Spacecraft Formation Flying Dynamics at L_2 and Operational Maneuvers Design

The case of the IRASSI Space Interferometer

Luisa dos Santos Buinhas

Full copy of the thesis approved by the Department of Aerospace Engineering of the Bundeswehr University Munich for obtaining the degree of

Doctor of Engineering (Dr.-Ing)

Advisors Committee:

1. Prof. Dr.-Ing. Christian Mundt (Chair)
2. Prof. Dr.-Ing. Roger Förstner (First Surveyor)
3. Dr. Ir. M.J. (Jeannette) Heiligers (Second Surveyor)

The doctoral thesis was submitted at the Bundeswehr University Munich on the 02nd of December, 2020 and accepted by the Department of Aerospace Engineering on the 10th of April, 2021. The oral examination took place on the 07th of May, 2021.

SPACECRAFT FORMATION FLYING DYNAMICS AT L_2 AND OPERATIONAL MANEUVERS DESIGN

THE CASE OF THE IRASSI SPACE INTERFEROMETER

by

Luisa DOS SANTOS BUINHAS

Research Associate of Aerospace Engineering,
University of the German Federal Armed Forces
born in Lisbon, Portugal.

Science is a wonderful thing
if one does not have to earn one's living at it.

Albert Einstein

Contents

SUMMARY

Formation flying and autonomy are two concepts that have increasingly become integral to space missions. Employing multiple spacecraft for achieving a common goal instead of a monolithic probe has the benefit of increasing mission robustness and flexibility. Onboard autonomy, on the other hand, confers a degree of intelligence and decision-making ability to the spacecraft. In turn, this allows overcoming communication delays and outages to ground stations, reduces ground segment availability demands and costs, and allows spacecraft to react in an unpredictable environment, maximizing the scientific potential of a mission.

One such mission to whom the concept of autonomy is relevant is the IRASSI mission, a free-flying interferometer designed for the observation of far-infrared phenomena in deep space. Built on precursor mission studies, IRASSI distinguishes itself by exploiting a unique operational concept that involves a continuous change of the physical separation of the spacecraft during observations. Furthermore, during its lifetime, IRASSI has to conduct a set of activities that support the science program. That includes, for example, the reconfiguration of the formation. These maneuvers need to both be safe and fuel-economical and respect all science requirements, without the intervention of ground personnel.

As a planned state-of-the-art facility, IRASSI brings simultaneously to the foreground unique challenges. As such, this thesis investigates the feasibility of the IRASSI mission by aggregating mission requirements into the formation-flying design and through the development of algorithms that simulate the operation of the formation as an independent entity.

A sequential approach underpins this research work. First, the IRASSI mission is introduced and the major high-level requirements are described. In connection to the wavelengths observed in the far-infrared, the spacecraft are to separate up to 850 m in a direction perpendicular to the target. Sensitive payload motivates the selection of a quasi-Halo orbit around the second Lagrange point of the Sun-Earth/Moon system, L_2. The ranging system is one of the payload instruments that warrants referral. It must operate at cold temperatures and is mounted opposite to the sunshield on each spacecraft. This ranging system permits the spacecraft to measure their relative separation during the science observations. The mission profile and its main phases are characterized, whereby an optimized transfer trajectory to L_2 with a duration of up to four months is succeeded by a five-year operational phase. Each science task can have a duration ranging between a couple of hours and over 8 days. ΔV budgets and a bespoke mechanical configuration set a preliminary individual spacecraft wet mass at 2.3 tons, of which nearly 5% is dedicated to fuel.

Thereafter, a bottom-up investigation of formation geometry requirements is pursued. Of particular interest, is the intervisibility requirement that stipulates that during the science phase the lasers of the ranging system must be within sight of one another. It is shown that the mechanical mounting of the ranging system severely limits where spacecraft can be positioned relative to each other. Other requirements include the relative positioning performance, sky access and science performance. The requirements are evaluated in an ephemeris around L_2, without the use of any thrust control. Even with passive drift magnitudes of up to 450 m and drift rates of 18 $\mathrm{mm\,s^{-1}}$ for large formations, compliance with the requirements was observed at the end of the 8 days. The first violations were detected at the two-week mark, keeping in mind that this is well outside the range of science-task durations. During the operational phase, a behavioral-type coordination control was elected as that which is most suitable for supporting autonomous operations for IRASSI. Furthermore, simple control feedback loops are suggested for implementation in face of the slow dynamics of perturbations acting in the vicinity of L_2.

The design and implementation of a task- and maneuver-planning tool compose the last part of this research. The tool, called iSCOUT, is supported by four modules with the joint aim of optimally planning the sequence of science tasks, computing the associated reconfiguration maneuvers and the paths to be followed by individual spacecraft during the science observations, while simultaneously delivering collision-free trajectories which ensure the intervisibility of the spacecraft. The modules are the Task-Planner Module, the Reconfiguration Module, the Collision- and Invisibility-Avoidance Module and the Baseline Pattern Module. Maneuvers are optimized, among others, on the basis of maneuver-time minimization and fuel management (including fuel consumption and fuel-balancing across the fleet). As such, iSCOUT aggregates the complete set of mission, formation geometry and functional requirements.

iSCOUT is ultimately intended to be executed onboard the spacecraft and support autonomous operations of the IRASSI interferometer. In its current standing, it serves well as a feasibility analysis tool that answers the goals of this research. As such, a comprehensive end-to-end mission simulation was carried out, where it was shown that 79% of observation tasks currently contained in the IRASSI catalog can be fulfilled, at a cost of 5.1 kg of fuel per spacecraft, after five years. Reconfigurations motivate nearly half of all fuel consumption. Over three-quarters of the mission can be dedicated to actual science observation, and the remaining time is allocated to maneuvers and activities, such as calibration of sensitive instruments. The conclusion follows, therefore, that even with the inclusion of the technical challenges of IRASSI, the mission can be successfully completed in the specified time frame.

Nonetheless, the preliminary nature of the tool leaves room for future improvements, namely concerning the completeness of motion models and of operational scenarios that can emulate off-nominal conditions, such as hardware malfunctions. The plasticity of the tool is ensured, for example, by the implementation of common functions and features that are used across different modules. Advancing iSCOUT can refine the obtained results and close the gap between a feasibility study and a high-fidelity mission simulation tool, agnostic to the type of application.

Overall, the present work showcases the complexities of operating a free-flying interferometry formation in space, whereby requirements of diverse origins (quality of science, the geometry of the spacecraft, visibility of metrology systems, target occultation, collision avoidance, etc.) must be taken into account in concert to deliver a unified optimal operational solution which fulfills all the mission's science goals. The understanding by mission planners of the impact of individual constraints and requirements on performance is particularly imperative nowadays, with the advent of mega-constellation satellite programs.

The research and implementation work carried out in this thesis contributes to the field of autonomous spacecraft formation flying on several levels. First, it specifically addresses and analyzes the influence of spacecraft design on day-to-day mission operations. Secondly, the detailed requirements analysis behind the Task-Planner Module and the Baseline Pattern Module provides special insight into the complexity of task-scheduling and observation-planning for astronomy missions. For both modules, optimization methods aimed at autonomously maximizing science performance are presented. The Baseline Pattern Module is of special importance as it reflects the first steps in understanding how formation configuration in physical space affects the quality of the science data obtained. Lastly, optimized maneuver-planning strategies that manage onboard resources are devised for producing safe trajectories which abide by mission-specific constraints, such as intervisibility.

KURZFASSUNG

Formationsflug und Autonomie sind zwei Konzepte, die für Weltraummissionen zunehmend an Bedeutung gewinnen. Der Einsatz mehrerer Raumfahrzeuge zur Erreichung eines gemeinsamen Ziels anstelle einer einzelnen Sonde hat den Vorteil, dass die Robustheit und Flexibilität der Mission erhöht wird. Die Autonomie an Bord wiederum verleiht dem Raumfahrzeug ein gewisses Maß an Intelligenz und Entscheidungsfähigkeit. Dies wiederum ermöglicht die Vermeidung von Kommunikationsverzögerungen und -ausfällen zu den Bodenstationen, reduziert die Anforderungen an die Verfügbarkeit und die Kosten des Bodensegments und erlaubt es dem Raumfahrzeug, in einer unvorhersehbaren Umgebung selbstständig zu reagieren und das wissenschaftliche Potenzial einer Mission zu maximieren.

Eine Mission, für die das Konzept der Autonomie von Bedeutung ist, ist die IRASSI-Mission: ein frei fliegendes Interferometer zur Beobachtung von Phänomenen im Weltraum im fernen Infrarotbereich. Auf der Grundlage von Vorlaufstudien zeichnet sich IRASSI durch ein einzigartiges Betriebskonzept aus, das eine kontinuierliche änderung der räumlichen Trennung der Raumfahrzeuge während der Beobachtungen vorsieht. Außerdem muss IRASSI während seiner Lebensdauer eine Reihe von Aktivitäten durchführen, die das wissenschaftliche Programm unterstützen. Dazu gehört zum Beispiel die Rekonfiguration der Formation. Diese Manöver müssen sowohl sicher als auch treibstoffsparend sein und alle wissenschaftlichen Anforderungen erfüllen, ohne dass das Bodenpersonal eingreifen muss.

Als geplante hochmoderne Anlage birgt IRASSI einzigartige Herausforderungen. Daher wird in dieser Arbeit die Machbarkeit der IRASSI-Mission untersucht, indem die Missionsanforderungen in das Design des Formationsfluges integriert und Algorithmen entwickelt werden, die den Betrieb der Formation als autonome Einheit simulieren.

Der Forschungsarbeit liegt ein sequenzieller Ansatz zugrunde. Zunächst wird die IRASSI-Mission vorgestellt und die wichtigsten Anforderungen beschrieben. Im Zusammenhang mit den im fernen Infrarot beobachteten Wellenlängen sollen sich die Raumfahrzeuge bis zu 850 m in einer Richtung senkrecht zum Ziel voneinander entfernen. Die sensible Nutzlast motiviert die Wahl einer Quasi-Halo-Umlaufbahn um den zweiten Lagrange-Punkt des Sonne-Erde-Mond-Systems, L_2.

Das Entfernungsmesssystem ist eines der Nutzlastinstrumente, die diese Wahl rechtfertigen. Seine Arbeitstemperatur ist sehr niedrig und daher auf jeder Sonde auf der sonnenabgewandten Seite des Sonnenschildes montiert. Mit diesem Entfernungsmesssystem können die Raumfahrzeuge während der wissenschaftlichen Beobachtungen ihren relativen Abstand zueinander messen. Das Missionsprofil und seine zwei Hauptphasen werden charakterisiert. Das Missionsprofil besteht aus einer optimierten Transferflugbahn nach L_2 mit einer Dauer von bis zu vier Monaten und eine darauf folgende fünfjährige Betriebsphase. Die Dauer jeder wissenschaftlichen Aufgabe kann zwischen einigen Stunden und mehr als 8 Tagen liegen. ΔV Budgets und eine maßgeschneiderte mechanische Konfiguration setzen eine vorläufige individuelle Startmasse des Raumfahrzeugs auf 2.3 Tonnen fest, von denen fast 5% für Treibstoff vorgesehen sind.

Danach wird eine Untersuchung der Anforderungen an die Formationsgeometrie durchgeführt. Von besonderem Interesse ist die Sichtbarkeitsanforderung, die vorschreibt, dass sich die Laser des Entfernungsmesssystems während der wissenschaftlichen Phase in Sichtweite zueinander befinden müssen. Es wird gezeigt, dass die mechanische Befestigung des Entfernungsmesssystems die relative Positionierung der Raumfahrzeuge stark einschränkt. Weitere Anforderungen sind die relative Positionierungsleistung, das Blickfeld des Himmels und die wissenschaftlichen Ziele. Die Anforderungen werden in einer Ephemeride um L_2 ausgewertet, ohne den Einsatz jeglicher Schubkontrolle. Selbst bei passiven Driftgrößen von bis zu 450 m und Driftraten von 18 $\mathrm{mm\,s^{-1}}$ für große Formationen wurde die Einhaltung der Anforderungen noch nach 8 Tagen beobachtet. Die ersten Verstöße wurden an der Zwei-Wochen-Marke festgestellt, wobei zu beachten ist, dass diese Zeitspanne weit außerhalb der Dauer der wissenschaftlichen Aufgaben liegt. Während der Betriebsphase wurde eine verhaltensorientierte Koordinationskontrolle eingesetzt, die am besten geeignet ist, den autonomen Betrieb von IRASSI zu unterstützen. Angesichts der langsamen Dynamik von Störungen, die in der Nähe von L_2 wirken, werden außerdem einfache Regelungsrückkopplungskreise zur Implementierung vorgeschlagen.

Der Entwurf und die Implementierung eines Tools für die Aufgaben- und Manöverplanung bilden den letzten Teil dieser Forschungsarbeit. Das iSCOUT genannte Programm setzt sich aus vier Modulen zusam-

men, deren gemeinsames Ziel es ist, die Abfolge der wissenschaftlichen Aufgaben optimal zu planen, sowohl die zugehörigen Rekonfigurationsmanöver als auch die von den einzelnen Raumfahrzeugen während der wissenschaftlichen Beobachtungen zu verfolgenden Pfade zu berechnen und gleichzeitig kollisionsfreie Flugbahnen zu liefern, die die Sichtbarkeit der Raumfahrzeuge untereinander gewährleisten. Die Module sind das Task-Planner Modul, das Rekonfigurationsmodul, das Kollisions- und Unsichtbarkeitsvermeidungsmodul und das Baseline Pattern-Modul. Die Manöver werden unter anderem auf der Grundlage der Minimierung der Manöverzeit und des Treibstoffmanagements (einschließlich des Treibstoffverbrauchs und des Treibstoffausgleichs in der Flotte) optimiert. Als solches aggregiert iSCOUT den kompletten Satz von Missions-, Formationsgeometrie und Funktionsanforderungen.

iSCOUT soll letztendlich an Bord des Raumfahrzeugs ausgeführt werden und den autonomen Betrieb des IRASSI-Interferometers unterstützen. In seiner jetzigen Form dient es als Instrument zur Analyse der Machbarkeit, das die Ziele dieser Forschungsarbeit erfüllt. Als solches wurde eine umfassende End-to-End-Missionssimulation durchgeführt, bei der gezeigt wurde, dass 79% der derzeit im IRASSI-Katalog enthaltenen Beobachtungsaufgaben mit einem Aufwand von 5.1 kg Treibstoff pro Raumfahrzeug in fünf Jahren erfüllt werden können. Fast die Hälfte des gesamten Treibstoffs wird für Rekonfigurationen benötigt. Mehr als 75% der Missionszeit können der eigentlichen wissenschaftlichen Beobachtung gewidmet werden, während die restliche Zeit für Manöver und Aktivitäten wie die Kalibrierung empfindlicher Instrumente gebraucht wird. Daraus ergibt sich die Schlussfolgerung, dass die Mission auch unter Berücksichtigung der technischen Herausforderungen von IRASSI in dem vorgegebenen Zeitrahmen erfolgreich abgeschlossen werden kann.

Nichtsdestotrotz lässt der vorläufige Charakter des Instruments Raum für künftige Verbesserungen, insbesondere in Bezug auf die Vollständigkeit der Bewegungsmodelle und der Betriebsszenarien, die außergewöhnliche Bedingungen, wie z. B. Fehlfunktionen der Hardware, nachbilden können. Die Flexibilität des Tools wird zum Beispiel durch die Implementierung gemeinsamer Funktionen und Merkmale gewährleistet, die in verschiedenen Modulen verwendet werden. Die Weiterentwicklung von iSCOUT kann die erzielten Ergebnisse verfeinern und die Lücke zwischen einer Machbarkeitsstudie und einem hochgradig realitätsgetreuen Missionssimulationswerkzeug schließen, das unabhängig von der Art der Anwendung ist.

Insgesamt zeigt die vorliegende Arbeit die Komplexität des Betriebs einer autonomen Interferometrieformation im Weltraum, wobei Anforderungen unterschiedlicher Herkunft (Qualität der Wissenschaft, Geometrie des Raumfahrzeugs, Sichtbarkeit der Messsysteme, Zielverdeckung, Kollisionsvermeidung usw.) gemeinsam berücksichtigt werden müssen, um eine einheitliche optimale Betriebslösung zu finden, die alle wissenschaftlichen Ziele der Mission erfüllt. Das Verständnis der Missionsplaner für die Auswirkungen individueller Einschränkungen und Anforderungen auf die Leistung ist heutzutage, mit dem Aufkommen von Satellitenprogrammen in Megakonstellationen, besonders wichtig.

Die in dieser Arbeit durchgeführten Forschungs- und Implementierungsarbeiten tragen auf mehreren Ebenen zum Bereich des autonomen Formationsfluges von Raumfahrzeugen bei. Erstens wird speziell der Einfluss des Raumfahrzeugdesigns auf den täglichen Missionsbetrieb untersucht und analysiert. Zweitens bietet die detaillierte Anforderungsanalyse des Task-Planner-Moduls und des Baseline-Pattern-Moduls einen besonderen Einblick in die Komplexität der Aufgaben- und Beobachtungsplanung für Astronomie-Missionen. Für beide Module werden Optimierungsmethoden vorgestellt, die auf eine autonome Maximierung der wissenschaftlichen Leistung abzielen. Das Baseline Pattern Modul ist von besonderer Bedeutung, da es die ersten Schritte zum Verständnis der Auswirkungen der Formationskonfiguration im physikalischen Raum auf die Qualität der gewonnenen wissenschaftlichen Daten darstellt. Schließlich werden optimierte Manöverplanungsstrategien entwickelt, die die Ressourcen an Bord verwalten, um sichere Flugbahnen zu erzeugen, die die missionsspezifischen Einschränkungen, wie z. B. die Sichtbarkeit, einhalten.

Acknowledgements

First and foremost I would like to express my sincere gratitude to Prof. Förstner for his continuous support throughout these six years. Prof. Förstner helped shaping my academic path and always brought in a refreshing point of view to our technical discussions with grace, patience and integrity. I enjoyed each of the projects I had the chance to work on, as they challenged me and enabled me to push the boundary a step further. Working at this institute under his leadership has been a wonderful pleasure above all, because of the freedom that I enjoyed in exploring each of the topics within a friendly and cozy atmosphere. I am equally obliged for his encouragement in this new venture into the entrepreneurial world.

I would also like to acknowledge my colleagues at ISTA for all the good moments we shared: coffee breaks, cake gatherings, chocolate recesses, nerdy jokes and conference getaways to exotic locations. I will carry these great memories with me for a long time.

An especial thanks to my mother and father, for all their support throughout my studies. Their encouragement and willingness to help were very important during crucial times. From them, I learned the importance of commitment. I am especially thankful to them for giving me my forever baby-sister, an endless source of fun and entertainment that I cannot imagine living without. They have helped me maintain my motivation and momentum throughout the PhD.

Last and certainly not least, I am grateful to all of my friends who checked up on me often to make sure I had all I needed during the mad rush of the last months. I would not have been able to get through them without our wine evenings, happy hours, spontaneous dinners, Bachata nights at the Pinakotheke and all the laughter that went along with that. My Munich family - I wouldn't trade it for the world!

List of Abbreviations

ACAS	Airborne Collision Avoidance System
AGN	Active Galactic Nucleus
ALMA	Atacama Large Millimeter Array
ASE	Autonomous Sciencecraft Experiment
BPM	Baseline Pattern Module
CAM	Collision- and Invisibility-Avoidance Module
CFRP	Carbon-fiber-reinforced polymer
CO	Carbon monoxide
CPU	Central processing unit
CR3BP	Circular-restricted three-body problem
Delta-DOR	Delta-differential one-way ranging
DLR	German Aerospace Center
DNA	Deoxyribonucleic acid
DSA	Deep-space Antenna
ESA	European Space Agency
ESPRIT	Exploratory Submillimeter Space Radio-Interferometric Telescope
ESTRACK	European Space Tracking
FIR	Far infrared
FIRI	Far-infrared Interferometer
FWHM	Full-width at half-maximum
GAIA	Global Astrometric Interferometer for Astrophysics
GMAT	General Mission Analysis Tool
GNC	Guidance, navigation and control
HEO	High elliptical orbit
HGA	High-gain antenna
HPBW	Half-power beam width
HSO	Herschel Space Observatory
IRASSI	InfraRed Astronomy Satellite Swarm Interferometer
iSCOUT	interferometer SCience and Operations maneUver-planning Tool
JCMT	James Clerk Maxwell Telescope
JVLA	Jansky Very Large Array
L_2	Second Lagrange point in any CR3BP
LGA	Low-gain antenna
LQG	Linear-Quadratic-Gaussian
LQR	Linear-Quadratic-Regulator
LS	Least squares
LVLH	Local Vertical Local Horizontal
MADS	Mesh-adaptive direct search
MAPGEN	Mixed-Initiative Activity Plan Generator
MAPPS	Mission Analysis and Payload Planning System
MIDI	MID-infrared Interferometric instrument
MIR	Mid-infrared
NASA	National Aeronautics and Space Administration
NIR	Near infrared
NNH	Nearest-neighbor heuristics
NOEMA	NOrthern Extended Millimeter Array
PD	Proportional-Derivative

PM	Propulsion module
RAAN	Right ascension of the ascending node
RAM	Random-access memory
ReM	Reconfiguration Module
SMA	Submillimeter Array
SNS	Semi-stochastic near-neighbor search
SOFIA	Stratospheric Observatory for Infrared Astronomy
SPICA	Space Infrared Telescope for Cosmology and Astrophysics
SPIRIT	Space Infrared Interferometric Telescope
TPF	Terrestrial Planet Finder
TPM	Task-Planner Module
TSP	Traveling Salesman Problem
VLTI	Very Long Telescope Interferometer
WMAP	Wilkinson Microwave Anisotropy Probe

List of Symbols

The symbols are listed alphabetically within each chapter. They are defined at the first instance of appearance and not multiplely defined across the chapters they are referenced in.

Chapter 2 – The IRASSI Mission

b	Interferometer baseline length (m)
n	Total number of spacecraft in the formation
$\boldsymbol{\delta x}, \boldsymbol{\delta y}, \boldsymbol{\delta z}$	Orthonormal basis vectors for $\mathscr{L}_2$ reference frame
λ	Wavelengths of the IRASSI targets (m)
$\mathscr{L}_2$	L_2-centered reference frame

Chapter 3 – Mission Analysis and Spacecraft Configuration

A_x, A_y, A_z	Amplitudes of a trajectory about the L_2 libration point along the $\delta x, \delta y, \delta z$ axes (km)
ΔV	Change in velocity capability of spacecraft ($\mathrm{m\,s^{-1}}$)
γ_{vis}	Elevation angle on the horizon of each ground station (deg)
$\Lambda_{E,nom}$	Insertion longitude in simulated trajectory (deg)

Chapter 4 – Formation Geometry

A_{ez}	Area of exclusion zone (m^2)
$A_{ez_{proj}}$	Projected exclusion zone area on the celestial sky (m^2)
A_{rest}	Percentage of total restricted area A_{rest} for observations
A_{ri}	Area of ranging invisibility (m^2)
A_{sky}	Total sky area (m^2)
A_sN	Asymmetry Number
$\boldsymbol{b}$	Vector of distance measurements (m)
B_{ij}	Baselines lengths between formation elements (m)
d	In-plane separation parameter (m)
g_{ij}	Geometric delay (m)
h_i	Out-of-plane component (height) of each telescope i (m)
h_{sc}	Height of the spacecraft (m)
i, j	Spacecraft identifier, $i, j = \{T_1, T_2, T_3, T_4, T_5,\}$
k	Condition number
L_i	Projected sampling length (m)
l_{ez}	Distance between a pair of spacecraft (m)
l_{ij}	Distances between any pair of telescopes i and j (m)
$l_{platform}$	Distance between the sunshield and ranging system, normal to $r_{sunshield}$ (m)
l_{ri}	Relative distance between a pair of ranging systems located in two different spacecraft, normal to $r_{sunshield}$ of a reference spacecraft (m)
q_{ez}	Radius q_{ez} of the base of the exclusion zone cone (m)
r_{dr}	Distance between the ranging system laser with respect to the line which passes through the center of the spacecraft, normal to $l_{platform}$ (m)
r_{ri}	Distance between l_{ri} and the line-of-sight of the laser (m)
$r_{sunshield}$	Radius of the sunshield (m)
T_i	Telescopes
x_{des}, y_{des}	Desired values for the projected baseline distances in a bespoke (Δx, Δy) plane parallel to the wavefront (m)
β	Internal angles of a polygonal formation arrangement (rad)
$\delta\boldsymbol{b}$	Deviations in vector $\boldsymbol{b}$ (m)

$\delta\boldsymbol{\Delta p}$	Deviations in vector $\boldsymbol{\Delta p}$ (m)
$\Delta\varphi_{ij}$	Shortest in-plane angular separation between any pair of telescopes i and j (deg)
$\boldsymbol{\Delta p}$	Correction of the estimated satellite positions (m)
$\boldsymbol{\Delta x}$, $\boldsymbol{\Delta y}$, $\boldsymbol{\Delta z}$	Orthonormal basis vectors for $\mathscr{L}$ reference frame
θ_{ez}	Semi-angle of the exclusion zone cone (rad)
θ_{ri}	Angle between the laser line-of-sight and l_{ri} (rad)
Λ	Anti-Sun vector longitude (deg)
Π_N	Plane of reference for formation geometry definition
$\mathscr{L}$	Local formation coordinate system

Chapter 5 – Formation Dynamics

$\boldsymbol{A}$	State matrix
D_ϕ	Formation deformation
$e_{\boldsymbol{\Delta r}}$	Position error (m)
f	Multiplication factor of components of vector $\boldsymbol{h}$
$\boldsymbol{h}$	Vector of out-of-plane component (heights)
M_E	Earth's mass (kg)
M_M	Moon's mass (kg)
M_S	Sun's mass (kg)
R_E	Median non-dimensional distance of the Earth to L_2
R_S	Median non-dimensional distance of the Sun to L_2
$\boldsymbol{n}_\phi$	Plane normal unit vector
t	Time elapsed since start time $t0$ (s)
t_0	Simulation start time (s)
$\boldsymbol{x}$	Six-dimensional state-space vector of the spacecraft
x_0	Distance of L_2 to the barycenter of the Sun/Earth-Moon system (km)
α_ϕ	Angular shift between the normal of the plane at time t and the normal at time t_0 (rad)
Δx, Δy, Δz	Components of vector $\boldsymbol{\Delta r}$ (m)
Δr	Distance between a reference point and a spacecraft (m)
δ_n	Switch function that determines if the orbit is Class I or Class II
$\nabla\mathbf{f}$	Gravity gradient at a given point (or spacecraft) (N)
$\boldsymbol{\nu}$	Vector denoting three orientation angles of a spacecraft
ρ	Mass ratio between the Earth-Moon barycenter and the combined system
σ_d	Standard deviation of Gaussian-distributed distance measurement errors (m)
σ_ν	Standard deviation of Gaussian-distributed orientation angles measurement errors (rad)
ϕ	Initial phase of the reference points' orbit around L_2(rad)

Chapter 7 – iSCOUT Architecture and General Considerations

d_{set}	Separation parameter set
F_i	Thrust force delivered by the actuator, parallel to the trajectory of a spacecraft (N)
f_i	Fuel mass of spacecraft i (kg)
$\dot{f}_i$	Fuel consumption rate of spacecraft i ($\mathrm{kg\,s^{-1}}$)
g_0	Standard gravitational acceleration at sea level ($\mathrm{m\,s^{-2}}$)
I_{sp}	Specific impulse of the thruster (s)
M_i	Mass of spacecraft i (kg)
$\ddot{\boldsymbol{r}}_{\boldsymbol{i}}$	Acceleration vector ($\mathrm{m\,s^{-2}}$)
S_0	Inertial reference frame
S_C	Initial ('current target') formation reference frame
S_N	Final ('next target') formation reference frame
$\boldsymbol{u}_{\boldsymbol{i}}$	Unit force direction vector
$\boldsymbol{x}, \boldsymbol{y}, \boldsymbol{z}$	Orthonormal basis vectors for reference frames
θ_C	Angle between S_0 and S_C (rads)
θ_N	Angle between S_0 and S_N (rads)

Chapter 8 – Optimization of Tasks Sequences

C	Set of to-be-completed tasks
D	Actual tour duration derived from tour sequence S
J	Overall score (cost) of a candidate task
J_{TPM}	Value of the objective functions over sequence S or over subset paths $s \in S$
$j_{i,k}$	Path lengths or score (cost) associated with performing task $l_k \in L_i$ from an initial task $l_i \in C$
L	Formation size associated with a long in-plane separation parameter (d =1000 m)
L_i	Set of all accessible tasks from a given task instance l_i
l_i	A task instance, $l_i \in C$
n_i	A target instance, $n_i \in N$
M	Formation size associated with a medium in-plane separation parameter (d =500 m)
N_i	Set of targets in the field of view of a spacecraft from a given target instance n_i
N_{past}	Number of completed tasks of a given type
N_{rel}	Relative amount of completed task types
N_{total}	Total number of observations tasks available of the same type
P	Priority of a candidate task
P_{rel}	Relative task priority
$\boldsymbol{p_i}, \boldsymbol{p_k}$	Position of current target i and candidate target k respectively
S	Formation size associated with a short in-plane separation parameter (d =10 m)
S	Tour sequence containing all selected paths s and associated scores j
s	An individual path connecting two tasks in sequence S
T_{rel}	Relative reconfiguration time of a task (s)
t_{BPM}	Duration of the scientific phase of a task (s)
t_i	Initial epoch (days)
t_{link}	Duration of uplink/downlink of telemetry and science data of a task (s)
t_{ReM}	Reconfiguration maneuver duration of a task (s)
t_{sci}	Target observation duration (s)
t_{total}	Total duration of a task (s)
$t_{i_k}*$	Final epoch for all tasks $l_k \in L_i$ (days)
Λ_k	Longitude of target candidate $n_k \in N_i$ (deg)
Φ_k	Latitude of target candidate $n_k \in N_i$ (deg)
Ω	Combined science duration of science tasks the catalog (days)
ω	Optional weighting factor
$\mathscr{D}$	User-specified minimum tour duration (days)

Chapter 9 – Optimization of Reconfiguration Maneuvers

$D_i, \dot{D}_i, \ddot{D}_i$	Position, velocity and acceleration of spacecraft i along $\boldsymbol{r_{trav,i}}$ (respectively in m, m s^{-1}and m s^{-2})
$f_{ReM,i}$	Fuel consumed by spacecraft i at the end of reconfiguration maneuver (kg)
J_f	Fuel-based objective function cost for reconfiguration maneuver (kg)
$J_{\Delta V}$	ΔV-based objective function cost for reconfiguration maneuver (m s^{-1})
n	Nominator of fuel or ΔV balancing performance metric
m	Denominator of fuel or ΔV balancing performance metric
$\boldsymbol{r_N}$	Formation center point position vector in S_0 (m)
$\boldsymbol{r_{0,fin,i}}$	Final resting position of spacecraft i in S_0 (m)
$\boldsymbol{r_{0,in,i}}$	Initial resting position of spacecraft i in S_0 (m)
$\boldsymbol{r_{trav,i}}$	Trajectory on which spacecraft i travels during a reconfiguration maneuver (m) in S_0 (m)
r_{Nx}, r_{Ny}, r_{Nz}	Components of vector $\boldsymbol{r_N}$ (m)
t	Time within a maneuver such that $t \in [t_0, t_{ReM}]$ (s)
t_0	Reconfiguration maneuver start time (s)
t_i	Maneuver duration of spacecraft i for a bang-bang thrust profile (s)
$t_{th,i}$	Thrust pulse width duration of spacecraft i for a bang-bang thrust profile (s)
t_σ	Maneuver duration of spacecraft σ, equal to formation maneuver time t_{ReM} (s)
$t_{w,i}$	Thrust pulse width duration of spacecraft i for a bang-coast-bang thrust profile (s)
$\boldsymbol{X}$	Independent vector for ReM maneuvers optimization

θ_T	Angle between telescope T_1 and an arbitrary vector in S_N (deg)
μ_f	Fuel-balancing weighting parameter for the ReM module
$\mu_{\Delta V}$	ΔV-balancing weighting parameter for the ReM module
τ_1, τ_3	Bang-associated time interval
τ_2	Coast-associated thrusting profile time interval

Chapter 10 – Optimization of Collision- and Invisibility-Avoidance Maneuvers

$\boldsymbol{a_1}, \boldsymbol{a_1}$	Acceleration experienced by spacecraft 1 and 2 in an L_2-centered reference frame
a_{max}	Maximum acceleration differences experienced by the spacecraft separated by relative distances of 1 km in an orbit around L_2 ($m\,s^{-2}$)
b_{ij}	Relative baseline estimation accuracy between spacecraft i and j (m)
$f_{CAM,i}$	Fuel consumed by spacecraft i associated with the perpendicular thrust
F_{per}	Thrust force perpendicular to the (ReM) trajectory of a spacecraft (N)
f_r	Fuel consumption ratio
f_{dr}	Fuel differences ratio
I_1	Nominal F_{per} magnitude interval (N)
I_2	Extended F_{per} magnitude interval (N)
$\boldsymbol{S}$	Independent vector for CAM maneuvers optimization
S_T	Telescope reference frame
$\boldsymbol{x_T}, \boldsymbol{y_T}, \boldsymbol{z_T}$	Orthonormal basis vectors of reference frame S_T (m)
$\boldsymbol{r_1}, \boldsymbol{r_1}$	Location in space of spacecraft 1 and 2 in an L_2-centered reference frame
$t_{c_{per,i}}$	Duration of the coast phase of the perpendicular thrust (s)
$t_{w_{per,i}}$	Thrust impulse width of the perpendicular thrust (s)
γ	Minimum safety distance parameter (m)
ΔV_r	ΔV consumption ratio
ΔV_{dr}	ΔV differences ratio
τ_{crit}	Critical propagation time (s)
φ_{per}	Angle of the F_{per} thrust relative to the spacecraft-Sun line (deg)

Chapter 11 – Optimization of Baseline Patterns

$F_{BPM,i}$	Thrust force parallel to the BPM trajectory of spacecraft i (N)
n	Total number of vertices in the polygon
$\boldsymbol{p_i^{form}}$	Reference point of spacecraft i
$\boldsymbol{l_i}$	Lever arms of spacecraft i
$t_{w,BPM}$	Thrust pulse width duration of baseline change maneuver
β	Interior angles of a formation polygon
δ	Central angles of a formation polygon
$\boldsymbol{Y}$	Independent vector for BPM Step 1 maneuvers optimization
$\boldsymbol{Z}$	Independent vector for BPM Step 2 maneuvers optimization

1

Introduction

Nature and nature's laws lay hid in the night;
God said 'Let Newton be!' and all was light.

Alexander Pope

It did not last: the devil shouting 'Ho.
Let Einstein be!' restore the status quo.

Sir John Collings Squire

1

1.1. BACKGROUND

THE concept of employing multiple cooperative satellites flying in a swarm has emerged over the last decades as an attractive replacement of traditional monolithic, single spacecraft for Earth-observation, astronomy and space exploration activities. Although developments concerning its use in deep space are still in infancy, the swarm approach benefits from increased mission robustness, higher reconfigurability, and superior instrument resolution. Achieving high resolution is particularly critical for astronomy missions.

The research work detailed in this manuscript is framed within the scope of a feasibility study of a free-flying interferometry mission. The mission is called InfraRed Astronomy Satellite Swarm Interferometer, or IRASSI, and the study was led by the German Aerospace Center, Space Administration (DLR, Bonn, Germany)[1] between 2014 and 2019. As an astronomy mission, IRASSI was designed for characterizing phenomena in the far-infrared with an unprecedented imaging resolution of 0.1 arcsec so as to understand the genesis of planets, star formation and evolution processes. In order to achieve this resolution, the five-element spacecraft formation must continuously drift during observations. IRASSI employs heterodyne detection in combination with a ranging system, which can provide inter-satellite distances with very high accuracy. Measuring inter-satellite distances is crucial for correlating the observations and achieving the required resolution at the collective system level.

Throughout the science phase, the spacecraft must perform complex operations that place stringent requirements on the relative position and drift of the formation. Different targets have different relative drift patterns and formation configuration requisites and it is, therefore, essential that all science maneuvers are tailored to each corresponding target. Being in deep space, the success of IRASSI is thus tied to the ability to autonomously derive observation task plans and optimal maneuvering strategies during critical science phases. Developing an understanding of the behavior of the spacecraft is thus a stepping stone in designing a formation concept that supports the scientific program of the IRASSI mission. This thesis reports the methodologies adopted in providing an assessment of the feasibility of the mission, taking into account a diverse set of formation constraints and science requirements.

1.2. MOTIVATION AND SCOPE OF RESEARCH

THE motivation for the present research is directly related to the unanswered challenges of IRASSI in the context of formation-flying.

1.2.1. SPACECRAFT-DESIGN-DRIVEN OPERABILITY

Operating an interferometer in space brings together a set of science goals and constraints which must be traded during the design phase in order to deliver a unified mission solution. These constraints stem from various sources. Some of the constraints are directly derived from the working principles of the science instruments on board the spacecraft (e.g., the maximum or minimum separation of formation elements). Others, depend on the *physical distribution* of such instruments on the bus. For instance, the sunshield mount relative to the prime direction of the collecting dish may affect the number of targets immediately available for observation due to partial occlusion of the field of view. Similarly, if an interferometer relies on bi-directional communication links, there is a limitation on where spacecraft can be positioned relative to each other before visibility is lost or interrupted.

A suitable selection of spacecraft configuration and data-flow architecture allows drawing an envelope of acceptable formation shapes and geometries. In turn, and together with the motion of the targets across the field of view, this formation configuration determines which science tasks can be performed at what stage of the mission. As it is clear, structural design and formation geometry have a major impact on overall technical feasibility and mission scheduling. This calls therefore for a bottom-up approach to systems engineering developments. Like a puzzle, the interconnectedness of singular elements ultimately determines how the full constellation performs in real time.

1.2.2. SCIENCE PERFORMANCE AND MAPPING OF PHYSICAL SPACE

In interferometry, there is a relationship between the physical separation of the elements and science performance. More importantly, the time evolution of the formation is the biggest determinant of how well the science goals are met.

[1] IRASSI-I financed under FKZ 50NA1326, IRASSI II - Phase 1 financed under FKZ 50NA1714, IRASSI II - Phase 2 financed under FKZ 50NA1816.

Whereas the relative separation is fixed for ground-based interferometers or limited for those relying on structural arrays, a free-flying formation adds a new dimension of flexibility. It allows exploring three-dimensional patterns which optimize the sampling of the celestial sky. It is essential to understand what geometric parameters are associated with these desirable patterns so that optimal relative trajectories can be prescribed to formation elements during science activities. This outlines a somewhat novel avenue of investigation, the first steps within which are addressed in this research work.

1.2.3. OPTIMAL FORMATION FLYING OPERATIONS AND MANEUVERS

Devising a mission scenario relies on deconstructing high-level requirements, framing them into functional and science activities and defining supportive information flow processes.

The science program requires that a minimum amount of targets are observed within the mission lifespan. Launch and cost restrictions limit the fuel mass constraints. Additionally, depending on the mechanical configuration of the spacecraft, only a portion of targets is available for observation at any point in time. One must pursue a trade analysis of possible conflicting variables to generate an optimal planning and ordering of activities.

Another challenge which is posed by operating a free-flying constellation is assigning trajectories in inertial space. From the science side, the relative positions must form specific patterns, as explained before. From the functional side, the trajectories must be fuel-economical and collision-free. Since spacecraft maneuver freely and independently from each other, they will require different amounts of fuel while taking different times to complete the maneuver. The mission is, however, contingent on all spacecraft operating at the same performance level. If fuel depletion occurs in spacecraft before the predicted mission end, science performance degrades and mission completion is at risk. Balancing fuel across the fleet is thus another aspect of formation-flying which must be addressed.

The fluidity and timeliness of data exchange among spacecraft are also critical for a successful mission. One of the design choices which must be made concerns thus the governance and self-ruling mechanisms of the fleet. If the spacecraft rely on the ground stations for the planning of activities and maneuvers, then this may relax computational requirements on board the spacecraft. However, a centralized architecture may prove inflexible in the advent of unexpected situations, such as hardware malfunctions. Conversely, autonomous formation planning places an emphasis on onboard processing capabilities, cooperative sensing, inter-satellite visibility and communications. A nascent field in formation flying, autonomy in space involves dedicated decision-making and planning algorithms intended to optimize operations in space, by removing the need of human supervisors and operators on the ground. A harmonious solution that trades mission complexity with onboard resources to guarantee a minimum performance level within IRASSI must be investigated.

1.3. RESEARCH QUESTIONS AND OBJECTIVES

IN the light of the research motivations, the overarching aim of this thesis is

> *to deliver a unified mission feasibility result for free-flying interferometers at L_2, with a particular focus on the IRASSI mission, encompassing a multi-disciplinary set of technical requirements that directly affect formation-flying operations.*

To address the research aim, the following research questions are posed and used as guidelines in the development of this thesis.

Research Question 1

How can a reference mission scenario be defined in support of the high-level mission requirements?

This first question involves **identifying different mission mythos** and performing a comparative analysis between the candidates according to technical practicability, cost and complexity before selecting the nominal one. For each scenario, the **mission phases** need to be defined and the launch windows and inertial trajectories must be determined. Additionally, preliminary estimations of **fuel and launch mass, ΔV and power budgets** and associated mission costs can be performed. The selection of the formation rendezvous strategy, together with the launch mass estimations can lead to a pre-selection of launchers. The preliminary

mission design is challenging mainly because of the highly interconnected disciplines involved: launcher and trajectory design, propulsion, spacecraft architecture, formation GNC, among others. Changes in each of the systems early on affect subsequent developments and consequently, during preliminary design studies, numerous iterations are required in order to keep mission objectives synchronized.

Research Question 2

What is the expected behavior of a free-flying formation in the vicinity of L_2 and what formation coordination strategies are applicable to an interferometer such as IRASSI?

This second question concerns the **aggregation of constraints for formation design** and probes potential formation organization schemes that suit formation missions operating far from Earth, establishing how spacecraft can or should be positioned relative to each other in nominal conditions. Preliminary considerations of formation design are relevant since they establish boundary conditions and allow mission planners to identify early on some of the potential impacts on overall mission performance. Answering this research question requires first and foremost, the **definition of a nominal formation geometry** according to high-level science and spacecraft configuration requirements. As a second step, the **formation dynamics** ought to be investigated with the spacecraft immersed in its nominal environment around L_2 and without any influence of control. This allows thus to assess the influence of disturbances on relative motion and define envelopes of free-drift which result in acceptable deviation of trajectories with respect to the nominal cases. Finally, the applicability of **autonomous guidance, navigation and control strategies** to IRASSI, as enablers of efficient and robust science- and maneuver-planning and as means to accomplish the mission objectives needs to be explored.

Research Question 3

How feasible is the mission once all formation constraints and science requirements are considered and how can a mission 'end-to-end' performance be evaluated? What maneuvering strategies guarantee the safety of the telescopes and deliver the maximum science return?

The last question requires first and foremost a definition of *feasibility* in the context of a mission study:

> *A feasibility assessment is an objective, in-depth analysis of the most relevant technical factors that impact a space mission in order to derive conclusions concerning the probability of successfully conducting the mission within the boundaries of all identified requirements and constraints. This analysis attempts to identify strengths and weaknesses of design choices and quantify resources needed for the completion of the mission.*

Addressing this last research question motivates a **simulation of all mission elements, that brings together science requirements** (physical separation during observations, to pointing accuracy of the interferometer, science return potential, trajectory evolution, etc.) **and functional constraints** (limited onboard resources, collision-avoidance, field-of-view unobstruction during motion, etc.) that are critical for the success of the mission and have previously been identified in answering Research Question 2. It should be mentioned that for the purpose of this study, technical factors (science, engineering and operations) were solely taken into account in the feasibility assessment of the mission and the planning of financial, logistical, legal and other material resources were not explicitly considered.

In this sense, to be able to evaluate the capabilities and limitations of the mission, an operations-planning tool is developed. The tool assists in the **sequencing of science observations** and computation of **optimal, safe maneuvers** according to onboard resources of a formation-flying interferometry mission. The algorithms of the tool are largely tailored to the IRASSI case. Answering this research question ultimately closes the gap in assessing the feasibility of this exceptional interferometry mission at a preliminary level, by generating representative solutions and determining expected outcomes throughout its operational phase.

1.4. THESIS STRUCTURE

IN light of the presented objectives, the structure of this thesis is illustrated in Figure 1.1 and is composed of three major parts:

- Part I: the first block addresses the major design requirements and preliminary results of the IRASSI mission. In Chapter 2, the scientific background motivating a far-infrared surveying campaign is provided and the IRASSI mission is introduced. Chapter 3 presents the mission phases, the ΔV budgets and the configuration of the spacecraft for the nominal mission scenario. Part I concerns Research Question 1.

- Part II: the second block is devoted to analyzing the operational boundaries of the formation. Chapter 4 uses the mission requirements and the spacecraft mechanical structure to deliver a formation geometry envelope during nominal operations. The relative dynamics under uncontrolled drift are investigated in Chapter 5 and the last chapter of this block, Chapter 6, examines applicable autonomous organization and control architectures to free-flying interferometry. Part II answers Research Question 2.

- Part III: building on the results of the first two blocks, the third block concerns the development of algorithms for optimizing reconfiguration and science maneuvers, thereby supporting the astronomy program of the mission. A tool, called iSCOUT, computes an epoch-dependent, optimal sequence of observation tasks and unifies the planning of the maneuvers with the challenging constraints. Chapter 7 outlines the skeleton of the tool and provides an overview of general model assumptions. The four modules of this tool are presented in Chapters 8 to 11. Chapter 8 introduces relevant details of the IRASSI target catalog, around which a straightforward approach to sequencing observations is devised. Chapter 9 is dedicated to the planning of reconfiguration maneuvers, using fuel- or ΔV-management as optimization criteria. The analysis is extended to heterogeneous formations. Chapter 10 addresses the refinement of trajectories by evaluating collision and invisibility conditions and deriving alternative optimal paths. The generation and commanding of formation patterns associated with science tasks are detailed in Chapter 11 followed by a combined performance assessment of iSCOUT in Chapter 12. Function-driven strategies which may frame future work within iSCOUT are discussed throughout the chapters. Part III regards Research Question 3.

Conclusions and Recommendations are presented in the final chapter of the thesis, Chapter 13, where the major findings are summarized and where an outlook for further investigation in the field of free-flying interferometry is provided.

Each chapter, excluding the introduction and conclusions, begins with a one-page *header* that includes an abstract, a citation referencing where the chapter has been published and a shortlist of the key contributors to the content of the chapter.

1.5. THESIS CONTRIBUTIONS

THE work performed throughout this thesis has resulted in a number of publications in international conference proceedings and journal submissions. In this section, the contributions are listed by their appearance order in the thesis.

- **L. Buinhas**, E. Ferrer-Gil and R. Förstner, *IRASSI InfraRed Astronomy Satellite Swarm Interferometry: Mission Concept and Description*, Proceedings of the 2016 IEEE Aerospace Conference (2016).

- **L. Buinhas**, E. Ferrer-Gil and R. Förstner, *IRASSI InfraRed Space Interferometer: Mission Analysis, Spacecraft Design and Formation Flying Overview*, Proceedings of the 68th International Astronautical Congress (2017).

- H. Linz, D. Bhatia, **L. Buinhas**, L. Lezius, E. Ferrer, R. Förstner, K. Frankl, M. Philips-Blum, M. Steen, U. Bestmann, W. Hänsel, R. Holzwarth, O. Krause and T. Pany, *InfraRed Astronomy Satellite Swarm Interferometry (IRASSI): Overview and study results*, Advances in Space Research, **65(2)**, 831-849 (2020).

- **L. Buinhas**, K. Frankl, H. Linz and R. Förstner, *IRASSI InfraRed Space Interferometer: Formation Geometry and Relative Dynamics Analysis*, Acta Astronautica **153**, 394-409 (2018).

1

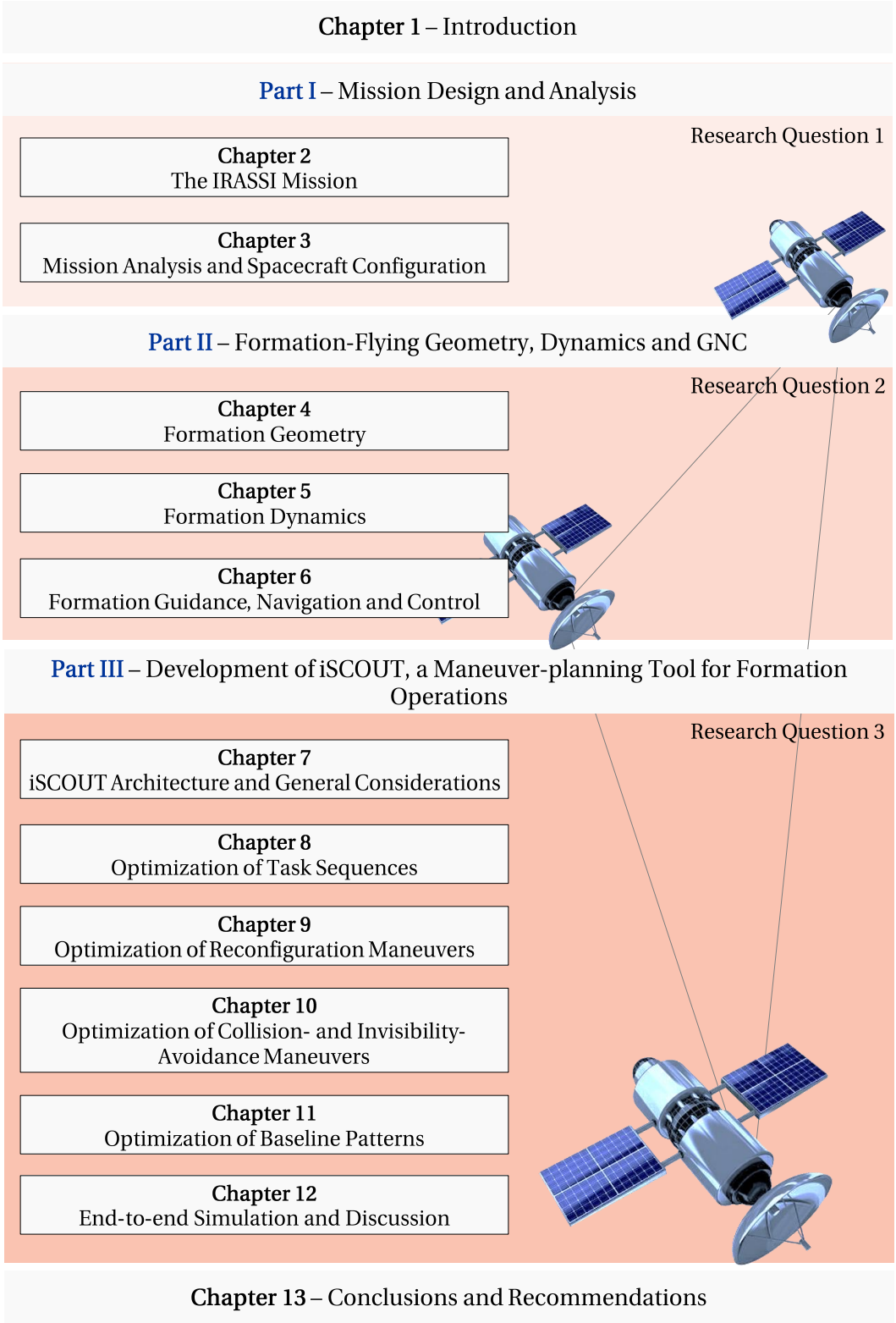

Figure 1.1: Thesis outline. Spacecraft credits: Creative Commons.

- **L. Buinhas** and R. Förstner, *Formation Reconfiguration Optimization for the IRASSI Space Interferometer*, Advances in Space Research, **67(11)**, 3819-3839 (2021).
- **L. Buinhas**, H. Linz, M. Philips-Blum and R. Förstner, *iSCOUT: Formation Reconfiguration and Science Planning Architecture for the IRASSI Space Interferometer*, Advances in Space Research, **67(11)**, 3840-3867 (2021).

I

Mission Design and Analysis

2

The IRASSI Mission

We have calcium in our bones, iron in our veins;
carbon in our souls, and nitrogen in our brains.
93 percent stardust, with souls made of flames,
we are all just stars that have people names.

Nikita Gill

ABSTRACT

This chapter introduces the IRASSI mission, which aims to further advance our current understanding of the evolution of galaxies and Earth-like planets and the processes leading to the creation of pre-biotic conditions. The scientific motivation for such an endeavor is presented, followed by the high-level mission requirements. The connection between accuracy requirements and the physical properties of the targets is shortly summarized. A stable environment in terms of gravitational disturbances and thermal variations motivates the selection of a large Halo orbit around the L_2 point of the Sun-Earth/Moon system, as the nominal destination of the interferometer. The distinguishing factor of IRASSI is, however, its free-flying concept, whereby the spacecraft drift continuously throughout the observation activities, in an expanding or contracting motion.

2.1. INTRODUCTION

IRASSI was a feasibility study undertaken by a consortium of partners between 2014 and 2019. It proposed observing stellar disks and protoplanetary regions using a constellation of five free-flying telescopes. In these regions of the cosmos, important chemical and physical processes in the far-infrared radiation spectrum can be observed, specifically between 1 and 6 THz, spanning wavelengths from 300 down to 50 µm. Observing such phenomena in these spectral ranges would greatly allow scientists to further their understanding of how pre-biotic conditions in Earth-like planets are formed. Although observations in this spectral range have been limited by the opacity of the atmosphere and by telescope size, recent technological developments are thought to provide solutions that bypass these limitations. In particular, the use of heterodyne detection in combination with a metrology system which measures the inter-satellite distance as the spacecraft drift apart during observations is a novel concept that distinguishes IRASSI from previous mission studies. The IRASSI formation is to be placed around the L_2 point of the Sun-Earth/Moon system.

The IRASSI consortium was headed by the German Aerospace Center, Space Administration (DLR, Bonn, Germany) and composed of different institutions, each responsible for specific technical disciplines. These are the Max Planck Institute for Astronomy (Heidelberg, Germany - high-level requirements and payload development), the Institute of Space Technology and Space Applications (Munich, Germany – mission analysis, spacecraft design, formation flying and relative navigation), the Institute of Flight Guidance (Braunschweig, Germany - attitude determination and sensor fusion) and finally, Menlo Systems GmbH as an industry partner (Martinsried, Germany – ranging system development).

2.2. SCIENCE BACKGROUND AND PRECURSOR MISSIONS

THE realm of astronomy has benefited immensely from recent advances in observation capabilities and from improvements in spatial (or angular) resolution that facilities can achieve. Over the past three decades, the Hubble telescope has been detecting galaxies and black holes in the furthest corners of the universe in the optical (100 nm–1 mm) and ultra-violet (UV, 10 nm–400 nm) wavelength ranges, with a spatial resolution better than 0.1 arcsec. Comparable resolution performance has been achieved with single-dish ground-based telescopes sampling the near-infrared (NIR) regions (780 nm–2500 nm) by means of deformable mirrors (that is, adaptive optics) to reduce the effect of atmospheric distortions. A higher resolution is yet achieved if observations by single-dish telescopes are combined with those of interferometers, such as the Very Long Telescope Interferometer (VLTI), creating long-baseline interferometry setups. At lower photon energies, such as in radio wavelengths, sub-mas resolution performance can be achieved with very-long-baseline interferometry techniques, the state-of-the-art currently represented by facilities such as the NOEMA [1], SMA [2] and particularly ALMA[1] [3]. However, although currently astronomers can access the sky at many wavelengths regimes with a high spatial resolution, the far-infrared (FIR), particularly of frequencies between 2–6 THz (30–300 µm), is a prominent exception. Figure 2.1 provides the electromagnetic spectrum overview.

Due to the presence of water vapor in the Earth's atmosphere, this portion of the spectrum is attenuated by 97 %–99 %, even at the driest observation locations in the world, such as ALMA, in the Chilean desert, and DOME-C, located in Antarctica [5]. As such, sophisticated airborne or space-based instrumentation which bypasses the atmosphere must be employed to observe phenomena in the FIR regime. In addition, the angular resolution has an inverse relation with the diameter of the collecting dish. Bringing achievable resolutions in the FIR to the sub-arcsec level implies that single-dish telescopes must be prohibitively large, demanding the use of interferometry for these regimes. Figure 2.2 depicts existing observation facilities in the radio and infrared wavelengths.

Until now, the resolution achieved in the FIR wavelengths has been limited, as FIR observation facilities are still in their infancy, compared to the NIR and the MIR regimes. The Herschel observatory remains at the vanguard of what is technically feasible in terms of angular resolution. None of the future planned single-dish satellite missions [6–8] aim to achieve an angular resolution below the arcsec-level in the FIR regime, although discontinued mission studies[9–11], did propose an interferometric approach exactly for this purpose.

As a consequence of these challenges, there remains a band of wavelengths, illustrated in Figure 2.2, which remains relatively unexplored at fine resolutions. This is the gap that IRASSI intends to fill, whilst both building on previous mission studies [9–13] and proposing novel concepts concerning relative navigation, swarm dynamics and calibration of such a state-of-the-art facility.

[1]The abbreviated names respectively for NOrthern Extended Millimeter Array (NOEMA) located in France, the Submillimeter Array (SMA) in Hawaii and the Atacama Large Millimeter Array (ALMA) in Chile.

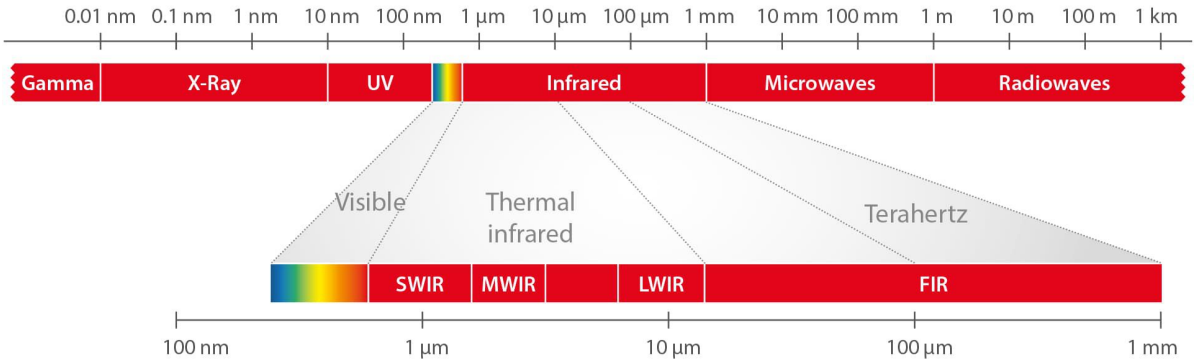

Figure 2.1: Wavelength ranges of electromagnetic radiation. Source: InfraTec [4].

2.2.1. ASTRONOMY IN THE FAR-INFRARED AND IRASSI

The discovery of over 4200 planetary systems outside of our Solar System [15] is one of the most exciting developments of modern astronomy. Of these, Earth-like planets are of particular interest as they can provide answers regarding the necessary environmental conditions that need to exist for life to materialize. In order to be able to characterize Earth-like planets, it is crucial to study the processes which lead to their formation by observing circumstellar disks and protoplanetary regions surrounding these planets. These regions are obscured by cold clouds of gas and dust, and only in FIR frequencies is it possible to look through the dust. The science cases for IRASSI [16] are enumerated below. Figure 2.3 shows a schematic of a protoplanetary disc.

1. Disk evolution
   Gas in stellar disks shapes the formation of planets and controls the dynamics of planetesimals, that is, the accretion of the first solid cosmic dust grains. Accurate gas-mass measurements provide insight into the evolution of disks and enable scientists to understand the formation environments of planets. Carbon monoxide (CO) can be used to measure velocity fields and differentiate gas heated by a central protostar and gas compressed from accretion shocks.

2. Star formation
   Stars are the essential building blocks of galaxies, determining the features of the planetary systems that may coalesce about them. Characterizing Earth-like planets requires studying the birth of stars. Stars are born within dust clouds. The energy exchange and cooling processes of clouds are largely attributed to inelastic collisions of molecules, which are detectable in the FIR. Together with ground-based observations, comparisons between the dynamics of atomic and molecular gas phases in these cold clouds would be possible.

3. Star evolution
   The course of stellar evolution and several stellar properties depend on the star mass and mass distribution at birth. Stellar evolution within molecular clouds is largely driven by a combination of infalling raw material due to gravitational forces and the transport of dust through accretion. Infall rates are thus an important measure of the change in protostar mass over time. These processes can be detected in the FIR. With novel developments in heterodyne detection instruments in terms of sensitivity and bandwidth, it will be possible to deliver high-resolution maps of dust-embedded objects and estimate with high accuracy and resolution true infall rates of material towards protostars.

4. Planet formation potential
   Water is a very important molecule conducive to the emergence of life. Detecting water or H_2O gas directly in debris and circumstellar disks at high resolution would provide valuable input in assessing the probability of planet-formation events through estimations of the location of the (water) snow line. The location of the snow line determines the distance in a star-forming region, such as nebulae, from

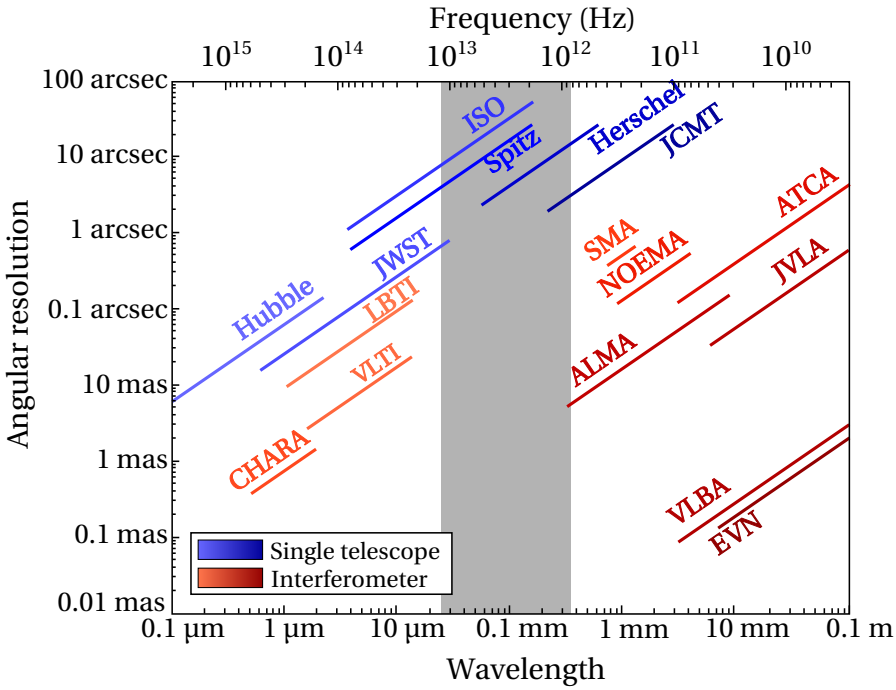

Figure 2.2: Angular resolutions achieved by different radio and optical infrared telescopes [14]. Indicated in blue are single-dish telescopes, all of which are space-based with the exception of the JCMT; and, in red, are ground-based interferometers. There is a gap, marked in gray, in the frequency-wavelength band (approximately 1 to 12 THz, or 350 to 25 µm), corresponding to far-infrared ranges: this range has not been explored with angular resolutions below 1 arcsec.

a central star, where it is cold enough for volatiles such as water[2] to condense into solid ice grains. It typically separates terrestrial planets from giant planets[3]. Promising studies [19, 20] pave the way for a facility like IRASSI to probe H_2O emissions from inside the water-snow line in the FIR in protoplanetary disks moderately close to Earth. In addition to water, measurements of gas mass are necessary to determine the planet-formation potential of protoplanetary disks. Certain unique features of atomic gas in the FIR have yet to be fully explored by scientists.

2.2.2. PREVIOUS MISSIONS AND CONTRIBUTIONS

While most of the launched formation-flying missions focused on Earth applications and on technology demonstration, space-based astronomy has been so far been materialized solely by single-element telescopes. IRASSI, therefore, inherits its layout from a mixture of past astronomy missions like Herschel [22] and studied interferometry mission concepts. Noteworthy studies include:

- TPF (Terrestrial Planet Finder) [23]: TPF was a NASA project aimed at detecting extrasolar terrestrial planets in nearby stars. Within the study, two architectures were considered, a visible-light coronograph and an infrared nulling interferometer. The interferometer architecture specifically intended to search for biomarkers in the atmosphere of such planets, such as CO_2 and water, and perform the final characterization of terrestrial bodies and gas giants within the mid-infrared band of 6.5 µm–18 µm. With a three-to-four-element formation separated by 100-m baselines, TPF set out to achieve approximately 25 mas in angular resolution. The concept relied on relative position control with centimeter-level accuracy. The TPF contained a catalog of 250 stars, each to be surveyed three times over the five-year mission. After consecutive delays over the course of more than a decade, TPF was finally canceled in 2011. The TPF interferometer architecture was the precursor of Darwin.

- Darwin [12]: after TPF, Darwin is the second-longest mission study of the list. Part of the program of the European Space Agency (ESA), Darwin underwent several design iterations with the number of formation elements varying from four to nine. In the most recent version, a central beam combiner spacecraft

[2] Other volatiles include ammonia, methane, carbon dioxide, carbon monoxide.

[3] For reference, the snow line of our Solar System lies currently at approximately 5 AU from the Sun [17] although during the early formation stages of planetesimals, nearly 4.6 billion years ago, this location was about half of that distance, at 2.7 AU from the Sun [18].

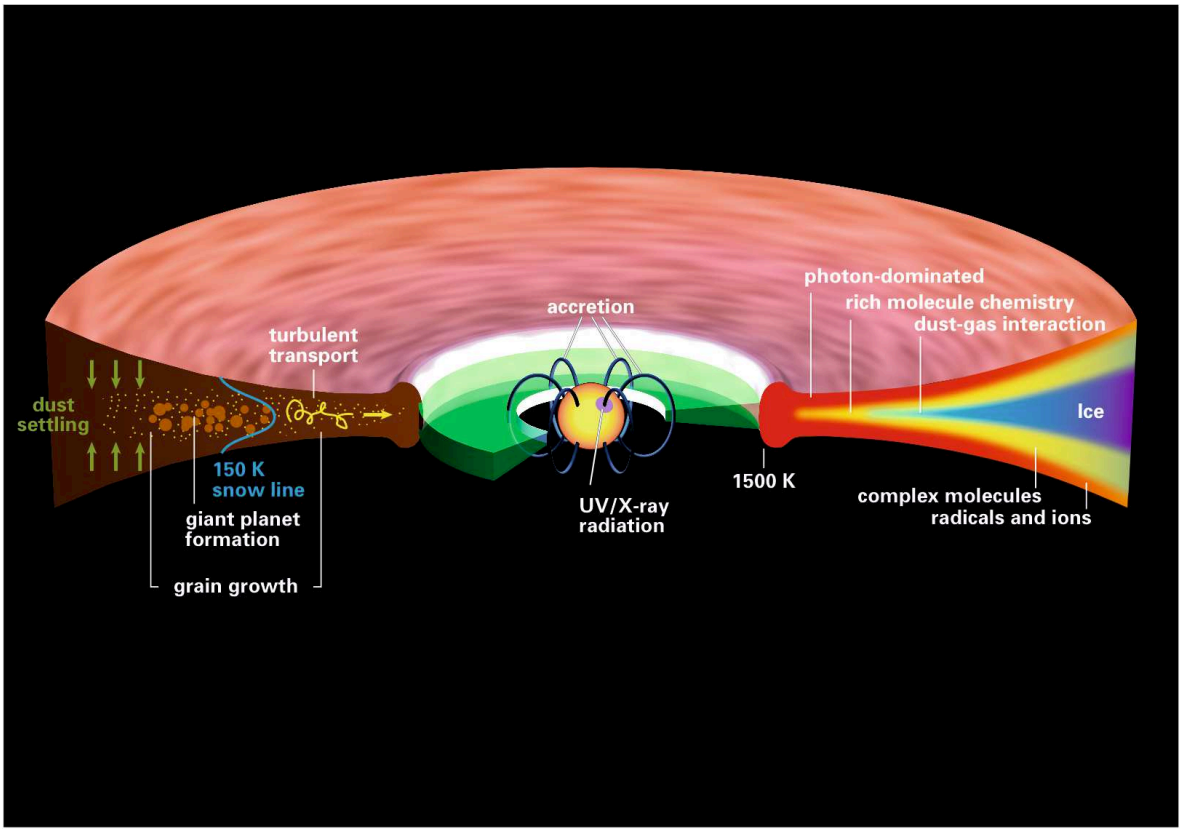

Figure 2.3: Sketch of the physical and chemical structure of a 1–5 million-year-old protoplanetary disk around a Sun-like star [21].

with spectrograph payload would receive redirected light of distant stars and planets from three other deputy telescopes. Direct planet detection and atmospheric spectroscopy were shared goals with TPF. Producing high-resolution infrared images was also Darwin's objective, allowing one to gain insight into various astrophysical processes. Sampling the mid-infrared at wavelengths of 6 µm–20 µm, a resolution of targets of 5 mas at 10 µm was foreseen for the longest baseline distances of 500 m. Such sensitive, high-resolution observations relied on controlling relative distances between the deputy telescopes at the µm-level and the distances between the telescopes and the beam combiner within 1 nm. The study ended in 2007 with the technology readiness level pointed as one of the biggest challenges to overcome for achieving feasibility.

- SPIRIT (Space Infrared Interferometric Telescope) [9, 10]: this NASA-sponsored mission study proposed to perform spectroscopy and high-angular resolution imaging in the subarcsec regime, targeting the FIR range of 25 µm–400 µm. It aimed at understanding how planetary systems arise from stellar desks, characterizing their composition and differentiating them according to their location in the disks. It also set out to investigate the origins and evolution of high-redshift galaxies. SPIRIT devised a formation concept of two light-collecting telescopes separated by a beam-combiner instrument mounted on a boom structure. The telescopes would sample the sky by sliding on the boom, to reach a maximum distance of 36 m.

- ESPRIT (Exploratory Submillimeter Space Radio-Interferometric Telescope) [11]: the concept of heterodyne detection in a free-flying interferometer was first explored in the ESPRIT study. Composed of a six-element formation with maximum baselines of 1 km, it proposed to explore the far-infrared band of 50 µm–600 µm with an angular resolution of 0.1 arcsec. A European-led initiative, ESPRIT was primarily aimed at designing the scientific instrumentation and overall architecture. One of the critical design choices was to employ a distributed correlator on board the spacecraft. This implied that all spacecraft were manufactured equally, guaranteeing redundancy and cost-savings.

- FIRI (Far-infrared Interferometer) [13]: this ESA study devised a classical concept of three large tele-

scopes orbiting a central beam-combiner module with baselines of up to 1 km. A tethered configuration and a free-flying solution were both considered during the study. FIRI proposed employing a hybrid of heterodyne and direct-detection techniques, promising an angular resolution of 0.02 arcsec while observing the far-infrared range of 25 µm–385 µm for high-resolution spectroscopy. Unveiling the formation of galaxies and the evolution of stars, planets and super-massive black holes by sampling at structures of dust in protoplanetary disks was the prime objective of FIRI.

IRASSI builds on the heritage of these studies to granularly resolve astronomical processes in the far-infrared, by replacing traditional centralized imaging systems with distributed science architectures, identifying the technology limitations associated with these novel concepts and taking a leap forward by supporting technology development for supporting such a mission.

2.3. IRASSI SCIENTIFIC OBJECTIVES

THE main goals of the mission and the justification for certain practical constraints is provided.

2.3.1. HIGH-LEVEL AND OPERATIONAL REQUIREMENTS

The main goal of IRASSI is to observe cold regions of space where Earth-like planets are likely to form, such as stellar disks, and investigate chemical and physical processes associated with the generation of these Earth-like planets. Such processes can be unveiled during the early phases of star formation in stellar disks when these regions are completely obscured by dust.

More particularly, the telescopes will analyze the distribution of relevant ionic, atomic and molecular species, by detecting their spectral signatures and the associated gas dynamics and the physical conditions surrounding these events which ultimately lead to pre-biotic conditions in Earth-like planets.

The science objectives dictate the technical specifications in order to fulfill the objectives of the mission. These high-level requirements are summarized in Table 2.1. The motivation for critical design choices is summarized in the next subsections.

Table 2.1: IRASSI high-level science and design requirements.

Parameter	**Required Value**
Number of telescopes (n)	5
Number of baselines	$10 \left[\frac{n(n-1)}{2}\right]$
Length of baselines	7-10 m (min) to 850 m (max)
Formation configuration	Free-flying in 3D
Size of telescope mirrors	3.5 m primary mirror
Wavelength (λ) range	50 to 300 µm
Frequency range	1 to 6 THz
Field of view (of each telescope)	3 to 19 arcsec (frequency-dependent)
Angular resolution	0.1 arcsec (at $\lambda = 300$ µm)
Telescope pointing accuracy	0.4 arcsec (requirement), 0.2 arcsec (goal)
Baseline measurement accuracy	5 µm
Noise temperature	$<$ 480 K/THz
Temperatures	80 K main dish; 4 K mixer

2.3.2. INTERFEROMETRY AND THE *(U, V)*-PLANE

As an interferometer, the angular resolution of IRASSI is determined by the length of the baselines. The term 'baseline' refers to the projected separation between two points of reference (located in two different space-

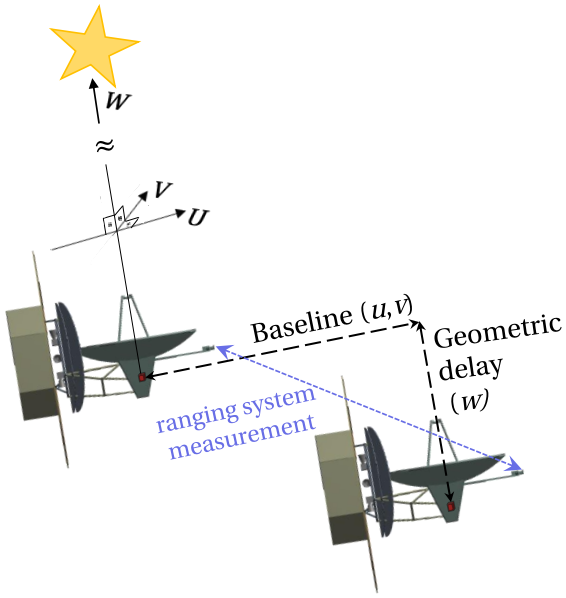

Figure 2.4: Illustration of the UVW reference frame.

craft), on a plane parallel to the incoming signal wavefront. In summary, the larger the baseline, the better the angular or spatial resolution of a target.

In order to reference the target, the UVW frame must be defined. The $\boldsymbol{W}$-axis connects the telescope detectors to the target and plane formed by the $\boldsymbol{U}$- and $\boldsymbol{V}$-axes, called the *(U, V)*-plane, is then parallel to the incoming wavefront. The specific direction of the $\boldsymbol{U}$- and $\boldsymbol{V}$- axes must be defined at the beginning of an observation and remains fixed during the whole observation period. The UVW reference system is illustrated in Figure 2.4. Note that the baseline is projected in the *(U, V)*-plane. There are a total of 10 baselines, in a five-spacecraft formation.

IRASSI relies on heterodyne detection which processes amplitude and phase information of incoming radiation. The heterodyne interferometer cross-correlates digitized wave signals containing the spectral information from each telescope pair (section 3.4.2 elaborates further on heterodyne detectors). This produces a set of visibilities (i.e., visibility function in the Fourier-transformed plane), at different locations in the *(U, V)*-plane. As baselines change, these sets of visibilities gradually populate the *(U, V)*-plane. The reference points of the baseline measurements are assumed to be the heterodyne instruments located inside the spacecraft.

The final target images are produced with postprocessing techniques. To obtain a high-quality image of a celestial object, the interferometer must scan as many points in the *(U, V)*-plane as possible.

BASELINE LENGTH AND ACCURACY

One of the high-level goals of IRASSI is to deliver a spatial resolution of 0.1 arcsec across the whole FIR frequency range, from 1 to 6 THz. Assuming a suitable sampling of the *(U, V)*-plane, a uniformly weighted sampling function will give rise to a synthesized beam, whose full-width at half-maximum FWHM is a function of the maximum baseline b_{max} at the lowest frequencies, that is, at the longest wavelengths λ_{max}. For a $FWHM = 0.1$ arcsec and given that the longest wavelengths of the IRASSI targets are $\lambda_{max} = 300\,\mu$m, the maximum baseline b_{max} is computed as [24]:

$$b_{max} = \frac{0.705\,\lambda_{max}}{0.1\text{ arcsec}} \approx 425\text{ m} \tag{2.1}$$

To account for noise due to high sidelobe levels of the uniform weighting scheme, a factor of 2 for the maximum baselines is introduced, bringing the maximum baseline lengths to 850 m.

In order to ensure that two heterodyne detectors correlate the signals from the same incoming wavefront, the geometric delay, also featured in Figure 2.4 as the w component, must be estimated very precisely. Uncertainties in the geometric delay lead to uncertainties in the phase of the recorded signals and a too-large uncertainty may therefore decorrelate the signals. In order to obtain an interference pattern, both wavefronts must be combined with a phase error below 30°. In terms of wavelength (λ), this geometric delay translates

into an accuracy knowledge requirement of approximately $\lambda/10$. The shortest wavelengths have thus the stringiest requirements. If the minimum wavelength to be observed, λ_{min} is 50 µm (cf. Table 2.1), then the geometric delay accuracy must be known within 5 µm. To determine the geometric delay, or the baselines, at this accuracy, a dedicated ranging system is employed and attitude sensors on board the spacecraft are also used. The baseline estimations in the *(U, V)*-plane are also based on the measurements of the ranging system.

Each spacecraft carries one ranging system mounted on an optical bench structure and each ranging system is equipped with four laser terminals. Each laser terminal must link to another spacecraft's laser terminal to measure continuously the relative distances between the two. The baselines and geometric delay are ultimately measured in a two-step process: 1) the ranging system lasers provide largely the separation between the two spacecraft and 2) the separation of the ranging system to the reference points (the heterodyne instruments inside the spacecraft), the attitude of the spacecraft from onboard sensors and all associated distance and angular measurement errors are then added to the process to produce a unified measurement of the geometric delay and baseline distances.

POINTING ACCURACY

Targets in the FIR are in general very faint and therefore large collecting areas (optical elements, such as mirrors) are necessary in order to increase the number of targets that can be detected. This motivates the choice of a 3.5-meter main mirror - a compromise between scientific potential and plausible dimensions which fit within a launcher's upper stage. This was also the size of Herschel's main mirror [22].

For a uniformly illuminated antenna with circular aperture of radius r the resulting power pattern (the 'primary beam') has a half-power beam width HPBW [24]:

$$HPBW = \frac{0.514\,\lambda}{r} \tag{2.2}$$

where λ is the target-emission wavelength. The pointing accuracy requirements depend thus on the lower-end of the wavelength operational range of IRASSI. With $\lambda_{min} = 50\,\mu\text{m}$, the $HPBW$ is 3 arcsec for a uniformly illuminated circular antenna. Modified designs for the main and secondary mirrors will slightly widen the main lobe by a factor of ≈1.1–1.4 [16]. Assuming a factor of 1.33 compared to the uniform illumination $HPBW$, the minimum requirement for the pointing accuracy is set to:

$$HPBW_{eff} = \frac{HPBW|_{\lambda_{min}=50\,\mu\text{m}}}{10} \times 1.33 = 0.4 \text{ arcsec} \tag{2.3}$$

However, in order to ensure high-quality interferometric data, it is suggested to pursue even higher accuracies. For instance, Napier [25] advocates a pointing accuracy of $\frac{HPBW}{20}$. Therefore, $HPBW_{eff} = 0.2$ arcsec would be the goal for the IRASSI pointing accuracy.

2.3.3. TARGET POPULATION AND SCIENCE OBSERVATIONS

The current catalog of potential targets[4] comprises 453 distinct objects, among them young stars (low-mass T Tauri stars and intermediate-mass Herbig stars) which are known to contain circumstellar gas and dust disks and which can be hosts to forming protoplanets; debris disks comprising of stars heavier than our Sun and remaining dust cloud material, where the planet formation might be more advanced; active galactic nuclei (AGNi) where the dynamics of neutral and ionized gas can be assessed; nearby galaxies and massive young stellar objects; high-mass star-forming regions and other special bright disk sources, such as prominent hot cores and hot corinos. An overview of the catalog entries is provided in Appendix D, whereas Figure 2.5 provides impressions of the IRASSI target population.

Each target is associated with a priority grade, an observation duration and the number of required visits. Detection observations require integration times between 0.1 to 8 days depending on the spectral type of the target and the distance to the target. The maximum duration of the observations of 8 days is allocated to debris disks, who similarly require a high number of revisits (they are very faint targets, which require long integration times), whereas massive objects require shorter observation times (they are bright sources in the FIR).

There is no differentiation of science activities *per se* as all targets involve the same operational processes. Similarly, there is no fixed formation configuration during the Science Observations subphase, as only high-level requirements demand that a free-drifting three-dimensional structure is observed. The minimum and

[4] The target list is to be updated periodically as potential sources are identified by the consortium partners.

(a) T Tauri surrounded by a gas and dust cloud. Credit: NASA.

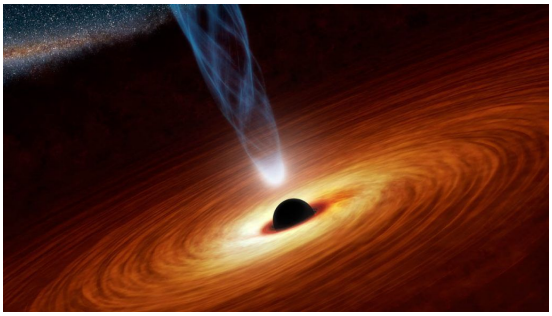

(b) AGN powered by accretion onto a supermassive black hole. Credit: MIT Kavli Institute.

(c) M81 Galaxy in infrared. Credit: NASA/JPL-Caltech.

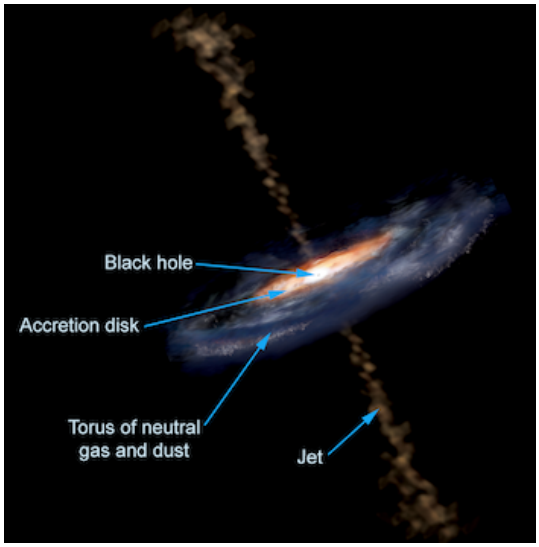

(d) Different features of an AGN. Credit: Aurore Simonnet, Sonoma State University.

Figure 2.5: Illustration of IRASSI targets.

maximum formation baselines (i.e., separation along the *(U, V)*-plane) of each observation are dictated by the target, but the three-dimensional arrangement of the formation leaves a degree of freedom for arranging the telescopes in preparation for an observation task. The boundary conditions for a formation geometry design are addressed in Chapter 4.

The nominal operational concept involves sampling one single target for each observation routine. For this target, the telescopes initiate the drift by means of a low-thrust maneuver at a baseline separation extremum (maximum or minimum) and finish the task at the other end. The observation details are summarized in Table 2.2.

2.4. ORBIT SELECTION

IT is of importance to the performance of the telescopes that observations are carried out unobtrusively and in stable conditions, avoiding violations of baseline measurement accuracies. This leads to the consideration of Lagrangian points, or libration points, as potential candidates around which the IRASSI spacecraft can fulfill its mission.

Lagrangian points are mathematical solutions to the Circular-Restricted Three-body Problem (CR3BP) [26]. The CR3BP describes the dynamics of a spacecraft around two primary massive bodies, without the former influencing their motion, i.e., the mass of the spacecraft is neglected with respect to the primaries. It also assumes that the primary bodies have circular orbits around their center of mass. In the CR3BP the trajectories and orbits of a spacecraft are determined solely by the gravitation interactions of the two primary bodies and the distance between the spacecraft and these bodies. At the exact Lagrangian point locations, however,

Table 2.2: Science observations for the IRASSI mission.

Science Observations	**Description**
Objective	Analyze the distribution of relevant ionic, atomic, and molecular species in circumstellar disks, detect their spectral signatures, the gas dynamics and the physical conditions leading to planet formation.
Observation duration (days)	0.1 to 8 days
Target visits	1 to 3
Priorities	1 to 4
Formation configuration	free-flying in 3D, at a maximum baseline of 850 m

the gravitational forces of the two primaries balance the centripetal force of the spacecraft. In the vicinity of Lagrangian points, the spacecraft can maintain a rather stationary position with respect to the two primary bodies even when disturbances (e.g. solar radiation pressure, the proximity of other planets, etc.) are considered and quasi-periodic orbits can be found around these points.

Of the five Lagrangian points, the so-called second Lagrange point, or L_2, of the Sun-Earth/Moon system is of particular interest to IRASSI. The L_2 point is located approximately 1.5 million km from the Earth, in the anti-Sun direction of the Sun-Earth line (the Earth and the Moon are treated as a single massive body, by considering their barycenter in the CR3BP). Because it allows spacecraft to remain relatively stationary with respect to the primaries, low energy expenditure is required for station-keeping. If the orbit around L_2 is large enough, thermal variations are minimized (compared, for instance, with the Earth, where heating/cooling cycles render sensitive instruments inoperable). And finally, it allows scientific observatories to point away from bodies, such as the Sun or the Earth, maintaining an unobstructed view of deep space. Example missions carried out to L_2 are, for instance, the WMAP (Wilkinson Microwave Anisotropy Probe) [27], HSO [22], Planck [28] or GAIA (Global Astrometric Interferometer for Astrophysics) [29].

In order to describe the IRASSI's nominal orbit, the L_2-centered reference frame, hereby termed $\mathscr{L}_2$, must be defined. As such, the following properties apply:

- the δx-axis is aligned with the ecliptic plane and its positive direction follows the anti-Sun direction (towards outer space);
- the δz-axis is aligned with the North and South ecliptic poles of the celestial sphere, with the positive sense in the North-pole direction;
- the δy-axis completes the right-handed reference frame.

This reference frame is illustrated in Figure 2.6(a). A quasi-Halo[5] orbit is selected for the mission, characterized by the following properties:

- quasi-periodic (frequency in δy-axis is nearly the same as the δx-δz-axes frequency);
- large amplitudes in the δy-component;
- a spacecraft in this orbit will not enter the antumbra region, i.e., it is free of eclipses;
- quasi-free ΔV transfer maneuvers.

[5]The prefix 'quasi' is coined since any orbit around L_2 is dynamically unstable, i.e., spacecraft will diverge from the reference Halo over time and 'escape' to outer space, in a heliocentric trajectory due to the solar radiation pressure, the movement of the Moon, among other disturbances.

These characteristics make Halo orbits ideal ones to carry out observations in the far-infrared, satisfying the high-level scientific requirements of the IRASSI mission. A quasi-Halo orbit around L_2 as seen from the Sun, is illustrated in Figure 2.6(b).

IRASSI's operational orbit is a large-amplitude quasi-Halo (800 000 km × 400 000 km) around L_2, with a period of six months. There is no requirement to maintain a fixed amplitude in each revolution, as long as the formation does not escape the vicinity of L_2 and maximum incursion limits are observed. This is addressed in section 3.3.

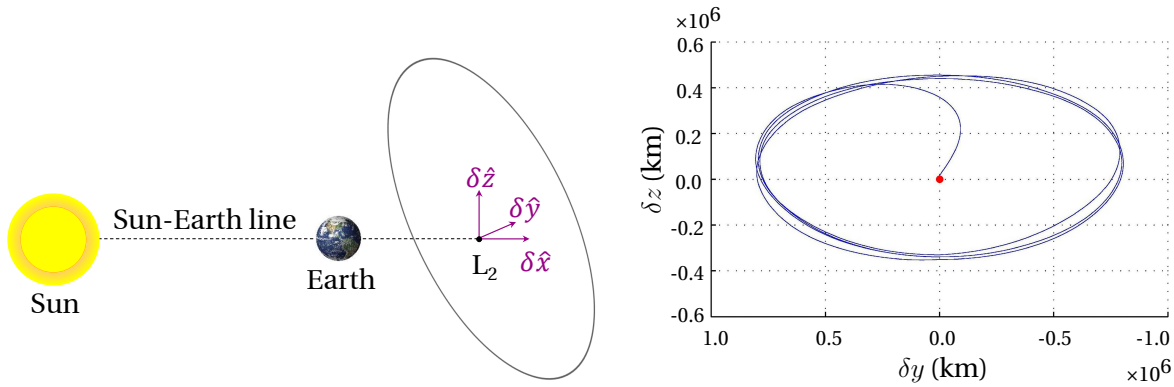

(a) $\mathscr{L}_2$ frame (b) Halo orbit [14]

Figure 2.6: L_2-centered reference frame and quasi-Halo orbit around L_2. The red dot (right) denotes the Earth.

2.5. Mission Overview

It is envisioned that the formation is launched with three launchers, in a 2-2-1 sequence. A propulsion module encapsulates each set of spacecraft. After injection into a highly elliptical orbit around Earth, the propulsion module is deployed from the launcher. After about 24 hours on this highly elliptical orbit, the cruise flight starts in direction to L_2. The spacecraft remain inside the propulsion module until the operational orbit is reached. Upon entering the Halo orbit around L_2, the spacecraft are deployed from the propulsion module and a set of health-check activities ensue to prepare the spacecraft for their five-year long operational life.

Once the spacecraft are operational, the scientific program of the mission can start. During observation tasks, the spacecraft shall drift continuously, expanding the baselines until a maximum of ≈850 m is reached, or conversely, contracting the baselines to a minimum of 7-10 m in the UVW frame. This drift is initiated by thrusters. The satellite distances do not have to be controlled but very accurately measured. An inter-satellite metrology via laser-based optical frequency combs shall provide these measurements to the correlator.

Although no symmetry is required, the spacecraft should be distributed in a three-dimensional configuration. The spacecraft are intended to be replicas of each other, i.e., have the same shape, volume and mass, as well as perform the same functions. This is expected to reduce overall mission complexity and costs (i.e., manufacturing), as well as to provide an element of redundancy. This redundancy allows for the failure of one of the elements without sacrificing the whole mission.

The selection of the reference scenario is a result of design trades, such as complexity and risk, and heritage from previous missions. Detailed logistics, financial assessments and scalability issues are nonetheless out of the scope of the present research.

2.6. Chapter Summary

This chapter introduced the most relevant aspects of the IRASSI mission. The underlying motivation for proposing the IRASSI mission is unveiled in the first section, together with an overview of previous mission studies upon which IRASSI is built. Novel technology developments, together with heterodyne detection methods, make the IRASSI mission a promising space-based facility for observations in the far infrared.

The high-level requirements are thereafter presented, which serve as the basis for the research of this thesis. A maximum baseline distance is set at 850 m, due to the strict spatial resolution requirement of 0.1 arcsec

at the longest wavelengths. Conversely, the pointing accuracy of 0.4 arcsec is directly related to the shortest wavelengths and the size of the primary mirror, whose diameter is set at 3.5 m, heritage of the Herschel Space Observatory.

The last subsection presents the nominal orbit of IRASSI, corresponding to a quasi-Halo orbit around the L_2 point of the Sun-Earth/Moon system. Finally, a brief outline of the mission is provided, where the free-flying nature of the interferometer is highlighted.

3

Mission Analysis and Spacecraft Configuration

The scientific man does not aim at an immediate result.
He does not expect that his advanced ideas will be readily taken up.
His work is like that of the planter - for the future.
His duty is to lay the foundation for those who are to come,
and point the way.

He lives and labors and hopes.

Nikola Tesla

ABSTRACT

Chapter 3 provides a system-level description of the IRASSI mission. The mission phases are identified, as are the activities and maneuvers contained within them. Three launch windows are available each year, starting approximately in March, July and December, with a duration of one month. The cruise to L_2 lasts between 90–120 days. Approximately 600 observation tasks are estimated to be fulfilled during the mission, with reconfiguration maneuvers accounting for more than half of the total ΔV estimations, at 225 $m\,s^{-1}$. The spacecraft are expected to weigh 2300 kg, a quarter of which is allocated to payload hardware and 5% is allocated to fuel.

3

Publication

L. Buinhas, E. Ferrer-Gil and R. Förstner, *IRASSI InfraRed Astronomy Satellite Swarm Interferometry: Mission Concept and Description*, Proceedings of the 2016 IEEE Aerospace Conference (2016).

Credits for the spacecraft ground visibility and mechanical design work belong to Eloi Ferrer-Gil. The information is added in this chapter for completeness.

3.1. INTRODUCTION

THE design of the mission activities and the architecture of the spacecraft are shaped by the science goals set out for IRASSI. A set of sensitive science instruments demands, for instance, the existence of certain operational rituals to ensure compliance with performance requirements, such as an intermittent calibration of attitude and ranging sensors. The same instruments are associated with lower thresholds of thermal variations and mechanical vibrations relative to other subsystems of the spacecraft. Payload instruments require thus a partition of the spacecraft on the basis of thermal and vibrational shielding.

In light of the high-level requirements of the mission, the phases of the mission are described in the first section, followed by the mission analysis describing the reference trajectory of the spacecraft, from their departure from Earth until the end of the mission. All maneuvers are identified, which, compounded by the subsystems' mass, lead to an estimation of the launch mass of the spacecraft in the final section of this chapter.

3.2. MISSION PHASES

THE IRASSI mission is divided into eight main phases, ranging from the pre-launch and launch activities until the end of the operational life of the telescopes. Of relevance to this work is the Nominal Operations phase. The remaining mission phases are briefly addressed in Appendix A and are summarized in Table 3.1 with the corresponding durations.

Table 3.1: IRASSI mission phases.

Phases and subphases	**Duration**
Pre-launch	8 hours
Launch	25 minutes
Deployment of Propulsion Modules	4 hours
Transfer Cruise to L_2	90 to 120 days
Deployment of Spacecraft	12 hours
Activation & Initial Formation	3 days
Subsystem & Payload Commissioning	30 days
Nominal Operations	5 years
Formation Reconfiguration	≈12 hours
Formation Pointing	6 hours
Scientific Observations	≈1 to 8 days
Calibration	4 hours
Uplink/Downlink	4 hours
Station-keeping	(once per orbit)

Nominal Operations constitute the longest phase of the mission and comprises a set of cyclic activities and subphases briefly described below. In total, the sequence of cyclic activities, called 'Observation Cycle' lasts from a few hours to over 8 days and repeats iteratively until either station-keeping maneuvers are required or off-nominal conditions arise. Based on the present work (the results of which are summarized in Chapter 12), it is expected that, over the course of the 5 years, around 600 observation cycles take place.

1. Formation Reconfiguration: before the beginning of each observation, each spacecraft must move individually to their specified positions. This may mean a rearrangement of the constellation in inertial space to cover a specified region of the sky.

2. Formation Pointing: after all spacecraft achieved their specified initial position, they must change their

attitude according to the region of the sky that is to be surveyed, such that the telescopes are aligned with the target.

3. Scientific Observations: most of the payload instruments operate exclusively during this subphase. Fine target-acquisition for high-accuracy pointing precedes the formation drift, which lasts for a number of hours up to 8 days until the maximum/minimum desired baseline length is reached. As aforementioned, this continuous drifting motion provides the coverage of the *(U, V)*-plane. The data collected is stored on board before being transmitted to the ground for post-processing.

4. Calibration: calibrations allow sensitive hardware to return to a known set point after a number of observation activities have been carried out. Given the precision requirements and the sensitivity of the science instruments involved, e.g., the heterodyne detectors, periodic corrections are foreseen. Other instruments, such as the ranging system, sensors or control actuators may also be calibrated when required, although less often than the heterodyne detectors.

   During calibrations, it is assumed that no particular relative position determination and attitude control requirements are in place and the spacecraft may drift freely - thus no maneuver is allocated during this subphase.

5. Uplink/Downlink: it comprises activities dedicated to downlinking the collected data from the payload subsystem and uplinking instructions from the ground for future operational procedures (e.g., target allocation schedules). In addition, overall housekeeping information from the spacecraft subsystems should be communicated to ground stations and control commands should be retrieved. Uplink/downlink of data can be carried out after or simultaneously with other subphases, as long as the spacecraft are visible from the ground and enough power is available.

   Due to the omnidirectional pattern of the low-gain antennas (LGA) and the pointing mechanism of the high-gain antennas (HGA), no particular maneuver is allocated during this subphase.

6. Station-keeping: impulsive corrections of the position of the spacecraft in their orbit outside scientific observation periods should occur periodically, nearly every 3-6 months.

3.3. MISSION ANALYSIS

THE present section provides an overview of the reference trajectory based on the selected operational orbit and the required ΔV estimations for IRASSI as well as a summary of the visibility analysis from the ground.

3.3.1. REFERENCE TRAJECTORY

The reference trajectory assumes hypothetical launch windows in 2029/2030 and the launch course used by Arianespace launchers for L_2 missions [30]. The launchers depart from the Guiana Space Center, in Kourou (French Guiana) and a direct transfer is used to reach the final orbit around L_2. This reference trajectory was simulated using the General Mission Analysis Tool (GMAT) [31]. The Earth was chosen as the primary, central body with the Moon and the Sun as point masses in the force model and solar radiation pressure was considered.

The motivation for choosing such a launch trajectory is threefold. First, preference was given to European-operated launch sites. Secondly, specific information regarding a launch to L_2 was available, contrary to other manufacturers. And finally, a launcher from the manufacturer (Ariane 5 ECA), has been used in the past for missions directed to L_2 as in the case of the Herschel Space Observatory and Planck [32]. Therefore, such a launch trajectory is proven feasible.

The reference trajectory of the constellation adopts the following profile:

- the launcher departs from the Guiana Space Center
- the launcher is inserted in a highly elliptical orbit (HEO) approximately 25 minutes after launch and 80° eastwards from the launch site;
- the propulsion module is propagated for approximately 24 hours before initiating the cruise phase from Earth to the Lagrange L_2 point;
- the propulsion module is propagated to the vicinity of L_2 by applying a first thrust correction maneuver;

- the propulsion module is propagated to its nominal quasi-Halo orbit around L_2 and a second thrust correction maneuver is applied;
- the deployment and separation maneuvers of the spacecraft from the propulsion module take place;
- station-keeping maneuvers begin to ensure the spacecraft remain in a quasi-Halo orbit for its five years of operations.

Table 3.2 presents an overview of the reference trajectory parameters simulated with the GMAT tool and Figure 3.1 presents a sample of the simulations obtained. The path followed by the spacecraft is shown, moving away from the Earth, and transferring to L_2, before entering the nominal orbit.

Table 3.2: Overview of the simulated reference trajectory parameters.

Parameter	**Value**
Simulation Tool	GMAT
Vehicle	Single propulsion module (containing five spacecraft)
Launcher trajectory	Ariane 5 ECA Flight 188
Launch site	Guiana Space Center
Launch site coordinates	5.2372° N, 52.7606° W
Insertion longitude $\Lambda_{E,nom}$	27.35° (80° east from launch site)
Simulated launch years	2029 and 2030
Orbit insertion altitude	850 km
Final nominal orbit	quasi-Halo

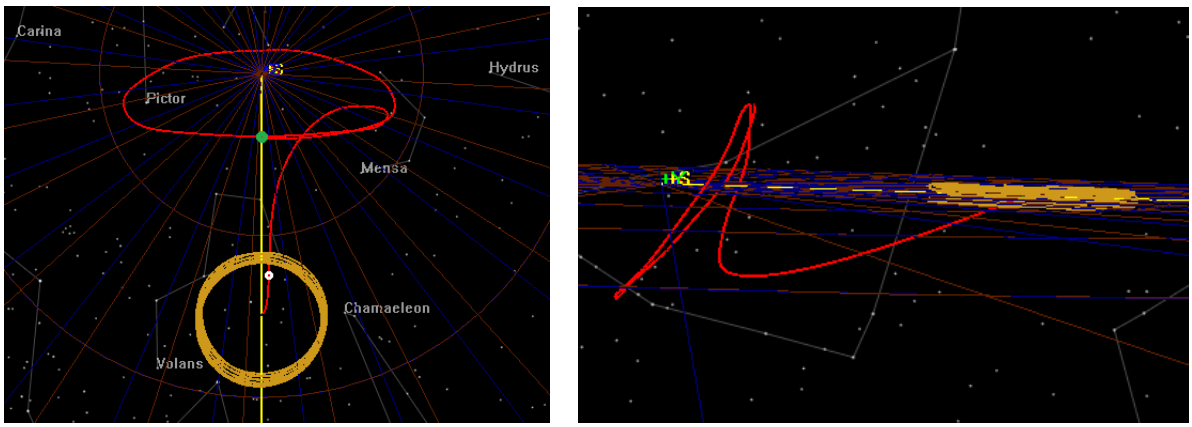

(a) View direction: -δz of $\mathscr{L}_2$ frame

(b) View direction: -δy of $\mathscr{L}_2$ frame

Figure 3.1: Simulation of the reference trajectory from Earth to L_2, in red. The yellow circles depict the Moon's orbit around the Earth. On the left, the white and green circles mark the points at which the propulsion module applies the first and second correction burns, respectively.

LAUNCH WINDOWS

The maximum amplitude values (in absolute terms) achieved in the δx-, δy- and δz- axis of the L_2-centered frame, of $\mathscr{L}_2$, depend highly on the time of launch. In order to select the candidate launch windows for IRASSI, the following aspects have been taken into account:

- Eclipse avoidance: the spacecraft should not enter the antumbra shadowed region of the Earth at any point during the Nominal Operations phase of the mission, in order to ensure solar power is continuously available. The lowest maximum amplitude value in the δz-axis for which the spacecraft can maintain their large-amplitude quasi-Halo orbit without drifting into an eclipse for a period of up to five years is $A_{z,min} = 270\,000$ km.

- Visibility: the highest maximum amplitude achieved in the δz-axis has a direct impact on the visibility from the ground stations, which are located across different latitudes on Earth. For amplitudes larger than $A_{z,max} = 550\,000$ km on the positive direction of the δz, there is an increased likelihood that the spacecraft cannot communicate with ground stations located in the Earth's Southern Hemisphere. The same is true for negative δz directions and Northern Hemisphere stations.

- Space loss: the maximum amplitudes on the δy-axis were determined so as to keep the space loss of the communications subsystem within an acceptable range. The current limit, $A_{y,max} = 850\,000$ km, may be altered in the future if necessary and if communications technologies evolve to cope with the Earth-L_2 distance.

The launch windows were calculated and ultimately selected on the basis of the reference trajectory and the aforementioned conditions. No maximum amplitudes δy_{max} lower than 600 000 km were obtained for the selected launch periods.

The launch optimization procedure based on bisection methods was implemented in GMAT. This procedure is described in Appendix A. The resulting launch windows for the years of 2029 and 2030 are presented in Table 3.3. In each year, three major periods were identified. According to the GMAT simulations, the transfer

Table 3.3: Launch windows for the years 2029 and 2030 for the IRASSI constellation.

Year	**Period 1**		**Period 2**		**Period 3**	
	From	**Until**	**From**	**Until**	**From**	**Until**
2029	19th March	18th April	19th July	17th August	04th December	04th January
2030	21st March	21st April	19th July	23rd August	27th November	30th December

has a duration of three to four months (90 to 120 days). The calculated average value for the ΔV of the first and second correction maneuvers, is of about 14 $m\,s^{-1}$ (in the anti-Sun direction) and 16 $m\,s^{-1}$, respectively, across all launch window periods. The burns are indicated in Figure 3.1(a).

3.3.2. ΔV BUDGET

The calculation of the total ΔV required is based on all maneuvers carried out throughout the course of the mission. The propulsion requirements associated with the different maneuvers are described before an overview of the corresponding ΔV is presented.

PROPULSIVE REQUIREMENTS

Two major maneuver types can be distinguished: orbit and formation control. Because the magnitude requirements differ for the various maneuver tasks, two propulsion systems have been devised.

The primary propulsion system is largely reserved for orbit-control maneuvers, such as station-keeping, deployment of spacecraft or momentum unload from saturated reaction wheels. The disposal of the spacecraft at the end of the mission is also delegated to primary thrusters. Such maneuvers have loose accuracy requirements and require thrust forces in the order of a few Newtons. Primary actuators consist of ten hydrazine-fueled thrusters, all duplicated for redundancy and distributed symmetrically on both sides of the service module (Sun- and anti-Sun-facing sides) to cancel out translational motion during actuation.

On the other hand, the secondary propulsion system is used for maneuvers requiring high stability and execution precision requirements, such as reconfiguration and baseline change maneuvers. Colloid thrusters, which employ a variety of metal solutions as propellant, can impart thrusting forces at submilliNetwon- or even at submicroNewton-levels.

CONTROL INTERVENTIONS OVERVIEW

Orbit-control maneuvers outside Nominal Operations encompass the transfer trajectory corrections, the deployment of the spacecraft and the disposal at the end of the mission.

The foreseen control interventions during the Nominal Operations phase and the associated actuators is provided below:

1. Formation Reconfiguration (secondary thrusters): maneuvers which lead the spacecraft to their new position prior to the observations. This leads to a change in formation geometry and pointing direction such that a new target is observed. The relative positions of the spacecraft in the formation must not remain fixed during the reconfiguration maneuver and no strict relative position determination requirements are in place, as long as the maneuver remains collision-free.

2. Formation pointing (reaction wheels): attitude change to align the telescope with the target

3. Momentum unload (primary thrusters): scheduled maneuvers to unload saturated reaction wheels

4. Baseline change (secondary thrusters): low-thrust, translational maneuvers which start the relative drift of the formation prior to the observations

5. Fine target-acquisition (reaction wheels/secondary thrusters): very small attitude maneuvers which provide the required telescope pointing accuracy (0.4 arcsec, cf. Table 2.1)

6. Station-keeping (primary thrusters): scheduled impulsive, translational maneuvers to ensure the spacecraft remain in a Halo orbit around L_2

7. Corrections when off-nominal situations arise:

   (a) of operational nature, such as malfunctions, when there is a collision risk or when formation requirements are violated

   (b) of performance nature, when image quality degrades.

TOTAL ΔV REQUIREMENTS

The total ΔV estimation required for the IRASSI mission is approximately 225 $\mathrm{m\,s^{-1}}$, from which 30 $\mathrm{m\,s^{-1}}$is allocated for the two correction maneuvers during the transfer phase, 1 $\mathrm{m\,s^{-1}}$each for Deployment and Disposal and the remaining amount for Nominal Operations.

A summary is provided in Table 3.4, where a total of 600 observation cycles is expected for the Nominal Operations phase (not including station-keeping), and station-keeping maneuvers are scheduled to take place twice per year (or once per orbit).

The estimations featuring in Table 3.4 were obtained in GMAT and with MATLAB within the frame of the IRASSI feasibility study, with the exception of the deployment of spacecraft, fine target-acquisition and momentum-unload maneuvers, which were conservatively estimated based on another studies [33, 34].

3.3.3. VISIBILITY TO GROUND

The analysis of visibility was carried out in the frame of the IRASSI feasibility study. It is summarized here for completeness and it is available in full in Reference [14].

The Deep Space Antennas (DSA) from the ESTRACK network were considered for the analysis. The location and geographic coordinates of these three DSAs are included in Table 3.5. The visibility precondition was defined as the elevation angle on the horizon of each ground station $\gamma_{vis} \geq 10°$. An illustration of how the elevation angle is defined is provided in Figure 3.2.

With such a setup, considering only single DSA antennas, the spacecraft are visible on average 10 hours per day, over the lifetime of the mission. However, using combinations of the DSA antennas (either subsets of two or all three DSA antennas), visibility would then average between 14.5 hours up to over 22 hours per day (naturally, the more ground antennas, the longer the visibility periods). There remain nonetheless days in which the spacecraft will remain invisible for a few hours. With careful planning and since the spacecraft can store data on board and operate autonomously during these short periods of time, such invisibility periods should not pose a problem.

Table 3.4: Total ΔV estimation per spacecraft. Maneuvers marked in gray denote strict control precision requirements.

Phase	Maneuver	ΔV ($m\,s^{-1}$)
Transfer to L_2	Correction near Earth	14
	Correction near L_2	16
Deployment of Spacecraft	Deployment	1
Nominal Operations	Formation Reconfiguration	128
	Momentum unload	11
	Baseline Change	15
	Fine target-acquisition	9
	Station-keeping	30
(End of Life)	Disposal	1
Total ΔV		225

Table 3.5: Geographical position of the Deep Space Antennas from the ESTRACK network.

Station	Location	Longitude	Latitude
DSA-1	New Norcia (Australia)	116.191° E	31.048° S
DSA-2	Cebreros (Spain)	4.368° W	40.453° N
DSA-3	Malargüe (Argentina)	69.398° W	35.776° S

3.4. IRASSI SPACECRAFT DESIGN

ALL elements of the IRASSI formation have the same shape, volume and mass, and perform the same functions. The spacecraft architecture and mass and power budgets were defined based on high-level and stability requirements of IRASSI(cf. Table 2.1), aiming at minimizing vibrations (from thermal and mechanical sources) which may cause misalignments within the telescopes [35].

3.4.1. MECHANICAL AND THERMAL ARCHITECTURE

The spacecraft is divided into two modules: a service module and a payload module. The service module contains the equipment which generates the strongest mechanical vibrations (including reaction wheels and thrusters) during operations. The payload module contains the sensitive equipment used during the scientific phase of the mission, such as telescopes, laser terminals, heterodyne detectors and attitude sensors.

The two modules also have different operating temperatures. Whereas the service module is not required to be cooled relative to the environment temperature, the payload module must be cooled up to 4 K due to infrared noise effects. Passive cooling down to 68 K can be achieved with the sunshield and corresponding thermal shields (enough for operating the main mirror of the telescope, cf. Table 1). Thereafter, active cooling systems, such as cryocoolers, should provide the required temperatures down to 4 K.

The two modules are separated by a sunshield. The overall architecture of one IRASSI spacecraft is illustrated in Figure 3.3. The thermal field of the spacecraft is presented in Figure 3.4, whereas details can be found in References [14, 35].

3.4.2. SPACECRAFT PAYLOAD SUBSYSTEM

Each IRASSI spacecraft is composed of the following seven subsystems: Payload, Structures and Thermal Control, Attitude and Orbit Control, Propulsion, Command and Data Handling, Communications and Power.

The Payload subsystem is at the core of the mission, as it contains all the scientific equipment necessary for detecting and processing the radiation signals from the observed target. The detailed description

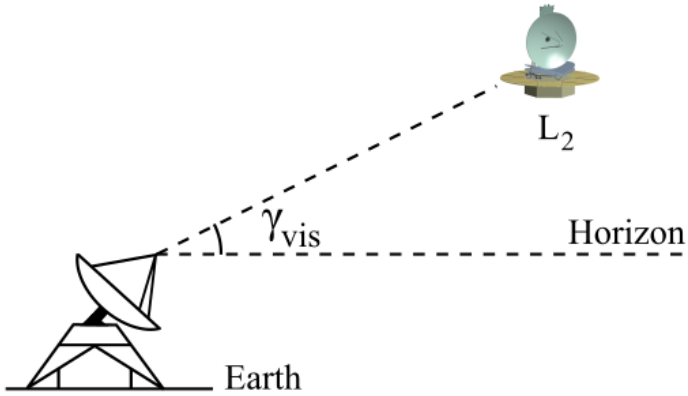

Figure 3.2: Elevation angle γ_{vis} [14]. An angle $\gamma_{vis} < 10°$ provides no visibility of the spacecraft to the ground stations.

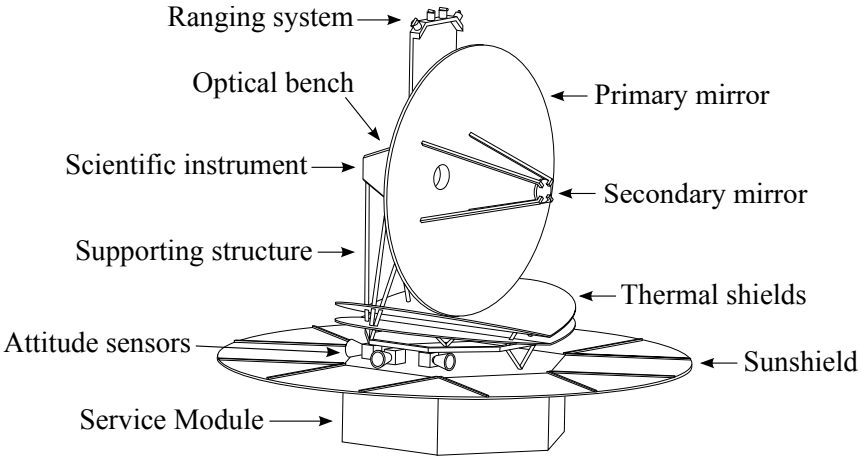

Figure 3.3: Mechanical configuration of the IRASSI spacecraft.

concerning the remaining subsystems is covered in References [14, 35].

Four major instrument groups compose the Payload subsystem:

1. Infrared telescope: it consists of the optical elements (mirrors) which reflect the incoming signal from a source and transmit it to the infrared instruments for processing. The primary mirror has a diameter of 3.5 m and the secondary mirror of 0.31 m.

2. Heterodyne detector: it includes all elements responsible for transforming the received signal into a digitized signal which is then sent to the correlator. A sequence of processes supports this detection technique.

   Firstly, the detected signal is combined with a local oscillator in a mixer instrument, in order to generate a low-frequency signal which is then amplified at the output. After being amplified, the signal is prepared for post-processing. That is, the signal is down-converted once again and divided into sub-bands. Each spacecraft is responsible for post-processing each sub-band.

   Finally, after being split into sub-bands, the signal is again electronically amplified without the addition of noise, digitized and sent either to the correlator on board the spacecraft or sent via an inter-satellite link to another spacecraft where it is correlated. An illustration of this process is given in Figure 3.5. In order to cover the desired frequency spectrum, between 1 THz and 6 THz, at least two mixers and local oscillators must be employed.

3. Distributed correlator: the importance of the correlator relates directly to the principle of interferometry. The goal of the correlator is to combine interferences of the detected wavefronts at different locations in space, to ultimately generate a synthesized image of a target. At each observation time step, 10

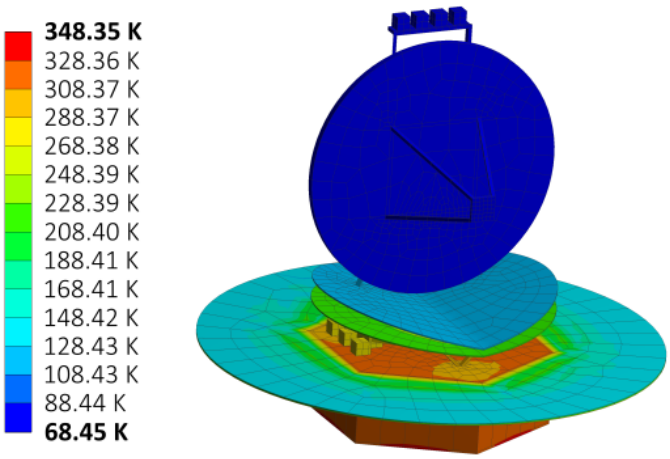

Figure 3.4: Thermal field of the IRASSI spacecraft [36].

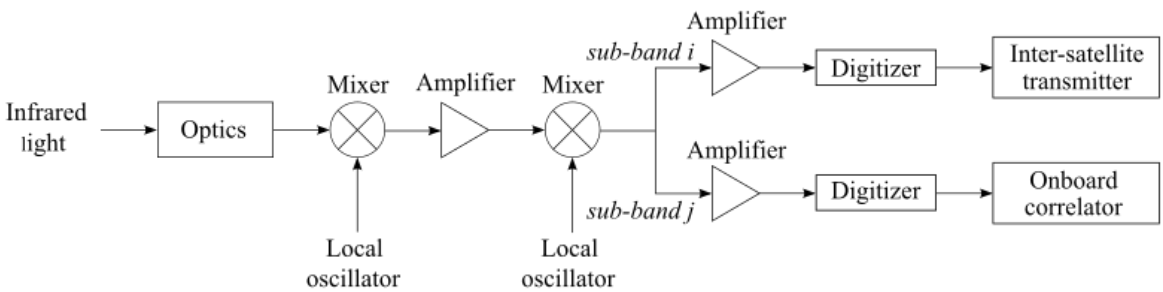

Figure 3.5: Elements of the heterodyne detector. Source: Ferrer *et al.* [35].

different interference measurements can be generated with the five-telescope interferometer.

Given that onboard correlation is computationally expensive, the process can be distributed among the five spacecraft, which use a sub-band of the total spectrum (this distributed correlation concept was firstly devised for the ESPRIT mission [11]). It relies then on inter-satellite links to exchange the data among spacecraft. From the total amount of data collected by each spacecraft, one-fifth will be fed to the local onboard correlator and the remaining four-fifths will be transmitted to the other spacecraft.

An added benefit of the distributed system is the increased redundancy: if one spacecraft ceases to be operational, 80% of the data required to generate an image of a target can still be recovered.

4. Ranging system: in order to ensure that every two measurements correlate the same detected signal at each location in space, they must be associated with a distance measurement between their respective spacecraft. The function of the ranging system is to provide this distance measurement.

   The ranging measurement is combined with a relative dynamics model of the formation and the onboard attitude sensors, to compute the geometric delay between incoming wavefronts at each spacecraft (Figure 2.4 illustrates the setup).

   The ranging system is divided into the main electronics unit, which is located in the service module, and the laser terminals, located in the payload module. The main electronics unit operates at the conventional temperature of the service module. On the other hand, misalignments, thermal gradients and relative distortions between the ranging lasers and the heterodyne detectors must be minimized. The laser terminals must thus be located in the cold payload module, where they can operate at cryogenic temperatures. The two components, the main electronics unit and the terminals, are connected through an optical fiber.

   There are four laser terminals, mounted atop the optical bench, as Figure 3.3 depicts. The laser terminals are not fixed. Instead, they are allowed to move within a range of ±90° both in azimuth and elevation, at an accuracy of 1 arcsec.

3.4.3. SPACECRAFT DIMENSIONS

The sunshield protects the payload module from incoming radiation from the Sun. The sunshield size largely determines the region of the celestial sphere that can be observed at one point in time, that is, the instantaneous sky access.

A larger sunshield is associated with higher instantaneous sky accessibility as it affords the spacecraft more freedom in terms of orientation. As a compromise between sky accessibility and structural mass, the sunshield diameter was set at 6 m. Additionally, the full length of the spacecraft totals 5.5 m. Figure 3.6 highlights the overall physical dimensions and Table 3.6 summarizes the specifications of the IRASSI spacecraft [36].

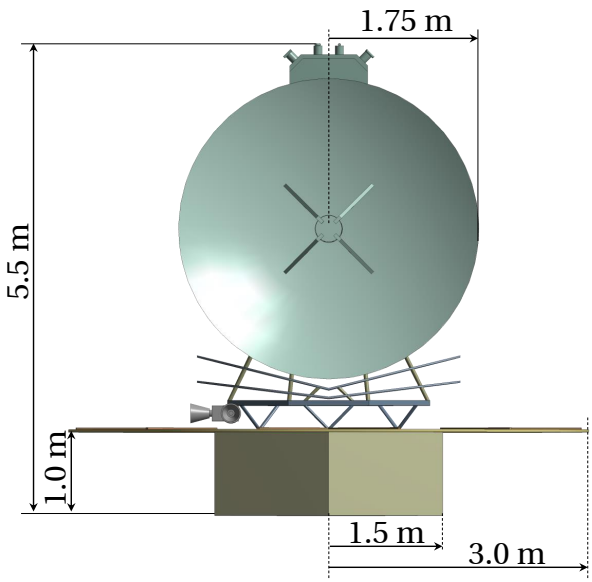

Figure 3.6: IRASSI spacecraft dimensions.

Table 3.6: Geometry and material specifications of the IRASSI spacecraft.

	Parameter	Property
Service Module	Shape	Hexagon
	Side length	1500 mm
	Height	1000 mm
	Material	Carbon-fiber-reinforced polymer (CFRP)
Sunshield	Shape	Circular
	Radius	3000 mm
	Material	Silver-Teflon/Aluminized Kapton
Payload Mod.	Structure material, Primary mirror, Secondary mirror	Silicon Carbide
	Optical bench and supports	Silicon Carbide/Zerodur and Titanium
	Thermal shields	CFRP

3.4.4. MASS AND POWER BUDGETS

The present section provides an overview of the wet and total mass budgets as well as of the estimated power budget. Details regarding dry mass calculations can be found in Reference [35], whereby a total dry mass of

approximately 2.2 tons is estimated per spacecraft, margins included.

WET MASS

The estimation of the fuel mass is a function of the ΔV required throughout the mission and of the properties of the propellant used to perform each maneuver. The ΔV required for each spacecraft are listed in Table 3.4, where gray-shaded maneuvers are associated with strict control precision requirements and non-shaded maneuvers represent those with loose precision requirements. This information is condensed in Table 3.7, which finally shows the fuel mass estimations based on state-of-the-art properties of each propulsion system type [37, 38] (again the colors refer to the respective precision requirements regimes). The estimated fuel mass for each spacecraft is 91 kg.

Table 3.7: Fuel mass estimation per spacecraft. The gray shading denotes the propulsion system associated with strict precision-requirement maneuvers.

Propulsion System	**Specific impulse (s)**	**ΔV ($m\,s^{-1}$)**	**Mass (kg)**
Primary/Chemical (Hydrazine)	230	73	76
Secondary/Electrical (Metal solutions)	2500	152	15
Total fuel mass			91

TOTAL MASS AND POWER REQUIREMENTS

The breakdown of estimated mass and power requirements for each spacecraft is presented in Table 3.8. Both for the total mass (dry and wet) and power calculations, a margin of 20% was considered. These constitute revised results from previous estimations [14, 35], where details regarding dry mass calculations can also be found.

The launch mass of each spacecraft is finally estimated at 2.3 tons. Furthermore, each spacecraft is expected to have a peak power requirement of 1780 W, provided by solar arrays with an area 8.4 m^2, fitted with multi-junction Gallium-Arsenide solar cells mounted on the sunshield.

Table 3.8: Subsystem mass and power budgets of the IRASSI spacecraft.

Subsystem	**Mass (kg)**	**Power (W)**
Payload	473.8	204.0
Structures and Thermal Control	831.5	170.0
Attitude and Orbit Control	120.5	393.5
Propulsion	107.5	122.0
Command and Data Handling	45.6	136.3
Communications	32.5	572.4
Power	217.6	185.3
Total (incl. 20% margin)		
Dry mass	2194.8	-
Wet mass	2304.0	

3.5. CHAPTER SUMMARY

THIS chapter presents a summary of the main phases of the mission, highlighting the Nominal Operations phase, which is composed of a set of science-related activities, called Observation Cycle, with a duration between 1 and 8 days. These time frames are mainly attributed to observations themselves and approximately 600 Observation Cycles are expected throughout the mission.

The results concerning mission analysis were presented, including the optimization process for the launch windows, and the total ΔV requirements for each spacecraft were estimated at 225 $\mathrm{m\,s^{-1}}$ for each spacecraft. In the years 2029/2030, three launch periods of about one month are available. A transfer time of three to four months is to be expected prior to the nominal start of the mission. Additionally, the formation is estimated to be visible from the ground for an average of 10 hours per day, using the Deep Space Network.

The preliminary architecture of the spacecraft was subsequently presented, with a focus on the Payload subsystem, which is at the center of the operating principle of interferometry, containing elements such as the optical mirrors, correlator instruments and the ranging system. The dimensions, mass and power budgets were given as were the overall dimension and properties of each individual spacecraft. Each spacecraft is expected to weigh about 2.3 tons.

II

Formation-Flying Geometry, Dynamics and GNC

4

Formation Geometry

Man is the best computer we can put aboard a spacecraft,
and the only one that can be mass produced with unskilled labor.

Werner von Braun

ABSTRACT

Chapter 4 outlines the steps taken in selecting a suitable formation geometry for the IRASSI interferometer. Firstly, four critical requirements are analyzed: the intervisibility of the ranging system, the relative positioning performance, the sky access and the science performance. After evaluating the impact of different formation arrangements on the aforementioned criteria, a three-dimensional nominal formation geometry is selected.

Publication

L. Buinhas, E. Ferrer-Gil and R. Förstner, *IRASSI InfraRed Space Interferometer: Mission Analysis, Spacecraft Design and Formation Flying Overview*, Proceedings of the 68th International Astronautical Congress (2017).

H. Linz, D. Bhatia, L. Buinhas, L. Lezius, E. Ferrer, R. Förstner, K. Frankl, M. Philips-Blum, M. Steen, U. Bestmann, W. Hänsel, R. Holzwarth, O. Krause and T. Pany, *InfraRed Astronomy Satellite Swarm Interferometry (IRASSI): Overview and study results*, Advances in Space Research, **65(2)**, 831-849 (2020).

Credits for the relative positioning method used in this chapter belong to Dr. Kathrin Frankl and MSc. Mathias Philips-Blum (Institute of Space Technology and Space Applications, University of the German Federal Armed Forces, Munich, Germany). The development of a science performance metric was done in conjunction with Dr. Hendrik Linz (Planet and Star Formation Department, Max Planck Institute for Astronomy, Heidelberg, Germany).

4.1. INTRODUCTION

THE first chapter of Part II provides a detailed analysis of the various constraints which impact the formation-definition procedure. At a first glance, there are numerous ways in how the spacecraft can be arranged in three-dimensional space. However, there are solutions which impair the operation of the science instruments (e.g., one spacecraft being placed in front of the mirror of another one) and not all solutions afford the same performance in terms of baseline estimation.

The mechanical architecture and physical distribution of the science instruments on the spacecraft are determinant factors in relative position assignment. The interferometer is, additionally, not static during science activities and therefore analyzing the evolution of the formation over time is imperative for determining which conditions deliver the best outcome in terms of science output.

Altogether these requirements contribute to constraining the solution space in defining a nominal formation geometry. The present chapter describes these requirements and assesses the impact of different relative position combinations on the operability of the formation. From this analysis, a nominal formation geometry is proposed and the relative dynamics of Chapter 5 is evaluated in terms of this nominal geometry.

4.2. ANALYSIS OF FORMATION REQUIREMENTS

OPERATIONAL requirements are related to four major preconditions which are addressed in this chapter:

1. Visibility of the ranging system
2. Relative positioning performance
3. Sky access
4. Science performance

Firstly, the visibility of the ranging system is one of the most crucial requirements in the arrangement of the spacecraft. If the spacecraft are distributed in a fashion which hampers the ranging system laser links, then the spacecraft are not able to determine their relative distances with the required accuracy. This requirement produces therefore areas in which spacecraft cannot be physically placed with respect to the other and affects mostly out-of-plane spacecraft. This issue is addressed in section 4.2.2.

Secondly, the relative positioning system performance is connected to the three-dimensionality requirement of the formation. The spacecraft must be distributed in 3D space and not arranged in a straight line or lying on the same plane. It is known that certain spatial arrangements of the spacecraft result in a degradation of determination performance of the relative distances and therefore a geometry must be found which minimizes this degradation. The relative positioning method is based on determining the satellites' positions using the distance measurements obtained from the ranging systems [39] and described in section 4.2.3 .

Thirdly, even when placed in a given formation that abides by Requirements 1 and 2, there are attitude restrictions as to where the telescopes can point to as the neighboring telescopes will occlude any target in the sky located in the same viewing direction. This results in exclusion zones characterized by areas in the instantaneous sky access which should be avoided by the telescopes when selecting the next target to observe based on a fixed formation setup. This is mostly relevant for short-baseline formations. This issue is addressed in section 4.2.4.

Finally, the process of optimizing the formation geometry is a complex one and mostly related to scientific performance. That is, following the nominal geometry established as a result of operational and geometric constraints, there still exist a set of possibilities that offer a solution to the mapping of the *(U, V)*-plane. More specifically, different combinations of relative positions and relative drift rates produce different coverages of the *(U, V)*-plane. section 4.2.5 describes ongoing efforts in attempting to establish requirements and, ultimately, to identify a set of optimized conditions which afford the best (or a set of best) *(U, V)*-plane mapping. Whereas Requirements 1 to 3 can be analyzed on a static basis, Requirement 4 demands a dynamic formation to fully evaluate the performance of the interferometer in light of the constraints imposed on the drift patterns.

The next subsection first introduces a general layout of the formation, upon which the analysis of the requirements is based. Thereafter, the subsections describe identified formation prerequisites.

4.2.1. GENERAL GEOMETRY DURING SCIENTIFIC OBSERVATIONS

A general nominal formation geometry during Scientific Observations is hereby presented. The spacecraft are distributed within a circle contained in a reference plane Π_N. The tridimensionality is afforded by an out-of-plane component (two spacecraft are positioned 'above' this plane, two are positioned 'below' the plane and the fifth one is on the plane). This general formation geometry is illustrated in Figure 4.1(a) and 4.1(b), where 'T_i' denotes the five telescopes.

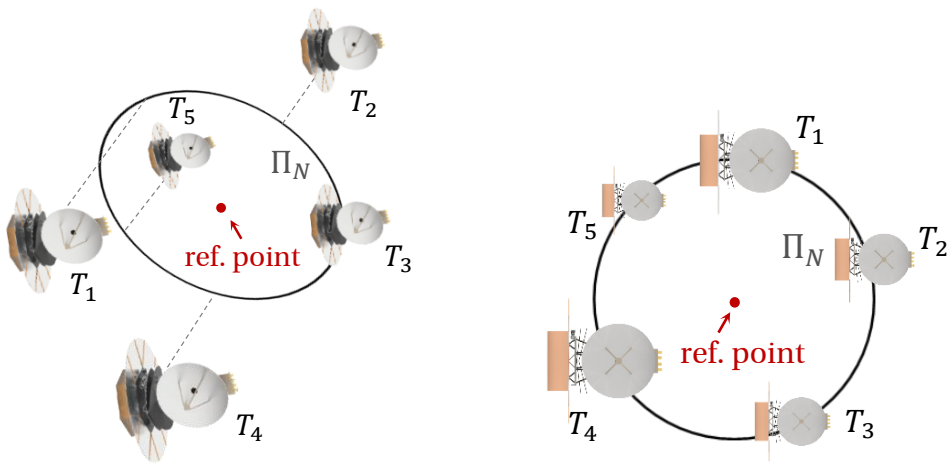

(a) Side view (b) Front view

Figure 4.1: General formation geometry arrangement relative to reference plane Π_N. Plane Π_N is aligned perpendicularly to the target direction.

From this general formation distribution, finding a formation that satisfies the four requirements described in section 4.2, depends on sizing the relative distances between the spacecraft (or analogously, the radius of the circle on which the formation is dispersed and the height above the reference plane). The first step is therefore to place a reference frame in a virtual formation center, relative to which all five spacecraft are positioned. This is illustrated in Figures 4.2(a) and 4.2(b). In Figure 4.2(a), the out-of-plane component (height) 'h_i' of each telescopes $i = \{T_1, T_2, T_3, T_4, T_5\}$ is shown and in Figure 4.2(b), the in-plane separation parameter 'd' is illustrated.

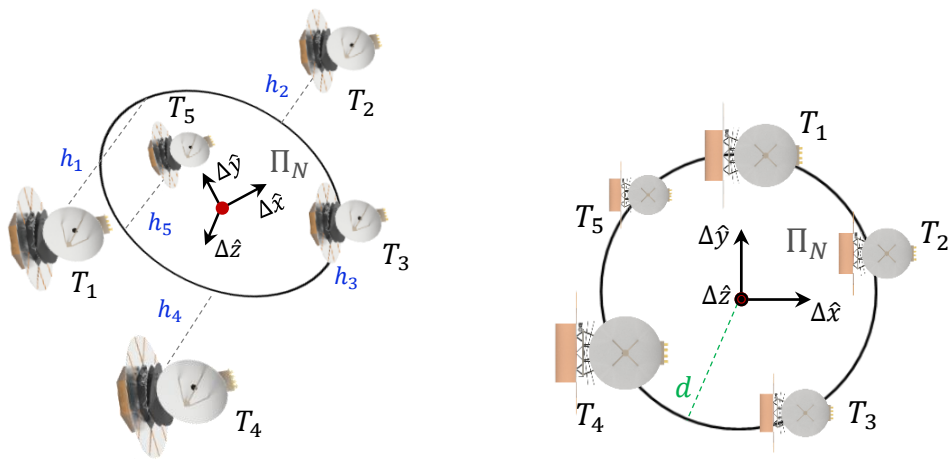

(a) Side view (b) Front view

Figure 4.2: General formation geometry arrangement relative to the local frame centered on the reference plane Π_N.

This local coordinate system $\mathscr{L}$ has the following properties:

- the Δx-axis parallel to the Sun-Earth line;

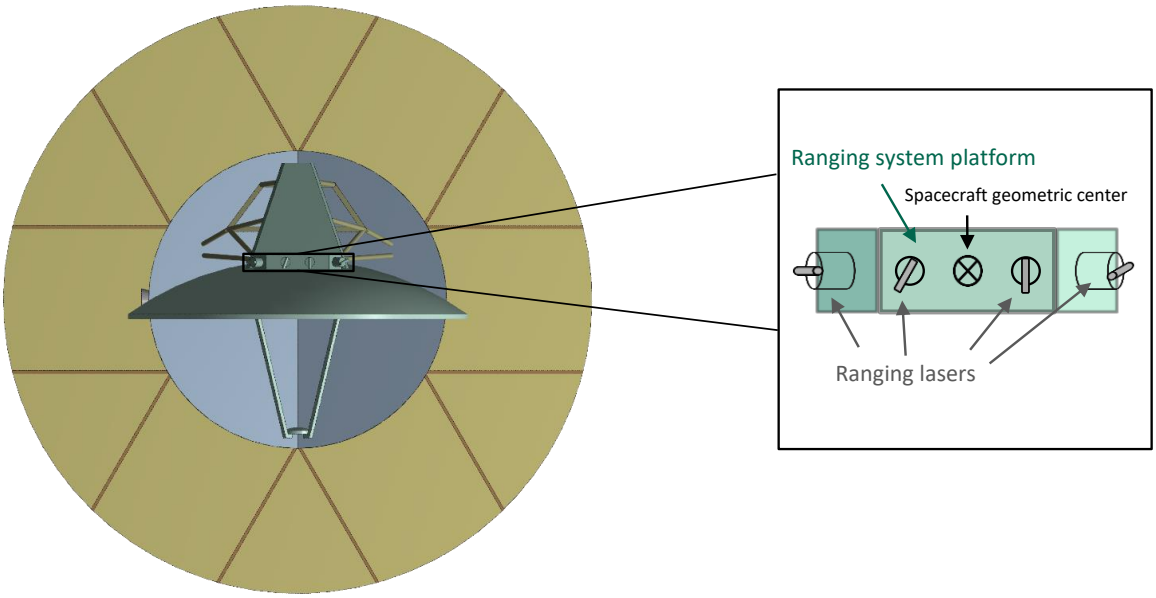

Figure 4.3: Illustration of ranging lasers mounted on the ranging system platform – top view.

- the Δz-axis normal to the ecliptic plane;
- the Δy-axis completes the right-handed reference frame.

This local $\mathscr{L}$ frame, whose origin is the 'formation center', moves about the L_2 Halo orbit and has the same orientation as the L_2-centered reference frame ('$\mathscr{L}_2$') described in Chapter 5. The geometry of the formation is described in light of the $\mathscr{L}$ reference frame. Assigning values to the coordinates of each spacecraft is a result of the requirements analysis which is described in the subsequent sections. As a basis, Requirement 1 requires that the out-of-plane component h_i is in the same order of magnitude as the in-plane separation d.

It must be remarked that the orientation of plane Π_N in the inertial frame is defined by the target direction. Therefore, although the reference frame remains fixed, the projection of d and h_i on the $(\Delta x, \Delta y, \Delta z)$ coordinates is target-dependent.

4.2.2. REQUIREMENT 1: VISIBILITY OF RANGING SYSTEM

Firstly, the visibility of the ranging system is one of the most crucial requirements in the arrangement of the spacecraft. As mentioned, the ranging system is responsible for measuring relative distances between spacecraft at very high accuracy levels in order to allow the telescopes to properly correlate the detected signals. If the spacecraft are distributed in a fashion that hampers the ranging system laser links, then the spacecraft are not able to determine their relative distances with the required accuracy.

The position and orientation of the ranging system lasers relative to the sunshield determine the sphere of inter-satellite visibility. This intervisibility between ranging systems becomes more restricted with increasing separation in the direction perpendicular to the plane of the sunshield, which occludes anything behind it.

Being mounted on a platform atop the optical bench, various combinations are possible, from the shape of the platform to its position and orientation on the optical bench, to the arrangement of the lasers on the platform and their orientation. Furthermore, for each link, it may be required that two, or even three, lasers are required for both flexibility and redundancy. It may also be the case that different spacecraft have different platform mounts to increase three-dimensionality flexibility. Attempting to optimize the geometry of the ranging system, and studying its impact on the formation geometry and visibility, quickly becomes a laborious process.

Therefore, first and foremost, the position and orientation of the ranging system lasers and platform shape need to be defined. Following the mechanical configuration design of early stages of IRASSI [35], the platform consists of a flat central part, parallel to the sunshield and a tilted part, on the edges. The platform is centered with respect to the geometric centerline which passes through the spacecraft. This is illustrated in Figure 4.3.

The tilted portion of the platform is such that the lasers mounted on this part, point directly to the edge

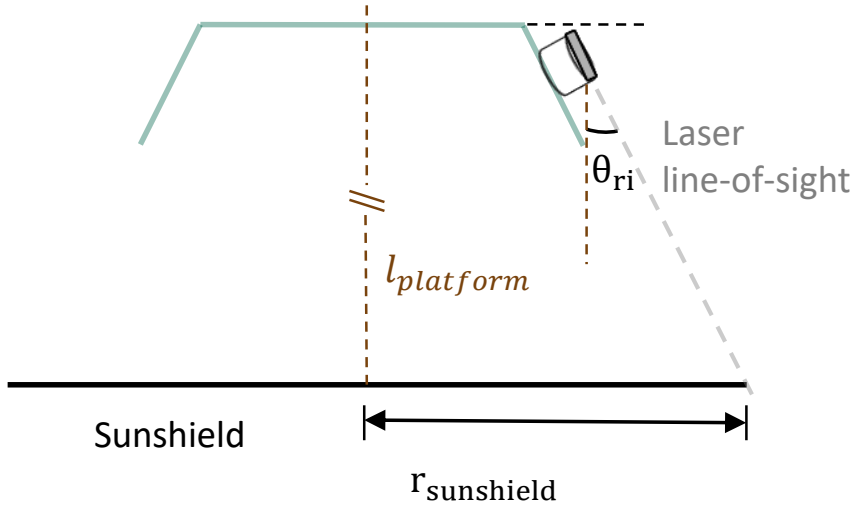

Figure 4.4: Illustration of the ranging system laser – side view. The laser is at the maximum deflection pointing to the edge of the sunshield. $r_{sunshield}$ refers to the radius of the sunshield and $l_{platform}$ is the distance between the sunshield and the ranging system platform, passing through the center of the spacecraft. The angle θ_{ri} is the instantaneous angle between $l_{platform}$ and the laser line-of-sight, pointing towards the edge of the sunshield.

of the sunshield. Note that the lasers are vectorizable (with a range between ±90° in azimuth and elevation). Hence the case considered is the limit case, with the laser pointed to the edge of the sunshield. This is depicted in Figure 4.4, where the subscript 'ri' refers to ranging invisibility. Note that the shape of the platform is assumed to be rectangular and therefore asymmetric with respect to the center of the sunshield. This means that the angle θ_{ri} will vary according to where in the platform the laser is mounted. This is addressed below. In addition, the dimensions of the mount (servomechanism) on which the lasers are positioned are neglected.

For each laser, depending on their position on the platform, a cone of invisibility may result, within which no other spacecraft should be positioned. This is illustrated in Figure 4.5, where the geometric relations between the line-of-sight of the laser and the area of ranging invisibility A_{ri} are shown. The three-dimensional area A_{ri} should be avoided by other spacecraft.

To determine A_{ri}, first and foremost, the position and orientation of the ranging system lasers needs to be conservatively assumed. As such, the present analysis postulates that the ranging lasers are centered with respect to the sunshield ($r_{dr} = 0$) and pointed directly to the edge of the sunshield. Thus, the angle θ_{ri} becomes simply the half-cone angle and r_{ri} is the radius of a symmetrical right cone. And l_{ri} passes through the center of the spacecraft.[1] As such, the angle θ_{ri} can be obtained from the spacecraft dimensions:

$$\arctan(\theta_{ri}) = \frac{r_{sunshield}}{l_{platform}} = 32.55° \tag{4.1}$$

A further assumption is that the sunshield of all spacecraft are perpendicular to the Sun direction. This means therefore that the line l_{ri} is aligned with the Δx-axis of the local formation reference frame $\mathscr{L}$.[2] and l_{ri} becomes solely a function of the in-plane parameter d (of Figure 4.2(b)), from whom the inter-satellite positions themselves depend on. Thus, for each telescope pair, i and j, the term l_{ri} may be expressed as:

$$l_{ri_{ij}} = \left|\left|\Delta x_j - \Delta x_i\right|\right|, \;\; i, j = \{T_1, T_2, T_3, T_4, T_5\} \wedge i \neq j \tag{4.2}$$

The required separation r_{ri} of the neighboring spacecraft in the Δy-Δz plane is finally obtained once l_{ri} is defined:

$$r_{ri_{ij}} = \sqrt{\left(\Delta y_j - \Delta y_i\right)^2 + \left(\Delta z_j - \Delta z_i\right)^2} \geq l_{ri_{ij}} \tan(\theta_{ri}) \tag{4.3}$$

[1] Removing this assumption would yield a nonconstant angle θ_{ri} and distance r_{ri}, giving rise to an orientation-dependent oblique elliptical cone of invisibility, asymmetrical with respect to l_{ri}.

[2] Although this assumption stipulates that the pointing of the spacecraft is 90° away from the Sun direction, the spacecraft have one full rotational degree of freedom around the Δx-axis in the $\mathscr{L}$ frame and l_{ri} will always be aligned with this axis, regardless of the pointing direction around it.

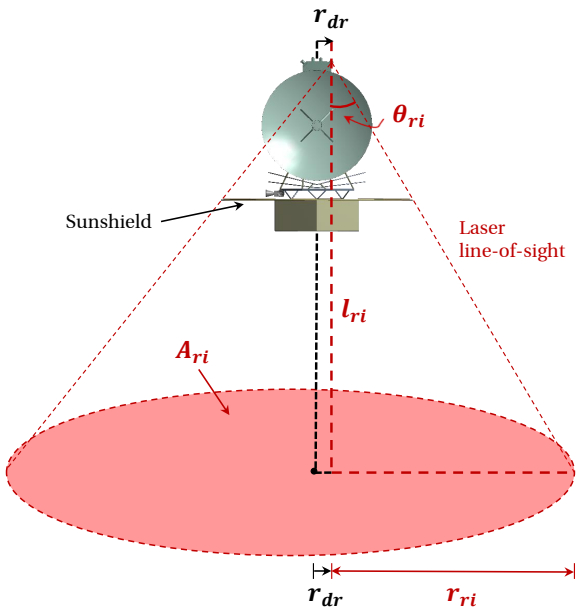

Figure 4.5: Illustration of the cone of invisibility of the ranging system. The line designated by l_{ri} is the relative distance between the ranging systems (perpendicular to the plane of the sunshield), r_{ri} is the distance between l_{ri} and the line-of-sight of the laser and the angle θ_{ri} defines the angle between the laser line-of-sight and l_{ri}. The term r_{dr} refers to the physical displacement of the ranging system laser with respect to the line which passes through the center of the spacecraft. These terms define the area A_{ri}, marked in red, which the neighboring spacecraft should avoid.

For each telescope pair, i and j, Equation 4.3 may be written as:

$$\sqrt{\left(\Delta y_j - \Delta y_i\right)^2 + \left(\Delta z_j - \Delta z_i\right)^2} \geq \left|\left|\Delta x_j - \Delta x_i\right|\right| \tan\theta_{ri} \tag{4.4}$$

Finally, given l_{ri}, the total the area of invisibility that a neighboring spacecraft A_{ri} should avoid is described as:

$$A_{ri} = \pi r_{ri}^2 \tag{4.5}$$

The magnitude of the distances l_{ri} and r_{ri} (respectively $||l_{ri}||$ and $||r_{ri}||$) is constant independent of the orientation of the spacecraft in inertial space. Nevertheless, ultimately, once the direction of the target is defined and if d and the dispersion along the plane Π_N are determined, one must then suitably size the out-of-plane heights h_i, obtain the respective Δy-Δz coordinates of the $\mathscr{L}$ system and abide by Equation 4.4, such that spacecraft stay outside each other's invisibility cone. The defined parameters in Figure 4.5 are summarized in Table 4.1.

4.2.3. REQUIREMENT 2: RELATIVE POSITIONING PERFORMANCE

As mentioned, this requirement concerns finding a formation geometry solution which minimizes the degradation of the performance of the relative positioning estimation algorithm. The spacecraft must be distributed in 3D space and not arranged in a straight line or lying on the same plane. The relative positioning method is based on determining the satellite positions using the distance measurements obtained from the ranging systems [39]. To this end, a nonlinear least-squares (LS) problem is formulated first. The LS problem is linearized, and solved by an iterative procedure thereafter. In each iteration, a linear equation system results, in the form of:

$$\boldsymbol{A} \cdot \boldsymbol{\Delta p} = \boldsymbol{b} \tag{4.6}$$

which is solved for $\boldsymbol{\Delta p} \in \mathbb{R}^n$, where $\boldsymbol{\Delta p}$ denotes a correction of the estimated satellite positions. Each row of matrix $\boldsymbol{A} \in \mathbb{R}^{m \times n}$ and vector $\boldsymbol{b} \in \mathbb{R}^m$ refers to distance measurements.

The expected accuracy of the solution strongly depends on the condition number k of matrix $\boldsymbol{A}$ [40]. The condition number $k(\boldsymbol{A})$ indicates the expected loss of accuracy in case of small variations $\delta\boldsymbol{b}$ in vector $\boldsymbol{b}$. More precisely, the expected (relative) error $\delta\boldsymbol{\Delta p}$ in $\boldsymbol{\Delta p}$ can be bounded by the product between the condition number $k(\boldsymbol{A})$ and the norm of the (relative) error $\delta\boldsymbol{b}$ in $\boldsymbol{b}$:

$$||\delta\Delta\boldsymbol{p}|| \leq k(\boldsymbol{A}) \cdot ||\delta\boldsymbol{b}|| \tag{4.7}$$

Table 4.1: Parameters for the visibility of ranging system.

Parameter	**Value**
$l_{ri_{ij}}$	$\|\|\Delta x_j - \Delta x_i\|\|$
$r_{sunshield}$ (m)	3.0
$l_{platform}$ (m)	4.7
θ_{ri} (deg)	32.55
r_{dr} (m)	0
r_{ri} limit	$l_{ri}\tan(\theta_{ri})$
A_{ri}	πr_{ri}^2

Hence, a small condition number, i.e., near to one, is preferred. The larger the condition number, the higher the potential errors in the positioning results, and the 'worse' is the selected formation geometry. If the deviations $\delta\boldsymbol{b}$ are assumed to cover only the error of the distance measurements, for example, the condition number reflects the increase of this measurement error that is induced by the formation geometry and thus, needs to be tolerated (if too high, then either the formation geometry must be changed to obtain a better condition number, or the associated degeneration of the estimation accuracy has to accepted). Similarly, a condition number of $k(\boldsymbol{A}) \approx 1000$ would result in a positioning error $||\delta\boldsymbol{\Delta p}||$ of 1 mm if a measurement error of 1 µm is assumed because $k(\boldsymbol{A}) \cdot ||\delta\boldsymbol{b}|| = 1000 \cdot 1\,\mu\text{m} = 1$ mm.

Figure 4.6(a) shows a two-dimensional example of three spacecraft arranged in an isosceles triangle: two spacecraft separated by 10 m form the base of this triangle and a third spacecraft is at the apex. If the height of the third spacecraft decreases, the condition number increases exponentially. This means that an arrangement of the spacecraft in a straight line should be avoided. With increasing height (≥ 60 m), the condition again degenerates. This is where the base angles of the triangle are about 80° or more. The lowest condition numbers are achieved when the height of the third spacecraft is between 3 m and 20 m, as Figure 4.6(b) shows. In this case, the condition number and thus, the potential error in the positioning result, is the lowest.

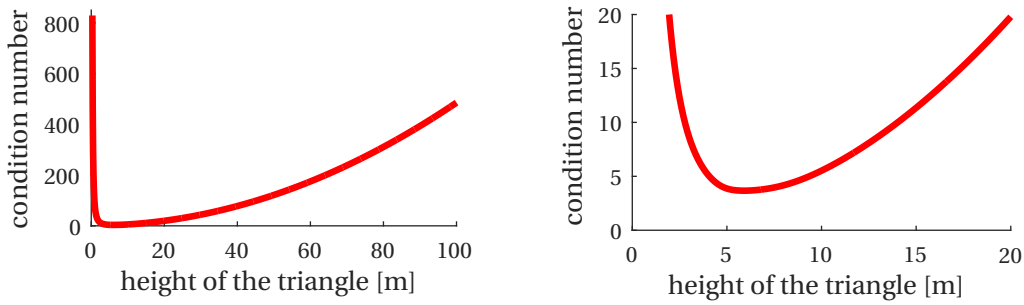

(a) Condition numbers vs. height

(b) Condition numbers vs. height - zoom

Figure 4.6: Condition numbers of a formation of three spacecraft arranged as an isosceles triangle.

The conclusion of this analysis is that the performance of the relative position algorithms is best when the height of an isosceles triangle (formed by three spacecraft) ranges from about a third to double the base length of this triangle. The shown example serves as an illustration for the basic procedure to evaluate the dependency of the formation geometry on the positioning accuracy. In the IRASSI mission, instead of three satellites in a two-dimensional space, five satellites in three-dimensional space are considered. Therefore, instead of evaluating the condition number for each subset of three satellites, the whole formation with all five satellites will be considered simultaneously. This results from the general principle of the LS algorithm, which minimizes the positioning error when it accesses all distance measurements, i.e., from one spacecraft

to any other spacecraft, at a moment in time. In the end, the goal is to select a formation geometry that satisfies the scientific requirements, i.e., which leads to a baseline accuracy of 5 µm (cf. Table 2.1) for each pair.

The positioning accuracy for the concrete IRASSI case study is evaluated by carrying out the following procedure:

1. Firstly, the distances between each spacecraft pair are calculated using the true spacecraft positions.
2. Then, the distance measurements are generated for each spacecraft pair by adding randomly generated measurement errors. The measurement errors are assumed to follow a Gaussian distribution with zero bias and 1 µm standard deviation. The measurement errors rely on an optical frequency-comb-based laser bench system from Menlo Systems GmbH, Martinsried, Germany.
3. The distance and attitude measurements are then passed to the relative positioning algorithm. A further input to the relative positioning algorithm is an initial guess of the spacecraft positions. These initial guesses are required because the relative position algorithm determines the spacecraft positions iteratively.
4. The initial guesses concerning the spacecraft positions and attitudes are produced by adding a randomly generated error to the true spacecraft positions. This error is assumed to follow a Gaussian distribution with zero bias and a standard deviation of 1 m. In operation, the initial guess of the spacecraft positions will be derived via absolute positioning using ESTRACK ground stations that measure range, range-rate and Delta-DOR (Differential One-way Ranging) of each satellite. The assumed error of 1 µm is, in the current standing, technically optimistic and refers to the expected positioning accuracy derived with ESTRACK ground stations in the future. The attitude errors are also random, Gaussian-distributed, but have a standard deviation of 0.1 arcsec.
5. After relaying the initial guesses to the relative positioning algorithm, the relative positioning algorithm can determine the spacecraft positions.
6. The relative positioning performance is then evaluated from the estimation error and the maximum baseline deviation. The estimation error is the sum of all differences between the estimated and true spacecraft positions. The maximum baseline deviation is the maximum of the absolute deviation between all true baselines and those calculated from the estimated spacecraft positions.

This procedure is carried out separately for each time instant, because the relative positioning algorithm is a snapshot method and thus, determines the instantaneous spacecraft positions. Figure 4.7 illustrates the relative position estimation procedure. If the maximum baseline deviation turns out to be smaller than the requirement baseline accuracy of 5 µm, then this formation geometry satisfies the scientific requirements.

4.2.4. REQUIREMENT 3: SKY ACCESS

The strongest determinant of the sky regions available to be observed at a given epoch is the sunshield. The sunshield limits the direction in which the spacecraft can observe, by nominally keeping the mirrors perpendicular to the direction of the Sun, and allowing a deviation of up to ±20° relative to the Δx axis. Within a simulation environment, the anti-Sun longitude is used to reference the simulation in place of the epoch. The accessible sky for the aforementioned sunshield-restricted attitude conditions for an initial anti-Sun vector longitude Λ of 85°, for instance, is illustrated in Figure 4.8, using a Plate Carrée projection [41]. In the image, the white areas denote the exclusion zones in the sky due to the sunshield and the blue area denotes the regions which are visible to the interferometer. The IRASSI sunshields and related attitude restrictions affect therefore about 48% of the celestial sky at each instant.

However, there may be further restrictions on the sky, depending on the selected target sampling strategy. The approaches described below broadly form two examples that illustrate how this process can be carried out:

- target-constrained sampling: in this case, the target is selected *a priori* from the regions of the sky that are available at a certain epoch, such that the absolute attitude of the spacecraft is defined in the celestial sphere. Thereafter, the separation of the formation over time in three-dimensional space must be computed such that the field of view of all spacecraft is not occluded during the drift of the formation, whilst simultaneously respecting Requirements 1 and 2. If all targets are selected first and the positions are subsequently determined, then no further exclusion zones have to be considered.

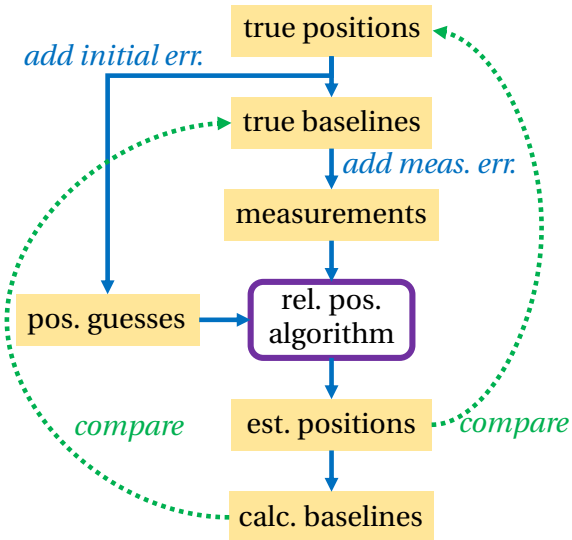

Figure 4.7: Relative position estimation procedure for a three-dimensional formation.

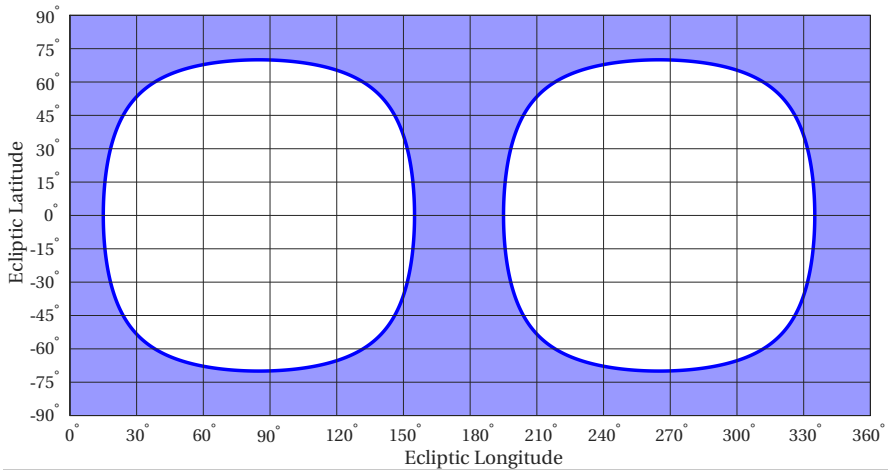

Figure 4.8: IRASSI instantaneous sky access for an anti-Sun vector longitude $\Lambda = 85°$.

- position-constrained sampling: in this case, the spacecraft's positions are selected first, abiding by Requirements 1 and 2. Only thereafter is the target selected. However, this limits the possible pointing direction of the telescopes, as they cannot target sources located 'behind' neighboring spacecraft. The result is that additional exclusion areas in the sky may have to be considered, reducing the pool of targets available at a given epoch.

Occlusion of the telescopes, even partially, is naturally undesirable as it leads to subtle phase shifts in the incoming wave signal which affect interferometric results. Additionally, hardware edges of other spacecraft may induce diffraction effects, changing the reception pattern of an antenna. The target-constrained sampling approach places the focus on the maximization of science return. This is the approach adopted in the development of iSCOUT and is therefore addressed in Part III of this thesis. Since it does not generate additional constraints in the sky, it will not be explored further in the present chapter. The position-constrained sampling, on the other hand, is analyzed due to its dependence on the formation geometry.

The issue of occlusion in the position-constrained sampling scheme is illustrated in Figure 4.9. The occlusion restrictions directly translate into considering an area around the neighboring spacecraft which should be avoided by the pointing telescope - the area is called 'exclusion zone' (to which the subscript 'ez' refers). This exclusion zone can be represented as a two-dimensional area surrounding a spacecraft (on the right-hand side of the image) on a plane perpendicular to the viewing direction of another telescope (that on the

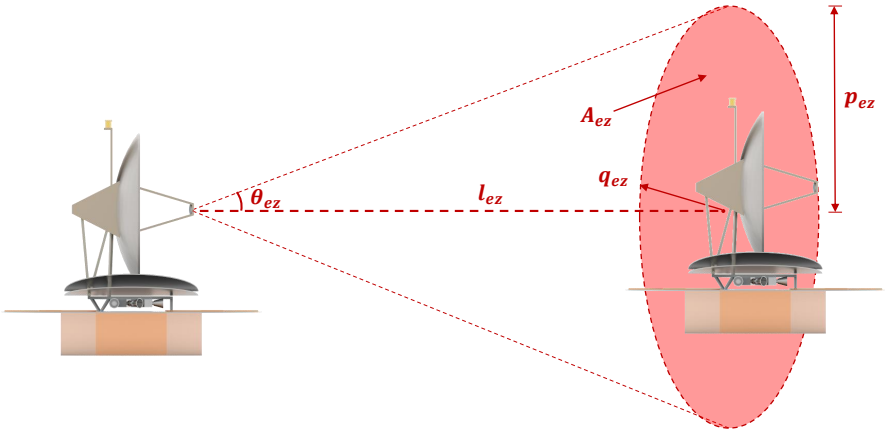

Figure 4.9: Illustration of exclusion zones. Given the θ_{ez} and the the relative distance l_{ez}, neighboring spacecraft should avoid incursions into area marked in red, A_{ez}, perpendicular to the target direction. The size of this area is given as a function of the cone base radius q_{ez}.

left-hand side of the image). A conical shape can then be used to estimate the size of the exclusion area. The height of the cone is defined by the physical separation of the telescopes. The base of the cone is solely dependent on the neighboring spacecraft's dimensions (width and height) and should also factor in safety margins due to signal diffraction effects. Since the sunshield must broadly be perpendicular to the Sun direction and the sunshield of both spacecraft are parallel, essentially the radius of the sunshield and the height of the spacecraft determine the size of the base of the cone, whereby an ellipse can be used as a first approximation for the base's geometry. With the radius of the sunshield $r_{sunshield}$ measuring 3 m, the height of the spacecraft h_{sc} totaling 5.7 m and considering a one-meter margin, the semi-major q_{ez} and semi-minor p_{ez} axes of the cone base are given as:

$$q_{ez} = r_{sunshield} + 1\,\mathrm{m} = 4\,\mathrm{m} \tag{4.8}$$

$$p_{ez} = \frac{h_{sc}}{2} + 1\,\mathrm{m} = 3.85\,\mathrm{m} \approx 4\,\mathrm{m} \tag{4.9}$$

The variables q_{ez} and p_{ez} respectively depend on the width and height of the spacecraft and define the dimensions of the base of the exclusion zone cone. Given the proximity of the two dimensions in Equations 4.8 and 4.9, the value of p_{ez} was rounded up to that of q_{ez} for simplification and one can then contemplate a right circular conical geometry. As such, in Figure 4.9, q_{ez} and p_{ez} are equal measures of the cone base radius, l_{ez} is the distance between the spacecraft, θ_{ez} is the cone semi-angle and A_{ez}, in red, identifies the area around a spacecraft which other telescopes should avoid pointing towards. The area A_{ez} is fixed for all spacecraft and simply calculated as:

$$A_{ez} = \pi \cdot q_{ez} \cdot p_{ez} = \pi \cdot q_{ez}^2 = \pi \cdot p_{ez}^2 \tag{4.10}$$

As the relative distance l_{ez} increases, the half-angle of this cone decreases. The result of this is that the instantaneous sky access is more limited when distances are small and, conversely, less restricted when l_{ez} is larger. This becomes clear from the circular cone half-angle equation, keeping in mind that the plane containing A_{ez} is perpendicular to the relative position vector $\boldsymbol{l_{ez}}$:

$$\theta_{ez} = \arctan\left(\frac{q_{ez}}{l_{ez}}\right) = \arctan\left(\frac{p_{ez}}{l_{ez}}\right) \tag{4.11}$$

The relative position vector $\boldsymbol{l_{ez}}$ between two spacecraft, i and j, is defined in the local $\mathscr{L}$ frame defined at the start of Section 4.2.1:

$$\begin{aligned} l_{ez_{ij}} &= \sqrt{\left(\Delta x_j - \Delta x_i\right)^2 + \left(\Delta y_j - \Delta y_i\right)^2 + \left(\Delta z_j - \Delta z_i\right)^2}, \\ i, j &= \{T_1, T_2, T_3, T_4, T_5\} \wedge i \neq j \end{aligned} \tag{4.12}$$

Finally, the projected exclusion zone area on the celestial sky $A_{ez_{proj}}$ is given by:

$$A_{ez_{proj}} = \pi \cdot \theta_{ez}^2 \tag{4.13}$$

Table 4.2: Parameters for exclusion zone of the sky.

Parameter	**Value**
$r_{sunshield}$ (m)	3
h_{sc} (m)	5.7
Margin (m)	1
q_{ez}, p_{ez} (m)	4
A_{ez}	$\pi \cdot q_{ez} \cdot p_{ez}$
$l_{ez_{ij}}$	$\sqrt{(\Delta x_j - \Delta x_i)^2 + (\Delta y_j - \Delta y_i)^2 + (\Delta z_j - \Delta z_i)^2}$
$\theta_{ez_{ij}}$	$\arctan\left(\frac{q_{ez}}{l_{ez_{ij}}}\right) = \arctan\left(\frac{p_{ez}}{l_{ez_{ij}}}\right)$
$A_{ez_{proj}}$	$\pi \cdot \theta_{ez}^2$

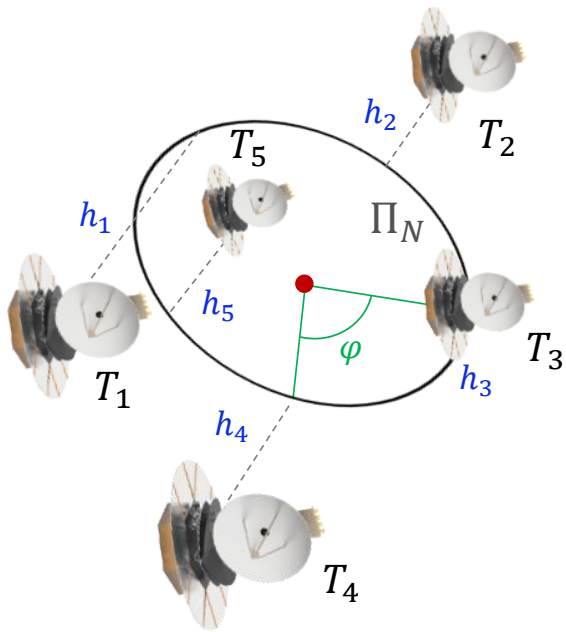

Figure 4.10: In-plane separation φ and out-of-plane h parameters. Π_N defines the reference plane.

With the dependence of $A_{ez_{proj}}$ on the cone semi-angle θ_{ez}, the size of $A_{ez_{proj}}$ will appear different, depending on whether the spacecraft are close to each other or far apart. Table 4.2 summarizes the parameters which define the exclusion zones.

The next paragraphs assess how the relative distance among spacecraft and their arrangement in inertial space affects the overall sky access of the interferometer. For this purpose, the formation geometry of Figure 4.2 is set as a reference, and the in-plane separation φ between consecutive telescopes, illustrated in Figure 4.10, is fixed at equal intervals of $\frac{2\pi}{5}$ =72°. For simplicity, the out-of-plane component set h is defined as a function of the separation parameter d, as summarized in Equation 4.14. The order in which the pool of out-of-plane component h is attributed to each telescope is arbitrary.

$$h = \left\{-d, -\frac{d}{2}, 0, \frac{d}{2}, d\right\}, \tag{4.14}$$

Two different pointing directions of the formation are analyzed and, for each, two different separation parameters d values are used, resulting in four different tested conditions. The pointing directions are parallel to the Δy-Δx plane and parallel to the Δz-Δx plane, whereas d is valued at 10 and 100 m. The pointing direction of the formation can be analogous to setting the orientation of the plane Π_N in the $\mathscr{L}$ reference frame. Due to sunshield restrictions, the Π_N plane may revolve boundlessly around the Δx-axis, but not the other two axes. Note that the pointing direction also defines the direction along which h, described in Equation 4.14, is expressed. When plane Π_N is parallel to the Δy-Δx plane, then $\boldsymbol{h_i} = h_i \boldsymbol{\Delta z}$; similarly, if plane Π_N is parallel to the Δz-Δx plane, then $\boldsymbol{h_i} = h_i \boldsymbol{\Delta y}$.

It should be remarked that the formation arrangement resulting from the assumed values of d and h_i, defined in Equation 4.14, does not necessarily abide by Requirements 1 and 2, as the interest here lies in simply evaluating how relative position constrains the science exercises during the operational phase by limiting access to regions of the sky.

The instantaneous sky access is given in Figures 4.11 and 4.12 with the corresponding labels. The labels denote which telescope pair is considered: for instance 'T_1-T_2' refers to the exclusion zone imposed on telescope T_1 by telescope T_2. Two exclusion zones of equal area arise for each telescope pair, located at diametrically opposite sides of the celestial sphere. For reference purposes, the 'first' telescope, T_1 was aligned with the in-plane axis defined by $\Delta x = 0$ and the assignment of out-of-plane separations h_i, $i = \{T_1, T_2, T_3, T_4, T_5\}$ corresponds to $h_i \in h = \left[d, -\frac{d}{2}, 0, -d, \frac{d}{2}\right]$.

Table 4.3: Percentage of exclusion zone A_{rest} affecting the celestial sky for different test conditions.

Formation pointing direction in the $\mathscr{L}$ frame	$\boldsymbol{A_{rest}}$	
	$\boldsymbol{d}$ **= 10 (m)**	$\boldsymbol{d}$ **= 100 (m)**
Parallel to Δy-Δx plane	16.00	0.17
Parallel to Δz-Δx plane	16.00	0.17

From Figures 4.11 and 4.12, it is clearly observable that smaller formations result in larger exclusion areas of the sky. Table 4.3 summarizes the percentage of total restricted area A_{rest} for observations according to the tested conditions, with A_{rest} defined by:

$$A_{rest} = \frac{\sum_{i}^{n} \sum_{j:j\neq i}^{n} A_{ez_{proj,ij}}}{A_{sky}} \tag{4.15}$$

where $A_{ez_{proj,ij}}$ is described by Equation 4.13 and $A_{sky} = 180° \times 360°$ deg^2 is the total sky area.

With the current setup, a one-order-of-magnitude increase of in-plane separation d, results in a total projected area approximately two orders of magnitude smaller. This is expected since the out-of-plane separation h is also scaled relative to d (and $\frac{d}{2}$). The distortion of the exclusion zones due to the Plate Carrée projection [41] increases in the direction of the poles, causing the projected areas to gradually lose the circularity observed at Equatorial latitudes. Further details of the transformation from the local $\mathscr{L}$ frame to the projected exclusion can be found in section Appendix B.1.1.

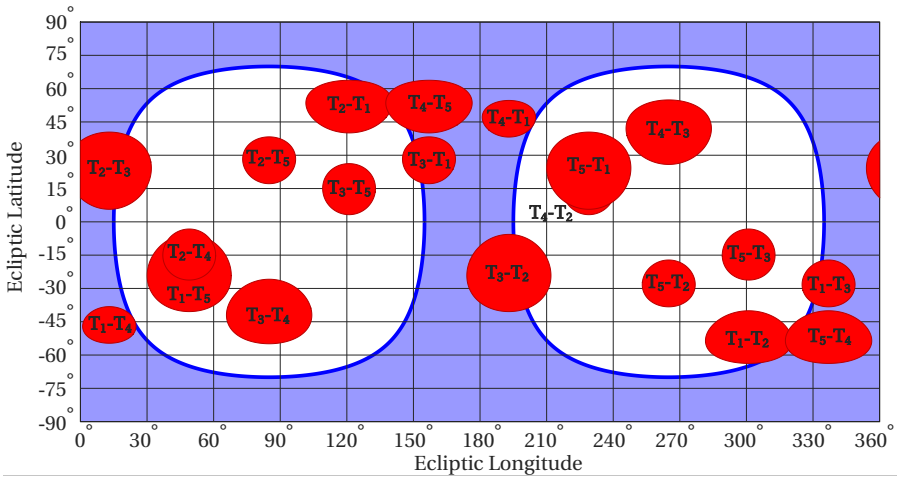

(a) $d = 10$ m

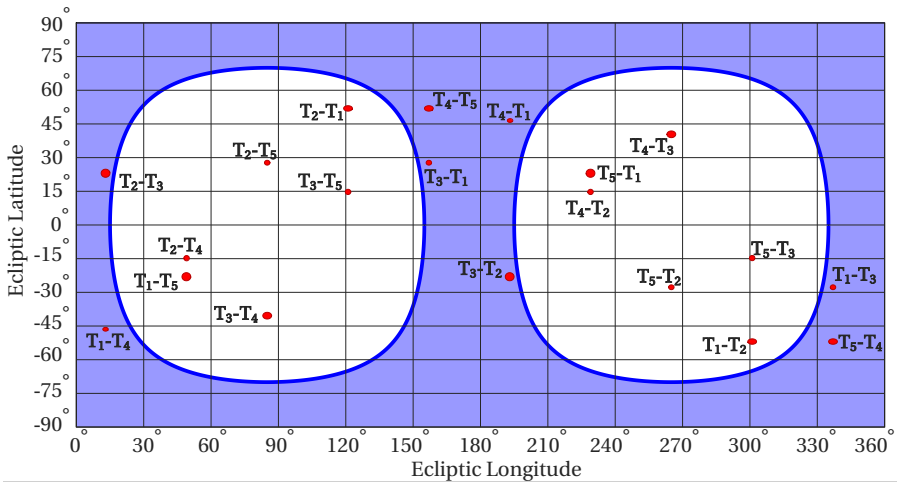

(b) $d = 100$ m

Figure 4.11: Instantaneous sky access for a formation pointing direction parallel to Δy-Δx plane for an anti-Sun vector longitude $\Lambda = 85°$.

Additionally, in general within Figures 4.11 and 4.12, the shortest the distance among telescope pairs, the larger the exclusion zone area (although the distortion of the projection may mask these effects). The relative distance $l_{ez_{ij}}$ between telescope pairs i and j can be computed with Equation 4.12. Alternatively, to provide a meaningful analysis of the impact of the relative separation parameters d and h on the sky access, $l_{ez_{ij}}$ can be calculated by simple trigonometry:

$$l_{ez_{ij}} = \sqrt{4d^2\left[1-\cos^2\left(\Delta\varphi_{ij}\right)\right] + (\Delta h_{ij})^2} \tag{4.16}$$

where $\Delta\varphi_{ij}$ is the shortest in-plane angular separation between any pair of telescopes, given by:

$$\Delta\varphi_{ij} = k\frac{2\pi}{5}: \;\; k = 1 \vee k = 2 \tag{4.17}$$

and Δh_{ij} is the separation of the spacecraft along the direction normal to the Π_N plane, such that:

$$\Delta h_{ij} = h_j - h_i \tag{4.18}$$

Tables 4.4 and 4.5 show the relationship between inter-satellite distances and size of the projection exclusion zone, respectively for the $d = 10$ m and $d = 100$ m conditions (which applies regardless of the orientation of the Π_N plane). The area $A_{ez_{proj}}$ was calculated using Equation 4.13.

Since the formation is arranged relative to the reference plane Π_N and the separation parameters are the same for the different plane Π_N orientations, the ratios between exclusion zone and total sky area are

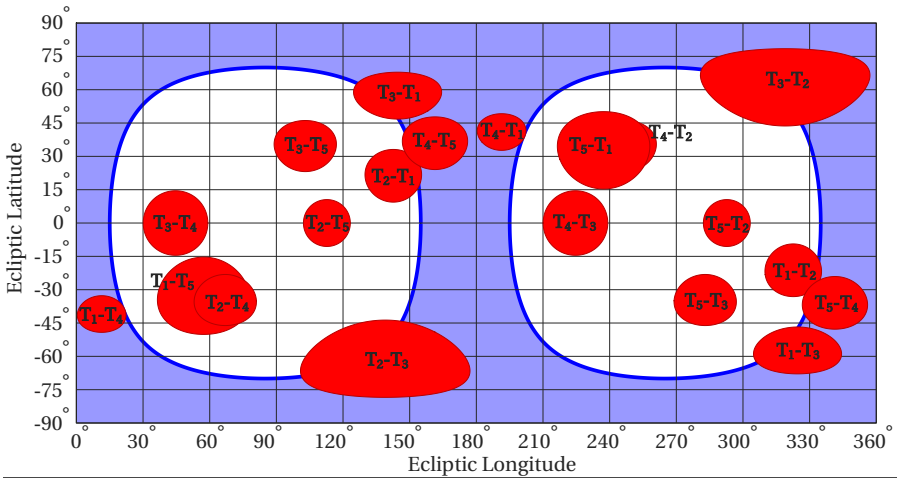

(a) $d = 10$ m

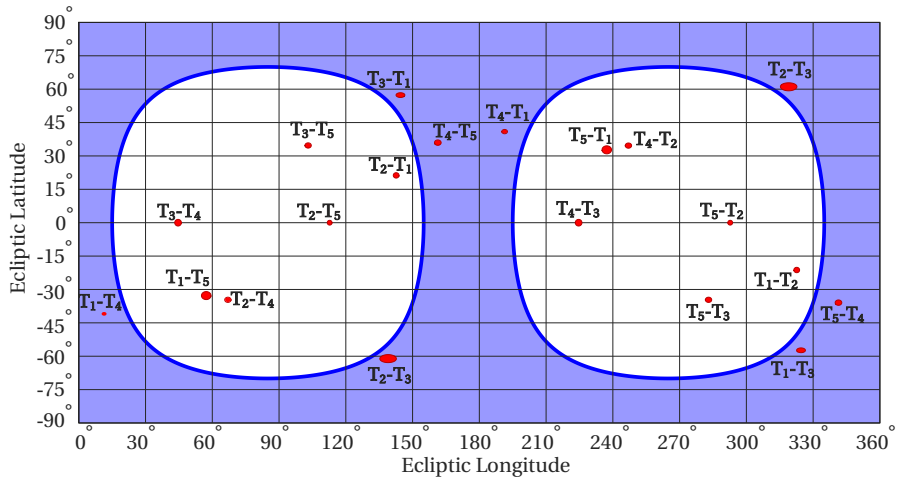

(b) $d = 100$ m

Figure 4.12: Instantaneous sky access for a formation pointing direction parallel to Δz-Δx plane for an anti-Sun vector longitude $\Lambda = 85°$.

maintained, as seen in Table 4.3. However, the location of the projected areas in the sky is contingent on the orientation of plane Π_N. For a fixed in-plane separation, for an orientation of the plane Π_N parallel to the Δz-Δx plane, the larger the out-of-plane separation, the lower the latitude of the projected exclusion zone (that is, exclusion zones will tend to the celestial Equator). Conversely, longer out-of-plane distances result in higher latitudes of the projected area for a Π_N orientation parallel to the Δy-Δx plane (that is, exclusion zones will tend to the celestial poles), for a fixed in-plane separation. Further results available in section Appendix B.1.2 demonstrate precisely the connection between h and projection latitude.

The importance of this analysis lies in understanding the relationship between relative-position assignment and sky visibility. If the formation can be adjusted 'on-the-fly', the ratio between separation parameters d or h can be dynamically regulated by mission planners over different observation tasks [3] and tailored accordingly, depending on whether the telescopes are sampling the polar regions or the Equatorial regions of the sky.

4.2.5. REQUIREMENT 4: SCIENCE PERFORMANCE

Finally, the process of optimizing the formation geometry is a complex one and mostly related to the performance of science activities, or the quality of the obtained results. That is, following a given geometry established as a result of previous requirements, there still exists a set of possibilities that offers a solution to the mapping of the *(U, V)*-plane. More specifically, different combinations of relative positions, attitudes

[3] By virtue of constant relative drift only, the relationship remains fixed.

Table 4.4: Relative distance and total projected area $A_{ez_{proj}}$ between telescope pairs, for $d = 10$ m.

Telescope pair	$l_{ez_{ij}}$ **(m)**	$\theta_{ez_{ij}}$ **(deg)**	$A_{ez_{proj}}$ **(deg^2)**	**Telescope pair**	$l_{ez_{ij}}$ **(m)**	$\theta_{ez_{ij}}$ **(deg)**	$A_{ez_{proj}}$ **(deg^2)**
$T_1 - T_2$	19.1	11.9	441.4	$T_2 - T_4$	19.7	11.5	415.2
$T_1 - T_3$	21.5	10.5	349.3	$T_2 - T_5$	21.5	10.5	349.3
$T_1 - T_4$	27.6	8.2	213.6	$T_3 - T_4$	15.4	14.5	663.2
$T_1 - T_5$	12.8	17.4	949.6	$T_3 - T_5$	19.7	11.5	415.2
$T_2 - T_3$	12.8	17.4	949.6	$T_4 - T_5$	19.1	11.9	441.4

4

Table 4.5: Relative distance and total projected area $A_{ez_{proj}}$ between telescope pairs, for $d = 100$ m.

Telescope pair	$l_{ez_{ij}}$ **(m)**	$\theta_{ez_{ij}}$ **(deg)**	$A_{ez_{proj}}$ **(deg^2)**	**Telescope pair**	$l_{ez_{ij}}$ **(m)**	$\theta_{ez_{ij}}$ **(deg)**	$A_{ez_{proj}}$ **(deg^2)**
$T_1 - T_2$	190.6	1.2	4.5	$T_2 - T_4$	196.7	1.2	4.3
$T_1 - T_3$	214.9	1.1	3.6	$T_2 - T_5$	214.9	1.1	3.6
$T_1 - T_4$	276.0	0.8	2.2	$T_3 - T_4$	154.3	1.5	6.9
$T_1 - T_5$	127.7	1.8	10.1	$T_3 - T_5$	196.7	1.2	4.3
$T_2 - T_3$	127.7	1.8	10.1	$T_4 - T_5$	190.6	1.2	4.5

and relative drift rates produce different coverages of the *(U, V)*-plane. Ongoing efforts aim to establish basic patterns in the formation motion configuration over time which produce, in general, agreeable *(U, V)*-plane coverage and hence synthesized images of the celestial targets. There is no universal optimal formation motion configuration / *(U, V)*-plane coverage or a simple figure-of-merit: this is dependent on the structure and geometry of the target being observed.

For ground-based interferometers with many antenna elements, such as ALMA (Atacama Large Millimeter Array) or JVLA (Jansky Very Large Array), the natural Earth rotation is used to fill the *(U, V)*-plane, as the projected baselines towards the targets change under this rotation. This natural rotation is not available for space interferometers located near L_2. There are interferometer concepts that introduce an artificial rotation of two or three space antenna elements around a common center (e.g., SPIRIT [10]), and in combination with a radial in/out motion of the satellites, quite dense sampling of the *(U, V)*-plane can be achieved over time [42]. Such concepts usually include, however, the need to have these antennas connected via a common mechanical structure (truss), and hence the practical maximum baseline lengths are limited to a few tens of meters. With IRASSI, a spatial resolution of 0.1 arcsec at the longest foreseen wavelengths of 300 µm is required, which demands maximum baseline lengths of several hundred meters.

In the current IRASSI concept, the five telescope elements will drift on approximately straight trajectories and with constant drift velocities. As a result, also the trails in the *(U, V)*-plane will be straight lines. Within this framework, boundaries can be specified to avoid a poor *(U, V)*-plane coverage. In particular, overly symmetric configurations (e.g., all satellites drifting with the same velocity, regularly spaced and with the same angles relative to each other) would result in degeneracies in the sampling function and particularly strong side lobes away from the center of the synthesized beam that follows as the Fourier transform of the *(U, V)* sampling function [24]. Furthermore, satellite paths that all start from (or converge to) one virtual intersection point should be avoided since the resulting trails in the *(U, V)*-plane would be straight radial lines instead of curved lines which would further limit the homogeneity of the *(U, V)*-plane coverage. Also, different drift velocities and different relative angles should be selected to cover more unique areas in the *(U, V)*-plane.

Figure 4.13 illustrates this issue, for a case in which the plane parallel to the wavefront (and also parallel to

the (*(U, V)*-plane) is aligned with (Δx, Δy) plane defined in Figure 4.1 and the target is therefore located in the direction of Δz. The projected satellite paths are shown, where the leftmost image illustrates an undesirable satellite path geometry, leading to strong degeneracies in the *(U, V)*-plane coverage, while the middle image shows a more acceptable configuration that will better sample the *(U, V)*-plane. In Figure 4.13(c), (x_i, y_i) are the coordinates of satellite Sat_i, β_i defines its corner angle in the projected shape of the formation in the (Δx, Δy) plane and L_i is the sampling length of Sat_i.

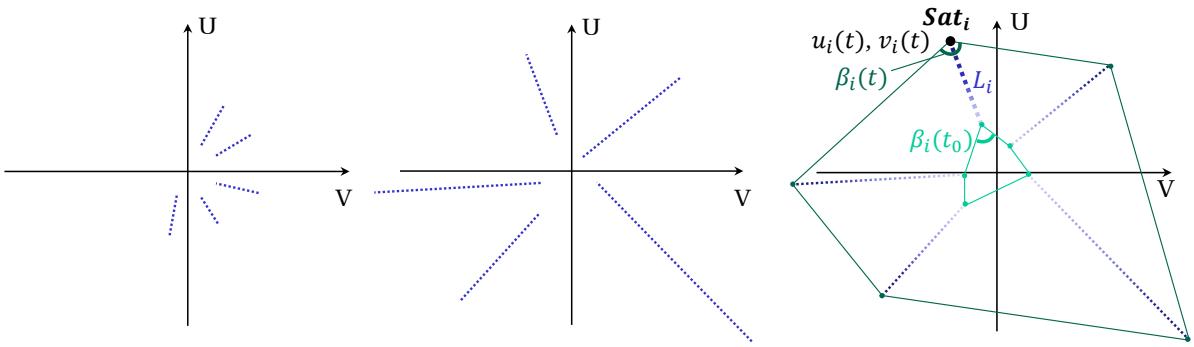

(a) Less desirable configuration (b) More desirable configuration (c) Corner angles

Figure 4.13: Illustration of the different (projected) satellite paths configurations.

Such requisites can be described in geometric terms. On a first approach, a certain 'asymmetry' seems to be desirable in the projected satellite paths, and therefore the difference between the internal angles β_i in this (Δx, Δy)-plane should be maximized. A measure of asymmetry, A_sN (Asymmetry Number), can thus be defined at each point in time t:

$$A_sN(t) \propto max\left[\sum_{i=1}^{n-1} \beta_{i+1}(t) - \beta_i(t)\right] \tag{4.19}$$

where n is the total number of spacecraft in the formation. Maximizing A_sN over an observation period would then correspond to finding the best relative position - attitude - relative drift rate combination across the whole formation which would yield an improved *(U, V)*-plane coverage. Different relative drift rates means that the angle β_i is not constant, and for the ith spacecraft one obtains:

$$\frac{\partial \beta_i(t)}{\partial t} \neq 0 \tag{4.20}$$

Additionally, the length of a projected baseline determines whether small or high spatial frequencies are probed. For example, by employing long baselines between the telescopes of an interferometer, one is susceptible to high spatial frequencies that carry information on such small spatial scales. Therefore, the relative distances can be fixed so as to probe finer spatial details of an intensity distribution:

$$\int_{t_0}^{t} |x_{i+1}(t) - x_i(t)\, dt| \geq x_{des} \wedge \int_{t_0}^{t} |y_{i+1}(t) - y_i(t)\, dt| \geq y_{des},\ i = 1, ..., 5. \tag{4.21}$$

where x_{des} and y_{des} are desired values for the projected baseline distances in the (Δx, Δy) plane parallel to the wavefront. Similarly, if for a given observation a fixed projected sampling length L_i has to be prescribed one can use:

$$[x_i(t) - x_i(t_0)]^2 + \left[y_i(t) - y_i(t_0)\right]^2 \geq L_i^2. \tag{4.22}$$

The final intensity distributions obtained by the free-flying interferometer are obtained *a posteriori*, for which the Fourier transform of the achieved (U, V) coverage (i.e., the *(U, V)* sampling function) plays an important role. This procedure is complex and the related deconvolution techniques are discussed in detail in Reference 24.

The metrics described in Equations 4.19 until 4.22 are useful for predicting, for example, how the *(U, V)*-plane is ultimately expected to be filled given a formation. Equally, they allow to somewhat prescribe changes in the formation geometry based on desirable *(U, V)*-plane coverage conditions.

Two remarks should be made here. The first one is that different relative drift rates, as translated by Equation 4.20, imply that the shape of the geometry is not maintained over the course of the observation period. Therefore, it should be ensured that a nominal formation geometry considers an envelope around it which accommodates slightly different formation shapes.

The second remark has to do with the fact that the relative distances can never physically be zero (which would mean a collision) and, therefore, there are automatically areas in the *(U, V)*-plane that cannot be sampled, (e.g., $u = v = 0$). In astronomy terms, this is called the 'missing zero-spacings information'. It means that the intensity contributions arising from very small spatial frequencies cannot be retained by the interferometer, and depending on the complexity of the structure of the celestial targets, also the information about the total intensity associated with that object is lost. One can attempt to compensate for such a deficiency by obtaining complementary information from the single telescopes and other space-based missions operating in the far infrared. In an ideal case, there should be an overlap between the spatial frequencies probed by the single-dish observations and the interferometer, which is hard to achieve for most of the relevant past, present and future mission with their small aperture sizes of 2.5 m–3.5 m (Herschel, SOFIA, SPICA). The long-term future might bring larger aperture single-dish missions like Millimetron [8] or the Origins Space Telescope [4] that will come with telescope sizes of 10 m–15 m. More information about interferometry and radio astronomy can be found, for example, in Reference 24.

Although the requirement is described here, these metrics reflect preliminary efforts at quantifying *(U, V)*-plane sampling by looking at formation patterns over time. Similarly, it only makes sense to evaluate performance under controlled dynamics, that is, when the free-drifting telescopes actively expand and contract (after an initial impulse), which is when the *(U, V)*-plane is filled with sample points. The conditions analyzed in Part II do not involve any control input prior to the observations and hence do not allow to properly evaluate the effect of the formation geometry on the science performance. This topic is instead explored in Part III of this thesis.

4.3. IRASSI NOMINAL GEOMETRY DURING SCIENCE OBSERVATIONS

GIVEN the aforedescribed requirements and constraints, a general nominal formation for IRASSI is defined. The shape of this formation is described by the in-plane and out-of-plane separation parameters, respectively, d and h. Specifically, the value of h of the telescopes is tailored to abide by the imposed requirements, whilst keeping its dependency on d: this means that regardless of the length of the baselines (i.e., irrespective of whether the formation is in a contracted or expanded state), the geometry is maintained.

The out-of-plane separation parameter set is thus:

$$\boldsymbol{h} = \{-4d, -2d, 0, 2d, 4d\}\, \boldsymbol{\Delta z}, \tag{4.23}$$

whereby each element of h is to be distributed by the five spacecraft and whereas d should be kept within the range:

$$10 \leq d \leq 1000 \tag{4.24}$$

Assuming that the pointing direction of the telescopes is perpendicular to plane Π_N and recalling Equation 4.16, the actual baselines B_{ij} between formation members which are used for the interferometry correlations (cf. Section 2.3.2) is given as:

$$B_{ij} = \sqrt{4d^2\left[1 - \cos^2\left(\Delta\varphi_{ij}\right)\right]} \tag{4.25}$$

whereas the geometric delay g_{ij} corresponds to:

$$g_{ij} = \sqrt{(\Delta h_{ij})^2},\ \ i, j = \{T_1, T_2, T_3, T_4, T_5\} \wedge i \neq j \tag{4.26}$$

It is possible to conclude from Equation 4.25 that the dispersion of the spacecraft is symmetric relative to plane Π_N and that the separation among spacecraft is greatest along a direction perpendicular to the plane. Table 4.6 provides the minimum and maximum baseline, geometric delay and relative distances among members of the formation, for different parameters of d. Generally, the ratio between maximum and minimum separations l_{ij} varies between about 2–3.5 among spacecraft, whereas the maximum baseline length has a proportion of about 1.6 relative to the minimum one. One of the top-level mission requirements is that

[4] https://asd.gsfc.nasa.gov/firs/

Table 4.6: Extrema of baseline B_{ij}, geometric delay g_{ij} and relative distances l_{ij} of the nominal formation, with varying d values.

Parameter	d = 10 m		d = 500 m		d = 1000 m	
	Min	Max	Min	Max	Min	Max
B_{ij} (m)	11.8	19.0	587.8	951.1	1175.6	1902.1
g_{ij} (m)	20.0	80.0	250.0	1000.0	2000.0	8000.0
l_{ij} (m)	23.2	82.2	638.7	1380.0	2319.9	8223.0

baselines lengths do not exceed 850–1000 meters during the observations. From a scientific point of view, this is clearly achieved for $d \leq 500$ m for certain spacecraft pairs, as shown in Table 4.6. However, from an operational point of view, the formation may benefit from acquiring their designated formation positions first and allow a certain amount of time after the start of the drift for residual vibrations to subside due to the (contraction/expansion) maneuver thrust, for calibration activities to take place, for locking the ranging system lasers and/or for acquiring the required attitude pointing precision towards the target and only then explore the full baseline length regime associated with each target for science observations. For targets demanding long baselines, this would mean extending the value of d to accommodate for such activities and, as such, $d = 1000$ m was selected as the limit.

It should also be mentioned that the nominal formation set out by specifying h according to Equation 4.23 is not the limit case for which the aforedescribed requirements are unconditionally met over time. Instead, an acceptable envelope can be defined around these conditions, whereby the spacecraft relative distances may deviate between ≈200 %–2500 %, depending on the formation pair being considered before Requirement 1 is violated, for instance. This envelope of acceptable inter-satellite distances is of interest when the spacecraft are expanding or contracting at different rates, as this would cause the nominal formation to degrade. Indeed, as seen in Section 4.2.5, a degradation of the nominal formation is desirable for better coverage of the *(U, V)*-plane. The present analysis sets thus the nominal case and the boundaries of this operational envelope of the formation.

Compliance with Requirements 1 to 3 is evaluated in Chapter 5 for a free-flying formation without thrust control. The implementation of Requirements 1, 2 and 4 is addressed in Chapter 11, where the baseline patterns and associated maneuvers are optimized for individual targets during the science phase of the mission.

4.4. CHAPTER SUMMARY

THIS chapter identifies and describes key geometrical and operational constraints requirements which must be considered during the operational part of the mission. They are the intervisibility of the ranging system, the baseline estimation accuracy, the accessibility of the sky and the scientific performance of the interferometer as a whole. The intervisibility of the ranging system is dictated by the sunshield dimensions, whereas the baseline estimation favors non-planar and non-linear formation arrangements due to the ambiguity of the relative positioning errors. These requirements have a direct impact on the performance of the formation and because they constrain the distribution of the spacecraft in three-dimensional space, they serve as a basis for the construction of a nominal formation geometry. From a generic formation distribution referenced with respect to a given plane Π_N, nominal in-plane and out-of-plane separation parameters are defined, culminating in a largely asymmetric formation.

Whereas the first two requirements depend on the ratios between relative distances, the sky access is directly dependent on the absolute distances among the spacecraft. Their evolution with respect to time is addressed in the next chapter in free-drift conditions, i.e., without any control input. Because evaluating science performance is only meaningful upon an optimized contraction or expansion of the baselines during science operations, the last requirement is addressed in Part III, in Chapter 11.

5

Formation Dynamics

The lack of understanding of something
is not evidence of God.
It's evidence of a lack of understanding.

Lawrence Krauss

ABSTRACT

Chapter 5 provides a detailed analysis of the formation dynamics in free-drift conditions in a Halo orbit around L_2. Firstly, an analytical model for relative motion is validated for short-term simulations, whereby relative position errors of up to 10% can be expected over time, depending on the location of the formation in the orbit. The modeling error is nonetheless independent of the selected epoch. Finally, the evolution of the formation over time is measured relative to the nominal initial conditions, set out in Chapter 4. A set of metrics, such as drift and drift rates, angular tilt, visibility of the ranging system, relative positioning performance and sky access are used to evaluate the change of the formation geometry. Whereas the overall deformation is independent of the location in the reference orbit, the orientation of the formation in inertial space affects the rate of change of the formation, with an orientation of the reference plane Π_N perpendicular to the ecliptic associated with a faster degeneration. Nonetheless, for the time scales of interest and all conditions tested, the nominal formation geometry remains stable over time and satisfies the formation requirements in free-drift conditions, without the risk of an imminent violation of geometry or performance requirements.

Publication

L. Buinhas, K. Frankl, H. Linz and R. Förstner, *IRASSI InfraRed Space Interferometer: Formation Geometry and Relative Dynamics Analysis*, Acta Astronautica **153**, 394-409 (2018).

5.1. INTRODUCTION

THE aim of this chapter is to provide an analysis of the relative motion among spacecraft in their orbit around L_2. The first step involves setting the equations of motion of the formation reference point, in its orbit around L_2, in Section 5.2. Thereafter, in Section 5.3, the equations of relative motion are provided. These are obtained by subtracting the equations of motion of the spacecraft relative to L_2 from the formation reference point.

The results of relative dynamics are presented in two phases. In the first phase, one single spacecraft relative to the formation center is considered, in Section 5.3, in order to validate the relative dynamics model and to gain insight into what parameters influence relative motion, when the dynamics are guided solely by gravitational forces of the Sun and the Earth-Moon primary bodies.

In the second phase, in Section 5.4, the equations of relative motion are extended to a five-spacecraft formation and a set of metrics are used to evaluate the change in formation geometry relative to the initial conditions in a free-drift environment for an orientation of the Π_N plane parallel to the ecliptic. The metrics include three of the requirements which were introduced in Chapter 4. The following passage, Section 5.5, compares the results with those obtained with a new orientation of Π_N plane, perpendicular to the ecliptic. Throughout this chapter, the spacecraft are treated as point masses.

There are a set of optimal geometry conditions for which science tasks can be performed. However, the deformation of the formation rises with time and during science tasks thrusters cannot be fired to control the formation and correct relative trajectories. It must be guaranteed that the formation performance does not degrade by virtue of the force environment during these critical periods. The relevance of this analysis is thus to determine the extent to which the formation geometry degenerates from a nominal departure point when no control is applied. This analysis is particularly relevant for targets associated with long observation windows and for instances of prolonged passiveness when calibration or communication activities may take place.

5.2. DYNAMICS OF FORMATION REFERENCE POINT AROUND L_2

BEFORE describing the equations of motion of the reference point contained in the Π_N-plane with respect to L_2, the reference frame of L_2 has to be defined. This coordinate system, designated $\mathscr{L}_2$, was previously introduced in Section 2.4. It lies on the Sun-Earth/Moon barycenter line and has the following properties:

- the δx-axis is aligned with the ecliptic plane and its positive direction follows the anti-Sun direction (towards outer space);
- the δz-axis is aligned with the North and South ecliptic poles of the celestial sphere, with the positive sense in the North-pole direction;
- the δy-axis completes the right-handed reference frame.

For visualization purposes, this is illustrated in Figure 5.1. The equations of motion for a spacecraft with respect to L_2 were derived by Richardson in 1980 [43]. Since the spacecraft are treated as point masses in this context, one may adapt this construction to the IRASSI case, by equivalently considering the reference point contained in the Π_N plane, relative to which the formation is arranged. These equations of motion are a three-dimensional, third-order analytical solution for Halo-type periodic motion about the collinear points of the circular-restricted problem (in this case applied to the Sun-Earth/Moon). These equations are obtained using a Lagrangian formulation, as a general approach, and applying the method of successive approximations (for the first and second-order), together with a Lindstedt-Poincaré method (third-order).

The advantage of this method is that the orbit of the spacecraft can be prescribed, by sizing the orbit amplitudes A_x, A_y and A_z, and the spacecraft can be initialized in any point in the orbit. The equations of motion of the formation reference point, with respect to L_2, are provided in Equations 5.1a to 5.1c:

$$\begin{aligned}\delta x = a_{21}A_x^2 + a_{22}A_z^2 - A_x\cos(\tau_1) + \left(a_{23}A_x^2 - a_{24}A_z^2\right)\cos(2\tau_1) + \\ + \left(a_{31}A_x^3 - a_{32}A_xA_z^2\right)\cos(3\tau_1)\end{aligned} \tag{5.1a}$$

$$\delta y = kA_x\sin(\tau_1) + \left(b_{21}A_x^2 - b_{22}A_z^2\right)\sin(2\tau_1) + \left(b_{31}A_x^3 - b_{32}A_xA_z^2\right)\sin(3\tau_1) \tag{5.1b}$$

$$\delta z = \delta_n A_z\cos(\tau_1) + \delta_n d_{21}A_xA_z\cos(2\tau_1 - 3) + \delta_n\left(d_{32}A_xA_z^2 - d_{31}A_z^3\right)\cos(3\tau_1) \tag{5.1c}$$

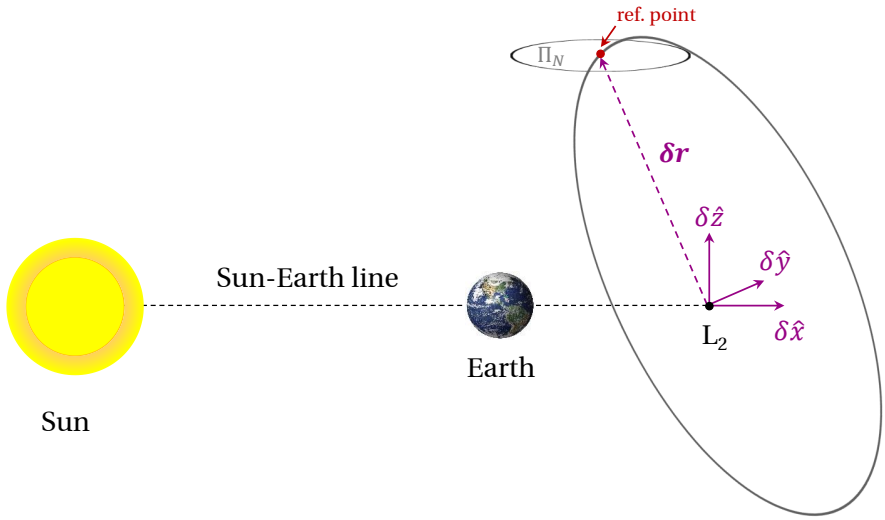

Figure 5.1: Illustration of L_2-centered reference, with respect to which the dynamics of the reference point of plane Π_N is described.

where the switch function δ_n determines whether the orbit is Class I or Class II and is given by:

$$\delta_n = 2 - n, \;\; n = 1,3 \tag{5.2}$$

and the a_{qw}, b_{qw} and d_{qw} are constants which are defined in Appendix, with $q = 1,2,3$ and $w = 1,2,3,4$. The angular term τ_1 is given by:

$$\tau_1 = \gamma\omega n_1 t + \phi \tag{5.3}$$

In Equation 5.3, ϕ corresponds to the initial phase of the reference points' orbit around L_2 and the term γ corresponds to the linearized frequency and is the mathematical solution to:

$$\gamma^4 + (c_2 - 2)\gamma^2 - (c_2 - 1)(1 + 2c_2) = 0 \tag{5.4}$$

where c_2 itself is a constant defined in Appendix C. In addition, the second term of Equation 5.3, ω, is the frequency correction, written in the general form as:

$$\omega = 1 + \sum_{n\geq 1} \omega_n, \;\; \omega_n < 1 \tag{5.5}$$

where the ω_n term is assumed to be of order $0(A_x^n)$ and it should be appropriately selected to remove the secular terms as they appear in the higher order solutions. For example, from the second-order solution, it is found that:

$$\omega_1 = 0 \tag{5.6}$$

and in third-order solutions that

$$\omega_2 = s_1 A_x^2 + s_2 A_z^2 \tag{5.7}$$

where s_1 and s_2 are constants defined in Appendix C.

Finally, still in Equation 5.3, the term n_1 corresponds to the orbital mean motion of the Earth/Moon around the Sun and t denotes the instantaneous time variable (making the connection between the temporal and angular domains).

Naturally, the amplitudes in the δx and δz axes are such that

$$A_x > 0$$

$$A_z \geq 0$$

Note that while the resulting orbits are symmetric with respect to the δy, they are not symmetric with respect to the δx and δz axes. This may produce effects in the relative dynamics at different points in the orbit.

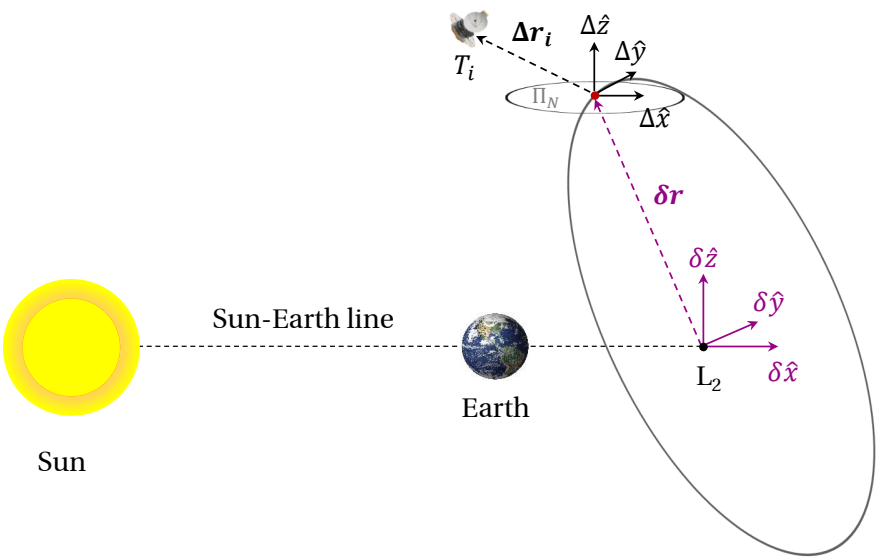

Figure 5.2: Illustration of the relative dynamics $\mathscr{L}$ coordinate system, with the origin fixed on the reference point contained in Π_N-plane, and of the L_2-centered frame $\mathscr{L}_2$.

The relative size of the periodic orbits defined by Equations 5.1a to 5.1c is obtained from the amplitude-constraint relationship [43]:

$$l_1 A_x^2 + l_2 A_z^2 + \Gamma = 0 \tag{5.8}$$

where l_1 and l_2 are constants defined in Appendix C and the definition of Γ is given by:

$$\Gamma \triangleq \gamma^2 - c_2 \tag{5.9}$$

From Equation 5.8 it is possible to conclude that the minimum allowable value for A_x occurs for $A_z = 0$, which then results in

$$A_x = \sqrt{\left|\frac{\Gamma}{l_1}\right|}.$$

A short analysis and discussion on the validity of Richardson's model are available in the Appendix C.2 section.

5.3. DYNAMICS OF SPACECRAFT RELATIVE TO FORMATION REFERENCE POINT

THE objective of the present section is to describe the evolution in time of the relative motion between two spacecraft or between a spacecraft and the formation reference point within the Π_N-plane, in free-drift conditions, given a set of initial parameters. No formation control is implemented. The dynamics of a spacecraft relative to the formation reference point, expressed in the coordinates in the local rotating $\mathscr{L}$ frame (defined in Section 4.2.1), are given in light of the coordinates δx, δy and δz, described by Equations 5.1a to 5.1c, and associated with the $\mathscr{L}_2$ frame of Section 5.2. A depiction of both coordinate systems is given in Figure 5.2.

For relative motion, the nonlinear equations of motion around L_2 of each spacecraft described in the frame of the circular restricted three-body problem must be subtracted. Roberts [44] devised a relative motion model which consists of evaluating the gravity gradient in three dimensions at a reference point (or spacecraft), $\nabla \mathbf{f_{ref}}$, and multiplying it by the distance Δr between the reference and a spacecraft, described by:

$$\Delta r = \sqrt{\left(\Delta x_T - \Delta x_{ref}\right)^2 + \left(\Delta y_T - \Delta y_{ref}\right)^2 + \left(\Delta z_T - \Delta z_{ref}\right)^2}. \tag{5.10}$$

This process is summarized in Equation (5.11):

$$\boldsymbol{\Delta \ddot{r}} = \boldsymbol{\delta \ddot{r}_T} - \boldsymbol{\delta \ddot{r}_{ref}} = \mathbf{f_T} - \mathbf{f_{ref}} = \nabla \mathbf{f_{ref}}\, \boldsymbol{\Delta r}. \tag{5.11}$$

The subscript 'T' refers to telescope and 'ref' to the formation reference point, located at the origin of the $\mathscr{L}$ frame , $(\Delta x_{ref}, \Delta y_{ref}, \Delta z_{ref}) = (0,0,0)$. The term on the left-hand side, $\boldsymbol{\Delta \ddot{r}}$, is the relative acceleration between the reference and the telescope and naturally $\boldsymbol{\ddot{r}_T}$ and $\boldsymbol{\delta \ddot{r}_{ref}}$ represent the gravitational acceleration exerted at the reference's and at the telescope's location respectively by the Sun-Earth/Moon system. For simplicity reasons, this gravity gradient model, as described in the subsequent equations, will be referred to as 'Roberts' model.

The equations of relative motion in non-dimensional form (in terms of the distances from L_2) for two point masses orbiting L_2 in the rotating $\mathscr{L}$ coordinate frame are provided in Equations 5.12a until 5.12c [44]:

$$\Delta \ddot{x} - 2\Delta \dot{y} - \Delta x = \varepsilon \Delta x \tag{5.12a}$$

$$\Delta \ddot{y} + 2\Delta \dot{x} - \Delta y = \vartheta \Delta x + \varpi \Delta y \tag{5.12b}$$

$$\Delta \ddot{z} = \xi \Delta x + \varsigma \Delta z \tag{5.12c}$$

where the variables ε, ϑ, ϖ, ξ and ς are described in Equations 5.13 until 5.17.

$$\begin{aligned} \varepsilon = &-(1-\rho_m)\left[\frac{1}{R_S^3} - \frac{3}{R_S^5}(x_0+\rho)(2\delta x_a + x_0 + \rho)\right] - \\ &-\rho\left[\frac{1}{R_E^3} - \frac{3}{R_E^5}(x_0 - 1 + \rho)(2\delta x_a + x_0 - 1 + \rho)\right] \end{aligned} \tag{5.13}$$

$$\vartheta = 3\delta y_a \left[\frac{(1-\rho)(x_0+\rho)}{R_S^5} + \frac{\rho(x_0 - 1 + \rho)}{R_E^5}\right] \tag{5.14}$$

$$\varpi = -(1-\rho)\left[\frac{1}{R_S^3} - \frac{3(x_0+\rho)\delta x_a}{R_S^5}\right] - \rho\left[\frac{1}{R_E^3} - \frac{3(x_0 - 1 + \rho)\delta x_a}{R_E^3}\right] \tag{5.15}$$

$$\xi = 3\delta z_a \left[\frac{(1-\rho)(x_0+\rho)}{R_S^5} + \frac{\rho(x_0 - 1 + \rho)}{R_E^5}\right] \tag{5.16}$$

$$\varsigma = -(1-\rho)\left[\frac{1}{R_S^3} - \frac{3(x_0+\rho)\delta x_a}{R_S^5}\right] - \rho\left[\frac{1}{R_E^3} - \frac{3(x_0 - 1 + \rho)\delta x_a}{R_E^5}\right] \tag{5.17}$$

In Equations 5.13 until 5.17, ρ refers to the mass ratio between the Earth-Moon barycenter (via the summation of Earth's and Moon's mass, respectively M_E and M_M) and that of the combined system, including the Sun's mass, M_S:

$$\rho = \frac{M_E + M_M}{M_E + M_M + M_S} \tag{5.18}$$

Additionally, the terms R_E and R_S are respectively the median distance of Earth and the Sun to L_2 and x_0 is the distance of L_2 to the barycenter of the Sun/Earth-Moon system, all terms dimensionalized by the Sun-Earth distance (1 AU). Similarly, the subscript 'a' in terms δx_a, δy_a and δz_a denotes the adimensional units of the prescribed coordinates of the reference around L_2, according to Equations (5.1a) to (5.1c). Unlike the latter, the equations of relative motion are coupled in the in-plane (Δx, Δy) and out-of-plane (Δz) directions.

By reordering the terms, the set of Equations 5.12 can be represented in the state-space format, such that:

$$\dot{\boldsymbol{x}} = \boldsymbol{A}\boldsymbol{x} + \boldsymbol{B}\boldsymbol{u} \tag{5.19}$$

where $\boldsymbol{x}$ is the state-space vector and $\boldsymbol{u}$ is the input command vector, $\boldsymbol{A}$ is the state matrix and $\boldsymbol{B}$ is the input matrix. Given that, at the present stage, no control is implemented, then $\boldsymbol{u} = 0$. The state vector $\boldsymbol{x}$ is defined as:

$$\boldsymbol{x} = \begin{bmatrix} \Delta x & \Delta y & \Delta z & \Delta \dot{x} & \Delta \dot{y} & \Delta \dot{z} \end{bmatrix}^T \tag{5.20}$$

and the state matrix $\boldsymbol{A}$ is described by:

$$\boldsymbol{A} = \begin{bmatrix} 0 & 0 & 0 & 1 & 0 & 0 \\ 0 & 0 & 0 & 0 & 1 & 0 \\ 0 & 0 & 0 & 0 & 0 & 1 \\ 1+\varepsilon & 0 & 0 & 0 & 2 & 0 \\ \vartheta & 1+\varpi & 0 & -2 & 0 & 0 \\ \xi & 0 & \varsigma & 0 & 0 & 0 \end{bmatrix} \tag{5.21}$$

The state variables of the spacecraft, Δx, Δy and Δz, are finally calculated by performing a step-wise integration (at each point in the orbit) of the linear-time varying system, such that:

$$\boldsymbol{x}(t) = e^{\int \boldsymbol{A}(t)dt}\Delta\boldsymbol{x}(0) \tag{5.22}$$

In addition, the initial values of the in-plane relative motion are given by Equations 5.23 to 5.25. These initial values were obtained by Roberts [45] to remove the secular drift, noting that the model prescribes an association between Δx and the initial out-of-plane component Δz. For the complete formulation of the analytical solution and approximations, the reader is referred to the work of Roberts [44, 45].

$$\begin{aligned}\Delta\dot{x}_0 = \frac{1}{2}\Bigg\{1 - \frac{(1-\rho)}{R_S^3} - \frac{\rho}{R_E^3} + \\ + \left[\frac{3(1-\rho)(x_0+\rho)}{R_S^5} + \frac{3\rho(x_0-1+\rho)(x_0+\rho)}{R_E^5}\right]\left(a_{21}A_x^2 + a_{22}A_z^2\right)\Bigg\}\Delta y_0\end{aligned} \tag{5.23}$$

$$\begin{aligned}\Delta\dot{y}_0 = \Bigg\{\frac{1}{2} - \frac{(1-\rho)}{2}\left[\frac{1}{R_S^3}\frac{3(x_0+\rho)^2}{R_S^5}\right] - \frac{\rho}{2}\left[\frac{1}{R_E^3} - \frac{3(x_0-1+\rho)^2}{R_E^5}\right] + \\ + \left[\frac{3(1-\rho)(x_0+\rho)}{R_S^5} + \frac{3\rho(x_0-1+\rho)}{R_E^5}\right]\left(a_{21}A_x^2 + a_{22}A_z^2\right)\Bigg\}\Delta x_0\end{aligned} \tag{5.24}$$

$$\Delta x_0 = \frac{a_{21}A_x^2 + a_{22}A_z^2}{3d_{21}A_xA_z}\Delta z_0 \tag{5.25}$$

5.3.1. VALIDATION OF ROBERTS' MODEL

The gravity gradient model for relative motion [44, 45] was implemented and solved numerically in MATLAB/Simulink and thereafter compared to the results obtained with the General Mission Analysis Tool[1] (GMAT, developed by NASA). In GMAT, Solar and planetary effects are considered (including the eccentricity of the Earth around the Sun which changes the location of the barycenter of the system in the Sun-Earth line and therefore changes the location of L_2). The epoch was arbitrarily selected as that of March 1st, 2030, at 12 o'clock.

A reference Halo orbit around L_2 was firstly selected, using Richardson's equations. The amplitude in the δz-axis of this orbit was set to $A_z = 400\,000$ km, which results in amplitudes corresponding to $A_x = 250\,272.869$ km and $A_y = 794\,070.722$ km. The period of this reference orbit is approximately 179.75 days and it belongs to Class 1, (meaning the direction of revolution about L_2 as viewed from the Earth is clockwise), by setting $\delta_n = 1$. The orbit is illustrated in Figures 5.3 and 5.4. An overview of the acceptable reference Halo orbit dimensions for the IRASSI mission can be found in Section 3.3.

From this reference Halo orbit, the spacecraft is positioned 200 meters and 125 meters (cf. Equation 5.25) respectively in the Δx_0 and Δz_0 directions away from the formation center point (the Δz_0 value is obtained using Equation 5.25). The initial positions for an initial phase $\phi = 0°$ are presented in Table 5.1, for both the center point and the spacecraft. As such, at the beginning of the simulations, the spacecraft and the formation reference point are above the ecliptic plane ($\delta z_0 > 0$), between the L_2 point and the Earth ($\delta x_0 < 0$). A simulation of 20 days was selected for the relative motion validation and the measurements are obtained in time-steps of 1 hour for both MATLAB and GMAT implementations.

In GMAT, a Cartesian axis system was created at the L_2 point and at the Chief. The initial conditions of the Chief were provided as Cartesian positions and velocities relative to L_2 and, similarly, the initial conditions of the Deputy were provided with respect to the Chief. A Runge-Kutta-89 propagator was selected. The Earth was chosen as the primary, central body with the Moon and the Sun as point masses in the force model and solar radiation pressure was considered. The GMAT data concerning absolute motion and relative motion of both spacecraft was collected through an output file reporting tool.

The evolution of the distance Δr and respective coordinates in the local $\mathscr{L}$ frame (centered on the formation reference point), as modeled with Roberts' relative motion equations, is shown in Figure 5.5. The distance is calculated according to Equation 5.10. This overall distance Δr between the spacecraft and the reference increases from an initial value of 236 m to 300 m over the course of 20 days, an average rate of 3.2 m/day in free-drift conditions. A decrease in absolute terms is observed for the Δx coordinate, from 200 m to

[1] from https://gmat.gsfc.nasa.gov/

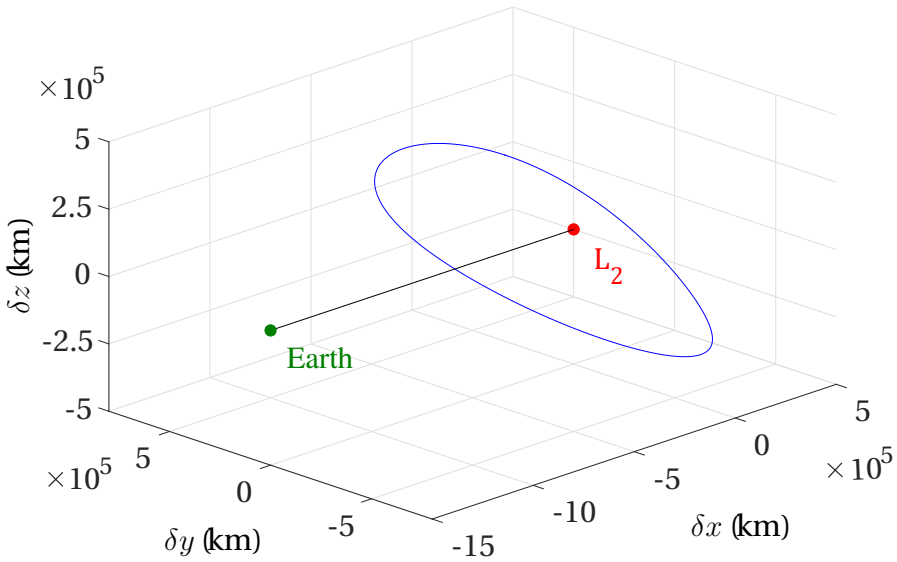

Figure 5.3: Halo orbit around L_2.

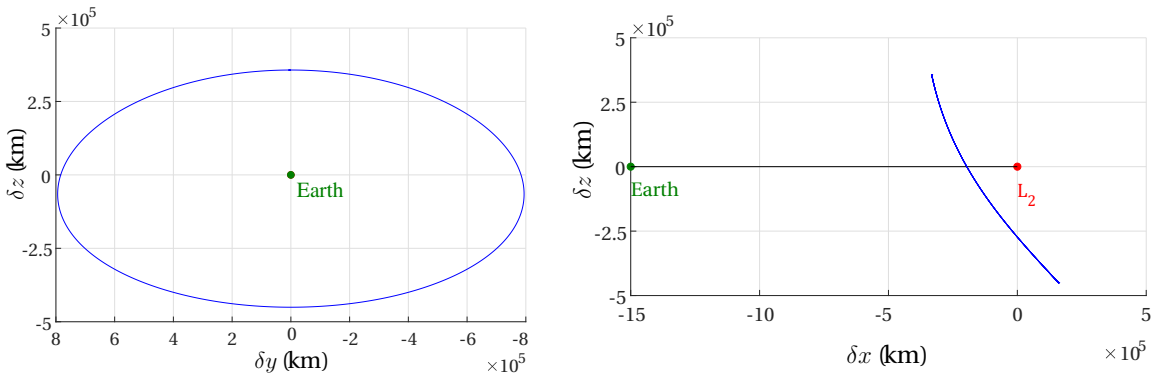

(a) δx-view (b) δy-view

Figure 5.4: 2D projections of Halo orbit around L_2.

170 m, and for the Δz coordinate from about 125 m to 70 m. This means therefore that the increase in distance Δr is governed by the magnitude increase from 0 m to 234 m of the Δy coordinate. The modeling errors of the relative positions and velocities between the gravity gradient model and GMAT are presented in Figure 5.6. The error was calculated by subtracting the analytical solution of Roberts' solution from GMAT's solution. From the plots, it is recognizable that the largest difference occurs for the Δx coordinate, at nearly 29 m after 20 days (or 1.45 m per day), whereby the steepest increase is observed within the first two weeks. The reason for this difference is mainly attributed to the dependence of Δx motion on the $\Delta \dot{y}$ velocity magnitude, as Equation 5.12a shows, whose initial value is estimated at 0.177 mm s^{-1}, which is likely underestimated. The reference point is further from L_2, but closer to the Earth than the telescope. The initial velocity of the reference point ($\delta \dot{y}_0 = 0.351$ km s^{-1}, cf. Table 5.1) causes it to move away from the Earth, subjecting it to a higher centrifugal force. With the Earth's gravity similarly acting on the reference, it moves in a Halo pattern. The neighboring telescope, further from Earth, requires a lower velocity to stay near the reference (which is correctly predicted by Roberts' model in this case), but the Halo rotation motion of the reference will cause the two to separate. The magnitude of this velocity, however, is indeed underestimated.

Conversely, GMAT predicts a more modest change along the Δz axis, of about 23 m, compared to the gravity gradient model (however, the deviation is positive due to the fact that both the GMAT and model values are negative). The Δz distance magnitude is thus overestimated by the gravity-gradient model. The deviation of the Δy coordinate is of only about -2.5 m on the first half of the simulation, growing to an order of

Table 5.1: Initial conditions of formation reference point and spacecraft.

	Reference (relative to L_2)		Telescope (relative to reference)	
Position	δx_0 (km)	−332 435.467	Δx_0 (m)	200.000
	δy_0 (km)	0.000	Δy_0 (m)	0.000
	δz_0 (km)	357 052.548	Δz_0 (m)	−125.258
Velocity	$\delta \dot{x}_0$ (km s^{-1})	0.000	$\Delta \dot{x}_0$ (mm s^{-1})	0.000
	$\delta \dot{y}_0$ (km s^{-1})	0.351	$\Delta \dot{y}_0$ (mm s^{-1})	−0.177
	$\delta \dot{z}_0$ (km s^{-1})	0.000	$\Delta \dot{z}_0$ (mm s^{-1})	0.000

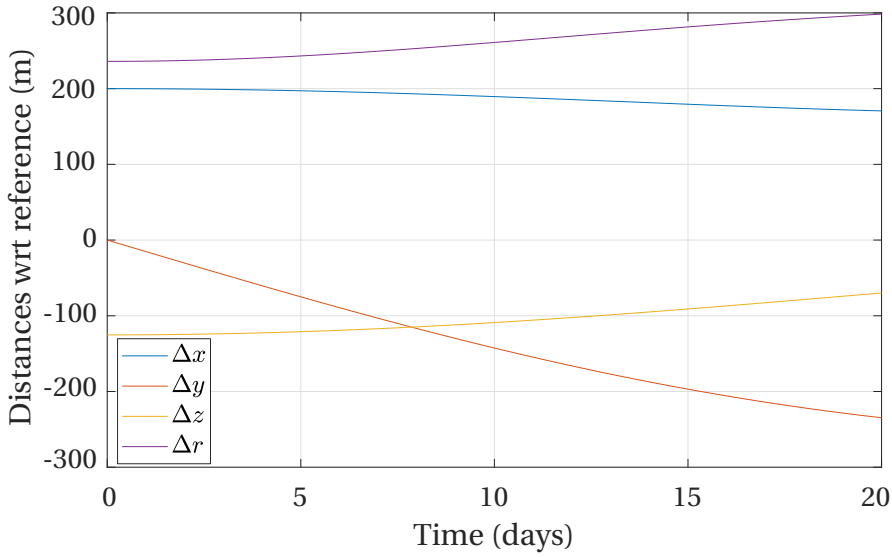

Figure 5.5: Evolution of the relative coordinates of the telescope relative to the reference point according to Roberts' model for an initial phase of the reference orbit of $\phi = 0°$.

magnitude greater over the last ten days. Again, both GMAT and model values are negative, but the absolute deviation is negative because the Δy distance magnitude is underestimated by the gravity-gradient model. A similar trend applies to the relative velocity $\Delta \dot{y}$ of Figure 5.6(b). The gravity-gradient model underestimates $\Delta \dot{x}$ by a maximum of 0.027 mm s^{-1} relative to GMAT at the 11th day of simulation, a value which sharply drops to less than 0.020 mm s^{-1} on the 20th day. And an underestimation of $\Delta \dot{z}$ by 0.015 mm s^{-1} is also observed over the first two weeks, after which the velocity deviation remains relatively constant.

The relative errors of relative and velocities are provided in Appendix C.3.1 in percentages, where it is observed that the coordinate that is modeled the poorest is Δz.

Note that the time scales of interest for modeling the relative dynamics of IRASSI correspond to the duration events in which the formation is in free drift. These are, for example, idle instances where the formation is performing calibration or communication tasks or even science observation activities - ranging from a couple of hours to two days, and occasionally one week. On these time scales, the deviation between GMAT and the gravity gradient model lies in the centimeter level for relative distances and micrometer per second for relative velocities. Therefore the gravity gradient model can be deemed as an acceptable tool for conducting a preliminary analysis on the relative motion under uncontrolled dynamics, at least for the selected epoch and a phase of $\phi = 0°$. In the next subsection, the modeling error is evaluated for different conditions.

Finally, note that the results obtained by Roberts [44, 45] were themselves compared and validated with

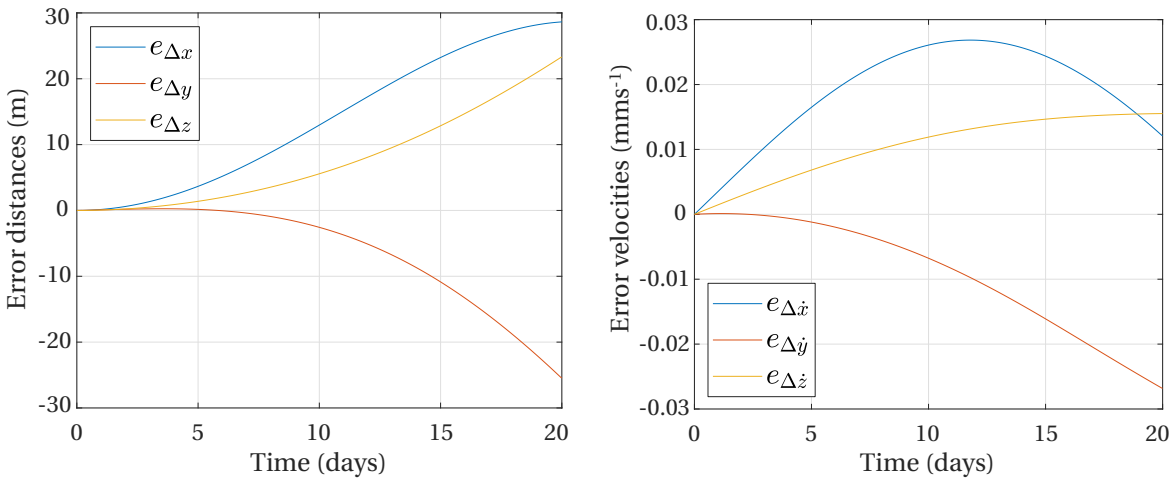

(a) Distance (b) Velocity

Figure 5.6: Relative motion modeling error (absolute) between GMAT and Roberts' model. Epoch of simulation is March 1st, 2030.

another simulation tool (STK Astrogator) for slightly different conditions. The results hereby presented, therefore, support previous research concluding that there is a good agreement between the analytical models and the numerical, more complex software for, at least, short-term periods.

5.3.2. Influence of Reference Point's Location on Relative Dynamics Modeling Error

This subsection addresses how the orbit of the formation reference may affect the relative dynamics with respect to neighboring spacecraft. It is clear that different orbit sizes may give rise to different relative dynamics (due to the dependency of $\boldsymbol{\Delta r}$ on $\boldsymbol{\delta r}$, shown by Equations 5.12 until 5.17). However, it is relevant to understand how, for example, for the same prescribed Halo orbit around L_2, the spacecraft move with respect to each other in free-drift conditions depending on where in the orbit they are (phase), in the relevant time scales.

Two parameters are hereby assessed: the initial phase ϕ of the reference and the epoch. Theoretically, the initial phase can be captured by the Roberts' model (due to its direct dependence on the reference's orbital adimensional coordinates δx_a, δy_a and δz_a in Equations 5.13 until 5.17. The epoch, however, cannot be captured by the Richardson/Roberts' models. The interest here is to see how the expected GMAT numerical solutions compare to the Roberts' model for the same orbit conditions when the simulation epoch varies throughout the year.

Initial Phase ϕ

According to Figures 5.3 and 5.4, the periodic Halo orbit is not completely symmetric. It may therefore be possible to detect differences in modeling performance of Roberts' equations, depending on where in the Halo orbit the formation reference is located. Certain conditions (for example, higher proximity to Earth) may be associated with higher modeling errors. Therefore, four different locations along the reference Halo orbit have been selected to measure the modeling error. The locations are given as a function the initial phase ϕ, which varies between 0° and 270° in steps of 90°, and are shown in Figure 5.7. The direction of ϕ increase indicates the sense of motion of the reference point along the orbit.

For each case, twenty-day simulations have been ran for the same orbit amplitudes as presented in Table 5.1. The initial distance of the spacecraft is also set as $\Delta x_0 = 200$ m and $\Delta z_0 = -125$ m away from the formation center point in the local $\mathscr{L}$ frame for an epoch of March 1st, 2030, at 12 o'clock. The evolution of the position error $e_{\boldsymbol{\Delta r}}$ and velocity error $e_{\boldsymbol{\Delta \dot{r}}}$ is shown in Figure 5.8 and Figure C.5 respectively in units and percentage. Additionally, the error is shown relative to the distances to the L_2 point and to the Earth-Moon barycenter in Figure 5.9. The position error $e_{\boldsymbol{\Delta r}}$ is measured by subtracting Equation 5.10 to the relative distance calculated by GMAT, as shown in Equation 5.26. The same procedure applies to velocities.

$$e_{\boldsymbol{\Delta r}} = \boldsymbol{\Delta r}_{|GMAT} - \boldsymbol{\Delta r} \tag{5.26}$$

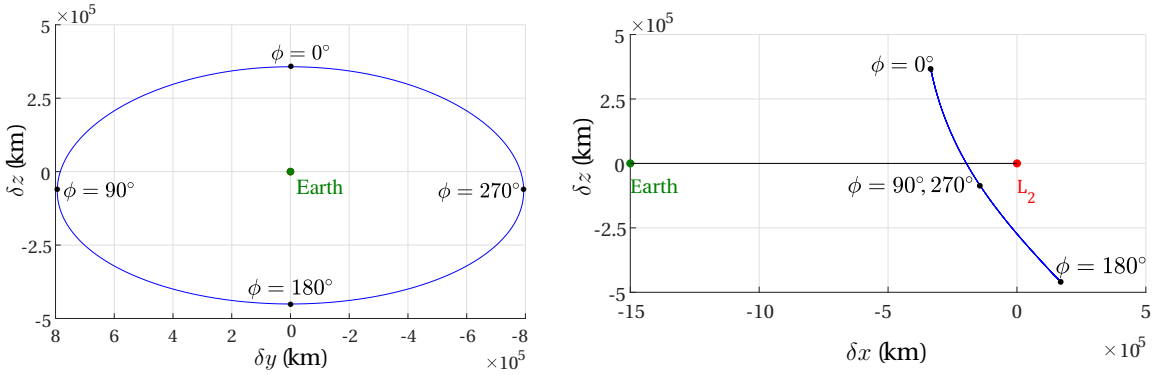

(a) δx-view (b) δy-view

Figure 5.7: 2D projections of Halo orbit around L_2.

Overall, from the four initial phase conditions, it is possible to see that the position estimated with the Roberts' model seems to deviate by 30-45 m after 20 days for all conditions, in Figure 5.8(a). The position is underestimated for the cases where the reference (and telescope) are closer to the Earth and moving along the Halo above the ecliptic for most of the time - that is, for initial phases corresponding to $\phi = 0°$ and $\phi = 270°$. Conversely, cases further from Earth on the southern hemisphere, $\phi = 90°$ and $\phi = 180°$, are overestimated and the associated magnitude of the deviations is lower than the former cases.

Along the orbit, the distance to Earth varies between 1.23×10^6 km and 1.73×10^6 km. Naturally, the fact that Richardson's model does not capture higher order (beyond third-order) gravitational effects or even solar radiation pressure is one of the reasons for the deviations. These effects influence the reference's orbit to a larger degree when they are closer to the primary bodies (Sun and Earth-Moon barycenter), which is why the magnitude of the deviation is higher for an initial phase of $\phi = 0°$ than for $\phi = 180°$, for instance[2]. Another reason is likely the estimation of the $\Delta\dot{y}_0$ of the Roberts' model. Inspecting Equations 5.12 until 5.17 and Equations 5.23 to 5.25 shows that regardless of the initial position of the reference point in the Halo orbit, the relative initial condition values of the telescope (position and velocity with respect to the reference) do not change and the spacecraft is always initiated with $\Delta\dot{y}_0 = -0.177$ mm s^{-1}. The initial velocity value $\delta\dot{y}_0$ on the Halo is maximum for $\phi = 0°$ and for $\phi = 180°$, and null for $\phi = 90°$ (tending to negative over the simulation time) and for $\phi = 270°$ (tending to positive over the simulation time). An added velocity $\Delta\dot{y}_0 = -0.177$ mm s^{-1}at the $\delta\dot{y}$ extrema ($\phi = 0°, 180°$) will lead to either an overestimation ($\phi = 180°$, $\delta\dot{y} < 0$) or underestimation ($\phi = 0°$, $\delta\dot{y} > 0$) of the relative position according to the sign of $\delta\dot{y}$. However, the integration error of the Roberts' model is higher when the reference and spacecraft are initialized with a null $\delta\dot{y}$. In this case, when the spacecraft is at an initial phase of $\phi = 270°$ and $\delta\dot{y}$ starts tending to positive (progressively underestimated by Richardson at it moves closer to Earth), the initial velocity of the spacecraft $\Delta\dot{y}_0 = -0.177$ mm s^{-1}is underestimated and subtracted from the (already underestimated) $\delta\dot{y}$. As a result, according to Roberts, the spacecraft separate more from the reference than the other cases and at a faster pace as observed in Figure 5.8(b). On the other hand, at $\phi = 90°$ the spacecraft is at the same distance from Earth as the $\phi = 270°$ case and $\delta\dot{y}$ increases in the negative sense and becomes again progressively underestimated as it moves further from the Earth. The added negative relative velocity $\Delta\dot{y}_0 = -0.177$, however, slightly accelerates the spacecraft in the Halo orbit in the Roberts' model and dampens the growth of the integration error over time, as observed by the inversion of the curve in Figure 5.8(b). This likely explains why the difference between the deviation of the two cases in the southern hemisphere ($\phi = 90°$ and $\phi = 180°$) is not as pronounced as the ones in the northern hemisphere ($\phi = 0°$ and $\phi = 270°$).

The relative errors of relative and velocities are provided in Appendix C.3.1 where it is shown that these are minor for all cases.

Finally, for completeness (and curiosity) the deviation of the predicted positions relative to GMAT is shown in Figure 5.9 as a function of the distance to L_2 and the Earth-Moon barycenter. These two locations, L_2 and the barycenter of the Earth-Moon system, are merely separated by a distance of approximately 1.5×10^6 km along the δx coordinate. Generally, in Figure 5.9(a), it can be observed that for the same sim-

[2]Low-order gravitational effects are considered in the Roberts' model by the adimensional terms δx_a, δy_a and δz_a in Equations 5.13 until 5.17.

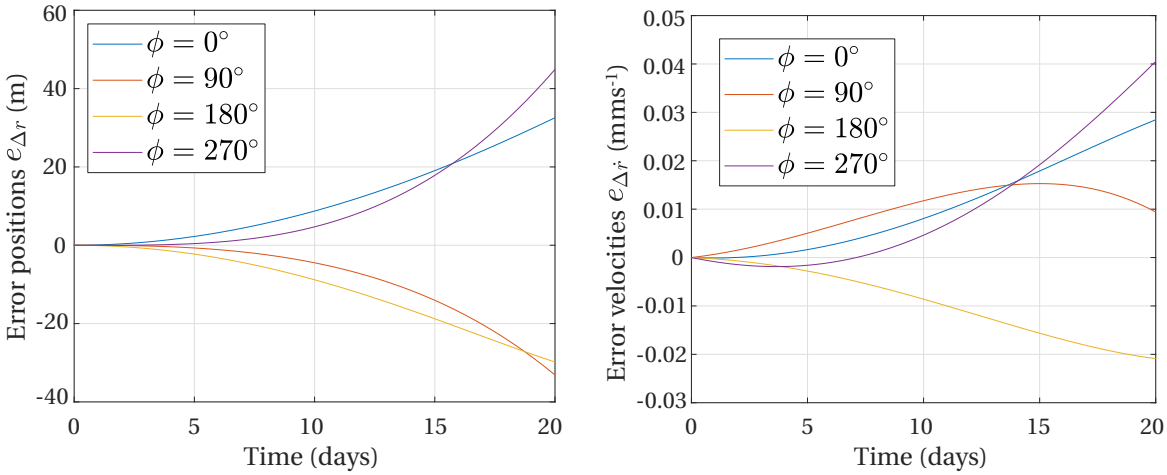

(a) Position (b) Velocity

Figure 5.8: Relative motion modeling error (absolute) between GMAT and Roberts' model for different initial phase values ϕ.

ulation time, the relative position error of the spacecraft increases with an increasing initial distance to L_2, although the magnitude of the deviation is greater for $\phi = 270°$ than for $\phi = 90°$ for the reasons explained above. Note that the initial distance to L_2 differs for $\phi = 0°$ and $\phi = 180°$ because the Halo orbit is asymmetric relative to the δz-axis. From Figure 5.9(b), the closest to Earth the initial position, the higher the magnitude of the deviation. The effect of the integration error due to the initial relative velocity $\Delta \dot{y}_0 = -0.177$ mm s^{-1}of the spacecraft is evident: whereas the deviation is relatively proportional to the distance for initial phases $\phi = 0°$ and $\phi = 180°$, this deviation becomes exponential when to an initial null $\delta \dot{y}$ the $\Delta \dot{y}_0$ is added to the spacecraft.

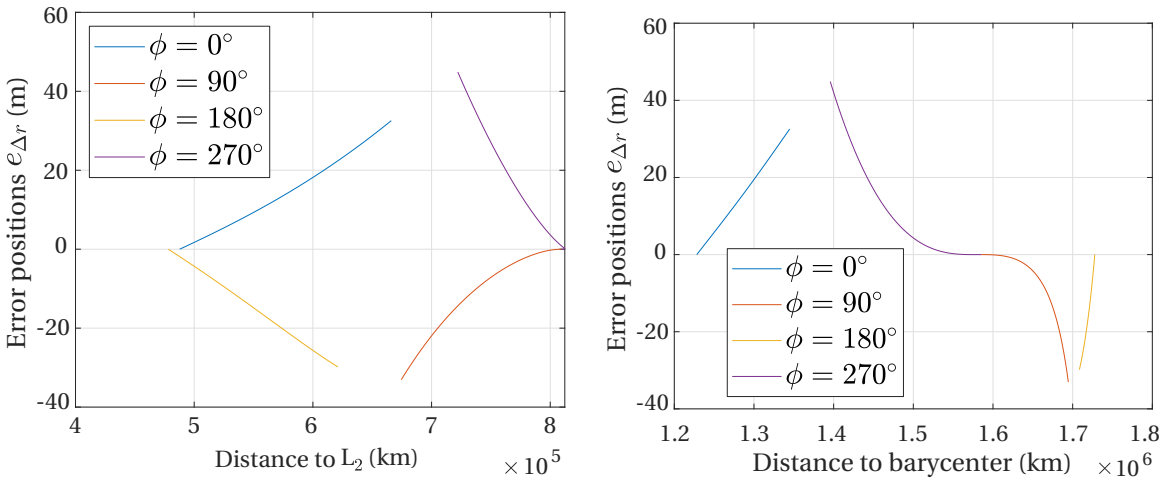

(a) Position/L_2 (b) Position/Barycenter

Figure 5.9: Relative motion modeling error (absolute) between GMAT and Roberts' model for different initial phase values ϕ, relative to distance to L_2 (left) and to the Earth-Moon barycenter (right).

As an extension of this analysis, the change in relative distance over time as predicted by the Roberts' model was evaluated by varying the initial phase ϕ, in steps of ϕ of 10°, resulting in 36 different simulation conditions. For brevity, results are hereby presented concerning the same initial phase values above ($\phi = 0°, 90°, 180°$ and $270°$). Initial phase values of $\phi = 0°$ and $\phi = 180°$ correspond respectively to cases of minimum and maximum observed relative drift after 20 days. The term ´drift', in this context, refers to the measured change in position relative to the initial positions.

The corresponding plots are presented in Figure 5.10, where drift is measured as a change in position of

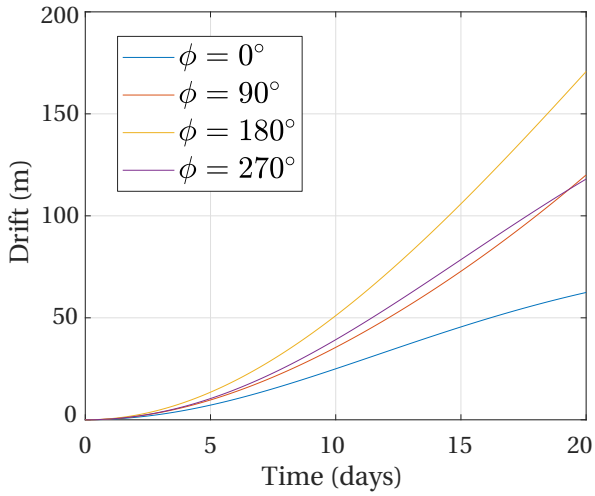

Figure 5.10: Drift over time for different initial phase values ϕ. Epoch of simulation is March 1st, 2030.

the spacecraft with respect to the reference and relative to the initial value. Note that this analysis no longer concerns the modeling error of the relative motion model. In free-drift conditions, therefore, the spacecraft is expected to deviate up to 170 m for an initial $\phi = 180°$, 62 m for $\phi = 0°$ and approximately 120 m for the other two cases ($\pm e_{\Delta r}(\%) \times ||\boldsymbol{\Delta r}||$) over twenty days. Over the time scales of interest for IRASSI, of 10 days or less, this drift ranges between 25 m and 51 m across all four cases. This drift must therefore be accounted for during prolonged idle periods if the spacecraft are reliant on certain relative geometries for intervisibility or if they must initiate an activity at a predefined set of relative distances.

EPOCH

The eccentricity of the Earth's orbit affects the location of the L_2 point in the Sun-Earth line. Richardson's model for halo-type motion about Lagrangian points assumes, however, circular orbits of the second primary body (the Earth-Moon system) around the first primary body (the Sun). In Appendix C.2 section, Richardson's model was validated for an epoch of March 1st, 2030. The Roberts' model is itself an extension of Richardson's model for relative motion and was validated against GMAT for the same epoch in Section 5.3. It may be reasonable, however, to investigate whether differences are observed in the modeling errors of the analytical solution for relative motion with respect to the numerical simulations.

For this purpose, a second epoch is considered, six months after the first one, whereby the relative dynamics between Robert's model and GMAT are compared for the same simulation time. The orbit amplitudes of the Chief are those presented in Table 5.1, for an initial phase of $\phi = 0°$. The initial distance between the spacecraft is also set as $\Delta x_0 = 200$ and $\Delta z_0 = -125$ m away from the formation center point in the local $\mathscr{L}$ frame. The resulting relative motion deviations are shown in Figure 5.11.

By comparing Figure 5.6 and Figure 5.11, little observable difference is detected between the errors of predicted relative dynamics of Roberts' model and that of GMAT for the two different epochs, six months apart. Therefore, the trends observed in the epoch of March 1st, 2030 apply to September 1st, 2030: the gravity-gradient model marginally underestimates the magnitude of the Δx and Δy coordinates and overestimates Δz. The value of the errors is slightly lower for the new epoch, where Δx peaks at 24 m, the Δy reaches 17 m and the Δz displays a deviation of -28 m (compared respectively to 29 m, 23 m and -25 m in Figure 5.6(a)). The same is true for the velocity errors, shown in Figure 5.11(b), whereby the peaks are lower in value for $\Delta\dot{x}$, $\Delta\dot{y}$ and $\Delta\dot{z}$ over the 20 days of simulation. The maximum values are thus $23\,\mu\mathrm{m\,s^{-1}}$ for $\Delta\dot{x}$, $11\,\mu\mathrm{m\,s^{-1}}$ for $\Delta\dot{y}$ and $-28\,\mu\mathrm{m\,s^{-1}}$ for $\Delta\dot{z}$, a decrease of approximately $4\,\mu\mathrm{m\,s^{-1}}$ for $\Delta\dot{x}$ and $\Delta\dot{y}$ and merely of $1\,\mu\mathrm{m\,s^{-1}}$ for $\Delta\dot{z}$ relative to the first epoch case, shown in Figure 5.6(b).

To avoid repetition and due to the proximity of the results between the epochs, the percentage error results are omitted. The conclusion follows therefore that the agreement between Roberts' and GMAT is largely independent of the selected epoch in GMAT for the time scales which are relevant for IRASSI[3].

[3] Presumably, the largest difference for the L_2 location relative to the ideal circular case (an assumption of the Richardson's and therefore of the Roberts' model) should occur for the perihelion and aphelion. Therefore, one may hypothesize that the largest deviation in modeling relative motion may occur for the dates coinciding with these two events. The perihelion for the year 2030 occurs on January 3rd

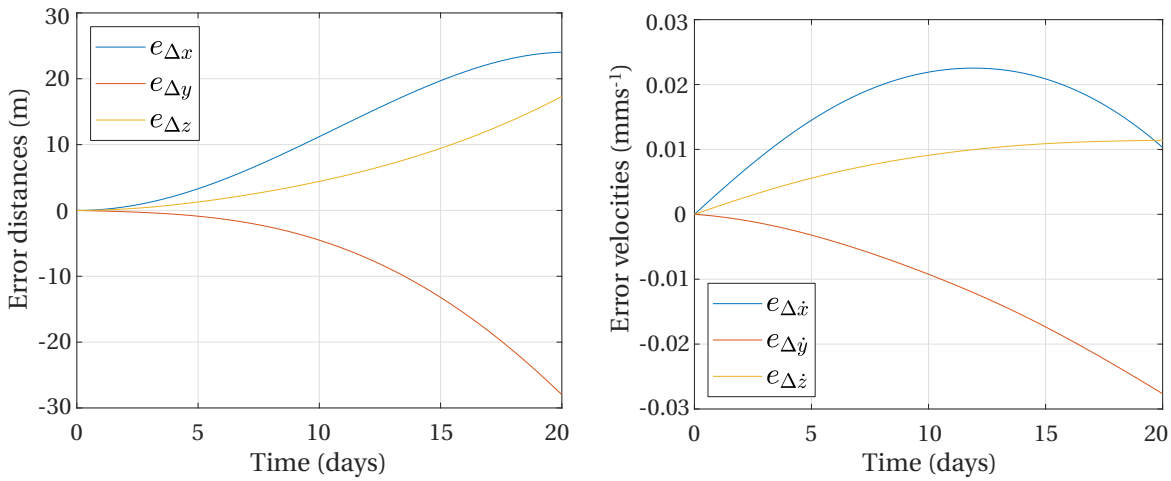

(a) Distances (b) Velocities

Figure 5.11: Relative motion modeling error (absolute) between GMAT and Roberts' model. Epoch of simulation is September 1st, 2030.

5.4. DYNAMICS OF THE IRASSI FORMATION AROUND L_2

THE present section extends the results of the formation dynamics to the IRASSI case, integrating the geometry definitions of Section 4.3 and focusing on the practical aspects of the motion of this formation without any position control input. The formation dynamics is analyzed in terms of the relative drift and drift rates relative to an initial formation geometry setup and in terms of the deformation and tilt of this geometry over time. Three of the four requirements identified in Chapter 4 are thereafter evaluated in free-drift conditions: the formation intervisibility, the relative positioning performance and the accessibility of the sky.

Building on the work of Chapter 4, the nominal formation geometry is illustrated generically in Figure 5.12, whereby the local coordinate system $\mathscr{L}$ is centered in the formation reference point, the in-plane separation φ between consecutive telescopes is fixed at equal intervals of $\frac{2\pi}{5}$ =72° and the out-of-plane separation parameter set h is given as a function of the in-plane separation term d:

$$h = \{-4d, -2d, 0, 2d, 4d\}\, \mathbf{\Delta z}, \tag{5.27}$$

whereby each element of h is to be distributed by the five spacecraft and whereas d should be kept within the range:

$$10 \leq d \leq 1000\,\text{m} \tag{5.28}$$

For the purpose of the study, two cases are generated for the IRASSI formation, one in which the formation is considered 'small' (d = 10 m) and one in which the formation is considered 'large' (d = 1000 m). The Π_N plane is oriented parallel to the Δy-Δx plane (parallel to the ecliptic plane), defining the pointing direction of the formation. The initial phase is set at $\phi = 0°$, unless explicitly stated otherwise during the analysis. For reference purposes, the 'first' telescope, T_1 was aligned with the Δx-axis. Table 5.2 provides the initial coordinate distances[4], considering that the allocation h_i among formation members of the h set is:

$$h_i = [4d, -2d, 0, -4d, 2d]\, \mathbf{\Delta z}, \;\; i = T_1, ..., T_5 \tag{5.29}$$

5.4.1. RELATIVE DRIFT AND DRIFT RATES

The results of the uncontrolled relative dynamics for eight-day simulations are presented for the imposed formation values as provided in Table 5.2. The corresponding relative drift and drift rates are presented in Figures 5.13 and 5.14 respectively for the small and large formation scenarios.

and the aphelion on July 4th. Indeed, post-hoc simulations for these dates agree with the derived conclusions, that different epochs throughout the year do not have any significant impact on the modeling error, and therefore it is deemed unnecessary to add further graphs to illustrate this point.

[4] Note that Equation 5.25 defines a value of Δz_0 associated with a value of Δx_0. The predicted values are shown below the table. Nevertheless Roberts asserts that a selection of a different value of Δz does not significantly affect model performance [45]. In addition, simulations carried out with the predicted values of Δz_0 showed that a slight increase in drift is observed for all spacecraft, but an order of magnitude lower than the relative distances among spacecraft. Relative velocities remained largely unchanged.

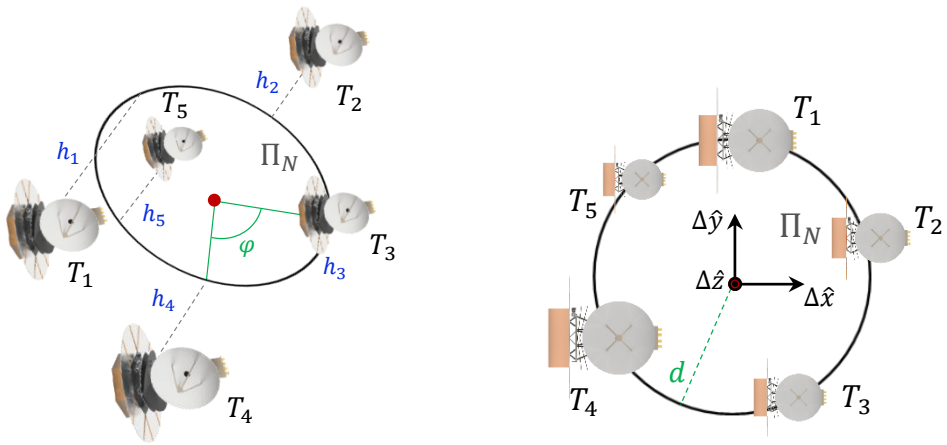

(a) Side view (b) Front view

Figure 5.12: General formation geometry arrangement relative to the local frame centered on the reference plane Π_N.

Table 5.2: Initial coordinates for the IRASSI formation, pointing to a direction parallel to the Δy-Δx plane, for two simulation conditions: small and large formation.

Tele-scope	**General formation coordinates**	**Small formation** $d = 10$ **m**	**Large formation** $d = 1000$ **m**
T_1	$(d, 0, 4d)$	$(10.0, 0.0, 40.0^{\text{i}})$	$(1000.0, 0.0, 4000.0^{\text{ii}})$
T_2	$(d\cos(\varphi), -d\sin(\varphi), -2d)$	$(3.1, -9.5, -20.0^{\text{iii}})$	$(309.0, -951.1, -2000.0^{\text{iv}})$
T_3	$(d\cos(2\varphi), -d\sin(2\varphi), 0)$	$(-8.1, -5.9, 0.0^{\text{v}})$	$(-809.0, -587.8, 0.0^{\text{vi}})$
T_4	$(d\cos(3\varphi), -d\sin(3\varphi), -4d)$	$(-8.1, 5.9, -40.0^{\text{v}})$	$(-809.0, 587.8, -4000.0^{\text{vi}})$
T_5	$(d\cos(4\varphi), -d\sin(4\varphi), 2d)$	$(3.1, 9.5, 20.0^{\text{iii}})$	$(309.0, 951.1, 2000.0^{\text{iv}})$

i $\Delta z_0 = -6.3$ m ii $\Delta z_0 = -626.3$ m
iii $\Delta z_0 = -1.9$ m iv $\Delta z_0 = -193.5$ m
v $\Delta z_0 = 5.1$ m vi $\Delta z_0 = 506.7$ m

From Figure 5.13(a) it is possible to observe that, for the small formation scenario, the relative drift varies between -5.1 m and 4.5 m. For the large formation scenario, Figure 5.14(a) shows that the relative drift varies between -514.7 m and 453.6 m. This means that for both scenarios, over time, some spacecraft will move closer while others will tend to drift apart. The first trend to notice regarding the relative motion is that it is proportional to the change in formation size. That is, given that the formation size in the large scenario is 100 times larger, the relative drift is 100 times higher in magnitude. The same linearity is, of course, observed for the drift rates, as seen in Figures 5.13(b) and Figure 5.14(b). The magnitude of the drift rates ranges between 5.7 and 18.5 $\mu\text{m}\,\text{s}^{-1}$ at the end of the simulation for the small formation and 100 times this amount for the large formation scenario, as the figures indicate. Increasing relative velocities translate into telescopes moving closer to each other over time.

Another aspect worth noting is that drift of the baselines is approximately linear with respect to time – at least for the time scales considered, 8 days. The same applies to the drift rate for half of the baseline pairs, whereas a parabolic relation is detected for the other half. Spacecraft pairs on different sides of the reference plane Π_N (e.g., $T_1 - T_2$, $T_1 - T_4$, $T_2 - T_5$, $T_4 - T_5$) are associated with a negative drift, but with a positive, parabolic drift-rate curve, whereas formation members on the same side (e.g., $T_1 - T_5$, $T_2 - T_4$) correlate with a positive drift and a linear, negative drift rate evolution.

For completeness, Appendix C.4 provides further information on relative drift metrics. The measured change in relative position is shown Figure C.6 and the proportion of drift relative to the initial distances is shown in Figure C.7, from where it is concluded that this drift ratio is generally inversely correlated to relative distance: the higher the initial separation, the lower the change over time of the drift as a proportion of initial

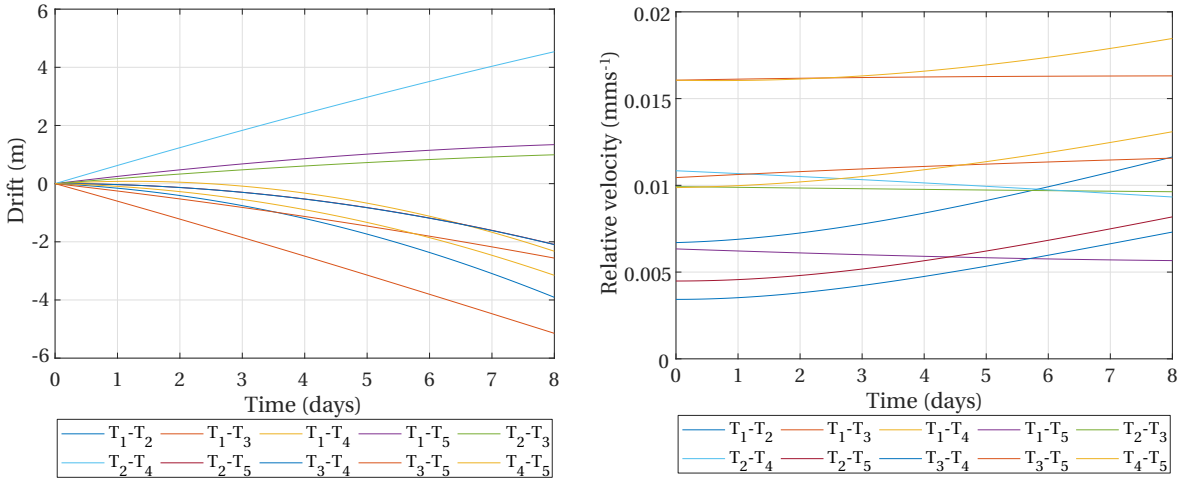

(a) Relative drift (b) Relative drift rate

Figure 5.13: Drift and drift rate profiles - small formation scenario.

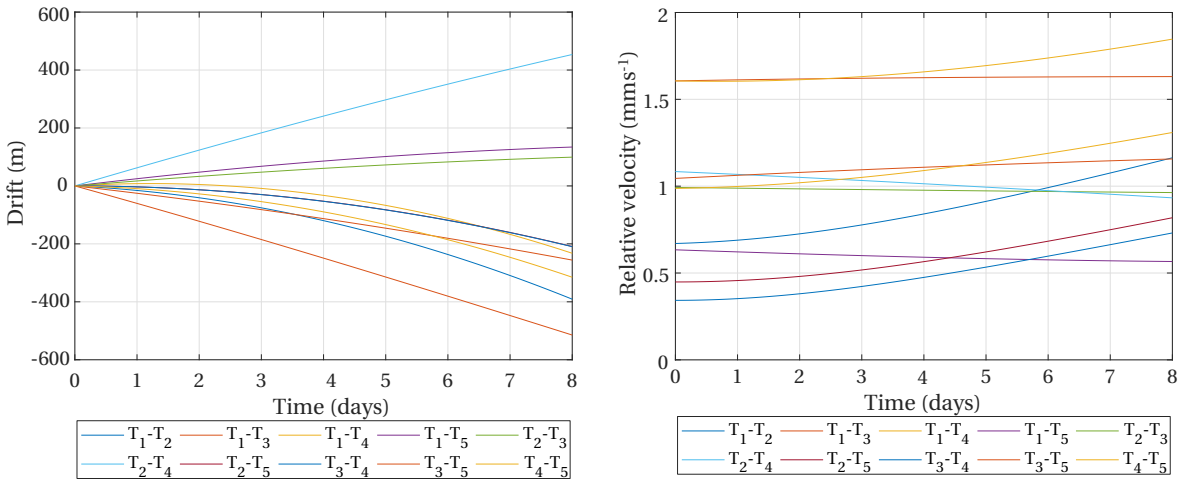

(a) Relative drift (b) Relative drift rate

Figure 5.14: Drift and drift rate profiles - large formation scenario.

relative distances. The Appendix C.4 also depicts the drift with respect to the formation reference point and the drift along individual coordinates relative to each other.

5.4.2. DEFORMATION UNDER UNCONTROLLED DYNAMICS

For a complete assessment of how the formation changes over time in free-drift conditions, the analysis is divided into three sets of metrics: formation deformation and tilt, internal angles and angular tilt of all planes formed by three-telescope sets. These are addressed in the three next subsections.

The results for all metrics are the same for the two formation scenarios due to their dependence on the geometry, rather than on the formation size. The ratios of the relative distances are the same for both the small and large nominal geometries.

FORMATION DEFORMATION AND Π_N-PLANE ANGULAR TILT

The change of the overall formation over time is analyzed according to Junge *et al.*[46]. They provide a two-step metric which measures the deformation of the formation relative to the (prescribed) initial conditions and the tilt of a given plane formed by three of these spacecraft. In general, this deformation metric can be used to evaluate the behavior of the formation at different points in the Halo orbit (or across different Halo-orbit families) and identify which locations are better suited for an energy-efficient formation flight. A

singular measure of deformation may thus provide an insight into how the overall shape and geometry of the formation changes over time when there exists a reference range of values (e.g., prescribed by requirements or defined in an ideal undisturbed environment).

Given that the minimum and maximum drift occur respectively for initial phases of $\phi = 0°$ and $\phi = 180°$ in the Halo orbit, as seen in Figure 5.10, the deformation is assessed at these two distinct locations. Based on the formulation of Junge *et al.*[46], the ϕ-dependent deformation is a function of the change of the relative distances of the spacecraft at a time t after the initial time, t_0. For the IRASSI case, with $n = 5$ spacecraft, the deformation is described by Equation (5.30), where $\boldsymbol{\Delta r}$ is the three-dimensional relative distance vector spanned by Δx, Δy and Δz.

$$D_\phi(t) = \sum_{j=1}^{n-1} \sum_{k=j+1}^{n} \left| \frac{\left|\left|\boldsymbol{\Delta r}_{\phi,j}(t) - \boldsymbol{\Delta r}_{\phi,k}(t)\right|\right|}{\left|\left|\boldsymbol{\Delta r}_{\phi,j}(t_0) - \boldsymbol{\Delta r}_{\phi,k}(t_0)\right|\right|} - 1 \right| \tag{5.30}$$

Junge *et al.* study the change in formation orientation by arbitrarily selecting three members of the cluster (a four-spacecraft formation arranged as a regular tetrahedron). However, given the asymmetric nature of the IRASSI formation geometry, angular changes concerning any set of three spacecraft may not be representative of the other nine sets. This analysis is performed later in the chapter, under 'Triplets Angular Tilt'. Therefore, instead of measuring a hypothetical angular tilt of the formation, the tilt of the reference Π_N plane is evaluated. This is achieved, firstly, by considering three points p_1, p_2 and p_3 contained in the Π_N plane, defined at the initial time t_0 as:

$$p_1 = (\Delta x_{0_{T_1}}, \Delta y_{0_{T_1}}, 0) \tag{5.31a}$$

$$p_2 = (\Delta x_{0_{T_3}}, \Delta y_{0_{T_3}}, 0) \tag{5.31b}$$

$$p_3 = (\Delta x_{0_{T_4}}, \Delta y_{0_{T_4}}, 0) \tag{5.31c}$$

The attitude of the Π_N plane is then defined by the corresponding plane normal unit vector:

$$\boldsymbol{n}_\phi(t) = \frac{\left(\boldsymbol{\Delta r}_{\phi,p_2}(t) - \boldsymbol{\Delta r}_{\phi,p_1}(t)\right) \times \left(\boldsymbol{\Delta r}_{\phi,p_3}(t) - \boldsymbol{\Delta r}_{\phi,p_1}(t)\right)}{\left|\left|\left(\boldsymbol{\Delta r}_{\phi,p_2}(t) - \boldsymbol{\Delta r}_{\phi,p_1}(t)\right) \times \left(\boldsymbol{\Delta r}_{\phi,p_3}(t) - \boldsymbol{\Delta r}_{\phi,p_1}(t)\right)\right|\right|} \tag{5.32}$$

Finally, the Π_N-plane tilt can then be evaluated, as the angular shift between the normal of the plane at time t and the normal at time t_0:

$$\alpha_\phi(t) = \arccos\left(n_\phi(t) \cdot n_\phi(t_0)\right) \tag{5.33}$$

The results are plotted in Figure 5.15, for both initial phase values. For $\phi = 0°$, the deformation value after eight days is measured at $D_{\phi=0°} = 0.75$, whereas the corresponding angle of tilt grows to $\alpha_{\phi=0°} = 1.3°$. The same metrics measured for $\phi = 180°$ are slightly lower for the deformation, with $D_{\phi=180°} = 0.71$, but larger for the tilt, with $\alpha_{\phi=180°} = 1.6°$. This divergence is interesting: whereas the plane Π_N seems to rotate more for $\phi = 180°$, the change in relative positions over time as measured by D decreases. This, however, seems to contradict the fact that the largest drift magnitudes around the orbit seem to occur for $\phi = 180°$, as Figure 5.10 illustrates (for the single spacecraft relative to reference case). The difference in initial conditions and the size of the formation may partly explain this discrepancy. One of the drawbacks of the deformation metric D is the fact that it provides no insight into which coordinate or spacecraft actually promotes the change in the formation (that is, it does not tell us how this change is distributed among formation pairs). D is simply an overall evaluation of the degree of formation deformation. It may well be therefore that the larger the number of spacecraft in the formation, n, the harder it may be to detect the influence of individual spacecraft on the change of relative distances over time.

More importantly, D does not translate into a measure 'goodness' or 'desirability' of formation geometry. A high deformation value relative to a reference simply means that the spacecraft are in a dynamic environment and such formation can still be acceptable, as long as operational and scientific requirements are met. In a realistic scenario, the usefulness of the deformation metric for IRASSI lies therefore in detecting off-nominal conditions which cause the formation to degrade significantly (exceeding the allowable deformation value D at a given location in space), thereby requiring a control input to return the formation to the original or desired state.

To complement the deformation analysis, two additional metrics were considered. These are the internal angles and the tilt of all telescope triplets, which are described in the next subsections.

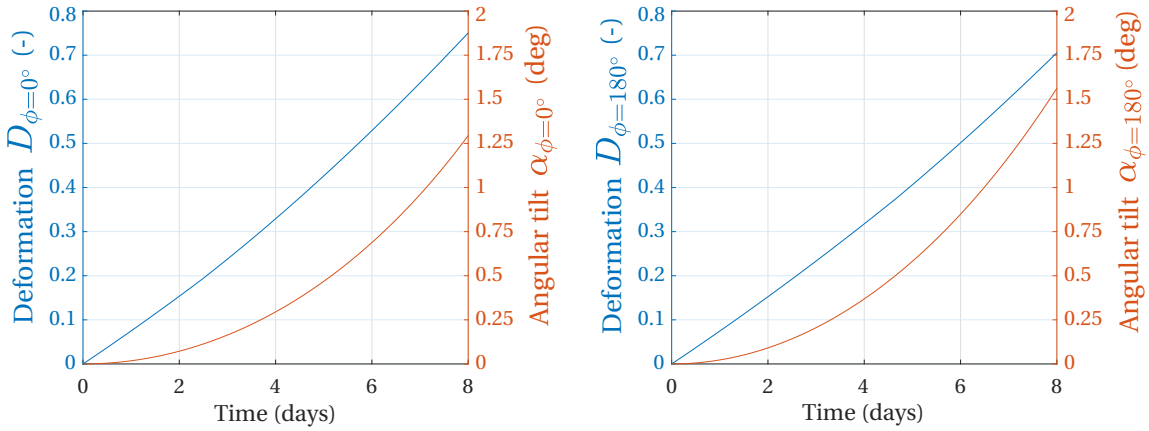

(a) $\phi = 0°$ (b) $\phi = 180°$

Figure 5.15: Formation deformation D_ϕ and angular tilt α_ϕ of plane Π_N. The metrics are independent of formation size.

5

INTERNAL ANGLES

To gain a deeper insight into how the formation geometry changes over time, the measured change of the internal angles of the triangles formed by each subset of three spacecraft are calculated. There are a total of 10 triangles in the formation, which results in 30 measured internal angles. The evolution of these internal angles over time is presented in Figure 5.16, where it may be concluded that it is comparable for both initial phase values ϕ.

Generally, in free dynamics conditions, some angles will become more acute, with decreases of nearly 22°, whereas others will become more obtuse, increasing up to 16° (not surprisingly, the maximum and minimum changes occur for the same spacecraft set: $T_2 - T_3 - T_4$). The angular change over the eight days is approximately linear for nearly all cases and the average change of all angles at the end of the simulation is of 7.1° for $\phi = 0°$ and 7.2° for $\phi = 180°$. The overall geometry of the formation is therefore largely maintained at both extrema of the Halo orbit. This also hints at the possibility that once a desired formation is achieved at the beginning of an Observation Cycle, very little control effort is expected to be required to counteract disturbances and formation requirement violations.

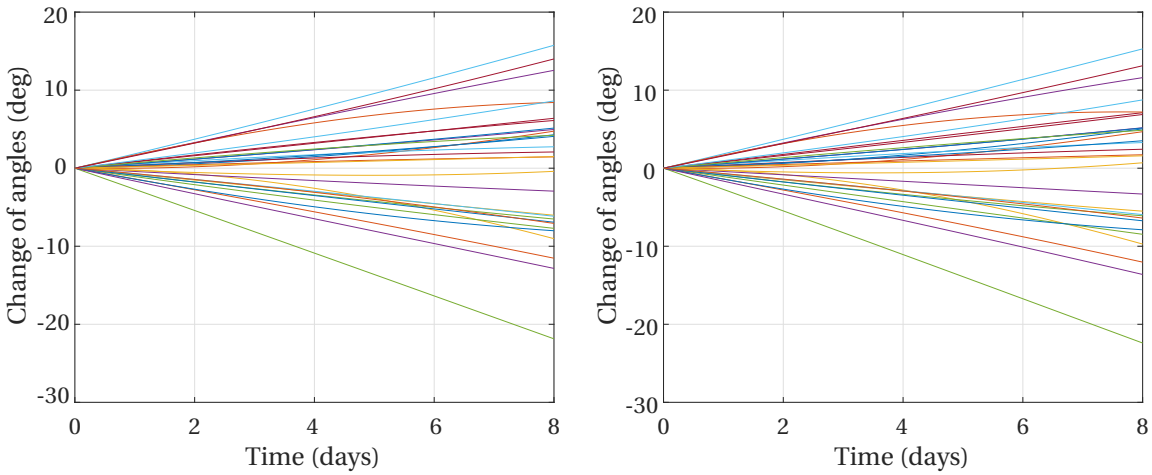

(a) $\phi = 0°$ (b) $\phi = 180°$

Figure 5.16: Internal angles. The metrics are independent of formation size.

Together with the formation deformation results from subsection 5.4.2, one may infer that the mild increase in average internal angle change (7.1° for $\phi = 0°$ vs. 7.2° for $\phi = 180°$) is associated with a mild decrease in the deformation metric D (0.75 for $\phi = 0°$ vs. 0.71 for $\phi = 180°$) which measures the change in relative

position.

TRIPLETS ANGULAR TILT

The angular tilt calculation was extended to all ten sets of three telescopes within the formation. This was done by replacing the term $\boldsymbol{\Delta r}$ in Equation 5.32 with the initial coordinates of the telescopes defined in Table 5.2. The results are shown in Figure 5.17 for both initial phase values ϕ.

Similar to the deformation D, a slightly lower value for the rate of change in orientation the triplets was found for $\phi = 180°$, in comparison to the $\phi = 0°$ case. The average tilt among all sets is 11.8 at the end of the simulation for the latter, compared to 11.7 for the former. This means therefore that the change of orientation of the planes is independent of orbit location.

It is interesting to observe that when the initial conditions of two out of the three spacecraft have an out-of-plane component ($\Delta z_0 \neq 0$), the angular tilt of the plane formed by these spacecraft is higher. Consider, for instance, the set $T_1 T_3 T_4$: with T_1 and T_4 having symmetrically opposed Δz_0 values, the tilt is approximately 18° at the end of the eight days for the $\phi = 0°$ case, more than one order of magnitude greater than the in-plane Π_N set of subsection 5.4.2, at $\alpha_{\phi=0°} = 1.3°$. This also shows that the evolution of the orientation of reference plane Π_N is indeed not representative of those formed by members of the formation.

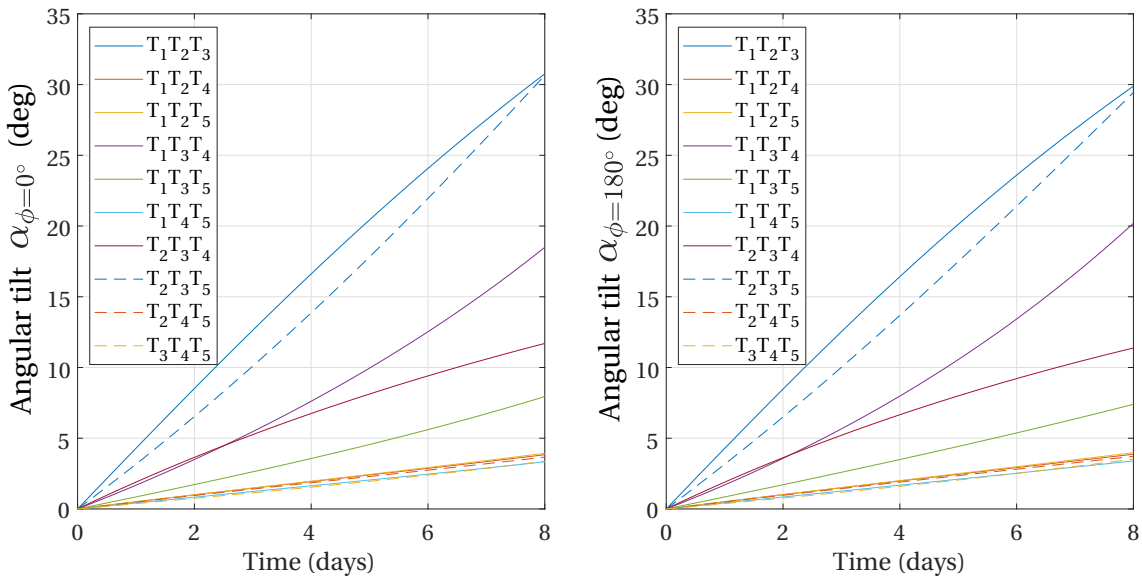

(a) $\phi = 0°$ (b) $\phi = 180°$

Figure 5.17: Triplets Angular Tilt. The metrics are independent of formation size.

Note in Figure 5.17 that, interestingly, the tilt of all triplets decreases with $\phi = 180°$, except the set $T_1 T_3 T_4$. The tilt of this set increases from approximately 18° for $\phi = 0°$ to 20° for an initial phase $\phi = 180°$. Given that the coordinates of the points considered for evaluating the tilt of reference plane Π_N are based on this set (cf. Equation 5.31), it is not surprising that an increase of tilt is observed for reference plane Π_N too in Figure 5.15.

Ultimately, deformation metrics (formation deformation, change in internal angles and triplets angular tilt) remain nearly constant with varying phase ϕ and the conclusion follows therefore that deformation is independent of location on the reference orbit.

5.4.3. REQUIREMENT 1: VISIBILITY OF RANGING SYSTEM

During the span of eight days, no loss of intervisibility was detected among the telescopes. That means that, given the nominal formation geometry, the passive drift of the formation shall allow for the ten baselines of the spacecraft to be computed continuously on board during activities which do not involve maneuvers.

The formation was propagated further in time to 140 days, both using Roberts' model and GMAT and both for the small and the large formation. The measured number of invisibility links, as proposed in Equation 4.4, is shown in Figure 5.18(a). Whereas within each model, expectedly no difference was found between small and large formation, the results in terms of intervisibility detection differ somewhat between those obtained with Roberts' model and GMAT. Using Roberts' motion model, it took a full 34 days before one laser link was

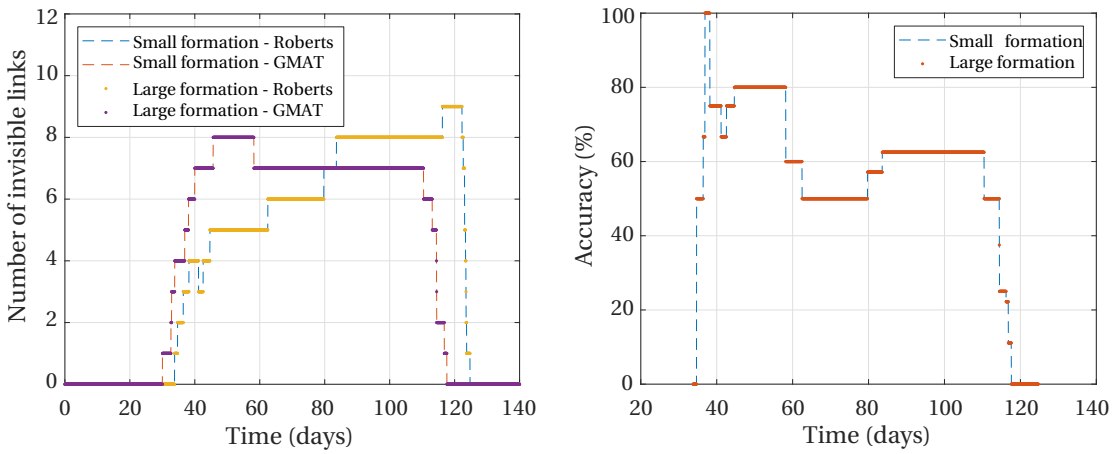

(a) Invisibility links (b) Accuracy

Figure 5.18: Number of invisible links and accuracy of predictions using Roberts' model.

lost between a pair in the formation. The number of laser links detected with Roberts' model rises with time until only one link remaining (between telescopes T_1-T_3) at day 117. Interestingly, with a rapid increase of the relative distance of the Δy and Δz coordinates and assuming that the lasers perform equally nominally at increased relative distances, full intervisibility of the formation is recovered at day 125. Only 2.5 days elapse between the maximum detected loss situation and full visibility recovery.

This pattern is somewhat observed with GMAT. However, the first loss of laser contact occurs within 30 days and the peak of invisibility for eight out of the ten baselines is observed at day 46 (10 weeks earlier than with Roberts' model). Throughout the simulated period, there are two links (compared with only one in the earlier case) that are never lost (between telescopes T_2-T_3 and T_3-T_5). A prolonged period of invisibility is detected between day 58 and 110 with GMAT, but within one week, full visibility is regained.

Thereafter, the results of the Roberts'-model-derived detection were compared with those obtained with GMAT. The accuracy is calculated as the ratio between the accurately predicted telescope pair and the total number of predicted pairs with Roberts' model. This is shown in Figure 5.18(b) in percentage terms. As a remark, this measure reflects how many pairs detected with the model are accurately individually identified (that is, also predicted by GMAT) and does not reflect the proportion between the identified number of lost links between the two models. The accuracy is independent of formation size. From Figure 5.18(b), it is visible that the accuracy of the detections using Roberts' model increases sharply as soon as intervisibility loss is detected (34 days) and decreases to half when the two-month mark is hit. The accuracy subsequently increases again to 62.5% and from day 110 it decreases nearly continuously until day 118, after which it remains null. Note that, as remarked, although 100% accuracy is achieved between days 37 and 38, the model-derived detection only captures three of the five lost links. At an average accuracy of 56% throughout the simulation, the model is only a mediocre predictor of intervisibility. However, the Roberts' model is suited only for short-time relative motion modeling. A 140-day simulation with GMAT, in fact, leads the free-drifting formation into a heliocentric orbit, where neither the Richardson's nor the Roberts' models apply any longer and, as such, this analysis (or comparison) stands as a mere trivial exercise.

5.4.4. REQUIREMENT 2: RELATIVE POSITIONING PERFORMANCE

The relative positioning performance is evaluated in light of the nominal formation setups defined in Table 5.2. The evaluation is made in terms of baseline estimation accuracy, defined as the deviation between the true baselines and those estimated from the spacecraft positions. As introduced in section 4.2.3, errors associated with the distance measurements provided by the metrology system and that of the telescope attitude sensors must be assumed. The nominal values selected are based on work carried out by partners within the IRASSI consortium [16, 39]. The distance measurement errors are hence assumed to be Gaussian-distributed, with zero mean value and a standard deviation $\sigma_d = 1\mu$m and the three orientation angles $\boldsymbol{\nu}$ of each satellite have a standard deviation of $\sigma_\nu = 0.1$ arcsec. No lever-arm distortions or lever-arm distance measurement errors are considered. These parameters define the nominal estimation errors case for the

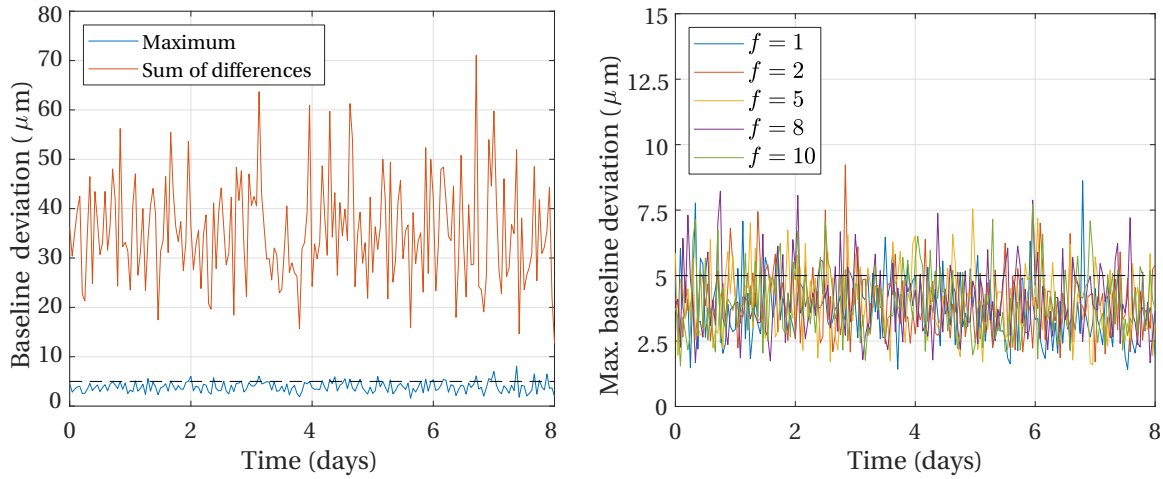

(a) Nominal formation

(b) Formation with varying f

Figure 5.19: Baseline deviation over time, for the nominal performance case: $\sigma_d = 1\,\mu$m and $\sigma_v = 0.1$ arcsec. The metrics are independent of formation size.

positioning performance analysis.

Figure 5.19(a) shows the maximum baseline error at each instant and the sum of differences between the estimated and true spacecraft baselines for the nominal performance case. Similar to the previous metrics, the results are dependent on the formation geometry and not on the formation size. The results of Figure 5.19(a) are therefore representative of both formation scenarios. The black line defines the required baseline estimation accuracy of 5 µm. It is visible from the plot that the maximum baseline deviation stays below the required value for the majority of the simulation time, with an average of the maximum values at 3.70 µm. The sum of the estimated baseline differences varies roughly between 15 µm and 70 µm. The selected formation geometry seems to be acceptable in terms of relative positioning, albeit at the upper limit of the allowable baseline estimation accuracy. There are indeed instances in which the limit is violated, using a Gaussian distribution of the errors.

The question may therefore arise as to whether: 1) different relative position ratios and/or 2) the assumed errors may have influenced the performance of the relative position estimation algorithm. A short sensitivity analysis is conducted to assess the impact of varying the nominal geometry and the nominal errors on the relative positioning performance.

Firstly, the ratios of relative distances are modified. This is done by assigning different values to the out-of-plane component set h. With d defined in Table 5.2, the new formation geometries are a function of varying factor f:

$$h = \left\{-fd, -\frac{f}{2}d, 0, \frac{f}{2}d, fd\right\}\Delta z \tag{5.34}$$

For the analysis, this parameter is tested at $f = \{1, 2, 5, 8, 10\}$, keeping in mind that $f = 4$ corresponds to the nominal geometry case. The resulting geometries do not necessarily abide by Requirements 1 and 3, since the focus is here is rather on evaluating the impact of different relative distance ratios on the performance of the baseline estimation. The estimation results are shown in Figure 5.19(b) and summarized in Table 5.3. As can be observed, there is no benefit in modifying the nominal formation geometry as the mean maximum baseline accuracy is slightly higher for conditions other than the nominal one. Subsequently, the assumed σ_d and σ_v errors are varied using the same nominal geometry as a basis. The distance measurement error is tested at $\sigma_d = \{0.1, 1, 5\}\,\mu$m and the angular errors at $\sigma_v = \{0.04, 0.1, 0.4\}$ arcsec, whereby the minimum values for both correspond to values experimentally achieved by internal project simulations and the maximum values are those set by the high-level requirements of the mission (cf. Table 2.1). The mean of the maximum estimated baseline is shown in Table 5.4, whereas the full results are plotted in Figure 5.20.

From the varying-error analysis it is possible to conclude that baseline estimations within a required accuracy of 5 µm are achievable for $\sigma_d \leq 1\,\mu$m and for $\sigma_v \leq 0.1$ arcsec with the present nominal geometry. Although demonstrated in laboratory during experimental research, it remains to be proven during space flight whether, as an integrated system, the baseline estimations are within the required range. Furthermore, the

Table 5.3: Average maximum baseline deviation with nominal errors and varying formation geometry. The colored cell identifies the nominal formation case.

Baseline deviation (μm)					
$f = 1$	$f = 2$	$f = 4$	$f = 5$	$f = 8$	$f = 10$
3.73	3.95	3.70	3.98	4.04	3.97

Table 5.4: Average maximum baseline deviation with nominal formation and varying error distribution. The colored cell identifies the nominal error case.

	Baseline deviation (μm)		
σ_v (arcsec)	σ_d (μm)		
	0.1	1	5
0.04	1.36	2.25	8.92
0.1[i]	3.32	3.70	9.65
0.4	12.56	13.80	16.71

[i] Omitted from Figure 5.20 for clarity.

position performance is more sensitive to changes in angular error than in distance measurement, which confirms previous findings [47].

Overall, the baseline estimation analysis shows that the required accuracy is achieved almost continuously with the nominal geometry for the nominal error parameters. As technology evolves and the technological readiness level of the IRASSI-developed systems increases, it is up to technicians and engineers to ensure that hardware becomes qualified for space operations and that the laboratory results are reproduced, validated and that the relative position accuracy below 5 µm is guaranteed throughout the mission. This is especially relevant for observations of targets at the shorter wavelengths (≈ 50 µm), which are associated with the strictest estimation requirements.

5.4.5. REQUIREMENT 3: SKY ACCESS

The evolution of the instantaneous sky access over time for the five spacecraft is provided in Figure 5.21 and Figure 5.22 for the small and large formation scenarios respectively. The sky access is evaluated for an initial anti-Sun vector longitude of $\Lambda = 345°$, which corresponds approximately to the epoch of March 1st, 2030, at 12:00 o'clock used in this chapter. The sunshields are perpendicular to the Sun's direction. The exclusion zones for the celestial targets are marked in red (bright red for the last time step and dark red for previous ones, indicating the direction of movement of the exclusion zones on the sky access).

One can observe how the uncontrolled formation drift affects the sky access, as spacecraft enter each other's field of view as they move (without changing their attitude). A remark should be made that, as well as the evolving exclusion zones, one should also see in Figures 5.21 and 5.22 an instantaneous sky access which spans eastwards over time. However, this would make the reading of the plot difficult and only the sky at the initial instant of the simulation is depicted.

By comparing Figure 5.21 and Figure 5.22, it is possible to visualize how proximity affects the projection of the exclusion zones in the sky, with the small formation scenario being naturally much more restrictive than the large formation case. The percentage of total restricted area over time, $A_{rest}(t)$, previously introduced in Chapter 4, is provided in Figure 5.23(b) and defined as:

$$A_{rest}(t) = \frac{\sum_{i}^{n} \sum_{j:j\neq i}^{n} A_{ez_{proj,ij}}(t)}{A_{sky}} \tag{5.35}$$

where $A_{ez_{proj,ij}}$ is described by Equation 4.13 and $A_{sky} = 180° \times 360°$ deg^2 is the total sky area. It is interest-

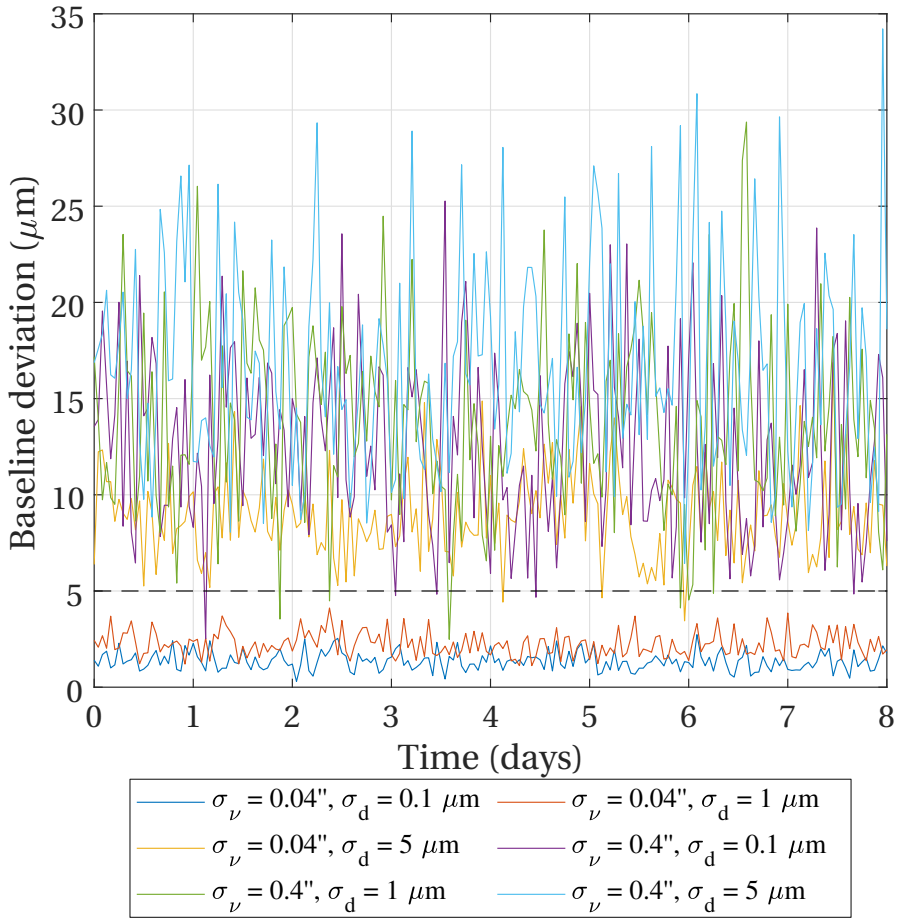

Figure 5.20: Baseline deviation over time for different σ_d and σ_ν values. The metrics are independent of formation size.

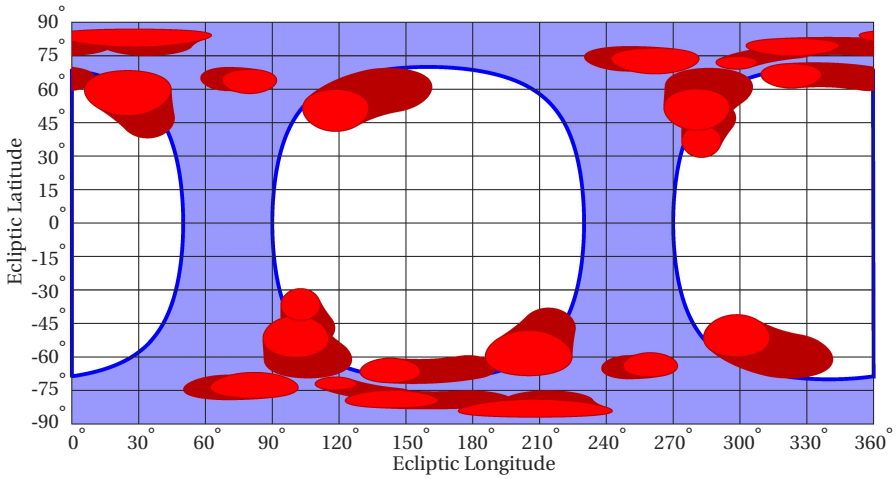

Figure 5.21: Sky access for the small formation scenario. The exclusion zones are marked in red.

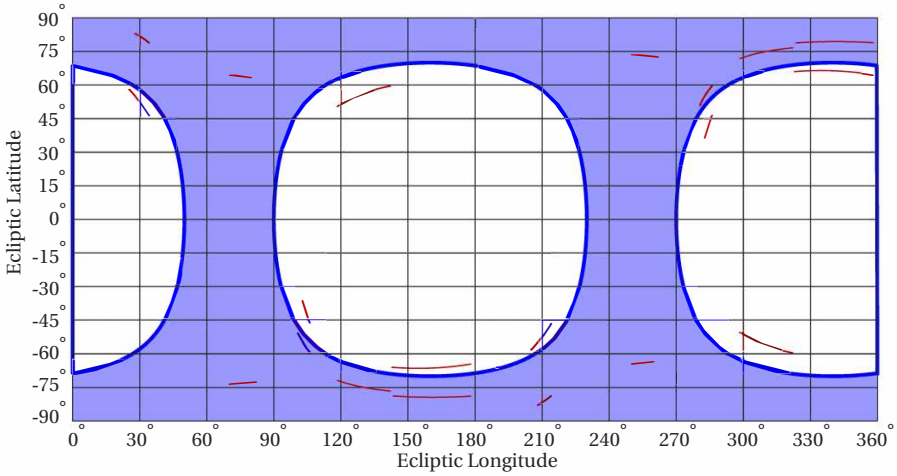

Figure 5.22: Sky access for the large formation scenario. The exclusion zones are marked in red.

ing to observe that, in Figure 5.23(a), A_{rest} initially decreases and thereafter increases. As one observes the negative drifts in Figures 5.13 and 5.14, the expectation is that the restricted area continuously increases, as spacecraft become closer to each other. However, A_{rest} (or rather $A_{ez_{proj,ij}}$) is affected by the relative change in distances between telescope pairs. Averaging the drift ratio (drift as a function of initial separations shown in the Appendix Figure C.7) provides a clue: the average drift of the formation increases initially, promoting a drop in A_{rest}; eventually, from approximately day 3, as the average drift decreases, the value of A_{rest} rises. This is shown Figure 5.23(b), where the curves for both small and large formation scenarios coincide. Over the 8-day simulation, the small formation occludes 4.3% of the total sky area on average, whereas the large formation only 4.4×10^{-4}%.

Obviously, only the exclusion zones which fall within the blue area restrict, in practice, the accessibility of the sky and the selection of possible targets, as explained in Section 4.2.4. Although no maximum value of sky exclusion area is imposed, a null value is never achievable and, thus, the minimization of exclusion must be pursued. With the selected nominal geometry, in the worst case (.i.e, for the small formation scenario) it can be observed that over 95% of the total sky remains unobstructed by the spacecraft in free-drift conditions. This can be deemed as an acceptable result, keeping in mind that a suitable target allocation strategy must therefore ensure that, at a given epoch, targets due for observation are not inaccessible due to neighboring telescopes throughout the whole observations period.

The simulated conditions correspond to a free drift, without any controlled relative motion. If a baseline change maneuver is given (to contract or expand the formation, as expected for the real IRASSI case) such that the initial nominal geometry of the formation is maintained, then one would observe exclusion zones that do

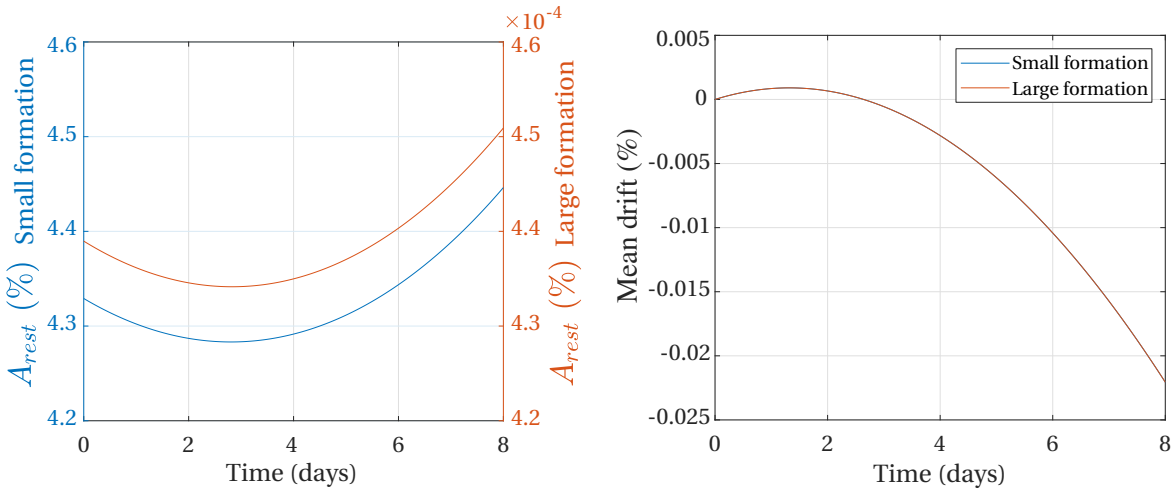

(a) A_{rest} (b) Mean drift

Figure 5.23: A_{rest} and mean drift over time for both small and large formation scenarios.

Table 5.5: Initial coordinates for the IRASSI formation, pointing to a direction parallel to the Δz-Δx plane, for two simulation conditions: small and large formation.

Tele-scope	**General formation coordinates**	**Small formation** $\boldsymbol{d}$ **= 10 m**	**Large formation** $\boldsymbol{d}$ **= 1000 m**
T_1	$(d, 4d, 0)$	$(10.0, 40.0, 0.0^{\mathrm{i}})$	$(1000.0, 4000.0, 0.0)$
T_2	$(d\cos(\varphi), -2d, -d\sin(\varphi))$	$(3.1, -20.0, -9.5)$	$(309.0, -2000.0, -951.1)$
T_3	$(d\cos(2\varphi), 0, -d\sin(2\varphi))$	$(-8.1, 0.0, -5.9)$	$(-809.0, 0.0, -587.8)$
T_4	$(d\cos(3\varphi), -4d, -d\sin(3\varphi))$	$(-8.1, -40.0, 5.9)$	$(-809.0, -4000.0, 587.8)$
T_5	$(d\cos(4\varphi), 2d, -d\sin(4\varphi))$	$(3.1, 20.0, 9.5)$	$(309.0, 2000.0, 951.1)$

not 'move' or span across the sky, but merely change in size. Should the baselines contract, nonetheless, then the target allocation procedure should ensure that at the closest point of approach the target is still visible and not occluded by neighboring spacecraft.

5.5. INFLUENCE OF Π_N-PLANE ORIENTATION ON FORMATION DYNAMICS

IN the previous subsection, the formation dynamics was analyzed for a pointing direction of the interferometer parallel to the Δy-Δx plane (i.e., parallel to the ecliptic plane). However, a different set of initial conditions, namely the orientation of plane Π_N, may give rise to a different relative motion profile, using the same nominal geometry. The analysis was repeated therefore for a new orientation of plane Π_N, parallel to the Δz-Δx plane (normal to the ecliptic plane) and for two formation sizes, 'small' ($d = 10$ m) and 'large' ($d = 1000$ m). The simulation duration remains at eight days. Figure 5.24 shows an illustration of the two orientations. The new set of conditions are summarized in Table 5.5, considering that the allocation h_i among formation members of the h set is:

$$h_i = [4d, -2d, 0, -4d, 2d]\ \boldsymbol{\Delta y},\ \ i = T_1, ..., T_5 \tag{5.36}$$

To avoid repetition, the results of all tested formation dynamics conditions are briefly summarized in Table 5.6. The metric means reflect the average of absolute values. The main findings which invoke a comment are addressed in the next paragraphs.

The new formation orientation gives rise to a slightly more mobile formation. Although in all cases the formation contracts in free-drift conditions, a formation with an out-of-plane component along the Δy-axis

Table 5.6: Formation dynamics results for two different formation pointing directions and two formation sizes.

Metric	**Formation pointing direction parallel to**			
	Δy-Δx plane		**Δz-Δx plane**	
	Small	**Large**	**Small**	**Large**
Drift (m), mean[i]	2.8	281.5	6.2	621.2
Drift rate (mm s^{-1}), mean[i]	11.1×10^{-3}	1.1	18.0×10^{-3}	1.8
Deformation				
$D_{\phi=0^\circ}$	0.8	0.8	1.5	1.5
Plane Π_N $\alpha_{\phi=0^\circ}$ (deg)	1.3	1.3	31.6	31.6
Internal angles change (deg), mean[i]	7.1	7.1	11.8	11.8
Triplets $\alpha_{\phi=0^\circ}$ (deg), mean[i]	11.8	11.8	24.0	24.0
Req. 1: visibility of ranging system				
No. invisible links	0.0	0.0	0.0	0.0
Req. 2: relative positioning performance				
Baseline deviation (µm), mean of maximum[ii]	3.7	3.7	3.7	3.7
Req. 3: sky access				
A_{rest} (%), mean[ii]	4.3	4.4×10^{-4}	4.7	4.8×10^{-4}

[i] Mean over sets at the end of simulation
[ii] Mean over time

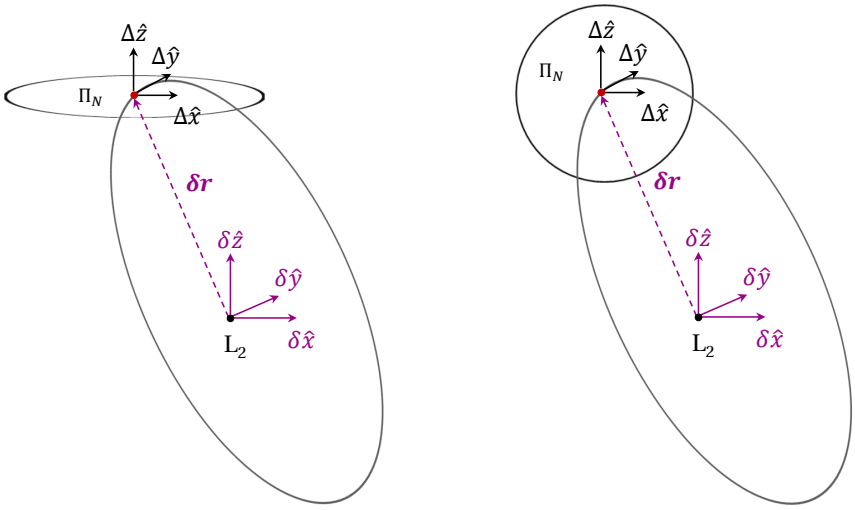

(a) Π_N plane parallel to Δy-Δx (b) Π_N plane parallel to Δz-Δx

Figure 5.24: Illustration of the two formation pointing orientations in the orbit around L_2.

leads to a shorter relative separation at the end of the eight days. Because telescopes come closer to each other, the average A_{rest} is slightly higher for the new formation orientation case. As a remark, although for all scenarios tested no telescope comes within 20 m of each other throughout the simulation (including for small formation scenarios), proximity during passive periods in orbit must nonetheless be monitored to ensure that no collisions occur.

With the Π_N plane parallel to the Δz-Δx plane, the deformation measure $D_{\phi=0^\circ}$ doubles compared to the previous orientation case and the detected changes in internal angles of each set of three telescopes are higher. The average change of spacecraft triplets also nearly doubles to 24°. Additionally, while previously the average was 7.1°, the new orientation raises this average change to 11.8°.

While there is no loss of visibility for any of the tested conditions over the eight days, it takes only 13 days with the new formation orientation (Π_N plane parallel to the Δz-Δx plane) for the first link, out of the ten, to be lost. This compares to 34 days with the previous orientation case, using Roberts'-model-based detection. The average maximum baseline deviations over time, however, remain the same.

Although the new orientation is associated with a higher rate of change of the nominal formation, this analysis concludes that over the time scales of interest, the nominal geometry remains stable over time and satisfies the formation requirements in free-drift conditions, independent of the orientation of the Π_N plane, that is, independent on the attitude of the geometry in inertial space.

5.6. CHAPTER SUMMARY

THIS chapter provides an analysis of the formation in free-drift conditions in a Halo orbit around the L_2 point. An analytical formulation for periodic motion in Halo orbits by Richardson [43] opens the chapter and, based on this model, the relative motion equations derived by Roberts [44] is thereafter introduced. The relative motion approximation is validated by considering a spacecraft in the vicinity of a formation reference point contained in the Π_N plane. The validation process consisted of evaluating the relative position and velocity errors of the model against the GMAT tool for different initial conditions over 20 days. The location of the reference point on the Halo orbit and the initial epoch were varied. The modeling error exhibited generally an exponential relationship with time. For Class-I Halo orbits, position errors of up to 45 m (or 10% of the relative separation) can be expected over the simulation time for different initial phases ϕ along the orbit. The modeling error was shown to be largely independent of the initial epoch. For the time scales of interest for IRASSI, eight days or less, Roberts' relative motion model was thus deemed very suitable due to the low magnitude of the deviations with respect to GMAT and it was used as a basis for the formation dynamics analysis.

Using the nominal formation geometry developed in Chapter 4, the dynamics were evaluated for a small (d = 10 m) and a large (d = 1000 m) formation scenarios for a total of eight days. Two different orientations

of the formation were also considered, whereby an orientation of plane Π_N parallel to the Δz-Δx resulted in a more dynamic formation due to the local gravity environment. Relative drift values of up to 15 m were observed for small formations and two orders of magnitude higher for the large formation scenarios. The same proportionality was naturally maintained in the relative velocities, the maximum of which was registered at approximately 1.8 $\mathrm{mm\,s^{-1}}$. The highest tilt of the planes formed by spacecraft triplets was detected for an orientation of plane Π_N parallel to the Δz-Δx, amounting to an average of 24°. This means that although the formation geometry is largely maintained, the orientation of the formation in inertial space changes considerably over time, at an average of 3°/day. The deformation of the formation, however, is independent of the location on the reference orbit.

The requirements identified in Chapter 4 were assessed for the free-drift conditions, namely the visibility of the ranging system, the relative position performance and the sky access. No loss of intervisibility was detected over the eight days of simulation. Depending on the orientation of the formation, it takes between two and four weeks until at least one of the ten metrology links is lost. Moreover, using nominal error assumptions regarding distance measurement and pointing accuracy, the baseline estimation accuracy largely remains under the required 5 µm with the nominal geometry, independently of formation size. Finally, over 95% and 99.9% of the total sky remains unobstructed for observations for a small and large formation respectively during the uncontrolled drift, independently of the orientation of the formation, which is deemed as an acceptable outcome. Overall, these metrics show that the nominal formation geometry remains stable over time and satisfies the formation requirements in free-drift conditions, independent of the orbit location and of the orientation of the formation, without the risk of an imminent violation of predefined conditions or a sudden change of performance.

6

Formation Guidance, Navigation and Control

We hunger to understand, so we invent myths
about how we imagine the world is constructed -
and they are, of course, based upon what we know,
which is ourselves and other animals.

So we make up stories about how the world was hatched from a cosmic egg
or created after the mating of cosmic deities
or by some fiat of a powerful being.

Carl Sagan

ABSTRACT

Chapter 6 deals with the selection of autonomous coordination and control architectures of the IRASSI interferometer, with a particular focus on the Nominal Operations phase. The Guidance, Navigation and Control (GNC) modes are firstly introduced, with a brief description of associated maneuvers and planning tasks. A bottom-up, distributed environment-sensing and maneuver-planning organization approach is envisaged and a behavior-based control coordination is largely deemed suited for the different GNC modes of a free-flying formation such as IRASSI.

6.1. INTRODUCTION

THE focus of the present chapter is the definition of the planning activities and of the formation organization structures which support the science program of the IRASSI mission. Since the geometry and dynamics envelopes of the formation have been defined, general control consideration must be set out, providing the backbone of the operational processes subject to optimization in the last part of this manuscript.

It should be remarked that although this research does not concern the implementation of formation flying control methods to simulate the maneuvers, it does outline a general framework for this purpose which can be used in future work.

6.2. OPERATIONAL MODES DURING NOMINAL OPERATIONS

DIFFERENT activities of the mission require various levels of planning and accuracy in execution. Although activities which involve a high degree of advance planning are of most concern to the present thesis, a short overview of the guidance, navigation and control (GNC) modes of IRASSI is hereby presented.

The GNC modes are closely associated with the phases/subphases and their maneuvers, both previously described respectively in Sections 3.2 and 3.3. The operational modes and associated control interventions are listed in Table 6.1. Gray-shaded cells indicate translations, whereas white-colored cells refer to attitude-related maneuvers or other GNC modes not requiring maneuvers. There is no overlap of maneuver types across different modes.

Table 6.1: GNC modes and maneuvers during Nominal Operations. Maneuvers highlighted in gray indicate translations.

GNC Modes	**Maneuver**	**Planning requisite**
Formation Reconfiguration	Formation Reconfiguration	Yes
Formation Pointing	Formation Pointing	Maybe
Scientific Observations	Baseline Change	Yes
	Fine target-acquisition	No
Calibration	-	-
Uplink/Downlink	-	-
Station-keeping (periodic)	Station-keeping	Yes
Momentum unload (intermittent)	Momentum unload	Maybe
Collision-avoidance (supervised)	Collision-avoidance	No

Formation reconfiguration, baseline-change and station-keeping maneuvers are those which demand the highest computational efforts for a suitable and optimal preparation preceding the execution. They all involve large translational maneuvers, that must be collision-free and can be optimized according to time or fuel resources, whilst simultaneously abiding by their respective functional and science requirements.

Although there is a fixed sequential slot for the reconfiguration and baseline-change maneuvers, the timing of the station-keeping or desaturation of reaction wheels (momentum unload) is variable. They can either be carried out in a standalone fashion or be combined with reconfiguration maneuvers since no operation of sensitive payload takes place. In the case of station-keeping maneuvers, the thrust magnitudes are also closer to reconfigurations than any other translation maneuver. Similarly, a slew of spacecraft to change its pointing direction could also be carried out in parallel to reconfigurations in order to free mission time for science observations. Finally, collision events arise only in off-nominal conditions, such as software or component failure events. Although relative distances must be continuously monitored and a suitable trajectory plan should prevent the materialization of collisions, when one or multiple spacecraft trigger the Collision-avoidance mode, an evasive maneuver(s) takes precedence over any other task. This represents an emergency requesting immediate action to safeguard the future of the mission.

6.3. AUTONOMY AND GUIDANCE DURING NOMINAL OPERATIONS

THE degree of autonomy devised for the IRASSI mission depends on a series of factors, such as visibility from the ground, complexity and cost of ground operations, communications bandwidth available between the formation and ground control and between the formation elements and onboard processing capabilities both in terms of software and hardware.

It is important to recognize that from a science perspective, there is no functional hierarchy within the formation. As twins, all spacecraft have the same construction and share the same responsibility in collecting and distributing observation data. All spacecraft share a communications link to the ground (X-band and Ka-band frequencies) and share a link among each other (X-band). Each element hosts memory storage [1] and processing facilities, for the correlation process of science data [35]. Since these resources are available and given that the formation is not always visible to the ground [14], it is then sensible to expect that the same scope of duties is extended to other functions outside of the observation periods. This means therefore that the planning tasks of the formation will be distributed and can be decoupled from the ground, conferring a degree of flexibility, redundancy, modularity[2] and responsiveness [3] to the free-flying interferometer. IRASSI is then a self-organizing and autonomous entity. This association is consistent with existing literature [50–54].

The high-level distributed network organization is schematized in Figure 6.1(b), where all spacecraft have full knowledge of each others' states and full capability for planning on an individual or cluster level. This contrasts with other available and classical formation autonomy architectures, such as centralized (those consolidated in a single controller with global knowledge, such as a ground station) or strictly decentralized (those concentrated on a leading member, who receives inputs from the ground and is in charge of mission-planning and of dissemination of commands to other members who remain uninformed of each others' states) [4] [58].

The activities which are shared among formation members, apart from observation tasks, are:

- relative motion determination: estimation of relative distances and velocities, via the metrology system.
- uplink: recovery of mission schedules from the ground, such as updates to the catalog and rearrangement of priorities to existing plans, retrieval of ranging information to update station-keeping procedures (tracking and command).
- downlink: transmission of science data and telemetry from the spacecraft to the ground stations.
- science planning: calculation of optimized sequences of targets to sample and the dissemination of such plans.
- maneuver planning and execution: calculation of optimized station-keeping, reconfiguration, baseline-change and collision-avoidance maneuvers as well as the implementation of the generated control commands.

Autonomy and distribution of planning functions imply that the effort is shared across the entire fleet. A coordinator craft distributes a set of discrete independent variables derived from a global pool on which constraints were imposed. The spacecraft compute the individual costs (e.g., the fuel or ΔV expense of moving from the current position to another) associated with the variable set. The results are returned to the coordinator who recombines the results according to a global objective function and generates the final optimal solution. The coordinator broadcasts the resulting plan to all remaining formation elements so that local controllers can compute their actuator strategy. Each individual satellite can still replan to optimize other local parameters ensuring that global constraints (e.g., time, intervisibility, collision-avoidance) are not violated.

[1] The minimum amount required of onboard memory storage capacity is of approximately 20 Tb.

[2] Modularity can be expressed as a mechanism which dismantles a complex system and re-writes it as a set of discrete pieces which interact and cooperate with each other through standardized interfaces [48].

[3] Responsiveness can be defined as the ability to acknowledge, react and adapt to uncertainty [49], increasing the resilience of the system considered.

[4] It is not uncommon, particularly in literature dating from the last decades, to use the terms *decentralized* and *distributed* interchangeably [55, 56] or to ascribe to *decentralization* a set of characteristics which pertain to distributed systems, such as *cooperation* [57]. As systems become more complex and the borders between computational intelligence and traditional space functions disappear, this fluidity of terms and characteristics make it difficult to conceive universal definitions of organizational structures. If cooperation is a feature lent to decentralization, one could similarly establish that IRASSI may act as a decentralized entity in which the role of the node who assigns tasks to the remaining formation elements is rotated among all members iteratively.

Parallelization of computing resources on a shared network is a way to take advantage of existing software and hardware capabilities within the fleet.

As explained above, the coordinator makes global decisions according to the planning task at hand and the role is then rotated amongst fleet members. This approach can also be applied to other functions, such as relative motion determination. The responsibility of communicating to the ground can also be assigned to a coordinator who disseminates the updates to the other formation elements and spacecraft then they take turns in handling ground communications. And lastly, distribution applies not only to guidance functions but also to navigation and control, as addressed in the next subsections.

A detailed depiction of a distributed architecture is shown in Figure 6.2, devised by Campbell, 2003 [59]. It features a fleet planner (i.e., a coordinator) and formation control loop for each spacecraft, with individual trajectory planners, control logic, and estimation and environment sensing. Sensing and estimation processes within IRASSI are shared via the metrology system and onboard computers. Campbell points out nonetheless that if the formation is immersed in a relatively stable environment and the relative dynamics between spacecraft are sufficiently slow, similar to the case of IRASSI in the vicinity of the Sun-Earth/Moon L_2 point, then feedforward-control techniques only might be suited to effectively drive the formation to its desired state. In this case, the connection between estimation and control blocks in each spacecraft loop may be removed. The control strategy is addressed in Section 6.5.

As a final remark, it should be mentioned that the quantification of computational requirements for the determination of relative positions, the planning of target sequences and associated maneuvers lies outside the activities foreseen in the frame of this research. Additionally, one may only speculate how advanced processing resources will be once (or if eventually) the mission materializes. Processor hardware shall exist on board anyway, and therefore the issue of scalability is not considered. It is assumed for practical purposes that sufficient processing capacity is equally available among all formation elements.

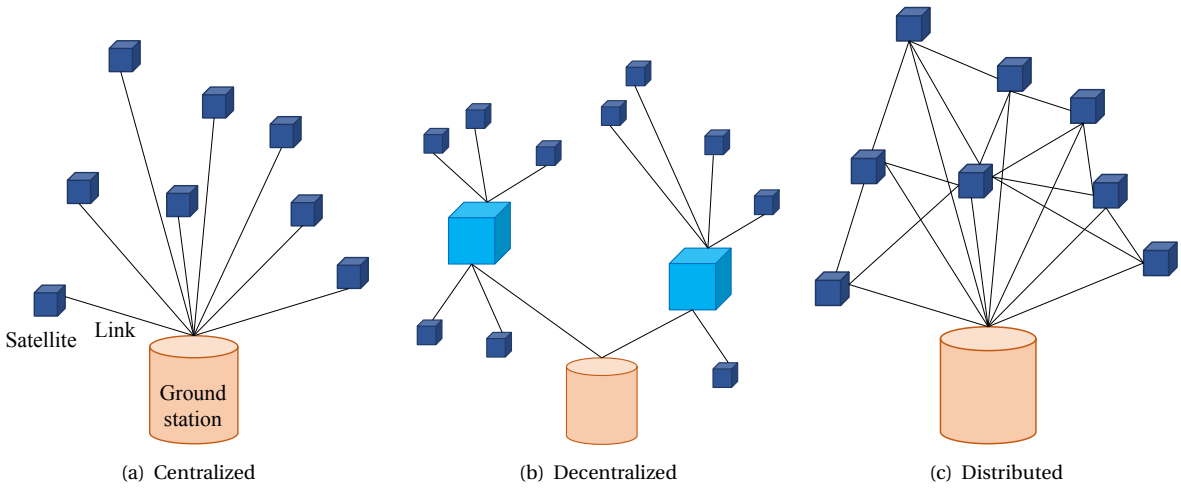

Figure 6.1: Organization of space networks.

6.4. NAVIGATION DURING NOMINAL OPERATIONS

MODELING orbital effects in deep space is a simpler task compared to Earth-orbiting missions due to the lower impact of disturbing forces on formation dynamics. On the other hand, inertial navigation at large distances from the Earth is challenging as absolute position measurements are either unavailable or of very low accuracy.

Luckily, the performance of the mission relies rather on the measurements of relative positions and velocities instead of on the knowledge of absolute states. As long as operational constraints and science goals are satisfied, a general agreement on the absolute positions of the interferometer in space suffices irrespective of its accuracy. Precise force modeling is irrelevant if the entire constellation experiences the same dislocation.

Within IRASSI, the determination of the positions in inertial space is performed by the ground stations. If

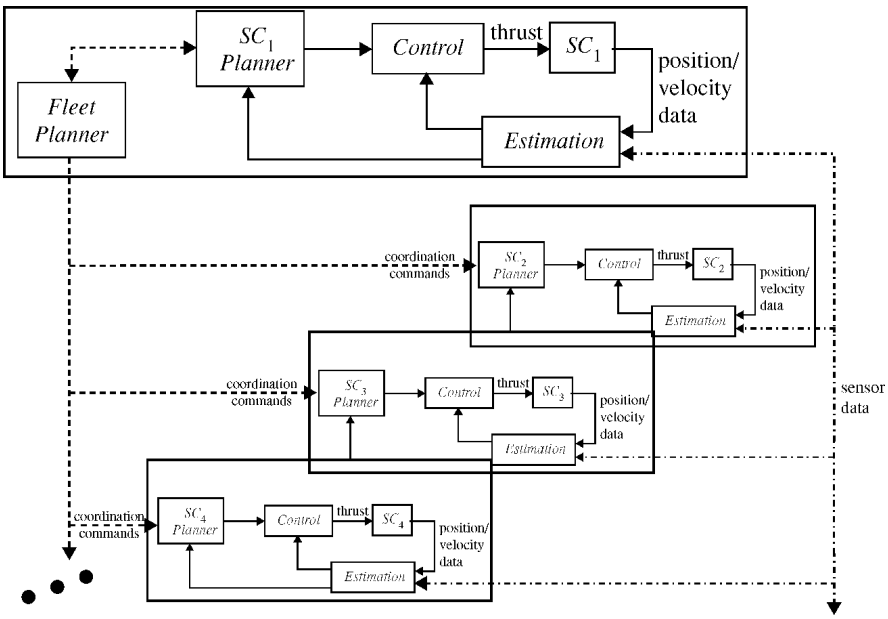

Figure 6.2: Architecture for distributed satellite systems, showing distributed planning and sensing. Source: Campbell, 2003 [59].

these are unavailable or not within reach due to visibility limitations, then internal propagation models are used. These models combine orbital and relative motion dynamics, for redundancy and accuracy, to estimate the current state of the spacecraft based on the previously determined fix. By means of the metrology system, the relative positioning estimator and the X-band antennas, all relative distances are known and shared (a two-way measurement is available for each spacecraft pair), as are positions and velocities in inertial space. Therefore, all formation members possess global knowledge of others' states.

The formation can exploit the observability and redundancy of the relative position measurements to frame controller actuation (and feedback). This information is expected to be continuously available during observations, whereby inter-satellite communication bandwidth is expected to be fully allocated for the transmission of measurement data (transmission of science data is foreseen to take place via the metrology laser link). Synchronization of these measurements is key in order to avoid latencies in the relative positioning estimator, which would have the dual effect of decreasing baseline estimation accuracies and introducing delays in the control feedback loops.

6.5. FORMATION CONTROL COORDINATION DURING NOMINAL OPERATIONS

SELECTING coordination strategies for IRASSI involves understanding the dependencies of the maneuvers on relative and/or absolute motion and may even differ among GNC modes. Performance-specific metrics are thus the biggest driving factor in defining a suitable formation coordination approach, in addition to standard functional design selection criteria such as computational complexity and speed or flexibility to optimize relevant variables (e.g. fuel or ΔV balance).

A short review of common coordination control procedures is firstly provided in the next subsection before their applicability to the IRASSI case is determined in Section 6.5.2.

6.5.1. REVIEW OF FORMATION CONTROL COORDINATION METHODS

Three major formation coordination schemes have been researched in literature: *leader-follower*, *behavioral* and *virtual structures*. These approaches are briefly described below.

LEADER-FOLLOWER COORDINATION STRATEGY

The leader-follower type of coordination is the most studied type of formation control coordination [54, 60–63], whereby a subset of elements track and maneuver relative to a 'chief' satellite who follows an absolute trajectory. Because the formation is referenced on the leading element, as illustrated in Figure 6.3(a), such schemes are suitable for formation-keeping or formation-translation maneuvers in centralized or hierarchically stratified formations. Variations of this top-down method include nearest-neighbor tracking and

barycenter-tracking [64]. The biggest advantage of this scheme is that the control architecture is easy to explore using standard control theory and formation stability is directly measurable. On the other hand, a blind reliance on both leader and follower working nominally subsumes this strategy: 1) if the follower fails, the formation is no longer preserved, since there is typically no feedback from the follower to the leader, and 2) if the leader fails, the formation as a whole might accordingly behave erroneously or be positioned in an unsuitable orbit. Lastly, since formation maneuvering is relegated to follower elements, these will always spend more fuel and therefore global fuel usage minimization and balancing cannot be guaranteed.

Mitigation of fuel or ΔV imbalances could be pursued by switching leadership roles among formation members. However, Tillerson *et al.* [65] as well as Douglass *et al.* [66] have shown that democratic formations (i.e., where the current state of each constituent satellite is equally weighted) consistently achieve both better fuel balance and minimal global fuel usage compared to formations which rotate the leading role.

VIRTUAL STRUCTURES COORDINATION STRATEGY

This scheme regards the formation as a single rigid body. Its elements are distributed relative to a virtual point or virtual leader, as shown in Figure 6.3(b), and during motion, the formation behaves as a rigid structure. In other words, a specified geometric, polygonal formation pattern is maintained during formation translation and rotation maneuvers. Initially emerging as a centralized framework for mobile robots [67–70], this approach has since evolved to parametrize decentralized, space-based formations [71–75], incorporate consensus protocols [76] and even devise mechanical-like joints as virtual links [77].

Although the nomination of a virtual leader in the formation is trivial, selecting a virtual point or center is not. This point can either be selected a priori and remain fixed [78], or be dynamic and specified by:

- the reference orbit [65], whereby the point is described by the nonlinear orbit equations. Since the determination of the point is not dependent on measurements, no dissemination of the information among the fleet is required. Because a massless point is not affected by perturbations, a disturbance model has to be included in the propagation to ensure that the spacecraft track a center that moves with formation.

- averaging the motion of the formation [79], including the disturbances, and agreeing upon it by consensus [80], such that the point tracks the 'unavailable' fuel mass. Since the point moves in inertial space and experiences accelerations, the averaging procedure can be used to adjust its location 'on the fly' to promote fuel balance. In this way, the center of the structure moves closer to elements that are more fuel-depleted or have a higher exhaust velocity, which is a cooperative solution to individual malfunctions, for instance. This does have a nonzero fuel cost for all remaining formation elements [65].

Since the positions of the formation are not interchangeable, the virtual structures approach is suited to high-precision science and formation-keeping tasks. Furthermore, prescribing a coordinated behavior of an inflexible entity in inertial space is a straightforward, computationally simple process. However, the strict requirements in preserving a structural-like movement and the lack of reconfiguration ability limit the realm of applications of this method. The selection of this approach trades therefore global resource (fuel/ΔV, time) efficiency with onboard processing power.

BEHAVIORAL COORDINATION STRATEGY

The basic principle of this decentralized approach is that two or more cooperative spacecraft in a dynamic environment are prescribed a set of behaviors or goals which are possibly conflicting and which compete for actuator resources. The accomplishment of a unified high-level (team) objective emerges from individual actions. Strongly influenced by biology [83–85], behavior-type schemes benefit from their inherent flexibility and the fact that explicit control feedback laws can be designed to correct for deviations of trajectories. These benefits come nonetheless at the expense of mathematical complexity and the fact that local control laws cannot always guarantee global optimal behavior or group stability if the environment is too complex [86]. This approach is widely used in multiagent robotics systems and typical behaviors can include a combination of team navigation, 'move-to-point', target-following, nearest-neighbor tracking, loose formation-keeping or obstacle-avoidance [86–92], as exemplified in Figure 6.4. It is also the underlying mechanism of airborne collision avoidance systems (ACAS) in planes[5]. Standard control formulations involve averaging individual competing behaviors, although other techniques have been proposed in order to increase robustness,

[5] ACAS averts mid-air collisions by warning pilots of the presence of other transponder-carrying aircraft or by issuing a conflict-resolution advisory action sequence for the aircraft involved, resolving the threat of collision. ACAS operates independently of ground-based equipment and air traffic control.

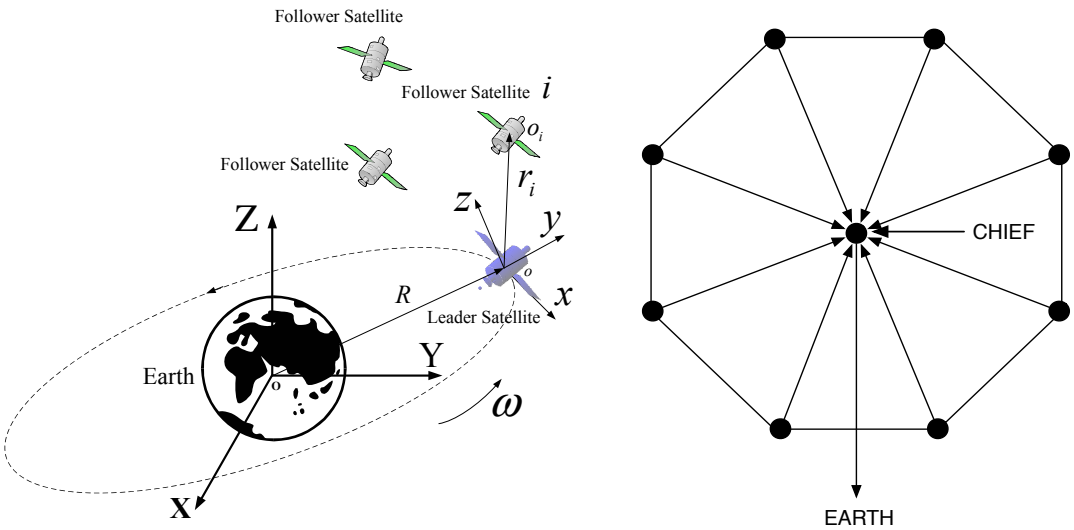

(a) Leader-follower coordination. Source: Yang *et al.*, 2008 [81].

(b) Virtual structures coordination. Source: Vasavada *et al.*, 2007 [82]

Figure 6.3: Illustration of leader-follower and virtual structures control coordination in spacecraft formations.

such as global and local knowledge balancing [93], task-output-hierarchy-based formulations [94], potential-function methods, whereby the sum of individual behavior potentials are null once the formation reaches its desired state [95], and similarly, the equilibrium-shaping approach where individual behaviors are described in the form of desired velocities [96]. Applications of behavior-type coordination range from industrial machine-automation, search and rescue, military and patrolling routines to extraterrestrial exploration by robot swarms. It is not tailored for directing rotational maneuvers or high-precision formation keeping.

6.5.2. CONTROL COORDINATION AND ALGORITHMS

Since attitude maneuvers are largely dependent on targets, it is then relevant to define formation coordination approaches to translation maneuvers. These are defined relative to the GNC modes and corresponding translation maneuvers identified in Table 6.1 of Section 6.2.

- Formation Reconfiguration: during reconfiguration maneuvers, no fixed formation geometry is required to be maintained. Instead, the nominal geometry devised in Chapter 4 is prescribed by the final positions of the elements in inertial space and the spacecraft must reach their destination in a timely manner. This time constraint demands both a minimum speed from the spacecraft in the absolute trajectories and a coordinated relative speed which guarantees that the spacecraft arrive at their destination near-simultaneously to perform preplanned observation tasks.

  For this purpose, a behavioral approach can be used, with goals set as 'move-to-point' and 'maintain relative velocity' within a specified margin. If anomalies are detected during the reconfiguration, this is directly communicated to all members and a democratic solution is reached. For example, if one spacecraft moves too slowly, it should be nudged by others to correct its reference trajectory to keep up with the planned schedule. Or similarly, the remaining four spacecraft recompute the thruster control command to slow down their velocity and wait for the faulty spacecraft to ensure all spacecraft initiate observations at the exact same instant. Standard Proportional-Derivative (PD) [72, 78] and Linear-Quadratic-Regulator (LQR) [97, 98] controllers should suffice to ensure nominal trajectories are restored.

- Baseline change: the final positions for reconfiguration are the initial positions for baseline change. The baseline change maneuver consists of a bang-coast-bang approach (details are available in Chapter 11). The 'coast' stage is when dedicated observation tasks take place and no control is exerted, but this is not necessarily the case during the 'bang' stage. As such, relative trajectories can be corrected employing a feedback control loop during the first 'bang'.

  Before the spacecraft initiate the formation contraction or expansion maneuver, they must agree on

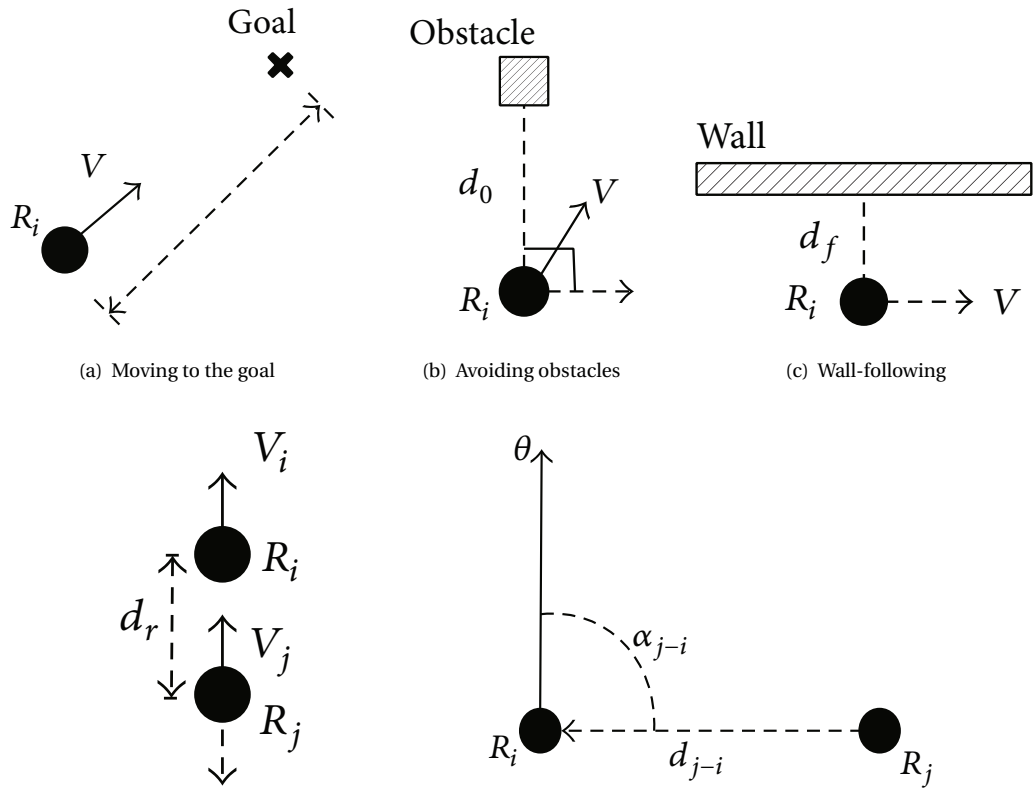

(a) Moving to the goal (b) Avoiding obstacles (c) Wall-following

(d) Avoiding robot (e) Keeping formation

Figure 6.4: Goal-oriented design of a robot in the behavioral coordination strategy. Source: Xu *et al.*, 2014 [86].

the location of the reference point. Similar to the virtual structures coordination approach, the IRASSI spacecraft will compute the 'virtual center' of the formation by averaging their near-static positions before the maneuver. The purpose of defining a reference virtual center is to achieve optimality conditions in the patterns that are generated in the *(U, V)*-plane and this point remains fixed during the baseline drift.

The baseline change maneuver ensues following a pre-planned trajectory. The coordination of the maneuver execution, however, does not follow a virtual structures approach: expansion/contraction of the formation resembles more a breathable mesh and can be equally framed within a behavior-type strategy. Typical design goals can be 'move-to-point', 'maintain relative velocity' or 'avoid sky occlusion of neighbor'.

Note that the term 'formation keeping' is not employed in this context! The formation does not have to maintain relative positions or a fixed geometry during the baseline change. What must be ensured is that the relative velocities during the first 'bang', computed in the planning stage, are observed within a tolerance margin which does not degrade the science-associated patterns at any point during the 'coast'.

With an internal motion model and baseline estimations of the metrology system, each spacecraft determines its own positions and velocities relative to the center and relative to each other during the maneuver. If during the 'bang' stage, violations of the behavior are detected, Lyapunov-based functions [66, 68, 87], PD [72, 79] and Linear-Quadratic-Gaussian (LQG) [99] controllers could be tailored to return the spacecraft to the planned trajectories. However, if there are violations during the 'coast stage', the formation can democratically decide on a case-by-case basis to either stop observation activities or continue by accepting lower performance.

- Station-keeping: these maneuvers can be performed individually to correct positions relative to an orbit. Although the spacecraft fly in each others' vicinity, they target a reference point in their respective

absolute trajectories, similar to the formation reconfiguration case. The control coordination is accordingly an 'absolute' approach and does not rely on any formation or relative parameters. Similar methods for formation reconfiguration apply to station-keeping.

- Collision-avoidance: these maneuvers are triggered once one or more spacecraft enter a predefined 'safety area' around another spacecraft. A formation 'emergency mode' is activated and all resources are channeled towards averting an impending crash. To ensure a safe evasion, a 'behavioral' control coordination approach is proposed. The two or more elements involved are prescribed a new velocity vector that deviates the inertial trajectories in a coordinated manner and ensures all conflicting elements leave the safety area as fast as possible. Lyapunov-based methods in combination with artificial potential functions [87, 96, 100] or passivity-based control [101] are candidate schemes for behavior coordination. A PD controller with a virtual force field, complemented by a decision-making algorithm which devises alternative semantics (based on the notions of *credibility* and *rejectability* functions) mapping to Boolean algebra has also been shown to avert collisions in a resource-efficient way [78].

As can be observed, behavior-based coordination seems the most widely applicable to IRASSI maneuver tasks due to the dependency of formation performance envelopes on rather elastic relative states. After receiving precomputed activity plans, each individual member can optimize its own goal-oriented control input based on internal, high-fidelity models. The maneuver output of each satellite is constrained to fall within a particular error ellipse around the designed trajectory, thus guaranteeing compliance with all formation requirements and constraints.

In this frame of distributed implementation, the spacecraft evolve in a parallel manner, removing the 'single-point-of-failure' that plagues centralized architectures and guaranteeing that formation performance is resilient to unexpected events. Table 6.2 summarizes the devised methods for each GNC mode associated with translation maneuvers. The choice of the control algorithms above is simply illustrative. Under slow dynamics, simplified control strategies such as PD a and LQR-based designs should be able to guarantee stability and a suitable trajectory response, but more sophisticated methods, e.g. nonlinear dynamic inversion [102], sliding mode [95, 96] and adaptive control [103, 104], can be equally implemented.

Table 6.2: Control coordination mechanisms for different GNC modes and associated maneuvers during Nominal Operations.

GNC Modes	**Maneuver**	**Control coordination**	**Potential algorithms**
Formation Reconfiguration	Formation Reconfiguration	Behavioral	PD, LQR
Scientific Observations	Baseline Change	Behavioral with virtual center determination	Lyapunov, PD, LQG
Station-keeping	Station-keeping	Absolute	PD, LQR
Collision-avoidance	Collision-avoidance	Behavioral	Lyapunov, passivity, PD

6.6. CHAPTER SUMMARY

THIS chapter provides an overview of the high-level processes involved in the planning of tasks and execution of maneuvers. The GNC modes of the formation during Nominal Operations are initially defined, where a focus is placed on those involving translation maneuvers which require a high degree of advance planning and a level of synchronization of the fleet, such as Formation Reconfiguration and Scientific Observation. These requirements do not necessarily apply to attitude maneuvers which are dependent on inertial references.

Thereafter, an analysis of the level of autonomy in planning and decision-making tasks is pursued. Since communication links are available to all spacecraft as are computational resources for data correlation, the formation can make use of these elements to reduce dependency from ground stations during the operational phase. As such, a bottom-up autonomous and distributed network has the best chance to ensure the

completion of the mission goals in a robust, resilient and time-efficient manner. All spacecraft are thus responsible for sensing the environment, pursuing relative motion estimations, scheduling observations and maneuvers and for broadcasting this information to others and to the ground. All elements possess then local and global knowledge of the formation states, while inertial navigation relies on a combination of ranging data from ground stations and internal motion models.

Finally, a brief overview of typical control coordination schemes was introduced. A behavioral-type of control coordination was selected for IRASSI, a scheme that involves prescribing one or more goals which compete for onboard resources of a spacecraft. A behavior-based technique is particularly suited to IRASSI because no formation-keeping has to be enforced at any point, but instead, an envelope of acceptable relative motion dynamics must be observed. The specific shape of this envelope is dependent on the GNC mode and maneuver considered. The behavioral coordination does rely on multidirectional continuous communication links within the interferometer. Standard PD, LQG and Lyapunov-based controllers are applicable for regulating deviations of reference relative trajectories in the event of violations of the envelope limits.

With this setup in mind, Part III of this research deals with the planning-optimization problem of the GNC modes, namely the Formation Reconfiguration and Scientific Observation.

III

Development of iSCOUT, a Maneuver-planning Tool for Formation Operations

7

iSCOUT Architecture and General Considerations

Science may have found a cure for most evils;
but it has found no remedy for the worst of them all -
the apathy of human beings.

Helen Keller

Abstract

The third part of the thesis details the development of algorithms that support IRASSI's science program and optimize maneuver-planning activities. These algorithms are part of the iSCOUT tool, which aims to deliver a unified mission performance simulation. This chapter introduces iSCOUT, by presenting an abstraction of its functionalities and the stream of information interchanged between its four modules. The modules are summarily described and the simplifications concerning the dynamics considered for the formation are defined. General considerations and trade-offs concerning design choices are given.

7.1. INTRODUCTION

The last part of the present thesis aims to investigate the feasibility of the IRASSI mission and deliver an end-to-end, bottom-up evaluation of mission budgets and achievable science performance. Several constraints have been introduced in Part II that have a direct impact on how a free-flying interferometer operates in space, such as the intervisibility of the ranging systems during motion or the need for an unobstructed field of view whilst observations take place. These constraints affect primarily maneuvering routines of the Nominal Operations phase, such as reconfigurations prior to observations or baseline-change during observations.

This calls therefore for an integrated simulation of the Nominal Operations phase of the mission. The **i**nterferometer **SC**ience and **O**perations mane**U**ver-planning **T**ool, or iSCOUT, was developed to answer this call.

iSCOUT is a MATLAB-based program developed in the frame of IRASSI, composed of four different modules with the joint aim of optimally planning the sequence of science tasks, computing the associated reconfiguration maneuvers and the paths to be followed by individual spacecraft during the science observations, while simultaneously delivering collision-free trajectories which ensure the intervisibility of the spacecraft. It integrates and builds on the constraints identified in Part II.

iSCOUT is ultimately intended to emulate a science and operations planner running on board the spacecraft to support formation autonomy-reliant activities and free resources from ground stations, whether it is operational time and cost, communication slots allocation or personnel. In its current version, iSCOUT can be used to perform preliminary task schedules, estimates of task and maneuver durations as well as of representative fuel mass budgets which shall be allocated to free-flying interferometry missions. More importantly, it allows for an initial analysis to be made concerning the formation patterns that must be generated in compliance with science goals. As such, iSCOUT is designed to be computationally simple. Therefore, rather than proposing a complex, time-consuming and interwoven multi-objective solution to the mission goals, the science and operations planning problem is framed as a set of sequential steps, whereby separate multi-variable single-objective functions address individual goals and requirements of the mission.

An end-to-end IRASSI mission performance simulation using iSCOUT is presented in Chapter 12, whereas each intermediary chapter is dedicated to the individual modules.

7.2. iSCOUT ARCHITECTURE

THE high-level design of iSCOUT is described in this section.

7.2.1. MODULES

The four modules of iSCOUT are briefly introduced:

- Task-Planner Module (TPM): assigns an optimized sequence of targets to observe within a specified target tour time frame.
- Reconfiguration Module (ReM): assigns optimized final positions and associated linear translation trajectories in inertial space for each of the targets of TPM, according to the science specifications.
- Collision- and Invisibility-Avoidance Module (CAM): refines the trajectories computed by the ReM to ensure they are collision-free and no loss of intervisibility occurs during translation maneuvers.
- Baseline Pattern Module (BPM): assigns optimized trajectories to individual spacecraft according to interferometric scanning pattern requirements, respecting operational conditions and geometric constraints stemming from the spacecraft mechanical architecture.

The modules can be run individually or in an integrated fashion. Although some of the parameters within iSCOUT are tailored to the requirements of IRASSI, the core optimization algorithms within each module are agnostic to their applications. Therefore, iSCOUT may well serve other free-flying or baseline-controlled interferometric missions, being also inspired by the Darwin mission [105].

Although the formation is not required to follow a given reference trajectory on the quasi-Halo orbit around the L_2 Lagrange point, station-keeping maneuvers ought to be periodically performed at a rate of once per orbit (or every 6 months) [14] to ensure that orbit amplitude limits are not surpassed or that the formation escapes the vicinity of L_2. Currently, iSCOUT does not support the provision of station-keeping maneuvers.

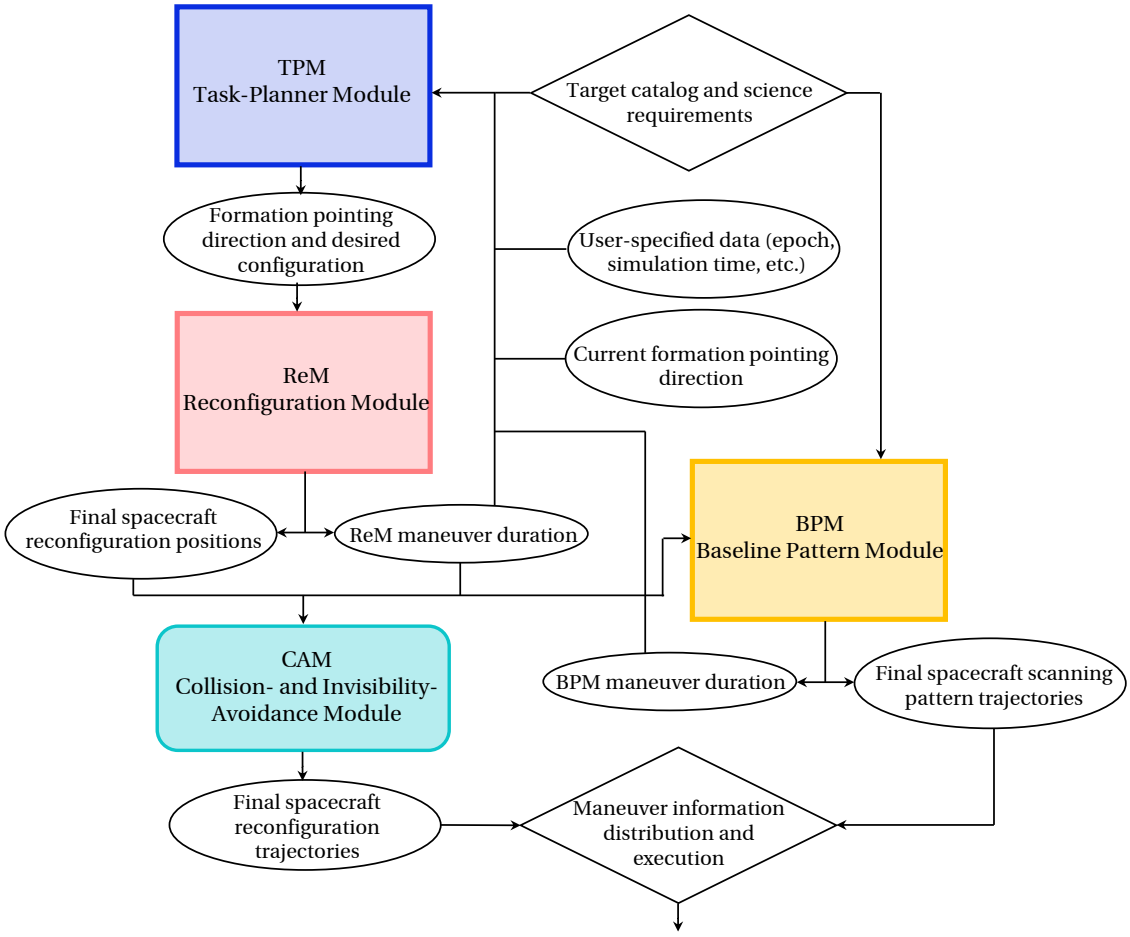

Figure 7.1: iSCOUT information flow diagram.

7.2.2. Information Flow within iSCOUT

The tool is composed of a set of sequential calculations aggregated by the modules, whereby the results of an optimization routine are fed to the next module as input. A general depiction of the tool is provided in Figure 7.1. At the start of the program, the user must indicate whether a full integrated simulation is to be carried out or if iSCOUT modules are to be run individually. If a full end-to-end simulation is desired, the tool is set to optimize upcoming reconfiguration and observation maneuvers for a given science task. The simulation is initialized by user-entered data, such as epoch, the duration of the simulation, the initial launch mass and fuel mass of the spacecraft and initial pointing direction. The epoch information is used by the TPM module to determine the direction of the anti-Sun vector, which, in turn, allows the algorithm to internally map the portions of the celestial sky which are available at the beginning of the simulation. Based on the formation current status, the TPM determines the 'next best observation task' for observation and the relevant output information is passed on to the ReM, which calculates the associated final positions and linear trajectories required for the new task. This information is disseminated to the CAM, which tests whether the linear trajectories previously calculated by the ReM are safe in terms of collisions and intervisibility. It is crucial that each individual spacecraft can determine where its neighbors are throughout the maneuver and as such the ranging system must be visible and provide relative position updates at specified time intervals. If formation elements fail the safety test, the reconfiguration trajectory is then refined until a collision-free, intervisible solution is achieved. Finally, the baseline patterns for the actual observation of the target are computed and the corresponding trajectories in inertial space are commanded. The TPM receives the updated status of the formation members at the end of the maneuver and the next task is selected. The procedure is iterated until the simulation time is exceeded.

Conversely, if a module (other than the TPM) is to be used separately, a predefined task sequence is loaded, and the chosen module iterates through the same maneuver type (reconfiguration for ReM/CAM or science for BPM) for the input target list. Else the TPM simply generates an optimal task sequence based

on the current conditions.

It is envisioned that after either the CAM or BPM trajectories are computed, the maneuver information is distributed among formation elements via a low-data-rate link of omnidirectional X-band antennas. The individual maneuvers shall then be executed in an open loop.

7.3. iSCOUT OPTIMIZATION ROUTINES

THE optimization processes associated with each module, including the algorithms, the constraints considered and the information inputs and outputs is provided in Table 7.1.

Over the months that iSCOUT was developed, different optimization algorithms have been implemented and tested within each of the modules. Ultimately, the selection was based upon computational speed, reliability of convergence to global minima, and most importantly, the suitability of the method to each specific problem. The latter is addressed in each of the respective chapters describing each module, Chapters 8 to 11, whereas the used methods are briefly described below.

A near-neighbor search is used for the TPM module, whereas the remaining modules use the mesh-adaptive direct search. The near-neighbor search method solves optimization problems by finding the point in a given set that is closest (or most similar) to a given value - e.g., selecting the solution which is associated with the lowest (or highest) value of a cost function. Its main applications include path-planning, pattern recognition and DNA sequencing. Its simplicity and therefore computational speed are among its primary advantages, whereas on a sequence of problems it is unlikely to deliver a globally optimal solution. Nearest-neighbor heuristics are applied to the TPM module of Chapter 8 to find optimal sequences of science tasks to be completed within a specified time window or even throughout a mission.

Direct search methods evaluate a set of points around the current one, in order to find one which returns a cost function value that is lower than the value at the current point. Because direct search does not use cost-function derivative information, it bypasses gradient discontinuities. Direct search methods can be classified into local and global optimization approaches. Local direct search is best suited to convex optimization problems, whereas a global search implementation is fit for problems with a low number of independent variables due to the higher computation time as the time required for solution-space exploration increases exponentially with the dimension of the search space. Direct search is employed within the ReM, CAM and BPM environments, Chapters 8 to 11, largely to deliver fuel-minimal and fuel-balanced (or the ΔV-analogous) maneuver solutions.

It should be noted that although optimization is a notable feature of this research, the aim here is not to procure an imperious optimization procedure but rather to devise a framework that is capable of delivering optimized task-planning and maneuver solutions while aggregating several mission constraints and requirements.

7.4. REFERENCE FRAMES

THREE coordinate systems of interest to the tool must be defined. The first one, S_0, is an orthonormal inertial reference frame with basis vectors $\{\boldsymbol{x_0}, \boldsymbol{y_0}, \boldsymbol{z_0}\}$, with a primary direction $\boldsymbol{x_0}$ pointing to the J2000 Vernal Equinox and secondary direction $\boldsymbol{z_0}$ pointing to the north ecliptic pole (parallel to the angular momentum vector of the Earth's orbit around the Sun); $\boldsymbol{y_0}$ completes the right-hand frame and both $\boldsymbol{x_0}$ and $\boldsymbol{y_0}$ lie in the plane of the ecliptic.

The second reference frame, S_C, has orthonormal basis vectors $\{\boldsymbol{x_C}, \boldsymbol{y_C}, \boldsymbol{z_C}\}$, with $\boldsymbol{x_C}$ pointing towards the current target C direction. S_C is represented by a quaternion rotation of S_0 by an angle θ_C, about an axis $\boldsymbol{i_C}$, whereby

$$\cos\theta_C = \frac{\boldsymbol{x_C} \cdot \boldsymbol{x_0}}{||\boldsymbol{x_C}||\,||\boldsymbol{x_0}||} \tag{7.1}$$

$$\boldsymbol{i_C} = \frac{\boldsymbol{x_C} \times \boldsymbol{x_0}}{||\boldsymbol{x_C} \times \boldsymbol{x_0}||} \tag{7.2}$$

The frames S_0 and S_C are centered in a virtual point, with respect to which the formation is arranged, before the reconfiguration ensues. Being the geometric midpoint, it is henceforth termed the 'formation center'.

Finally, the third coordinate frame, S_N, has orthonormal basis vectors $\{\boldsymbol{x_N}, \boldsymbol{y_N}, \boldsymbol{z_N}\}$ from which $\boldsymbol{x_N}$ points in the direction of next target N. Similar to S_C, S_N is represented by a quaternion rotation of S_0, by an angle θ_N, about an axis $\boldsymbol{i_N}$, as described by Equations 7.1 and 7.2 and a translation of S_0 by a vector S_N is fixed in the

Table 7.1: Summary of optimization routines for individual iSCOUT modules.

Module	Goal	Constraints	Algorithm	Input data	Output data
Task-Planner Module (TPM)	Minimize score (criteria: target priority, total maneuver duration, cumulative frequency)	Exclusion zones (sunshield)	Nearest-neighbor search	Epoch, simulation duration, target catalog, initial (or current) formation pointing direction; ReM and BPM maneuver duration	Final formation pointing direction, desired formation configuration
Reconfiguration Module (ReM)	Minimize fuel/ΔV consumption and post-maneuver fuel/ΔV differences	User-specified (e.g., max. maneuver duration, max. traveled distance)	MADS[a]	Initial spacecraft positions in S_0[b], final formation pointing direction, desired formation configuration	ReM final spacecraft positions in S_0, ReM maneuver duration
Collision- and Invisibility-Avoidance Module (CAM)	Minimize fuel/ΔV consumption and post-maneuver fuel/ΔV differences	Collision avoidance and ranging intervisibility	MADS	ReM final spacecraft positions in inertial frame, ReM maneuver duration	Final spacecraft trajectories in S_0
Baseline Pattern Module (BPM)	Step 1: Maximize central angle and interior angle differences given a *(U, V)*-plane-projected geometry Step 2: Minimize fuel/ΔV consumption and post-maneuver fuel/ΔV differences	Collision avoidance, ranging intervisibility, baseline estimation accuracy, sky access, desired scanning length, trajectory projections in *(U, V)*- plane	Step 1: MADS Step 2: MADS	Desired target scanning length, observation duration, ReM final positions in S_0	Final spacecraft positions and trajectories in S_0, BPM maneuver duration

[a] Mesh-adaptive direct search
[b] S_0 denotes an inertial frame and it is described in section 7.4.

formation center after the reconfiguration maneuver. The vectors $\boldsymbol{r_{C,i}}$ and $\boldsymbol{r_{N,i}}$ denote respectively the positions of the ith spacecraft before and after the maneuver in the inertial frame S_0, where $i = \{T_1, T_2, T_3, T_4, T_5\}$ ('T' denotes telescopes). The coordinate systems are depicted in Figure 7.2(a).

7.5. FORMATION BASELINES AND SEPARATION

ALTHOUGH the general formation geometry has been introduced in Part II, this information is hereby summarized in the context of iSCOUT and with the respective frames. The formation is arranged in a three-dimensional configuration. For a given target N, the formation center is contained in a plane Π_N perpendicular to the target direction, determined by the aforedefined vectors $\{\boldsymbol{y_N}, \boldsymbol{z_N}\}$. The distribution of the spacecraft on the Π_N plane is determined by the baseline associated with the target being observed (given as a function of separation parameter d), and the distribution normal to the plane (that is, the 'height' h above/below the Π_N plane, along the $\boldsymbol{x_N}$ axis) is determined by intervisibility requirements.

The parameter d defines the in-plane separation of each telescope relative to the formation center whilst the telescopes are equally spaced by an angular distance of $\frac{2\pi}{5}$ (or 72°). Three separation parameter $d \in d_{set}$ lengths have been set according to the IRASSI high-level requirements:

- $d = 10$ m, resulting in 'short' baselines, when the formation is at its most contracted state
- $d = 500$ m, resulting in 'medium' baselines, when the formation explores the middle portions of the *(U, V)*-plane
- $d = 1000$ m, resulting in 'long' baselines, when the formation is at its most expanded state

with the this triple set d_{set} summarized as:

$$d_{set} = \{10, 500, 1000\} \tag{7.3}$$

For a given attitude of a spacecraft in inertial space (determined by the direction of the target), no neighboring telescope can be placed directly in a direction normal to the sunshield. This results in a set of acceptable heights to be assigned to the telescopes at each observation instance:

$$h = \{-4d, -2d, 0, 2d, 4d\} \tag{7.4}$$

The separation of the spacecraft is always higher in a direction normal to plane Π_N. Figure 7.2(b) shows the distribution of the formation relative to the plane Π_N. The corresponding minima and maxima values for the interferometer baselines, geometric delays and relative distances for these nominal d parameters are available in Table 4.6.

7.6. SPACECRAFT MOTION DYNAMICS

7.6.1. GENERAL CONSIDERATIONS

For the planning of the maneuvers, it would be ideal that:

1. reconfigurations and target-associated repositioning of spacecraft occur swiftly to allow the operational time to be allocated to science as much as possible;
2. science-associated maneuvers during observations, such as expansions or contractions, should be of enough magnitude to allow the required scan length to be fulfilled within the specified observation window, but should not cause induce vibrations or disturbances in the mechanical structure of the telescopes.

As outlined in earlier stages of the IRASSI study, two propulsion systems are employed [35]: chemical hydrazine-based thrusters (capable of Newton-level thrust force) and electrical colloid thrusters (which apply micro- to milliNewton thrust force magnitudes).

Hydrazine-based thrusters are particularly suitable for periodic station-keeping or even contingent escape maneuvers, but too inefficient (and thus prohibitively expensive at launch) for recurring mission maneuvers, such as reconfigurations. This means therefore that reconfiguration and science maneuvers share the secondary thrusters and that they compete for the upper and lower bounds of deliverable thrust. Reconfiguration maneuvers are in this sense limited to the highest thrust delivered by the colloid engines.

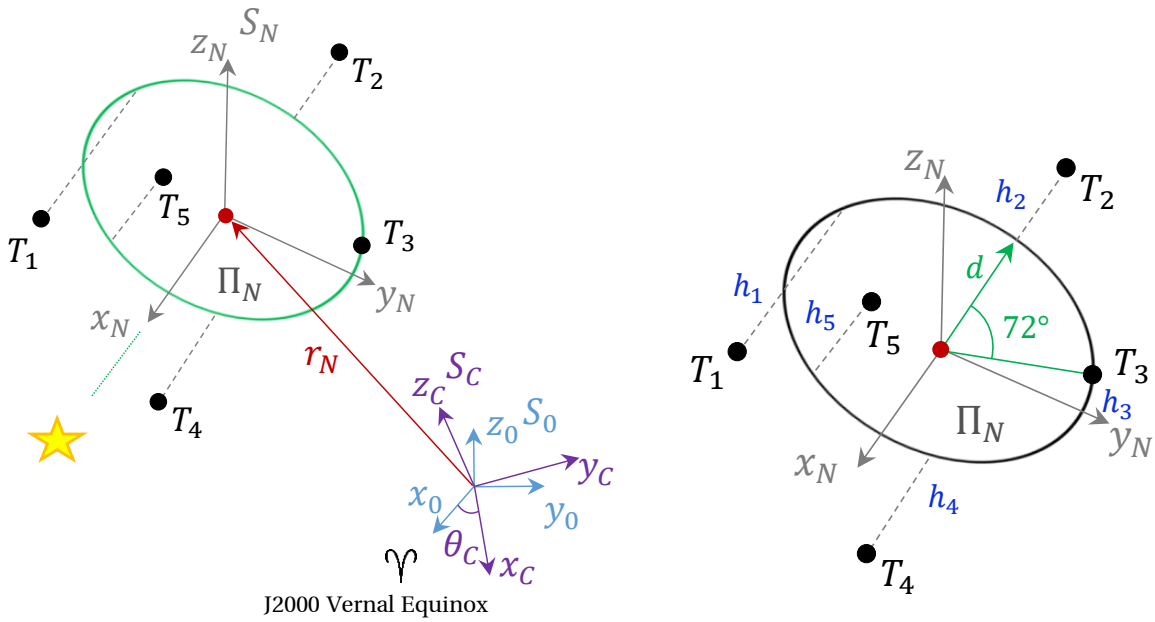

(a) Reference frames

(b) Formation separation

Figure 7.2: Reference frames and formation separation for iSCOUT modules.

7

For the present study, Busek colloid thrusters[1] are assumed as actuators, which deliver a maximum of 20 mN of thrust to the spacecraft. Although this is the current state-of-the-art, future developments may allow the range of thrust to be expanded at an efficient expenditure of resources, which would be desirable for reconfiguration maneuvers.

7.6.2. Model Assumptions and Dynamics

The following assumptions are made for simplification purposes:

1. The spacecraft are in free space (as if exactly at L_2 and no gravity gradient acts on the spacecraft, due to the close proximity of the telescopes). In reality, the spacecraft experience a gravity-gradient-induced acceleration difference acting on them, which translates to a drift of approximately 1 meter/day for relative separations of less than 100 meters (or an order of magnitude higher for inter-satellite distances of about 1 km) [106], for a formation placed in a Halo orbit with an amplitude of 800 000 km × 400 000 km around L_2. Given that the duration of the ReM reconfiguration maneuvers does not generally exceed a third of a day (or 8 hours), it is plausible to assume that the local dynamics are determined exclusively by the actuators. For the BPM trajectories, 2.9% of the total target population requires an observation duration longer than 3 days, which may mean a deviation between the approximated and the real trajectories of a few hundred meters. However, the BPM module is by itself a very computationally-intensive program and because of the additional computational effort required for the precise integration of the individual trajectories, it was deemed appropriate to simplify the formation dynamics as if the spacecraft are in free space (although it is foreseen in the future to complement the interferometer dynamics with a suitable relative motion model). Even during idle periods, in-between observation slots, the relative distance between the spacecraft shall nonetheless not exceed 10 km.

2. The spacecraft are modeled as point masses. As such, all maneuvers are purely translational and decoupled from attitude maneuvers;

3. The mass of the spacecraft is constant throughout the maneuver;

4. Each thruster vector can be pointed in any direction. There are 16 colloid thrusters distributed in two planes, above and below the sunshield, to provide full control and redundancy of translations in three axes (see Figure 7.3);

[1] Online source: NASA, "20-mN Variable Specific Impulse (Isp) Colloid Thruster," https://ntrs.nasa.gov/archive/nasa/casi.ntrs.nasa.gov/20160005350.pdf

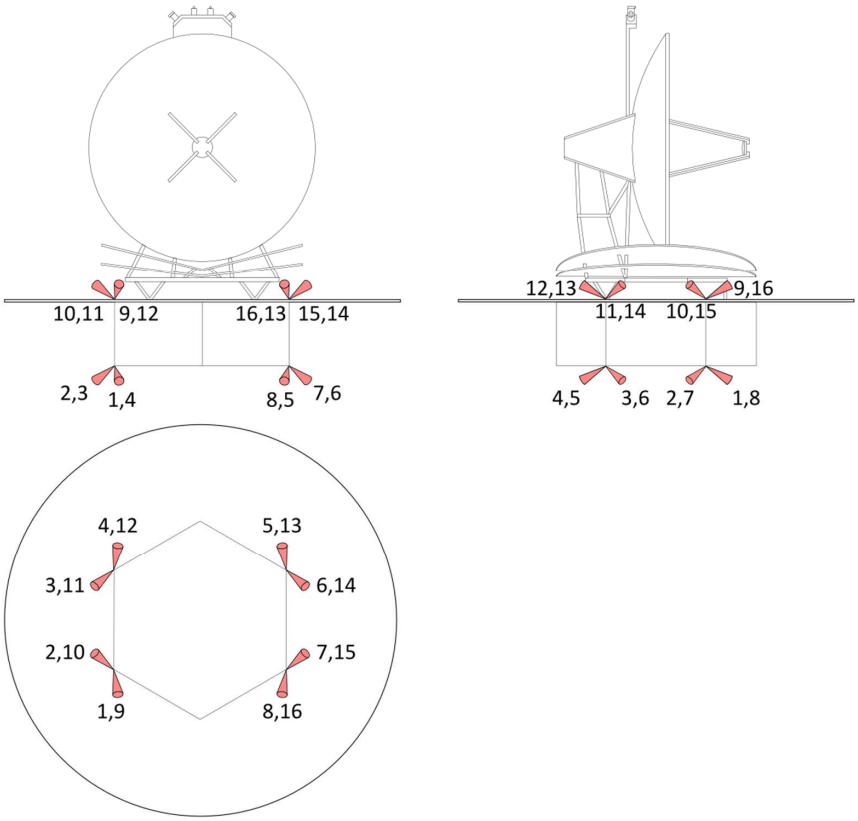

Figure 7.3: Thruster configuration of the secondary propulsion system. Credit: Eloi Ferrer-Gil.

5. The position of each spacecraft is determined precisely in an inertial frame (no error considerations are made);

The actuators are assumed to be the Busek colloid thrusters, as introduced in the previous section, and the following motion dynamics apply:

$$M_i \ddot{\boldsymbol{r}}_{\boldsymbol{i}} = \begin{cases} F_i \boldsymbol{u}_{\boldsymbol{i}}, & \text{if } f_i(t_0) > 0, ||\boldsymbol{u}_{\boldsymbol{i}}|| \neq 0. \\ 0, & \text{otherwise.} \end{cases} \tag{7.5}$$

$$\dot{f}_i = \begin{cases} -\frac{F_i}{I_{sp} g_0}, & \text{if } f_i(t_0) > 0, ||\boldsymbol{u}_{\boldsymbol{i}}|| \neq 0. \\ 0, & \text{otherwise.} \end{cases} \tag{7.6}$$

where M_i is the mass of the ith spacecraft (kg), $\ddot{\boldsymbol{r}}_{\boldsymbol{i}}$ is the acceleration vector ($\mathrm{m\,s^{-2}}$) in the S_0 frame, F_i is the thrust force delivered by the actuator (N), $\boldsymbol{u}_{\boldsymbol{i}}$ is a unit force direction vector, f_i is the instantaneous fuel mass of the spacecraft (kg) and $\dot{f}_i$ is the fuel consumption rate ($\mathrm{kg\,s^{-1}}$), I_{sp} is the specific impulse of the thruster (s) and g_0 is the standard gravitational acceleration at sea level ($\mathrm{m\,s^{-2}}$).

Each spacecraft has a launch mass of 2.3 tons and the fuel mass is decremented accordingly after each maneuver.

7.7. iSCOUT SOFTWARE AND HARDWARE BASE

iSCOUT was developed in MATLAB's 2019 version. In its current standing, iSCOUT is run on a network of 32 processing units (Intel(R) Xeon(R) Silver 4108 CPU) with a nominal processing speed of 1.80 GHz, each with 8 cores and 32 Gb of RAM. The optimization routines with each module employ both parallelization and vectorization for maximizing computer resources and processor performance.

Whereas optimal individual maneuvers within the ReM, CAM and BPM modules take between 1 and 370 seconds to compute, the TPM can generally construct sequences of 45 tasks per hour. The suitability of modern space-qualified processors for supporting iSCOUT is discussed Chapter 9, with reference to future developments foreseen in space-based hardware.

7.8. iSCOUT Architecture Advantages and Limitations

In its current standing, iSCOUT is embedded with a set of modular functions designed for achieving task schedules and maneuver-planning solutions efficiently. It is clear that solving each of the problems associated with the modules demands achieving a set of goals, often conflicting, while having to consider several parameters that independently influence the goals. For a feasibility assessment tool that can perform a preliminary end-to-end mission simulation whilst aggregating several of the mission constraints, the operations and maneuver-design problems are framed as a series of multi-variable, single-objective functions. Four main advantages arise from the simplicity of this approach in relation to an overarching multi-objective problem:

1. the ability to separate and assess the influence of variables on each optimization problem
2. the ability to detect shortcomings or technical infeasibility of high-level mission requirements
3. the ease in implementation
4. the low computation complexity level and computation time

On the other hand, the simplified design of the modules and force model assumptions do, however, limit the accuracy of the tool, particularly, for long-term mission planning. Current limitations include:

1. the absence of gravity gradients and control feedback loop to correct the trajectories
2. the omission of station-keeping maneuvers
3. the modularity of iSCOUT requires the TPM module to make assumptions concerning the output of two other modules (reconfiguration maneuver duration of the ReM and baseline-change maneuver duration of the BPM)

Addressing the accuracy concerns of iSCOUT will nonetheless increase the complexity of the tool and decrease its computational efficiency.

7.9. Chapter Summary

The present chapter showcases the high-level architectural design of the iSCOUT tool, a modular program akin to an operations planner that aims to perform science-task scheduling and compute optimal collision-free reconfiguration and science-related maneuvers, abiding by functional requirements and formation constraints. These functions are performed by the four different modules of iSCOUT, which are described in the next four chapters. The tool is intended to address the need of simulating and of measurably evaluating the feasibility of IRASSI. Future versions of the tool may potentially be tailored for onboard utilization for real-time mission planning.

Two execution modes are supported, an integrated simulation mode and execution on an individual module basis. The optimization procedures selected for each module were identified, whereby a nearest-neighbor search is implemented for devising optimal task sequences and a direct search method is used for maneuver-planning.

The most relevant reference frames, an inertial one and a local formation one, were defined as were the separation requirements, ensuring acceptable formation geometry envelopes. Three different separation parameters are used in the simulations, described by the set $d_{set} = \{10, 500, 1000\}$. The spacecraft separation is higher along the direction of the target than on the plane defined perpendicularly to this direction.

Free-space dynamics are assumed in an open-loop maneuver-control configuration. In the current version of iSCOUT, only the secondary (electric-based) propulsion system is of relevance. Station-keeping maneuvers, which typically employ chemical thrusters, are not supported.

The problems within iSCOUT are optimized locally within each module. Future versions of the program may bring it closer to being implemented in realistic scenarios. This can be by developing more elaborate dynamics models, using a global optimization strategy across all modules or by extending the support to station-keeping maneuvers. Further work within iSCOUT is discussed in detail in Chapters 8 to 11.

8

Optimization of Tasks Sequences

Our posturings, our imagined self-importance,
the delusion that we have some privileged position in the universe,
are challenged by this point of pale light.

Our planet is a lonely speck in the great enveloping cosmic dark.

Carl Sagan

ABSTRACT

This chapter introduces the IRASSI science targets and describes the method within iSCOUT that is devised to optimize the sequence of observations. For a given epoch (or initial anti-Sun vector longitude), the Task-Planner Module detects which targets are available for observation and preserves in a candidate list those who remain in the field of view once the associated observation task is completed. Using time efficiency, target priority and target diversity metrics, two decision-making algorithms are compared to assess how task sequences are built over the lifetime of the mission. Results show that nearest-neighbor heuristics produce savings in maneuver time (and thus fuel) of up to 30% compared to a semi-stochastic near-neighbor search. This module builds the maneuvering strategy around science requirements. Alternative scanning strategies are proposed at the end of the chapter to potentially increase science returns and minimize time and fuel consumption required for maneuvering in-between tasks.

Credits for the catalog input and general developments within this chapter are owed to Dr. Hendrik Linz (Planet and Star Formation Department, Max Planck Institute for Astronomy, Königstuhl 17, 69117 Heidelberg, Germany, linz@mpia-hd.mpg.de), who endured extensive discussions via e-mail, telephone and in-person meetings.

8.1. INTRODUCTION

IRASSI'S main function is to observe targets in the far-infrared. It is first and foremost necessary to distinguish between *target* and *task*. Whereas a target refers to a celestial source of infrared radiation, a task refers to all activities associated with observing a target (the collection of science data, the calibration of instruments, the downlinking of processed data and the required reconfiguration maneuvers). One target requires at least one task to be carried out. There are currently 784 pre-planned science tasks to be fulfilled over the five-year operational lifetime associated with 453 targets. Due to the diverse nature of the targets in terms of scientific interest and location in the celestial sky, there must be a balance between science return and operational viability upon selection of the task sequence.

The main motivation for devising a science activities' planning module stems therefore from the fact that time and physical resources in space are scarce. Additionally, certain targets, particularly those close to the celestial equator, are only available for observation during certain times of the year. An efficient solution that maximizes science return and procures savings in energy expenditure, computational and operational processes is thus imperative. The Task-Planner Module (TPM) was created to address these concerns.

The TPM is the first module of iSCOUT. It determines which celestial targets will be observed within a specified time window, taking into account its characteristics, such as its sky coordinates, emission frequencies, and the associated formation configuration requirements, such as minimum and maximum desired baseline lengths as recorded in the mission catalog. The output of TPM is the final sequence of tasks (or the next best subsequent task if the tool is run integrally), the required pointing direction and initial and final formation configurations, which serve as input of the next module, the ReM (or Reconfiguration Module, see Chapter 9). The target catalog is expected to be dynamically updated as the nominal phase of IRASSI befalls. This module allows for a real-time rescheduling of the science activities of the interferometer as new scientific information becomes available.

8.2. PREVIOUS CONTRIBUTIONS

8.2.1. SCIENCE SCHEDULING AND PLANNING

Traditional mission design concepts using predefined and immutable sequences of commands have evolved in the past decades to become fluid, malleable and adaptable to unpredictable environments. Having the ability to react to unforeseen events or unknown terrains is particularly useful to reprogram activities in missions operating far from Earth, such as those conducting deep-space astronomy or planetary exploration.

The first demonstrator of onboard autonomous planning and fault management was the Deep Space One's Remote Agent [107]. The Remote Agent flight software had built-in encoded operational rules and constraints and received from the ground a set of goals to achieve during its experimental mission. However, the agent's software itself was tasked with generating the sequence of activities to accomplish the goals (using priorities, heuristics and models) and with executing them. It also included a monitoring function able to perform subsystem failure diagnosis and recovery during the execution of the plans. Similar developed systems took shape in the Continuous Activity Scheduling Planning Execution and Replanning [108], tested on the Deep Space Four for creating accurate topological maps of the Tempel 1 comet and for determining gas compositions of its coma, in the Mixed-Initiative Activity Plan Generator [109] (MAPGEN), an onboard task-sequencing and scheduling tool for the Mars Exploration Rover mission, and in the Autonomous Sciencecraft Experiment [110] (ASE) which flew on the Earth Observing-1 mission and aimed at supporting research on the spectral and spatial resolution of volcanic events. In particular, the MAPGEN and ASE, developed in the early 2000s, were complex day-to-day tactical planners which organized coordinated high-level activities and provided schedules that ensured an efficient and conflict-free utilization of onboard resources, taking into account time constraints, the health status of subsystem components, hardware availability and competition for sensors, actuators and processors according to user-generated goals, priorities or flight rules. The heritage of some of these tools has also been incorporated into unmanned underwater [111] and surface vehicles [112].

Several breakthroughs on automation of ground and spacecraft planning tasks came also from the European side [113–117]. Of particular interest to iSCOUT, is the Mission Analysis and Payload Planning System (MAPPS), a high-fidelity, modular tool used by science operations and investigator teams specifically to plan and simulate science routines for ESA's Solar System missions [118]. Although MAPPS is not yet fully automated and does not operate on board the spacecraft, it works online, parallel to ongoing missions, such as the MarsExpress, VenusExpress, Rosetta, BepiColombo and JUICE missions, among many others. It manages input from ground users, such as operation requests, spacecraft pointing requests or event requests with

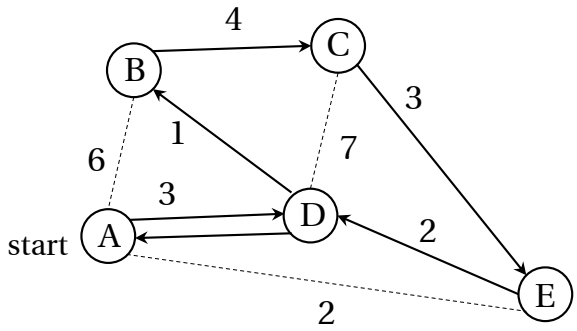

Figure 8.1: Solution of a traveling salesman problem: the arrows denote the shortest possible route that connects every city. The dashed lines show discarded paths. The distance between cities is assumed to be the same in both directions.

opportunity and constraint windows (e.g., for communications and telemetry downlink) and allows time-based simulations of the spacecraft and experiment models to detect potential conflicts [118]. It can perform short-term to long-term activity scheduling, but crucially, during short-term planning tasks, MAPPS detects whether resource consumption conforms to allocated resources at the end of the medium-term planning cycle. A configurable 2D mapping panel and an interactive 3D visualization display round up MAPPS' main functions. The majority of MAPPS utilities and user interfaces have been developed in C++.

All of these contributions focus on operational autonomy and responsiveness, by providing architecture descriptions of ground-space segment interactions, information workflows and planning interfaces. However, they do not address the optimization and selection mechanisms associated with science task-planning. In the IRASSI case, 784 observation tasks must be performed over the course of the mission, on the basis of a set of metrics. Deciding the order in which these tasks should be performed, with respective target-availability constraints, is akin to the *Traveling Salesman Problem*.

8.2.2. THE TRAVELING SALESMAN PROBLEM

8

A well-known challenge in combinatorial optimization, the Traveling Salesman Problem [119] (TSP) has applications in manufacturing, logistics and general activity-planning. In its classical formulation, the TSP contains a list of N cities, $N \in \mathbb{Z}^+$, connected by paths. The path length $P_{i,j}$ connects city pair i and j and typically the problem attempts to find a route that minimizes the sum of the paths lengths for a set number of cities that need to be visited at least once, before returning to the point of departure. Figure 8.1 shows a schematic of the TSP. The analogous problem within IRASSI could be expressed as:

> *Given a list of targets, what is the most (time- or fuel-) efficient sequence of observation tasks that maximizes science returns within five years?*

In this analogy, maneuver events which link any two observation tasks correspond to the TSP paths.

The following aspects characterize the IRASSI problem:

1. The lengths of the paths correspond to the metrics used to evaluate candidate tasks and they are not known *a priori*. These metrics are dependent on all previously sampled targets (or the task history) of the same sequence. Path lengths connecting two tasks are thus asymmetric.

2. Subsets of targets are available at different times of the year and whereas the task pool reduces as the mission progresses, certain targets have to be revisited. But time delays are not acceptable: if a target leaves the field of view before the observation task is complete, this candidate task must obligatorily be discarded and similarly, the observation time itself cannot be subject to optimization.

3. There is no fixed number of maximum tasks and the target catalog itself may increase as new information is collected by the telescopes. Priorities of targets and tasks may also change dynamically over the mission.

There exist several algorithms which attempt to solve the TSP. The most trivial solution is by exhaustive search, that is, for a fixed number of cities, compute all city permutations and identify the cheapest route. The computational speed, in this case, scales with a polynomial time complexity of $\mathcal{O}(N!)$ and therefore, calculating all permutations becomes unfeasible even for 10 or 20 cities [120, 121]. The most suitable method

for solving large instances, currently holding a record of nearly 86 000 cities [122], is the so-called branch-and-cut method [123]. It is merely an organized way of performing an exhaustive search. In short, this approach applies firstly, a linear-programming relaxation for fast convergence, together with a cutting-plane algorithm [124] as means to find optimization variables that are feasible but discarded in the first step, and finally, a branch-and-bound routine. Branch-and-bound involves defining a search tree, whereby the *branches* represent subsets of the solutions explored by the algorithm. As solutions along the branch are searched, the branch is compared to lower or upper *bounds* of the current optimal solution. If a branch does not produce an improvement compared to the best current one, it is discarded by the algorithm. This, however, relies on a fixed number of cities (tasks) imposed on a tour.

Variations of the branch-and-bound algorithm include the imposition of resource availability [125] or temporal [126] constraints, which respectively may mimic whether or not a target finds itself in the field of view of the telescopes and the starting time or duration of an observation task. Temporal constraints may inclusively emulate target priorities, such that one might impose that an observation of a target of low priority may not start before an observation of a high-priority one. But these algorithms fail to account for the dependency of the path length between two consecutive tasks on previous instances of the tour.

Heuristics-based algorithms have equally been developed to search paths over large sets of data expeditiously. They seek to find a tour (typically via a *greedy* search) that terminates as soon as a feasible solution has been constructed. Nearest-neighbor and Christofides are such examples. In the former case, the traveler always chooses to move to the next closest unvisited city and yields on average a 25% worse path than the best shortest tour [127]. The Christofides [128] method starts by constructing minimum spanning trees over the to-be-visited cities, aggregating them with paths that connect to an odd number of other cities, to ultimately find a non-repetitive tour route. In the worst case this method produces tours 50% longer than the shortest one. However, the Christofides approach is not applicable to IRASSI as the path lengths (metrics) separating two tasks are not symmetric (they rely on the past route taken) and do not obey triangle inequality rules.

Similarly, mutations of the TSP incorporate uncertainties regarding the availability of the paths which only become apparent to the traveler upon reaching an adjacent site [129]. These are solved using competitive analysis, that is, by minimizing the ratio between the worst-case distance cost of a planned route to the distance cost of the shortest possible path computed offline, where all road blockages are known beforehand. An analogous road blockage in the IRASSI case would correspond to the impossibility of performing a maneuver in-between two observation tasks. However, it suffices that a target is within the field of view for a path to be available and its distance cost predictable.

Attempting to observe as much as possible while minimizing the 'cost' of observing (whereas this cost is directly dependent on past observations), are naturally conflicting criteria. The task-sequencing problem is simultaneously more complex and constrained than any of the solutions proposed. The approach taken has therefore focused on refining the initial conditions provided to the TPM module, by generating a surrogate catalog 'on-the-fly', and implementing two heuristics optimization algorithms for comparison: a nearest-neighbor and a semi-stochastic near-neighbor procedure.

Nearest-neighbor heuristics (NNH) are known to be sub-optimal [130], but reach a feasible solution in a relatively short time. The interest in devising a dynamic catalog is to accommodate task sequences which limit the impact of reconfiguration time and thus ensure that any sub-optimal solution found by the nearest-neighbor method is as close to the best possible performing one. Nevertheless, the possibility of using local search algorithms to refine tours generated by NNH under certain circumstances is addressed in Section 8.5.5.

8.3. IRASSI TARGET CANDIDATES

8.3.1. TARGET CLASSIFICATION

THE current catalog has been shortly introduced in Section 2.3.3. The 453 objects are associated with 784 science tasks with a combined science duration of $\Omega = 1597$ days, or approximately 4.4 years, to be fulfilled (as much as possible) during the operational phase of the mission. All remaining time shall be allocated to other supporting tasks, from retargeting, reconfiguration, station-keeping, calibration, communications, etc. These targets are categorized according to types and relative priorities and they are tagged with a priority grade, the duration of the observation task, the number of visits, the desired scanning length, their emission sensitivity and their location in the celestial sky. They are broadly aggregated in Table 8.1, whereas Table D.1 of Appendix D shows all catalog entries. Emission-sensitive targets are highlighted in gray and this is elaborated further in Section 8.4.1.

The total number of tasks refers to the number of targets multiplied by the number of visits. For ease, task

Table 8.1: Target categorization for IRASSI.

Target type (No.)	Priority	No. targets	Observation duration	No. visits
T Tauri stars and disks (I)	1 or 2	94	≤ 1 day	2
Herbig Ae/Be stars (II)	2	139	≤ 3 days	2
Debris disks (III)	1, 2 or 3	14	≤ 8 days	3
Massive objects (IV)	1 or 2	16	≤ 1 day	1
Galaxies (V)	1 or 4	85	≤ 3 days	1
High-mass star-forming regions (VI)	1, 2 or 3	20	≤ 1 day	1
Hot cores and corinos (VII)	1, 2 or 3	25	≤1 day	1
FU-Orionis-class stars/objects (VIII)	1 or 2	35	≤ 3 days	3
AGNi (IX)	1 or 3	25	≤ 1 day	1

priority or task type will be used to refer to the priority or type of the target that a task is associated with.

In Table 8.1, priority is shown in descending order, such that a 'high-priority' target receives a score of 1 and 'low-priority' one, a mark of 4. Approximately 9% of the tasks are of first priority, with the highest proportion, at approximately 74%, being associated with second. The lowest priority targets are galaxies and related science tasks make up about 9% of all tasks.

Observation durations range between 0.1 and 8 days. The histogram featured in Figure 8.2 shows the observation task distribution with the respective duration and the cumulative frequency. Approximately half of the total observation time is dedicated to tasks which require a target-sampling duration of less than 1.5 days and a quarter to those requiring between 1.5 and 2.8 days.

8.3.2. ACCESSIBLE SKY AND TARGET DISTRIBUTION

The region of the celestial sky which is available for observation is calculated according to the spacecraft's design, whereby the telescope mirrors point nominally in a direction perpendicular to the Sun's direction, allowing for a ±20° attitude change relative to the observed direction. Figure 8.3 and Figure 8.4 show the sky access for a single telescope located in L_2 at two different times of the year, that is, for two different initial anti-Sun vector longitudes. In the figures, these 'forbidden' regions are then colored in white (containing red-marked targets) and the 'accessible' portions of the celestial sphere are marked in blue (containing yellow-marked targets).

From Figures 8.3 and 8.4, it can be observed that as time passes, the instantaneous sky access continuously shifts 'eastwards' in longitude and targets move in and out of the field of view continuously. Targets close to the celestial equator can be observed twice per year for a maximum of ≈40.5 days on each installment. With increasing latitudes, this visibility restriction decreases. For instance, targets located at latitudes of 45° can be observed a combined ≈117 days per year. Targets with a latitude of 70° and above are available in the sky all year long.

The distribution of target priorities with respect to latitude is shown in Figure 8.5. About 38% of all targets are concentrated in the equatorial regions, particularly in the latitude band between −15° and 15°. Whereas, in general, Priority-3 targets seem well distributed across all latitude ranges, Priority-1 and Priority-4 targets are predominant in the southern hemisphere. Priority-2 targets, however, are shown to be concentrated near the celestial Equator and in the high latitude regions of about −65° and 60°. This is also the most populous priority group.

With respect to longitude, Priority-1 and Priority-3 targets exhibit a uniform distribution across all ranges, excluding a gap between 90° and 150°. A mild concentration of Priority-4 targets at longitude values of 30°, 180° and 330° is observed. Priority-2 targets are nonetheless dominant and concentrated in longitude bands between 67° and 85° and between 236° and 253°. In fact, and curiously again, approximately 38% of all targets fall in the aforementioned longitude bands. The distribution of target priorities according to longitude is

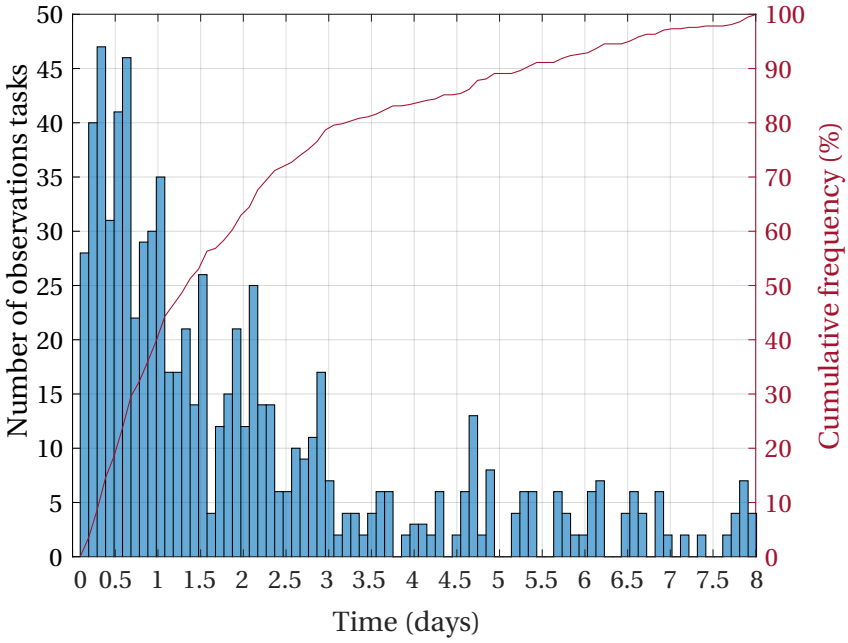

Figure 8.2: Distribution of the number of observations by duration and cumulative frequency.

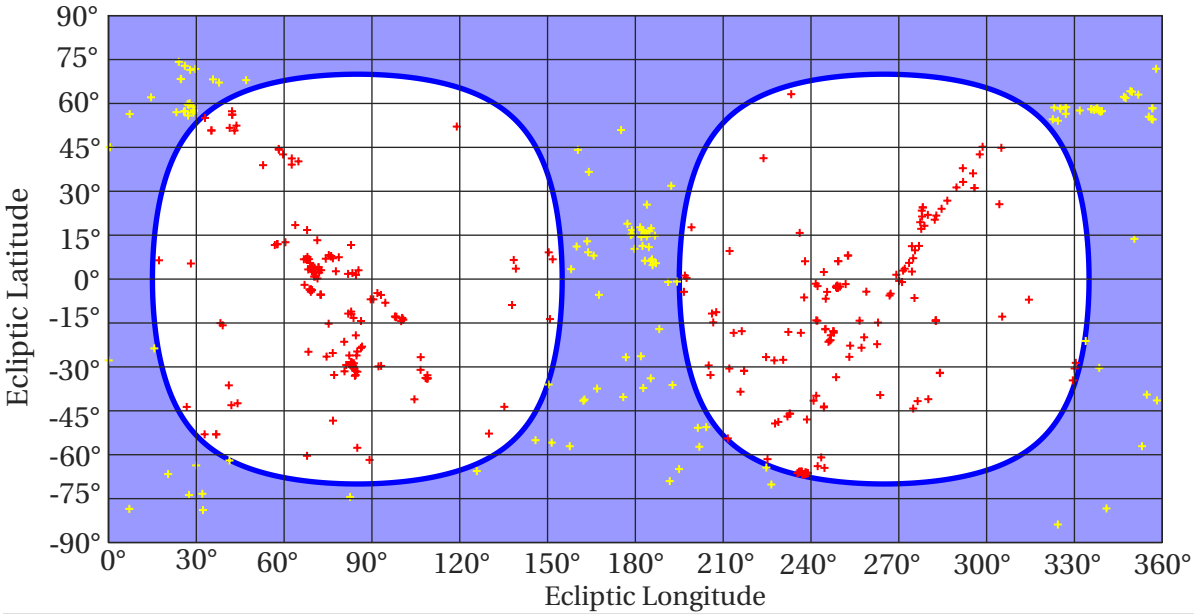

Figure 8.3: Instantaneous sky access for an anti-Sun vector longitude $\Lambda = 85°$.

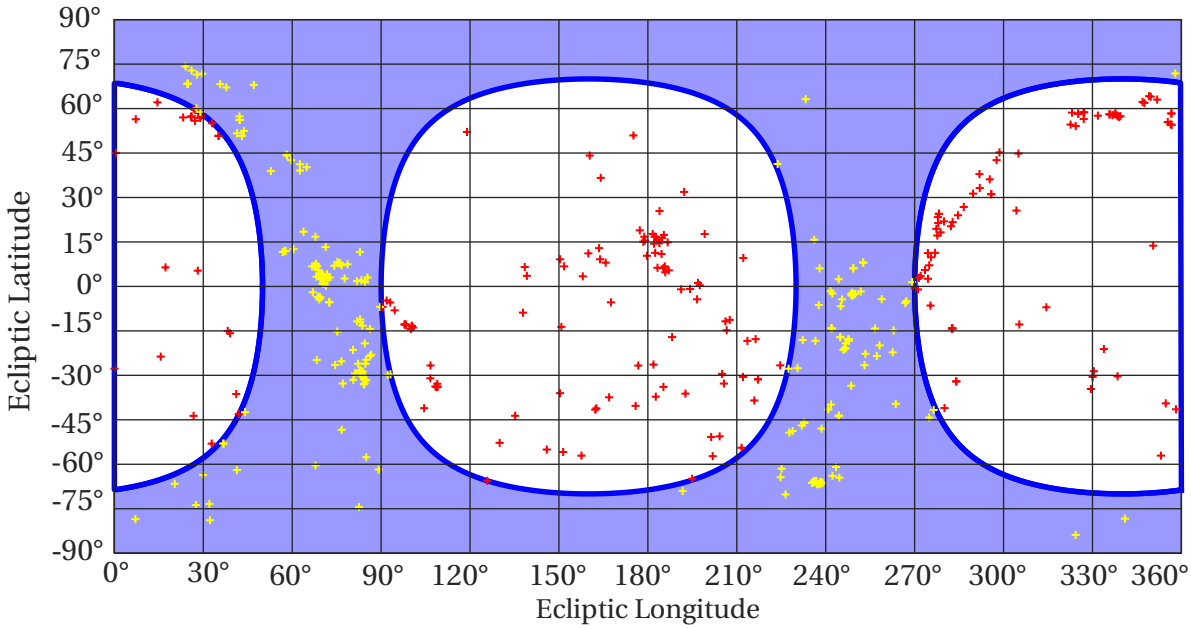

Figure 8.4: Instantaneous sky access for an anti-Sun vector longitude $\Lambda = 160°$.

featured in Figure 8.6. The figure shows that depending on the time of the year, the mission is more likely to sample certain target priority levels and that crucially, when crossing longitude ranges between 110° and 120° or between 305° and 323°, chances are that no targets are available for observation and the interferometer may remain idle. These longitude bands could, for example, be allocated for the execution of station-keeping maneuvers.

For completeness, the distribution of target types with latitude and longitude is shown in Appendix D.

8.4. TASK-PLANNER MODULE (TPM)

THE overarching goal of the TPM is to ensure that as many scientifically relevant targets as possible are observed in the most (fuel- and time-) efficient manner. An analysis of the planning strategy is provided followed by the adopted methodology and the implemented task-selection decision-making methods.

8.4.1. TASK PLANNING STRATEGY: EFFICIENCY VS. SCIENCE PERFORMANCE

There are numerous ways in which the science activities may be planned and the sequence of observations optimized from the diverse set of targets. One possibility would be to carry out as many observation tasks as possible within the operational lifetime of the mission. In order to maximize the number of tasks, the strategy would then be to select tasks with the lowest associated observation duration and reconfiguration maneuvers. This would, however, not guarantee that high-priority targets are selected within this time frame, particularly because they make up only 9% of the target population (and half of those exceed an observation duration of one day).

The other extreme would be to give importance only to the quality of targets and disregard the quantity. In this case, generally observing the targets in ascending order of priority would be reasonable and high-priority targets with multiple required visits would have their science tasks fulfilled soon after they enter the accessible region of the sky. However, this may be inefficient from a time and fuel point of view, especially if spacecraft have to perform an elaborate reconfiguration maneuver to sample the next target, located on a different portion of the celestial sky.

Table 8.2 provides an overview of the relationship between the number of tasks and observation duration, including the distribution of the latter with target priority. The first noteworthy trend is that even though short-observation targets (≤ 1 day) make up the majority of the target population at 53%, they are mostly associated with single tasks. It is the long-observation targets (≥ 1 day) that compose nearly three-fifths of the total observations. Of these, more than 35% require an observation duration higher than 3 days. Approximately 24% and 62% of short-duration Priority-1 and Priority-2 targets respectively are associated with

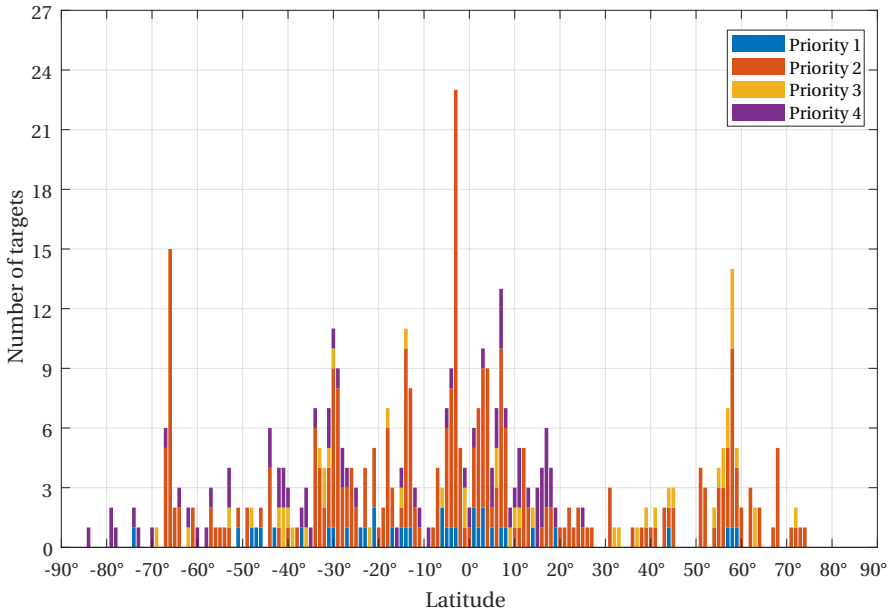

Figure 8.5: Distribution of target priorities relative to celestial latitude.

Table 8.2: Observation duration distribution in numbers and percentage of targets, according to their priority.

Parameter	**Distribution with observation duration**				
	< 1 day	≥ 1 day	≥ 3 days	≥ 5 days	≥ 7 days
Targets					
Total (%)	242 (53%)	213 (47%)	77 (17%)	41 (9%)	10 (2%)
Priority 1	17	20	8	5	2
Priority 2	108	187	65	34	7
Priority 3	43	6	4	2	1
Priority 4	74	0	0	0	0
Observation tasks					
Total (%)	328 (42%)	460 (58%)	163 (21%)	86 (11%)	21 (3%)
Priority 1	22	46	20	12	4
Priority 2	187	396	131	68	14
Priority 3	45	18	12	6	3
Priority 4	74	0	0	0	0

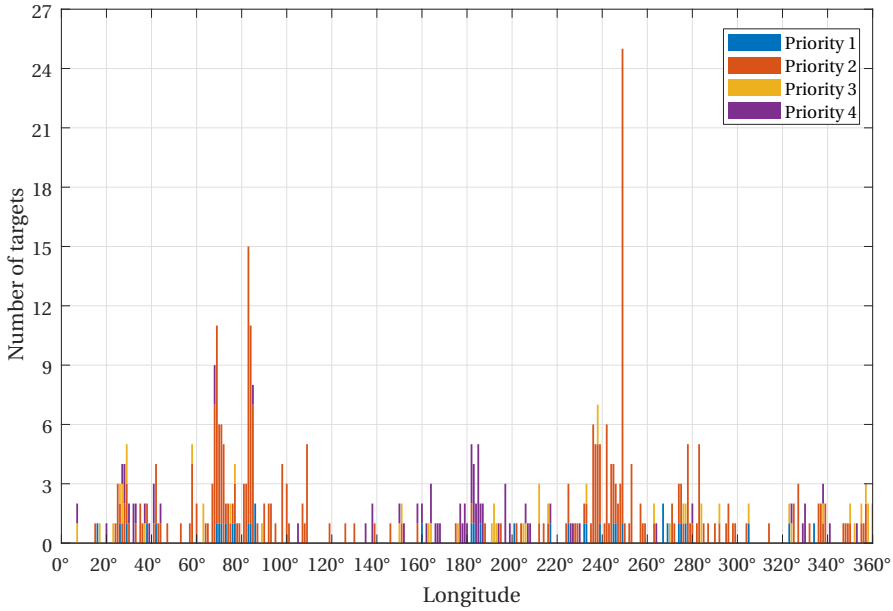

Figure 8.6: Distribution of target priorities relative to celestial longitude.

multiple observations compared to 2% of third priority ones, whereas none of the Priority-4 targets require revisits regardless of duration. This means that if quantity is indeed the criterion that determines the sequence of science activities, a disproportional sampling of lower priority targets ensues. Therefore, a compromise between efficiency and science return is perhaps imperative in the planning decision-making procedure.

Note, however, that the observation time is not the only determinant of the total task duration. The reconfiguration time must also be considered.

8

TARGET PROXIMITY AND RECONFIGURATION TIME

All reconfiguration maneuvers are carried out to abide by baseline configuration requirements dictated at the outset by the target catalog. Naturally, any time dedicated to these maneuvers detracts from time which could potentially be allocated for science. In order to optimally order the tasks, an estimation of the time required for these maneuvers should be carried out (without actually having to pursue complex calculations to derive exact optimized values).

It would be intuitive to think that targets which are close to each other in the celestial sky would be associated with a shorter reconfiguration maneuver compared to a target pair associated with a high angular separation. This would indeed be the case if the formation was linear or planar, not interchangeable and the length of the baseline remained approximately constant across different targets. In such cases, the reconfiguration would be akin to a rigid-body rotation of the formation; an average rotation rate could simply be multiplied by the angular separation between targets to estimate the maneuver time. However, the IRASSI case consists of a three-dimensional dispersion of interchangeable elements with variable baseline requirements for different targets. Given that the distance traveled by each spacecraft differs significantly in a reconfiguration maneuver, angular separation of targets alone becomes a poor predictor of maneuver duration. Assuming equal thruster parameters, the maneuver duration is then largely dictated by the length of the translation trajectories or the differences between the current and subsequent formation size. This is illustrated by Table 8.3, where the formation maneuver duration is defined as the time the slowest spacecraft takes to complete the maneuver. Three formation configurations are considered depending on separation parameter d values: a short baseline 'S' with length corresponding to 10 m, a medium baseline 'M' of 500 m, and a long baseline 'L' of length 1000 m - all naturally three-dimensional formations.

In Table 8.3, it is possible to observe that an increasing angular separation between targets is associated with a nonlinear increase in maneuver duration, but only when baseline distances are maintained. When the reconfiguration maneuver involves an expansion or contraction of the baselines, the maneuver time remains nearly equal across different target separations. In addition, a baseline contraction or expansion is always more time-consuming than maintaining the baseline constant. A full description of the reconfiguration pro-

Table 8.3: Maneuver duration for different target separations and formation configurations.

Formation size (initial-final)	Maneuver duration (hours)		
	Target separation		
	5°	45°	90°
S-S	0.12	0.87	1.30
M-M	0.99	6.14	9.14
L-L	1.17	8.68	12.96
S-L	13.44	13.37	13.41
L-S	13.68	13.65	13.65

cedure is provided in Chapter 9.

The importance of this is that if the total duration is used as a selection criterion for generating task schedules, the reconfiguration maneuver time must be appropriately estimated by the TPM (even before the reconfiguration maneuvers are actually computed by the ReM).

SCANNING ORDER FOR EMISSION-SENSITIVE TARGETS

After each reconfiguration maneuver, the formation either expands or contracts. At the longest baselines, there may be instances in which the interferometer may not be able to correlate the flux of the emissions (or very minimally). This may be an issue for certain targets if the formation starts at the longest baselines, as the spacecraft cannot record the interference fringes at the start of the observation and rather the fringes are found as the formation contracts.

Although it is early to predict with exactness, most targets are not vulnerable to this effect. Disk-type targets, for example, are well-defined sources in the infrared and it is relatively simple to predict *a priori* up to which baseline lengths it is safe to perform measurements. Similarly, active galactic nuclei (AGNi) should have a compact and central emission flux, which affords the flexibility of being able to start the measurements at either end of the baseline length (minimum or maximum). For massive young stellar objects, high-mass star-forming regions and hot cores, correlated flux loss at long baselines is more concerning, since apart from a disk, also an envelope forms around the source structure. Because of this envelope, the limit of the baseline length is too imprecise to be determined beforehand.

Furthermore, the issue of flux loss is target-dependent. There may be wavelengths in the far-infrared that are very detectable, but which are associated with correlated flux loss at long baselines or, conversely, highly excited molecular lines from very compact (little correlated flux loss) regions that are also weaker (bad detectability). Good modeling techniques prior to the science campaign of IRASSI could provide further insights.

With this information, initial scanning requirements were placed on tasks associated with the targets identified above (massive objects, high-mass star-forming regions and hot cores and corinos, respectively target groups IV, VI and VII), such that the formation elements initiate the observation at the shortest baseline and expand during the observations. This affects 61 targets, or about 13% of the total target population and none of the targets require revisits. These are henceforth referred to as 'emission-sensitive targets' and highlighted in gray in Table 8.1. For the remaining targets, only the scanning length (i.e., the difference between the longest and shortest baseline length) is of importance and it is therefore irrelevant whether a target is first sampled at the longest or shortest required baseline.

SCANNING ORDER EFFECT ON RECONFIGURATION TIME

Given that the thrust magnitude is fixed at the maximum limit of 20 mN for reconfiguration maneuvers, this raises the question of whether reconfiguration time can be minimized by instead selecting the order of the scanning (expansion or contraction) appropriately and individually for each target, in order to avoid unnecessary maneuvering time and resource expenses. This would institute that the initial reconfiguration separation is equal to (or determined by) the final separation of the last observation for non-emission-sensitive targets. The advantage of this setup is that it achieves minimal consumption of fuel and time, as most of the

maneuvers can be kept well below 10 hours, as shown in Table 8.3. This has a positive impact on the mission as a whole as more time can be dedicated to science.

In this light, a dynamic catalog concept has been devised, whereby the initial (and final) formation configurations of all (non-emission-sensitive) targets immediately available for the next task are adjusted according to the final formation settings of the current target. For example, assume that the current observation task involves a formation contraction during science activities. At the end of the observation, the formation finds itself at its shortest baseline, e.g. with $d = 10$ m. For all non-emission-sensitive candidates for the next observation, the following applies:

- if the target of a candidate task is tagged with an *intermediate*[1] desired scanning length, the observation task will have its initial separation set to its shortest baseline, $d = 500$ m, and its final separation set to $d = 1000$ m.
- if the target of a candidate task is tagged with an *long* desired scanning length, the observation task will have its initial separation set to its shortest baseline, $d = 10$ m and its final separation set to $d = 1000$ m.

Only then is the feasibility of the tasks evaluated. The task-selection process is described in the next section.

8.4.2. METHODOLOGY

The metrics used to evaluate observation tasks are first introduced followed by the decision-making procedures where the connection with the TSP is revisited. The model dynamics described in Section 7.6.2 apply and so does the separation parameter set $d_{vec} = \{10, 500, 1000\}$ defined in Section 7.5.

TARGET-SELECTION METRICS

A weighted sum of three criteria is used to evaluate candidate tasks:

1. Relative reconfiguration time T_{rel} (i.e., time efficiency)
   The first criterion respects the requirement that most of the time of the mission should be allocated to science observations. That is, if the expected reconfiguration maneuver duration is relatively long, then it consumes mission time to the detriment of science. This maneuver corresponds to the associated translations and any required interchange in position slots among formation members. If iSCOUT is operated on a module-by-module basis, the TPM has no access to this information and the expected reconfiguration maneuver time t_{ReM} is estimated by means of spline interpolation.

   The interpolated values are based on the values obtained in Table 8.3 which portray typical reconfiguration times for different separation parameters d (introduced in Section 7.5 and for different target angular separations. Four different spline functions are defined: three for cases in which the initial formation baseline length (short, medium or long) does not change during reconfiguration and one for when it does (that is, for emission-sensitive targets).

   Else, if iSCOUT is operated in an integrated mode the value of t_{ReM} is provided by the ReM module (details on are provided in Chapter 9, cf. Equation 9.9).

   The relative reconfiguration time for a given target is thus given by:

$$T_{rel} = \frac{t_{ReM}}{t_{total}} \tag{8.1}$$

   with

$$t_{total} = t_{ReM} + t_{cal} + t_{link} + t_{BPM} \tag{8.2}$$

   and where t_{cal} is the calibration time, t_{link} is the time slot allocated for uplink/downlink of telemetry and science data and t_{BPM} is the duration of the scientific phase for the considered task. Again, if iSCOUT is integrally operated, t_{BPM} is provided by the BPM module (described in Chapter 11, cf. Equation 11.3), otherwise t_{BPM} is approximated by the maximum allowable value of t_{BPM}:

$$t_{BPM,max} = 1.4 t_{sci} \tag{8.3}$$

   which corresponds to the combined time of the baseline-change maneuver and target observation duration t_{sci} as provided by the catalog.

[1] Targets associated with intermediate scanning lengths are not sampled at separation parameters $d < 500$ m.

IRASSI assumes $t_{cal} = t_{link} = 4$ hours. t_{total} refers then to the total task time.

From Equations 8.1 and 8.2, it is possible to see that if the reconfiguration maneuver duration t_{ReM} is large enough compared to the science phase t_{BPM} term, T_{rel} will approach ≈ 1. As such, T_{rel} is a measure of efficiency, as the lowest its value is, the higher the chances that in the future further tasks are conducted.

2. Relative task priority P_{rel}
The second criterion has to do with the fact that higher-priority targets should be observed more regularly than low-priority ones, due to their scientific relevance. As such, the relative priority of the associated task is calculated simply as:

$$P_{rel} = \frac{P - P_{min}}{(P_{max} - P_{min})}, \tag{8.4}$$

where P is the priority of a candidate task and P_{min} and P_{max} are respectively the minimum and maximum possible task priorities (where $P_{min} = 1$ and $P_{max} = 4$, cf. Table 8.1).

Using solely criteria 1 and 2 could, however, result in tours that are likely locally confined to isolated regions of the sky and whose sequences of tasks are defined by the ascending order of priorities. Since there is a correlation between target priority and target type, this is not necessarily desirable since after collecting a certain amount of science data from a target type or a region, the interferometer should move on to observing new portions of the sky and other target types. Therefore, in order to balance maneuvering time, science relevance and data heterogeneity, the third criterion was introduced.

3. Relative amount of completed task types N_{rel} (i.e., task diversity)
This third criterion tracks the cumulative frequency of previous task types in a given tour. N_{rel} is the ratio between the number of completed tasks of a given type N_{past} and the total number of observations tasks available of the same type N_{total} (i.e., including revisits), multiplied by an optional weighting factor ω:

$$N_{rel} = \frac{N_{past}}{N_{total} \times \omega}. \tag{8.5}$$

In the above equation ω is the ratio between the user-specified minimum tour duration $\mathscr{D}$ (in days) and the duration of the combined to-be-completed science observation tasks available in the catalog, Ω, which currently totals 1597 days. With $C \in \mathbb{Z}$ denoting the set of all to-be-completed tasks:

$$\omega = \frac{\mathscr{D}}{\Omega} = \frac{\mathscr{D}}{\sum_{c=1}^{C} t_{sci_c}} : 0 < \omega \leq 1. \tag{8.6}$$

In the above equation, ω is automatically set to 1 if $\mathscr{D} > \Omega$. Whether the factor ω is applied to Equation 8.5, is decided by the user. The advantage of this parameter is that it makes the decision-making process agnostic with respect to the size of the catalog: if only so many targets can be realistically observed within the specified time window ($\mathscr{D} < \Omega$), then N_{total} is scaled to reflect this limit. Naturally, this simple scaling process of N_{total} assumes a uniform distribution of targets in longitude, which is not necessarily true, as explained in Section 8.3.2. As time passes and the number of observable targets becomes lower, the less accurate this approximation becomes. Naturally, as the selected tour duration value increases, $\omega \to 1$.

All three criteria scores reflect relative values, with a theoretical value between 0 and 1 (P_{rel} will in fact be exactly zero for Priority-1 tasks). Finally, the function which determines the overall score of a candidate task is:

$$J = \frac{T_{rel} + P_{rel} + N_{rel}}{3} \tag{8.7}$$

The factor $\frac{1}{3}$ was simply applied to normalize the score function to a maximum value of 1.

TASK-SEQUENCING ALGORITHM

The TPM receives user-defined variables, such as initial epoch t_i (in days, or alternatively, the anti-Sun vector longitude value), the minimum tour duration $\mathscr{D}$ (in days) and a logical answer to whether a non-unity ω factor

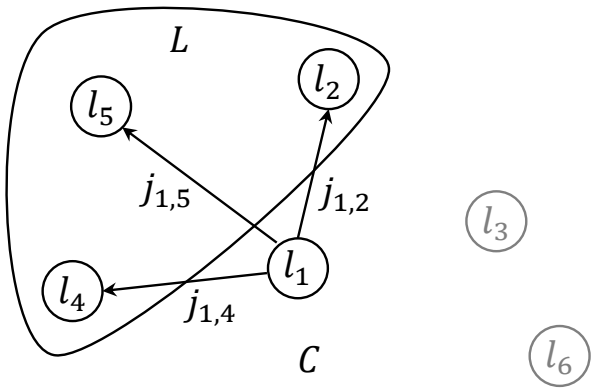

Figure 8.7: Diagram of the IRASSI-TSP analogy.

is to be used in the metric calculations. At the start of the simulation, the target-task catalog[2] is loaded and a map containing all accessible targets at the epoch is generated. A surrogate catalog to be dynamically updated as the tour sequence progresses is simultaneously initiated with default properties equal to the original target catalog.

To make the analogy with the TSP, one can define the set C as that containing all to-be-completed tasks of the catalog. The subset L_i represents accessible tasks from a given task instance l_i which can be evaluated using the score function of Equation 8.7. The path lengths $j_{i,k}$ are defined by the score or cost associated with performing task $l_k \in L_i$ from the starting task $l_i \in C$. The observable task score set J_i contains all possible path lengths connecting l_i to candidate tasks. The tour sequence S is a set of s number of paths, with $j_{i,k} \in S$. The actual tour duration D is defined by:

$$D = \sum_{c=1}^{s} j_{c_{i,k}} \tag{8.8}$$

8

and the tour ends once $D \geq \mathscr{D}$. Figure 8.7 schematizes the IRASSI-TSP analogy, with the set of observable tasks $L_1 = \{l_2, l_4, l_5\}$ from the catalog set $C = \{l_1, \cdots, l_6\}$ and the score set $J_1 = \{j_{1,2}, j_{1,4}, j_{1,5}\}$. Tasks l_3 and l_6 are unreachable because the targets associated with them are unobservable. The full TPM sequencing algorithm is described below.

1. Compute available task set L_i from the set of targets within the field of view N_i, such that the latitude and longitude of each target candidate $n_k \in N_i$, respectively Φ_k and Λ_k, respect the following conditions for $t = t_i$:

$$(\Lambda_k(t), \Phi_k(t)) \notin A_{ez_{proj}} = \text{proj}\left(q_{ez}, \boldsymbol{l_{ez}}, t\right), \tag{8.9}$$

   where $A_{ez_{proj}}$ is the projected the sunshield-associated exclusion zone on the celestial sphere, $q_{ez} = 3$ m (the sunshield radius), $\boldsymbol{l_{ez}} = (1.10, 0, 0)$ m in the $\mathscr{L}$ frame (1.10 m is the distance of the detector from the sunshield) and proj$(*, *, *)$ is a function which executes this projection (the procedure is explained in Chapter 4.2.4 and Appendix B).

2. If no task has yet been completed, select the initial task l_i, associated with target n_i, randomly using a uniform distribution, from a pool of available targets in N_i.

3. Remove $n_k = n_i$ from N_i if n_i is associated with more than one task in order to avoid two consecutive tasks being performed in connection with the same target. Update L_i accordingly.

4. Perform a check functions on L_i: if the list is empty, no tasks are available because either

   (a) no targets are within the field of view, i.e., $N_i = \varnothing$ *or*

   (b) all tasks l_k associated with reachable targets in $N_i \neq \varnothing$ have been completed.

[2] The catalog can be the raw list of targets with zero completed tasks to be fulfilled during the mission provided or contain a pre-completed task set saved from a previously generated tour. If the latter is true, the initial target will be set as the last target from the tour.

The program adds then a 24-hour waiting period to the current tour epoch, resulting in an update of the time variables e.g., $D = D + 1$ days, and the program returns to Step 1. In the first year of operations, for example, the chances that a non-visited target will be within reach after a 24-hour waiting period is 74%, rising to 83% after 48 hours.

5. Estimate $t_{ReM_{i,k}}$ (via spline interpolation, cf. Table 8.3) and $t_{total_{i,k}}$ and update the dynamic catalog (i.e., set the properties of initial and final formation separation) for all tasks $l_k \in L$.

6. Calculate a final epoch t_i* for all tasks, corresponding to the end of candidate observation tasks, such that (cf. Equation 8.1):

$$t_{i_k}* = t_i + t_{total_{i,k}} \; \forall \; l_k \in L \tag{8.10}$$

7. Remove from list N_i targets $n_k \in N_i$ which do not satisfy the condition described by Equation 8.9, when setting $t = t_{i_k}*$, to ensure that at the end of each candidate task, the corresponding target is still within the field of view. Update L_i accordingly.

8. Repeat Step 4. At this stage, the list L_i is updated and shall contain all available observation tasks.

9. Calculate the set J_i to attribute a cost associated with each observation task

10. Select the next task l_k (based on either method introduced in the next subsection), update the catalog and generate a record on the mission task-progress database with the completion status of l_k and with the required initial and final separation recorded in the dynamic catalog at the current instance l_i.

The process is iterated until $D \geq \mathscr{D}$ or the mission database contains all tasks prescribed by the catalog, as illustrated by the pseudocode below.

DECISION-MAKING PROCEDURES

TWO decision-making methods are implemented for constructing task sequences: a nearest-neighbor and a semi-stochastic near-neighbor procedure. The solutions obtained with each are compared in the next section.

Nearest-neighbor heuristics (NNH) Nearest-neighbor optimization is the process via which task sequences are generated by always selecting the next lowest $j_{i,k}$ value, $j_{i,k} \in J_i$. This means thus that the selection score described in Equation 8.7, for example, penalizes potential tasks requiring comparatively longer reconfiguration maneuvers. Likewise, the score discourages the algorithm to select the next task if it is of a type that has been observed disproportionally frequently relative to other type populations, even if the target has a high priority.

In order to grasp the relative effect of criteria T_{rel} and P_{rel}, that is, the trade-off between efficiency and priority, Table 8.4 shows the value of the objective function J_{TPM} at the start of the simulation, when $N_{rel} = 0$. The table is colored according to the value of J_{TPM}: the darker the color, the lower the J_{TPM} and vice-versa. As expected, high-priority tasks with the lowest T_{rel} have the lowest J_{TPM} value, at the top-left corner of the table; tasks linked with the lowest P_{rel} requiring relatively long reconfiguration time occupy the bottom-right corner with the highest J_{TPM}. It is possible to observe from the table, for example, that the algorithm would select a Priority-2 task with a $T_{rel} = 0.10$ ($J_{TPM} = 0.14$) over a Priority-1 task with $T_{rel} = 0.50$ ($J_{TPM} = 0.17$). Additionally, since $J_{TPM} \approx 0.25$ both for a Priority-3 task with a short reconfiguration time and a high-priority task with $T_{rel} = 0.75$, the value of N_{rel} would be the deciding factor in determining the next task. Note that N_{rel} will have, at the early stages of the simulation, markedly different values for differing task types. This is due to the abundance of observation tasks associated with certain types, such as T Tauri stars and disks (188 observation tasks) and Herbig Ae/Be stars (278 observations), which together make up ≈ 60% of all tasks. For example, it will take about 17 more observations of the type Herbig Ae/Be stars compared to Massive objects to obtain the same value of N_{rel}.

Naturally, the NNH is not a guarantee of a globally optimum solution. However, because the initial observation positions (i.e., final positions of the reconfiguration maneuver) are set dynamically and adapted to each sequence's instance, the solutions provided via the NNH method can be considered a good approximation of a hypothetical optimal tour.

Algorithm 1 TPM task-sequencing algorithm.

Define:
d_{vec}, q_{ez}, l_{ez}, t_{cal}, t_{link}

Require:
$\mathscr{D} > 0$, $t_i \in \mathbb{R}_{\geq 0}$, $\omega_{bool} \in \{0, 1\}$

Initialize:
[task, catalog] = retrieveCatalog
ω = getOmega(catalog, ω_{bool})
$D = 0$

while $D < \mathscr{D}$ **or** task < size(catalog) **do**
  $[L_i, N_i]$ = getList$\left(t_i,\ \text{catalog}\right)$
  if task = 0 **then**
    $[l_i, n_i]$ = firstTask(L_i)
    catalog = updateCatalog$\left(l_i,\ \text{'completed'}\right)$
  end if
  $L_i = L_i\,(N_i \triangle n_i)$;
  D = checkList(L_i);

  $\left[t_{total}, \text{catalog}_\text{d}\right]$ = estimateTime$\left(\text{catalog}\,(l_i, L_i)\right)$
  $t_i* = t_i + t_{total}$
  $[L_i*, N_i*]$ = getList$\left(t_i*,\ \text{catalog}\,(l_i, L_i)\right)$
  $L_i = L_i \cap L_i*$
  D = checkList(L_i)

  J_i = calcMetrics$\left(t_{total},\ \text{catalog}_\text{d}\,(l_i, L_i),\ \omega\right)$
  l_k = selectNextTask(J_i)

  Update:
  $l_i = l_k$, $D = D + \left(t_{i_k}* - t_i\right)$, $t_i = t_{i_k}*$, task = task + 1
  catalog = updateCatalog$\left(l_i, \text{'completed'}\right)$
end while

Table 8.4: Relative importance of P_{rel} and T_{rel}, when $N_{rel} = 0$.

Priority	P_{rel}	J_{TPM}			
		T_{rel}			
		0.10	**0.25**	**0.50**	**0.75**
P_1	0.00	0.03	0.08	0.17	0.25
P_2	0.33	0.14	0.19	0.28	0.36
P_3	0.66	0.25	0.30	0.39	0.47
P_4	1.00	0.37	0.42	0.50	0.58

Table 8.5: Minimum number of tasks necessary to be available for at least two candidates to be considered by the SNS, for different thresholds.

Threshold	No. of tasks
3%	34
5%	21
10%	11

Semi-stochastic near-neighbor search (SNS) To escape the trap of local minima in devising optimal long-term task sequences, a second method is introduced. This method, called a semi-stochastic near-neighbor search (SNS), relies on the following three steps:

1. ordering the candidate tasks by ascending J_i values
2. setting a threshold to identify top candidates out of the available pool
3. choosing the next task employing a uniformly distributed random process

As such, the SNS algorithm samples the solution space more amply than the NNH at each instance and may be able to deliver different solutions, e.g., produce more observation tasks within the same time window.

The threshold value may itself be subject to optimization. In the present study, three values are selected: 3%, 5% and 10%. The number of top candidates is rounded up to the nearest integer. Note that selecting the top candidate would emulate the NNH behavior. However, depending on the threshold value, there may be instances in which only one target is available. This is shown in Table 8.5 where the minimum number of candidates is given for at least two tasks to be traded. Note also that because the SNS is itself stochastic[3], there is a very low likelihood that two equal sequences are produced.

8.5. RESULTS AND DISCUSSION

THE simulation setup is presented in this section followed by the obtained results and respective analysis. The results are split into a short-term example tour, which demonstrates the effect of using the ω parameter in the scoring process, and a representative long-term tour which compares the effect of the two optimization algorithms.

8.5.1. TPM SIMULATION PARAMETERS

The following assumptions hold within the TPM module:

1. The field of view is the same for all members of the interferometers (relative member distances are negligible compared to interferometer-target distances and therefore target direction can be assumed equal)
2. The interferometer is located at the L_2 point of the Sun-Earth/Moon system, at the center of the celestial sphere. The rotation rate of L_2 about the Sun, is the same as the Earth's, corresponding to 360 deg in 365.25 days or 0.9856 deg/day. This is therefore the rotation rate of the field of view of the interferometer. Keplerian motion is assumed.
3. The mean equinox of J2000 is used to define the celestial reference coordinate system
4. Since spacecraft are treated as point masses, attitude maneuvers are not considered. Adjusting the pointing of the formation from one target to the next involves thus a translation maneuver and the term 'retargeting' does not apply. Instead, the term 'reconfiguration' is herein used.
5. Although attitude maneuvers are not considered by iSCOUT, the estimation of t_{ReM} is calculated by considering the shortest possible attitude change between two targets. For example, consider current

[3]The term 'semi-stochastic' is employed because the threshold that is imposed does not allow a random task selection of the full candidate pool.

Table 8.6: Simulation parameters for the Task-Planner Module.

Dependency	Parameter	Value
Reconfiguration and science maneuvers	$t_{BPM} \approx t_{sci}$	Target-dependent, between 2.5 hours and 8 days
	t_{ReM}	Target-dependent, up to 14 hours
Operational activity	t_{cal}	4 hours
	t_{link}	4 hours
TPM algorithm variables	Ω	1597 days
	Field-of-view slew rate	0.9856°/day
	Prioritization of:	
	targets	Yes
	tasks	No (can be accommodated if needed)
	Initial formation pointing direction	Randomly selected from accessible sky

target n_i with a position $\boldsymbol{p_i}$ defined by Cartesian coordinates (Λ_i, Φ_i) and a candidate target n_k with position $\boldsymbol{p_k}$ defined by Cartesian coordinates (Λ_k, Φ_k). If the Cartesian separation between these two targets in the celestial sky

$$\angle(\boldsymbol{p_k}, \boldsymbol{p_i}) = \arccos\left(\frac{\boldsymbol{p_i} \cdot \boldsymbol{p_k}}{||\boldsymbol{p_i}||\,||\boldsymbol{p_k}||}\right) \tag{8.11}$$

corresponds to 175°, the reconfiguration maneuver will not correspond to a full 175° reorganization of the formation. Instead, the following ensues:

(a) a 180° attitude maneuver is assumed, followed by

(b) a 5° reconfiguration translation

This would correspond to the most resource-efficient way to maneuver in a realistic scenario as the current setup of the tool models the spacecraft as point masses. For practical purposes, this means therefore that for reconfiguration maneuvers, candidate targets are, at most,

$$\angle(\boldsymbol{p_k}, \boldsymbol{p_i})\big|_{max} = 90° \tag{8.12}$$

away.

Additionally, Table 8.6 summarizes the parameter values considered in the TPM simulation environment.

8.5.2. EXAMPLE TASK TOUR - EFFECT OF ω

Two 100-day simulations are performed to demonstrate the effect of introducing ω in the scoring process and discuss its utility to the user. The first one does not apply any temporal scaling to N_{rel} (cf. Equations 8.5 and 8.6) and simply assumes $\omega = 1$. The second one scales N_{rel} with the combined to-be-completed science observation tasks available in the catalog, Ω, such that $\omega = \frac{100}{1597} \approx 0.063$.

The NNH selection process is used. The initial anti-Sun vector longitude is set to $\Lambda = 85°$ for both simulations. The simulation is initiated from the beginning of the IRASSI mission, with an empty record of past observation tasks. The first task l_1 of the first simulation, i.e., for the $\omega = 1$ condition, is selected at random from the available list L_i at the initial instant. However, the first task of the second simulation, i.e., for $\omega \approx 0.063$ is set equal to that of the first simulation.

The results are presented in Tables 8.7 and 8.8 and the sequences are shown in Figure 8.8, where the numbers correspond to the targets. The first target is 331. Table 8.9 provides a summary of the results. Over the 100 days, 28 and 34 tasks are conducted respectively for $\omega = 1$ and for the $\omega \approx 0.063$ case, a 21% increase.

This increase is naturally associated with the selection of shorter tasks, although the maneuver duration is, on average, 10 minutes longer (3.44 vs. 3.27 hours). Another difference lies in the fact that for the $\omega = 1$ case, only Priority-1 targets are observed, whereas with $\omega \approx 0.063$, 26% of the tasks are associated with Priority-2 targets. Of the total tasks completed, 32% are associated with previously observed targets, a reduction of 7% compared to the $\omega = 1$ case. No passive days are recorded for both simulations, that is, there are always targets in the field of view of the interferometer.

What is noteworthy, however, is that by scaling N_{rel} with $\omega \approx 0.063$, a balanced proportion of task types are completed. Whereas with $\omega \approx 0.063$, between 94 %–96 % (mean= 95.4 ± 0.7%) of the various types remain to be observed, with $\omega \approx 0.063$, the range is significantly wider at 81 %–100 % (mean=94.4 ± 5.5%). As such, the $\omega \approx 0.063$ tour guarantees a diverse sequence of tasks, without necessarily detracting from observing high-priority targets. It is therefore suggested that users scale the target diversity metric N_{rel} with the minimum tour duration $\mathscr{D}$.

8.5.3. IRASSI TASK TOUR - NNH AND SNS

To emulate the operation of the TPM, task tours with minimum duration $\mathscr{D} = 5$ years were generated. Four different tour sets were generated: one using NNH and three SNS-based tours, each with different thresholds: 3%, 5% and 10%. They are henceforth designated as SNS-3, SNS-5, SNS-10. The simulation conditions are summarized in Table 8.10. The initial anti-Sun vector longitude is fixed at $\Lambda = 85°$. The simulation is initiated from the beginning of the IRASSI mission, i.e., no observations have been made prior to this point, but all four conditions start at the same task.

Because of the stochasticity of the SNS tours, each tour was repeated five times and the results reflect the averages of the runs. Results were extracted at yearly intervals and summarized in Table 8.11.

The first trend that is visible is that tours generated by the SNS can outperform the NNH in terms of the number of tasks, albeit only by up to 1.4%. This increase corresponds to the 630 tasks of the SNS-5 and is achieved without detriment to the overall metrics. Appendix D.3 contains more extensive information concerning these results - see, for example, Table D.2. However, due to the stochastic nature of the SNS, a consistently higher number of tasks cannot be guaranteed. In fact, results show that, on average, the number of tasks completed using the SNS approach does not differ from the NNH. Surprisingly, this also applies to the mean performance J_{TPM} even though the average maneuver time t_{ReM} is 43% higher for SNS-10, 28% for SNS-5 and 19% for the SNS-3. Since the duration of the science phase (t_{BPM}) is the dominant term of Equation 8.2, the increase in average t_{ReM} is not sufficient to affect T_{rel} and thus J_{TPM}.

One interesting aspect to note is that the number of idle days is lower for the SNS tours than for the NNH. This means that the spacecraft in SNS tours spend less time waiting around for a target (or a target that has not yet had all of its associated tasks completed) to come within view. However, within the SNS tours, the higher the threshold, the higher the t_{ReM}. Therefore, given that the number of tasks per day is the same for the SNS and NNH, the formation spends more time maneuvering in-between tasks for SNS sequences. This indicates thus that the NNH tour is more fuel-efficient than any of the SNS tours.

As expected, the number of single tasks decreases with increasing SNS threshold values, such that, nearly 30% of the tasks selected with the SNS-3 emulate those of the NNH. Conversely, when comparing the SNS tours, one may observe that the range between minimum and maximum decreases with an increasing threshold value, whilst averaging 621 tasks at the end of the five years. This is perhaps unexpected, since, for instance, for the SNS-3 with 30% of the tasks selected only having one candidate, one might suppose that the number of tasks will tend to converge to the vicinity of that obtained with the NNH. This may therefore indicate that the magnitude of the range between the minimum and maximum number of tasks in the SNS case may be attributed to stochasticity.

8.5.4. METRICS ANALYSIS

Following the results of the last two sections, Section 8.5.2 and 8.5.3, an analysis of the behavior of the metrics over time is warranted. For example, by observing Tables 8.7 and 8.8, which have a duration of only 100 days, it is noticeable that P_{rel} will largely remain near zero (as low-priority targets are penalized in the decision-making process), as will N_{rel}, as the task database starts to be populated. The relative reconfiguration time T_{rel} is therefore generally the biggest determinant of the next task for the early stages of the mission.

On the other hand, in appendix Table D.3, which shows the yearly evolution of the NNH metrics for a five-year simulation, it is noticeable that as time passes, the mean values of P_{rel} and, in particular, N_{rel}, rise and will tend to one. The variation of T_{rel} over time is significantly lower and by the second quarter of the first year, T_{rel} loses its dominance completely in the J_{TPM} scoring value. The correlation value between

Table 8.7: Sequence results of Example Task Tour, $\omega = 1$.

Target No.	Visit No.	Target Type	Cumulative duration (days)	T_{rel} (10^{-2})	P_{rel} (10^{-2})	N_{rel} (10^{-2})	j (10^{-2})
331	1	VI	0.00	0.00	0.00	0.00	0.00
74	1	II	1.48	1.03	0.00	0.00	0.34
442	1	III	6.51	7.59	0.00	0.00	2.53
440	1	III	11.39	6.24	0.00	2.38	2.87
243	1	V	12.87	9.97	0.00	0.00	3.32
197	1	I	14.04	3.41	0.00	0.00	1.14
74	2	II	15.68	10.64	0.00	0.36	3.67
197	2	I	16.82	1.54	0.00	0.53	0.69
442	2	III	21.902	8.43	0.00	4.76	4.40
441	1	III	28.64	3.30	0.00	7.14	3.48
440	2	III	33.48	5.25	0.00	9.52	4.93
441	2	III	40.19	2.84	0.00	11.90	4.92
442	3	III	45.14	6.16	0.00	14.29	6.81
11	1	IV	46.71	18.1	0.00	0.00	6.05
232	1	IX	47.93	3.51	0.00	0.00	1.17
357	1	VII	48.96	14.9	0.00	0.00	4.96
441	3	III	56.00	7.30	0.00	16.67	7.99
163	1	I	63.27	3.91	0.00	1.06	1.66
167	1	I	70.85	0.42	0.00	1.60	0.67
29	1	II	74.07	0.18	0.00	0.72	0.30
28	1	II	75.01	1.01	0.00	1.08	0.69
29	2	II	78.22	0.03	0.00	1.44	0.49
28	2	II	79.17	1.01	0.00	1.80	0.90
167	2	I	86.72	0.08	0.00	2.13	0.74
163	2	I	93.75	0.46	0.00	2.66	1.04
92	1	II	96.24	0.71	0.00	2.16	0.96
17	1	V	99.36	2.30	0.00	1.18	1.16
343	1	VII	100.19	0.75	0.00	4.00	1.58

Table 8.8: Sequence results of Example Task Tour, $\omega = 0.063$.

Target No.	Visit No.	Target Type	Cumulative duration (days)	T_{rel} (10^{-2})	P_{rel} (10^{-2})	N_{rel} (10^{-2})	j (10^{-2})
331	1	VI	0.00	0.00	0.00	0.00	0.00
74	1	II	1.48	1.03	0.00	0.00	0.34
442	1	III	6.51	7.59	0.00	0.00	2.53
243	1	V	8.12	17.65	0.00	0.00	5.88
225	1	IX	9.13	9.72	0.00	0.00	3.24
197	1	I	10.55	20.09	0.00	0.00	6.70
74	2	II	12.18	10.64	0.00	5.74	5.46
197	2	I	13.33	1.54	0.00	8.49	3.35
357	1	VII	14.49	24.55	0.00	0.00	8.18
401	1	VIII	16.97	1.19	33.33	0.00	11.51
442	2	III	21.85	4.92	0.00	38.02	14.31
75	1	II	25.53	9.32	33.33	11.49	18.05
8	1	IV	26.61	1.09	33.33	0.00	11.48
80	1	II	27.19	1.55	33.33	17.23	17.37
403	1	I	34.40	0.24	33.33	16.99	16.85
432	2	II	35.66	26.67	0.00	22.98	16.55
245	1	V	36.46	1.59	33.33	18.79	17.90
432	1	II	37.50	11.82	0.00	28.72	13.51
401	2	VIII	40.23	10.41	33.33	15.21	19.65
403	2	I	47.57	1.88	33.33	25.48	20.23
404	1	I	52.79	0.01	33.33	33.98	22.44
139	1	II	56.28	10.47	0.00	34.47	14.98
206	1	I	61.18	0.09	0.00	42.47	14.19
139	2	II	64.34	1.36	0.00	40.21	13.86
29	1	II	67.57	0.51	0.00	45.96	15.49
373	1	VIII	71.20	8.76	0.00	30.42	13.06
376	1	VIII	73.09	3.08	0.00	45.63	16.24
17	1	V	76.39	7.70	0.00	37.58	15.09
167	1	I	84.22	3.63	0.00	50.97	18.20
29	2	II	87.49	1.69	0.00	51.70	17.80
28	1	II	88.42	0.10	0.00	57.44	19.18
167	2	I	96.03	0.79	0.00	59.49	20.07
28	2	II	96.98	0.62	0.00	63.19	21.27
373	2	VIII	100.61	8.90	0.00	60.84	23.25

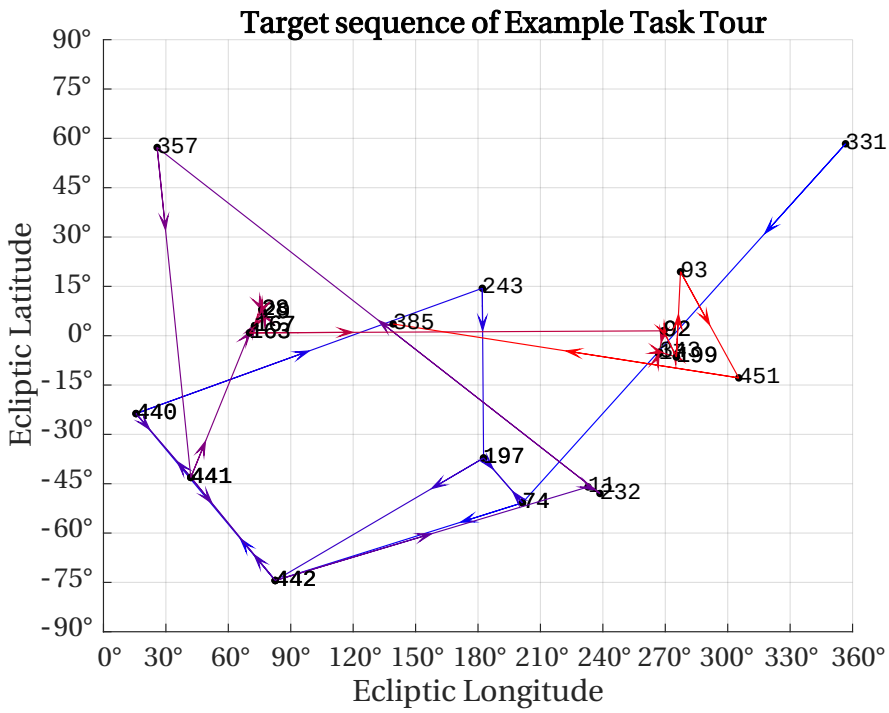

(a) $\omega = 1$

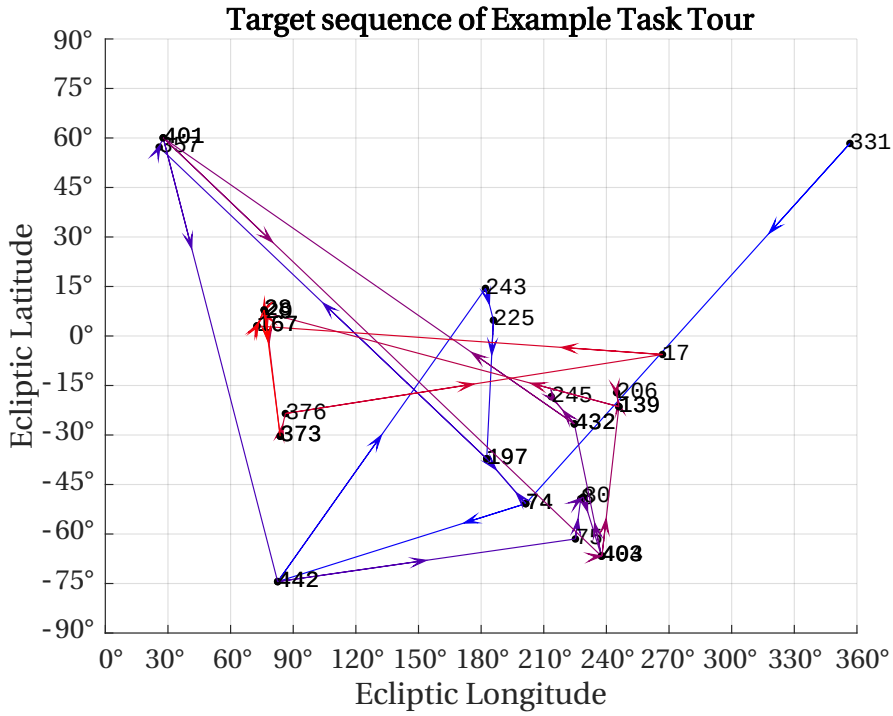

(b) $\omega = 0.063$

Figure 8.8: 100-day sequences for the Example Task Tour for different ω parameters.

P_{rel} and J_{TPM} is the highest of the three metrics and stands at an average of 0.86 (cf. Appendix D.3.2). A correlation factor of only 0.49 was found for T_{rel}. It is suspected that this is due to the fact that the calculation of target sequences is already optimized (for non-emission-sensitive targets) to guarantee that the order of the scanning does not generate unnecessary reconfiguration maneuvers, keeping t_{ReM} and thereby T_{rel} low

Table 8.9: Summary results of Example Task Tour. With $t_{BPM} \approx t_{sci}$, t_{BPM} becomes a measure of the observation duration.

Parameter	$\omega = 1$	$\omega = 0.063$
Repeated target visits (%)	39	32
Remaining tasks of (%)		
Type I	97	96
Type II	97	96
Type III	81	95
Type IV	94	94
Type V	98	96
Type VI	95	95
Type VII	92	96
Type VIII	100	95
Type IX	96	96
No. idle days	0	0
Mean t_{BPM} (days)	3.34	2.49
Mean tasks per day	0.28	0.34
Mean t_{ReM} (hours)	3.27	3.44

Table 8.10: Simulation parameters for the IRASSI Task Tour.

Simulation parameter	**Value**
$\mathscr{D}$	5 years
ω	1
Optimizer	NNH, SNS-3, SNS-5, SNS-10

in comparison with the other two metrics (cf. Equation 8.1).

As such, it is clear that different metrics will be predictors of the J_{TPM} value at different times of the mission. This information may be useful in the context of devising more elaborate algorithms which could explore these properties to generate alternative sequences using alternative score metrics after a certain amount of mission time has elapsed. This topic is explored further in the 'Conclusions and Future Work' section.

8.5.5. CONCLUSIONS AND FUTURE WORK

From the results, it can be concluded that the NNH task-selection algorithm seems to provide better fuel-savings than the SNS over the long term. As such, this algorithm will be used to generate the end-to-end simulation of Chapter 12. The relative priority metric P_{rel} proved to be the biggest determinant of the task-sequence selection procedure overall, using equal weights in the J_{TPM} scoring process.

The TPM module assumes[4] that each observation window or task is exclusively dedicated to one single target and that reconfiguration maneuvers subservient to the target ought to occur prior to observations. Although this scenario may represent an ideal case from a time-target availability and onboard resources

[4]The premise is obviously a result of current mission requirements established by IRASSI's science team.

Table 8.11: Results of TPM's IRASSI Task Tour. With $t_{BPM} \approx t_{sci}$, t_{BPM} becomes a measure of the observation duration.

Parameter	**NNH**	**SNS-3**	**SNS-5**	**SNS-10**
Completed tasks (min-max)	621	609 to 629	615 to 630	613 to 624
Mean completed tasks (%)	79	79	79	79
Mean no. idle days	344	328	329	325
Mean no. single tasks available for SNS	–	186	143	104
Mean tasks per day	0.34	0.34	0.34	0.34
Mean t_{BPM} (days)	1.97	1.98	1.97	1.96
Mean t_{ReM} (hours)	2.14	2.55	2.73	3.05
Mean J_{TPM} (-)	0.29	0.29	0.29	0.29

point of view, it is not necessarily the most efficient solution. Therefore, the next subsections detail possible avenues for future investigation.

OPTIMIZATION ALGORITHM AND METRICS

The metrics used within TPM place an emphasis on sampling efficiency from a maneuvering point-of-view, on target priority and diversity. This, however, assumes that at least one target is always available for observations. Whereas in the early stages of the mission, this is certainly the case, target scarcity gradually becomes a concern over time. One possible way to remedy this is to design a multi-objective algorithm that minimizes waiting times in-between targets over a tour. Another approach could perhaps consider an algorithm switch at a bespoke instant in time during the mission (or after achieving a sufficient value of N_{rel} for all task types and with the highest-priority tasks having been completed) to devote resources to observing targets as much as possible until the end of the mission once the number of targets available falls below a certain threshold. Algorithms such as the *split-interval scheduling* [131], which attempts to find sequences of tasks over non-intersecting segments of time to maximize mission profits, could prove useful in this case. Vidal *et al.* [132] provide a modeling and algorithmic design for combinatorial problems with time characteristics.

The NNH algorithm in the present work could also serve as a mechanism for generating starting tours for the short- and medium-term observations using local search procedures [127, 133], which explore the solution space to a higher degree than the NNH. This would entail a modification of the target-selection criteria or metrics in the current standing, but could push the solutions to within 1-2% of the global optimum [134]. Using local search algorithms may be suitable in situations where the maximum allowable number of targets N associated with a maximum t_{total} is fixed, e.g., if operating payload instruments for longer than $\sum_{n=1}^{N} t_{total_n}$ will cause a memory storage overload. This may also imply that the metrics become dependent only on the maneuver itself instead of on the history of the tour (which is imposed by the 'target diversity' criterion N_{rel}).

MODULE COMPLEXITY

The TPM was developed to cope with the preliminary character of the IRASSI study. Currently, only limited information concerning the science tasks is available in the catalog. As such, all science activities are deemed observation tasks with no differentiation in nature (e.g., detection of gases vs. measuring accretion rates in protostars) or in order of execution. This differentiation could accrue to the prioritization of tasks being considered differently from the priorities of the targets as in the current procedure.

The catalog can be extended to account for target characteristics and prioritization of different tasks as more information becomes available either before or during the mission. This requires an adaptation of the task-selection metrics. As missions progress and more astronomy data is available, the decision-making procedures should be able to adapt 'on-the-fly' accordingly. Therefore, implementing such automated procedures which evolve online would increase the complexity of the module and could bring the TPM closer to supporting a real mission.

In addition, if there are temporal constraints on certain observation activities due to ground personnel or due to communications unavailability, these can be incorporated within the module in the future.

TRADING SCIENCE PRIORITIES WITH MISSION-TIME SAVINGS

Maneuver duration is decoupled from observation duration. As such, a high-priority target may require an observation window as short as 3 hours and a reconfiguration maneuver of 12 hours. However, in the same time frame, one could observe instead five other targets of lower priority which are associated with very short reconfiguration times. Whether this is beneficial from a scientific point of view, is a discussion to be relayed to astronomers and one the author cannot judge. In any case, a future analysis in this regard should not be excluded and the implementation of such a strategy would require a global optimization method to be employed, which should include efficiency metrics stemming from target-aggregation within an observation window, instead of a nearest-neighbor search.

TRADING SCIENCE PERFORMANCE WITH FUEL SAVINGS

As aforestated, the prioritization of science for individual targets requires that reconfiguration maneuvers are performed systematically before any observation. Since colloidal engines are devised for these maneuvers, they are extremely time-consuming and may limit the number of observations that can be performed during the operational phase of the mission. An interesting question one could pose is whether a small decrease in science performance for certain targets could be acceptable by simply reorienting the spacecraft (instead of changing the size of the baselines and moving the spacecraft) before the expansion/contraction maneuver. This is particularly relevant to IRASSI, given the high concentration of targets in certain regions of the celestial sphere. This strategy would demand that attitude models are included in iSCOUT and that input from science experts is provided for an assessment of the degradation in science performance in each case.

Similarly, aggregating several targets with comparable desirable baseline requirements and observation times in a single observation task before proceeding to changing the baselines, instead of having consecutive tasks for each target, could also be a feasible option. This option has been explored by Bailey *et al.* [135] for a two-spacecraft formation, whereby retarget, reorient and resize strategies have been devised to guarantee fuel economy and fuel balance in light of an observation goal. In their work, using a 'chained local optimization' [136] algorithm, Bailey *et al.* showed that mixing targeting and reorientation maneuvers before resizing is significantly more efficient than imaging stars separately, particularly when separation angles between targets is relatively small. Although no mission time limitations or target availability constraints are considered, a multi-tier optimization loop which accounts for both could perhaps extend this work and be useful to IRASSI-type missions.

These aspects reinforce the idea that alternative strategies in sampling the targets and organizing the sequence of science events must be investigated in the future. An analysis should consider different operational aspects and combinations of targets and their characteristics, such that the global and individual science return over an observation window does not degrade below a certain threshold. Independent parameters may include:

1. how many targets in an expansion or contraction maneuver can be observed
2. the maximum acceptable target separations in the sky (or combinations thereof)
3. the maximum acceptable duration of individual target observations (or combinations thereof)

8.6. CHAPTER SUMMARY

THE present chapter introduced the setup of the Task-Planner Module. A survey describing the evolution of autonomous task-planning tools was provided and several algorithms which attempt to solve the TSP, akin to the IRASSI task-sequence optimization problem, were presented. Given the peculiarities of the IRASSI case, a nearest-neighbor search and semi-stochastic near-neighbor procedure were pre-selected for further analysis, respectively the NNH and the SNS.

The targets from the current catalog were presented, whereby Priority-2 targets, the most populous group, were shown to be concentrated in certain regions of the celestial sphere, namely close to the Equator and near the 236°–253° band. It was also shown that although target separation was correlated with reconfiguration maneuver time, the biggest predictor of maneuver duration was the initial and final formation size. This led to a task-planning strategy that determined the initial and final configurations of the formation dynamically for each task, rather than pre-programming it before the sequences, as a means to ensure fuel and time efficiency.

The eligibility of a task candidate was evaluated using a weighted sum of three metrics: the relative reconfiguration-maneuver time, the relative priority of the to-be-observed target and how often the same target type has been previously observed. The NNH and SNS algorithms were used to generate five-year mission tours. Results showed that although there were instances in which the SNS outperformed the NNH by observing up to 1.4% more tasks without detriment to the overall metrics, this cannot be guaranteed due to the stochastic nature of the SNS. On average, the number of completed tasks was the same, but the average maneuver time required by the SNS amounted to a 43% increase relative to the NNH, which makes the SNS algorithm more expensive in terms of fuel. The NNH was then selected for generating IRASSI task sequences.

The last part of the chapter describes a pathway for further research in the context of task-planning for IRASSI. For instance, although the NNH offers promising results by devising realistic tours quickly and in a computationally efficient manner, more complex algorithms could be used to refine NNH-generated solutions. Of particular relevance to future work, is how to best leverage overall time dedicated to science without sacrificing the completion of specific observation goals and how to best aggregate maneuvers with an acceptable decrease of science returns. These are practical aspects that affect the feasibility of the mission and should be subject to a more in-depth investigation. The difficulty lies instinctively in determining what 'best' is in this case and perhaps such a discussion requires a harmonization of goals between astronomers (who aspire to maximize science returns), engineers (who work at the limit of what is technically achievable) and mission managers (who would like to drive mission costs to a minimum).

9

Optimization of Reconfiguration Maneuvers

An experiment is a question which science poses to Nature and a measurement is the recording of Nature's answer.

Max Planck

ABSTRACT

To address the challenge of finding suitable relative positions in three-dimensional space which satisfy science goals over long periods of time, a reconfiguration procedure has been devised. The method assigns optimized post-maneuver positions of the individual telescopes for the next to-be-observed target. A mesh-adaptive direct search algorithm is selected for the optimization and two cost functions are analyzed: a fuel-based and a ΔV-based one, both pursuing a balanced use of these resources across the fleet. The effect of simulation variables such as initial wet mass and fuel mass balance, thruster settings and cost-function weighting parameters is evaluated with respect to overall used fuel and fuel balance, ΔV and ΔV balance and maneuver duration. Results show that for wet-mass-imbalanced cases, cost functions should be tuned differently for optimal fuel and ΔV management. This is not necessarily the case for homogeneous or fuel-mass imbalanced cases. The analysis also suggests that the ΔV-based function produces more consistent optimal ΔV-balancing potential across different sets of initial conditions and shows less variability in individual maneuvers than the fuel-based function.

Publication

L. Buinhas and R. Förstner, *Formation Reconfiguration Optimization for the IRASSI Space Interferometer*, Advances in Space Research, **67(11)**, 3819-3839 (2021).

9.1. INTRODUCTION

RECONFIGURATION maneuvers precede science activities and observation routines. They entail a set of formation configuration adjustments, such as re-targeting, formation rotations and separation changes by means of translations in inertial space. Such maneuvers are part of the Formation Reconfiguration GNC mode introduced in Chapter 6.

The Reconfiguration Module (ReM) was designed to prescribe optimal trajectories in inertial space, while accommodating science requirements, such as initial separation and target direction, and formation geometry configurations. The ReM receives the observation plan generated by the TPM and outputs a set of final spacecraft positions.

The formation reconfiguration methodology presented in this chapter builds on the approach devised for the Darwin mission [12, 137]. The main differences lie in IRASSI being a decentralized free-flying five-element interferometer, which must be distributed in three-dimensional space, whereas Darwin has a fixed centralized planar configuration of its four-element formation. As a result, the solution space for formation reconfiguration positions is much larger. The reconfiguration strategies seek either the minimization of overall fuel consumed and fuel differences across the formation or minimization of ΔV expended and ΔV differences, simultaneously guaranteeing time-optimal maneuvers.

IRASSI is a homogeneous formation, in that both wet mass and fuel mass are equal for all elements. However, this work extends the analysis to other formation cases, with elements of differing wet and fuel masses, in order to formulate generalizable mathematical expressions for optimal maneuver-planning.

9.2. PREVIOUS CONTRIBUTIONS

THE interest in devising optimal formation reconfiguration strategies has been well documented in the past two decades. Methods for optimal repositioning of spacecraft on the basis of fuel consumption and balancing were found by Beard *et al.* for planar formations, allowing both for two-dimensional 'rigid-body' formation rotations about a point in space [79] and three-dimensional constrained [71] (or fixed configuration) and unconstrained [138] rotations in space. In all three cases, a combination of bang-bang and bang-coast-bang thrust profiles was used. However, the proposed schemes do not allow for the interchangeability of the formation elements or a resize of the baselines. In addition, the analysis is restricted to single-maneuver simulations, providing no insight on the long-term effects of the selected optimization parameters on spacecraft resources, such as onboard fuel or ΔV capacity.

Subsequently, Burgon *et al.* [137] builds on this research enhancing the optimization method by allowing for reconfigurations which involve adjusting the baselines lengths and changing configuration within the formation slots. This is applied to the planar case of the Darwin mission. The paper provides an analysis of the impact of cost-function parameters on the performance of the algorithm using time, fuel and fuel-balance metrics in free space. Also in the context of the Darwin mission, Junge and Ober-Blöbaum [139] devised a reconfiguration maneuvering technique around a target periodic (nonperturbed) manifold around the Lagrange L_2 point. The method aims to achieve fuel-optimal solutions while penalizing collision-prone situations. The formation member states and controls are discretized, for which equality constraints are obtained and thereafter the nonlinear optimization problem is solved numerically.

However, most of the research conducted thus far in formation flying and reconfiguration maneuver optimization has focused on geocentric applications. Richards *et al.* [140] designed a fuel-optimal trajectory-planning architecture, combining position assignment, plume-impingement prevention and collision-avoidance constraints for formation reconfiguration and proximity operations applications near Earth. The path planning problem employs linear programming by adopting logical equality and inequality constraints, achieving thus global minimum solutions. Commercial software is used for solving the linear cost function. A similar approach is taken by Tillerson *et al.* [98], whereby high-level ΔV maps of global fuel costs are generated from a distributed calculation of predicted costs for the repositioning of individual elements. Minimization of total ΔV expenditure during reconfiguration of large constellations in geosynchronous orbits is also used as the optimization criteria in the work of De Weck *et al.* [141], which employs an auction-based position assignment logic. The reconfigurations use a mixture of Hohmann transfers, plane-change and phasing maneuvers. And Vaddi *et al.* [61] use analytical Hill-Clohessy-Wiltshire modeled-formations to find two-impulse optimal fuel and, inherent to the method, fuel-balanced solutions, closely matching numerical optimization results.

Armellin *et al.* [142] developed a low-thrust-based propulsion method which addresses reconfiguration maneuvers and station-keeping for short baseline (< 1 km) planar formations. Collision avoidance is considered in the fuel-optimal algorithm and the formations are distributed in elliptical orbits around the Earth.

Linearized dynamics are adopted to bypass the computational burden and allow the method to be implemented for real-time applications. For the same reason, maneuver durations are of the order of the reference orbital period. However, to compensate for linearization errors, a feedback control loop augments the control sequence by correcting for disturbances such as drag, planetary nonsphericity and sensor noise.

A two-stage path planning method for reconfiguration of clusters was devised by Aoude *et al.* [143], whereby in the first step a Rapidly-exploring Random Trees algorithm is used for fast convergence and without differential constraints, followed by a second smoothing step which improves the first solution by solving a nonlinear cost function, (containing nonlinear dynamics and constraints) about the initial feasible solution. This approach considers the coupling between positions and attitudes of all spacecraft, solving the trajectory design and attitude planning problems simultaneously in six degrees of freedom with applications to deep space missions.

Sun *et al.* [144] develop later a closed-loop brainstorm approach inspired by swarm-intelligence for fuel-optimal two-impulse maneuvers, using formation configuration requirements and collision avoidance as constraints for planar formation cases around Earth. Since circular orbits are assumed, the optimization involved selecting the best time and control input that meet the constraints. The complexity and computation load of the algorithm is nonetheless a disadvantage.

As can be concluded, a wealth of research has been dedicated to formation-flying and reconfiguration topics. It seems, however, that most of the contributions have focused on the design of optimal techniques without evaluating the influence of different initial spacecraft resource conditions or the behavior of the methods in the long term, after successive maneuvers. The present study aims to take the first steps in modeling how spacecraft resources are managed during reconfiguration periods in the IRASSI cluster based on formation and operational requirements and over extended periods of time. There are particular similarities between IRASSI and Darwin and therefore the reconfiguration analysis builds on the research devised by Burgon *et al.* [137], placing an emphasis on the selection of suitable optimization laws which accommodate the complexities of the IRASSI mission with acceptable computational effort. As such, efficient resource-management strategies are pursued in the search for time-optimal reconfiguration solutions.

9.3. RECONFIGURATION MODULE (REM)

THE approach devised for iSCOUT' ReM module is introduced in this section.

9.3.1. IRASSI RECONFIGURATION MANEUVER REQUIREMENTS

The relative positions of the spacecraft are dictated largely by the targets that are observed. For instance, targets emitting radiation at higher frequencies require shorter baselines and vice-versa. In addition, operational and geometrical constraints dictate that a three-dimensional configuration is used and that the laser terminals are intervisible, as aforedescribed. As such, the final position of the reconfiguration maneuvers corresponds to the initial position of the spacecraft when the science activities ensue, immediately before the expansion/contraction thrust pulse. During the reconfiguration maneuvers, no science tasks take place.

The computation of the final reconfiguration positions is carried out by the ReM, the second module of iSCOUT. The reconfiguration maneuvers entail a translation of the individual spacecraft in inertial space (the gravity gradient between the spacecraft is negligible, as addressed in section 7.6.2). This is done in several steps. Firstly, the primary mirrors must be pointed in the direction of the target[1]. For this purpose, the arrangement of the formation takes place relative to a plane perpendicular to the target direction in the celestial sphere. This arrangement is dictated by the required target baseline and other aforementioned constraints. Given that the spacecraft perform equal functions and no hierarchy is commanded, an infinite number of solutions that conform to these conditions are possible. In order to find a feasible solution, each reconfiguration maneuver is framed as an optimization problem taking into account the following goals:

1. Maneuver time: the operational phase should prioritize science tasks (combined duration of 4.5 years) over functional tasks; as such, reconfiguration maneuvers should be time-minimal so as not to consume time that could potentially be allocated for science tasks.

2. Spacecraft resources:

[1] Note that simultaneously, the sunshield should remain perpendicular to the Sun direction, with a maximum attitude deviation of ±20°. As such, most targets can only be observed at specific times throughout the year. This is accounted for in the planning sequence of the TPM module

(a) Fuel and fuel balance: given the large population of tasks and the impact of fuel mass on mission cost and mass budgets, the maneuvers should be fuel-minimal. Since the spacecraft operate independently, there is a risk that one spacecraft inadvertently expends more fuel than the others over time. Naturally, this affects the capacity of the interferometer to fulfill the science goals. In order to prevent fuel deprivation on one or multiple spacecraft, fuel balance must be taken into account.

(b) ΔV and ΔV balance: alternatively, spacecraft resource management may be expressed as a function of the ΔV. This is particularly suited to formations with differing launch masses.

Note that these optimization goals compete with each other. For example, to ensure fuel-use equalization, it may be required that certain spacecraft travel further, increasing overall fuel consumption. Fine-tuning the prioritization of these goals is part of the methodology described in the next subsection.

9.3.2. METHODOLOGY

The setup for the IRASSI reconfiguration analysis and optimization is analogous to that developed for the Darwin case [137]. Whereas the reference frames of relevance, the IRASSI formation geometries and the model dynamics were introduced in sections 7.4 to 7.6.2, the optimization problem is addressed in this section.

GEOMETRY OPTIMIZATION NOTE

Since ReM aims to find post-maneuver positions that satisfy a list of requirements, one may wonder if, for instance, the requirements can be expressed as constraints in the optimization problem. Whereas the d parameter must be fixed *a priori* because it is defined by science, this option would allow the 'out-of-plane' variable h to be optimized for each telescope.

The constraints associated with h are defined by intervisibility conditions among the telescopes and baseline accuracy thresholds. Although the spacecraft must always keep the sunshield normal to the Sun (with a tolerance of ±20°), they can survey targets in any direction normal to the Sun vector. This means that when a new target is selected and if the direction of the Sun is known, a new attitude in inertial space is commanded and a new position assignment must take intervisibility into account. With the new attitude defined, no neighboring telescope can be placed directly in a direction normal to the sunshield for each spacecraft.

However, the computational complexity of this approach is a disadvantage. It requires a minimum of five independent variables, twenty constraints of intervisibility (four lasers × five spacecraft) and twenty constraints of baseline accuracy. Alternatively, to bypass such an expensive processing procedure, a set of acceptable heights h can be defined (and traded during the optimization) such that $h_i \in h = \{h_1, \ldots, h_5\}$ which results in full compliance with intervisibility requirements (for all possible anti-Sun vector directions in the inertial frame) and baseline accuracy limits. Since this approach simplifies the optimization procedure in terms of complexity and computational time, without necessarily detracting from a potentially optimal fuel and fuel-balance result, this option was selected. The full examination of the optimization parameters is given in the subsections ahead.

OPTIMIZATION

The aim of the ReM is to calculate optimized final reconfiguration positions which satisfy the science and functional goals (formation pointing direction, configuration and baseline length for a given target, intervisibility and baseline estimation accuracy) in terms of maneuver time, fuel and fuel balance.

The three-dimensional configuration, described in the previous subsection, is centered in the formation center point, with individual telescopes dispersed relative to plane Π_N. This formation center point can be located anywhere in inertial space, following the translation maneuver. This is described by the vector $\boldsymbol{r_N} = \{r_{Nx}, r_{Ny}, r_{Nz}\}$ in S_0. Furthermore, the rotation of this plane Π_N around the $\boldsymbol{x_N}$ axis, is not fixed and can be used as a further independent variable in the 'local' target-associated frame S_N, indicated by the angle θ_T relative to an arbitrary vector in S_N (this setup is illustrated in Figure 9.1). As such, the independent vector can be described as:

$$\boldsymbol{X} = \{r_{Nx}, r_{Ny}, r_{Nz}, \theta_T\} \tag{9.1}$$

The in-plane (y_N, z_N) coordinates of the spacecraft are determined by the separation d associated with the target being observed. The out-of-plane height is determined by the set h. Since the arrangement of the set h elements, $h = \{h_1, \ldots, h_5\}$, is not fixed in any particular order and all satisfy intervisibility requirements, there are 5! = 120 possible assignment combinations. In addition, due to the decentralized nature of the formation, any spacecraft can occupy any of the five positions in inertial space. This results, again, in 5! = 120

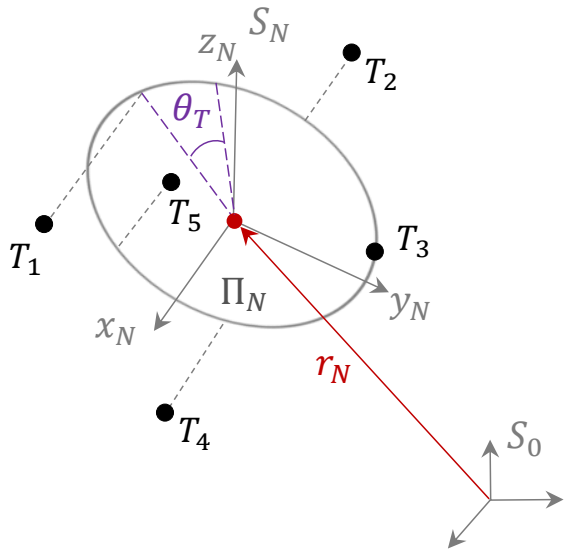

Figure 9.1: Independent variables $\boldsymbol{r_N}$ and $\boldsymbol{\theta_T}$.

possible permutations. This means therefore that for each optimization variable set $\boldsymbol{X}$, there are $120 \cdot 120 = 14400$ potential combinations to trade (compared to six for Darwin's centralized planar formation [137]).

In order to simplify the problem of competing optimization goals (time, fuel and fuel balance or ΔV and ΔV balance), time-optimality was selected for all reconfiguration maneuvers, such that the allocation of science tasks is prioritized throughout the operational mission lifetime. Prior to the maneuver, the spacecraft are idle, at rest. Each spacecraft has to fire the thrusters to initiate the maneuver and eventually reverse the thrust direction in order to come to a rest again. Given that the thrust force is the same for all spacecraft, the spacecraft which travels the furthest in a reconfiguration maneuver is the slowest to arrive at the final position if a bang-bang thrust profile is used. This dictates the total duration of the maneuver, as the maneuver is only deemed complete when all spacecraft have arrived at their assigned destinations.

However, the other spacecraft can economize propellant if they coast in-between firing periods, such that at the end all spacecraft arrive at their final positions at the same time. Given that the distance traveled during the translation maneuver is different for each spacecraft, the coast/firing periods have to be calculated for each element of the formation, such that the fuel mass and fuel balance across the formation are calculated. This is described in the next subsection.

By implementing a combination of bang-bang and bang-coast-bang thrust profiles across the formation for time-optimal maneuvers, then fuel economy and fuel-use equalization can be found by pursuing the optimization of the spacecraft's final position. Two optimization objective functions are proposed, one fuel-based and another that is ΔV-based. The first attempts to find an optimum between overall fuel mass use during the maneuver and remaining fuel mass balance among formation members:

$$J_f = \sum_i^n \left(f_i\left(t_0\right) - f_i\left(t_{ReM}\right)\right) + \mu_f \sum_i^n \sum_{j:j>i}^n \left|f_i\left(t_{ReM}\right) - f_j\left(t_{ReM}\right)\right| \qquad i,j = \{T_1, T_2, T_3, T_4, T_5\} \tag{9.2}$$

where $f_i\left(t_0\right)$ is the initial fuel mass of the ith spacecraft and $f_i\left(t_{ReM}\right)$ is the final fuel mass of the ith spacecraft and $\boldsymbol{X}$ is the independent vector as defined in Equation 9.1. The first part of the objective function addresses fuel use and represents the total amount of fuel mass expended by the whole formation during the maneuver. The second part of the equation concerns fuel balance and represents the sum of the fuel differences among cluster members at the end of the maneuver. The term μ_f is the weighing of the second part of the equation. Note that the fuel balance concerns the equalization of the post-maneuver remaining fuel, rather than promoting equalization in fuel use among telescopes during the maneuver. The motivation is that if, for any reason (e.g., a malfunction), a spacecraft is fuel-deprived, then the best approach is to allow this spacecraft to remain close to its initial position and command other spacecraft to move, conserving as much as possible the remaining propellant in the faulty spacecraft.

A natural outcome of implementing this cost function is that due to the dependency of the fuel mass calculation on the spacecraft mass (as shown in the following subsection), there is the risk that in cases where launch mass differs among formation elements or when μ_f is improperly tuned, significantly more overall propellant is used in attempting to equalize the post-maneuver's fuel. Heavier spacecraft would simply be pushed to travel further. Therefore, a second optimization routine attempts to overcome this issue by re-writing the objective function of Equation 9.3 in terms of ΔV.

Similar to J_f, this new routine attempts to find an optimum between combined exerted ΔV for the maneuver and the differences between remaining ΔV available for individual spacecraft after the maneuver, by means of the weighing parameter $\mu_{\Delta V}$:

$$J_{\Delta V} = \sum_{i}^{n} \left(\Delta V_i\left(t_0\right) - \Delta V_i\left(t_{ReM}\right)\right) + \mu_{\Delta V} \sum_{i}^{n} \sum_{j:j>i}^{n} \left|\Delta V_i\left(t_{ReM}\right) - \Delta V_j\left(t_{ReM}\right)\right| \qquad i,j = \{T_1, T_2, T_3, T_4, T_5\} \tag{9.3}$$

where the ΔV calculation is naturally connected to the fuel mass by the following expression:

$$\Delta V_i = g_0 I_{sp} \ln\left[\frac{M_i}{M_i - \left(f_i\left(t_0\right) - f_i\left(t_{ReM}\right)\right)}\right] \tag{9.4}$$

As such, $J_{\Delta V}$ attempts to balance post-maneuver spacecraft resources regardless of spacecraft mass.

Minimizing J_f and $J_{\Delta V}$ becomes then a function of the weighting parameters μ_f and $\mu_{\Delta V}$. It shall be evaluated whether different ranges of optimality can be found, by virtue of fine-tuning μ_f and $\mu_{\Delta V}$ values across different initial conditions. Note that J_f and $J_{\Delta V}$ optimize for different parameters (fuel and fuel balance vs. ΔVand ΔV balance), so the goal is not necessarily to compare performance between them within each metric in this case, but to understand the effect of the weighting parameters on spacecraft resource use in general.

Both objective functions are analyzed: first, in an IRASSI context, and thereafter in a general formation flying context. A mesh-adaptive direct search (MADS) algorithm [145] is used for the optimization. For each variable set $\boldsymbol{X}$, two function costs, J_f and $J_{\Delta V}$, are calculated for the 14400 potential position combinations and the lowest one is returned and stored in the algorithm's database. The process is iterated until the variable set $\boldsymbol{X}$ meets the stopping criteria (e.g. objective function cost J_f and $J_{\Delta V}$ below a certain threshold). If a solution set $\boldsymbol{X_N}$ is found for target N, the positions of all spacecraft in inertial space are computed and the next reconfiguration maneuver optimization procedure starts for the next target.

The MADS method solves optimization problems by searching a set of points (mesh) around the current point in the pursuit of an improvement of the cost function. A scalar multiple of a set of randomly generated vectors is added to the current point to form the mesh. The MADS version used in this work is thus not deterministic, as the choice of the polling directions has a probability component. As part of the direct search methods family, it bypasses the need of computing cost function gradients to generate solutions. Its selection as an optimization algorithm is motivated by two main aspects:

1. the ability to achieve convergence to global minima [145] when no constraints are imposed, as in the ReM case. The low number of independent variables (four) also makes the direct search a suited algorithm.

2. the suitability for parallel computing environments: as a distributed-type entity, all spacecraft share an inter-communications link and processing facilities, for the correlation process of science data. Parallelization of computing resources on a shared network for science activities and maneuver-planning is a way to take advantage of existing software and hardware capabilities within the fleet. This allows the solution space to be searched expeditiously.

OBJECTIVE FUNCTION PARAMETERS

For a given variable set $\boldsymbol{X}$, the total duration of the maneuver t_{ReM} is given by the spacecraft σ which takes the longest to arrive at the final position using a bang-bang thrusting profile. In order to identify the slowest spacecraft σ and obtain t_{ReM}, the reconfiguration maneuvers for all spacecraft using a bang-bang thrust profile are calculated. The dynamics of each formation element i are governed by Equation 7.5 during the maneuver and the trajectory on which the spacecraft travel is described by the difference between the final $\boldsymbol{r_{0,fin}}$ and initial resting position $\boldsymbol{r_{0,in}}$ in S_0:

$$\boldsymbol{r_{trav,i}} = \boldsymbol{r_{0,fin,i}} - \boldsymbol{r_{0,in,i}} \tag{9.5}$$

Along this trajectory, the spacecraft fire the thrusters continuously in the direction of travel for half of the distance $\frac{||\boldsymbol{r_{trav}}||}{2}$ and reverse the thrust for the remaining $\frac{||\boldsymbol{r_{trav}}||}{2}$. For each of these sections, using Equation 7.5, the acceleration is given by:

$$\frac{||\ddot{\boldsymbol{r}}_{\boldsymbol{trav,i}}||}{2} = \frac{F_i}{M_i} \tag{9.6}$$

By rearranging Equation 9.6 and given that $||\boldsymbol{r_{trav,in}}|| = ||\dot{\boldsymbol{r}}_{\boldsymbol{trav,in}}|| = 0$, one obtains:

$$||\ddot{\boldsymbol{r}}_{\boldsymbol{trav,i}}|| = \frac{2F_i}{M_i},\ ||\dot{\boldsymbol{r}}_{\boldsymbol{trav,i}}|| = \frac{2F_i}{M_i} t_{th,i},\ ||\boldsymbol{r_{trav,i}}|| = \frac{2F_i}{M_i}\frac{t_{th,i}^2}{2} \tag{9.7}$$

where $t_{th,i}$ is the thrust duration associated with each of the sections $\frac{\ddot{\boldsymbol{r}}_{\boldsymbol{trav,i}}}{2}$ for the ith spacecraft. The maneuver duration t_i for each spacecraft is then given by $t_i = 2t_{th,i}$ for a bang-bang thrust profile. Using Equation 9.7 and for a constant thrust F_i, the individual maneuver times can be expressed as a function of the traveled distance $||\boldsymbol{r_{trav,i}}||$ and wet mass M_i:

$$t_i = 2\sqrt{||\boldsymbol{r_{trav,i}}||\frac{M_i}{F_i}} \tag{9.8}$$

The slowest spacecraft σ and associated with a given variable set $\boldsymbol{X_N}$, is then identified as that for which t_i is maximum, determining the total maneuver duration of the formation t_{ReM}:

$$t_{ReM} = t_\sigma = \max_{1\leq i\leq 5} t_i \tag{9.9}$$

The other spacecraft will travel on their trajectories, employing a bang-coast-bang profile. Naturally, for each, the duration of the coast has to be adjusted such that all spacecraft complete their maneuvers at the same time t_{ReM}. As such, three distinct time intervals τ_1, τ_2 and τ_3 representing the durations of the bang-coast-bang thrust profile respectively are defined for the remaining four spacecraft:

$$\begin{aligned} \tau_1 &= [0, t_{w,i}[\\ \tau_2 &= [t_{w,i}, (t_{ReM} - t_{w,i})[\\ \tau_3 &= [(t_{ReM} - t_{w,i}), t_{ReM}] \end{aligned} \tag{9.10}$$

where t_w is the thrust pulse width for spacecraft i and τ_1 and τ_3 have the same duration. Let $D_i(t)$ be the distance of spacecraft i along $\boldsymbol{r_{trav,i}}$ at time t. The associated acceleration $\ddot{D}_i(t)$, velocity $\dot{D}_i(t)$ and position $D_i(t)$ equations for a bang-coast-bang profile are then:

$$\begin{array}{llll} \ddot{D}_i(t) & \dot{D}_i(t) & D_i(t) & \\ \frac{F_i}{M_i} & \frac{F_i}{M_i} t & \frac{1}{2}\frac{F_i}{M_i} t^2 & t \in \tau_1 \\ 0 & \frac{F_i}{M_i} t_{w,i} & \frac{F_i}{M_i}\left(t_{w,i} t - \frac{t_{w,i}^2}{2}\right) & t \in \tau_2 \\ -\frac{F_i}{M_i} & \frac{F_i}{M_i}(t_{ReM} - t) & \frac{F_i}{M_i}\left(t_{w,i}(t_{ReM} - t_{w,i}) - \frac{(t_{ReM}-t)^2}{2}\right) & t \in \tau_3 \end{array} \tag{9.11}$$

At $t = t_{ReM}$, the distance traveled is $D_i(t_{ReM}) = ||\boldsymbol{r_{trav,i}}||$, with $\boldsymbol{r_{trav,i}}$ defined in Equation 9.5, and can be described as:

$$D_i(t_{ReM}) = \frac{F_i}{M_i} t_{w,i}(t_{ReM} - t_{w,i}) \tag{9.12}$$

whereby rearranging the terms and solving for $t_{w,i}$ such that $t_{w,i} \leq \frac{t_{ReM}}{2}$, results in

$$t_{w,i} = \frac{t_{ReM}}{2} - \sqrt{\frac{t_{ReM}^2}{4} - \frac{M_i}{F_i} D_i(t_{ReM})} \tag{9.13}$$

For the slowest spacecraft σ, it becomes evident that

$$t_\sigma = 2t_{w,\sigma} = t_{ReM} \tag{9.14}$$

Using Equation 7.6 and given that there are two periods of thrust for each maneuver, the fuel consumed by the ith spacecraft is:

$$f_{ReM,i} = -2t_{w,i}\dot{f}_i = 2t_{w,i}\frac{F_i}{I_{sp}g_0} \tag{9.15}$$

The final fuel masses for each spacecraft are:

$$f_i(t_{ReM}) = f_i(t_0) - f_{ReM,i} \tag{9.16}$$

Correspondingly, the ΔV_i value for each formation element can then be calculated using Equation 9.4. Figure 9.2 portrays, at last, the thrust profiles used during reconfiguration.

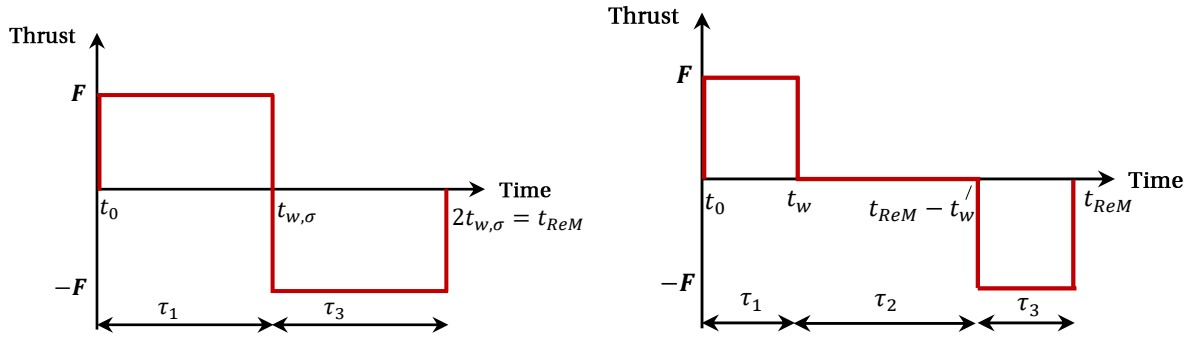

(a) Bang-bang

(b) Bang-coast-bang

Figure 9.2: Illustration of thrust profiles during reconfiguration maneuvers. The thrust vectors are parallel to the spacecraft's trajectories. Adapted from Burgon (2010) [137].

9.4. RESULTS AND DISCUSSION

THE simulation setup is presented in this section followed by the obtained results and respective analysis.

9.4.1. REM SIMULATION PARAMETERS

The initial simulation variables used for all maneuvers in the ReM module are based on preliminary estimations for the IRASSI mission [14], assuming colloidal thruster parameters. They are featured in Table 9.1. The selected optimization solver is mesh-adaptive and is part of MATLAB's Global Optimization Toolbox [146].

For demonstrative purposes, the reconfiguration maneuvers are computed consecutively according to the predefined sequence of targets. However, the science-related translation maneuvers which take place in-between reconfigurations are considered, such that the initial position prior to the reconfiguration maneuver, is the final position of the previous observation task.

For each maneuver, fuel-related and ΔV-related optimization metrics were retrieved, as shown in Table 9.2, along with the maneuver duration for each cost function. The metrics were nondimensionalized as follows:

- Total fuel and ΔV: relative to initial total values (the sum of fuel and ΔV in the formation)
- Sum of fuel and ΔV differences: relative to initial total values (the sum of fuel and ΔV in the formation)[2].
- Maneuver duration: relative to total the tour or maneuver allocated time ($\propto \frac{t_{ReM}}{\mathscr{D}}$). The allocated time includes the observation duration and all associated maneuvers (reconfiguration and expansion/contraction of baselines during observations).

The metrics reflect solely the spacecraft resources used during the formation reconfiguration maneuvers, according to the assumptions described in the previous chapter. No considerations are made to account for attitude control maneuvers or station-keeping.

[2]This nondimensionalization of the sum of the fuel differences is meant to provide a measure relative to reference mass or ΔV values. This does mean that, in reality, the resulting fuel differences can surpass 100% if one or multiple spacecraft suffer a sudden depletion of the tanks, for example.

Table 9.1: Simulation parameters for the IRASSI formation.

Simulation parameter	Value
i	$\{T_1, T_2, T_3, T_4, T_5\}$
F_i	$20 \cdot 10^{-3}$ N
$I_{sp,i}$	2500 s
Optimizer	Mesh-adaptive direct search

Table 9.2: Optimization metrics.

Metric	Expression
Total fuel used (kg)	$\sum_i^n \left(f_i(t_0) - f_i(t_{ReM})\right)$
Sum of fuel differences (kg)	$\sum_i^n \sum_{j:j>i}^n \left\lvert f_i(t_{ReM}) - f_j(t_{ReM})\right\rvert$
Total ΔV expended (m s^{-1})	$\sum_i^n (\Delta V_i(t_0) - \Delta V_i(t_{ReM}))$
Sum of ΔV differences (m s^{-1})	$\sum_i^n \sum_{j:j>i}^n \left\lvert \Delta V_i(t_{ReM}) - \Delta V_j(t_{ReM})\right\rvert$

9.4.2. EXAMPLE IRASSI TOUR

In order to analyze the effect of the weighting parameters μ_f and $\mu_{\Delta V}$, on a preliminary basis, a general tour of 20 targets, involving 19 reconfiguration maneuvers over the course of approximately 11 weeks, was generated for two different values for each, $\mu_f, \mu_{\Delta V} = \{0, 500\}$. When $\mu_f = 0$, it represents the case when optimization minimizes only fuel and when $\mu_{\Delta V} = 0$, only ΔV.

For this tour, all spacecraft were initialized with a wet mass of $M_i = 2300$ kg and a fuel mass of $f_i = 15$ kg, such that no fuel imbalance existed at the beginning of the tour. After each maneuver, both the fuel mass f_i and spacecraft wet mass M_i were decremented accordingly. The initial target's unit vector is $\boldsymbol{N} = [1, 0, 0]$ (coinciding with S_0) and all subsequent targets are associated with their real locations in the ecliptic frame. All formation configurations are three-dimensional and the maneuvers use three baseline combinations, {short, medium, long} where correspondingly $d = \{10, 500, 1000\}$ m. For instance, a maneuver designated 'S-L' describes a formation pointing to target C, with a separation parameter $d = 10$ m, performing a translation maneuver such that the final configuration has a separation parameter $d = 1000$ m and points to a new target N. This reconfiguration maneuver, 'S-L' represents a formation expansion, whereas the inverse sequence would describe a formation contraction.

The cost functions, J_f and $J_{\Delta V}$, include the metrics described in Table 9.2. The fuel-related metric results are presented in Figure 9.3 and Figure 9.4, whereas the ΔV results are shown in Appendix E.1.1, in Figure E.1 and Figure E.2. The mean traveled distance by the fleet is also shown in Appendix E.1.1, in Figure E.3. Figure 9.5 shows the duration of each maneuver and all results are summarized in Table 9.4 in adimensional form. The remaining fuel of Table 9.4 reflects that of the entire constellation.

Figure 9.3 shows the fuel used for each individual maneuver for the whole fleet. For the cases in which

Table 9.3: Parameters for Example IRASSI Tour.

Simulation parameter	Value
$M_i(t_0)$	2300 kg
$\mu_f, \mu_{\Delta V}$	$\{0, 500\}$
$f_i(t_0)$	15 kg

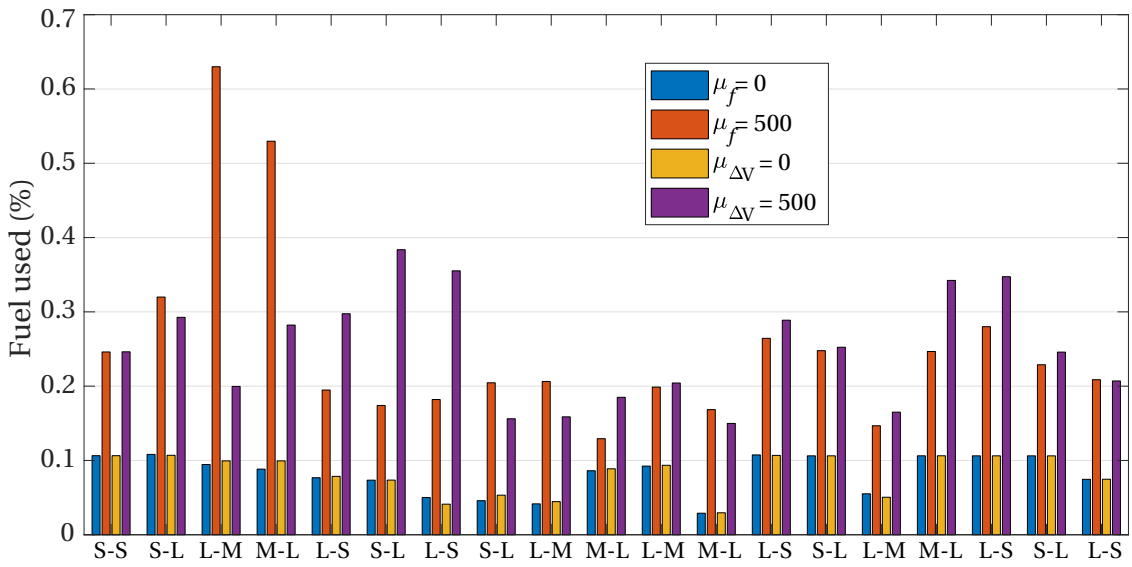

Figure 9.3: Fuel used per maneuver for Example IRASSI Tour.

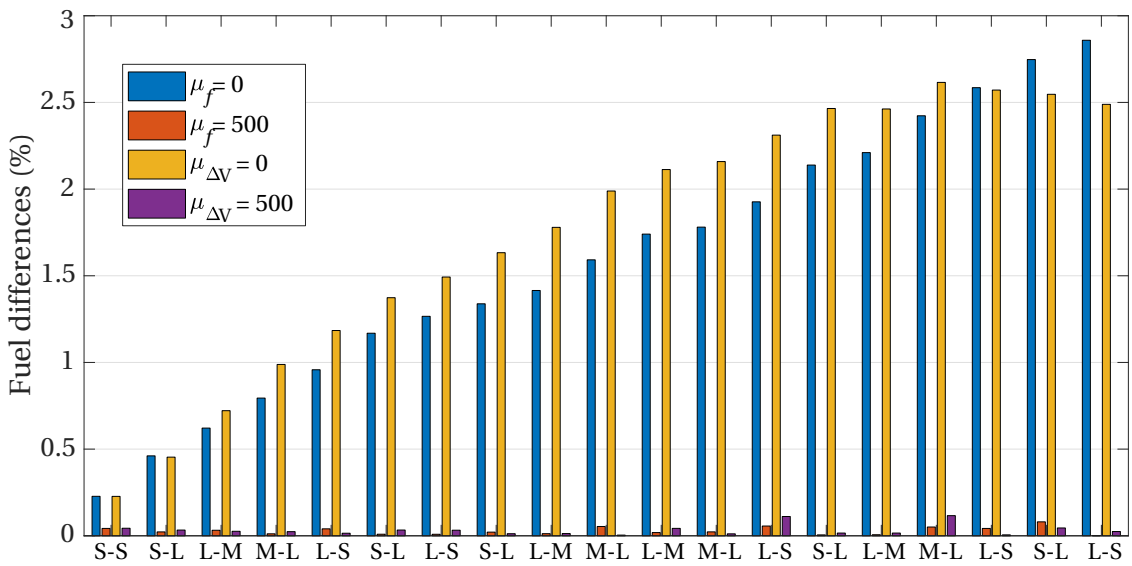

Figure 9.4: Sum of fuel differences per maneuver for Example IRASSI Tour.

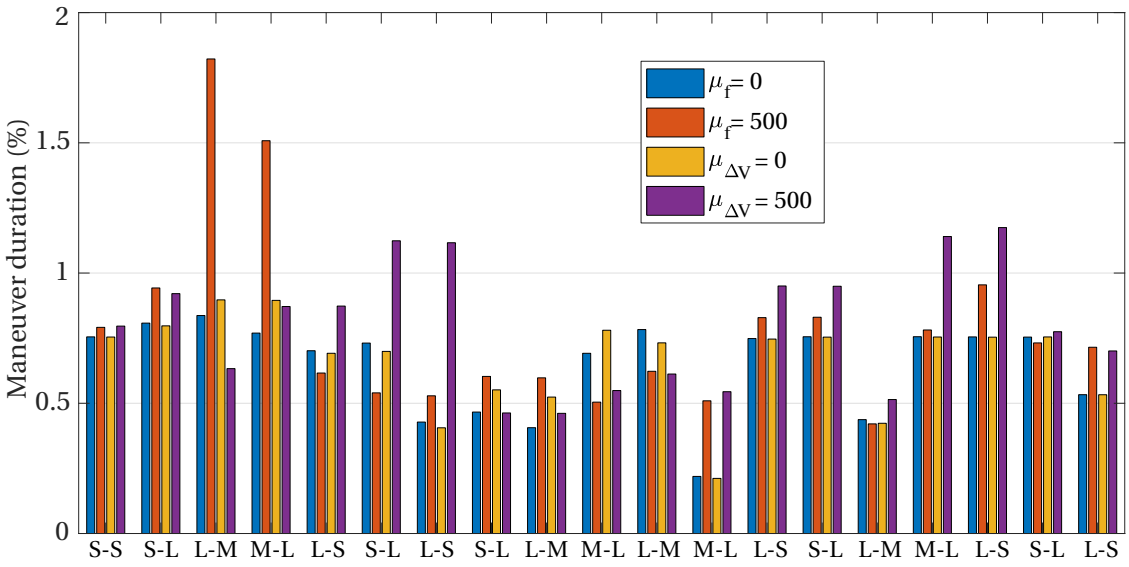

Figure 9.5: Maneuver duration per maneuver for Example IRASSI Tour.

Table 9.4: Summary of results for Example IRASSI Tour.

Metric	**Mean value per maneuver**			
	$\mu_f = 0$	$\mu_f = 500$	$\mu_{\Delta V} = 0$	$\mu_{\Delta V} = 500$
Total fuel used (%), mean	0.08	0.25	0.08	0.25
Sum of fuel differences (%), mean	1.59	0.03	1.77	0.03
Total ΔV expended (%), mean	0.08	0.25	0.08	0.25
Sum of ΔV differences (%), mean	1.59	0.03	1.76	0.03
Maneuver duration (%), mean	0.65	0.78	0.67	0.80
Distance traveled per spacecraft (km), mean	2.00	6.88	2.07	6.47
Remaining				
fuel (%)	98.44	95.19	98.43	95.24
ΔV (%)	98.45	95.21	98.43	95.25

$\mu_f = \mu_{\Delta V} = 0$, there is very little difference in fuel consumption between the two objective functions, both requiring a mean fuel consumption of 0.08% of the total fuel (or ≈60 grams) per maneuver as summarized in Table 9.4. However, with an increase in weighting parameters to $\mu_f = \mu_{\Delta V} = 500$, more than three times more fuel is expended respectively (for each cost function) as the spacecraft try to equalize their final fuel masses or ΔV capabilities. The sum of the fuel differences is presented in Figure 9.4. Naturally, with $\mu_f = \mu_{\Delta V} = 0$, no fuel balancing is observed and the differences in spacecraft resources rise over time at a similar pace for the two cost functions. The trends observed in Figure 9.3 and Figure 9.4 are respectively observed for the ΔV metrics' plots, shown in Figure E.1 and Figure E.2 of Appendix E.1.1.

Concerning the duration of the maneuver, shown in Figure 9.5, it is possible to observe that the $J_{\Delta V}$ function takes on average 18 minutes more to complete the maneuver than J_f (a difference of 0.02% of the allocated 11 weeks). With $\mu_f = \mu_{\Delta V} = 500$, as the spacecraft are commanded to travel further in order to balance their post-maneuver fuel mass or ΔV, there is a natural rise in maneuver time compared to $\mu_f = \mu_{\Delta V} = 0$.

Longer distances are associated with higher weighting parameters and resource consumption. On av-

erage, for each additional 60 grams (or 0.08%) of used fuel, each spacecraft travels approximately another ≈1.10 km. The standard deviations of Figure E.3 also show that higher weighting parameters demand more equitable traveled distances. This a natural consequence of better fuel and ΔV balancing.

Overall, the fuel-based objective function J_f seems to be more effective at balancing resources (both fuel and ΔV). However, when it comes to resource consumption, the results are split. For example, for ΔV expenditure: for $\mu_f = \mu_{\Delta V} = 0$, J_f is more economical and for $\mu_f = \mu_{\Delta V} = 500$, $J_{\Delta V}$ is the cost-effective one. This likely means that the two objective functions require different weighting parameters to achieve a comparable result for the same metric. The evaluation of this effect over ranges of μ_f and $\mu_{\Delta V}$ values is explored in the next subsection. In addition, the embedded stochasticity in the mesh-adaptive optimization algorithm (which determines the direction of the search in the quadri-dimensional solution space, as there are four independent variables) contributes to the differences in results.

9.4.3. EFFECTIVE ENVELOPES

Since the weighting parameters μ_f and $\mu_{\Delta V}$ of respective Equations 9.2 and 9.3 influence the objective function results and determine the extent to which spacecraft resources are balanced, it is of interest to mission designers to select appropriate μ_f and $\mu_{\Delta V}$ values. Ideally, an optimum range can be identified, whereby a suitable resource balance solution is achieved without sacrificing significant amounts of fuel or ΔV.

Table 9.5: Parameters for effective envelopes analysis.

Case studies	**Simulation parameter**	**Value**	**Initial sum of differences**	
			Fuel (kg)	**ΔV (m s^{-1})**
Case A	$M_i\,(t_0)$	$\{1700, 2000, 2300, 2600, 2900\}$ kg		
	$\mu_f, \mu_{\Delta V}$	$10^{-3} \leq \mu_f, \mu_{\Delta V} < 10^3$	0.00	446.01
	$f_i\,(t_0)$	15.00 kg		
Case B	$M_i\,(t_0)$	2300 kg		
	$\mu_f, \mu_{\Delta V}$	$10^{-3} \leq \mu_f, \mu_{\Delta V} < 10^3$		
B.1		15.00 kg	0.00	0.00
B.2		$\{14.40, 15.00, 15.00, 15.00, 15.00\}$ kg	2.40	25.75
B.3	$f_i\,(t_0)$	$\{13.65, 15.00, 15.00, 15.00, 15.00\}$ kg	5.40	57.92
B.4		$\{14.40, 14.55, 14.55, 14.55, 15.00\}$ kg	2.40	25.75
B.5		$\{13.65, 13.95, 13.95, 13.95, 15.00\}$ kg	5.40	57.92

In order to identify the optimal ranges of the weighting parameters for each cost function, two different case sets, A and B, are tested for a single randomly selected maneuver, repeated 20 times in order to achieve enough consistency with the optimization algorithm. For both sets, the parameters μ_f and $\mu_{\Delta V}$ are varied between 0.001 and 1000. However, the initial conditions for spacecraft wet mass M_i and fuel mass f_i differ. In Case A all spacecraft are initialized with the same f_i, but with different M_i (such that the average mass of the formation is 2300 kg). This emulates general formation conditions which do not necessarily reflect IRASSI. The selection of these values is merely aimed at demonstrating the behavior of the algorithms in mass-imbalanced formations. In Case B, all spacecraft have the same M_i, but five different initial fuel conditions are tested. Case B.1 corresponds to that in which the spacecraft are initialized with null fuel and ΔV capability differences. Cases B.2 to B.5 correspond to different initial fuel mass conditions and emulate potential non-nominal scenarios, such as malfunctions. Cases B.2 and B.4 have an equal initial sum of fuel differences, but with differences distributed among one and several spacecraft respectively. The same applies to Cases B.3 and B.5. Although Case B.1 is, in theory, the most representative case of IRASSI, the interest in simulating different conditions lies in attempting to determine consistent (and generalizable) optimal envelope across different formation compositions and initial conditions, lending a measure of robustness to the optimization law. The case sets are summarized in Table 9.5. For both case sets a semi-logarithmic scale is

adopted. A total time of 1.48 days is allocated for this single target.

CASE A

The fuel-related metric results for J_f are presented in Figure 9.6(a) and Figure 9.6(b), while Figure 9.6(c) displays the corresponding maneuver duration. The ΔV-related metrics are shown in Appendix E.2.1 (Figures E.7(a) to E.7(c)). An 'effective' interval is one in which changes in μ_f or $\mu_{\Delta V}$ produce changes in the evaluated metrics. In general, within an effective interval, fuel balancing requires higher fuel expenses, the rate of required fuel increases with μ_f and lower balancing of resources are associated with lower μ_f. The same applies to ΔV balancing and $\mu_{\Delta V}$ envelopes.

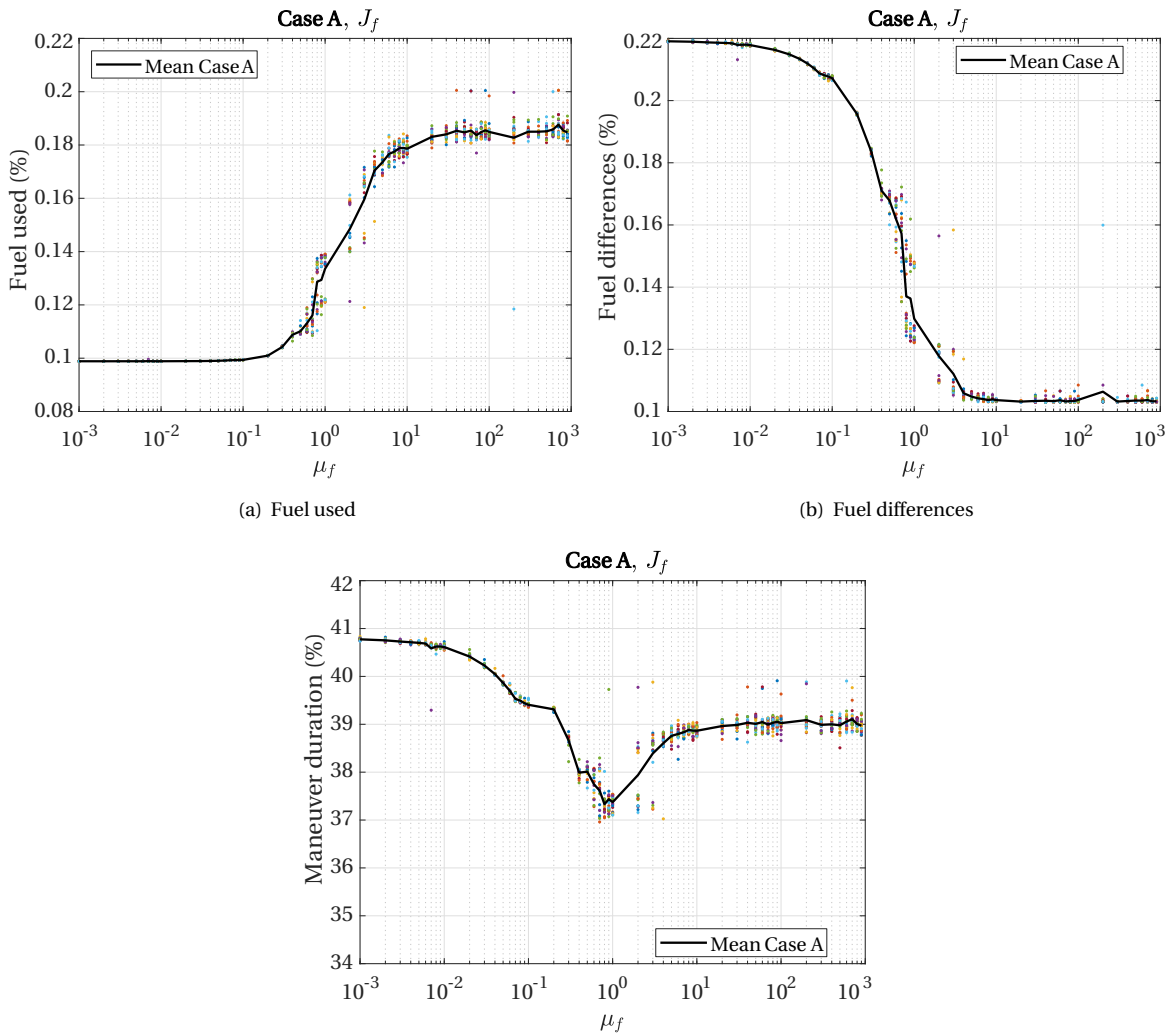

(a) Fuel used

(b) Fuel differences

(c) Maneuver duration

Figure 9.6: Fuel metrics and maneuver duration for Case A and J_f.

In terms of fuel consumption, in Figure 9.6(a), the most pronounced effect of μ_f occurs for $0.1 \leq \mu_f \leq 10$. The variance in fuel consumption for $\mu_f < 0.1$ is nearly undetectable, with the difference between maximum and minimum fuel consumption lying in the sub-milligram level, whereas for $\mu_f > 1$, this difference reaches nearly 0.05% (or 38 grams) of the total fuel. The sum of fuel differences, shown in Figure 9.6(b), displays broader range of effective μ_f between 0.01 and 5. With an increase of μ_f beyond 5, no improvement in fuel balancing is detected, on average. It is nonetheless interesting to capture the effect of an increasing μ_f: with a single reconfiguration, post-maneuver summed fuel differences can decrease from nearly 164 grams (0.22% of the initial formation fuel) with $\mu_f < 0.01$ to about half of that for $\mu_f \geq 5$, for an initially fuel-balanced formation. Fuel and fuel balance compete nonetheless for the interval of $0.1 \leq \mu_f \leq 5$, whereas in the range of $0.01 \leq \mu_f \leq 0.1$ a slight improvement in fuel balance is achieved without sacrificing fuel. Similar behavior

is observed for ΔV (cf. Figure E.7(a) and Figure E.7(b)), but over a much narrower range of $\mu_{\Delta V}$ values and seemingly with lower variability between repetitions. In percentage terms, less ΔV is expended nonetheless for higher $\mu_{\Delta V}$ than for the fuel case.

In general, the maneuver duration decreases from a maximum of nearly 41% of the allocated time (14.5 hours) of the total mission time to a minimum of around 34% (13.3 hours) for $\mu_f = 0.8$, as depicted in Figure 9.6(c). Thereafter, i.e. is for $\mu_f > 0.8$, the maneuver duration increases again. A minimum duration of 12.1 hours (37.3% of allocated time) is observed in Figure E.7(c) for the same $\mu_{\Delta V} = 0.8$ value.

To summarize, the following can be reported from the single-maneuver analysis of Case A:

- For wet-mass imbalance, the $\mu_{\Delta V}$ effective range is significantly narrower than that of μ_f.
- $\mu_f = 0.1$ and $\mu_{\Delta V} \approx 0.5$ provides a modest fuel- and ΔV-balancing effect with negligible fuel and ΔV sacrifice.
- $\mu_f = \mu_{\Delta V} \approx 0.8$ provide the best maneuver duration.
- $\mu_f \approx 10$ and $\mu_{\Delta V} \approx 5$ provide respectively the best fuel and ΔV equalization but requiring significant propellant consumption. These are also generally the upper boundary of effective parameters.

CASE B

The fuel-related metric results of Case B are presented in Figure 9.7(a) and Figure 9.7(b), whereas the maneuver duration is shown in Figure 9.7(c). The ΔV-related metrics are shown in Appendix E.2.2 (Figures E.11(a) to E.11(c)). For all figures of Case B, each line reflects the mean of 20 repetitions.

Fuel consumption, shown in Figure 12, will rise at around $\mu_f \approx 0.1$ and plateau from $\mu_f > 4$ for Case B.1, and from about $\mu_f > 1$ for Cases B.2 and B.3, whilst monotonously increasing for Cases B.4 and B.5. As such, it can be concluded that the effect of μ_f is dependent on the initial fuel mass conditions. Specifically, on the *distribution* of f_i among formation elements: the more spacecraft have uneven initial fuel masses, the more the algorithm will try to compensate for it during the maneuver, by commanding several spacecraft to move further such that at the end of the maneuver, fuel equalization is achieved. This correlation is discordant with the findings of a similar analysis carried out by Burgon et al. [137] and this is attributed to the magnitude of the fuel differences considered: the fuel differences considered by Burgon et al. were not large enough to capture the effect of fuel distribution on fuel consumption. Finally, the upper bound of effective μ_f for Cases B.4 and B.5 in the present analysis is out of the range of the simulated μ_f values. It is also noteworthy that when fuel mass imbalances are concentrated on one spacecraft (Cases B.2 and B.3), the effective range is narrower than in other cases.

Case B.1 demands the least fuel consumption overall, although Cases B.2 and B.3 do seem more efficient strictly in the range between $1 \leq \mu_f \leq 8$. Again, this relation is not observed in the work of Burgon et al. [137]. However, the explanation for the discrepancy in the findings is, in this case, not only attributed to the magnitude of the initial fuel differences considered, but also to the length of the maneuver. The maneuvers considered in the present work are significantly more demanding than in Darwin's case (the IRASSI spacecraft must travel further to reconfigure between formation geometries with baseline lengths one order of magnitude higher or more than Darwin), whereby the associated increased fuel expenditure for fuel balancing of Case B.2 and B.3 is detected 'earlier' with a single maneuver. Indeed, different tests were made in the frame of the present work, where shorter reconfiguration maneuvers were required from the formation, and results showed that additional fuel consumption of Cases B.2 and B.3 (compared to Case B.1) only became apparent over time, after subsequent maneuvers. This means that for a single maneuver, more demanding reconfiguration properties may conceal granularity effects of μ_f (or $\mu_{\Delta V}$) parameters which would otherwise be visible with shorter maneuvers.

The fuel differences of Figure 9.7(b) are subtracted from their respective initial fuel mass values, with positive values representing a decrease in post-maneuver f_i equalization, and negative values corresponding to a desirable increase in post-maneuver f_i balance. The best fuel balance capacity among the five scenarios corresponds to Cases B.4 and B.5. This is due to the fact that individual fuel differences are lower (than in the remaining cases). Therefore, the optimization algorithm is able to find reconfiguration solutions that result in small increments/decrements in fuel differences for each element pair, but which produce a substantial impact on the total sum of fuel differences. These residual improvements are met with great fuel consumption penalties, however.

The maneuver duration profiles of Figure 9.7(c) diverge among the cases for $\mu_f > 0.01$. For Case B.1, the maneuver duration decreases with increasing μ_f, which is not observed for the other four cases.

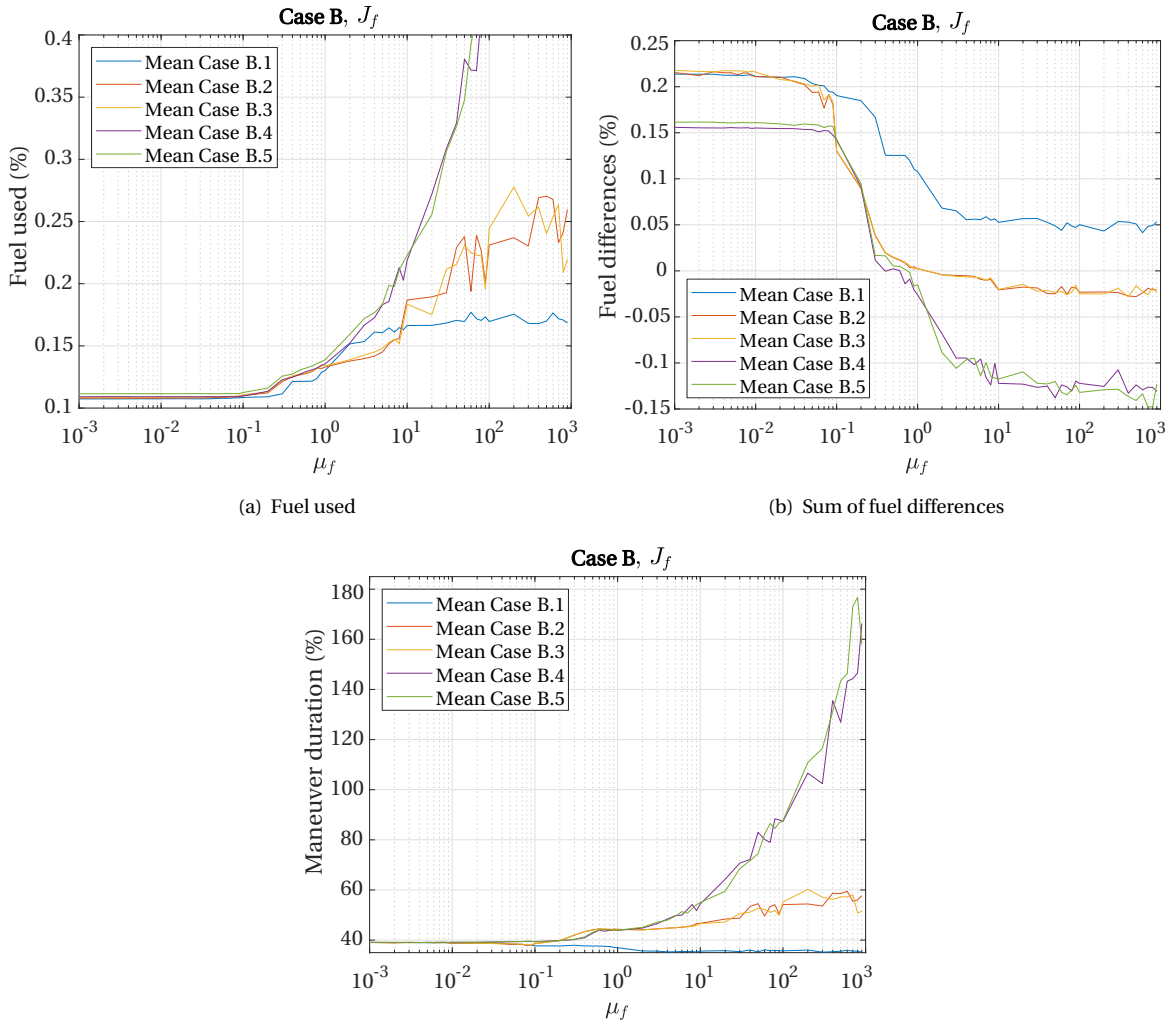

(a) Fuel used

(b) Sum of fuel differences

(c) Maneuver duration

Figure 9.7: Fuel metrics and maneuver duration for J_f of Case B.

The analysis for the ΔV-related metrics are omitted for brevity reasons, since similar trends are observed, but the following points summarize the single-maneuver analysis of Case B:

- The more distributed the fuel-mass imbalance, the narrower μ_f and $\mu_{\Delta V}$ effective ranges.
- $\mu_f = \mu_{\Delta V} \approx 0.1$ provides a modest fuel- and ΔV-balancing effect with negligible fuel and ΔV consumption sacrifice for all cases.
- $\mu_f = \mu_{\Delta V} \approx 0.9$ provides the best maneuver duration for fuel-imbalanced formations (Cases B.2 to B.5).
- $\mu_f = \mu_{\Delta V} \approx 4$ provide respectively the best fuel and ΔV equalization and are generally the upper boundary of effective parameters.

Finally, the same trends concerning fuel consumption, fuel differences, ΔV expenditure, ΔV equalization and maneuver duration have been observed for varying actuator parameters, such as thrust force F_i and specific impulse I_{sp}, for both J_f and $J_{\Delta V}$. This is demonstrated in the Appendix section E.2.1.

In order to evaluate the effect of these parameters in the long term, the metrics are analyzed in the context of a multi-maneuver tour.

9.4.4. IRASSI TOUR ANALYSIS

The present subsection aims to show the effect of a varying μ_f, $\mu_{\Delta V}$ on tours composed of 200 different reconfiguration maneuvers, for which a total time of ≈602 days is allocated. Two tour groups, Tour A and Tour

B, are considered, whereby the initial fuel mass conditions of Case A and Case B, described in the previous section, apply respectively. The variation of μ_f and $\mu_{\Delta V}$ is restricted to intervals of interest identified in the single-maneuver cases. A summary of the simulation parameters is provided in Table 9.6.

Table 9.6: Parameters for IRASSI Tour analysis.

Tours	Simulation parameter	Value	Initial sum of differences	
			Fuel (kg)	ΔV (m s^{-1})
Tour A	$M_i(t_0)$	$\{1700, 2000, 2300, 2600, 2900\}$ kg		
	$\mu_f, \mu_{\Delta V}$	$\mu_f = \mu_{\Delta V} = 0,\ 10^{-2} \leq \mu_f, \mu_{\Delta V} < 10$	0.00	446.01
	$f_i(t_0)$	15.00 kg		
Tours B	$M_i(t_0)$	2300 kg		
	$\mu_f, \mu_{\Delta V}$	$\mu_f = \mu_{\Delta V} = 0,\ 10^{-2} \leq \mu_f, \mu_{\Delta V} < 10$		
B.1		15.00 kg	0.00	0.00
B.2		$\{14.40, 15.00, 15.00, 15.00, 15.00\}$ kg	2.40	25.75
B.3	$f_i(t_0)$	$\{13.65, 15.00, 15.00, 15.00, 15.00\}$ kg	5.40	57.92
B.4		$\{14.40, 14.55, 14.55, 14.55, 15.00\}$ kg	2.40	25.75
B.5		$\{13.65, 13.95, 13.95, 13.95, 15.00\}$ kg	5.40	57.92

To compare the efficiency of each tour, a performance metric is used, similar to that introduced by Burgon et al. [137], which quantifies the relationship between fuel- (or ΔV-) balancing capacity with fuel consumption (or ΔV expended). More specifically, the metric is described as:

$$\text{fuel or } \Delta\text{V balancing performance} = \frac{\text{percent increase in fuel or } \Delta\text{V balancing}}{\text{percent increase in fuel or } \Delta\text{V expended}} \tag{9.17}$$

If n designates the nominator of Equation 9.17 and m the denominator, then the performance is calculated as described in Table 9.7. Since the initial fuel- and ΔV -balancing values are null for certain tours (fuel-based Tour A and Tour B.1), these cases are compared to the fuel-only and ΔV-only optimal tours, i.e., $\mu_f = \mu_{\Delta V} = 0$.

Table 9.7: Performance metric calculation dependencies.

Tours	Parameter	Fuel or ΔV balancing performance
Tour A (fuel), Tour B.1	n	Relative to $\mu_f = \mu_{\Delta V} = 0$ tour
Tour A (ΔV), Tour B.2 - Tour B.5	n	Relative to initial values, $f_i(t_0)$ or $\Delta V_i(t_0)$
All	m	Relative to $\mu_f = \mu_{\Delta V} = 0$ tour

TOUR A

Selected μ_f values of interest and their effect on fuel consumption and fuel balancing are shown in Figure 9.8 for the IRASSI Tour A, whereas Figure E.12 of Appendix E.3 shows the effect on expended ΔV and ΔV-balancing for the same tour and for specific $\mu_{\Delta V}$ values. The results shown correspond to the mean of the five repetitions.

This tour is initially fuel-balanced and from Figure 9.8 it can be seen that this remains the case over time for the higher values of μ_f. An $\mu_f = 0.09$ shows a 33% improvement in fuel-balancing relative to $\mu_f = 0$ case, but at no fuel penalty, a trend also observed in the section 9.4.3. This tour is not ΔV-balanced at the beginning of the simulation. One interesting observation is that for the $J_{\Delta V}$ function, fuel differences improve (relative

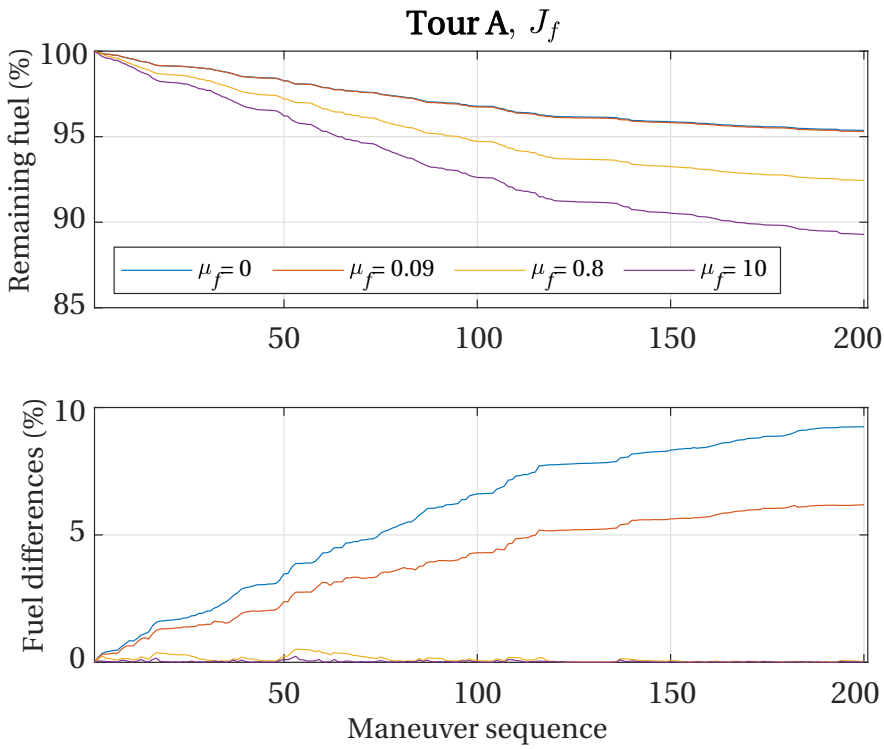

Figure 9.8: IRASSI Tour A with varying μ_f parameter: total fuel remaining (top) and fuel differences (bottom).

to the $\mu_{\Delta V} = 0$ tour) only for $\mu_{\Delta V} \leq 0.2$, whereas ΔV-balancing continues to improve for $0.2 \leq \mu_{\Delta V} \leq 5$. This is shown in Figure E.13.

The tour performance results are shown in Figure 9.9. A 'high performance' is associated with a positive increase of fuel balance (or similarly reduction in fuel differences) percentages relative to the ratio of fuel consumption (the same applies to ΔV). The μ_f and $\mu_{\Delta V}$ values of performance peak designate those for which the highest performance is detected, whereas the range concerns positive performance values. These are indicated in Figure 9.9. Table 9.8 and Table 9.9 summarize the main findings concerning this analysis.

9

TOUR B

The previous analysis is repeated for the Tour B group. The results are summarized in Table 9.8 and Table 9.9. From the former, it can be observed that for Tour B.1, the peak occurs for lower values of μ_f and $\mu_{\Delta V}$ than for other cases, which means that significant reductions in fuel differences can be achieved at low fuel consumption levels relative to $\mu_f = \mu_{\Delta V} = 0$, although this stems from the nature of nominator n in Equation 9.17.

For Tours B.2 – B.5, both cost functions seem to show a good agreement between the peak values of μ_f and $\mu_{\Delta V}$. From Table 9.6, given that the ΔV imbalance in these cases is solely due to the fuel imbalance, the $J_{\Delta V}$ function seems able to minimize ΔV differences and consumption better than the J_f counterpart concerning fuel. Maneuver times are nonetheless nearly identical between both functions.

For the tour analysis, it can be reported that:

- The range 0.2–0.4 is identified more often with higher performance for both μ_f and $\mu_{\Delta V}$ for heterogeneous formations.
- ΔV-based function produces more consistent optimal performance peaks across different sets of initial conditions than the fuel-based function.
- Wet-mass imbalanced formations (Tour A) require lower values of μ_f and $\mu_{\Delta V}$ for optimal results.
- Initially fuel-balanced formations (Tour B.1), such as IRASSI, require for optimal performance $\mu_f = \mu_{\Delta V} \approx 0.05$.
- For initially fuel-uneven formations (Tour B.2-B.5), $\mu_f = \mu_{\Delta V} \approx 0.2$ is generally the lowest boundary for which no increase in fuel- or ΔV-balancing performance is achieved.

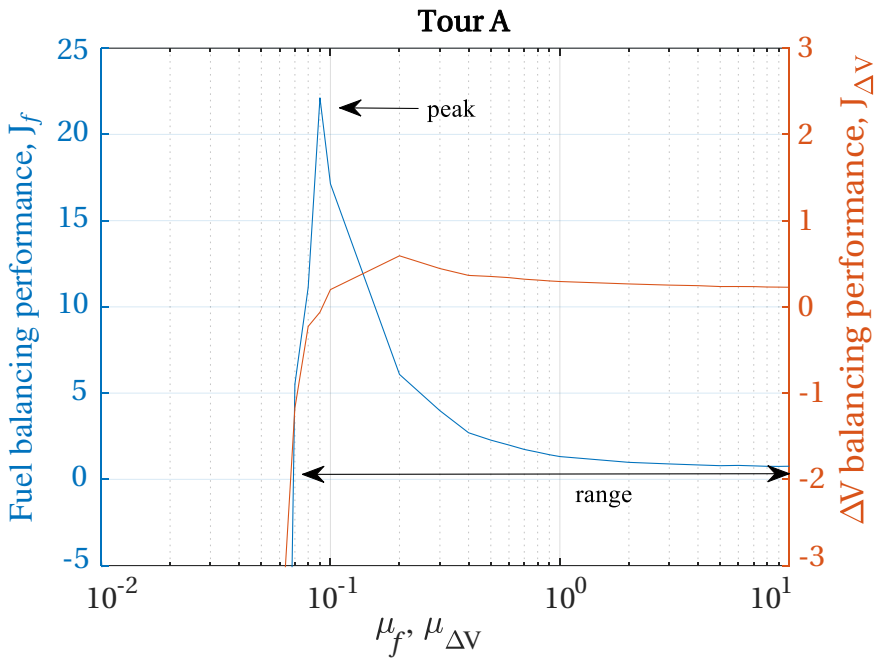

Figure 9.9: IRASSI Tour A fuel- and ΔV-balancing performance.

Table 9.8: Fuel and ΔV-balancing performance metric results.

Tours	μ_f for performance peak, fuel	μ_f of performance range, fuel	$\mu_{\Delta V}$ for performance peak, ΔV	$\mu_{\Delta V}$ of performance range, ΔV
A	0.09	0.07–10	0.20	0.10–10
B.1	0.05	0.01–10	0.05	0.02–10
B.2	0.30	0.30–10	0.30	0.30–10
B.3	0.40	0.30–10	0.40	0.30–10
B.4	0.30	0.20–10	0.30	0.20–10
B.5	0.20	0.20–10	0.20	0.20–10

9.4.5. CONCLUSIONS AND FUTURE WORK

The analysis conducted concerning the effect of weighting parameters on spacecraft resource management provided an insight into effective envelopes relevant for expressing reconfiguration maneuvers cost functions.

It can be concluded that for homogeneous formations such as IRASSI, either a fuel- or ΔV-based cost function with a weighting parameter valued at 0.05 is expected to provide the best compromise between resource balance and resource consumption. For heterogeneous formations, a ΔV-based function with parameter $\mu_{\Delta V}$ ≈0.2–0.4 is suggested.

With the tour results, one can estimate that over the five years of the IRASSI mission, nearly 15-20% of the total secondary propellant may be dedicated to reconfiguration maneuvers, whereas over 5% of the mission time (or a combined 95 days) is allocated to such maneuvers.

Finally, the ReM module described in the present chapter benefits from simplifications which may limit its application to a real mission. In this frame, the topics addressed in the next subsections could be used as guidelines for improvement of the module:

Table 9.9: Metric results for peak μ_f and $\mu_{\Delta V}$ at the end of tours.

Tours	J_f			$J_{\Delta V}$		
	Remaining fuel (%)	**Fuel diff.[i] (%)**	**Duration[ii] (%)**	**Remaining ΔV(%)**	**ΔV diff. (%)**	**Duration (%)**
A	95.30	6.18	5.17	95.13	48.91	5.17
B.1	95.18	5.36	5.03	95.22	5.54	5.03
B.2	93.69	1.16	5.06	93.73	0.86	5.06
B.3	92.14	1.21	5.05	92.17	1.07	5.05
B.4	93.51	0.22	5.04	93.55	0.15	5.04
B.5	93.88	4.19	5.05	93.91	4.00	5.05

[i] Differences
[ii] Cumulative maneuver duration

MODEL ASSUMPTIONS AND DYNAMICS

The motion model used in this analysis (and described in section 7.6.2) assumes that the spacecraft are in free-space, without considering gravity gradients between spacecraft. In order to increase the accuracy of the dynamics and of the maneuvers, gravity and disturbances such as the solar radiation pressure, could be included.

This would, in addition, require a feedback control loop which would need to be suitably tuned for removing the perturbation effects on the trajectories.

OPTIMIZATION ALGORITHM

A multi-objective optimizer could be implemented and compared to the multi-variable, single-objective function of the present analysis. In fact, a weighted-sum approach has known drawbacks [147], the most significant of which relates to the dominance of one variable (e.g., fuel used) over another (e.g., fuel balance), leading to inconsistent distances to the optimal Pareto set across different maneuvers.

The impact on computation time should nonetheless be examined in order to understand whether the multi-objective method merits implementation for near real-time onboard computation of reconfiguration maneuvers of spacecraft.

OPTIMIZATION CONSTRAINTS

In the present chapter, it was demonstrated that a ΔV-based function displayed significantly less variability than the fuel-based one. It could be of interest to study whether placing constraints on the maximum distances that spacecraft are allowed to travel has an impact on minimizing the variability of fuel-based functions.

Alternatively, if the thrusters are allowed to vary their magnitude (compared to the present case in which they operate at the maximum output), time constraints could also be prescribed or included in the multi-objective optimizer.

SIMULATION CONDITIONS

The studied initial conditions included heterogeneous formation where either the launch mass or fuel mass differed among elements. Simulating the combined effect of these two aspects could aid in gaining further insights into the maneuvering dynamics of heterogeneous formations.

ONBOARD PROCESSING AVAILABILITY

The suitability of optimization methods for real-time processing on board, considering hardware limitations and speed of convergence of the algorithms on a distributed network, could be investigated.

In the frame of this study, on a virtual network of 16 cores (3.50 GHz), using vectorization, each maneuver within ReM takes about 1-105 seconds to process (largely driven by the 14400 combinations which must be

traded at each iteration). Modern space-proven processors are at least an order of magnitude slower than general desktop computers, the state-of-the-art of the former being the European GR740[3] (250 MHz) and the American High-Performance Spaceflight Computing[4] (HPSC, 500 MHz). Using such state-of-the-art space-qualified processors (and disregarding other speed-loss-inducing sources, such as motherboard bus speed, memory, software system, etc.), at least five minutes are expected for each maneuver.

It is however to expect that processor technology advances significantly in the coming years, particularly considering NASA's ambitions of bringing quantum computing to space [5]. One can therefore be hopeful, if not optimistic, that sufficient processing capacity will be available for a timely convergence of the algorithms at the time when IRASSI (or a similar mission) launches.

9.5. CHAPTER SUMMARY

IN order to support mission autonomy and ensure compliance with science goals, a Reconfiguration Module, responsible for repositioning the formation prior to observations, was devised. For this purpose, a survey of existing literature was firstly presented, whereby it was concluded that in-depth analyses of long-term effects of formation maneuvers on spacecraft resource consumption and management, particularly in the context of heterogeneous formations, were not available. This gap set out the scope of the research, along with the motivation of setting up a maneuver-optimization procedure that was computationally simple in nature for real-time and onboard applications.

Next, the maneuver requirements, namely fuel and fuel balance as well as ΔV and ΔV balance were identified. Two weighted-sum optimization functions were described and implemented in light of these requirements, with respective weighting parameters μ_f and $\mu_{\Delta V}$. The weighting parameters μ_f and $\mu_{\Delta V}$ determined the relationship between resource consumption and resource balance. Higher weighting parameters ensure a more balanced use of resources across the fleet but demand a higher consumption of fuel and ΔV. The tuning of these parameters for different simulation conditions was a core task within the analysis.

Four independent variables were used to determine the final positions of the reconfiguration maneuvers for each spacecraft. The geometry of the final positions considered intervisibility and functional constraints as well as the required baselines associated with the next to-be-observed target. For each solution set, 14 400 combinations are traded to account for the interchangeability of positions within the formation. The spacecraft follow linear translation trajectories in inertial space, connecting their initial and final positions, using a combination bang-bang and bang-coast-bang thrust profiles to ensure time-optimal reconfigurations. The simulation conditions included a mixture of heterogeneous formations, with either different initial wet mass or fuel mass among elements and homogeneous formations (representing IRASSI). Single maneuvers and tours containing 200 maneuvers were used to derive reconfiguration scenarios.

Results showed that, generally, parameter values $\mu_f > 10$ and $\mu_{\Delta V} > 5$ seem ineffective. For formation with equal wet mass and fuel mass, parameters $\mu_f = \mu_{\Delta V} \approx 0.05$ provide the most cost-effective compromise. Conversely, heterogeneous formations may benefit by using a ΔV-based cost function to plan reconfiguration maneuvers over the long term, with a weighting parameter within the range of $\mu_{\Delta V} \approx$0.2–0.4. Metrics associated with the ΔV-based function also show less variability for individual maneuvers than those associated with the fuel-based one.

An outlook for future improvements within the ReM module, particularly concerning motion models and the optimization procedure was proposed. The investigation of the suitability of such methods for onboard processing hardware is also suggested. The ReM stands nonetheless as a robust method to optimize linear trajectories efficiently (in terms of computation complexity and time) for formation-flying applications, where full control over the relative weight of the optimization metrics is given to mission planners.

The ReM is a crucial module within iSCOUT. It receives the sequence of targets meant for observation from the TPM, described in Chapter 8 to formulate suitable reconfiguration strategies. Since these are constraint-free, the next module, the Collision-Avoidance and intervisibily Module (CAM) assesses whether conjunction events or loss of visibility links occur and refines the ReM trajectories if necessary.

[3] https://www.gaisler.com/doc/gr740/GR740-UM-DS-2-3.pdf
[4] https://ntrs.nasa.gov/archive/nasa/casi.ntrs.nasa.gov/20180003537.pdf
[5] https://www.nasa.gov/feature/ames/quantum-supremacy/

10

Optimization of Collision- and Invisibility-Avoidance Maneuvers

Simplicity is
the ultimate sophistication

Leonardo da Vinci

ABSTRACT

The Collision- and invisibility Avoidance Module (CAM) computes curvilinear trajectories for reconfiguration maneuvers that are compliant with safety requirements. The final positions and the total maneuver time remain fixed with respect to the plan of the Reconfiguration Module (ReM), but a perpendicular thrusting force is added to the nominal thrust vector, itself parallel to the trajectory. The exact magnitude and direction of the perpendicular thrusting vector are subject to a mesh-adaptive search optimization, as is the duration of its coasting period. Nearly 6% of previously generated trajectories of homogeneous formations require modification by the CAM module due to safety violations. Results show that, due to these modifications, over 300% additional resource consumption (fuel or ΔV) may be required relative to the amount of resources previously allocated by the ReM. Violations involving more than three pairs of spacecraft require the highest amounts of additional resources and computation time. Invisibilities, which typically are associated with multi-spacecraft violations, are therefore significantly more likely than collisions to consume higher amounts of fuel or ΔV and require longer processing times for the computation of solutions.

10.1. INTRODUCTION

DURING reconfigurations, a set of safety requirements apply to the formation. The first one is the minimum separation distance, to ensure that collisions do not occur. The second one is that the ranging system lasers mounted on each spacecraft must be intervisible, at least periodically, to ensure that the accuracy of the estimation of relative distances does not degrade below a given threshold.

Since the ReM module does not consider these requirements to compute the linear reconfiguration trajectories, the Collision- and invisibility Avoidance Module (CAM) was conceived to address these requirements. The CAM checks whether the ReM trajectories are safe and redesigns these trajectories in case a violation of safety requirements is detected. The CAM uses a set of flexible parameters to optimize the maneuvers as a function of fuel and fuel differences or of ΔV and ΔV differences.

The tours generated with the ReM module are the focus of this analysis. It includes thus the case of IRASSI, a homogeneous formation, as well as formations either with wet-mass imbalances or fuel-mass imbalances.

10.2. PREVIOUS CONTRIBUTIONS

iSCOUT is intended to support autonomous operations and, as such, allow spacecraft to react immediately as soon as a violation is detected. A short review of online, reactive, autonomous trajectory-planning methods with collision-avoidance constraints and control feedback laws with potential applications to the IRASSI mission, has been introduced in Section 6.5.1, in the context of goal-based (behavioral) control coordination. In its current standing, however, iSCOUT underlying motion models assume free-space dynamics, without consideration of disturbing forces or off-nominal situations, such as conjunctions, and thus in an open-loop configuration. For the calculation of safe trajectories, offline path-planner methods are of relevance.

Most of the literature of Section 9.2 which considered collision-avoidance constraints in the offline path-planning process of reconfigurations, dealt with single-step strategies. That is, final reconfiguration positions are automatically considered as collision-avoidance constraints in the path-planning algorithm [98, 140, 142]. Other research work examples complement this review. For example, Kim, Mesbahni and Hadaegh (2004) devise a heuristics approach akin to a 'bouncing ball' to determine the optimal control forces that steer spacecraft to predefined relative states (positions and velocities) while abiding by minimum separation distance requirements. When a collision is detected between a pair of spacecraft, a sudden change in the direction of the control force ('bouncing') ensues for both spacecraft. The algorithm is given the initial spacecraft states relative to the inertial frame, but the individual inertial states during the maneuver, however, are unspecified *a priori* and are instead a product of the optimal control forces solution calculated by the bouncing-ball algorithm. This way, the trajectories are energy-optimal and collision-free.

Wang and Schaub (2010) propose an open-loop, short-range collision-avoidance strategy for deep-space formations by using electrostatic forces. The alternative trajectory is composed of three patched conic sections ('repel–attract–repel') and is achieved by applying constant charge magnitudes. The magnitude of the charge and the charge switching times are subject to optimization whilst minimum-distance and path-geometry constraints ensure that the alternative trajectory maneuver is safe and symmetric. At the end of the maneuver, the original relative motion direction of the spacecraft involved is restored. The authors recognize, however, the difficulty in adapting the algorithms to large spacecraft formations due to computational complexity.

The reconfiguration problem within iSCOUT is nonetheless split into two steps. The first one, addressed by the ReM, simply calculates unconstrained optimal trajectories. The second one, addressed by the CAM, uses safety constraints for finding alternative trajectories bounded by initial and final positions as well as total maneuver time. A two-stage setup is also proposed by Sultan *et al.* [150] for deep-space formation-flying applications, who devise a trajectory parametrized by cubic polynomials and define a set of way-points that satellites must pass. The first stage solves an unconstrained, energy-optimal problem that finds the location of the final way-point (the endpoint) for each spacecraft. If no proximity violations are detected for the single way-point, this trajectory will be a straight cubic-parametrized line. Else, the second stage introduces way-points and deals with way-point separation in collision-prone trajectories. The new trajectories are assessed and the process is repeated either by introducing new way-points or modifying the positions or velocities of existing ones until safe trajectories are found for all spacecraft. Each way-point is associated with a location and velocities, yielding thus six optimization variables for each way-point for each spacecraft. The authors highlight the scalability of their method to large satellite constellations which achieves solutions speedily.

Open-loop, collision-free reconfiguration maneuvers in free-dynamics environments are also implemented by Li *et al.* [151]. Li *et al.* use predefined initial and final positions of each spacecraft to generate trajecto-

ries containing both a straight-line component connecting these two points, using a bang-coast-bang thrust profile, and an orthogonal element (perpendicular to the linear component), which employs simply a bang-bang approach. The trajectories are parametrized respectively by a velocity component parallel to the linear trajectory and a perpendicular one. Both velocity components limits are pre-computed from actuator properties and spacecraft orientations. Evolutionary algorithms are used to solve a single-objective cost function seeking the minimization of collisions, path lengths, maneuver execution time, fuel consumption and fuel distribution. The analysis is extended to a five-spacecraft formation, although complexity and difficulty in finding feasible solutions rise with the size of the formation. One of the biggest drawbacks of this method is the fact that it leads to the formation being asynchronous: each spacecraft executes a maneuver of different durations. In highly time-constrained missions, such as IRASSI, the telescopes have to be coordinated so as to initiate observations simultaneously and in order not to miss observation window opportunities.

Although none of the aforementioned manuscripts mentioned the issue of intervisbility in free-flying formations, these contributions form a starting point for the CAM. The approach devised therefore is a modification of the algorithm proposed by Li *et al.*. Thrust forces, instead of velocities, are implemented within the CAM and, for a given avoidance maneuver, the execution time is fixed by that computed previously by the ReM. Additionally, collision avoidance within the CAM is not used to calculate the cost function but is instead expressed by inequality constraints. The path lengths term is similarly removed from the cost functions, but coasting time associated with orthogonal components are introduced as independent variables within the CAM.

10.3. COLLISION- AND INVISIBILITY-AVOIDANCE MODULE (CAM)

THIS module refines the linear paths calculated by the ReM in case collisions and/or intervisibility loss events are detected. If no collisions or loss of visibility occurs, no action is taken by the CAM and the iSCOUT tool can then either distribute the ReM maneuver information to the spacecraft or relay this information to the BPM module, which then proceeds to compute the baseline patterns as described in the next chapter.

However, if either violation is detected, an alternative trajectory is computed to ensure the safety of the formation and compliance with the relative positioning requirements. The alternative trajectory employs an additional thrust force perpendicular F_{per} to the (ReM) trajectory of each spacecraft.

Although collisions must be avoided at all times, the accuracy in the relative distances' determination is not at the micrometer level outside science activity periods and, as such, intervisibility is not required on a continuous basis. The discretization procedure for the two constraints, collision avoidance and intervisibility, thus differs.

10.3.1. RELATIVE POSITION ESTIMATION DURING INVISIBILITY: CRITICAL PROPAGATION TIME

In the vicinity of L_2, the spacecraft experience a gravity-gradient-induced acceleration acting on them. The absolute accelerations which the spacecraft experience differ depending on the position of the interferometer in the orbit. These accelerations deviate up to $a_{max} = 6.9 \times 10^{-9}$ m s^{-2} for in-orbit distances of 1 km (see Philips-Blum *et al.*, 2018 [47]).

From a relative positioning perspective, this means that either the acceleration estimator model for relative distance estimations is extremely precise or, if the propagation model considers a constant acceleration throughout the orbit, then (inter-laser distance) updates from the ranging system at certain propagation time intervals $[0, \tau]$ are required to correct biases in the relative distance estimation determinations. If the acceleration difference between two telescopes, telescope 1 and telescope 2, located in different points in space with positions $\boldsymbol{r_1}(t)$ and $\boldsymbol{r_2}(t)$, equals a_{max}:

$$||\boldsymbol{a_2} - \boldsymbol{a_1}||_2 = a_{max} \tag{10.1}$$

then, in order to stay within the submeter-level region of relative distance accuracy over time $t \in [0, \tau]$, the propagation time is then given by [47]:

$$1\,\mathrm{m} < ||\boldsymbol{r_1}(t) - \boldsymbol{r_2}(t)||_2 = \left|\left|\frac{\tau^2}{2} \cdot (\boldsymbol{a_2} - \boldsymbol{a_1})\right|\right|_2 = \frac{\tau^2}{2} \cdot a_{max} \tag{10.2}$$

By rearranging the terms or Equation 10.2, the critical propagation time can be obtained:

$$\tau_{crit} \leq \sqrt{\frac{2 \cdot 1\,\mathrm{m}}{a_{max}}} \approx 4.7\,\text{hours} \tag{10.3}$$

The onboard relative motion estimation model should therefore receive updates from the metrology system, at most, every 4 hours and 40 minutes to ensure a collision-free environment during idle periods. As such, the CAM module checks whether there are periods of invisibility which last longer than $\tau_{crit} = 4.7$ hours during the reconfiguration and collision-avoidance maneuvers.

For the sake of simplicity, throughout this analysis, an invisibility instance is a period of invisibility with an associated duration higher than 4.7 hours. Shorter invisibility events are within propagation time requirements and therefore do not count as a violation.

10.3.2. RELATIVE POSITION ESTIMATION DURING INTERVISIBILITY

Once the lasers are intervisible, the 'snapshot' baseline estimation method described in Section 4.2.3, based on least-squares optimization, is used to complement the onboard propagation model of relative motion and derive the relative positions of the spacecraft. With intervisibility guaranteed and with the stated error assumptions, the accuracy at a given time instant becomes solely a function of the instantaneous formation geometry.

For completeness, the nominal assumed errors are reiterated here. These are:

- the distance measurement errors, assumed to be Gaussian-distributed with zero mean value and a standard deviation $\sigma_d = 1$ µm;
- the three orientation angles ν of each satellite, also using a Gaussian distribution, with zero mean value and a standard deviation $\sigma_\nu = 0.1$ arcsec.

No lever-arm distortions or lever-arm distance measurement errors are considered. During intervisibility between each of the 20 laser links, therefore, the relative positions are computed at time-steps of one second for each link.

10.3.3. METHODOLOGY

The maneuver requirements are analogous to those described in section 9.3.1 in terms of spacecraft resources: fuel or ΔV consumption should be minimal and balanced across the formation. However, the CAM maneuver time is limited by that previously calculated by the ReM module, t_{ReM}. The model dynamics described in Section 7.6.2 apply.

ORIENTATION DURING THE MANEUVER

During reconfiguration, the spacecraft maintain their attitude, pointing towards the target. Let S_T denote the telescope reference frame centered on the telescope's detectors, with basis vectors $\{\boldsymbol{x_T}, \boldsymbol{y_T}, \boldsymbol{z_T}\}$, where $\boldsymbol{x_T}$ points towards the target (parallel to the nominal trajectory), $\boldsymbol{z_T}$ is normal to the sunshield (parallel to the spacecraft-Sun line) and $\boldsymbol{y_T}$ completes the right-hand frame of the orthonormal system.

Figure 10.1 shows the orientation of the spacecraft at the start of the CAM maneuver, with F and F_{per} being respectively the nominal thrust parallel to the ReM trajectory and F_{per} is the thrust perpendicular to F, and φ_{per} is the angle of the thrust relative to the spacecraft-Sun line. This angle dictates the direction of F_{per}, whereas the magnitude of F_{per} determines the deviation relative to the nominal path, that is, how far each spacecraft travels.

OPTIMIZATION

If either collisions or loss of intervisibility are detected in the ReM trajectories, an alternative path has to be computed. The time to perform this surrogate CAM maneuver is bound by t_{ReM}, calculated by the ReM and described in the previous chapter.

The CAM maneuver involves departing from the nominal ReM trajectory by applying thrust $F_{per,i}$ perpendicular to the trajectory (simultaneous to the nominal one F_i parallel to the trajectory) at the initial instant and for a specified duration of time. The direction of this $F_{per,i}$ thrust is reversed once the maximum deviation from the nominal trajectory is reached, and twice more two return to the nominal trajectory. Again, in order to guarantee resource savings, the spacecraft are allowed to coast in-between firing periods. The thrusting scheme is illustrated in Figure 10.2. All spacecraft arrive therefore at their destinations simultaneously.

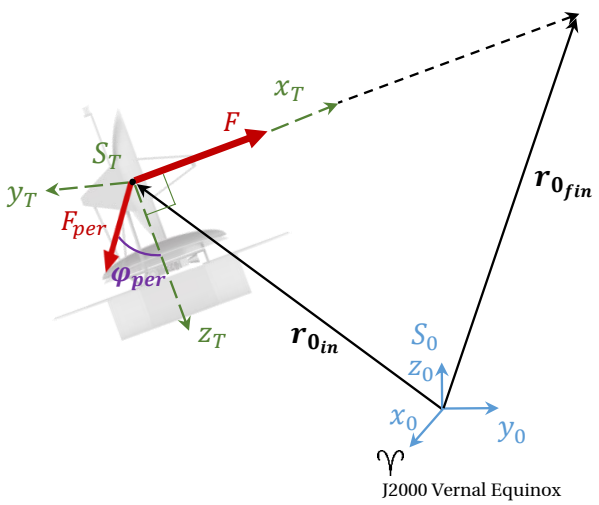

Figure 10.1: Spacecraft orientation during the CAM maneuver and thrust geometry.

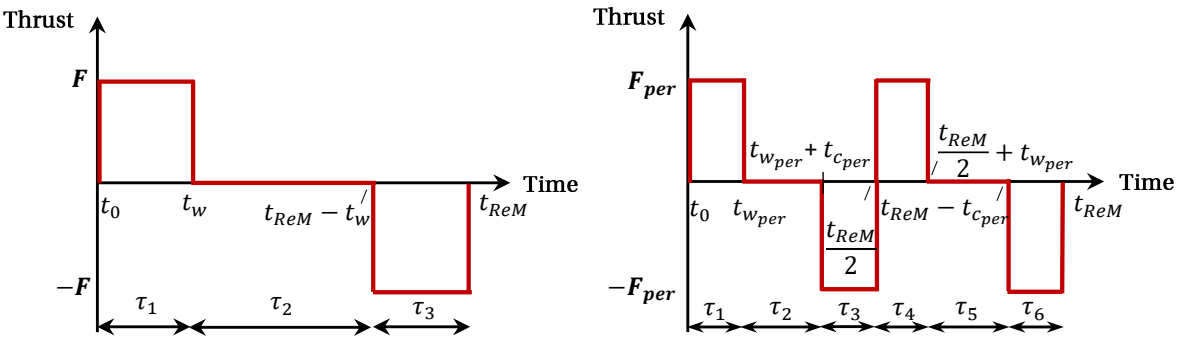

(a) Parallel thrust

(b) Perpendicular thrust

Figure 10.2: Comparison between thrust profiles during reconfiguration maneuvers. The parallel thrust has a fixed magnitude of 20 mN and is used by the ReM to compute linear trajectories while the perpendicular thrust is calculated by the CAM. Both shown examples use a bang-coast-bang approach.

To delimit the possible solution set in inertial space, there are three optimization variables attributed to each spacecraft i: the direction of the perpendicular thrust component $\varphi_{per,i}$ the magnitude of this thrust $F_{per,i}$ and the duration of the coast phase associated with the perpendicular thrust pulse $t_{c_{per,i}}$. It results in an independent vector with the 15 variables defined by:

$$\boldsymbol{S} = \left\{\varphi_{per,i}, F_{per,i}, t_{c_{per,i}}\right\} \tag{10.4}$$

where the thrust angle range is $0 \leq \varphi_{per,i} \leq 2\pi$, the coasting duration is bound by the interval $0 \leq t_{c_{per,i}} \leq t_{ReM}$ and the maximum thrust magnitude $F_{per,i}$ is user-specified. Ideally, the higher the coast phase $t_{c_{per,i}}$, the higher the fuel savings.

Similar to the ReM module, overall resource savings and resource balance among formation elements are pursued by means of two optimization objective functions, a fuel-based one and a ΔV-based one, the selection of which is specified by the user. They are recalled below:

$$J_f = \sum_i^n \left(f_i\left(t_0\right) - f_i\left(t_{ReM}\right)\right) + \mu_f \sum_i^n \sum_{j:j>i}^n \left|f_i\left(t_{ReM}\right) - f_j\left(t_{ReM}\right)\right| \tag{10.5}$$

$$J_{\Delta V} = \sum_i^n \left(\Delta V_i\left(t_0\right) - \Delta V_i\left(t_{ReM}\right)\right) + \mu_{\Delta V} \sum_i^n \sum_{j:j>i}^n \left|\Delta V_i\left(t_{ReM}\right) - \Delta V_j\left(t_{ReM}\right)\right| \tag{10.6a}$$

$$\Delta V_i = g_0 I_{sp} \ln \left[\frac{M_i}{M_i - \left(f_i(t_0) - f_i(t_{ReM}) \right)} \right] \tag{10.6b}$$

with

$$i, j = \{T_1, T_2, T_3, T_4, T_5\}$$

The weighting parameters values μ_f and $\mu_{\Delta V}$ of respective Equations 10.5 and 10.6a can equally be selected by the user.

The mesh-adaptive direct search (MADS) introduced in Chapter 9 and used by the ReM is also employed by the CAM[1]. However, differently from the ReM, the CAM optimization process is constrained by the collision- and invisibility-avoidance requirements, as well as relative position estimation accuracies. The constraints used for the computation of optimized trajectories are presented in Table 10.1, where the minimum safety distance parameter γ is set at $\gamma = 10$ m.

Table 10.1: Nonlinear constraints for CAM.

Constraint (ref. frame)	**Expression**
Collision avoidance (S_0)	$\sqrt{\left[x_{0,i}(t) - x_{0,j}(t)\right]^2 + \left[y_{0,i}(t) - y_{0,j}(t)\right]^2 + \left[z_{0,i}(t) - z_{0,j}(t)\right]^2} \geq \gamma,$ $\forall t \in [t_0, t_{ReM}]$
Intervisibility (S_T)	$\sqrt{\left[x_{T,i}(t) - x_{T,j}(t)\right]^2 + \left[y_{T,i}(t) - y_{T,j}(t)\right]^2} \geq \left\|z_{T,i}(t) - z_{T,j}(t)\right\| \tan(\theta_{ri}),$ $\forall t_{ReM} \geq \tau_{crit} \wedge \Delta t = [t, t+1] : \Delta t \geq \tau_{crit}$
Relative pos. estimation accuracy (S_0)	$b_{ij}(t) \leq 1m$ $\forall t_{ReM} \geq \tau_{crit} \wedge \Delta t = [t, t+1] : \Delta t \geq \tau_{crit}$

There are several ways in which collision- and invisibility-avoidance maneuvers can be pursued. It has been proposed that a time term is added to the independent vector for optimization [105] determining the starting time of the departure from the ReM trajectory. However, for a five-spacecraft formation, this would lead to an additional five parameters subject to trade-off by the mesh-adaptive algorithm, increasing the computational time and complexity. Imposing a departure from the nominal ReM-generated trajectory at $t = 0$, as proposed by Li *et al.* [151], accomplishes overall fuel savings as the algorithm allows telescopes to coast for most of the journey in case an alternative trajectory has to be computed.

OPTIMIZATION FUNCTION PARAMETERS

The dynamics of each formation element i are governed by Equations 7.5 and 7.6 during the maneuver. The introduction of a perpendicular thrust element simultaneous to the nominal parallel one, however, does require additional fuel consumption which is proportional to the thrust impulse width of the perpendicular thrust, $t_{w_{per,i}}$:

$$t_{w_{per,i}} = \frac{t_{ReM} - 2t_{c_{per,i}}}{4} \tag{10.7}$$

The fuel consumption associated with the perpendicular thrust is therefore given by:

$$f_{CAM,i} = -4 t_{w_{per,i}} \dot{f}_i = 4 t_{w_{per,i}} \frac{F_{per,i}}{I_{sp} g_0} \tag{10.8}$$

[1] It should be remarked that prior to deciding on a final optimizer for the CAM, two other methods of MATLAB's Global Optimization Toolbox [146] were implemented and compared: a genetic algorithm and a surrogate one. However, none of them proved to be useful in finding good solutions. The genetic algorithm required more runs than the MADS for convergence and the surrogate method was slower and no more accurate than the MADS.

Table 10.2: Simulation parameters for the IRASSI formation.

Simulation parameter	**Value**
i	$\{T_1, T_2, T_3, T_4, T_5\}$
$I_{sp,i}$	2500 s
γ (collision-avoidance)	10 m
τ_{crit} (invisibility-avoidance)	4.7 hours
σ_d (relative position estimation)	1 µm
σ_v (relative position estimation)	0.1 arcsec
Optimizer	Mesh-adaptive direct search

Together with Equation 9.15, the total fuel consumption for a collision- or visibility-loss-avoidance maneuver is[2]:

$$f_{av,i} = f_{ReM,i} + f_{CAM,i} = -4t_{w_{per,i}} \frac{1}{I_{sp}g_0} \left(2t_{w,i} + 4t_{w_{per,i}} F_{per,i}\right) \tag{10.9}$$

As in the ReM, the ΔV_i value for each formation element can then be calculated using Equation 10.6b and the corresponding ΔV_{av} is given as a function of $f_{av,i}$. It should also be highlighted that as soon as one violation is detected, alternative trajectories are sought for the full constellation and not simply for the telescope pairs involved. This is to ensure that any alternative path among the pairs involved will not itself violate non-modified trajectories.

10.4. RESULTS AND DISCUSSION

To illustrate the functioning of the CAM module, first an example CAM maneuver is presented, followed by an analysis of the IRASSI tours. These tours were generated by the ReM module and presented in section 9.4.4. Each tour ReM maneuver is screened to assess whether collision or invisibility events are detected. If that is the case, then an alternative trajectory is calculated by the CAM.

The simulation setup is firstly presented followed by an analysis of violations events obtained with the ReM tours. The obtained results and discussion are featured in the subsequent section. For curiosity, the need for maneuvering was also investigated for the effective-envelope single maneuvers of ReM (cf. section 9.4.3) and is presented in Appendix F.

10

10.4.1. CAM SIMULATION PARAMETERS

The simulation setup is the same as for the ReM module, whereby spacecraft employ colloidal-based propulsion, and the optimization solver, the MADS, is part of the MATLAB's Global Optimization Toolbox [146]. The simulation parameters and initial mass conditions are reiterated in Table 10.2.

Each trajectory and constraint is evaluated with the time-resolution of one second. For each maneuver, fuel-related and ΔV-related optimization metrics were retrieved (cf. Table 9.2). The results are shown as a function of the additional fuel, f_r, and ΔV, ΔV_r, *and* of the additional sum of fuel and ΔV differences obtained with the CAM maneuvers, respectively, f_{dr} and ΔV_{dr} used by the CAM. The f_r and ΔV_r are given as the ratios of:

$$f_r = \frac{f_{CAM} - f_{ReM}}{f_{ReM}} \tag{10.10a}$$

$$\Delta V_r = \frac{\Delta V_{CAM} - \Delta V_{ReM}}{\Delta V_{ReM}} \tag{10.10b}$$

The f_{dr} and ΔV_{dr} ratios are obtained via the same method: the sum of differences of fuel or ΔV obtained with CAM subtracted and divided by that of the original ReM maneuver. The results are also shown in terms of the computation time necessary to achieve convergence.

[2] Note that Equation 10.9 denotes a suboptimal way of computing the magnitude of $f_{av,i}$. The consideration of the resultant of the two perpendicular force magnitudes F_i and $F_{per,i}$ associated respectively with fuel consumptions $f_{ReM,i}$ and $f_{CAM,i}$ would result in an optimal $f_{av,i,opt}$ value, such that $f_{av,i,opt} = \sqrt{f_{ReM,i}^2 + f_{CAM,i}^2}$.

10.4.2. EXAMPLE CAM MANEUVER

Exemplified is a single collision- and invisibility-avoidance maneuver. The original nominal trajectory, shown in Figure 10.3(a), involves a collision of all ten spacecraft pairs at the origin of the inertial frame S_0, the half-point of the 10-hour maneuver, and one invisibility instance. This invisibility event is detected between telescope pair $T_3 - T_4$ and lasts for the whole maneuver. The initial position coordinates $\boldsymbol{r_{0,in}}$ of the formation are:

$$\boldsymbol{r_{0,in}} = \begin{bmatrix} -208.5 & -328.8 & -135.9 \\ 126.5 & 184.2 & 8.6 \\ 73.2 & -30.7 & -60.8 \\ -172.0 & -142.9 & -2.0 \\ 180.7 & 318.1 & 190.1 \end{bmatrix} \text{ m} \tag{10.11}$$

The final commanded positions mirror the initial positions, such that $\boldsymbol{r_{0,fin}} = (-1) \cdot \boldsymbol{r_{0,in}}$. All spacecraft are initialized with 15 kg of fuel and 2300 kg of wet mass.

The avoidance maneuver, in Figure 10.3(b) is calculated using $\mu_f = 0.05$. The collision threat is removed and all spacecraft are intervisible throughout the maneuver for periods longer than $\tau_{crit} \approx 4.7$ hours[3]. Figure 10.4 shows the distance among all spacecraft pairs for the original trajectory and the CAM-modified one. The safety distance of $\gamma = 10$ m is indicated by the dashed line. By measuring the relative positions at all instants when ranging-system laser links are available (i.e., when telescopes are intervisible), it is possible to observe that the maximum difference between the true and estimated positions never rises above 11 µm, using the baseline estimation snapshot method described in Section 4.2.3.

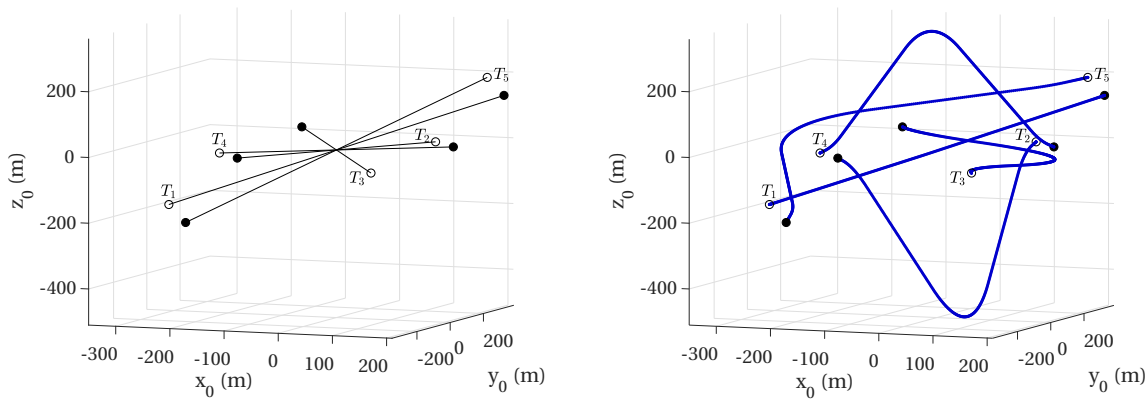

(a) Original trajectory (b) CAM trajectory

Figure 10.3: CAM Example Maneuver: the CAM designs an alternative trajectory for collision- and invisibility-avoidance. White spherical markers denote initial positions and black markers the final positions.

10

All spacecraft perform the avoidance maneuver distinctively, obtaining different trajectory lengths and coasting/thrusting durations. They all achieve the commanded final position in the specified time of 10 hours without violating any of the constraints or maximum values prescribed to the independent variables. The optimized variables, i.e., the angle of the perpendicular thrust component $\varphi_{per,i}$, the magnitude of the thrust $F_{per,i}$ and associated coasting duration $t_{c_{per}}$, are presented in Table 10.3. Telescope T_1 coasts for the majority of the maneuver (recall that there are two coasting periods associated with the perpendicular thruster), whereas the thrust magnitude of telescope T_2 is the highest.

10.4.3. COLLISION AND INVISIBILITY EVENTS FOR REM TOURS

Firstly, it must be assessed whether the spacecraft violate safety requirements at any point within the ReM tours. The tours were presented in section 9.4.4 and each is composed of 200 maneuvers within a total operation time of ≈602 days. Each tour is repeated five times, giving a total of 1000 maneuvers for each initial condition and each cost function. The initial mass conditions are reiterated in Table 10.4 respectively. The weighting parameter values μ_f and $\mu_{\Delta V}$ are those which provided the best fuel and ΔV-balancing performance within the ReM, according to the specific initial conditions.

[3] Invisibility instances of durations well below 4.7 hours remain between six different pairs of telescopes, but these do not pose a concern to relative position estimation with accuracy requirements below one meter.

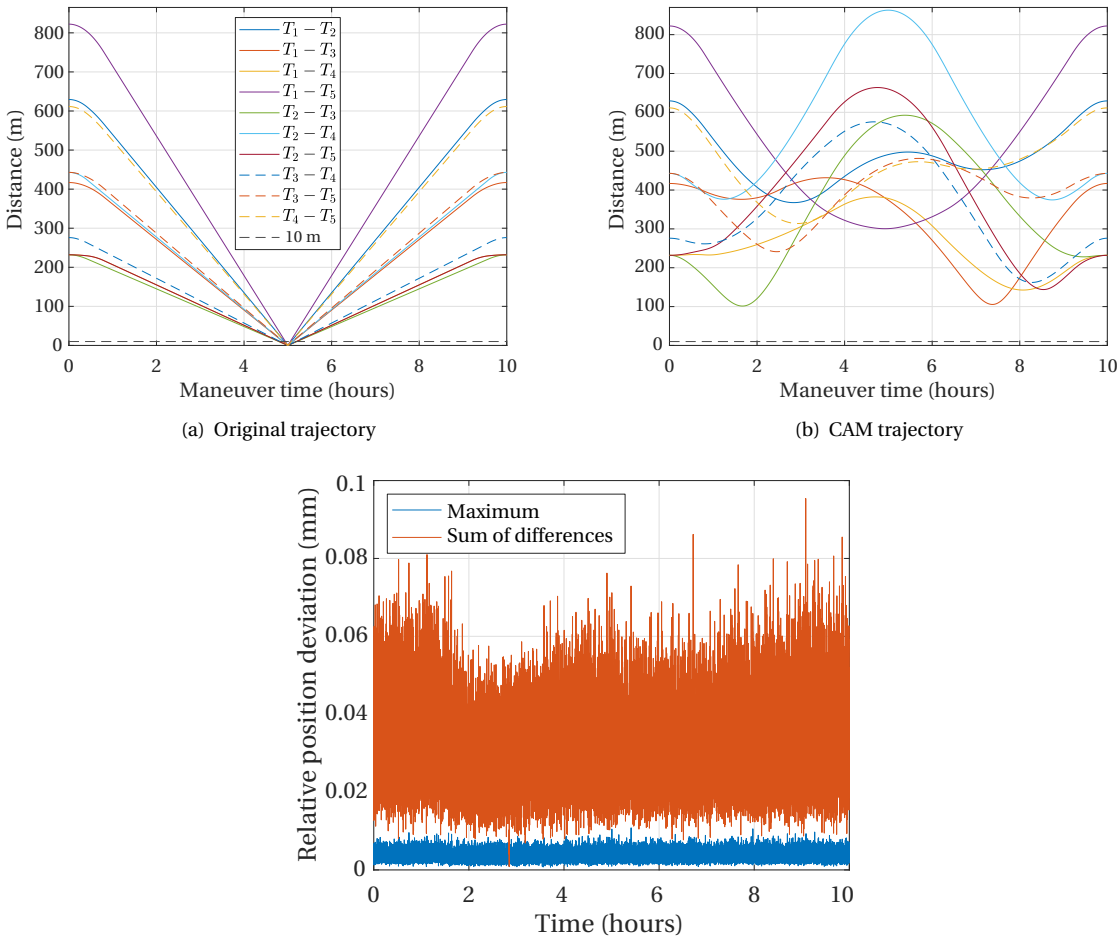

(a) Original trajectory

(b) CAM trajectory

(c) CAM trajectory

Figure 10.4: Distance of telescope pairs with collision risk (top left) and collision-avoidance (top right). The legend on the top-left-hand plot applies to the right-hand plot. The estimated relative position deviations relative to the true positions are shown on the bottom plot.

10

The violation instances are shown in Table 10.5. For each tour and cost function, the values reflect the mean of the five repetitions. The 'Total' columns show the ratio between the number of maneuvers with detected collision or invisibility violation and the number of tour maneuvers (200). The 'Pairs' columns show the mean number of spacecraft pairs involved in collision or invisibility events over the tours. The last column, 'Duration', shows the average ratio between the duration of invisibility and the duration of the reconfiguration maneuver for each pair. No relative position estimations which violate the accuracy threshold of one meter were detected during reconfiguration.

In terms of collisions, the B.3 tour shows the highest incidence rate at about 12-13% for both cost functions (or about 25 detections out of 200), while the other tours have a detection rate which never exceeds 6% (or 12 detections). On average, collisions of any tours involve up to 1.2 pairs of spacecraft.

With regards to invisibilities, the B.5 tour has the highest proportion of instances for the J_f cost function, at 7.2%, and the B.4 tour that of the $J_{\Delta V}$, with 6.7%. A minimum of ten instances are detected for B.1 (for $J_{\Delta V}$). The number of invisible pairs, on average, is between 2.3 and 3.0, whereas the average invisibility duration varies between ≈53% and 57% (corresponding to approximately 7 and 7.5 hours). Upon closer inspection, there were instances whereby up to 8 ranging links out of 20 became invisible in a single reconfiguration maneuver.

Tours A, with an initially unbalanced wet mass, and B.1, associated with a homogeneous formation, have the lowest proportions of collision events. Overall, the need for alternative trajectories due to invisibilities and collisions, is typically consistent for concentrated fuel imbalances (Tours B.2 and B.4). Curiously, there is a divergence been the fuel-imbalance distribution cases in terms of collisions, with Tours B.3 registering the highest proportion and Tour B.5 the lowest. Given that the values reflect the averages of five repetitions,

Table 10.3: Independent variables results for Example CAM maneuver.

Telescope	φ_{per} (deg)	F_{per} (mN)	$t_{c_{per}}$ (hours)
T_1	-119.58	6.81	4.51
T_2	118.05	18.28	2.32
T_3	-79.81	11.16	0.05
T_4	143.37	14.76	2.79
T_5	-144.99	11.95	2.24

Table 10.4: Parameters for IRASSI Tour analysis.

Tours	μ_f	$\mu_{\Delta V}$	Mass (kg)	Initial sum of differences	
				Fuel (kg)	ΔV (m s^{-1})
Tour A	0.09	0.20	$M_i(t_0) = \{1700, 2000, 2300, 2600, 2900\}$ $f_i(t_0) = 15.00$	0.00	446.01
Tours B			$M_i(t_0) = 2300$		
B.1	0.05	0.05	$f_i(t_0) = 15.00$	0.00	0.00
B.2	0.30	0.30	$f_i(t_0) = \{14.40, 15.00, 15.00, 15.00, 15.00\}$	2.40	25.75
B.3	0.40	0.40	$f_i(t_0) = \{13.65, 15.00, 15.00, 15.00, 15.00\}$	5.40	57.92
B.4	0.30	0.30	$f_i(t_0) = \{14.40, 14.55, 14.55, 14.55, 15.00\}$	2.40	25.75
B.5	0.20	0.20	$f_i(t_0) = \{13.65, 13.95, 13.95, 13.95, 15.00\}$	5.40	57.92

it is unlikely that this effect may be attributed to chance (the MADS algorithm is stochastic). It may well be that the algorithm implemented within the ReM attempted to minimize the resource differences by finding peculiar final position combinations for Tour B.3. In addition, the J_f cost function is generally associated with 6% higher number of collisions and invisibilities than the $J_{\Delta V}$ function, on average.

Although invisibilities tend to occur more often than collisions, there is only a chance of 0.1% that both collision risk and invisibility instances occur within a single reconfiguration maneuver. This is because collision events are associated with short ReM trajectories (i.e., when the baseline parameter d is maintained between an initial and final 'short' baseline configuration) and invisibility events involve longer trajectories and longer maneuver duration times (e.g., when the baseline parameter d is maintained between an initial and final 'long' baseline configuration). Figures 10.5 illustrate this relationship. The top plots show the number of collision and invisibility pairs as a function of maneuver time and the bottom plots as a function of traveled distance. All simulation sets of Table 10.4 are considered here. It is clear that collisions are typical for maneuvers shorter than 3 hours and distances lower than 700 m. On the other hand, invisibility instances prevail for maneuver duration over 7 hours and traveled distances between 1.5 and 3 km. Figures 10.5(b) and 10.5(d) also show that the number of mutually invisible pairs rises with increasing maneuver duration and trajectory length.

10.4.4. CAM MANEUVERS FOR IRASSI TOURS

The present subsection shows the additional fuel and ΔV (f_r and ΔV_r), as well as their respective summed differences (f_{dr} and ΔV_{dr}), required by the CAM maneuvers. The tours are composed of 200 different reconfiguration maneuvers, for which a total time of ≈602 days is allocated. The initial fuel and wet mass conditions of the two tour groups, Tour A and Tour B, described in the previous section, apply respectively. Of the five repetitions of each ReM-generated tour, one is randomly selected for the CAM module demonstration.

Table 10.5: Detected collisions and invisible pairs during reconfiguration maneuver.

Tours	Collisions				Invisibilities					
	Total (%)		Pairs		Total (%)		Pairs		Duration (%)	
	J_f	$J_{\Delta V}$	J_f	$J_{\Delta V}$	J_f	$J_{\Delta V}$	J_f	$J_{\Delta V}$	J_f	$J_{\Delta V}$
A	0.7	1.4	1.0	1.1	5.6	5.7	2.6	2.7	56.6	53.2
B.1	0.7	0.2	1.0	1.0	5.4	4.8	2.7	3.0	53.7	53.9
B.2	4.8	5.7	1.1	1.1	5.6	5.8	2.9	2.8	56.9	57.8
B.3	13.2	11.8	1.2	1.2	6.5	6.1	2.3	2.9	57.2	57.2
B.4	4.7	4.6	1.1	1.2	6.3	6.7	2.7	2.6	55.9	54.6
B.5	1.4	1.7	1.0	1.0	7.2	6.3	2.6	2.7	54.5	54.0

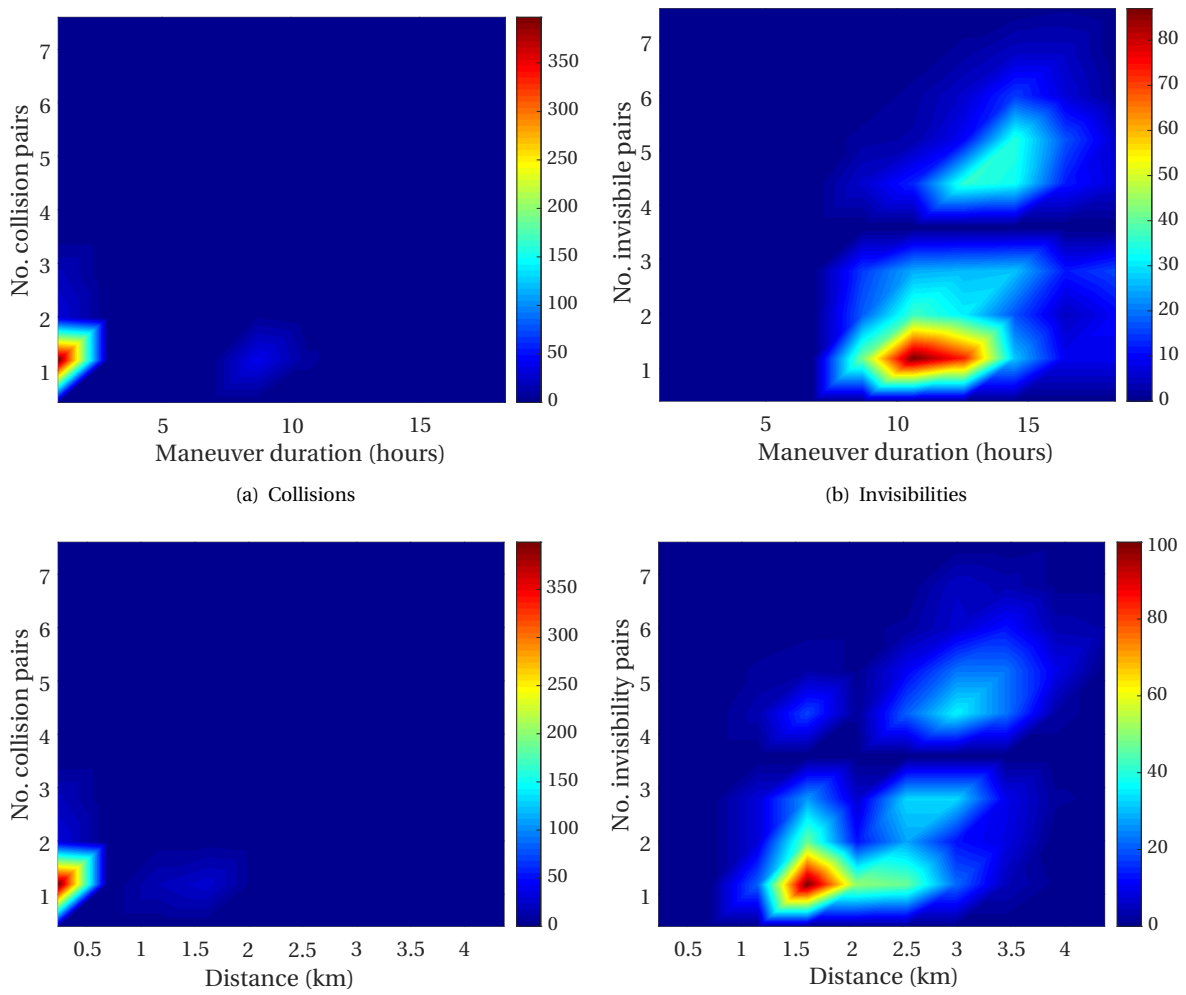

(a) Collisions (b) Invisibilities

(c) Collisions (d) Invisibilities

Figure 10.5: Number of telescope pairs involved in collision and invisibility instances as a function of maneuver duration and ReM trajectory distance.

The metrics are the additional resources and the computation time associated with CAM maneuvers. To

maintain the same structure as in the ReM tours, results are discriminated between J_f and $J_{\Delta V}$ functions, although the focus is not to compare the performance of the metrics between the two functions. Throughout the analysis, no relative position estimation errors higher the required maximum of one meter were detected during the CAM maneuvers and the analysis focuses therefore on collision- and invisibility-avoidance constraints.

ACHIEVING CONVERGENCE WITH THE MADS

During the analysis, two issues regarding convergence within the CAM module became apparent:

1. due to the imposed constraints and the setup of the optimization process (thrust profile and independent variables) convergence of the MADS was rare. To improve the rate of successful convergence to a solution, a loop was implemented whereby the initial guesses for the independent variables S of the MADS were randomized values at each iteration.

2. with the perpendicular thrust limited to $F_{per} = 20$ mN (as per hardware limitation [38]), with the proposed setup, convergence with the randomized trials was still unachievable or the speed of convergence of the algorithm was unreliably slow - in the order of 45-60 minutes. To cope with this issue, after 40 iterations (totaling approximately 10 minutes) the limit of F_{per} was relaxed. A new upper bound of $F_{per} = 200$ mN was imposed, an order of magnitude higher than the current theoretical physical limit [38].

A strong improvement in the success rate of the CAM calculations was observed by implementing these two steps. There were nonetheless instances for which the upper limit of $F_{per} = 200$ mN was not enough to guarantee convergence. This is attributed to the setup of the optimization process and recommendations for future work in this context are proposed in section 10.4.5.

This means that for the cases in which convergence was achieved, the highest of the five $F_{per,i}$ values in the formation for a given CAM maneuver will belong to either of the two intervals I_1 or I_2:

$$I_1 = [0, 20]\,\text{mN} \tag{10.12a}$$

$$I_2 = [20, 200]\,\text{mN} \tag{10.12b}$$

When the maximum $F_{per,i} \in I_1$, this instance is denoted F_{per1}, otherwise if the maximum $F_{per,i} \in I_2$, it is denoted F_{per2}.

ADDITIONAL RESOURCES

The additional resources required for CAM-generated alternative trajectories relative to the original (straight-line) ReM ones are summarized in Table 10.6. The table reflects the averages for each tour for one repetition. Results show that over 300% more fuel or ΔV may be required for an alternative trajectory in comparison to those computed by the ReM.

Whereas the $J_{\Delta V}$ function was previously associated with 6% less collision- and invisibility events in ReM trajectories, the function was shown to be more expensive in terms of additional ΔV than the J_f function concerning fuel. Conversely, the additional ΔV differences are lower with the $J_{\Delta V}$ than the fuel differences of J_f. Since these results reflect a single repetition of the CAM for each maneuver, they are not generalizable.

Although the initial sum of ΔV differences at the beginning of the simulation for Tour A amounts to 446 m s^{-1}, a change in ΔV differences is barely detectable for all alternative maneuvers of this tour. The breakdown of each CAM maneuver for Tour A is presented in Figure 10.6(a) for the $J_{\Delta V}$ function. The abscissa shows the maneuver number and the nature of the violation: 'I' for invisibility and 'C' for collision. The numbers atop bars represent the number of spacecraft pairs associated with the violation. It is possible to infer that the higher the number of spacecraft associated with the violation, the higher the ΔV_r, or the additional ΔV required for generating an alternative trajectory. Collisions also seem to require less additional fuel than invisibility events.

Concerning Tours B, the distribution of fuel imbalance does not seem to have an impact on the f_r and f_{dr} metrics (the absolute fuel consumption and fuel differences naturally follow the same trends as those identified in Chapter 9 within each tour). Figure 10.6(b) shows the results for the heterogeneous formation case, Tour B.1, in terms of fuel consumption. A rise in the number of pairs involved in a violation is accompanied by an increase in both additional fuel consumption and fuel differences among elements. There are, however, instances, where a reduction in f_{dr} is observed. For maneuver 54, for example, this reduction corresponds to 25% at an additional fuel consumption of 144%. Finally, similar to what is observed in Tour A, the single collision event is associated with the lowest f_r.

Table 10.6: Results for the IRASSI Tours' CAM maneuvers.

Tours	J_f		$J_{\Delta V}$	
	Fuel (%)	**Fuel diff.[i] (%)**	**ΔV(%)**	**ΔV diff. (%)**
A	300	52	323	0
B.1	160	30	268	72
B.2	186	126	110	61
B.3	98	2	87	1
B.4	130	68	187	64
B.5	166	13	295	113

[i] Differences

The distribution of additional fuel and ΔV resources is shown in Figure 10.7(a) in semilog scale. As can be observed, there is a clear progression of the amount of additional resources required to execute the CAM maneuver and the number of spacecraft pairs involved in the violation.

CONVERGENCE ANALYSIS AND COMPUTATION TIME

Table 10.7 shows the proportion of events for each of the maximum ranges of F_{per}. The values in the first columns show the ratio between the number of F_{per1} instances and the total violation events of the tour, whereas the second column shows the same for F_{per2}. The proportion of non-convergent solutions relative to total violation events of the tour is shown in the third column.

Overall, there is a chance between approximately 50 %–75 % that a safe alternative trajectory is found for thrust magnitudes between [0, 20] mN (F_{per1}). Curiously, allowing the range of F_{per} to increase up to 200 mN (F_{per2}) had little impact on fuel-imbalanced tours (Tours B.2 to B.5), but it is enough that convergence to a solution is found for Tours A and B.1. Indeed, no solution is found for Tours B.2 to B.5 between 19 %–53 % of the times. Upon close inspection, 89% of total non-convergent events were intervisibility-related violations involving on average 4.1 spacecraft pairs. The remaining 11% were associated with collisions involving a mean of 1.7 pairs.

The distribution of maximum F_{per} values is also shown in Figure 10.7(b). Whereas F_{per2} events are loosely distributed among the number of formation pairs, F_{per1} events occur significantly more often for low numbers of telescopes involved in a given violation. On average, the number of pairs associated with F_{per1} instances corresponds to 1.4 and rising to 3.7 pairs for F_{per2} instances. This clearly indicates that the higher the number of pairs, the more likely it is for a higher thrust to be demanded from the algorithm - that is, the further the spacecraft will travel away from the nominal trajectory. Similarly, higher computation times are associated with F_{per2} instances and a higher number of pairs. Each calculation of F_{per2} takes on average 11.5 minutes, compared with 2.5 for F_{per1} maneuvers.

These results show that the MADS optimization algorithm either does not converge (after 60 iterations) or spends significant amounts of time finding solutions when a violation involves more than three of four pairs of spacecraft. Even though non-convergent events and F_{per2} maneuvers represent, on average, a minority of maneuvers of the whole of the tour (200 maneuvers), never exceeding a combined 5% of the total tour maneuvers, it is not acceptable that such maneuvers are expensive in terms of computation time, thrust and hence onboard resources (fuel and ΔV). Alternative strategies are discussed under 'Conclusions and Future Work', in section 10.4.5.

METRICS AS A FUNCTION OF VIOLATION TYPE

The overall metric averages discriminated between the type of violations, are presented in Table 10.8. Invisibilities require 199% more fuel and 248% more ΔV than the ReM trajectories, which corresponds to 2.5–3.5 more than fuel and ΔV required for collision-avoidance maneuvers. Although collisions do not increase resource differences, the results show that resources are approximately 70% more unbalanced at the end of invisibility-avoidance maneuvers compared to the original ReM trajectory.

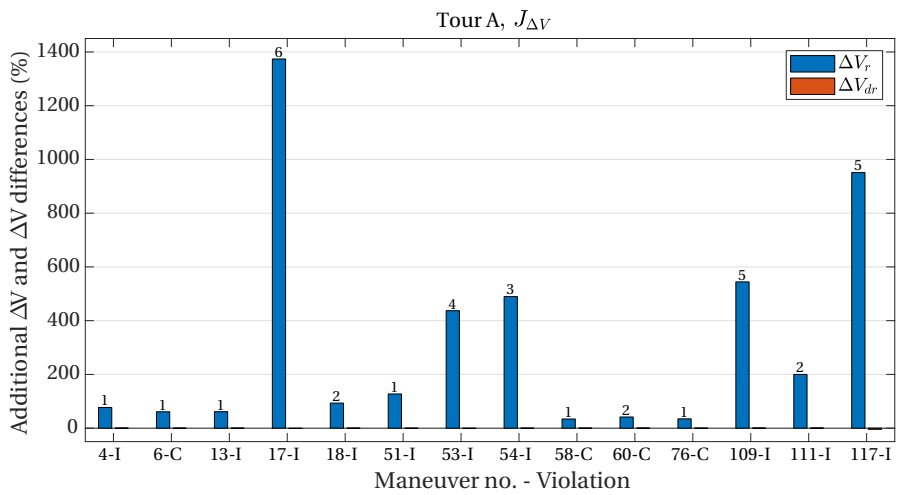

(a) Additional ΔV and ΔV differences for Tour A, $\mu_{\Delta V} = 0.2$

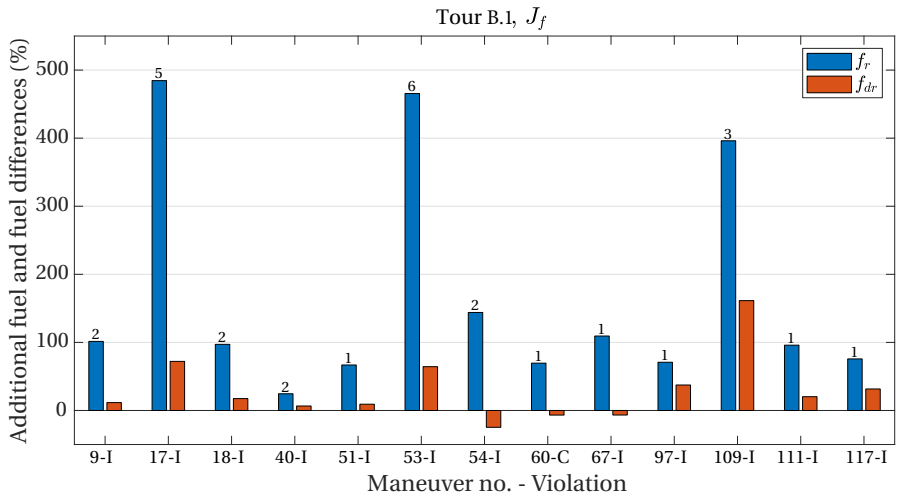

(b) Additional fuel and fuel differences for Tour B.1, $\mu_f = 0.05$

Figure 10.6: Additional resources and resource differences for Tour A and B.1. 'I' violations refer to invisibilities and 'C' to collisions. The numbers of pairs involved in each violation are shown on top of the bars.

10

F_{per1} events are nearly balanced between the two violation types. However, due to the fact that invisibilities often involve several pairs of spacecraft, as shown in Table 10.5, there is a need to spend more fuel to resolve these violations and therefore 74% of all F_{per2} instances are connected to invisibility-avoidance maneuvers. For Tours B.2 to B.5, in 28% of the times that a violation is detected, no solution is found because of invisibilities. Invisibilities make up 89% of all non-convergent events.

The difficulty in resolving intervisibility violations among several pairs is reflected in the computation time, at over 8 minutes for each CAM maneuver - double that required to calculate collision-avoidance maneuvers, on average. In comparison, each straight-line ReM maneuver takes, at most, 30 seconds to compute. The imposition of safety constraints together with thrust magnitudes limitations, therefore, have a strong impact on the rate of production of collision- and invisibility-free, alternative trajectories.

10.4.5. CONCLUSIONS AND FUTURE WORK

The analysis concerning the need for alternative trajectories shows that up to 13% of ReM maneuvers for a given tour may require an alternative trajectory. For homogeneous formations such as IRASSI, this value is around 6%. Overall, albeit by 6% margin, $J_{\Delta V}$ performed slightly better in achieving violation-free trajectories.

It was also shown that the collisions and invisibility periods occur in the same reconfiguration maneuver at a rate of one in every 1000 maneuvers, since collision events are prone to occur in short-duration (typically,

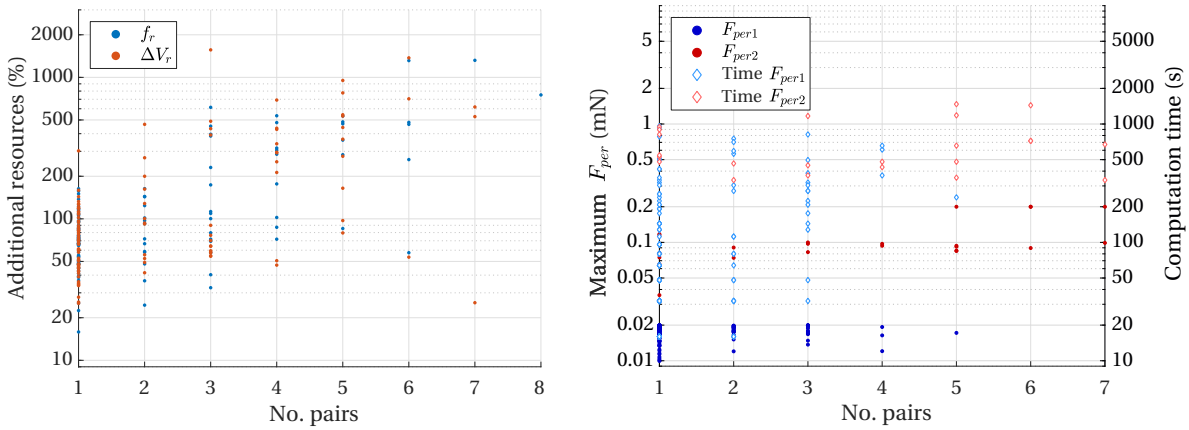

(a) Resources (b) Maximum F_{per}

Figure 10.7: Distribution of additional resources and maximum F_{per} with number of pairs involved in collision or intervisibility violations.

Table 10.7: Proportion of events for each of the maximum F_{per} ranges of CAM maneuvers for tours.

Tours	F_{per1} (%)		F_{per2} (%)		NC[i] (%)	
	J_f	$J_{\Delta V}$	J_f	$J_{\Delta V}$	J_f	$J_{\Delta V}$
A	75	57	25	43	0	0
B.1	69	50	31	50	0	0
B.2	63	67	0	0	37	33
B.3	76	73	3	8	21	19
B.4	75	56	0	9	25	35
B.5	69	47	0	0	31	53

[i] Non-convergent

10

of less than 3 hours) and short-distance (less than 700 meters of displacement) reconfiguration maneuvers, as opposed to invisibility periods which are largely present for long-duration (of over 7 hours) and long-distance (of more than 1.5 km of displacement) reconfiguration maneuvers.

Depending on the tour type, over 300% more fuel or ΔV might be required for an avoidance maneuver compared to the original ReM trajectory. However, since only a small fraction of ReM trajectories require an alternative path and reconfiguration maneuvers are generally cost-effective (in Chapter 9 it was shown that ≈95% of the secondary propellant and ΔV capacity are still available after 200 maneuvers), this increase is not likely to generate fuel-starvation on any spacecraft before the end of the mission. This does indicate, however, that the optimal positions calculated by the ReM are potentially sub-optimal if the trajectory is modified by the CAM module.

Given the similarities of the methodologies, the avenues for further work within the CAM largely match those of the ReM module. Furthermore, ideally, the ReM should be able to deliver trajectories that are free of any safety violations. However, the imposition of constraints does result in a higher computation time as observed in section 10.4.4. Given that on average only 13% or less of the maneuvers require a refinement of the ReM trajectory, there is no particular need to include collision- and invisibility-avoidance in the ReM unless powerful processors are used to guarantee that mission time is not unnecessarily used to calculate reconfiguration maneuvers. However, the fact that not all alternative solutions of the CAM complied with the physical limitations of the thrusters ($F_{per,i} \leq 20$ mN) does require that the current CAM setup is adapted. Suggestions for future investigation and improvements are made in the following subsections.

Table 10.8: Summary for the IRASSI Tours' CAM maneuvers according to violation (collision or invisibility).

Metric	**Collisions**	**Invisibility**
f_r (%)	80	199
f_{dr} (%)	0	68
ΔV_r (%)	71	248
ΔV_{dr} (%)	-1	70
F_{per1} events (%)	48	52
F_{per2} events (%)	26	74
NC[i] events (%)	11	89
Computation time[ii] (min)	3.9	8.2

[i] Non-convergent, applies only to Tours B.2 to B.5
[ii] Does not include computation time for non-convergent events

INTER-MODULAR LOOP

If CAM maneuvers:

- require 300% more fuel or ΔV than the original ReM trajectory;
- involve a higher computation time than the ReM;
- are not always compliant with the thrust magnitude limit of $F_{per,i}$ = 20 mN;

then one can consider devising a loop between the CAM and the ReM, such that in cases where multiple pairs of spacecraft violate safety requirements, a new ReM position can be delivered that is both collision-free and fully intervisible during the reconfiguration maneuver.

THRUST PROFILE AND OPTIMIZATION VARIABLES

In order to ensure compliance with the maximum thrust magnitudes of colloidal engines, other strategies on how to operate the engines can be devised. For instance, the imposition of the four coasting periods $t_{c_{per,i}}$ associated with the perpendicular thrust $F_{per,i}$ to be equal, could be removed. Similarly, the start time of $F_{per,i}$ could also be subject to trades in the optimization, instead of imposing that the perpendicular thrust starts automatically with the CAM maneuver. Perhaps the demand that the total CAM maneuvers maintain the same duration as the original ReM ones is the biggest contributor to the algorithm not finding a suitable solution. This would require a sensitivity analysis, since too long of a maneuver or cumulatively long CAM maneuvers may impact the ability to pursue science activities in the allocated operational slots and targets may leave the field of view of the interferometer.

In summary, the effect of varying the different $t_{c_{per,i}}$ times for each spacecraft, of varying the start time of $F_{per,i}$ and of adding time to the complete reconfiguration maneuver could be individually investigated to complement the present work. The inclusion of each of these parameters in the optimization process, however, increases the current number of independent variables of set $\boldsymbol{S}$ from 15 to at least 20 (one per spacecraft). This could further affect negatively the computation time.

SIMULATION PARAMETERS

If all of the methods described above fail to produce a measurable change in compliance with $F_{per,i} < 20$ mN, it may be warranted to revise high-level system requirements and mission drivers. For instance:

- for cases where no solution is found by the CAM algorithm within a reasonable amount of time, the ReM could be run again for the same science task such that a new final position is calculated and used by the CAM. Additionally, a modified ReM routine that takes into account the CAM constraints (collision avoidance, intervisibility and relative position estimation accuracy) could be used to generate new final positions.

- if a science task is of extreme importance, but requires $F_{per,i} > 20$ mN, the primary propulsion system could instead, and exceptionally, be activated for the associated CAM maneuver
- similar to what has been proposed in Chapter 8, alternative strategies for sampling targets should be sought in the pursuit of optimal science performance. If the target separation for two consecutive science tasks is small enough (e.g., less than 5°), then perhaps reconfiguration maneuvers should indeed be forgone such that the spacecraft only change their attitude.

10.5. CHAPTER SUMMARY

THE CAM module is proposed for refining trajectories associated with the ReM which contain either violations of proximity limits among spacecraft or periods of invisibility between the laser links. Its setup resembles that of the ReM, in that alternative maneuvers are sought in terms of minimization of fuel and fuel differences or of ΔV and ΔV differences. The final positions and the time to complete the collision- or invisibility-avoidance maneuver are dictated by the ReM. A mesh-adaptive direct search is equally reused as the optimization algorithm. However, safety constraints are imposed on the algorithm, namely the avoidance of collisions and invisibility periods with a duration of 4.7 hours to ensure that the uncertainty of the relative distance measurements does not surpass the one-meter limit during reconfigurations.

The analysis conducted in this chapter provided valuable insights into the rate at which violation of constraints occur for ReM-generated maneuvers, the onboard physical and computational resources required for bypassing these transgressions, their dependence on the number of pairs involved and the violation type (collision or invisibility).

Up to 6% of the ReM trajectories require an avoidance maneuver for homogeneous, IRASSI-type formations. The need for alternative trajectories due to invisibilities and collisions, is highest for a small fuel imbalance (1.35 kg) concentrated on one spacecraft (Tours B.3). Interestingly, collision and invisibility transgressions are rarely present in the same ReM trajectory. This is owed to the fact that the collision risk arises largely for short ReM distances and invisibility instances for long-duration, long-distance ReM maneuvers.

Although differences between the additional fuel and ΔV required for executing a CAM maneuver were detected for respectively the J_f and the $J_{\Delta V}$ cost functions, these are merely attributed to the stochasticity of the optimization algorithm. Over 300% more resources may be required compared to that of the initially calculated by the ReM. This is accompanied by over 100% more resource differences among formation elements. Results also showed that not only did invisibilities require between 2.5 and 3.5 times more resources than collisions compared to the original ReM-calculated resources, the average computation time for generating an invisibility-free trajectory, at over 8 minutes, was double that of producing collision-free maneuvers. Because the ReM takes one order of magnitude less time to produce a new solution, it is proposed to investigate a new setup of iSCOUT in the future, whereby a second run of the ReM is called when the first run produces a trajectory with violations involving several pairs of spacecraft. This second iteration of the ReM could formulate a new final position of the reconfiguration maneuver by taking into account the CAM (collision-avoidance and intervisibility) constraints. This may prove to expedite computations instead of forcing the CAM to find alternative paths for fixed final formation positions.

Although a solution within the initially imposed thrust limit of 20 mN is found for the majority of the ReM-generated trajectories with violations, there is at least 25% chance that the thrust magnitude is not enough to seek viable alternatives, particularly when violations involve more than three or four pairs of spacecraft. Increasing the thrust limit to 200 mN solved all of the remaining trajectories for homogeneous and wet-mass imbalanced formations (Tours B.1 and A respectively), but had a negligible impact on fuel-imbalanced cases (Tours B.2 to B.5). For overcoming this issue, recommendations for further investigation include changing the thrust profile during CAM maneuvers and studying the feasibility of using the primary propulsion system for exceptional reconfiguration maneuvers to ensure compliance with the safety constraints (minimum separation distance and intervisibility).

The CAM module is called intermittently, as instances of constraint violations are detected in the ReM trajectories. It receives the reconfiguration-maneuver data and makes the necessary modifications. Once this step is completed, the CAM returns the information to the iSCOUT coordinator that proceeds to disseminating and ordering the planning and execution of the maneuvers to each spacecraft. ReM and CAM maneuvers precede science observations. The next module, the Baseline Pattern Module (BPM), calculates the patterns that spacecraft follow during the expansion or contraction of the formation. The BPM thus takes over once the spacecraft have arrived at their final reconfiguration destinations.

11

Optimization of Baseline Patterns

The meeting of two personalities
is like the contact of two chemical substances:
if there is any reaction, both are transformed.

Carl Gustav Jung

ABSTRACT

The Baseline Pattern Module generates trajectories associated with the science observations. These entail a very low magnitude initial thrust to change the length of the baselines, by either contracting or expanding them. The thrust is applied for a certain duration of time, followed by a coasting phase and another (symmetric) thrusting stage. It is during the coasting phase that observations take place as no operation of the engines is allowed due to the sensitive payload. In order to compute the BPM maneuver, a two-step optimization process is devised. The first step selects the final positions of the spacecraft according to desired patterns and strict geometric constraints and the second one determines the magnitude and duration of individual thrusts. Both steps employ a mesh-adaptive pattern search for optimization. Results show that thrust magnitudes in the mN range suffice for the majority of tasks, whilst keeping ΔV expenditure within 0.35 $m\,s^{-1}$. The constraints are fulfilled and preliminary response functions associated with the formation baseline patterns are simulated.

Credits for the relative positioning method used in this chapter are owed to Dr. Kathrin Frankl and MSc. Mathias Philips-Blum (Institute of Space Technology and Space Applications, University of the German Federal Armed Forces, Munich, Germany). The development and analysis of the method which calculates the response function of the interferometer was performed jointly with Dr. Hendrik Linz (Planet and Star Formation Department, Max Planck Institute for Astronomy, Heidelberg, Germany).

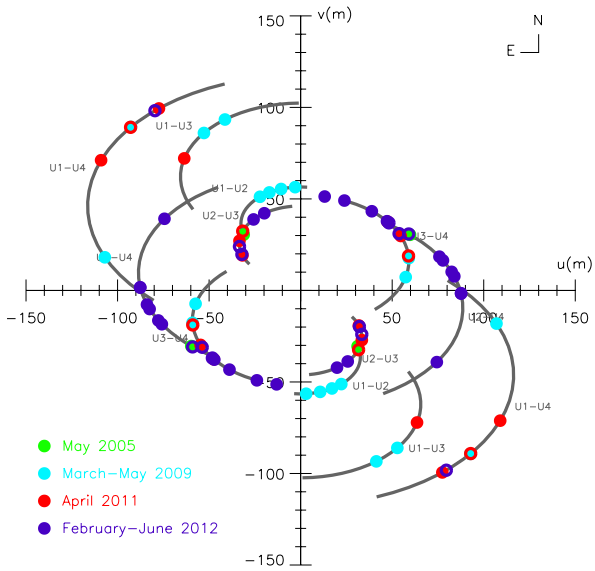

Figure 11.1: *(U, V)*-plane coverage (on-sky orientation) of the mid-IR interferometric observations of NGC 3783, a spiral galaxy of the Centaurus constellation. The different colors represent the various observing runs in 2005 May (green), 2009 March and May (light blue), 2011 April (red), and 2012 February to June (violet). Source: Hönig et al. (2013) [152].

11.1. INTRODUCTION

AFTER spacecraft have reached their final reconfiguration positions, the science-related activities commence. These include not only the re-calibration of the science instruments if required, but crucially the completion of observation tasks as well as the computation and execution of the maneuver that initiates the expansion or contraction of the baselines.

The Baseline Pattern Module, BPM, is responsible for the planning of the baseline change maneuvers. More specifically, its goal is to prescribe the linear trajectories which the spacecraft must follow during the observations in a resource-efficient and resource-balanced manner. The patterns generated by these trajectories result in bespoke *(U, V)*-plane coverage and response functions which must be fused with target measurements made by the interferometer. Since only suitable response functions can be used for interferometry and there is a dependency of these on the formation baselines for every instant the measurements are taken, the trajectories must be designed according to predefined science requirements. The requirements loosely dictate the drift velocities, the direction of motion or the scanning length during BPM maneuvers. This target-constrained sampling approach places the focus on the maximization of science return, whilst simultaneously considering the avoidance of collisions, invisibility events and sky obstruction in the planning of these maneuvers.

The mapping from physical space to the *(U, V)*-plane is many-to-one as there is an infinite number of physical configurations which result in a single (u, v) coordinate. Altogether, the content outlined in this chapter concerning the mapping of physical space onto the interferometric response functions reflects preliminary efforts in finding optimal formation trajectory patterns which enable the generation of desirable astronomy images that ultimately contribute to the furthering of our current understanding of phenomena in the far-infrared.

11.2. PREVIOUS CONTRIBUTIONS

THE patterns obtained when sampling the sky are directly associated with the type of interferometry instruments and the location of the interferometers. For instance, ground-based interferometers observing the sky produce curved patterns in the *(U, V)* map due to the Earth's rotation. Such an example is given in Figure 11.1, using the mid-infrared beam combiner instrument *MIDI* of the VLTI in Chile.

Space-based interferometers do not have the luxury of achieving the same natural rotation at the same time scales. Alternative strategies of sampling the sky can be sought by exploring environmental perturbations that induce relative accelerations [153, 154] in the case of free-flying interferometers, particularly if located in the vicinity of Earth. DeCou shows, however, that formation flying strategies that require pro-

pellant expenditure beyond station-keeping are not viable for low-Earth orbit constellations with propulsive efficiencies lower than I_{sp} = 3000 s. Hussein and Scheeres. [155, 156] devise closed-form analytical solutions that predict image quality for a minimum number of passive satellites in a formation distributed in a plane or line and for circular sun-synchronous, eccentric or perturbed orbits [155, 156]. The image quality optimization procedure is framed as that which supplies a maximum of pixels of resolution in the coverage plane. Linear formation arrangements around the Earth are suited to formations with sufficiently small maximum baselines (or conversely, requiring an orbit with a sufficiently high orbit radius).

In deep space, the only mechanism to generate trajectories that produce suitable images is to use thrusters. Hussein et al. [157] propose an intermittent thrusting strategy for dual-spacecraft interferometry, whereby the spacecraft follow a path on Riemannian manifolds. The manifolds are constructed by applying geometry constraints. The constraints involve defining a paraboloid virtual structure along which a thrust-induced spiral evolves. The spiral defines coverage characteristics, whereas the depth of the paraboloid determines the focusing properties of the apertures. The motion-planning problem is formulated in an optimal control setting, using time as an independent variable on a single objective function that uses a weighted sum of fuel expenditure and image quality. Image quality is given as a function of the signal-to-noise ratio, which is maximized by minimizing the relative speeds between the spacecraft in the formation. As explained by the authors, as a spacecraft moves more slowly, more time is spent in the neighborhood of a relative position state in space. This leads to more photon collection at that state, and thus a stronger signal. Although it may seem that minimizing fuel consumption is equivalent to minimizing relative speeds (and thus maximizing image quality), the authors show in previous work [158] that a tradeoff is necessary. Attitude and maintenance of line-of-sight are not considered.

Chakravorty and Ramírez [159] frame the calculation of fuel-optimal maneuvers as a traveling salesman problem for multi-element interferometry missions following spiral trajectories. Imaging maneuvers correspond to consecutively reaching different positions in cylindrical coordinates (r, θ) at each point in time in the plane normal to the target direction. Their results show that efficient imaging maneuvers require a tradeoff between the total time allowed for the maneuver, the number of satellites in the formation and the propulsion system. Fuel-optimal solutions typically correspond to the loosest spirals, that is, the spiral with the maximum possible spiraling rate $\frac{\partial r}{\partial \theta}$. Additionally, as the number of satellites in a constellation increases, shorter maneuver times are required and the total fuel cost of an imaging maneuver is reduced. As an example, using electric propulsion (I_{sp} = 7000 s) and considering 8 spacecraft executing one hundred imaging maneuvers, each over 24 hours would require 63% of their launch mass to be propellant. With their design, the authors prove that imaging solutions are feasible for multispacecraft formations using state-of-the-art propulsive technologies, both in deep space and in the near-Earth environment.

Complementing the latter is the extension to cases where the target direction changes with time and, similarly, where the relative distances to the target are time-variant in orbits around the Earth [160]. Both of these cases involve re-designing the cost function to include a closed-loop controller. Other sampling strategies involved previously introduced 'rigid-body' formation rotations about a point in space [79] and three-dimensional constrained [71] (or fixed configuration) and unconstrained [138] rotations in space.

These are all interesting points of departure for devising a strategy that fulfills imaging requirements for the IRASSI mission. Their lack of applicability to the IRASSI case, however, is largely motivated by the fact that the mission is currently designed for avoiding the usage of thrusters in-between target samples. The change of the baselines is initiated by the thrust, but during the observations, the spacecraft must strictly passively drift. Additionally, spiral trajectories have not been evaluated in terms of line-of-sight maintenance ability between elements. The fact that each spacecraft have four laser links to their neighbors which must remain visible throughout observations, makes a spiral-like trajectory challenging unless several laser terminals are provisioned for each pair link.

To avoid mixing science performance metrics with functional metrics, such as fuel usage, in a single objective function as done in previous work [155–158], a two-step optimization is devised. The first step uses target-specific catalog information to derive an envelope of suitable geometries constrained by a set of geometric and functional requirements. The second one uses onboard resources expenditure (fuel and/or ΔV) and balance.

11.3. BASELINE PATTERN MODULE (BPM)

THE BPM receives parameters associated with the next observation (or a sequence of tasks) as an input from the mission catalog as well as the final reconfiguration positions in the inertial frame S_0 calculated

by the ReM module. The latter are used as initial positions for the calculation of the BPM science trajectories.

Similar to the ReM, the trajectories designed by the BPM consist of three phases (bang-coast-bang), whereby the drifting phase (or coast) corresponds to the science observation. The differences lie in the fact that in this case, all spacecraft are allowed to drift (versus only four in the ReM) and the thrust magnitudes are allowed to differ among formation elements (which was fixed in the ReM), such that the start of observations is synchronized among all formation members.

11.3.1. *(U, V)*-PLANE COVERAGE REQUIREMENTS

Achieving desirable pattern combinations of the formation baselines is one of the most critical functions of iSCOUT. The relationship between formation geometry and its mapping onto the *(U, V)*-plane has been detailed in section 4.2.5. It will be shortly summarized here.

Ground-based telescope arrays take advantage of Earth's natural rotation to produce curved patterns in the plane. This natural rotation is obviously not available in the vicinity of L_2 and the spacecraft must be thrusted to initiate coverage. Different combinations of relative positions, relative drift rates and even attitudes produce different coverage patterns. Due to internal calibration requirements and the high sensitivity of the onboard instruments, continuous operation of the thrusters is discarded during observations and hence the resulting trajectories and generated patterns are straight ones.

Although there is no universal optimal *(U, V)*-plane coverage or a simple figure-of-merit, certain characteristics which generally determine suitable coverage are:

- asymmetry in motion: for instance, regularly-spaced spacecraft, with the same drift rate degenerate the synthetization procedure
- symmetry in the interferometric beam: the more uniquely covered areas of the plane, the better. The formation should expand or contract in different directions and with different lengths; uncovered areas in the *(U, V)*-plane coverage should be kept small since these will boost the unwanted sidelobes in the so-called 'dirty beam' of the interferometer, which is the response function of the interferometer to the incoming brightness signals [24].

These two requirements seem to compete with each other, as the more asymmetric the drift rates, the less likely the patterns will cover unique portions of the plane. There is thus a confined region of the solution space which can be used for trading of these requirements. Since attitude maneuvers are not considered in iSCOUT, optimization of plane mapping becomes then a function of fine-tuning the relative drift rates given a set of initial positions. An example showcasing undesirable and desirable patterns is provided in section 11.3.3.

11.3.2. METHODOLOGY

During observations, the formation will either expand or contract in order to cover as many unique points in the *(U, V)*-plane as possible. An expansion or contraction maneuver associated with science activities is thus designated a BPM maneuver. The starting position of the spacecraft is the final position of the reconfiguration maneuvers computed by the ReM module.

In order to abide by the science requirements and ensure the feasibility of the maneuver, a two-step optimization approach is devised: the first step seeks to find the best scanning patterns in the *(U, V)*-plane at the end of the maneuver considering geometric formation configuration limitations which affect, for example, intervisibility or minimum proximity limits. The second step sizes the thrusting phase and thrusting magnitude of each formation individual while minimizing and balancing fuel or ΔV consumption. Using a multi-variable, multi-objective optimization routine (instead of the two-step approach) was discarded in order to explicitly prioritize science over resource management.

BPM STEP 1: BASELINE PATTERN OPTIMIZATION

The first step of the BPM uses the final three-dimensional coordinates of each spacecraft as the independent variables to quantify the asymmetry of the polygonal shape of the formation projected in the *(U, V)*-plane. The resulting projection is expressed in *(u, v)* coordinates. With the shape that is produced from this projection, the five central angles δ (as measured by two consecutive vertices) and five interior angles β are measured, as illustrated in Figure 11.2. Using only one of either of these parameters would conflict with the desirable sampling of different areas in the *(U, V)*-plane, highlighted in Section 11.3.1.

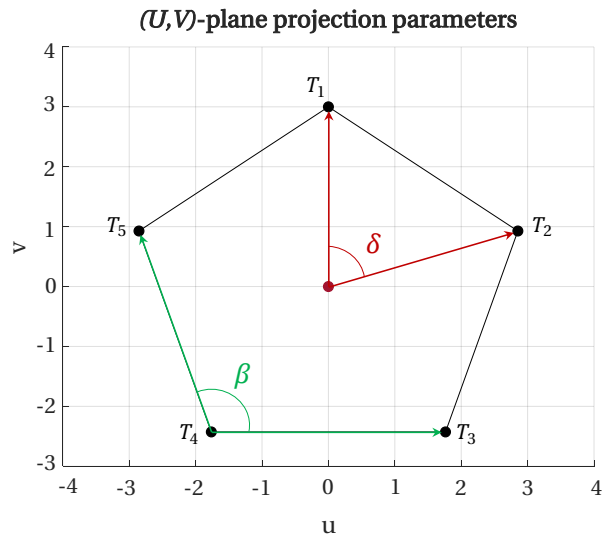

Figure 11.2: *(U, V)*-plane projection parameters for BPM: central angle δ (red) and interior angle β (green).

The independent vector set $\boldsymbol{Y}$ contains the three-dimensional coordinates of each spacecraft in the local S_N frame (cf. Section 7.4), a total of 15 variables:

$$\boldsymbol{Y} = \{x_{N,i}, y_{N,i}, z_{N,i}\} \tag{11.1}$$

From these coordinates, the projection of the trajectories in the *(U, V)*-plane is computed and the optimization scheme returns the solution $\boldsymbol{Y_{BPM}}$ which maximizes the following cost function:

$$J_{BPM,1} = \sum_{l}^{n} \sum_{m:m>l}^{n} |\delta_l(t_{BPM}) - \delta_m(t_{BPM})| + \sum_{l}^{n} \sum_{m:m>l}^{n} \left|\beta_l(t_{BPM}) - \beta_m(t_{BPM})\right| \tag{11.2}$$

where the subscripts l and m are the vertices of the polygon, coinciding with the projected positions of the five telescopes, $\{T_1, T_2, T_3, T_4, T_5\}$, n is the total number of vertices in the polygon ($n = 5$) and t_{BPM} is the total maneuver duration time:

$$t_{BPM} = 2t_{w,BPM} + t_{sci} \tag{11.3}$$

which is composed of two short symmetric impulse phases $t_{w,BPM}$ and the time allocated for the observation of the target, t_{sci}. The calculation of t_{sci} is addressed in the next subsection.

The first part of Equation 11.2 addresses the difference between two consecutive central angles at the end of the maneuver. Each central angle is defined by a vector connecting the origin of the *(U, V)*-plane and the (projected) positions of two spacecraft i and j (which form two consecutive vertices):

$$\cos\delta_l = \frac{(u_i, v_i)\cdot(u_j, v_j)}{||(u_i, v_i)\cdot(u_j, v_j)||} \quad l = 1, \ldots, n \tag{11.4}$$

Each pair of consecutive central angles share therefore one vertex. Similarly, the second part of the objective function concerns the sum of the differences between the five interior angles after the BPM maneuver. Each interior angle connects three vertices, i, j and k, and is defined by two vectors according to the following formula:

$$\cos\beta_l = \frac{(u_i - u_j, v_i - v_j)\cdot(u_k - u_j, v_k - v_j)}{||(u_i - u_j, v_i - v_j)\cdot(u_k - u_j, v_k - v_j)||} \quad l = 1, \ldots, n \tag{11.5}$$

It must be remarked, however, that the objective function defined by Equation 11.2 can only be used in its current form if a set of geometrical conditions are met: namely, if the relative order of the vertices is the same before and after the BPM maneuver. That is, each δ_l angle is defined by the same spacecraft i and j, at $t = 0$ and at $t = t_{BPM}$. The same applies to the five β_m angles, which must be individually defined by the same i, j and k telescopes. This is ensured both by constraining the optimization algorithm and setting strict upper

and lower bounds on the independent variables of set $\boldsymbol{Y}$ according to the scientific requirements associated with the target being observed.

Because the solution space is confined to acceptable regions to a large extent due to catalog-based parameters and thus via the selection of the upper and lower bounds of the independent variables, the search for the solution set $\boldsymbol{Y_{BPM}}$ becomes typically one in which feasible regions around constraints are easily found. There is thus not a significant advantage in using intricate optimization methods (e.g., highly stochastic or gradient-based). As such, due to its reliability, the MADS previously used in the ReM and CAM module is also used in the BPM module.

The constraints are imposed on the optimization function in order to accommodate for predefined desired scanning patterns associated with the target as well as other functional requirements, described in Chapter 4. The full list of constraints is summarized in Table 11.1 and shortly described thereafter. It is clear from Table 11.1 that due to the different nature of the constraints, they are described in different reference systems. The first two (collision avoidance and intervisibility) also apply to the CAM module.

Collision avoidance It ensures that the final positions in inertial space do not violate safety requirements. The minimum safety distance parameter γ is set at $\gamma = 10$ m. This constraint is mostly applicable for contraction maneuvers.

Intervisibility In order to ensure that the projected patterns in the *(U, V)*-plane do not result in formation configuration solutions that impair the ranging system lasers from linking to each other (at end of the expansion/contraction maneuver), this condition is imposed. The angle θ_{ri} refers to the angle of range invisibility and is a function of the spacecraft's mechanical configuration, such that θ_{ri} =32.55° (cf. Chapter 4).

In Step 1 intervisibility is evaluated solely at $t = t_{BPM}$. Step 2 handles intervisibility during the maneuver. Differently from the CAM, intervisibility must be guaranteed at all points in the BPM trajectory, instead of intermittently during reconfiguration, due to heterodyne detection and onboard correlation processes.

Baseline estimation accuracy Chapter 4 introduced the baseline estimation procedure, whereas a preliminary evaluation of the baseline in free-dynamics conditions over a span of 8 days was provided in Chapter 5. Its use in the context of science activities is now explored.

Whereas the coverage of the *(U, V)*-plane is evaluated in (u, v) coordinates, the baseline estimation accuracy is dependent on the geometry of the constellation in three-dimensional space, as well as on the relative attitude between spacecraft. The baseline estimation accuracy requirement prevents thus the optimization algorithm from finding post-maneuver positions in inertial space which violate the baseline estimation accuracy of 5 µm.

In a real mission setting, relative distance measurements (from the ranging system) and relative attitude measurements (from star trackers together with the ranging system) are used to estimate the baselines. In the simulated environment, the absolute positions of the spacecraft in the inertial frame S_0 are used instead to derive the sensor measurements and thereafter, to determine the formation baselines and the associated accuracies (cf. Figure 4.7).

First, a local swarm coordinate system using a spacecraft as a reference (origin), named SV1, is initialized. The x-axis is described by a line connecting the telescope reference points of SV1 and a second spacecraft, named SV2. A third spacecraft, named SV3, is located in the x-y-plane (see Figure11.3(a)) and defines the y-axis. The z-axis completes the right-handed coordinate system and has the same direction as the z-axis of the satellite's body coordinate system (shown in Figure 11.3(b)). Next, the inertial coordinates of the five SVs are transformed into this local system. The formulas of the transformation can be found in previous work of Philips-Blum *et al.*. 2018 and the method is also addressed by Frankl *et al.* 2017.

Now, the true baselines between the telescope reference points (the detectors) and the true distance vectors between the ranging sensors are determined from the transformed true coordinates. Further, two major sources of errors are introduced in the measurement chain: distance measurement errors and attitude errors. The distance measurement errors emulate those introduced by the ranging system. These distance measurement errors are modeled as random, Gaussian-distributed, with zero mean value and a standard deviation of 1 µm. The attitude errors simulate those originating from star-trackers and the angular measurements of the ranging system. The errors are associated with each of the three orientation angles α of each satellite, having also a Gaussian distribution, but with a standard deviation of 0.1 arcsec. These assumptions concerning the sensor errors result from internal project estimations.

Table 11.1: Nonlinear constraints for BPM Step 1. Constraints marked with '*' are also implemented on Step 2 and evaluated at all time steps, $\forall t \in \{t_0, \ldots, t_{BPM}\}$.

Constraint (ref. frame)	**Expression**
Collision avoidance* (S_0)	$\sqrt{\left[x_{0,i}(t_{BPM}) - x_{0,j}(t_{BPM})\right]^2 + \left[y_{0,i}(t_{BPM}) - y_{0,j}(t_{BPM})\right]^2 + \left[z_{0,i}(t_{BPM}) - z_{0,j}(t_{BPM})\right]^2} \geq \gamma,$
Intervisibility* (S_T)	$\sqrt{\left[x_{T,i}(t_{BPM}) - x_{T,j}(t_{BPM})\right]^2 + \left[y_{T,i}(t_{BPM}) - y_{T,j}(t_{BPM})\right]^2} \geq \left\|z_{T,i}(t_{BPM}) - z_{T,j}(t_{BPM})\right\| \tan(\theta_{ri})$
Baseline estimation accuracy* (S_0)	$b_{ij}(t) \leq 5\mu\text{m}$
Sky access* (S_N)	$\sqrt{\left[y_{N,i}(t_{BPM}) - y_{N,j}(t_{BPM})\right]^2 + \left[z_{N,i}(t_{BPM}) - z_{N,j}(t_{BPM})\right]^2} \geq \left\|x_{N,i}(t_{BPM}) - x_{N,j}(t_{BPM})\right\| \tan(\theta_{ez}),$
Scanning length (UVW)	$\sqrt{[u_i(t_{BPM}) - u_i(t_0)]^2 + [v_i(t_{BPM}) - v_i(t_0)]^2} \leq b_{des} \cdot (1 + tol)$ (Maximum) $\sqrt{[u_i(t_{BPM}) - u_i(t_0)]^2 + [v_i(t_{BPM}) - v_i(t_0)]^2} \geq b_{des} \cdot (1 - tol)$ (Minimum)
Disjointed projected trajectories (UVW)	If $L_i = \{(u_i, v_i) \mid v_i = (u_i - u_i(t_0)) \frac{v_i(t_{BPM}) - v_i(t_0)}{u_i(t_{BPM}) - u_i(t_0)} + v_i(t_0)\}$ and $L_j = \{(u_j, v_j) \mid v_j = (u_j - u_j(t_0)) \frac{v_j(t_{BPM}) - v_j(t_0)}{u_j(t_{BPM}) - u_j(t_0)} + v_j(t_0)\}$, then $L_i \cap L_j = \emptyset$

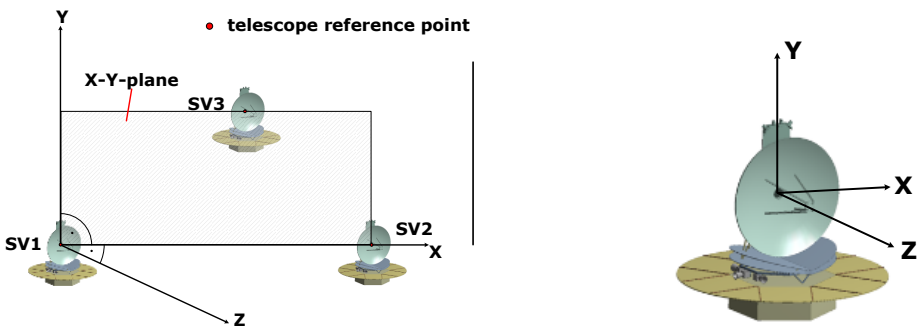

(a) Swarm coordinate system

(b) Satellite coordinate system

Figure 11.3: Local swarm coordinate system (left), satellite coordinate system with telescope reference point (red) (right) for the baseline estimation procedure.

The following step is the generation of initial guesses for the positions of the telescope reference points. Using these positions and the orientation angles α, an approximation value for the distances between the sensors is computed, as shown in Equation 11.6. The result of this formula is the computed distance $d_{i\to j}^{sat\,i}$ (Figure 4.7, rel. pos. algorithm) between the sensors of satellites i and j given in the coordinate system of satellite i. Other parameters are the telescope reference points $\boldsymbol{p}_i^{form}$,$\boldsymbol{p}_j^{form}$ of each satellite defined in the swarm coordinate system as well as the lever arms $\boldsymbol{l}_i^{sat\,i}$,$\boldsymbol{l}_j^{sat\,j}$ in the respective body-frame coordinate systems. The lever arm is the position vector of the sensors relative to the telescope reference point. The last parameters are the rotation matrix $\boldsymbol{R}^T\left(\boldsymbol{\alpha}_j^{form}\right)$ to rotate the lever arm l_j into the swarm coordinate system and the matrix $\boldsymbol{R}\left(\boldsymbol{\alpha}_i^{form}\right)$ to rotate a term from the swarm coordinate system into that one of satellite i. The parameter $\boldsymbol{\alpha}$ is a vector containing the three orientation angles of the satellites in the inertial system.

$$d_{i\to j}^{sat\,i} = \left\|\boldsymbol{R}\left(\boldsymbol{\alpha}_i^{form}\right)\cdot\left(\boldsymbol{p}_j^{form} - \boldsymbol{p}_i^{form} + \boldsymbol{R}^T\left(\boldsymbol{\alpha}_j^{form}\right)\cdot\left(\boldsymbol{l}_i^{sat\,i}\right)\right) - \boldsymbol{l}_i^{sat\,i}\right\|_2 \tag{11.6}$$

In the estimation step, a trilateration problem is solved by least-squares optimization to determine the relative positions of the telescope reference points.

A further step in the relative positioning algorithm is the calculation of the design matrix. This is done by the differentiation of Equation 11.6 with respect to the unknown positions of the telescope reference points. The equation system is finally transformed into a normal equation system, with the difference of the measured and computed distances as measurements and the corrections of the initial telescope reference points as unknowns. The algorithm runs several iterations until a threshold value for the correction of the estimated positions will be reached. In the last step, the final baselines can be compared to the true baselines, yielding $\hat{b}_{ij}$.

In a five-element formation, there are 20 one-way measurements (each of the 10 baselines is independently estimated by the two laser links of a pair of spacecraft). If any of the 20 measurements in $\hat{b}_{ij}$ exceed the required 5 µm for a given variable set $\boldsymbol{Y}$, the baseline estimation accuracy constraint is violated. This solution is then discarded and the algorithm proceeds to finding a new variable set.

The imposition of this constraint in Step 1 ensures that the final positions of the BPM maneuver result in a constellation geometry which complies with the baseline estimation requirements, whereas Step 2 addresses the baseline estimations' accuracy *during* the maneuver.

Sky Access This constraint prevents the occultation of the target by ensuring that at no point during the drift there is an incursion of neighboring telescopes in the field of vision of one another. The issue of accessing the sky and the geometry of these parameters was described first in section 4.2.4. Within iSCOUT, targets are firstly selected prior to proceeding to the position optimization of the formation - a procedure titled 'target-constrained sampling'. The role of this constraint is to ultimately prevent a drift pattern that results in the spacecraft violating a volume of space which must be unobstructed for a proper target observation.

The semi-angle of the cone which determines an exclusion area, θ_{ez}, is a function of the telescope's field of view. Apart from the pure geometrical target occultation, a safety margin to account for diffraction effects

that broaden the reception pattern of an antenna was included (see the contributions of Napier 1999 for details). At the longest operational wavelengths of IRASSI (300 µm), the center of the primary beam of an IRASSI antenna will have a FWHM[1] of ≈19″ (cf. Table 2.1). It is assumed that, in addition to the geometric cross-section, the antennas have to obey an additional angular separation of $\frac{19''}{2} \times 10$ in order to be outside of the innermost antenna reception side lobes. The θ_{ez} is thus scaled as $\theta_{ez} = \frac{19''}{2} \times 10 = 0.026°$.

Scanning length This constraint imposes a minimum and maximum pattern scanning length. The variable b_{des} is the target-related scanning length, available from the mission catalog and tol specifies a tolerance around this prescribed value. This adjustment factor can be specified by the user, adjusted to each target and/or each spacecraft, varying between $-1 \leq tol \leq 1$. Typically, the larger the value, the larger the solution space and hence the higher the potential value of $J_{BPM,1}$, but the longer the algorithm takes and less control over the final pattern one has, making unpredictable outcomes of the final Fourier-transformed response function $G(u, v)$ more likely. The default values for IRASSI are $tol = \pm 0.2$, the sign of which is adjusted depending on whether an expansion or contraction maneuver is considered.

Disjointed projected trajectories The initial coordinates of the formation, delivered by the ReM, ensure that projected *(u, v)* coordinates fall on each of the *(U, V)*-plane's quadrants. To maintain this distribution during the BPM maneuver and to guarantee that *(U, V)*-plane is covered as much as possible, no intersections of the projected trajectories are allowed.

BPM STEP 2: RESOURCE MANAGEMENT OPTIMIZATION

The second step of the BPM calculates the thrust-impulse duration of the formation, $t_{w,BPM}$, and the individual thrust magnitudes of the spacecraft, F_i in order to ensure continuous intervisibility in a collision-free environment and with baseline estimation of sufficient accuracy, as the spacecraft reach their final positions $\boldsymbol{Y_{BPM}}$ (calculated by the first step of the BPM module). The vector set $\boldsymbol{Z}$ contains six independent variables:

$$\boldsymbol{Z} = \{F_{BPM,i}, t_{w,BPM}\} \tag{11.7}$$

where the maximum thrust duration $t_{w,BPM}$ and the thrust force can be specified by the user. By default, $t_{w,BPM}$ is restricted to $0 \leq t_w \leq 0.2\, t_{sci}$, where t_{sci} is the time allocated for the observation of the target. This means that, with two thrust impulses, the total t_{BPM} time can be, at most, 40% higher than the science duration t_{sci}.

The optimization goal is expressed as a fuel-based or ΔV-based (user-specified) objective function, similar to those used for both the ReM and the CAM, to ensure overall resource savings and resource balance among formation elements. Although the weighting parameter can be set by the user, its default parameters for the IRASSI case are $\mu_f = \mu_{\Delta V} = 0.05$, as determined in Chapter 9. The cost functions of Step 2 are summarized below:

$$J_{BPM,2_f} = J_f \Big|_{\mu_f = 0.05} \tag{11.8a}$$

$$J_{BPM,2_{\Delta V}} = J_{\Delta V} \Big|_{\mu_{\Delta V} = 0.05} \tag{11.8b}$$

where J_f and $J_{\Delta V}$ are described by Equations 9.2 and 9.3 respectively.

The trajectories are discretized in time steps of one second and the algorithm evaluates constraint violations at each step for each $\boldsymbol{Z}$ set. The optimization returns the solution set $\boldsymbol{Z_{BPM}}$ containing the thrusting time and individual magnitudes which simultaneously deliver the lowest amount of fuel consumption (or ΔV expenditure) during the science maneuver and the lowest post-maneuver summed fuel (or ΔV) differences.

Four of the constraints devised for Step 1 are applied to Step 2, as indicated in Table 11.1:

- Collision avoidance
- Intervisibility
- Baseline estimation accuracy
- Sky access

[1] Full width at half maximum

However, unlike Step 1, these constraints are evaluated for all $t \in \{t_0, \ldots, t_{BPM}\}$ instead of only on the final instant.

A MADS algorithm was also used for Step 2. However, similar to the CAM module, the initial conditions were subject to a multi-start selection process, using a random distribution, within the range values prescribed above for t_w and F_i.

MAPPING PHYSICAL SPACE ONTO THE INTERFEROMETRIC BEAM

The response function $G(u, v)$ of the interferometer is loosely obtained by measuring the baseline from the projected distances in the *(U, V)*-plane at each observation instance (i.e., 10 data points, corresponding to the 10 immediate baselines, per timestamp); mapping this information to a logical coverage matrix, with the origin of the data at its center, and Fourier-transforming the resulting matrix [161]. The result is a theoretical synthesized interferometric beam (called 'dirty beam', akin to a response function). The pseudocode below illustrates this process.

Algorithm 2 BPM transformation from physical space onto the interferometric beam.

```
Define:
Number of samples along trajectory: N_s

Require:
Five BPM trajectories in S_N frame: T_{S_N} ∈ ℝ

Initialize:
N_b = NumberBaselines(T_{S_N})
T_UVW = alignPlane(T_{S_N})
[u, v] = transformCoordinates(T_UVW)
B_uv = getBaselineMatrix(u, v)
uv_max = max(u, v)

for n_b = 1 : 1 : 2*N_b do
    for n_s = 1 : 1 : N_s do
        coverage(B_uv(n_b, n_s, 1)+uv_max, B_uv(n_b, n_s, 2)+uv_max) = 1
        coverage(~ B_uv(n_b, n_s, 1)+uv_max, ~ B_uv(n_b, n_s, 2)+uv_max) = 0
    end for
end for

Beam = FourierTransform(coverage)

function getBaselineMatrix(u, v)
    for n_b = 1 : 1 : 2*N_b do
        for n_s = 1 : 1 : N_s do
            for i = 1 : 1 : 4 do
                for j = i + 1 : 1 : 5 do
                    BaselineMatrix(n_b, n_s, 1)= ||u(n_s, i) − u(n_s, j)||
                    BaselineMatrix(n_b, n_s, 2)= ||v(n_s, i) − v(n_s, j)||
                end for
            end for
        end for
    end for
    return BaselineMatrix
end function
```

It should be mentioned that there is one last step in the image-processing chain from the part of the astronomy or science team. The real intensity distribution on the sky as measured by the interferometer is convolved with the synthesized beam to obtain the final target images (the so-called 'dirty images'). However, this step no longer involves the motion of the formation, instead, it relies on the previously-obtained dirty beam. The goal of the BPM is therefore to deliver a suitable dirty beam that can be convolved with the

Table 11.2: Comparison of BPM patterns using Step 1.

Metric parameter	**'Less desirable'**	**'More desirable'**
Sum of central angle δ_l differences (deg)	916.0	71.5
Sum of internal angle β_l differences (deg)	852.3	194.1

intensity distributions measurements.

11.3.3. EXAMPLE BPM PATTERNS

In order to illustrate the effect of the symmetry requirements addressed in Section 11.3.1, two examples of IRASSI-like maneuvers are given: one in which an undesirable pattern is achieved and one in which the opposite is true. To obtain the trajectories for the first case, hereby termed the 'less desirable patterns' case, the asymmetries are maximized without employing any of the constraints introduced in Section 11.3.2. In the second case, the 'more desirable patterns' case, the constraints are switched on in the asymmetry optimization.

These two examples are shown in Figures 11.4 and 11.5. Note how in the 'less desirable patterns' case of Figure 11.4(a), the difference between the scanning lengths is high (nearly two orders of magnitude difference among certain spacecraft pairs) and the spacecraft find themselves concentrated in certain regions of the Π_N-plane (e.g., T_1 and T_3, T_4 and T_5).

This extreme asymmetry of the 'less desirable patterns' is reinforced by the fact that the summed differences of central angles and internal angles are extremely high, as shown in Table 11.2. Recall that these angles are used to calculate the objective function of the BPM Step 1, in Equation 11.2.

The result of this is that the dirty-beam is largely asymmetric and there is no clear compact core at the center of the beam and thus the side lobes become faint only at extremely large $G(u, v)$ values (Figure 11.5(a) is zoomed in for viewing purposes). Conversely, in the 'more desirable pattern case', the mild asymmetries in spacecraft trajectories, that is the scanning length among formation elements, shown in Figure 11.4(b), result in a neat, evenly distributed lobe structure with a clear compact Gaussian core with lobes that fade radially quickly (Figure 11.5(b) is also zoomed in).

Although some asymmetry is desirable for a good *(U, V)*-plane coverage, this example illustrates the effect that the constraints have on the generation of a suitable geometry. With the imposed constraints the sum of differences of central angles or internal angles should never rise above ≈ 250°.

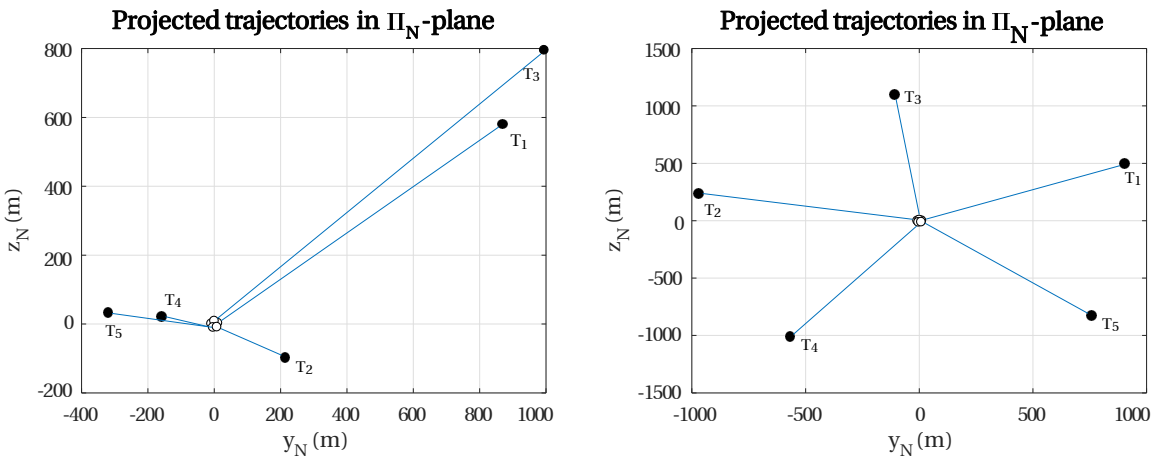

(a) Less desirable pattern

(b) More desirable pattern

Figure 11.4: Different patterns of the projected trajectories in the Π_N-plane.

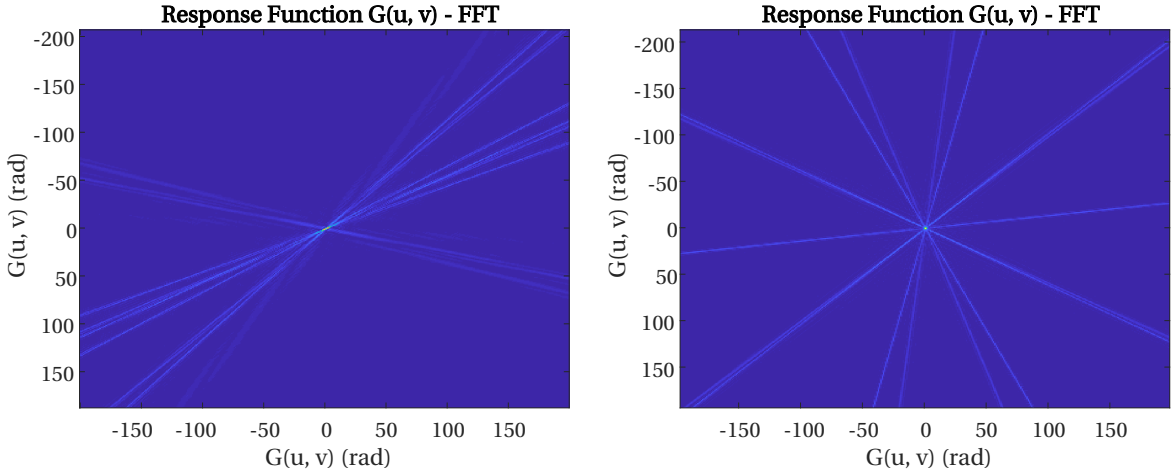

(a) Less desirable pattern

(b) More desirable pattern

Figure 11.5: Different patterns of the final response function $G(u, v)$, or 'dirty-beam', resulting from the projected trajectories.

11.3.4. EXAMPLE BPM MANEUVER AND ANALYSIS

As an example, a detailed analysis was carried out for two targets using the simulation parameters described in Section 11.3. The thrust duration of the BPM maneuvers is restricted to $0 \leq t_w \leq 0.2 t_{sci}$. The $F_{BPM,i}$ is capped at 200 mN, similar to the CAM module for guaranteeing convergence.

The two targets are identified by their order in the catalog: Target 232, corresponding to the small and faint Circinus constellation, and Target 163, a T Tauri disk called CITau. A maximum tolerance tol=0.2 was allowed for the generation of the trajectories and the ΔV-based optimization function $J_{BPM,2_{\Delta V}}$ with $\mu_{\Delta V} = 0.05$ was selected. The spacecraft were initialized with the parameters described in Table 11.3. The computed trajectory patterns, the corresponding *(U, V)*-plane coverage and dirty beam/response function (output of BPM Step 1) are shown from Figure 11.6(a) to Figure 11.8(b), for the two targets. The solutions in terms of applied thrust, BPM maneuver duration and expended fuel (output of BPM Step 2) are presented in Table 11.4.

The first maneuver involves a contraction of the baselines, from an initial in-plane (Π_N) separation parameter d=1000 m (cf. Section 7.5), requiring a nominal scanning length of $b_{des} = 500$ m. On the other hand, the second target demands a baseline expansion from an initial in-plane separation parameter $d = 10$ m and a scanning length of $b_{des} = 1000$ m.

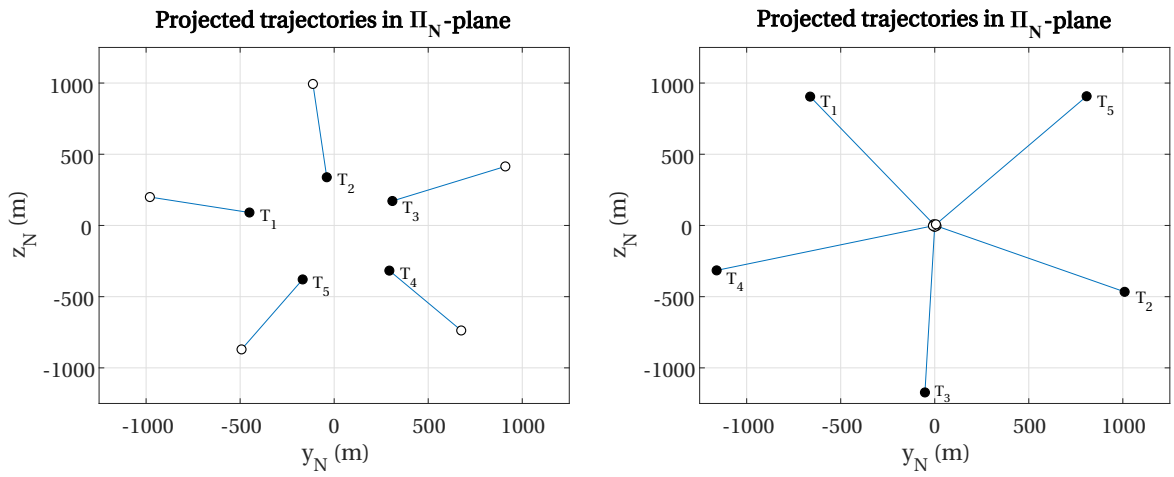

(a) Target 232

(b) Target 163

Figure 11.6: Projection of trajectories in Π_N-plane.

In Figure 11.6(a) and Figure 11.6(b), the distribution of the projected trajectories in the Π_N plane is shown,

Table 11.3: Simulation parameters for the Example BPM Maneuver.

Simulation parameter	**Value**
i	$\{T_1, T_2, T_3, T_4, T_5\}$
$I_{sp,i}$	2500 s
M_i	2300 kg
f_i	15 kg
$t_{w,BPM,max}$	$0.2\,t_{sci}$
γ (collision-avoidance)	10 m
τ_{crit} (invisibility-avoidance)	1 s
σ_d (baseline estimation)	1 µm
σ_v (baseline estimation)	0.1 arcsec
θ_{ez} (sky access)	0.026°
tol (scanning length)	±0.2
Optimizer	Mesh-adaptive direct search

Table 11.4: Summary of results of BPM's science trajectory patterns generation.

BPM Step	**Metric parameter**	**Target 232**	**Target 163**
-	Initial d (m)	1000	10
-	Scanning length b_{des} (m)	500	1000
Step 1	Sum of central angle δ_l differences (deg)	61.1	48.7
	Sum of internal angle β_l differences (deg)	161.9	81.4
Step 2	$t_{w,BPM}$ (hours)	1.47	14.3
	t_{BPM} (days)	0.97	7.85
	$F_{BPM,i}$ (mN)	$\{3.0, 7.2, 14.9, 13.3, 7.6\}$	$\{0.2, 0.4, 0.2, 0.1, 0.4\}$
	Total ΔV ($\mathrm{m\,s^{-1}}$)	0.21	0.05
	Sum ΔV diff. ($\mathrm{m\,s^{-1}}$)	0.28	0.06
	Drift velocity during observations ($\mathrm{mm\,s^{-1}}$, in inertial frame S_0)	$\{6.5, 15.4, 32.1, 28.7, 16.4\}$	$\{4.1, 7.4, 4.1, 1.8, 7.5\}$
	Drift velocity as projected on Π_N plane ($\mathrm{mm\,s^{-1}}$, S_N frame)	$\{6.5, 7.8, 7.7, 6.8, 7.0\}$	$\{0.7, 0.5, 0.5, 0.6, 0.6\}$

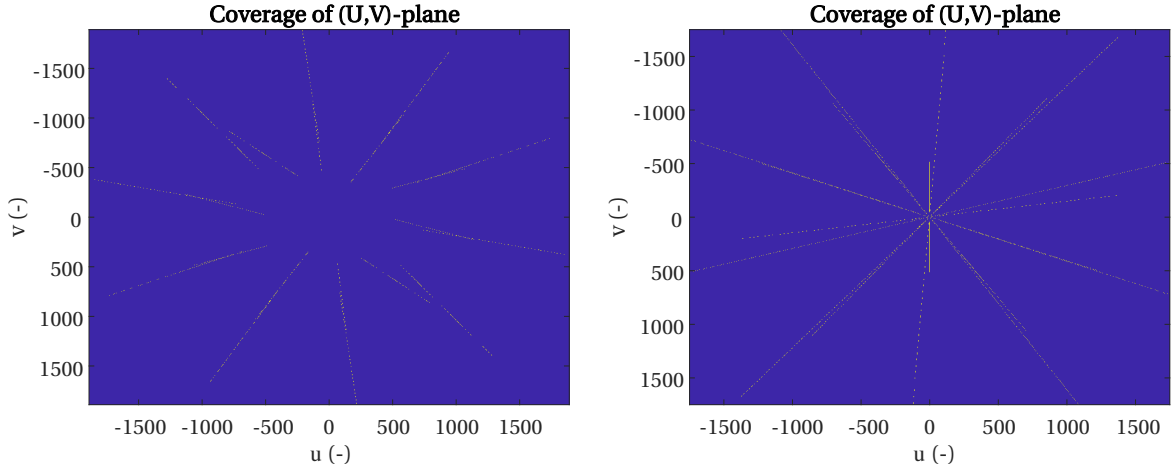

(a) Target 232 (b) Target 163

Figure 11.7: Coverage of *(U, V)*-plane associated with the baseline patterns.

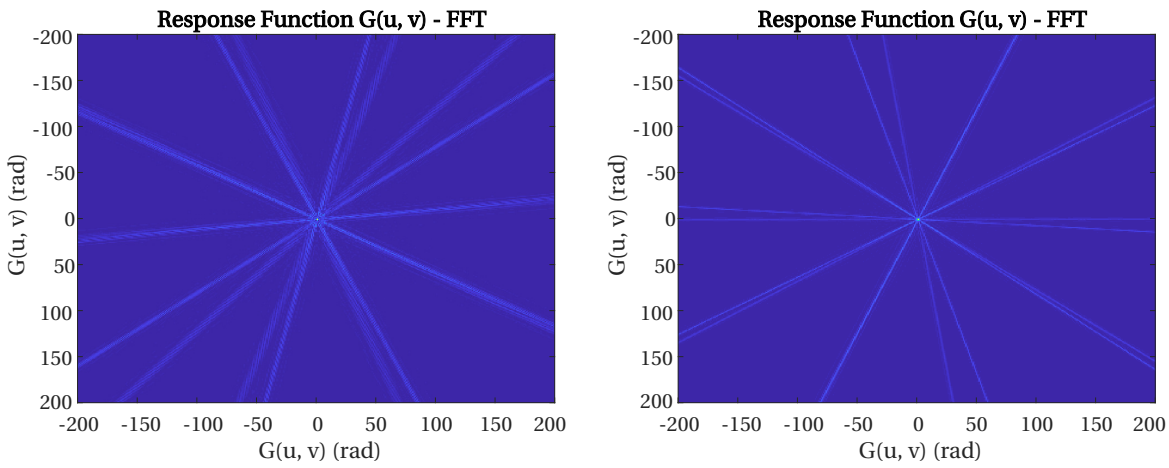

(a) Target 232 (b) Target 163

Figure 11.8: Response function ('dirty beam') associated with the baseline patterns.

with a portion of each of the quadrants covered, followed by the corresponding *(U, V)*-plane coverage. All imposed requirements are fulfilled. A compact core in the dirty-beam image forms; the side-lobes, due to the straight spacecraft trajectories, are also straight lines and are clearly weaker than the core. This is a desirable situation since the finally restored intensity distribution of an astronomical source will be the convolution of the real intensity distribution on the sky with this dirty beam. After all, this beam response then has to be removed from the final astronomical images by post-processing steps (e.g., CLEAN or maximum-entropy methods). The two cases are different in that for Target 163, a large range of baseline lengths (from short to long) is covered, while for Target 232 just intermediate and long baselines have been secured (which can be implemented for science targets that just need this high spatial resolution and where the science happens on the smallest spatial scales).

From Table 11.4, it is possible to observe that for long observation durations such as that of Target 163, resulting in $t_{BPM} \approx 7.85$ days, very low levels of thrust are required, with $F_{BPM,i}$ varying from 0.08 mN for telescope T_4 and 0.36 mN for T_5 and drift velocities in the order of $\mathrm{mm\,s^{-1}}$. The low level of $F_{BPM,4} = 0.08$ mN is mostly related to the fact that telescope T_4 remains in the vicinity of the plane Π_N throughout the BPM maneuver, moving in a near bi-dimensional trajectory, whereas the other spacecraft are required to move in three-dimensional space during the expansion and thus require more thrust force. Conversely, targets that must fulfill the scanning lengths over shorter observation times will drift with higher velocities. These reach

a maximum of 32.1 $\mathrm{mm\,s^{-1}}$ for Target 232, with thrust magnitudes $F_{BPM,i}$ of up to 14.9 mN in the S_0 frame. The magnitude of the drifts of the y_N and z_N coordinates, as projected in the Π_N plane varies between 6.5–7.8 $\mathrm{mm\,s^{-1}}$.

It should be remarked that achieving convergence to a solution for BPM Step 1 whilst guaranteeing that all requirements are fulfilled strongly depends on the initial conditions provided to the optimization solver. Namely, on the limits placed on the independent variable values. These limits reduce the solution space of the variables to a resulting envelope of acceptable geometries for which a constraint-violation-free solution is likely to be found. On the other hand, a mere 'dead-reckoning' approach, with a randomized initial guess is likely to be non-compliant with the imposed constraints even if it delivers an optimal solution, simply because certain requirements compete with each other: for instance, the baseline accuracy (defined as a constraint) and the asymmetry of the projected trajectory patterns (part of the cost function, cf. Equation 11.2). The more asymmetric the patterns, the more the baseline estimation accuracy degenerates due to high incursions of the telescopes on the x_N axis, and the more visibility issues are likely to arise. The baseline accuracy is a high-level mission requirement which must be fulfilled, as introduced Chapter 2, and is therefore as relevant as the achieved asymmetry. One alternative to this setup is to include certain terms, such as baseline accuracy, in the objective function and employing a multi-objective solver instead of a single-objective one.

11.3.5. CONCLUSIONS AND FUTURE WORK

This module aggregates several functional requirements for delivering optimal trajectories from a resource-usage and science point of view. Simulations have shown that there is a dependency of the consumed resources and drift velocities on the duration of the observation tasks (or t_{BPM}). The longer the t_{BPM}, the longer the spacecraft are allowed to coast and the slower they move relative to their initial positions, thereby saving ΔV resources. Conversely, shorter observation windows require faster maneuvers and the spacecraft will both spend more ΔV and have a less balanced post-maneuver ΔV distribution.

The work set out in this chapter circumscribes initial attempts to relate physical spacecraft separation and science performance in space. Future work goals in this context are described in the following subsections.

IMAGE-BASED OPTIMIZATION

The set of characteristics identified for producing general agreeable *(U, V)*-plane coverage, however, could be transferred to the final Fourier-transformed images, such that the pattern optimization is closer to the final synthesized images of the celestial targets, instead of being contained in intermediate steps. One could potentially optimize the brightness and the distribution of the lines on the dirty beam images by employing machine-learning and pattern-recognition algorithms which associate such arrangements with a suitable visibility function. For a good beam, the intensity levels of the outer parts of the beam image should be clearly fainter than for the central main peak. The central part of the beam image, on the other hand, should be compact and as close to a circular shape as possible.

ALTERNATIVE PATTERNS AND SCANNING STRATEGIES

Should technology advancements allow, other means of scanning the *(U, V)*-plane could be employed instead of linear expansion/contraction trajectories. Multiple-pulse thrusting or continuous thruster operation would yield respectively step-like and curved projected paths, such as the spirals introduced earlier in this chapter, and perhaps allow more uniform areas of the *(U, V)*-plane to be surveyed. An analysis of the effect of firing thrusters while operating sensitive instruments would have to be performed.

RELATIVE MOTION MODELS

The results presented in Chapter 5, have demonstrated that there is a continuous drift between spacecraft. This drift amounts to over 600 meters depending on the initial conditions of the formation. Because the spacecraft are assumed to be in free space in the current setup, not modeling gravity-induced disturbances may, in effect, not truthfully represent the trajectory patterns which are achieved for observation tasks which have a duration of several days. The inclusion of these disturbances should be part of future improvements of the BPM module.

11.4. CHAPTER SUMMARY

ASTRONOMY images produced by interferometers rely on measurements which must be correlated at each sample instance. The correlation involves temporal and physical separation information. Image quality is largely dependent upon the number of samples collected and the physical separation between spacecraft.

The BPM module was thus developed with the aim of generating optimal patterns in physical space that, when transformed to the spatial frequency domain, can contribute to producing meaningful infrared images.

These trajectories are computed by means of a two-step process. The first one guarantees that the response functions have a confined center with uniformly spread side-lobes with an intensity significantly weaker than the core. This is achieved by trading off asymmetries in the physical trajectories and drift rates with a minimum distribution of the trajectories in the physical Π_N plane. The second step addresses the means to achieve these trajectories, that is, the most resource-efficient and resource-balanced way to reach the final positions that use the thrusting time and magnitudes as independent variables. With a bang-coast-bang thrust profile, the observations take place during coasting. A set of constraints are imposed in the optimization process, namely intervisibility, baseline accuracy, sky access and desired scanning length and a mesh-adaptive direct search method is employed in both optimization steps.

From a maneuvering point of view, the science requirements detailed in this chapter can be met with a suitable choice of upper and lower bounds of the independent variables. These bounds are specified by task-specific information contained in the catalog, such as desired baseline length. The analysis conducted in the frame of this chapter has shown that baseline changes of about 1000 m over short observation windows (a couple of hours) require the highest consumption of resources, as the spacecraft must move fast to reach their final positions within the specified time. Conversely, shorter baseline changes over long observation periods (lasting several days) require the lowest resource consumption, as the thrusting phase is significantly reduced compared to the first case and spacecraft can comfortably coast at very low drift rates.

The BPM is the last module of iSCOUT. The next section focuses on presenting end-to-end simulation results representative of the IRASSI mission.

12

End-to-end Simulation and Discussion

There is no demand for women engineers, as such,
as there are for women doctors;
but there's always a demand for anyone who can do a good piece of work.

Edith Clarke

ABSTRACT

The task and maneuver-planning framework introduced in Chapter 7 was developed in the frame of the IRASSI study and is intended for performing preliminary formation-flying mission simulations and feasibility analysis. Its modularity allows users to optimize different sets of problems with specific constraints to form a global picture of what can be achieved within a given mission. This chapter performs thus a complete simulation of a five-year mission of IRASSI, whereby it is shown that 621 out of the total 784 tasks are successfully completed at a penalty of 34% of ΔV expenditure. Although over 76% of the time is dedicated to observations, idle periods represent 8% of the total mission time - an issue that can be minimized by extending the IRASSI catalog. 5% of all reconfiguration trajectories must be re-designed due to collision and invisibility occurrences. The most costly module in terms of ΔV per maneuver and computation time is the CAM.

Publication

L. Buinhas, H. Linz, M. Philips-Blum and R. Förstner, *iSCOUT: Formation Reconfiguration and Science Planning Architecture for the IRASSI Space Interferometer*, Advances in Space Research, **67(11)**, 3840-3867 (2021).

12.1. INTRODUCTION

As a first step of an evolving tool, iSCOUT is capable of performing feasibility analysis of several types of activities from task scheduling, to optimization of reconfiguration and science-related maneuvers, bringing together a set of elements (quality of science, the geometry of the spacecraft, visibility of metrology systems, target occultation, collision avoidance, etc.) which are crucial for assessing the viability of formation-flying missions.

This modular tool was introduced in Chapter 7 and subsequent chapters detailed the methodology followed in its development and embedded functionalities. Embodying the culmination of these efforts, this chapter aims to showcase the results of a long-term mission simulation in the context of IRASSI.

12.2. HIGH-LEVEL OPERATION AND SIMULATION PARAMETERS

THE sequential set of operations within iSCOUT are recalled below:

1. The Task Planner Module (TPM) delivers a science-task sequence within a user-specified tour window, based on a weighted metric which takes into account time efficiency, priority and diversity of task candidates.

2. The Reconfiguration Module (ReM) calculates straight trajectories of individual spacecraft in inertial space, setting the final reconfiguration positions according to requirements associated with the to-be-observed target. The trajectories are time-optimal and the user can specify the degree to which fuel-minimization and fuel-balancing are achieved in the reconfiguration maneuver.

3. The Collision- and invisibility Avoidance Module (CAM) checks for collisions and invisibility instances during the ReM maneuver. If such safety violations are detected, an alternative trajectory with the duration and final positions generated by the ReM is calculated, using fuel-minimization and fuel-balancing as optimization parameters.

4. The Baseline Pattern Module (BPM) provides formation expansion or contraction linear trajectories which maximize pattern asymmetries, whilst abiding by a set of science and functional requirements, such as intervisibility, sky access or baseline estimation accuracy.

The planning of these activities is distributed on a network of onboard processors and information concerning, e.g., the solutions of the modules are exchanged among formation elements via the X-band antenna. Individual spacecraft controllers can compute their own actuator strategy. Each satellite can still replan to optimize other local parameters ensuring that global constraints (e.g., time, intervisibility, collision-avoidance) are not violated.

The end-to-end simulation has a duration of five years. The modules are run sequentially and the simulation parameters share commonalities with those of the previous chapters. The goal is thus to obtain long-term optimized task sequences and to analyze how resources are managed across the fleet in ideal, free-space conditions for IRASSI-like maneuvers of different nature.

Table 12.1 summarizes the simulation parameters and those marked with an asterisk ('*') apply also to the CAM and BPM modules. Given the fact that higher savings and better balancing of ΔV was achieved relative to fuel using the fuel-based cost function, and due to the demonstrated lower variability in individual maneuvers, the ΔV-based cost function was selected with a corresponding parameter $\mu_{\Delta V} = 0.05$. This value was shown to have the best ΔV-balancing performance.

It should also be remarked that on the basis of the CAM analysis in Chapter 10, that is, due to the fact that convergence of the optimization algorithm for the ΔV cost function within the nominal maximum magnitude of the colloid thrusters of 20 mN [1] was only observed 50% of the times for nominal mass distribution conditions (case B.1), the upper limit of F_{per} for the end-to-end simulation was correspondingly increased to 200 mN.

12.3. END-TO-END SIMULATION RESULTS

THE results of the science task tour for a period of five years are first shown. The resources used by each module are thereafter summarized, followed by an analysis of the accuracy of the TPM in estimating parameters of other modules in its task-evaluation procedure.

[1] Online source: NASA, "20-mN Variable Specific Impulse (Isp) Colloid Thruster," https://ntrs.nasa.gov/archive/nasa/casi.ntrs.nasa.gov/20160005350.pdf

Table 12.1: Parameters for the IRASSI end-to-end simulation. Parameters marked with an asterisk ('*') apply also to the CAM and BPM modules.

Module	Simulation parameter	Value
TPM	Tour duration $\mathscr{D}$	5 years
	Initial target	331
	Initial simulation longitude	85°
	Optimization method	Nearest-neighbor heuristics (NNH)
	Estimation of t_{ReM}	Spline interpolation
	Estimation of t_{BPM}	$2t_{w,BPM,max} + t_{sci}$
ReM	Subscript i correspondence*	$\{T_1, T_2, T_3, T_4, T_5\}$
	Weighting parameter* $\mu_{\Delta V}$	0.05
	Specific impulse* I_{sp}	2500 s
	ReM nominal thrust force F	20 mN
	Initial launch mass M_i	$\{2300, 2300, 2300, 2300, 2300\}$ kg
	Initial fuel mass f_i	$\{15, 15, 15, 15, 15\}$ kg
	Initial ΔV ΔV_i	$\{160.4, 160.4, 160.4, 160.4, 160.4\}$ m s^{-1}
	Optimization method*	Mesh-adaptive direct search (MADS)
CAM	CAM maximum perpendicular thrust force F_{per}	200 mN
	Minimum separation distance* γ	10 m
	Critical propagation time τ_{crit}	4.7 hours
BPM	BPM maximum nominal thrust force F_{BPM}	200 mN
	Critical propagation time τ_{crit}	1 s
	Standard deviation of distance measurements σ_d (relative position estimation)	1 µm
	Standard deviation of attitude angles σ_v	0.1 arcsec
	Sky exclusion semi-angle θ_{ez}	0.026°
	Maximum tolerance values tol	±0.2

12.3.1. TASK ASSIGNMENT (TPM)

The total number of completed observations within the operational mission lifetime is 621, an average of ≈124 tasks per year. That means that using the optimization scheme proposed in Section 8.4.2 and nearest-neighbor heuristics (NNH), 79% of observations are completed relative to the current standing of the catalog, with 163 observations (or 21%) remaining. All Priority-1 observations are completed within the first two years, even though more than two-thirds (cf. Table 8.2) have a science campaign duration (t_{BPM}) of more than one day. The low associated maneuver times t_{ReM} and the fact that the ratio N_{rel} between cumulative frequency of each completed task type and total observations to be completed is low in the initial stages of the mission, ensures thus that the highest-priority tasks are completed early on.

The average value of P_{rel} increases steadily until the third year, as lower priority tasks slowly populate the mission sequence. In the third year alone, 48 Priority-4 tasks (with a very short observation duration of less than one day, cf. Table 8.2) are carried out, which corresponds to over a quarter of all tasks conducted that year. In comparison, in the second year, 99% of all completed tasks are of Priority 2. In the fourth and fifth years, the proportion of completed Priority-2 tasks increases again and P_{rel} decreases accordingly.

At least one task of each type is executed in all but the second year, which misses only Type-III and Type-IX tasks. The proportion of remaining observations at the end of the five-year operational lifetime varies between 0 %–35 % for all tasks, with five out of the nine types below 15%. For Type-V targets, a record 97.6% of all observations are completed. Types II and VIII have completed observation rates comparable to the overall population (77% and 82% respectively), whereas Type-I tasks fare well below the average, at 65%. This is attributed to the high concentration of Type-I targets in particular areas of the celestial sky (as can be observed in Figures D.1 and D.2 of Appendix D), which only allows for a combined four-week observation window per year.

It is interesting to note that even though 21% of the total observations remain to be completed after five years, the overall proportion of tasks associated with highly emission-sensitive targets (Types IV, VI and VII) is lower, at about 10%. Given that the high-priority population is under-represented in this group (compared to the total observation population) and that emission-sensitive targets are associated with demanding t_{ReM} values and short observation durations, the skewness towards higher completion rates can only be explained by the fact that N_{rel} is low in the first two years. In fact, by the third year, the algorithm tries to compensate the diversity of the sampled population so far by observing under-represented target types, such as emission-sensitive ones (Type IV, VI and VII). This is likely a contributing factor to the increase in T_{rel} between the second and third year, combined with the fact that the mean science phase duration t_{BPM} reaches a minimum of 1.39 days in the third year.

As depicted in Table 12.3, whereas N_{rel} steadily (and expectedly) increases over time, the peak value of P_{rel} is achieved in the third year, whereas T_{rel} and J_{TPM} reach a maximum in the fourth year, after which a decrease is subsequently observed for these metrics. It is also worth mentioning that T_{rel} decreases by ≈54% between the first and second year, not because of longer observation durations (in fact, the opposite is true), but because the average t_{ReM} is lower. This coincides with the lowest amount of observed emission-sensitive targets and with the time window when 99% of Priority-2 targets are observed. Given that these are very concentrated in certain regions of the sky, the time required for reconfiguration between these targets is thus low and motivates the lowest t_{ReM} value of all the five years.

Finally, the number of days where no observation is detected is nil in the first two years of the mission, increasing to 11 in the third year. Thereafter, in the fourth and fifth years, the interferometer spends respectively 37% and 55% of the operational time idly waiting for a target to enter the field of view. As the catalog is extended with other potential target candidates in the far-infrared or if the IRASSI mission lends itself to other astronomy tasks or exploration pursuits, downtimes can be further minimized.

12.3.2. MANEUVER PLANNING (REM, CAM AND BPM)

Every observation task entails both a ReM and a BPM maneuver. CAM maneuvers are, however, required only upon detected safety violations using ReM-generated trajectories.

In the simulated five-year tour, 5% of reconfiguration maneuvers required intervention by the CAM. Invisibility violations motivate 93.5% of all CAM maneuvers, involving an average of 3.5 spacecraft pairs. Conversely, collisions make up the remaining 6.5% and only affect one single pair for each instance.

With the parameters of Table 12.1, the management of ΔV resources across the fleet was evaluated throughout the mission. At the end of the 621 observations tasks 65.9% of the initial ΔV is still available for the full formation, whereas the ΔV differences amount to 6.3% of the total initial ΔV. With a combined total of 1271 maneuvers (among the ReM, CAM and BPM), this means that, on average, maneuvers require 21.5 cm s^{-1} of

Table 12.2: Number of observations over time for IRASSI end-to-end simulation.

Parameter	No. observation tasks											
	Start		Year 1		Year 2		Year 3		Year 4		Year 5	
	c[i]	r[ii]	c	r	c	r	c	r	c	r	c	r
Total Cumulative	0	784	124	660	274	510	459	325	563	221	621	163
Per target priority												
Priority 1	0	68	67	1	68	0	68	0	68	0	68	0
Priority 2	0	579	56	523	204	375	313	266	381	198	427	152
Priority 3	0	63	1	62	2	61	30	33	44	19	54	9
Priority 4	0	74	0	74	0	74	48	26	70	24	72	2
Per target type												
Type I	0	188	22	166	61	127	82	106	103	85	122	66
Type II	0	278	47	231	118	160	173	105	199	79	215	63
Type III	0	42	15	27	15	27	20	22	28	14	36	6
Type IV	0	16	3	13	5	11	10	6	12	4	15	1
Type V	0	85	8	77	10	75	59	26	81	4	83	2
Type VI	0	20	3	17	5	15	16	4	19	1	20	0
Type VII	0	25	4	21	8	17	15	10	18	7	20	5
Type VIII	0	105	18	87	48	57	67	38	80	25	86	19
Type IX	0	25	4	21	4	21	17	8	23	2	24	1
Per target emission sensitivity												
Low	0	723	114	609	256	471	418	305	514	209	566	157
High	0	61	10	51	18	43	41	20	49	12	55	6

[i] Completed
[ii] Remaining

Table 12.3: Yearly average results of TPM's IRASSI Task Tour.

Parameter	Start	Year 1	Year 2	Year 3	Year 4	Year 5
Completed tasks (%)	–	16	35	59	72	79
Completed tasks	–	124	274	459	563	621
No. idle days	–	0	0	11	134	199
Mean tasks per day	–	0.34	0.41	0.50	0.28	0.16
Mean t_{BPM} (days)	–	2.51	2.08	1.46	1.77	2.43
Mean t_{ReM} (hours)	–	2.87	0.92	2.27	2.75	2.20
Mean Performance (-)						
J_{TPM}	–	0.09	0.21	0.36	0.43	0.40
T_{rel}	–	0.05	0.02	0.07	0.09	0.07
P_{rel}	–	0.15	0.33	0.56	0.52	0.41
N_{rel}	–	0.08	0.27	0.46	0.67	0.72

ΔV (or 20.1 grams of fuel). Figure 12.1 shows the evolution of ΔV expenditure and ΔV differences across the formation. Table 12.4 presents the breakdown of resources per telescope. The fuel metrics correspond to the fuel results achieved using the ΔV-based cost function, with $\mu_{\Delta V} = 0.05$.

The remaining ΔV per spacecraft varies between 62% and 69% at the end of the mission, corresponding to a net fuel consumption between 4.7 and 5.7 kg. Nearly half of these resources are dedicated to reconfiguration maneuvers as shown in Table 12.5. With typically low thrust values, BPM maneuvers required nearly 30% of the total ΔV. Each BPM maneuver requires on average 13.4 cm s^{-1} of ΔV (or 12.3 grams of fuel). What is noteworthy, however, is that with only 5% of maneuvers, the CAM module requires over a fifth of onboard ΔV. Adaptation of the thrust profiles could potentially be investigated in the future, as proposed in Chapter 10, in order to assess whether improvements in resource-usage metrics can be found. For clarity, the ΔV and average thrust metrics associated with the CAM in Table 12.5 refer exclusively to the perpendicular thrust F_{per}, keeping in mind that the simultaneous nominal thrust, which is applied in the direction of the trajectories, is accounted for by the ReM row. Similarly, the duration of the CAM maneuver is accounted for by the ReM.

The cumulative duration of reconfiguration maneuvers accounts for 5.63% of the total mission time, whereas the average reconfiguration lasts approximately 3.98 hours. The longest maneuver is registered at a duration of 17.5 hours. Furthermore, 11.3% is allocated to functional tasks, such as calibration, communications to ground and exchange of telemetry data. The remaining 83.07% of the mission time is associated with BPM module activities: the duration of the thrust associated with baseline expansion or contraction maneuvers makes up 6.67% of the total mission (on average, 4.7 hours) and 76.4% is dedicated to actual target observations.

12.3.3. IMPLICATIONS OF EMPLOYING A PRIMARY PROPULSION SYSTEM FOR CAM AND BPM MANEUVERS

As discussed in Chapters 10 and 11, the upper limit of the secondary colloid thrusters was raised from the commercially advertised maximum magnitude of 20 mN to an artificial limit of 200 mN to ensure convergence of the optimization procedures and compliance with the science requirements, in the face of the current design of the iSCOUT modules. Different avenues to pursue a revisit to the issue of convergence were proposed, ranging from a redesign of the profile of the thrusts and a different selection of optimization variables to the addition of a loop between the ReM and CAM modules and even usage of the primary propulsion system in instances where the 20 mN upper limit is violated.

Although some of these suggestions can be addressed in a future study, the implications of using the chemical-based primary propulsion system are hereby discussed. Taking the results of the end-to-end simulation (that is, with an average of 54.7 m s^{-1} of ΔV spent out of the initially available 160.4 m s^{-1}) and a worst-

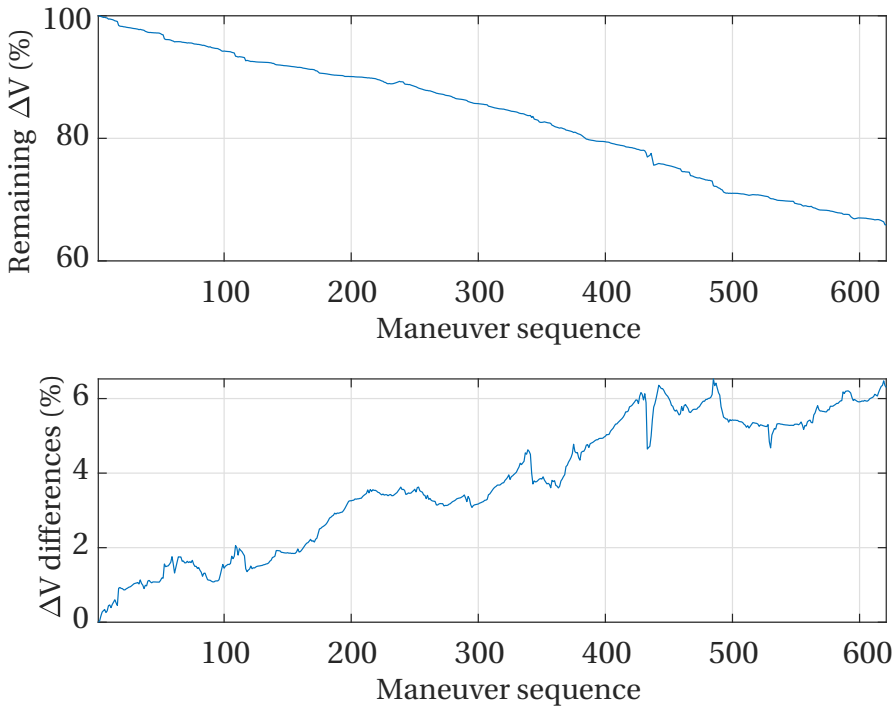

Figure 12.1: Total ΔV remaining (top) and ΔV differences for the IRASSI end-to-end simulation.

Table 12.4: Resource usage per spacecraft.

Tele-scope	Remaining ΔV (%)	Net ΔV usage (m/s)	Remaining fuel (%)	Net fuel usage (kg)
T_1	64.44	56.62	64.37	5.34
T_2	66.83	52.79	66.76	4.99
T_3	62.22	60.18	62.15	5.68
T_4	67.18	52.24	67.10	4.93
T_5	68.73	49.75	68.66	4.70

Table 12.5: Resource usage and maneuver duration per module.

Module/activity	Share of ΔV expenditure (%)	Mean thrust (mN)	Total maneuver duration (%)
ReM	48.37	20.00	5.63
CAM	21.85	31.89	(5.63)
BPM	29.78	14.20	83.07
observation ($\propto t_{sci}$)	0.00	0.00	76.40
baseline change ($\propto 2t_{w,BPM}$)	29.78	14.20	6.67

case assumption that all CAM and BPM maneuvers are performed by the primary propulsion system, the following applies:

- the CAM and BPM are responsible for 51.63% of the total ΔV expended, or 28.2 $\mathrm{m\,s^{-1}}$
- the primary propulsion system relies on hydrazine as propellant, with a specific impulse I_{sp} of 230 s
- using Equation 9.4 and assuming an initial launch mass of 2300 kg, one obtains a total of additional propellant mass of 28.6 kg

Given that with the colloid thrusters (I_{sp} = 2500 s), the same CAM and BPM maneuvers would require only 2.6 kg, a net mass penalty of 26.0 kg (28.6−2.6) must be considered for employing the primary propulsion system, with the current iSCOUT setup. This 26.0 kg mass penalty must be added to the currently considered total propellant mass of 109.2 kg (cf. Section 3.4.3), a 24% increase in fuel mass (or correspondingly 1% in launch mass).

Another option is simply to employ more colloid thrusters. Nonetheless, a combination of a redesign of the thrust profile together with a investigation of the use of more powerful secondary (electric) thrusters should be pursued before considering the addition of more colloid thrusters, as the mass penalty of propulsion hardware would be higher than the mass penalty of electric-based propellant mass. A suitable distribution of additional thrusters around the center of gravity of the spacecraft ought to furthermore be investigated in the latter case.

12.3.4. ESTIMATION ACCURACY OF t_{ReM} AND t_{BPM}

As explained in Chapter 8, for the evaluation of candidate tasks, the TPM depends on parameters which are generated by other modules. This is the case of the t_{ReM} and t_{BPM} values, used to calculate the total time associated with the task. Equation 8.2 is reproduced below for clarity:

$$t_{total} = t_{ReM} + t_{cal} + t_{link} + t_{BPM} \tag{12.1}$$

where t_{ReM} is the reconfiguration maneuver time, t_{cal} is the calibration time, t_{link} is the time slot allocated for uplink/downlink of telemetry and science data and t_{BPM} is the duration of the scientific phase for the considered task. Since TPM does not have access to the t_{ReM} and t_{BPM} values, these values are estimated.

The estimation of t_{ReM} is based on an interpolation of a matrix containing previously computed reconfiguration durations. The estimation accuracy is thus measured as that of TPM's estimated t_{ReM} and the real t_{ReM} computed by the ReM for the same maneuver. Results indicate that the calculation of t_{ReM} by the TPM seems to persistently underestimate the reconfiguration maneuver duration, as Figure 12.2(a) shows. This leads to an estimated error with a median of 1.73 hours per reconfiguration maneuver. Over the five-year mission and the 621 tasks, this represents an accumulated error of 47.4 days, or 2.6% of the total mission time.

In order to improve these estimations in the future, more samples can be incorporated in the pool of values which TPM uses for interpolation and/or a correction factor can be added in the TPM.

The estimation of the t_{BPM} is pursued by the following strategy: in the BPM, an upper limit can be set to the thrust time, $t_{w,BPM,max}$ when an expansion/contraction maneuver is to be computed. For example, the default value is given as a function of t_{sci}:

$$t_{w,BPM,max} = 0.2\,t_{sci} \tag{12.2}$$

With two thrust impulses, the total t_{BPM} time can be, at most, 40% higher than the science duration:

$$t_{BPM,max} = 2\,t_{w,BPM,max} + t_{sci} = 1.4\,t_{sci} \tag{12.3}$$

The TPM takes this maximum value, $t_{BPM,max}$, as a proxy for t_{BPM}. Since this is a maximum limit, the result is that the t_{BPM} will be conservatively overestimated by the TPM relative to the real value computed by the BPM. This is shown in Figure 12.2(b), where the difference between the estimated and real t_{BPM} is presented. At a median error of 3.91 hours per baseline-change maneuver, an accumulated error of 101 days at the end of the mission, corresponding to a total of 5.5% of the operational lifetime, is obtained. With this knowledge, and similar to the t_{ReM} case, correction factors can be applied to the TPM using the current iSCOUT setup.

With the t_{ReM} underestimated and the t_{BPM} overestimated, one obtains a net overestimation of the overall maneuver time that corresponds to 2.9% of mission time. This means that in the end-to-end IRASSI simulation, nearly 53 days are available and can be used in the calculation of mission time margins (e.g., unforeseen events that require mission downtime or even time needed for onboard processing of maneuvers).

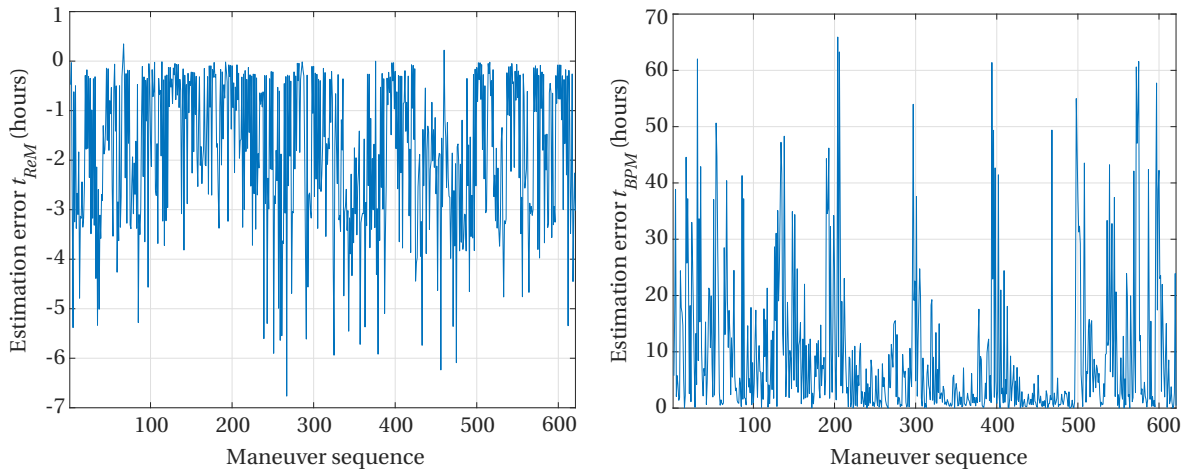

(a) t_{ReM} (b) t_{BPM}

Figure 12.2: Difference between estimated and obtained times of t_{ReM} and t_{BPM}. The estimated values are calculated by the TPM, whereas the obtained t_{ReM} and t_{BPM} are respectively computed by the ReM and BPM modules.

12.3.5. COMPUTATION TIME

The time required for the computation of tasks and maneuvers is presented in Table 12.6. The CAM requires the highest amount of time per solution, at over 6 minutes, followed by the BPM Step 2 process (which involved finding the thrust duration and magnitude for the expansion/contraction phase prior to the observations). Recall that a CAM maneuver takes effect when proximity or visibility violations are detected.

Typically, the higher the number of spacecraft pairs involved in such violations, the longer the computations take. For example, the average computation time required for computing alternative trajectories is merely 45 seconds for violations involving one spacecraft pair but rises to over 10 minutes for four or more pairs. The highest computation time was registered for an invisibility violation involving 7 spacecraft pairs, at 24 minutes. A full mission simulation, like that presented in this chapter, takes an average of three days to calculate.

12.3.6. CONCLUSIONS

With the assumptions made throughout the construction of iSCOUT, it can be concluded that an IRASSI mission can be successfully completed within the five years, as the large majority of science tasks are fulfilled, costing an average of 34% of the initially available onboard resources. The functional and geometric requirements are met with the use of both linear- and nonlinear-constrained optimization.

The long computation times associated with some of the modules, namely the CAM and the BPM Step 2, may naturally have implications for a space-borne use of iSCOUT in the future. Since the computation time is not considered in the planning of activities within iSCOUT, this must be an added feature to the tool if the formation must recursively compute the sequences of their own tasks and maneuvers. Achieving convergence within a reasonable amount of time is important not only because it maximizes mission returns, but because there may be a need of reacting to an unpredictable environment in a timely fashion. As outlined in the 'Future Work' section of Chapter 9, compatibility with onboard processors should be investigated. Additionally, architecture-level tradeoffs should conduce to the selection of dedicated software and programming languages that are enablers of onboard autonomy and time-sensitive computation solutions - and which may preclude the use of interpreted language, like MATLAB.

The current architecture of iSCOUT is driven by top-down high-level mission requirements which were defined at the outset of the IRASSI feasibility study. In Chapter 3, for example, a combined 143 $\mathrm{m\,s^{-1}}$ of ΔV was estimated for reconfiguration and baseline change maneuvers. Simulations show that only 38% of the initially planned ΔV is actually required for such maneuvers over the five years of nominal operations. This information could be used to iterate mass budgets of the spacecraft in the future (keeping in mind all simplifications used in the simulation).

Similarly, the strategies outlined in Chapters 8 to 11 place a strong emphasis on science performance. In the respective 'Future Work' sections, several issues were raised and discussed, primarily concerning the fea-

Table 12.6: Computation time for individual modules.

Parameter	Module	Computation time (s)
Mean per task or maneuver	TPM	81
	ReM	105
	CAM	371
	BPM Step 1	< 1
	BPM Step 2	207
Total tour	TPM	50 402
	ReM	65 100
	CAM	11 504
	BPM Step 1	620
	BPM Step 2	128 548

sibility of the design choices. Several alternative methods were proposed, ranging from the task-sequencing procedures (observing multiple targets in a single task instead of one target), the optimization frameworks (multi-objective algorithms) to thrusting strategies (for achieving curved or step-like trajectory patterns to improve science returns). Each proposed adaptation results from the in-depth analysis throughout Part III of this thesis and can be identified as a bottom-up approach to improving the iSCOUT tool. Finally, a comparison of iSCOUT with standard mission-planning methods could additionally add value to this research.

12.4. CHAPTER SUMMARY

THE present chapter provides the results of a complete five-year IRASSI mission simulation. A synopsis of the tool is given, followed by the parameters used in the simulation. Results associated with the TPM module show that 79% of all tasks available in the catalog can be completed within five years in ideal conditions. All Priority-1 tasks are carried out, followed by over 97% for Priority-4 tasks. Priority-3 tasks benefit from a completion rate of 86%, whereas 26% of Priority-2 tasks remain unfulfilled.

Due to the three-dimensionality of the formation, 95% of ReM-generated trajectories are free of collisions and ranging-system invisibility events. ReM maneuvers consume 48% of the total of expended onboard resources and require an average of 21 $\mathrm{cm\,s^{-1}}$ of total ΔV per single maneuver. Altogether, ReM maneuvers require 5.6% of the total mission time.

The provision of resource-efficient escape trajectories during reconfiguration for the remaining 5% of ReM trajectories is handled by the CAM module, which does however require higher consumption of ΔV and fuel per maneuver than any other module at 1.9 $\mathrm{m\,s^{-1}}$ and uses nearly 22% of consumed ΔV. With the artificial increase of the upper limit of F_{per} to 200 mN, convergence was achieved 100% of the times that the CAM module was called.

An average ΔV expenditure of 13.4 $\mathrm{cm\,s^{-1}}$ is registered for the baseline change maneuvers, generated by the BPM Step 2. Overall, nearly 30% of consumed ΔV resources are dedicated to the BPM maneuvers, which make up 6.7% of the mission time. The remaining 76.4% of the full mission time is dedicated to the actual scientific observations.

It was also observed that time parameters t_{ReM} and t_{BPM} are respectively under- and overestimated by the TPM module. Overall, the net result of this discrepancy is that there are an additional 53 days (or 2.9% of the total mission) available, indicating that initial TPM estimates were conservative. At an early mission-planning stage, this extra time could be purposed for the calculation of time budget margins. Such margins could correspond to mission downtime due to malfunctions or to required periods allocated to onboard processing of maneuvers, which remain unaccounted for in the current version of iSCOUT.

It is thus concluded that an IRASSI mission can be successfully completed in the specified time frame and future advancements within iSCOUT can refine these results and close the gap between a feasibility study

and a high-fidelity mission simulation.

13

Conclusions and Recommendations

In 399 B.C. Socrates was accused of introducing new gods
and questioning accepted gods.
He was sentenced to death by a jury of 500 of his peers.

His philosophy did not pass peer review.

Don L. Anderson

13.1. CONCLUSIONS

This thesis was motivated by the need to assess the feasibility of a free-flying interferometry mission that must operate independently in deep space and fulfill a set of complex science tasks over the course of five years. It departed from the stated aim:

> *to deliver a unified mission feasibility result for free-flying interferometers at L_2, with a particular focus on the IRASSI mission, encompassing a multi-disciplinary set of technical requirements that directly affect formation-flying operations.*

To achieve this objective, the thesis was divided into three parts. The contributions and main findings of each part, driven by three research questions respectively, are discussed below.

PART I - MISSION DESIGN AND ANALYSIS

The first part of the thesis considered the question:

Research Question 1

How can a reference mission scenario be defined in support of the high-level mission requirements?

This question was answered in a broad sense in **Chapters 2** and **3**, respectively where the main mission drivers were introduced and the nominal mission scenario was presented.

Chapter 2 provided an overview of precursor missions upon which IRASSI's concept is built on. Whereas past missions relied on precise formation control or mechanical structural connecting observing elements, IRASSI bypasses these requirements by employing a metrology system in combination with heterodyne detection, overcoming technical limitations from the past. The maximum baseline distance of 850 m is owed to the stringent resolution requirements of 0.1 arcsec at the longest wavelength of 300 µm. The mechanical configuration of IRASSI draws largely from the heritage of previous astronomy missions. This is the case of the main mirror, for instance, whose diameter of 3.5 m matches that of the Herschel Space Observatory. Due to these dimensions, one single launcher is potentially prohibitively small to host the full formation and the spacecraft are envisioned to be launched in a triple 2-2-1 sequence.

Chapter 3 defines the mission phases and nominal trajectory of IRASSI, delivering an estimation of mass and power budgets. Eight major phases compose the mission, including the Launch, the Transfer Cruise to L_2, the Deployment of the Spacecraft and the Nominal Operations. The Nominal Operations phase is the longest phase of the mission. It comprises itself of a set of science-related activities such as Formation Reconfiguration, Scientific Observations or Calibration of the instruments. These activities form an Observation Cycle and have a combined duration ranging between 1 and 8 days. The duration of the observations is the biggest factor in determining the span of the Observation Cycle and approximately 600 Observation Cycles are expected throughout the mission. Three launch periods of about one month are available in the studied years of 2029 and 2030. The duration of the Transfer Cruise is expected to last between three and four months and once in its nominal orbit, the formation is foreseen to be visible from ground stations for 10 hours per day on average.

The mission required ΔV totals 225 $\mathrm{m\,s^{-1}}$. Due to differing magnitude requirements for the various maneuver tasks, two propulsion systems have been devised: a primary one, consisting of hydrazine-fueled thrusters reserved for orbit-control maneuvers, and a secondary one, based on colloid thrusters for operation exclusively during the Nominal Operations phase. The spacecraft are expected to weigh 2300 kg, a quarter of which is allocated to payload hardware and 5% is allocated to fuel (1% to electric propulsion and 4% to chemical propulsion). A peak power requirement of 1780 W is expected, provided by solar arrays with an area of 8.4 $\mathrm{m^2}$ mounted on the sunshield.

Main findings of Part I

- After a maximum transfer cruise of four months, deployment of the spacecraft and the commissioning of the payload, nearly 600 observation tasks are expected over the five-year Nominal Operations mission phase.
- A suitable orbit design requires station-keeping maneuvers only once every six months.
- Preliminary mass budgets estimate a launch mass of 2.3 tons per spacecraft (including 20% margin), of which 5% is allocated to fuel.

The first research question considered the first building blocks towards a mission design that satisfies high-level requirements. The next part of the research addresses specific challenges that must be considered in the development and simulation of a multi-element spacecraft formation.

PART II - FORMATION-FLYING GEOMETRY, DYNAMICS AND GNC

The second part of the thesis considered the question:

Research Question 2

What is the expected behavior of a free-flying formation in the vicinity of L_2 and what formation coordination strategies are applicable to an interferometer such as IRASSI?

This first part of this question was answered in **Chapters 4** and **5**, where a step-by-step analysis demonstrated that an envelope of nominal formation geometries could be defined and that even when immersed in the L_2 environment, the degradation of the formation was minimal for the time scales corresponding to those of the Observation Cycle. **Chapter 6** investigated formation organization structures for IRASSI with particular focus on the Nominal Operations phase of the reference scenario.

Key geometrical and operational constraints that must be strictly respected during the operational phase of the mission were identified in **Chapter 4**. These are the intervisibility of the ranging system, the baseline estimation accuracy, the accessibility of the sky and the scientific performance of the interferometer as a whole. The intervisibility of the ranging system is affected by the sunshield dimensions and relative mounting location, whereas the baseline estimation accuracy dictates that an asymmetric three-dimensional formation configuration is preferred over e.g., a planar one, due to the ambiguity of the relative positioning errors. Ensuring sky accessibility prevents any spacecraft from entering another's field of view and occluding a target during observations. And finally, science performance has a double dependency on the science instruments and on the relative drift patterns of the formation. As such, it is up to mission planners to design optimal formation trajectories that deliver the best contribution to the imaging procedures. Together, these four requirements constrain the distribution of the spacecraft in three-dimensional space and they serve as a basis for constructing a nominal formation geometry.

The nominal formation geometry is thus defined with respect to a plane Π_N perpendicular to the target direction. The telescopes are distributed uniformly along a circle with a radius d contained in the Π_N plane and separated by an out-of-plane distance h. The out-of-plane distance is the height above the plane and scales with d, such that $h \propto kd$, $k = \{0, 2, 4\}$, resulting in the formation being dispersed along the target direction to a higher extent than in perpendicular direction. The minimum and maximum circle radius are $d = 10$ m and $d = 1000$ m, and correspond respectively to the small and large formation scenarios. An envelope around this nominal formation geometry allows a deviation between 200 %–2500 % of the relative distances before a violation of constraints takes place, depending on the formation pair being considered.

Chapter 5 investigated the evolution of the formation over time, in an L_2 environment and in control-free conditions. The first step of this process consisted of implementing an analytical relative motion model in MATLAB and validating it using NASA's General Mission Analysis Tool (GMAT) considering a full-force model. It was shown that over the course of nearly three weeks, a relative distance error of up to 10% was expected, reducing to a fourth of that for time scales of the Observation Cycle - approximately 8 days. The modeling

error was verified for different positions along the Halo orbit and for different epochs, in order to capture the eccentricity effects of Earth's orbit around the Sun.

With the nominal formation geometry developed in **Chapter 4**, the relative motion model predicted relative drift magnitudes of up to 45 m and drift rates of 1.8 $\mathrm{mm\,s^{-1}}$ for small formations at the end of the 8 days. A linear relationship between these quantities and formation size was observed, such that large formations were associated with two orders of magnitude higher drift and drift rates compared to the small formations. The orientation of the formation in the inertial frame was shown to change at a maximum rate of 3°/day. In these free-drift conditions, three out of the four formation configuration requirements identified in **Chapter 4** were assessed. No loss of intervisibility was detected over the eight days of simulation. In fact, depending on the initial orientation of the formation in space, it takes between two and four weeks until at least one of the ten metrology links is lost. Moreover, using nominal error assumptions regarding distance measurement and pointing accuracy, the baseline estimation accuracy largely remains under the required 5 µm, independently of formation size. Finally, over 95% and 99.9% of the total sky remains unobstructed for observations for a small and large formation respectively during the uncontrolled drift, which for a position-constrained target-sampling approach is an exceptional outcome in that a vast majority of the celestial sky is available for science tasks at any given time.

From the analysis contained in **Chapter 6**, it was concluded that IRASSI should be treated as an autonomous, self-organizing and distributed agency, given that it operates far from Earth with limited contact opportunities to the ground and considering that inter-satellite links for communication are available to all spacecraft. These links can be used to explore the parallelization of computation processes for science and maneuver planning activities, reducing dependency from ground stations, boosting mission robustness and increasing resilience to unanticipated events during the operational phase. Finally, a behavioral-type coordination control, which involves prescribing one or more formation goals competing for onboard resources of a spacecraft, is especially suitable for IRASSI for the majority of the GNC modes of the mission. Throughout the operational phase, the formation must respect the envelope around a nominal formation geometry and relative motion dynamics, without having to strictly enforce formation-keeping. Formation goals such as 'avoid collisions', 'reach final reconfiguration positions' or 'maintain intervisibility' are some of the objectives that can be prescribed in such a coordination framework. Due to the slow dynamics of the L_2 environment, standard PD, LQG or Lyapunov-based controllers can be employed for regulating deviations of reference relative trajectories in the event of violations of the envelope limits.

Main findings of Part II

- The major requirements affecting the design of a nominal formation geometry are the intervisibility of the ranging system, the baseline estimation accuracy, the accessibility of the sky and the scientific performance.
- The nominal formation geometry is characterized by being elongated in the target direction and distributed uniformly around the axis connecting the formation center and the target.
- The nominal formation geometry remains stable over time and satisfies the formation requirements in free-drift conditions, independent of formation size, orbit location and orientation of the formation, without the risk of an imminent violation of predefined conditions.
- Sharing of computing resources on a communications network is a way to take advantage of existing software and hardware capabilities within the fleet to increase autonomy and a behavioral-type coordination scheme should underpin the organization of the formation.

The second research question led to the outline of prerequisites that must be satisfied during the Nominal Operations phase. The last part of this research work addresses the technical feasibility of the mission, bringing together all mission objectives and constraints identified in the first and second parts.

PART III - DEVELOPMENT OF ISCOUT, A MANEUVER-PLANNING TOOL FOR FORMATION OPERATIONS

The third part of the thesis considered the question:

Research Question 3

How feasible is the mission once all formation constraints and science requirements are considered and how can a mission 'end-to-end' performance be evaluated? What maneuvering strategies guarantee the safety of the telescopes and deliver the maximum science return?

This question motivated the development of a simulation environment that is able to aggregate all mission parameters to deliver a unified assessment of the practicability of the mission. The architecture of this modular environment, called iSCOUT (**i**nterferometer **SC**ience and **O**perations mane**U**ver-planning **T**ool), is introduced in **Chapter 7**. Assembled in MATLAB, iSCOUT is supported by four modules with the joint aim of optimally planning the sequence of science tasks, computing the associated reconfiguration maneuvers and the paths to be followed by individual spacecraft during the science observations, while simultaneously delivering collision-free trajectories which ensure the intervisibility of the spacecraft. The four modules are: 1) Task-Planner Module (TPM), 2) Reconfiguration Module (ReM), 3) Collision- and Invisibility-Avoidance Module (CAM) and 4) Baseline Pattern Module (BPM). As such, **Chapters 8** to **11** detail the methodologies associated with each module, whereas **Chapter 12** provides end-to-end simulation results of a five-year IRASSI mission using the iSCOUT tool.

In **Chapter 8**, which describes the TPM, it was shown that a methodical selection of science tasks was needed, given that a large proportion of targets are located in concentrated regions of the celestial sky and can therefore only be observed within a time window in particular seasons of the year. The initial and final formation size were the major determinants of reconfiguration maneuver duration. In order to minimize unnecessary maneuver time that detracts from observation opportunities and minimize fuel expenditure, a dynamic task-planning strategy that determined the initial and final configurations of the formation 'on-the-fly' for each task candidate was devised. Thereafter, the eligibility of a task candidate was evaluated using a weighted sum of three metrics: the relative reconfiguration-maneuver time, the relative priority of the to-be-observed target and how often the same target type has been previously observed. A nearest-neighbor search was selected for constructing task sequences during missions.

Chapter 9 describes reconfiguration maneuvers optimization procedure within the ReM. This procedure selects the final positions of the spacecraft that return the lowest value of two user-defined cost functions: a fuel-based and a ΔV-based one, both pursuing a balanced use of these resources across the fleet by virtue of the respective weighting parameters values μ_f and $\mu_{\Delta V}$. Higher weighting parameters ensure a more balanced use of resources across the fleet but demand a higher consumption of fuel and ΔV. During reconfigurations maneuvers, a mixture of bang-bang and bang-coast-bang thrust profiles are used to ensure time-optimality. During the bang phases, a constant thrust magnitude of 20 mN is used. For identifying the best-performing μ_f and $\mu_{\Delta V}$ values, maneuver tours using different initial fuel and wet mass conditions were simulated using a range of μ_f and $\mu_{\Delta V}$ values. The fuel- and ΔV-balancing performance of each tour was thereafter assessed. Results showed that for homogeneous formations (with equal wet mass and fuel mass), parameters of $\mu_f = \mu_{\Delta V} \approx 0.05$ provide the most cost-effective compromise. Conversely, heterogeneous formations may benefit from using a ΔV-based cost function to plan reconfiguration maneuvers over the long term, with a weighting parameter within the range of $\mu_{\Delta V} \approx$0.2–0.4. In individual maneuvers, metrics associated with the ΔV-based function also showed less variability than those associated with the fuel-based one.

A safety analysis of the ReM maneuvers led to the development of the CAM module introduced in **Chapter 10**. The CAM module procures a refinement of the ReM linear trajectories in case collisions or invisibility periods between metrology systems are detected. The safety analysis shows that collisions were present nearly exclusively in short-baseline reconfiguration maneuvers and involve an average of 1.2 pairs of spacecraft. Invisibilities, on the other hand, occurred for long-baseline reconfigurations and involve 2–8 pairs. The ReM trajectories are modified by the addition of a second thrust, perpendicular to the nominal trajectory connecting the initial and final reconfiguration positions. A bang-coast-bang profile is used for the secondary, perpendicular thrust. The direction, magnitude and coasting time of this thrust are independent variables of the same cost functions used in the ReM (using the best fuel- and ΔV-balancing performance μ_f and $\mu_{\Delta V}$ values). The higher the number of telescope pairs involved, the higher the computation time for achieving an alternative trajectory with the CAM and the higher the fuel or ΔV expended. In fact, over 300% more resources may be required with a CAM maneuver than initially allocated with the ReM.

BPM, the last module of iSCOUT, was presented in **Chapter 11**. It dealt with the calculation of formation

expansion or contraction maneuvers during observation tasks. As such, the BPM generates optimal trajectory patterns in physical space that, when transformed to the spatial frequency domain, lead to the interferometer generating high-quality infrared images. A two-step process is used for designing baseline-change trajectories. The first one maximizes asymmetries. The second step searches for the most resource-efficient and resource-balanced solution, in terms of fuel or ΔV, using thrust magnitude and coasting time as independent variables. The four requirements identified in **Chapter 4** are considered in the optimization process as constraints, to ensure that during the expansion or contraction of the formation, visibility is not lost or that spacecraft do not occlude each others' field of view. In addition, geometric patterns associated with science requirements, such as distribution of the trajectories in the Π_N plane and desired scanning length, are equally described as constraints. The analysis conducted within the BPM showed that drift rates in the order of a few $\mathrm{mm\,s^{-1}}$ are to be expected. Nonetheless, similar to the CAM module, the upper limit of the thrust was increased to 200 mN to ensure that the aforestated requirements are fulfilled, with baseline changes of about 1000 m over short observation windows (a couple of hours) demanding the highest consumption of resources in the fleet. A mesh-adaptive direct search is the selected optimization procedure for the maneuver-planning algorithms of **Chapters 9**, **10** and **11**.

With the simulation environment implemented within iSCOUT, the feasibility analysis of an integral IRASSI mission over the five-year lifetime was performed. This was the focus of **Chapter 12**. Each spacecraft was initialized with 15 kg of fuel, or 160.4 $\mathrm{m\,s^{-1}}$ of ΔV. Results show 621 observation tasks, or 79% of all tasks available in the catalog, can be completed within five years in ideal conditions. More specifically, the completion rate ranges between 74% and 100% across the four task priorities with the lowest associated with Priority-2 and the highest related to Priority-1 tasks. The onboard consumed resources average 34.1 % of the total initially available. In addition, 95% of ReM-generated trajectories are free of collisions and ranging invisibility events. Of the total consumed onboard resources, 48% are used by ReM maneuvers which require altogether 5.6% of the total mission time. The remaining 5% of ReM trajectories require an intervention by the CAM module, whose share of consumed ΔV totals nearly 22% of the total ΔV expended. Invisibility violations are behind 93.5% of all CAM interventions, involving an average of 3.5 pairs of telescopes. The CAM demands the highest consumption of ΔV and fuel per maneuver than any other module at 1.9 $\mathrm{m\,s^{-1}}$. Conversely, the lowest ΔV expenditure per maneuver is registered for the BPM at 13.4 $\mathrm{cm\,s^{-1}}$. Nearly 30% of consumed ΔV is dedicated to BPM maneuvers, which make up 6.7% of the mission time. The remaining 76.4% of the full mission time is dedicated to the actual scientific observations.

Under nominal conditions and with the stated assumptions of iSCOUT, it was possible to demonstrate that the mission can be successfully completed in the specified time frame if the trusting capability of the thrusters is increased from 20 mN to 200 mN. A fuel mass penalty of 26 kg was estimated if all CAM and BPM maneuvers are to be pursued with the hydrazine-based primary propulsion system, a 24% increase to the current spacecraft total propellant mass of 109.2 kg.

Over the course of iSCOUT's development, several avenues for future work were identified, overcoming the present limitations of the tool. This is conducive to leaving a set of guidelines that should be explored in order to bridge the gap between a feasibility study and a high-fidelity mission simulation.

Main findings of Part III

- Under nominal conditions, 79% of observation tasks can be fulfilled, with nearly two-thirds of fuel tanks still full at the end of the mission.
- Over three-quarters of the mission can be dedicated to actual science observation. The remaining amount of time is allocated to maneuvers and functional tasks, such as calibration or communications.
- Homogeneous formations such as IRASSI benefit from weighting parameters of $\mu_f = \mu_{\Delta V} \approx 0.05$.
- Despite intervening on only 5% of the ReM trajectories, the CAM module is both the most expensive one in terms of onboard resources (fuel and ΔV) and computation time per maneuver.

13.2. RECOMMENDATIONS

Advancements within iSCOUT and a refinement of the current IRASSI mission should complement the work developed throughout this thesis. Hence the following recommendations are proposed for future work:

- iSCOUT modules
  - Task-Planner Module (TPM)
    - Optimization algorithm and metrics: local-search procedures that complement the NNH algorithm could be implemented to improve NNH solutions. In addition, multi-objective optimization could be considered not only for selecting tasks based on time efficiency, task priority and diversity, but also for minimizing idle periods due to target scarcity.
  - Reconfiguration Module (ReM)
    - Optimization algorithm and constraints: as in the TPM case, the applicability of a multi-objective optimization algorithm could be investigated, such that nondominated points in the objective space of fuel and fuel balance (or ΔV and ΔV balance) are preserved, together with the respective solution values in the decision space. This could also lead to considering maneuver time and thrust magnitude in the decision-making procedure of the ReM. Constraints such as traveled distance or even thrust direction could similarly be used to improve the current multi-variable, single-objective optimization setup. Proximity constraints could also be incorporated in order to bypass the need for CAM module interventions.
    - Simulation conditions: the ReM considered separately fuel-mass and wet-mass imbalances across the formation. Addressing both sources of mass imbalances simultaneously could lead to further insights into the formation behavior over time.
  - Collision- and invisibility-Avoidance Module (CAM)
    - Thrust profile: adopting different modes of operation of the secondary engines in the generation of alternative, safe trajectories during reconfiguration could prove to be a valuable effort. Varying the duration of coasting periods, the duration of the reconfiguration maneuver itself, the starting time of the perpendicular thrust and even removing the imposition of perpendicularity of the CAM thrust are potential avenues for examination. The expected improvement of this module would then be measurable in terms of resource savings per maneuver and computational time.
  - Baseline Pattern Module (BPM)
    - Image-based pattern optimization: machine-learning and pattern-recognition algorithms applied to the final, post-processed images that are able to reverse-engineer formation trajectories can be viable alternatives to producing suitable *(U, V)*-plane coverage. Recent developments in this field make these concepts promising candidates for science and mission-planning purposes in the near future.
- iSCOUT architecture design choices
  - Catalog information: tasks being differentiated in the future (e.g., gas detection vs. measurement of accretion rates in protostars) could lead to a new task-prioritization scheme, where the order of execution is taken into account. This requires introducing new task-selection metrics. Moreover, if catalog extensions occur periodically during the operational phase of the mission, relevant metrics (e.g., target diversity, that accounts for the total population of tasks of the same type) should be scalable in real-time to incorporate new entries as soon as these become available.
  - Onboard execution and processing: iSCOUT is currently an *ex-ante* mission-planning tool, executed on a network of ground-based processors. However, with technology advances, it is foreseeable that more complex operation planners run on board the spacecraft in order to support formation autonomy-reliant activities and reduce costs, freeing resources from ground stations, such as communication slots and personnel. Future iterations of iSCOUT could be adapted for onboard use, enabling distributed space-based facilities to compute day-to-day routines independently from operators. Similarly, the suitability of optimization methods for real-time processing on board, considering hardware limitations and speed of convergence of the algorithms on a distributed network, ought to be investigated.

  - Perturbations on motion dynamics: relative motion model for L_2 environments which accounts for gravity gradients can be included in order to produce more realistic trajectories during passive drift phases or idle periods, such as uplink/downlink of telemetry. Similarly, the implementation of control feedback loops for governing relative motion would allow to simulate off-nominal scenarios and to evaluate the ability of the formation to react to an unpredictable environment.
  - Attitude models: attitude motion was not considered in this research beyond error assumptions in the baseline estimation accuracy. Simulating both orientation maneuvers and disturbances are important aspects of an astronomy mission that relies on precise pointing mechanisms to achieve its goals.
  - Station-keeping: although orbit control was simulated and associated fuel budgets calculated during the Mission Analysis phase, this was not considered in the development of iSCOUT. Future improvements of the iSCOUT tool may thus consist of the provision of station-keeping maneuvers.
  - Inter-modular loops: to facilitate the exchange of information between modules and the conflict-resolution capacity of iSCOUT, modules should be interconnected and able to generate new solutions upon request.
  - Alternative operational scenarios: an in-depth analysis of any mission requires the consideration of realities outside the nominal one. As such, configuration files containing a set of bespoke initial conditions could be loaded onto iSCOUT and the effect of simulation parameters on mission performance could then be evaluated. Emulated conditions can include, for example, actuator malfunctions or the imposition of temporal constraints on certain observation activities due to ground personnel or communications unavailability. Typically, such exercises deliver invaluable insights to mission planners and ultimately allow for detailed design iterations of complex systems.

- Mission and system-level design choices
  - Trading science and function: Priority-1 tasks are among the least abundant in the catalog. Since the mission was built around delivering the highest science returns, an interesting question to pose scientists is whether several low-priority targets could occasionally be observed in place of a single high-priority one. This quantity vs. quality dichotomy is one that saves fuel and potentially observation time that can be used to expand the mission lifetime. Attitude-change maneuvers in place of reconfiguration maneuvers could similarly save onboard resources and prolong the mission.
  - Actuators: using two propulsion systems operating at different magnitudes leaves a void in-between the two regimes, as registered by the CAM. Perhaps future technology developments will naturally overcome this issue. However, the impact of switching in-between propulsion systems during times coinciding with or near science observations may be subject to future analysis.
  - Alternative pattern and scanning strategies: the top-down requirement of using linear patterns due to thrust usage limitations during observation could be removed should technology developments allow. It could be subject to research whether curvilinear or spiral trajectories could realistically be obtained, how much improvement in *(U, V)*-plane coverage is achieved and whether there are long-term effects on spacecraft fuel consumption by devising such ambitious patterns. As science is at the center of IRASSI, this critical aspect is a final recommendation for future work from this thesis.

REFERENCES

[1] K. F. Schuster, R. Neri, F. Gueth, A. Castro-Carrizo, J. Pety, B. Gautier, B. Lefranc, S. Blanchet, P. Dumontroty, D. Broguière, O. Gentaz, S. Mahieu, V. Pietu, J. Boissier, M. Bremer, M. Krips, J. Winters, and R. García, *NOEMA: a powerful millimeter wave interferometer using next generation technology (Conference Presentation),* in *Ground-based and Airborne Telescopes VII*, Vol. 10700 (International Society for Optics and Photonics, SPIE Astronomical Telescopes + Instrumentation, 2018, Austin, Texas, United States, 2018) p. 107000R.

[2] P. T. Ho, J. M. Moran, and K. Y. Lo, *The submillimeter array,* The Astrophysical Journal Letters **616**, L1 (2004).

[3] J. C. Webber, *The ALMA telescope,* in *2013 IEEE MTT-S International Microwave Symposium Digest (MTT)* (IEEE, Seattle, WA, USA, 2013) pp. 1–3.

[4] InfraTec, *Glossary - Electromagnetic Spectrum,* `https://www.infratec.eu/sensor-division/service-support/glossary/infrared-radiation/` (2020), [Online; accessed 16-April-2020].

[5] N. Schneider, J. Urban, and P. Baron, *Potential of radiotelescopes for atmospheric line observations: I. observation principles and transmission curves for selected sites,* Planetary and Space Science **57**, 1419 (2009).

[6] P. R. Roelfsema, H. Shibai, L. Armus, D. Arrazola, M. Audard, M. Audley, C. Bradford, I. Charles, P. Dieleman, Y. Doi, L. Duband, M. Eggens, J. Evers, I. Funaki, J. Gao, M. Giard, A. di Giorgio, L. González Fernández, M. Griffin, F. Helmich, R. Hijmering, R. Huisman, D. Ishihara, N. Isobe, B. Jackson, H. Jacobs, W. Jellema, I. Kamp, H. Kaneda, M. Kawada, F. Kemper, F. Kerschbaum, P. Khosropanah, K. Kohno, P. Kooijman, O. Krause, J. van der Kuur, J. Kwon, W. Laauwen, G. de Lange, B. Larsson, D. van Loon, S. Madden, H. Matsuhara, F. Najarro, T. Nakagawa, D. Naylor, H. Ogawa, T. Onaka, S. Oyabu, A. Poglitsch, V. Reveret, L. Rodriguez, L. Spinoglio, I. Sakon, Y. Sato, K. Shinozaki, R. Shipman, H. Sugita, T. Suzuki, F. van der Tak, J. Torres Redondo, T. Wada, S. Wang, C. Wafelbakker, H. van Weers, S. Withington, B. Vandenbussche, T. Yamada, and I. Yamamura, *SPICA — a large cryogenic infrared space telescope: unveiling the obscured universe,* Publications of the Astronomical Society of Australia **35** (2018), https://doi.org/10.1017/pasa.2018.15.

[7] J. Staguhn, E. Amatucci, L. Armus, D. Bradley, R. Carter, D. Chuss, J. Corsetti, A. Cooray, J. Howard, D. Leisawitz, M. Meixner, S. Moseley, A. Pope, J. Vieira, and E. Wollack, *Origins Space Telescope: the far infrared imager and polarimeter FIP,* in *Space Telescopes and Instrumentation 2018: Optical, Infrared, and Millimeter Wave*, Vol. 10698 (International Society for Optics and Photonics, SPIE Astronomical Telescopes + Instrumentation, 2018, Austin, Texas, United States, 2018) p. 106981A.

[8] N. S. Kardashev, I. D. Novikov, V. N. Lukash, S. V. Pilipenko, E. V. Mikheeva, D. V. Bisikalo, D. S. Wiebe, A. G. Doroshkevich, A. V. Zasov, I. I. Zinchenko, P. Ivanov, V. Kostenko, T. Larchenkova, S. Likhachev, I. Malov, V. Malofeev, A. Pozanenko, A. Smirnov, A. Sobolev, A. Cherepashchuk, and Y. Shchekinov, *Review of scientific topics for the Millimetron space observatory,* Physics-Uspekhi **57**, 1199 (2014).

[9] D. Leisawitz, C. Baker, A. Barger, D. Benford, A. Blain, R. Boyle, R. Broderick, J. Budinoff, J. Carpenter, R. Caverly, P. Chen, S. Cooley, C. Cottingham, J. Crooke, D. DiPietro, M. DiPirro, M. Femiano, A. Ferrer, J. Fischer, J. Gardner, L. Hallock, K. Harris, K. Hartman, M. Harwit, L. Hillenbrand, T. Hyde, D. Jones, J. Kellogg, A. Kogut, M. Kuchner, B. Lawson, J. Lecha, M. Lecha, A. Mainzer, J. Mannion, A. Martino, P. Mason, J. Mather, G. McDonald, R. Mills, L. Mundy, S. Ollendorf, J. Pellicciotti, D. Quinn, K. Rhee, S. Rinehart, T. Sauerwine, R. Silverberg, T. Smith, G. Stacey, H. Stahl, J. Staguhn, S. Tompkins, J. Tveekrem, S. Wall, and M. Wilson, *The space infrared interferometric telescope (SPIRIT): High-resolution imaging and spectroscopy in the far-infrared,* Advances in Space Research **40**, 689 (2007).

[10] D. Leisawitz, T. T. Hyde, S. A. Rinehart, and M. Weiss, *The Space Infrared Interferometric Telescope (SPIRIT): the mission design solution space and the art of the possible,* in *Space Telescopes and Instrumentation 2008: Optical, Infrared, and Millimeter*, Vol. 7010 (International Society for Optics and Photonics, SPIE Astronomical Telescopes + Instrumentation, 2008, Marseille, France, 2008) p. 701028.

[11] W. Wild, T. de Graauw, F. Helmich, A. Baryshev, J. Cernicharo, J. Gao, A. Gunst, A. Bos, J.-W. den Herder, B. Jackson, V. Koshelets, H.-J. Langevelde, P. Maat, J. Martin-Pintado, J. Noordam, P. Roelfsema, L. Venema, P. Wesselius, and P. Yagoubov, *ESPRIT: a study concept for a far-infrared interferometer in space,* in *Optical and Infrared Interferometry*, Vol. 7013 (International Society for Optics and Photonics, SPIE Astronomical Telescopes + Instrumentation, 2008, Marseille, France, 2008) p. 70132R.

[12] A. Leger and T. Herbst, *DARWIN mission proposal to ESA,* arXiv preprint arXiv:0707.3385 (2007).

[13] F. P. Helmich and R. Ivison, *FIRI — A far-infrared interferometer,* Experimental Astronomy **23**, 245 (2009).

[14] L. Buinhas, E. Ferrer-Gil, and R. Förstner, *IRASSI: InfraRed astronomy satellite swarm interferometry — Mission concept and description,* in *2016 IEEE Aerospace Conference* (IEEE, Big Sky, MT, USA, 2016) pp. 1–20.

[15] J. Schneider *et al.*, *Interactive extra-solar planets catalog,* (2010), [Online; accessed 17-April-2020].

[16] H. Linz, D. Bhatia, L. Buinhas, M. Lezius, E. Ferrer, R. Förstner, K. Frankl, M. Philips-Blum, M. Steen, U. Bestmann, W. Hänsel, R. Holzwarth, O. Krause, and T. Pany, *InfraRed Astronomy Satellite Swarm Interferometry (IRASSI): Overview and study results,* Advances in Space Research **65**, 831 (2020).

[17] D. Jewitt, L. Chizmadia, R. Grimm, and D. Prialnik, *Water in the small bodies of the solar system,* Protostars and Planets V , 863 (2007).

[18] R. G. Martin and M. Livio, *On the evolution of the snow line in protoplanetary discs,* Monthly Notices of the Royal Astronomical Society: Letters **425**, L6 (2012).

[19] S. Notsu, H. Nomura, D. Ishimoto, C. Walsh, M. Honda, T. Hirota, and T. Millar, *Candidate water vapor lines to location the h_2o snowline through high-dispersion spectroscopic observations. i. the case of a t tauri star,* The Astrophysical Journal **827**, 113 (2016).

[20] S. Notsu, H. Nomura, D. Ishimoto, C. Walsh, M. Honda, T. Hirota, and T. Millar, *Candidate water vapor lines to locate the h2o snowline through high-dispersion spectroscopic observations. ii. the case of a herbig ae star,* The Astrophysical Journal **836**, 118 (2017).

[21] T. Henning and D. Semenov, *Chemistry in protoplanetary disks,* Chemical Reviews **113**, 9016 (2013).

[22] G. Pilbratt, J. Riedinger, T. Passvogel, G. Crone, D. Doyle, U. Gageur, A. Heras, C. Jewell, L. Metcalfe, S. Ott, *et al.*, *Herschel Space Observatory - An ESA facility for far-infrared and submillimetre astronomy,* Astronomy & Astrophysics **518** (2010), https://doi.org/10.1051/0004-6361/201014759.

[23] C. Beichman, P. Lawson, O. Lay, A. Ahmed, S. Unwin, and K. Johnston, *Status of the terrestrial planet finder interferometer (TPF-I),* in *Advances in Stellar Interferometry*, Vol. 6268 (International Society for Optics and Photonics, SPIE Astronomical Telescopes + Instrumentation, 2006, Orlando, Florida , United States, 2006) p. 62680S.

[24] A. R. Thompson, J. M. Moran, and G. W. Swenson Jr, *Interferometry and synthesis in radio astronomy* (2nd Edition, John Wiley & Sons, 2001).

[25] P. J. Napier, *in Synthesis Imaging in Radio Astronomy II,* in *ASP Conference Series*, Vol. 180 (1999) p. 37.

[26] J. L. Junkins and H. Schaub, *Analytical Mechanics of Aerospace Systems,* Texas A&M University (2001).

[27] C. L. Bennett, M. Bay, M. Halpern, G. Hinshaw, C. Jackson, N. Jarosik, A. Kogut, M. Limon, S. Meyer, L. Page, D. N. Spergel, G. S. Tucker, D. T. Wilkinson, E. Wollack, and E. L. Wright, *The Microwave Anisotropy Probe mission,* The Astrophysical Journal **583**, 1 (2003).

[28] J. A. Tauber, N. Mandolesi, J.-L. Puget, T. Banos, M. Bersanelli, F. R. Bouchet, R. C. Butler, J. Charra, G. Crone, J. Dodsworth, *et al.*, *Planck pre-launch status: The Planck mission,* Astronomy & Astrophysics **520**, A1 (2010).

[29] L. Eyer, B. Holl, D. Pourbaix, N. Mowlavi, C. Siopis, F. Barblan, D. Evans, and P. North, *The GAIA mission,* in *XI Hvar Astrophysical Colloquium* (Hvar Observatory, Hvar, Croatia, 2013).

[30] Arianespace, *ARIANE 5: User's Manual*, Tech. Rep. (Issue 5, Revision 1, 2011).

[31] S. P. Hughes, *General Mission Analysis Tool (GMAT)*, (2007).

[32] S. Leboucher, *ARIANE 5: Data relating to Flight 188*, Tech. Rep. (Arianespace, Guiana Space Center, Kourou, French Guiana, 2009).

[33] S. Martin, D. P. Scharf, R. Wirz, O. Lay, D. McKinstry, B. Mennesson, G. Purcell, J. Rodriguez, L. Scherr, J. R. Smith, *et al.*, *Design study for a planet-finding space interferometer*, in *Aerospace Conference, 2008 IEEE* (IEEE, Big Sky, MT, USA, 2008) pp. 1–19.

[34] T. Ikenaga and M. Utashima, *Study on the Stationkeeping Strategy for the Libration Point Mission*, Transactions of the Japan Society for Aeronautical and Space Sciences, Aerospace Technology Japan **10**, 11 (2012).

[35] E. Ferrer, L. Buinhas, and R. Förstner, *System Design and Thermal Stability Analysis for the IRASSI Infrared Space Interferometer*, in *AIAA SPACE 2016* (AIAA, Long Beach, CA, USA, 2016) p. 5496.

[36] L. Buinhas, E. Ferrer-Gil, and R. Förstner, *IRASSI InfraRed Space Interferometer: Mission Analysis, Spacecraft Design and Formation Flying Overview*, in *68th International Astronautical Congress* (Adelaide, Australia, 2017).

[37] Arianegroup - Orbital Propulsion Center, *1N Hydrazine Thruster*, `http://www.space-propulsion.com/spacecraft-propulsion/hydrazine-thrusters/1n-hydrazine-thruster.html` (2020), [Online; accessed 08-April-2020].

[38] National Aeronautics and Space Administration (NASA), *20-mN Variable Specific Impulse (Isp) Colloid Thruster* , `https://ntrs.nasa.gov/archive/nasa/casi.ntrs.nasa.gov/20160005350.pdf` (2020), [Online; accessed 08-April-2020].

[39] K. Frankl, M. E. Copur, and B. Eissfeller, *Geometric snapshot method for the autonomous relative positioning of formation flying satellites in real-time*, in *27th AAS/AIAA Space Flight Mechanics Meeting*, 396 (San Antonio, TX, USA, 2017).

[40] A. K. Cline, C. B. Moler, G. W. Stewart, and J. H. Wilkinson, *An estimate for the condition number of a matrix*, SIAM Journal on Numerical Analysis **16**, 368 (1979).

[41] F. Botley, *A new use for the plate carree projection*, Geographical Review , 640 (1951).

[42] R. Juanola-Parramon, G. Savini, D. Fenech, and C. Walsh, *An end-to-end Far-infrared Interferometer Instrument Simulator (FIInS)*, in *Space Telescopes and Instrumentation 2014: Optical, Infrared, and Millimeter Wave*, Vol. 9143 (International Society for Optics and Photonics, SPIE Astronomical Telescopes + Instrumentation, 2014, Montréal, Quebec, Canada, 2014) p. 91434I.

[43] D. L. Richardson, *Analytic construction of periodic orbits about the collinear points*, Celestial mechanics **22**, 241 (1980).

[44] J. Roberts, *Development of a relative motion model for satellite formation flying around L_2*, (2004).

[45] J. Roberts, *Satellite formation flying for an interferometry mission* (PhD thesis dissertation, Cranfield University, 2005).

[46] O. Junge, J. Levenhagen, A. Seifried, and Dellnitz, *Identification of halo orbits for energy efficient formation flying*. in *International Symposium Formation Flying* (2002).

[47] M. Philips-Blum, T. Pany, K. Frankl, L. Buinhas, and B. Eissfeller, *Advancements of the relative positioning in space within the IRASSI mission concept*, in *2018 AAS/AIAA Astrodynamics Specialist Conference* (Snowbird, UT, USA, 2018).

[48] R. N. Langlois, *Modularity in technology and organization*, Journal of economic behavior & organization **49**, 19 (2002).

[49] O. Brown and P. Eremenko, *Fractionated space architectures: A vision for responsive space,* Tech. Rep. (Defense Advanced Research Projects Agency - DARPA, Arlington, VA, 2006).

[50] R. Zlot and A. Stentz, *Market-based multirobot coordination for complex tasks,* The International Journal of Robotics Research **25**, 73 (2006).

[51] Y.-P. Tian, *Frequency-domain analysis and design of distributed control systems* (John Wiley & Sons, 2012).

[52] S. D'Amico, M. Pavone, S. Saraf, A. Alhussien, T. Al-Saud, S. Buchman, R. Byer, and C. Farhat, *Miniaturized Autonomous Distributed Space System for Future Science and Exploration,* in *International Workshop on Satellite Constellations and Formation Flying* (International Astronautical Federation's Astrodynamics Committee Delft, Delft, Netherlands, 2015) pp. 1–20.

[53] M. Mosleh, K. Dalili, and B. Heydari, *Distributed or monolithic? a computational architecture decision framework,* IEEE Systems journal **12**, 125 (2016).

[54] J. Scharnagl, F. Kempf, and K. Schilling, *Combining distributed consensus with robust h_∞-control for satellite formation flying,* Electronics **8**, 319 (2019).

[55] J. van der Horst and J. Noble, *Distributed and centralized task allocation: When and where to use them,* in *2010 Fourth IEEE International Conference on Self-Adaptive and Self-Organizing Systems Workshop* (IEEE, Budapest, Hungary, 2010) pp. 1–8.

[56] L. Samsó, J. Quirce, and J. Becedas, *Distributed satellite systems: The next big thing is already here,* in *Small Satellite Systems and Services Symposium* (Mallorca, Spain, 2014).

[57] M. Resnick, *Turtles, termites, and traffic jams: Explorations in massively parallel microworlds* (Mit Press, 1997).

[58] P. Baran, *On distributed communications networks,* IEEE transactions on Communications Systems **12** (1964), 10.1109/TCOM.1964.1088883.

[59] M. E. Campbell, *Planning algorithm for multiple satellite clusters,* Journal of Guidance, Control, and Dynamics **26**, 770 (2003).

[60] A. K. Bondhus, K. Y. Pettersen, and J. T. Gravdahl, *Leader/follower synchronization of satellite attitude without angular velocity measurements,* in *Proceedings of the 44th IEEE Conference on Decision and Control* (IEEE, Seville, Spain, 2005) pp. 7270–7277.

[61] S. Vaddi, K. T. Alfriend, S. Vadali, and P. Sengupta, *Formation establishment and reconfiguration using impulsive control,* Journal of Guidance, Control, and Dynamics **28**, 262 (2005).

[62] N. Basilico, N. Gatti, and F. Amigoni, *Leader-follower strategies for robotic patrolling in environments with arbitrary topologies,* in *Proceedings of The 8th International Conference on Autonomous Agents and Multiagent Systems-Volume 1* (International Foundation for Autonomous Agents and Multiagent Systems, Budapest, Hungary, 2009) pp. 57–64.

[63] S. Varma and K. D. Kumar, *Multiple satellite formation flying using differential aerodynamic drag,* Journal of Spacecraft and Rockets **49**, 325 (2012).

[64] P. Wang and F. Y. Hadaegh, *Coordination and control of multiple microspacecraft moving in formation,* (1996).

[65] M. Tillerson, L. Breger, and J. P. How, *Distributed coordination and control of formation flying spacecraft,* in *Proceedings of the 2003 American Control Conference*, Vol. 2 (IEEE, Denver, CO, USA, 2003) pp. 1740–1745.

[66] E. Douglass, M. J. Holzinger, J. W. McMahon, and A. Jaunzemis, *Formation control problems for decentralized spacecraft systems,* in *AAS/AIAA Astrodynamics Specialist Conference* (AAS/AIAA, Hilton Head, SC, USA, 2013).

[67] M. A. Lewis and K.-H. Tan, *High precision formation control of mobile robots using virtual structures,* Autonomous robots **4**, 387 (1997).

[68] P. Ogren, M. Egerstedt, and X. Hu, *A control lyapunov function approach to multi-agent coordination,* in *Proceedings of the 40th IEEE Conference on Decision and Control (Cat. No. 01CH37228)*, Vol. 2 (IEEE, Orlando, FL, USA, 2001) pp. 1150–1155.

[69] B. J. Young, R. W. Beard, and J. M. Kelsey, *A control scheme for improving multi-vehicle formation maneuvers,* in *Proceedings of the 2001 American Control Conference.(Cat. No. 01CH37148)*, Vol. 2 (IEEE, Arlington, VA, USA, 2001) pp. 704–709.

[70] W. Ren and R. Beard, *Virtual structure based spacecraft formation control with formation feedback,* in *AIAA Guidance, Navigation, and control conference and exhibit* (AIAA, Monterey, CA, USA, 2002) p. 4963.

[71] R. W. Beard, T. W. McLain, and F. Y. Hadaegh, *Fuel optimization for constrained rotation of spacecraft formations,* Journal of Guidance, Control, and Dynamics **23**, 339 (2000).

[72] R. W. Beard, J. Lawton, and F. Y. Hadaegh, *A coordination architecture for spacecraft formation control,* IEEE Transactions on control systems technology **9**, 777 (2001).

[73] W. Ren and R. W. Beard, *Decentralized scheme for spacecraft formation flying via the virtual structure approach,* Journal of Guidance, Control, and Dynamics **27**, 73 (2004).

[74] W. Ren and R. W. Beard, *Formation feedback control for multiple spacecraft via virtual structures,* IEE Proceedings-Control Theory and Applications **151**, 357 (2004).

[75] M. Xin, S. Balakrishnan, and H. J. Pernicka, *Position and attitude control of deep-space spacecraft formation flying via virtual structure and θ-d technique,* Journal of Dynamic Systems, Measurement and Control **129**, 689 (2007).

[76] L. Dong, Y. Chen, and X. Qu, *Formation control strategy for nonholonomic intelligent vehicles based on virtual structure and consensus approach,* Procedia Eng **137**, 415 (2016).

[77] Y. Liu, J. Gao, C. Liu, F. Zhao, and J. Zhao, *Reconfigurable formation control of multi-agents using virtual linkage approach,* Applied Sciences **8**, 1109 (2018).

[78] R. Beard, *Architecture and algorithms for constellation control*, Tech. Rep. (Jet Propulsion Laboratory, California Institute of Technology, Pasadena, CA, Tech. Rep, 1998).

[79] R. W. Beard, T. W. McLain, and F. Y. Hadaegh, *Fuel equalized retargeting for separated spacecraft interferometry,* in *Proceedings of the 1998 American Control Conference. ACC (IEEE Cat. No. 98CH36207)*, Vol. 3 (IEEE, Philadelphia, PA, USA, 1998) pp. 1580–1584.

[80] M. Holzinger and J. McMahon, *Decentralized mean orbit-element formation guidance, navigation, and control: Part 1,* in *AIAA/AAS Astrodynamics Specialist Conference* (AIAA/AAS, Minneapolis, MN, USA, 2012) p. 4515.

[81] E. Yang, A. T. Erdogan, T. Arslan, and N. H. Barton, *Adaptive formation control and bio-inspired optimization of a cluster-based satellite wireless sensor network,* in *2008 NASA/ESA Conference on Adaptive Hardware and Systems* (IEEE, Noordwijk, Netherlands, 2008) pp. 432–439.

[82] H. A. Vasavada, *Four-Craft Virtual Coulomb Structure Analysis for 1 to 3 Dimensional Geometries*, Ph.D. thesis, Virginia Tech, Blacksburg, VA, USA (2007).

[83] C. W. Reynolds, *Flocks, herds and schools: A distributed behavioral model,* in *Proceedings of the 14th annual conference on Computer graphics and interactive techniques* (1987) pp. 25–34.

[84] M. J. Mataric, *Designing emergent behaviors: From local interactions to collective intelligence,* in *Proceedings of the Second International Conference on Simulation of Adaptive Behavior* (1993) pp. 432–441.

[85] L. Steels, *The artificial life roots of artificial intelligence,* Artificial Life **1**, 75 (1993).

[86] D. Xu, X. Zhang, Z. Zhu, C. Chen, and P. Yang, *Behavior-based formation control of swarm robots,* Mathematical Problems in Engineering **2014** (2014), https://doi.org/10.1155/2014/205759.

[87] C. R. McInnes, *Autonomous ring formation for a planar constellation of satellites,* Journal of Guidance, Control, and Dynamics **18**, 1215 (1995).

[88] K. Sugihara and I. Suzuki, *Distributed algorithms for formation of geometric patterns with many mobile robots,* Journal of robotic systems **13**, 127 (1996).

[89] T. Balch and R. C. Arkin, *Behavior-based formation control for multirobot teams,* IEEE transactions on robotics and automation **14**, 926 (1998).

[90] B. B. Werger, *Cooperation without deliberation: A minimal behavior-based approach to multi-robot teams,* Artificial Intelligence **110**, 293 (1999).

[91] B. Young and R. W. Beard, *A decentralized approach to elementary formation maneuvers,* in *IEEE Transactions on Robotics and Automation, Princeton University* (IEEE, San Francisco, CA, USA, 2002).

[92] G. Lee and D. Chwa, *Decentralized behavior-based formation control of multiple robots considering obstacle avoidance,* Intelligent Service Robotics **11**, 127 (2018).

[93] L. E. Parker, *Designing control laws for cooperative agent teams,* in *[1993] Proceedings IEEE International Conference on Robotics and Automation* (IEEE, Atlanta, GA, USA, 1993) pp. 582–587.

[94] G. Antonelli, F. Arrichiello, and S. Chiaverini, *Experiments of formation control with multirobot systems using the null-space-based behavioral control,* IEEE Transactions on Control Systems Technology **17**, 1173 (2009).

[95] V. Gazi, *Swarm aggregations using artificial potentials and sliding-mode control,* IEEE Transactions on Robotics **21**, 1208 (2005).

[96] D. Izzo and L. Pettazzi, *Equilibrium shaping: distributed motion planning for satellite swarm,* in *Proc. 8th International Symposium on Artificial Intelligence, Robotics and Automation in Space - iSAIRAS* (Munich, Germany, 2005).

[97] D. Hoffman, *Station-keeping at the collinear equilibrium points of the earth-moon system,* NASA JSC-26189, September (1993).

[98] M. Tillerson, G. Inalhan, and J. P. How, *Co-ordination and control of distributed spacecraft systems using convex optimization techniques,* International Journal of Robust and Nonlinear Control: IFAC-Affiliated Journal **12**, 207 (2002).

[99] J. Russell Carpenter, *Decentralized control of satellite formations,* International Journal of Robust and Nonlinear Control: IFAC-Affiliated Journal **12**, 141 (2002).

[100] J.-C. Latombe, *Robot motion planning*, Vol. 124 (Springer Science & Business Media, 2012).

[101] J. R. Lawton and R. W. Beard, *Synchronized multiple spacecraft rotations,* Automatica **38**, 1359 (2002).

[102] I. Yang, D. Lee, and D. S. Han, *Designing a robust nonlinear dynamic inversion controller for spacecraft formation flying,* Mathematical Problems in Engineering **2014** (2014), https://doi.org/10.1155/2014/471352.

[103] M. S. De Queiroz, V. Kapila, and Q. Yan, *Adaptive nonlinear control of multiple spacecraft formation flying,* Journal of Guidance, Control, and Dynamics **23**, 385 (2000).

[104] J. McMahon and M. Holzinger, *Decentralized mean orbit-element formation guidance, navigation, and control: Part 2,* in *AIAA/AAS Astrodynamics Specialist Conference* (AIAA/AAS, Minneapolis, MN, USA, 2012) p. 4516.

[105] R. Burgon, *Manoeuvre Planning Architecture for the Optimisation of Spacecraft Formation Flying Reconfiguration Manoeuvres*, Ph.D. thesis, Cranfield University (2010).

[106] L. Buinhas, K. Frankl, H. Linz, and R. Förstner, *IRASSI infrared space interferometer: Formation geometry and relative dynamics analysis,* Acta Astronautica **153**, 394 (2018).

[107] D. E. Bernard, G. A. Dorais, C. Fry, E. B. Gamble, B. Kanefsky, J. Kurien, W. Millar, N. Muscettola, P. P. Nayak, B. Pell, *et al.*, *Design of the remote agent experiment for spacecraft autonomy,* in *1998 IEEE Aerospace Conference Proceedings (Cat. No. 98TH8339)*, Vol. 2 (IEEE, Snowmass, CO, USA, 1998) pp. 259–281.

[108] S. Chien, R. Knight, A. Stechert, R. Sherwood, and G. Rabideau, *Using iterative repair to increase the responsiveness of planning and scheduling for autonomous spacecraft,* (1999).

[109] M. Ai-Chang, J. Bresina, L. Charest, A. Chase, J.-J. Hsu, A. Jonsson, B. Kanefsky, P. Morris, K. Rajan, J. Yglesias, *et al.*, *Mapgen: mixed-initiative planning and scheduling for the mars exploration rover mission,* IEEE Intelligent Systems **19**, 8 (2004).

[110] A. Davies, S. Chien, V. Baker, T. Doggett, J. Dohm, R. Greeley, F. Ip, R. Castan, B. Cichy, G. Rabideau, *et al.*, *Monitoring active volcanism with the autonomous sciencecraft experiment on eo-1,* Remote Sensing of Environment **101**, 427 (2006).

[111] K. Rajan, C. McGann, F. Py, and H. Thomas, *Robust mission planning using deliberative autonomy for autonomous underwater vehicles,* ICRA Robotics in challenging and hazardous environments (2007).

[112] T. Huntsberger, H. Aghazarian, D. Gaines, M. Garrett, and G. Sibley, *Autonomous operation of unmanned surface vehicles (USV's),* in *Proc. IEEE ICRA Workshop on Robots in Challenging and Hazardous Environments* (Citeseer, 2007).

[113] J. Bermyn, *Proba-project for on-board autonomy,* Air & Space Europe **2**, 70 (2000).

[114] M. J. Woods, R. S. Aylett, D. Long, M. Fox, and R. Ward, *Developing autonomous ai planning and scheduling technologies for remote planetary exploration,* in *7th ESA Workshop on Advanced Space Technologies for Robotics and Automation* (ASTRA 2002, Noordwijk, The Netherlands, 2002).

[115] O. Camino, M. Alonso, D. Gestal, J. de Bruin, P. Rathsman, J. Kugelberg, P. Bodin, S. Ricken, R. Blake, P. P. Voss, *et al.*, *Smart-1 operations experience and lessons learnt,* Acta Astronautica **61**, 203 (2007).

[116] B. Wille, M. T. Wörle, and C. Lenzen, *Vamos–verification of autonomous mission planning on-board a spacecraft,* IFAC Proceedings Volumes **46**, 382 (2013).

[117] P. Di Lizia, F. Bernelli-Zazzera, A. Ercoli-Finzi, S. Mottola, C. Fantinati, E. Remetean, and B. Dolives, *Planning and implementation of the on-comet operations of the instrument sd2 onboard the lander philae of rosetta mission,* Acta Astronautica **125**, 183 (2016).

[118] P. Van Der Plas, *MAPPS: A science planning tool supporting the ESA Solar System missions,* in *14th International Conference on Space Operations* (SpaceOps Conferences, Daejeon, Korea, 2016) p. 2512.

[119] E. L. Lawler, *The traveling salesman problem: a guided tour of combinatorial optimization,* Wiley-Interscience Series in Discrete Mathematics (1985).

[120] R. Bellman, *Dynamic programming treatment of the travelling salesman problem,* Journal of the ACM (JACM) **9**, 61 (1962).

[121] H. A. Abdulkarim and I. F. Alshammari, *Comparison of algorithms for solving traveling salesman problem,* International Journal of Engineering and Advanced Technology **4**, 76 (2015).

[122] D. L. Applegate, R. E. Bixby, V. Chvatal, and W. J. Cook, *The traveling salesman problem: a computational study* (Princeton university press, 2006).

[123] M. Padberg and G. Rinaldi, *A branch-and-cut algorithm for the resolution of large-scale symmetric traveling salesman problems,* SIAM review **33**, 60 (1991).

[124] H. Marchand, A. Martin, R. Weismantel, and L. Wolsey, *Cutting planes in integer and mixed integer programming,* Discrete Applied Mathematics **123**, 397 (2002).

[125] A. Fest, R. H. Möhring, F. Stork, and M. Uetz, *Resource-constrained project scheduling with time windows: A branching scheme based on dynamic release dates*, Tech. Rep. (Technical University of Berlin, 1999).

[126] P. Brucker, T. Hilbig, and J. Hurink, *A branch and bound algorithm for a single-machine scheduling problem with positive and negative time-lags,* Discrete applied mathematics **94**, 77 (1999).

[127] D. S. Johnson and L. A. McGeoch, *The traveling salesman problem: A case study in local optimization,* in *Local search in combinatorial optimization*, edited by E. H. L. Aarts and J. K. Lenstra (John Wiley and Sons, London, 1997) pp. 215–310.

[128] N. Christofides, *Worst-case analysis of a new heuristic for the travelling salesman problem*, Tech. Rep. (Carnegie-Mellon Univ Pittsburgh Pa Management Sciences Research Group, 1976).

[129] A. Bar-Noy and B. Schieber, *The canadian traveller problem,* in *Proceedings of the 2nd ACM-SIAM Symposium on Discrete Algorithms (SODA)*, Vol. 91 (SODA91: Conference on Discrete Algorithms, San Francisco, CA, USA, 1991) pp. 261–270.

[130] G. Gutin, A. Yeo, and A. Zverovich, *Traveling salesman should not be greedy: domination analysis of greedy-type heuristics for the tsp,* Discrete Applied Mathematics **117**, 81 (2002).

[131] R. Bar-Yehuda, M. M. Halldórsson, J. Naor, H. Shachnai, and I. Shapira, *Scheduling split intervals,* SIAM Journal on Computing **36**, 1 (2006).

[132] T. Vidal, T. G. Crainic, M. Gendreau, and C. Prins, *Timing problems and algorithms: Time decisions for sequences of activities,* Networks **65**, 102 (2015).

[133] J. Hurink and J. Keuchel, *Local search algorithms for a single-machine scheduling problem with positive and negative time-lags,* Discrete Applied Mathematics **112**, 179 (2001).

[134] S. Lin and B. W. Kernighan, *An effective heuristic algorithm for the traveling-salesman problem,* Operations research **21**, 498 (1973).

[135] C. A. Bailey, T. W. McLain, and R. W. Beard, *Fuel-saving strategies for dual spacecraft interferometry missions,* The Journal of the Astronautical Sciences (2001), https://doi.org/10.1007/BF03546233.

[136] O. Martin, S. W. Otto, and E. W. Felten, *Large-step markov chains for the traveling salesman problem,* Complex Systems **5**, 299 (1991).

[137] R. Burgon, P. C. Roberts, J. A. Roberts, and F. Ankersen, *Maneuver planning optimization for spacecraft formation flying missions,* The Journal of the Astronautical Sciences **56**, 545 (2008).

[138] R. W. Beard and F. Y. Hadaegh, *Fuel optimized rotation for satellite formations in free space,* in *Proceedings of the 1999 American Control Conference (Cat. No. 99CH36251)*, Vol. 5 (IEEE, San Diego, CA, USA, 1999) pp. 2975–2979.

[139] O. Junge and S. Ober-Blöbaum, *Optimal reconfiguration of formation flying satellites,* in *Proceedings of the 44th IEEE Conference on Decision and Control* (IEEE, Seville, Spain, 2005) pp. 66–71.

[140] A. Richards, T. Schouwenaars, J. P. How, and E. Feron, *Spacecraft trajectory planning with avoidance constraints using mixed-integer linear programming,* Journal of Guidance, Control, and Dynamics **25**, 755 (2002).

[141] O. L. De Weck, U. Scialom, and A. Siddiqi, *Optimal reconfiguration of satellite constellations with the auction algorithm,* Acta Astronautica **62**, 112 (2008).

[142] R. Armellin, M. Massari, and A. E. Finzi, *Optimal formation flying reconfiguration and station keeping maneuvers using low thrust propulsion,* in *Proceedings of the 18th International Symposium on Space Flight Dynamics (ESA SP-548)*, 548 (Jointly organized by the German Space Operations Center of DLR and the European Space Operations Center of ESA, Munich, Germany, 2004) pp. 429–434.

[143] G. S. Aoude, J. P. How, and I. M. Garcia, *Two-stage path planning approach for solving multiple spacecraft reconfiguration maneuvers,* The Journal of the Astronautical Sciences **56**, 515 (2008).

[144] C. Sun, H. Duan, and Y. Shi, *Optimal satellite formation reconfiguration based on closed-loop brain storm optimization,* IEEE Computational Intelligence Magazine **8**, 39 (2013).

[145] C. Audet and J. E. Dennis Jr, *Mesh adaptive direct search algorithms for constrained optimization,* SIAM Journal on optimization **17**, 188 (2006).

[146] *MATLAB Global Optimization Toolbox (R2019a)*, 1 Apple Hill Drive, Natick, MA 01760-2098, USA.

[147] R. T. Marler and J. S. Arora, *The weighted sum method for multi-objective optimization: new insights,* Structural and multidisciplinary optimization **41**, 853 (2010).

[148] Y. Kim, M. Mesbahi, and F. Y. Hadaegh, *Multiple-spacecraft reconfiguration through collision avoidance, bouncing, and stalemate,* Journal of Optimization Theory and Applications **122**, 323 (2004).

[149] S. Wang and H. Schaub, *Electrostatic spacecraft collision avoidance using piecewise-constant charges,* Journal of guidance, control, and dynamics **33**, 510 (2010).

[150] C. Sultan, S. Seereeram, R. K. Mehra, and F. Y. Hadaegh, *Energy optimal reconfiguration for large scale formation flying,* in *Proceedings of the 2004 American Control Conference*, Vol. 4 (IEEE, Boston, MA, USA, 2004) pp. 2986–2991.

[151] S. Li, R. Mehra, R. Smith, and R. Beard, *Multi-spacecraft trajectory optimization and control using genetic algorithm techniques,* in *2000 IEEE Aerospace Conference. Proceedings (Cat. No. 00TH8484)*, Vol. 7 (IEEE, Big Sky, MT, USA, 2000) pp. 99–108.

[152] S. Hönig, M. Kishimoto, K. Tristram, M. Prieto, P. Gandhi, D. Asmus, R. Antonucci, L. Burtscher, W. Duschl, and G. Weigelt, *Dust in the polar region as a major contributor to the infrared emission of active galactic nuclei,* The Astrophysical Journal **771**, 87 (2013).

[153] A. B. DeCou, *Station-keeping strategy for multiple-spacecraft interferometry,* in *Space Astronomical Telescopes and Instruments*, Vol. 1494 (International Society for Optics and Photonics, Orlando, FL, United States, 1991) pp. 440–451.

[154] E. M. Kong, D. W. Miller, and R. J. Sedwick, *Exploiting orbital dynamics for interstellar separated spacecraft interferometry,* in *Proceedings of the 1999 American Control Conference (Cat. No. 99CH36251)*, Vol. 6 (IEEE, San Diego, CA, USA, 1999) pp. 4153–4157.

[155] I. Hussein, D. Scheeres, and D. Hyland, *Interferometric observatories in earth orbit,* Journal of guidance, control, and dynamics **27**, 297 (2004).

[156] I. I. Hussein and D. J. Scheeres, *Effects of Orbit Variations and J2 Perturbations on a Class of Earth-Orbiting Interferometric Observatories,* The Journal of the Astronautical Sciences **53**, 147 (2005).

[157] I. I. Hussein, D. J. Scheeres, A. M. Bloch, D. C. Hyland, and N. H. McClamroch, *Optimal motion planning for dual-spacecraft interferometry,* IEEE Transactions on Aerospace and Electronic Systems **43**, 723 (2007).

[158] I. I. Hussein, D. J. Scheeres, and D. C. Hyland, *Control of a satellite formation for imaging applications,* in *Proceedings of the 2003 American Control Conference, 2003.*, Vol. 1 (IEEE, Denver, CO, USA, 2003) pp. 308–313.

[159] S. Chakravorty and J. Ramirez, *Fuel optimal maneuvers for multispacecraft interferometric imaging systems,* Journal of guidance, control, and dynamics **30**, 227 (2007).

[160] J. Ramirez and S. Chakravorty, *Two-stage controller algorithm for multi-spacecraft interferometric imaging systems,* IEEE Transactions on Aerospace and Electronic Systems **46**, 1248 (2010).

[161] J. W. Cooley and J. W. Tukey, *An algorithm for the machine calculation of complex fourier series,* Mathematics of computation **19**, 297 (1965).

[162] R. L. Burden and J. D. Faires, *The bisection algorithm,* Numerical analysis , 46 (1985).

A

Complementary Information on Mission Analysis

A.1. Description of Mission Phases before Nominal Operations

1. Pre-Launch
   Pre-launch activities comprise of final checkouts of hardware and software equipment prior to launch, preparations of the launch pad, fueling and tank pressurization of the launcher and its stages and preparation of the synchronized and countdown sequences.

2. Launch
   The Launch phase is initiated by the removal of the umbilical circuit from the ground, followed by the irreversible engine ignition sequences. Three launchers are used to deploy the five-element formation, in a 2-2-1 sequence. The Launch lasts until the upper stage engines shut down after intercepting the desired highly elliptical orbit around Earth. Launch capacity is highly dependent on available technology and given the time distance between the present research work and a hypothetical IRASSI launch, specific decisions concerning launcher types, maximum allowable mass, etc., cannot be reached.

3. Deployment of Propulsion Modules
   The propulsion modules are deployed after insertion in the highly elliptical near-Earth orbit, preceding the Transfer Cruise to L_2.

4. Transfer Cruise to L_2
   The transfer starts immediately after the deployment of the propulsion module and finishes with the deployment of the individual spacecraft. During this phase, the module travels from the near-Earth highly elliptical orbit into deep space, reaching the vicinity of L_2. Intermediary corrections are made in order to adjust the trajectory of the propulsion module and ultimately achieve the final orbit around L_2 successfully.

5. Deployment of Spacecraft
   Following the transfer and preceding the Activation & Initial Formation phase, the spacecraft are deployed in the target orbit. During this deployment process, either the propulsion module or the newly-ejected spacecraft should perform a collision-avoidance maneuver to allow for the safe continuation of the deployment of the remaining spacecraft and avoid contact with both the propulsion module or soon-to-be-ejected spacecraft.

   In addition, once all spacecraft are deployed, the disposal of the propulsion module should be ensured, such that it will not obstruct the orbits of spacecraft around L_2. A potential burn maneuver could thrust the propulsion module in the anti-Sun direction, for instance.

6. Activation & Initial Formation
   After the formation deployment, vital subsystems need to be activated. Batteries supply power for the initial reorientation and attitude correction of the spacecraft, and solar array deployment. The initial Sun acquisition, deployment of antennas and other necessary appendages is performed, followed

by the initiation of the communication units, checks on the overall health of the spacecraft and preliminary testing of onboard equipment. The spacecraft should also acquire the initial constellation geometry in the operational L_2 orbit.

7. Subsystem & Payload Commissioning
   This phase prepares all the vital and scientific apparatus for their nominal activities during the mission. Besides regular checks to functions such as thermal balance and radiation shielding, which ensure the survival of the payload, all scientific instruments should be initiated and verified for instance, by sending and receiving telemetry from the scientific instruments via the data-handling subsystem and monitoring the produced contents.

A.2. LAUNCH-WINDOW OPTIMIZATION PROCEDURE

The launch window optimization procedure is described in the pseudocode of the next page. The core algorithm consists of nested loops employing a bisection method [162] to its control variables. The trajectory prescribed is that of Ariane 5 Flight 188 [32]. The nominal values of the simulation parameters are:

$$\delta\dot{x}_{nom} = \delta\dot{z}_{nom} = 0 \tag{A.1a}$$

$$\Lambda_{E,nom} = 27.35° \tag{A.1b}$$

where $\delta\dot{x}_{nom}$ and $\delta\dot{x}_{nom}$ relate to the vicinity of the L_2 orbit, in the $\mathscr{L}_2$ frame, and $\Lambda_{E,nom}$ is the longitude of the propulsion module once it intercepts the HEO orbit. The same variables without the subscript ('nom') refer to the measured values. The 'RAAN' term refers to the Right-ascension of the Ascending Node of the HEO orbit. Finally, subscripts 'u' and 'l' refer respectively to upper and lower boundary values.

Algorithm 3 IRASSI launch-window selection in the years of 2029 and 2030.

```
Define:
δẋ_nom, δż_nom, Λ_E,nom

Require:
Launch time boundaries: t_u, t_l > 0
RAAN boundaries: RAAN_u, RAAN_l > 0
ΔV lower boundary: ΔV_l > 0
ΔV_esc upper boundary: ΔV_esc, u > 0

Initialize:
Sat, Propulsion Module (PM)

for Date = January 1st, 2029 : 1 : December 31st 2030 do
    while Λ_E − Λ_E,nom ≥ 10^−3 do
        Update: PM.Epoch = Epoch(Date, t)
        while |δż − δż_nom| ≥ 10^−3 do
            Update: PM.RAAN

            while PM escapes to heliocentric orbit during transfer do
                Propagate PM Near Earth for 25.7 hours
                Update: ΔV_esc
                Apply ΔV_esc and Propagate PM Transfer for 50 days
                if |δẋ − δẋ_nom| ≤ 10^−5 then
                    ΔV upper boundary: ΔV_u = ΔV_esc
                end if
            end while

            while |δẋ − δẋ_nom| ≥ 10^−5 do
                Propagate PM Near Earth for 25.7 hours
                Update: ΔV
                Apply ΔV and Propagate PM Transfer to δẋ = 0 and δẏ = 0
                Propagate PM Transfer to L2-orbit insertion point
                Measure |δẋ − δẋ_nom| and apply bisection to ΔV
            end while
            Measure |δż − δż_nom| and apply bisection to RAAN
        end while
        Measure |Λ_E − Λ_E,nom| and apply bisection to launch time t
    end while

    /* Assume Sat is deployed from PM */
    Propagate Sat around L2 for 5 years & Perform station-keeping every 6 months
    if δ_y,max ≤ A_y,max ∧ A_z,min ≤ δ_z,max ≤ A_z,max then
        Add Date to launch-window database
    end if
end for
```

B

Complementary Analysis of Formation Geometry

The present appendix chapter aims to complement and support the analysis of the Formation Geometry addressed in Chapter 4. The representation of the formation in the celestial sphere is described and results concerning further formation geometry conditions, demonstrating the relationship between relative position assignment and sky accessibility.

B.1. Formation Geometry and Sky Access

In order to perform a transformation of the formation arrangement in the local coordinate system $\mathscr{L}$ devised in Section 4.2.1 to the exclusion zone area projected onto the celestial sphere, the ecliptic celestial coordinate system S_0 is firstly described. S_0, is an orthonormal inertial reference frame with basis vectors $\{\boldsymbol{x_0}, \boldsymbol{y_0}, \boldsymbol{z_0}\}$, with a primary direction $\boldsymbol{x_0}$ pointing to the J2000 Vernal Equinox and secondary direction $\boldsymbol{z_0}$ pointing to the north ecliptic pole (parallel to the angular momentum vector of the Earth's orbit around the Sun); $\boldsymbol{y_0}$ completes the right-hand frame and both $\boldsymbol{x_0}$ and $\boldsymbol{y_0}$ lie in the plane of the ecliptic [1].

If the Earth revolves around the Sun in one year, then the Sun-Earth line moves, defined by the $\boldsymbol{\Delta x}$-axis, along the x_0-y_0 plane at a rate of 360 deg/year or 0.9856 deg/day. The simulation epoch *or* the initial anti-Sun vector longitude define then the angular displacement of the $\boldsymbol{\Delta x}$-axis on the x_0-y_0 plane of S_0, that is, the phase λ at which the exclusion zone is evaluated. For example, when the spacecraft longitude coincides crosses the Vernal Equinox axis, $\lambda = 0$. Since the radius of the celestial sphere is considered to be infinite, any point within it can be considered the center. This applies to the spacecraft and they are thus located at the origin of S_0. The size of the sphere can be adjusted for representation purposes. And finally, the coordinate system $\mathscr{L}$ is set to be centered on one of the spacecraft pair being analyzed for the study.

B.1.1. Conical Projection onto Sphere

Once the relative distance between spacecraft $\boldsymbol{l_{ez}}$ and the cone half-angle θ_{ez} are known (cf. Table 4.2), the cone which defines the exclusion zone must be projected on a sphere. This sphere has a radius equivalent to the relative distance value $||\boldsymbol{l_{ez}}||$. Let us denote $\boldsymbol{l_{ez}}$ as:

$$\boldsymbol{l_{ez}} = l_{ez_x}\boldsymbol{\Delta x} + l_{ez_y}\boldsymbol{\Delta y} + l_{ez_z}\boldsymbol{\Delta z} \tag{B.1}$$

where l_{ez_x}, l_{ez_y} and l_{ez_z} are scalar values at the simulation epoch and $\boldsymbol{\Delta x}$, $\boldsymbol{\Delta y}$ and $\boldsymbol{\Delta z}$ are the basis vectors of the local frame $\mathscr{L}$. Then the height of the cone is scaled such that:

$$\boldsymbol{l_{ez_{sc}}} = \boldsymbol{l_{ez}} \cos(\theta_{ez}) \tag{B.2}$$

and the corresponding scaled cone radius $q_{ez_{sc}}$ becomes:

$$q_{ez_{sc}} = ||\boldsymbol{l_{ez}}|| \sin(\theta_{ez}) \wedge \boldsymbol{q_{ez_{sc}}} \perp \boldsymbol{l_{ez_{sc}}} \tag{B.3}$$

[1] This coordinate system is also described and used in Chapter 7.4

$\boldsymbol{q_{ez_{sc}}}$ denotes any vector connecting the center of the cone base to any point on its outer radius. This process is illustrated in Figures B.1(a) and B.1(b), respectively first, in a two-dimensional example whereby the magnitudes of $\boldsymbol{l_{ez_{sc}}}$ and $\boldsymbol{q_{ez_{sc}}}$ are shown, and then on celestial sphere with the appropriate vectorial representation.

B

With this new geometrical reference, the base of the scaled cone defines the exclusion zone. If each point ρ circumscribing this area is defined as $\rho = (\rho_x, \rho_y, \rho_z)$ in the local $\mathscr{L}$ frame, then the latitude Φ and longitude Λ values of ρ become:

$$\Phi_\rho = \frac{\pi}{2} - \tan^{-1}\left(\frac{||\boldsymbol{\Delta\hat{z}} \times \boldsymbol{\rho}||}{\boldsymbol{\Delta\hat{z}} \cdot \boldsymbol{\rho}}\right) \tag{B.4}$$

$$\Lambda_\rho = \tan^{-1}\left(\frac{\rho_y}{\rho_x}\right) + \lambda, \tag{B.5}$$

where $\boldsymbol{\Delta\hat{z}}$ is the unit vector of the local $\mathscr{L}$ reference frame, $\boldsymbol{\rho}$ is the vector connecting the the origin of the $\mathscr{L}$ frame and point ρ and λ is the angular phase of $\boldsymbol{\Delta x}$ along the x_0-y_0 plane of the inertial frame and keeping in mind that the z_0-axis of the inertial sphere onto which the celestial sky is projected, is parallel to the Δz-axis of the local $\mathscr{L}$ frame. The conversion from date in a J2000 standard epoch to λ, in degrees, is a simplified multiplication of the number of days elapsed from the J2000 Vernal Equinox and the field-of-view slew rate of $\frac{360^\circ}{365.25 \text{ days}} = 0.9856^\circ/\text{day}$. Given that the rate of change of the true equinox with respect to the Vernal Equinox of the J2000 is approximately 1.4° per century, this is deemed a reasonable simplification.

The final projection of the exclusion zone on the celestial sphere is shown in Figure B.1(c), along with the respective latitude and longitude values of point ρ, respectively Φ_ρ and Λ_ρ.

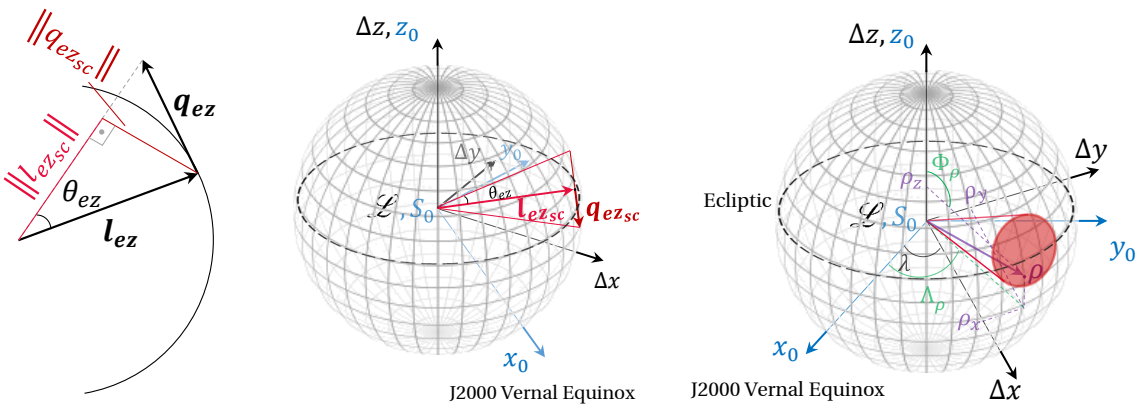

(a) 2D representation (b) 3D representation (c) Final projection

Figure B.1: Illustration of the exclusion zones projection onto celestial sphere.

B.1.2. ADDITIONAL EXCLUSION ZONE RESULTS

To further illustrate the effect of relative position assignment, the analysis on the exclusion zones is expanded in this subsection. The setup of the analysis is the same as that described in Section 4.2.4 and will not be reiterated here in entirety. Two different pointing directions of the telescopes are analyzed and, for each, two different values of the out-of-plane component h are tested. In these examples, h becomes a function of factor f, whilst retaining its dependency on d as shown in Section 4.2.4:

$$h_i = \left\{-fd, -\frac{f}{2}d, 0, \frac{f}{2}d, fd\right\}, \quad i = \{T_1, T_2, T_3, T_4, T_5\} \tag{B.6}$$

The factor receives the value of $f = 0.1$ and $f = 10$, whereas d is set at $d = 100$ m. The corresponding exclusion zone projections are show in Figures B.2 and B.3. It is noteworthy how a low value of the out-of-plane component h ($0 \leq ||h|| \leq 10$ m) with respect to d ($d = 100$ m), shifts exclusion zone projections to lower latitude regions for a Π_N orientation parallel to the Δz-Δx plane and to higher latitudes for a Π_N orientation parallel to the Δy-Δx plane in comparison with a higher out-of-plane component h value ($0 \leq ||h|| \leq 1000$ m).

A change of h in the Δz affects only the latitude of the projection, since it induces a change in the $l_{ez_{sc_z}}\boldsymbol{\Delta z}$ component and thus in the ρ_z value, as explained in the previous section. If $l_{ez_{sc_x}}\boldsymbol{\Delta x}$ and $l_{ez_{sc_y}}\boldsymbol{\Delta y}$ remain

unchanged changed, so does ρ_x and ρ_y, and hence the longitude. This is observed in Figures B.2(a) and B.2(b), when the orientation of Π_N is parallel to the Δy-Δx plane.

Conversely, a change of h in either the Δy or Δx directions, affects both the longitude (due to the term $||\boldsymbol{l_{ez_{sc}}}||$ in Equation B.4) and the latitude, since ρ_x and ρ_y depend on the $l_{ez_{sc_x}}\boldsymbol{\Delta x}$ and $l_{ez_{sc_y}}\boldsymbol{\Delta y}$ components of $\boldsymbol{l_{ez_{sc}}}$. This is why a longitudinal shift, apart from the latitude deviation, is observed between Figures B.3(a) and B.3(b).

The results in terms of total exclusion zone relative to celestial sky area projection area, A_{rest}, as described by Equation 4.15, are summarized in Table B.1. For the small formation case hereby considered, that is, $f = 0.1$, the exclusion zone affects a quarter of one percent of the celestial sky, whereas for the large formation case, with $f = 10$, the exclusion zones make up only 0.009% of the total sky area. Lastly, in Figures B.2(b) and B.3(b), all exclusion zones fall exclusively on the accessible sky, that is, outside the 'forbidden' region dictated by the sunshields.

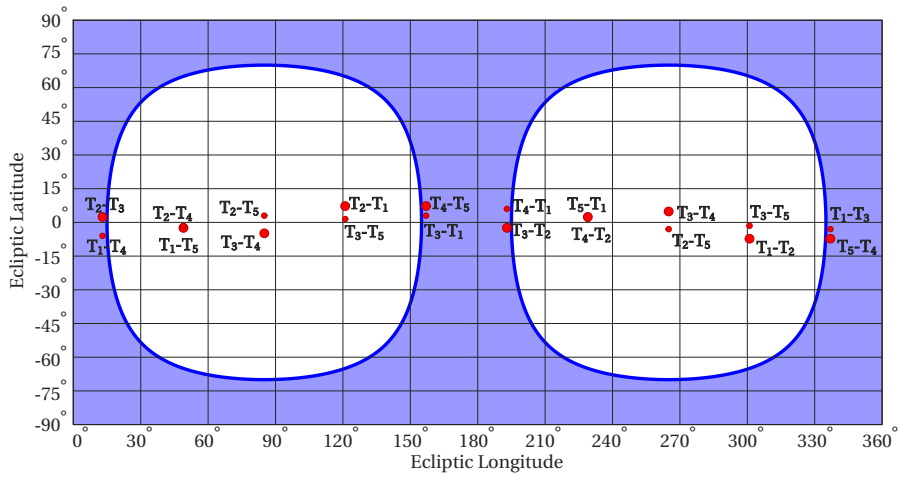

(a) $f = 0.1$ m

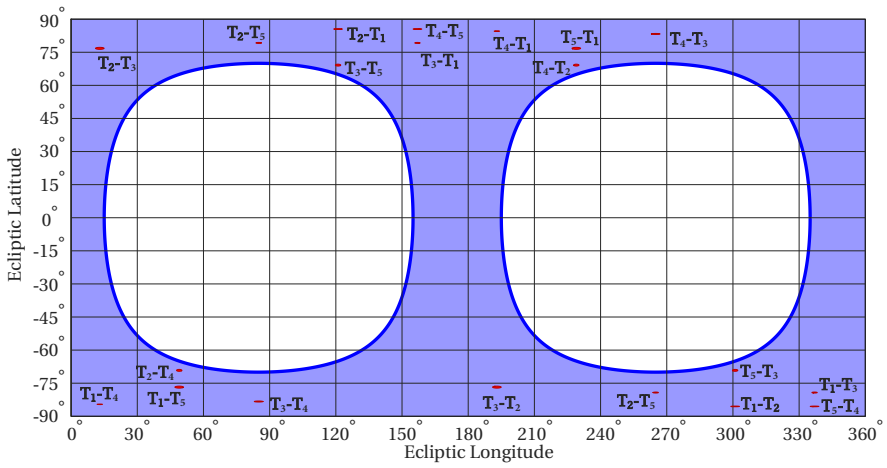

(b) $f = 10$ m

Figure B.2: Instantaneous sky access for a formation pointing direction parallel to Δy-Δx plane for 12th June.

B

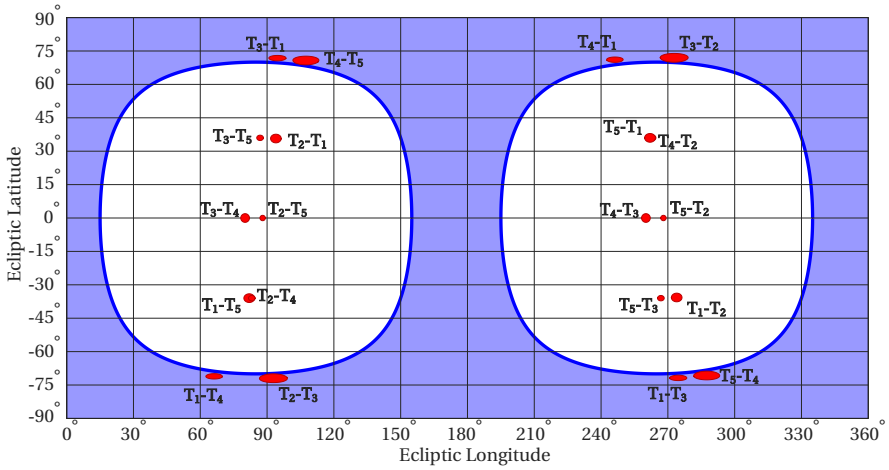

(a) $f = 0.1$ m

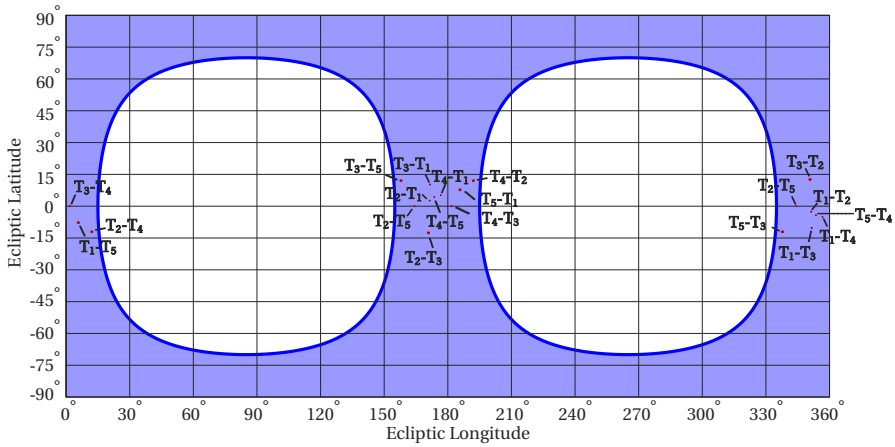

(b) $f = 10$ m

Figure B.3: Instantaneous sky access for a formation pointing direction parallel to Δz-Δx plane for 12th June.

Table B.1: Percentage of exclusion zone A_{rest} affecting the celestial sky for different values of factor f, by setting $d = 100$ m.

Formation pointing direction in the $\mathscr{L}$ frame	A_{rest}	
	$f = 0.1$	$f = 10$
Parallel to Δy-Δx plane	0.250	0.009
Parallel to Δz-Δx plane	0.250	0.009

C

Complementary Analysis of Formation Dynamics

The present appendix accompanies the Formation Dynamics assumptions and results introduced in Chapter 5. The first part of the chapter defines the variables used in the linearized third-order solution for periodic motion along Halo orbits in the circular-restricted problem. In addition, the validity of this model and its simplifications is demonstrated for short-term simulations, which calculate the ephemeris of the formation based on numerical integration.

The second section of this appendix presents the relative errors of positions and velocities of the Roberts' model. And the last section provides additional formation dynamics results that complement section 5.4.

C.1. Constant Definition and Results

C.1.1. Constant Definition

The following sets of equations shall define the constants presented from Equations 5.12 through Equation 5.9. They were introduced in Chapter 5.2 as part of Richardson's analytical solution [43] for describing Halo-type periodic motion about collinear Lagrange points.

$$a_{21} = \frac{3c_3\left(k^2-2\right)}{4\left(1+2c_2\right)} \tag{C.1}$$

$$a_{22} = \frac{3c_3}{4\left(1+2c_2\right)} \tag{C.2}$$

$$a_{23} = \frac{3c_3\gamma}{4kd_1}\left[3k^3\gamma - 6k(k-\gamma)+4\right] \tag{C.3}$$

$$a_{24} = \frac{3c_3\gamma}{4kd_1}\left(2+3k\gamma\right) \tag{C.4}$$

$$\begin{aligned} a_{31} = &-\frac{9\gamma}{4d_2}\left[4c_3\left(ka_{23}-b_{21}\right)+kc_4\left(4+k^2\right)\right]+ \\ &+\left(\frac{9\gamma^2+1-c_2}{2d_2}\right)\left[3c_3\left(2a_{23}-kb_{21}\right)+c_4\left(2+3k^2\right)\right] \end{aligned} \tag{C.5}$$

$$\begin{aligned} a_{32} = &-\frac{1}{d_2}\left\{\frac{9\gamma}{4}\left[4c_3\left(ka_{24}-b_{22}\right)+kc_4\right]+\right. \\ &\left.+\frac{3}{2}\left(9\gamma^2+1-c_2\right)\left[c_3\left(kb_{22}+d_{21}-2a_{24}\right)-c_4\right]\right\} \end{aligned} \tag{C.6}$$

$$b_{21} = -\frac{3c_3\gamma}{2d_1}\left(3k\gamma-4\right) \tag{C.7}$$

$$b_{22} = -\frac{3c_3\gamma}{d_1} \tag{C.8}$$

$$b_{31} = \frac{3}{8d_2}\left\{8\gamma\left[3c_3\left(kb_{21}-2a_{23}\right)-c_4\left(2+3k^2\right)\right]+ \right. \\ \left. +\left(9\gamma^2+1+2c_2\right)\left[4c_3\left(ka_{23}-b_{21}\right)-kc_4\left(4+k^2\right)\right]\right\} \tag{C.9}$$

$$b_{32} = \frac{1}{d_2}\left\{9\gamma\left[c_3\left(kb_{22}+d_{21}-2a_{24}\right)-c_4\right]+ \right. \\ \left. +\frac{3}{8}\left(9\gamma^2+1+2c_2\right)\left[4c_3\left(ka_{24}-b_{22}\right)+kc_4\right]\right\} \tag{C.10}$$

$$d_{21} = -\frac{c_3}{2\gamma^2} \tag{C.11}$$

$$d_{31} = \frac{3}{64\gamma^2}\left(4c_3a_{23}+c_4\right) \tag{C.12}$$

$$d_{32} = \frac{3}{64\gamma^2}\left[4c_3\left(a_{23}-d_{21}\right)+c_4\left(4+k^2\right)\right] \tag{C.13}$$

And with

$$c_n = \frac{1}{\chi_L^3}\left[(-1)^n\mu+(-1)^n\frac{\left(1-\mu\right)\chi_L^{n+1}}{\left(1+\chi_L^{n+1}\right)^{n+1}}\right] \tag{C.14}$$

where μ denotes the mass ratio of the Earth+Moon binary, M_E and M_M respectively, relative to the mass of the system, which also includes the mass of the primary body, the Sun, M_S:

$$\mu = \frac{M_E+M_M}{M_E+M_M+M_S} \tag{C.15}$$

Additionally,

$$d_1 = \frac{3\gamma^2}{k}\left[k\left(6\gamma^2-1\right)-2\gamma\right] \tag{C.16}$$

$$d_2 = \frac{8\gamma^2}{k}\left[k\left(11\gamma^2-1\right)-2\gamma\right] \tag{C.17}$$

For the frequency correction of Equation 5.5:

$$s_1 = \frac{1}{2\gamma\left[\gamma\left(1+k^2\right)-2k\right]}\left\{\frac{3}{2}c_3\left[2a_{21}\left(k^2-2\right)-a_{23}\left(k^2+2\right)-2kb_{21}\right]- \right. \\ \left. -\frac{3}{8}c_4\left(3k^4-8k^2+8\right)\right\} \tag{C.18}$$

$$s_2 = \frac{1}{2\gamma\left[\gamma\left(1+k^2\right)-2k\right]}\left\{\frac{3}{2}c_3\left[2a_{22}\left(k^2-2\right)+a_{24}\left(k^2+2\right)+2kb_{22}+5d_{21}\right]- \right. \\ \left. -\frac{3}{8}c_4\left(12-k^2\right)\right\} \tag{C.19}$$

where

$$k = \frac{1}{2\gamma}\left(\gamma^2+1+2c_2\right) = \frac{2\gamma}{\left(\gamma^2+1-c_2\right)} \tag{C.20}$$

The linearized frequency γ is computed from the solution to the fourth-order equation below:

$$\gamma^4+\left(c_2-2\right)\gamma^2-\left(c_2-1\right)\left(1+2c_2\right)=0 \tag{C.21}$$

For the amplitude-constraint relationship of Equation 5.8:

$$l_1 = a_1+2\gamma^2 s_1 \tag{C.22}$$

$$l_2 = a_2+2\gamma^2 s_2 \tag{C.23}$$

where

$$a_1 = -\frac{3}{2}c_3\left(2a_{21}+a_{23}+5d_{21}\right)-\frac{3}{8}c_4\left(12-k^2\right) \tag{C.24}$$

$$a_2 = \frac{3}{2}c_3\left(a_{24}-a_{22}\right)+\frac{9}{8}c_4 \tag{C.25}$$

C.1.2. CONSTANT NUMERICAL RESULTS

The constants are implemented in MATLAB [146] and the results are verified by matching the condition to that selected by Richardson [43]. First and foremost, the amplitude in the δz-axis, A_z, must be set to A_z=125 000 km. The remaining obtained constant values are presented in Table C.1.

From Table C.1 it can be concluded that the values are very much equal or comparable to those obtained by Richardson. Eventual discrepancies may lie in floating-point accuracies of MATLAB. The model is therefore deemed as correctly implemented and Richardson's results are verified.

C.2. VALIDATION OF RICHARDON'S MODEL FOR HALO-TYPE ORBITS

The Lindstedt-Poincaré approach developed by Richardson [43] summarized by Equations 5.1a to 5.1c, provides an uncontrolled periodic solution of a spacecraft orbiting the vicinity of the L_2 point of two larger primary bodies, in a Halo orbit. In order to evaluate the linearization error of the analytical solution, simulations were carried out for different initial conditions, namely for different orbit amplitudes (the selection of different orbit locations and times of the year was analyzed for the relative motion and is referred to in the body of the paper, in Section 5.3.2).

The Richardson's Model was implemented in MATLAB and compared with the numerical solutions of GMAT. The GMAT setup is the same as the relative dynamics analysis in Chapters 5.3 and 5.4 - the Earth was chosen as the primary, central body with the Moon and the Sun as point masses in the force model and solar radiation pressure was considered. The modeling error was evaluated for two cases, Case 1 and Case 2, whose properties are presented in Table C.2. Case 1 corresponds to the nominal one, analyzed in Chapters 5.3 and 5.4. For both Case 1 and Case 2 the initial position of the formation reference point reflects a phase $\phi = 0°$ at the start. The simulation time was fixed at 20 days, with time steps of 1 hour for both MATLAB and GMAT. The error was calculated by subtracting the analytical solution of Richardson from GMAT's solution. The selected simulation epoch was arbitrarily selected as March 1st, 2030, at 12 o'clock.

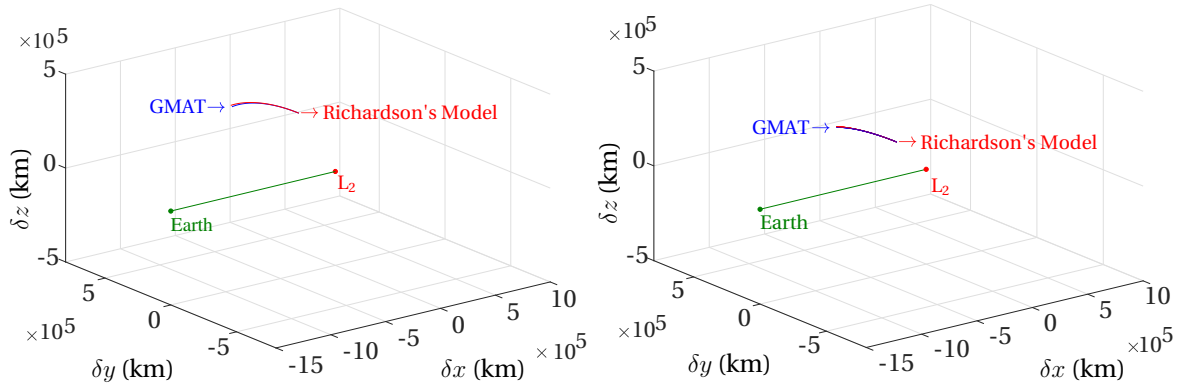

(a) Case 1

(b) Case 2

Figure C.1: Halo motion for 20 days of simulation. Comparison between GMAT and Richardson's model in a L_2-centered frame.

At a first glance, little difference is observed for both cases of Figure C.1 between GMAT's numerical model and Richardson's analytical solution. However, it becomes clear that, over time, there is a divergence between the two models, particularly with respect to the motion along the δx-axis, as Figure C.2(a) and Figure C.2(b) show.

For Case 1, after 20 days, the difference in absolute terms corresponds to 7 853 km, 2 413 km and 7 693 km, respectively for the δx-, δy- and δz-axes. Comparatively, for Case 2, the divergence is less pronounced, with a deviation of 1 144 km in δx, -673 km in δy and -3 636 km in the δz-axis. Thus the magnitude of the modeling error is dependent on the amplitudes of the selected Halo orbits: a larger Halo (Case 1) will deviate more significantly than a smaller one (Case 2). Moreover, the negative values of the δx coordinate seem consistently overestimated by Richardons' model[1]. In percentage terms, however, this is not necessarily observed. Comparing Figures C.3(a) and C.3(b), for instance, the deviation percentage between GMAT and Richardson's

[1]For clarity, in the simulation considered, the values of the δx coordinate are negative both for GMAT and in Richardson's model, but since in the latter case the absolute value is greater than in the former case, the error is positive in the images of Figure C.2. This also explains why the percentage error is negative in Figure C.3.

C

Table C.1: Obtained values of the constants for Halo orbits around L_2, according to Richardson's formulas [43].

Parameter	**Value**
a_1 (km)	$1.495978706910 0 \times 10^{11}$
n_1 (rad/sec)	$1.991024040237 8 \times 10^{-7}$
μ	$3.040225128781 5 \times 10^{-6}$
γ	2.056973404245 4
k	3.187171114207 2
Γ	$2.907831619558 5 \times 10^{-1}$
c_2	3.940356423816 9
c_3	−2.979676594960 7
c_4	2.970091265856 5
s_1	$-7.444634962151 0 \times 10^{-1}$
s_2	$1.250447633303 1 \times 10^{-1}$
l_1	$-1.482777467620 2 \times 10^{1}$
l_2	1.673639727373 9
a_1	−8.527916738204 7
a_2	$6.154760311329 7 \times 10^{-1}$
d_1	$2.931678895403 6 \times 10^{2}$
d_2	$1.497882726546 0 \times 10^{3}$
a_{21}	−2.052907801343 4
a_{22}	$-2.516416738793 6 \times 10^{-1}$
a_{23}	$8.962370495326 2 \times 10^{-1}$
a_{24}	$1.065986435879 7 \times 10^{-1}$
a_{31}	$7.806035504216 9 \times 10^{-1}$
a_{32}	$8.369473363112 7 \times 10^{-2}$
b_{21}	$4.913377038045 5 \times 10^{-1}$
b_{22}	$-6.271951050331 0 \times 10^{-2}$
b_{31}	$8.552539705521 5 \times 10^{-1}$
b_{32}	$2.043371799002 7 \times 10^{-2}$
d_{21}	$3.521127741779 0 \times 10^{-1}$
d_{31}	$1.882885174152 7 \times 10^{-2}$
d_{32}	$3.940147723881 5 \times 10^{-1}$

Table C.2: Initial conditions of formation reference point relative to L_2.

Parameters	**Case 1**	**Case 2**
A_x (km)	250 272.869	221 566.865
A_y (km)	794 070.722	703 086.472
A_z (km)	400 000.000	200 000.000
Initial Position δx_0 (km)	−332 435.467	265 324.918
Initial Position δy_0 (km)	0.000	0.000
Initial Position δz_0 (km)	357 052.550	180 937.186
Initial Velocity $\delta \dot{x}_0$.000 (km s^{-1})	0.000	0.000
Initial Velocity $\delta \dot{y}_0$.000 (km s^{-1})	0.352	0.304
Initial Velocity $\delta \dot{z}_0$.000 (km s^{-1})	0.000	0.000

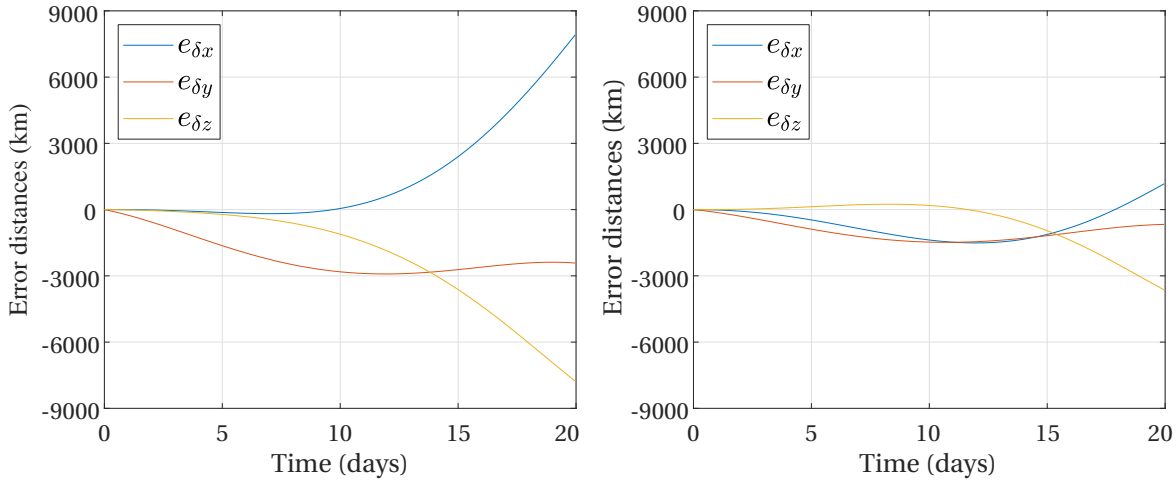

(a) Case 1 (b) Case 2

Figure C.2: Halo motion modeling error (absolute) between GMAT and Richardson's model.

model is comparable for both cases for the δy and δz coordinates at the 20-day mark at less than 0.5% and 3.5% respectively. The percentage error for the δx coordinate, on the other hand, is approximately 5.5 times greater for Case 1 than for Case 2. The percentage error is given as the ratio between the distance error (shown in Figure C.2) and the real instantaneous value of each coordinate determined with GMAT.

From these simulations, it can be concluded that the analytical solution will always lead to a divergence of the trajectory relative to the numerical case. However, Richardson's analytical solution provides a useful approximation for up to 10 to 20 days, seldom exceeding an error percentage of 1% over the first two weeks for the tested initial conditions. Given that for the IRASSI mission, scientific activities take place over the course of typically 48 hours (occasionally during one week), this analytical solution is then a reasonable tool to model the motion of a spacecraft in a Halo orbit around L_2 on a preliminary basis.

C.3. VALIDATION OF ROBERTS' MODEL

C.3.1. GENERAL CASE

The general case corresponds to the first tested case in section5.3.1, with an epoch arbitrarily selected as that of March 1st, 2030, at 12 o'clock and an initial phase $\phi = 0°$.

Figure C.4(a) shows the percentage error of relative distances whereas Figures C.4(b) and C.4(c) show the

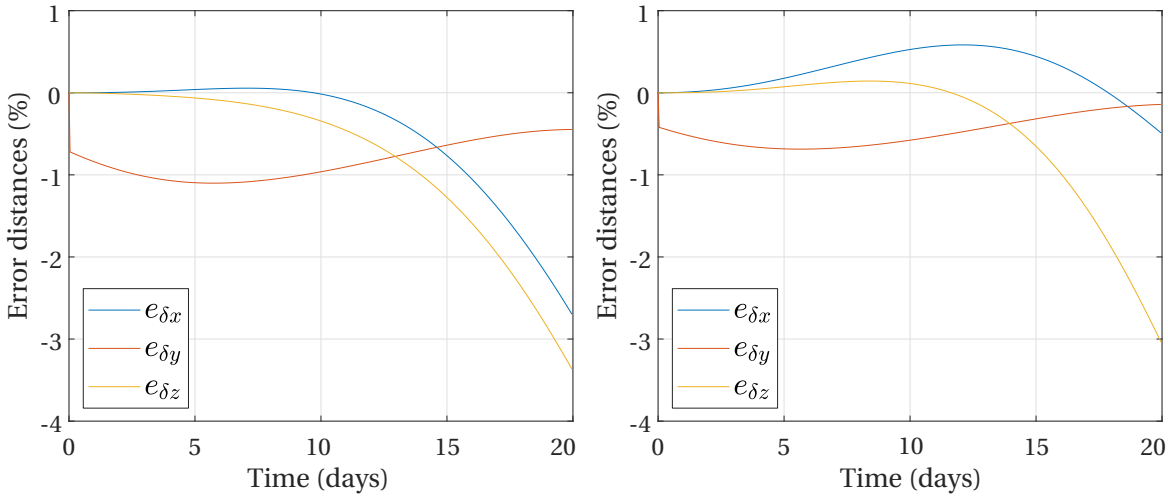

(a) Case 1 (b) Case 2

Figure C.3: Halo motion modeling error (percentual) between GMAT and Richardson's model.

percentage error of velocities. The percentage error is given as the ratio between the distance or velocity errors (shown in Figure 5.6) and the real instantaneous value of each coordinate distance or velocity determined with GMAT. At the end of the simulation, the error along the Δx-axis amounts to approximately 14% of distance along the same coordinate. The percentage error of Δy is the lowest of the three, at less than 10% over the simulated time of 20 days and it is positive given that the direction of the movement is increasing along the negative direction of the Δy-axis. This is interesting to observe: although the deviation of Δy rises fast in the last half of the simulation (as Figure 5.6(a) shows), the model captures the change in the Δy coordinate better than in the other two cases (Δx and Δz). In particular, it is clear that the lowest absolute error, corresponding to Δz is also the one which is modeled the poorest with the gravity-gradient equations of relative motion since the percentage of the error rises to nearly -50% of the real distance along the same coordinate: that is, the Roberts' model significantly overestimates the magnitude of the Δz position, in the negative direction of the same axis.

The percentage error of the relative velocity along the Δy coordinate, $e_{\Delta \dot{y}}$, shows that the gravity-gradient model increasingly underestimates $\Delta \dot{y}$ over time, reaching a maximum of 25% at the end of the simulation. This leads to the conclusion that even though the distance is proportionally better modeled than the other coordinates with Roberts' model, this is only true because of the limited simulation time. The parabolic increase in the $\Delta \dot{y}$ percentage error would eventually lead to biases in the Δy distance and, due to the motion coupling shown in Equations 5.12a to 5.12c, contribute to modeling errors in the other two coordinates (Δx and Δz). Conversely, the percentage error of $\Delta \dot{z}$ decreases from approximately 27% to less than 21% over the 20 days. The percentage error of $\Delta \dot{x}$ is shown separately in Figure 5.6(b), where a high overestimation by the gravity-gradient model is detected. The graph shows two interesting peaks around day 13, with extrema at about 161 000 % and -65 000 %. This is because GMAT predicts that $\Delta \dot{x}$ increases positively for the first week (not directly obvious in the graph due to the scale) and thereafter continuously decreases, reversing its direction on the 13th day around which the peaks are observed and retaining values very close to zero. On the other hand, Roberts' model predicts a monotonous $\Delta \dot{x}$ increase in magnitude in the negative direction. The mean percentage error is 513% in the first half of the simulation and -306% in the last five days.

INFLUENCE OF REFERENCE POINT'S LOCATION ON RELATIVE DYNAMICS MODELING ERROR

INITIAL PHASE ϕ

Overall, from Figure 5.8(a) the Roberts' model seems slightly more accurate in the vicinity of the extrema values of δz, when the phase is $\phi = 0°$ or $\phi = 180°$ for the simulation time considered. But interestingly, the percentage of the error of Figure C.5(a), albeit minor for all cases, is slightly higher for $\phi = 0°$, at nearly 10%, than for $\phi = 180°$, at 8.6%. The same trend is visible in Figure C.5(b), where the lowest deviation percentages are for initial phases $\phi = 180°$ and $\phi = 270°$. The percentage error of the velocities is nearly double to that of the positions for each case at the end of the simulation but nearly comparable for the first half. The percentage error is given as the ratio between the distance or velocity errors (shown in Figure 5.8) and the real

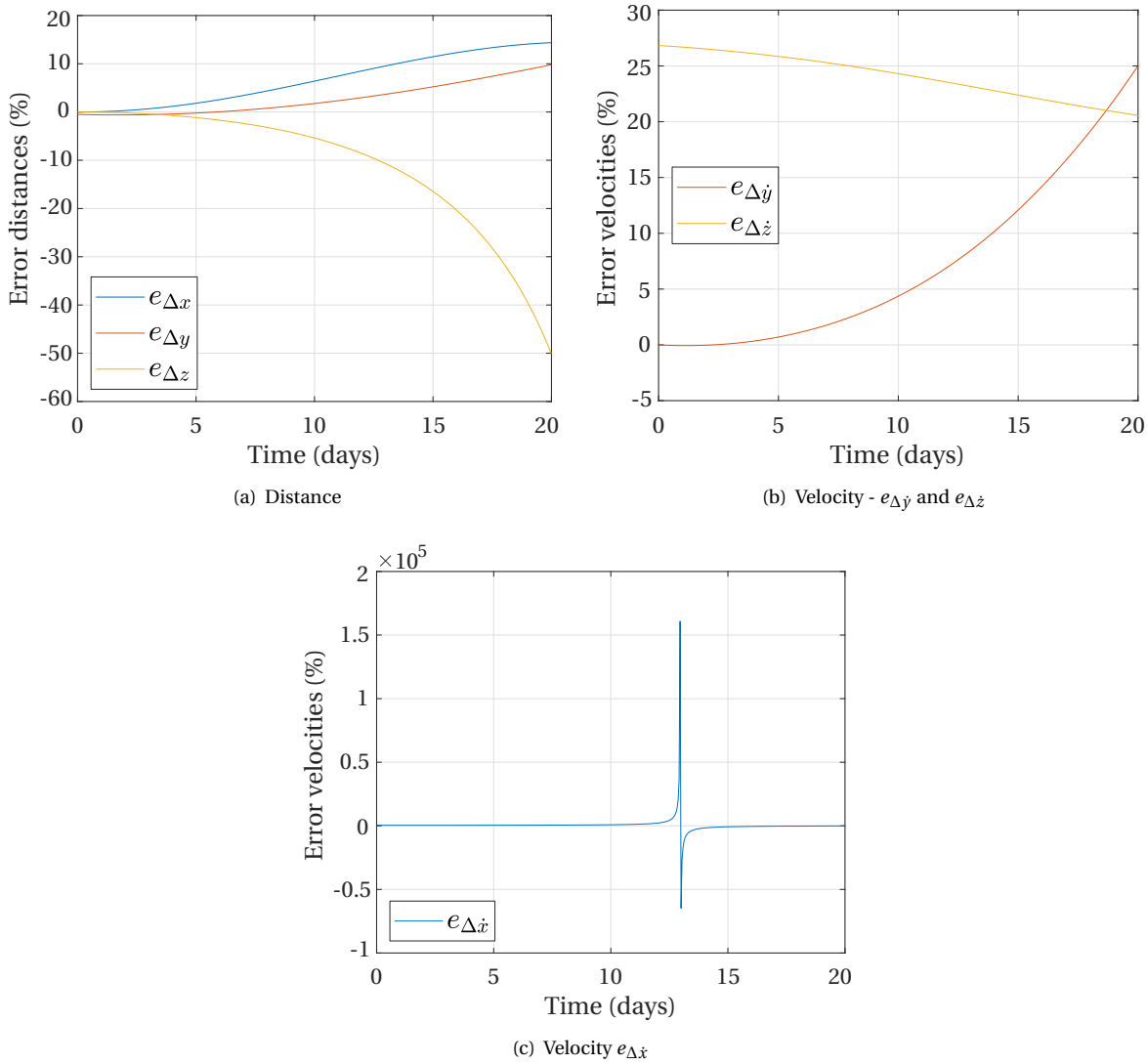

(a) Distance

(b) Velocity - $e_{\Delta \dot{y}}$ and $e_{\Delta \dot{z}}$

(c) Velocity $e_{\Delta \dot{x}}$

Figure C.4: Relative motion modeling error (percentage) between GMAT and Roberts' model. Epoch of simulation is March 1st, 2030.

instantaneous value of each coordinate distance or velocity determined with GMAT.

C.4. DYNAMICS OF THE IRASSI FORMATION AROUND L_2

C.4.1. ADDITIONAL RELATIVE DRIFT RESULTS

To further understand the relative motion of the formation under uncontrolled dynamics, the analysis of the relative drift is expanded in this subsection. The initial conditions of the spacecraft are defined in Table 5.2 for the small and large formation scenarios. The Π_N plane is oriented parallel to the Δy-Δx plane (parallel to the ecliptic plane), defining the pointing direction of the formation. The initial phase corresponds to $\phi = 0°$.

Figure C.6 shows the evolution of the relative distance among spacecraft pairs for both scenarios. As observed in Section 5.4.1, the majority of the pairs experiences a decrease in separation. Note in Figure C.7, however, that the ratio between the change in position (drift) and initial separation is inversely proportional to the measured distance among spacecraft: the drift is proportionally larger for closer pairs than for more separated pairs.

The drift along the coordinate relative to the formation reference point, located on reference plane Π_N, as a function of time, is shown in Figure C.8 and Figure C.9 respectively for the small and large formation scenarios. Similarly, in Figures C.10 and C.11, the drift along each coordinate is plotted relative to the others in order to offer a parallel for the diagrams of the more typical LVLH (Local Vertical Local Horizontal) frame

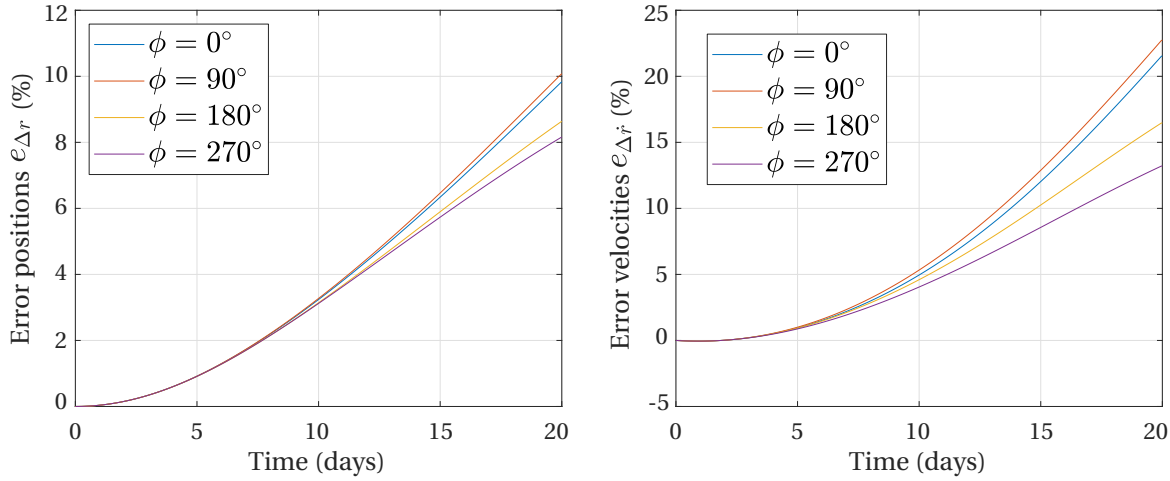

(a) Position (b) Velocity

Figure C.5: Relative motion modeling error (percentage) between GMAT and Roberts' model for different initial phase values ϕ.

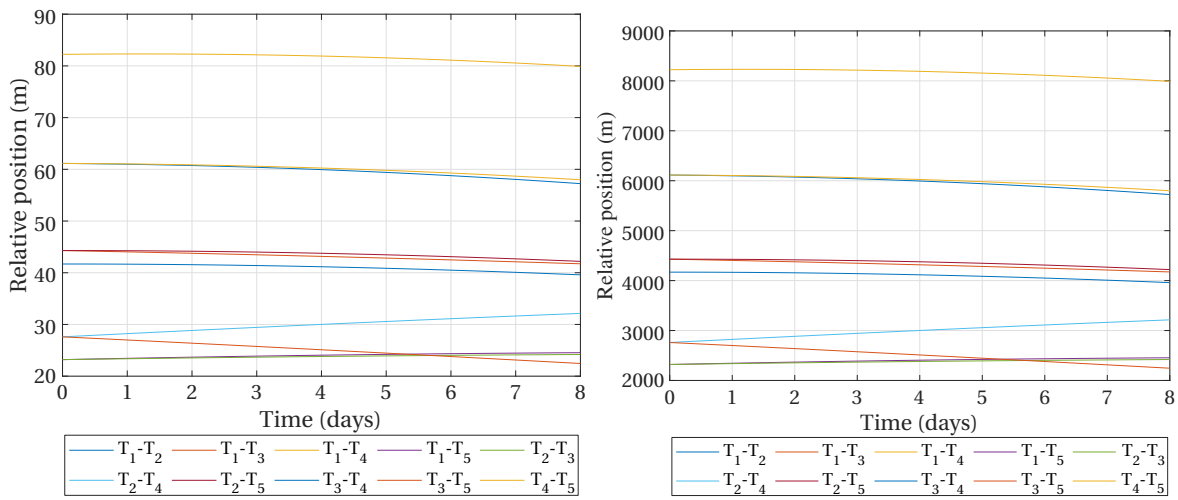

(a) Small formation (b) Large formation

Figure C.6: Relative position over time for both formation scenarios

for Earth-orbiting formations.

From Figure C.10 and Figure C.11, it is possible to see that changes along the Δz coordinates are significantly smaller than for the Δx and Δy for the initial part of the simulation, but an exponential increase brings it to a magnitude change of a total of 2 meters for the small formation scenario (and two orders of magnitude greater for the large formation scenario), comparable with the changes along the Δx-axis. The higher the initial Δz_0, the higher the out-of-plane drift, and the further away from the primaries (Δz_0>0), the more the telescopes will be pulled towards the reference point along Δz. The highest value of Δx_0, for T_1, is associated with the highest drift along the Δy coordinate, as a result of the coupling in Equations 5.12a until 5.12c.

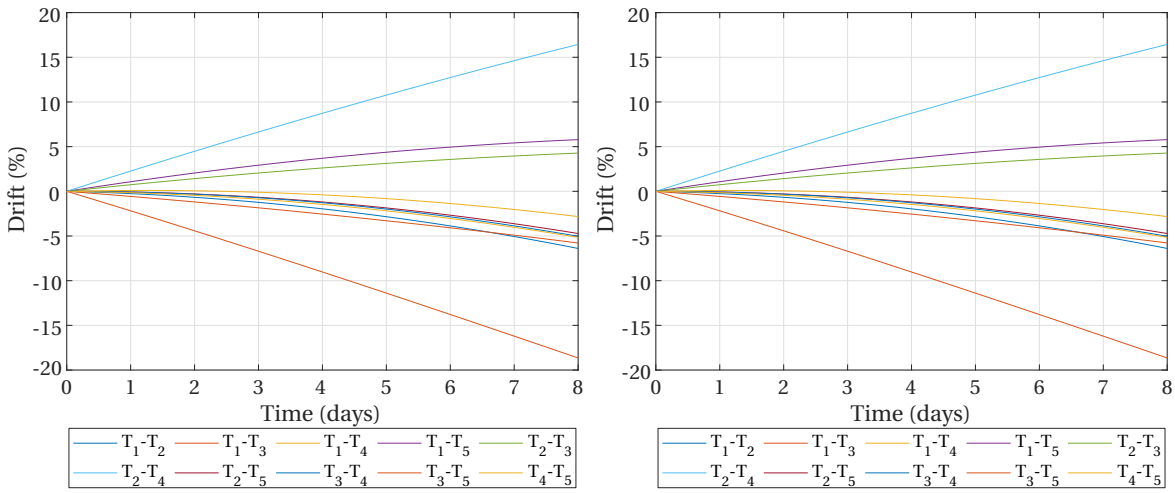

(a) Small formation (b) Large formation

Figure C.7: Drift percentage over time for both formation scenarios.

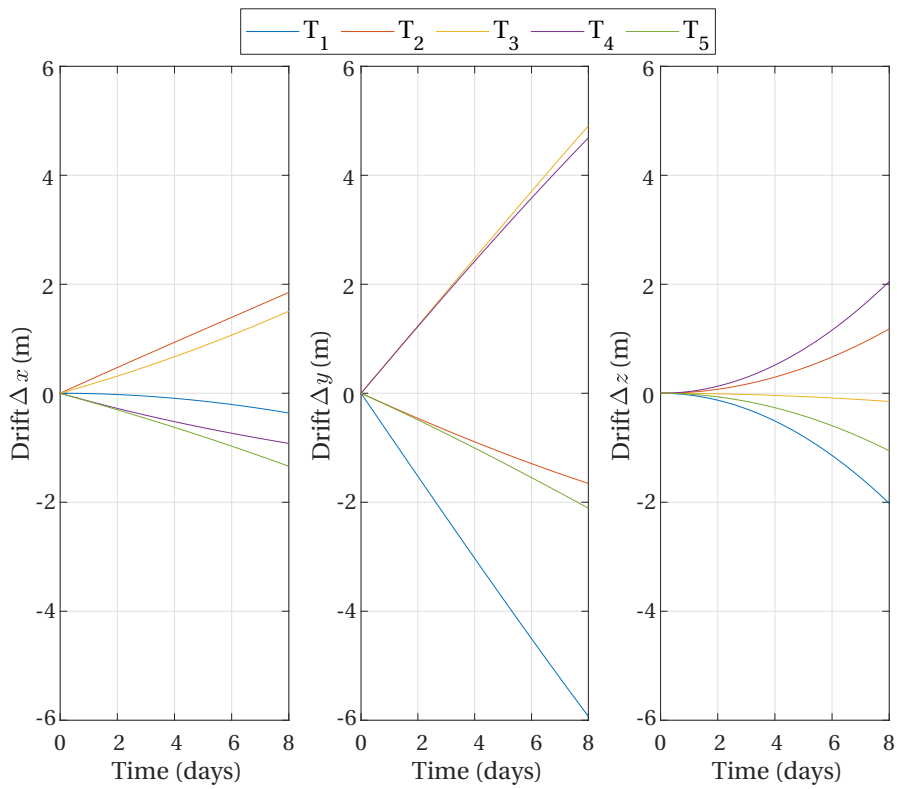

Figure C.8: Time-evolution of drift relative to formation reference point - small formation scenario.

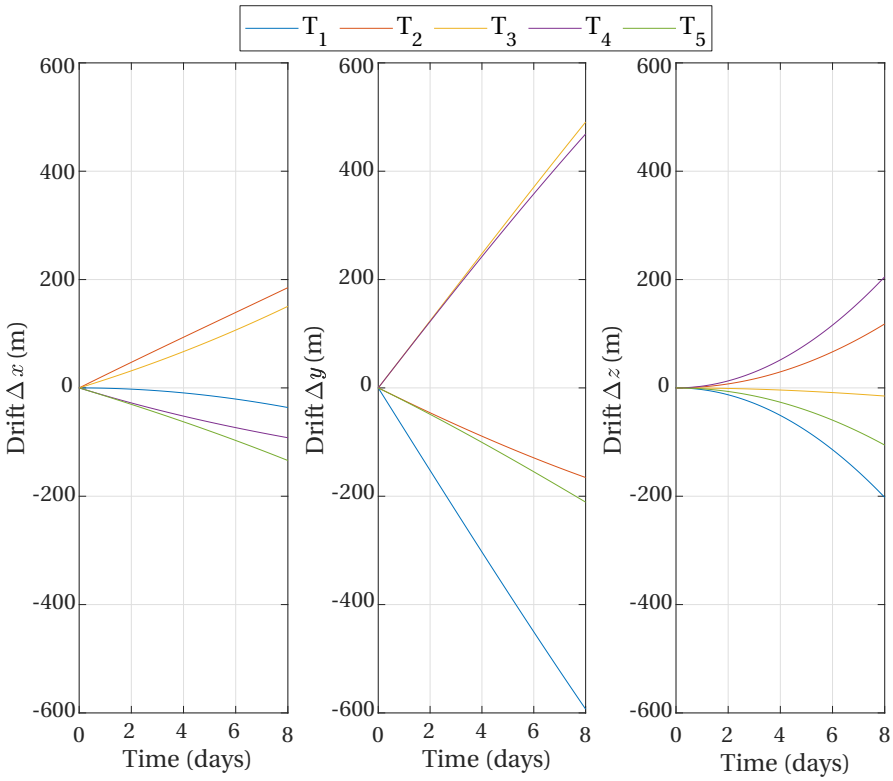

Figure C.9: Time-evolution of drift relative to formation reference point - large formation scenario.

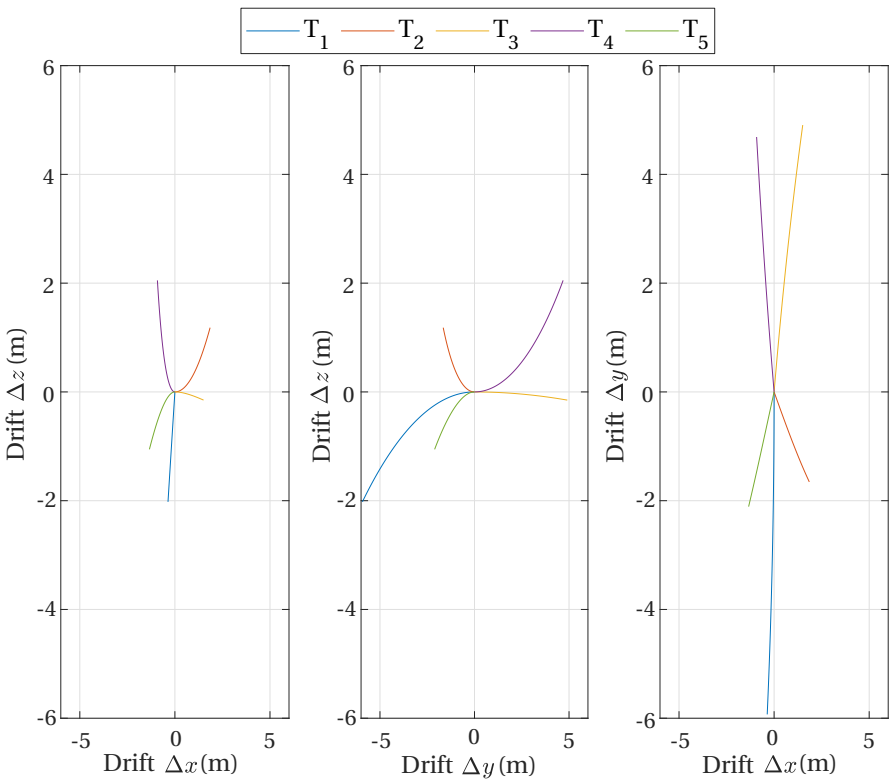

Figure C.10: Drift along coordinates relative to formation reference point - small formation scenario.

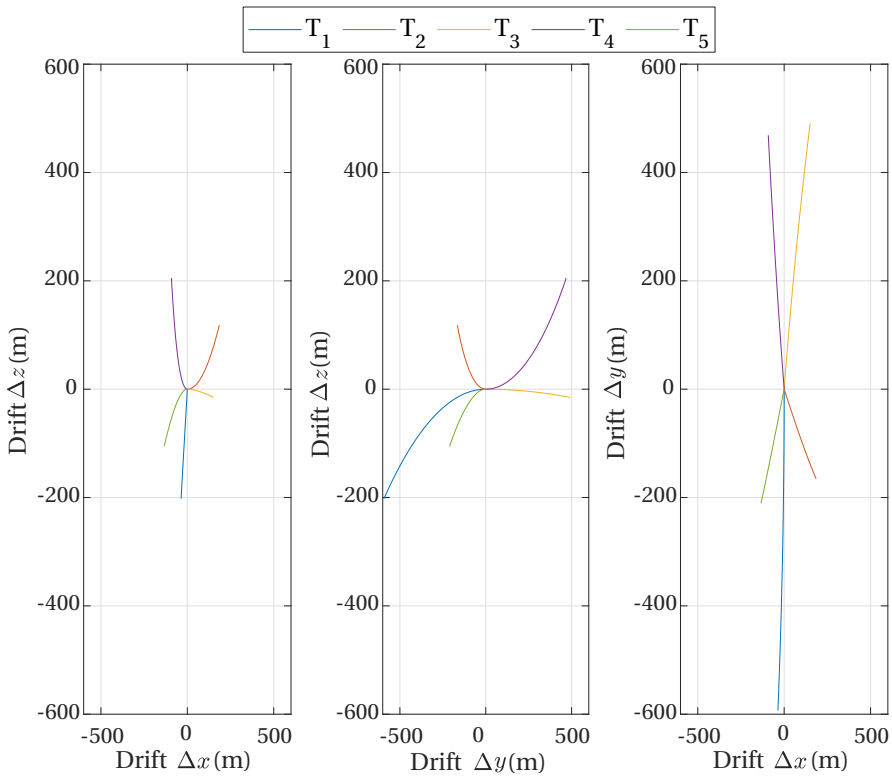

Figure C.11: Drift along coordinates relative to formation reference point - large formation scenario.

D

Complementary Analysis of TPM

The present appendix chapter aims to complement and support the analysis of the Task-Planner Module (TPM), introduced in Chapter 8. Entry values of IRASSI catalog targets are summarized and the distribution of target types is presented. Tour results discretized at annual intervals for different TPM task-sequencing algorithms are compared.

D.1. IRASSI Catalog

The IRASSI catalog is the main source of information of iSCOUT. It contains a list of targets identified in the frame of the IRASSI feasibility study. Each target contains specific information which determines the overall sequence of science observations (TPM) and shapes the formation maneuver requirements prior (ReM/CAM) and during the observations (CAM). Table D.1 provides an overview of the entry values for each target.

D.2. Target Distribution

Figure D.1 shows the distribution of target types with latitude. It is visible from the plot, for example, that there is a large concentration of Type-I targets (T Tauri stars and disks) near the equatorial regions and that Type-V targets (galaxies) are predominant in the latitude ranges below 20°. Type-II targets (Herbig Ae/Be stars) are common in the latitude regions between −35° to −25° an in the high latitudes of the northern hemisphere, >55°. With one exception, all Type-III targets (debris disks) are located in the southern hemisphere. Of the total 61 emission-sensitive types (Types IV, VI and VII), 44 are located in the northern hemisphere, including all of the Type-VI targets.

The distribution of target types with respect to longitude is shown in Figure D.2, where it can be observed that target groups are generally aggregated by area. For instance, the vast majority of Type-V targets are situated within the 160°-205° band. Conversely, no target of Types III, IV, VI and VII can be found in the longitude range of 100°-230°, whereas in the same region only two Type-I targets are found. The elusive Type-VI targets (high-mass star-forming regions) exist only in the longitude ranges below 65° and above 300° and Type-I targets are severely concentrated in two regions, at around 70°-80° and again in the vicinity of 235°-250°. Since these two regions are separated by 180°, the opportunity to observe these target types arises only twice a year and the observation window for each one lasts for approximately two weeks.

D.3. IRASSI Task Tour

D.3.1. Additional SNS-5 Tour Results.

Table D.2 shows the breakdown of the SNS-5 tour per repetition.

D.3.2. Additional NNH Tour Results.

Table D.3 shows the metrics breakdown of the NNH tour on an annual basis. Figure D.3(a) shows the evolution of the three metrics over the five-year simulation and the average annual metric correlation relative to J_{TPM} is shown in Figure D.3(b). The overall correlation values are presented in Table D.4.

D

Table D.1: Catalog entry values.

Parameter	**Possible value and value ranges**
Ecliptic longitude	$[0°, 360°[$
Ecliptic latitude	$[-90°, 90°]$
Priority	{1, 2, 3, 4 }
Number of visits	{1, 2, 3}
Observation duration	[0.1, 8] days
Target name	{...}
Target type	{Massive young stellar objects, Galaxies and galactic center, Herbig stars or disks, T Tauri stars or disks, Active Galactic Nuclei (AGNi), High-mass forming regions, Hot Cores or Hot Corinos, FU-Orionis class stars and objects or debris disks}
Target no.	{I, II, III, IV, V, VI, VII, VIII, IX}
(U, V)-plane scan length	{intermediate, long}
Emission sensitivity	{low, high}

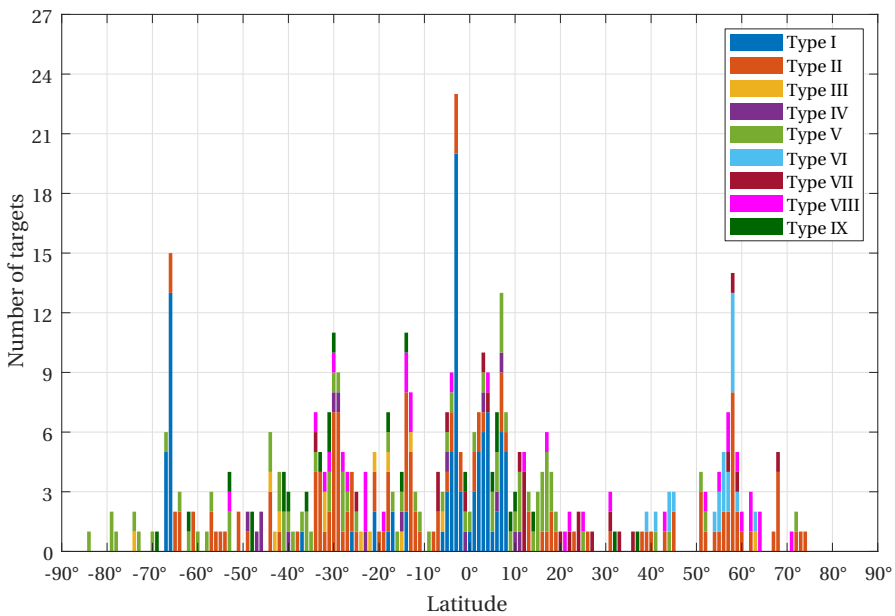

Figure D.1: Distribution of target types relative to celestial latitude.

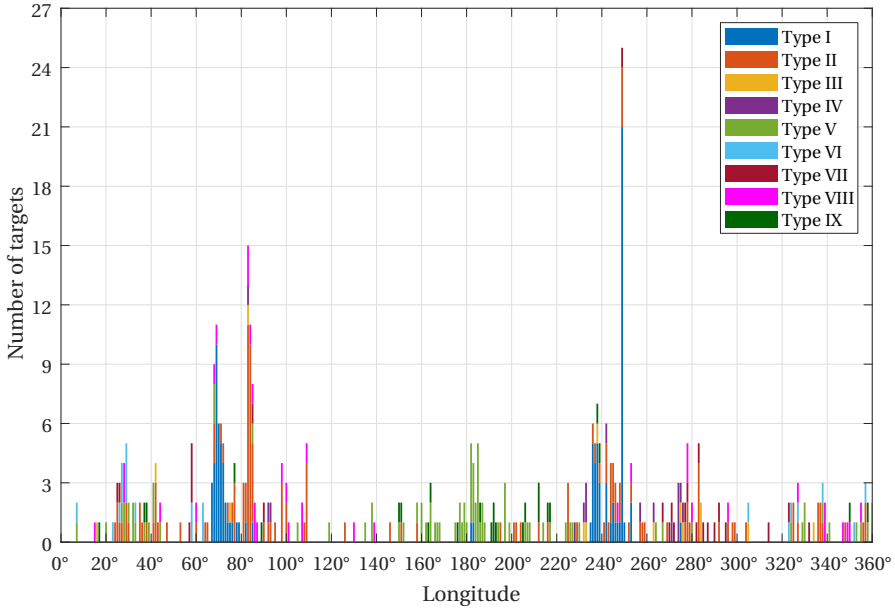

Figure D.2: Distribution of target types relative to celestial longitude.

Table D.2: Results of TPM's IRASSI Task Tour for the SNS-5 algorithm. With $t_{BPM} \approx t_{sci}$, t_{BPM} becomes a measure of the observation duration.

Parameter	**SNS-5**				
	Rep. 1	**Rep. 2**	**Rep. 3**	**Rep. 4**	**Rep. 5**
Completed tasks (%)	80	79	79	78	79
Completed tasks	630	616	621	615	619
No. idle days	310	331	323	343	339
No. single tasks available	144	142	140	146	143
Mean tasks per day	0.35	0.34	0.34	0.34	0.34
Mean t_{BPM} (days)	1.97	1.98	1.97	1.96	1.96
Mean t_{ReM} (hours)	2.55	2.83	2.85	2.82	2.63
Mean J_{TPM} (-)	0.29	0.29	0.29	0.29	0.29

Table D.3: Yearly average results of TPM's IRASSI Task Tour for the NNH algorithm.

Mean Performance	**NNH**					
	Start	**Year 1**	**Year 2**	**Year 3**	**Year 4**	**Year 5**
J_{TPM}	–	0.093	0.208	0.361	0.426	0.399
T_{rel}	–	0.046	0.021	0.070	0.089	0.065
P_{rel}	–	0.151	0.333	0.557	0.519	0.414
N_{rel}	–	0.082	0.271	0.457	0.669	0.718

D

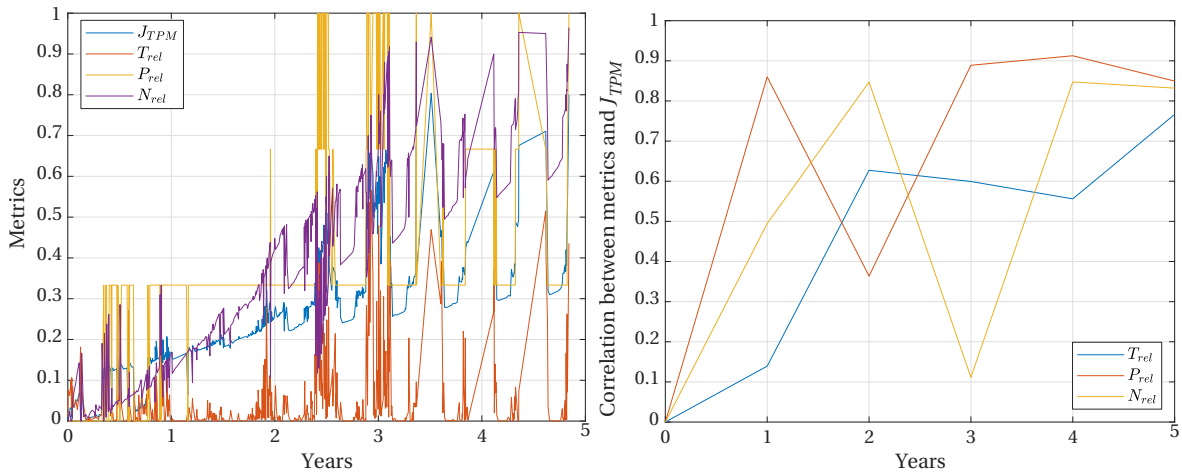

(a) Metric

(b) Yearly metric correlations

Figure D.3: Evolution of metrics over time and correlation of individual metrics with J_{TPM} taken at yearly intervals.

Table D.4: Correlation of individual metrics to overall J_{TPM}.

Metric	**Correlation value**
T_{rel}	0.49
P_{rel}	0.86
N_{rel}	0.82

E

Complementary Analysis of ReM

The present appendix section aims to complement the analysis of the Reconfiguration Module (ReM), introduced in Chapter 9. The following subsections provide details at the formation level on ΔV metrics and distance traveled and on the resource management of individual spacecraft and the variation of simulation parameters such as thrust force and specific impulse. The chapters and subchapters follow the same structure as Chapter 9.

E.1. Example IRASSI Tour

E.1.1. Additional formation results

The ΔV-associated results of Section 9.4.2 are shown in Figures E.1 and E.2. Figure E.3 shows the mean distance traveled with the corresponding standard deviations.

E.1.2. Individual results

The results presented in Section 9.4.2 are hereby discriminated by spacecraft. The fuel used and ΔV expended are shown for both the fuel-based and ΔV-based cost functions, such that it is possible to inspect how resources are managed according to each cost function (even though they optimize for different resources). These results are provided in Figures E.4 and E.5. Additionally, the distance traveled in inertial space is presented in Figure E.6. In all figures, $T_i, i = 1, \cdots, 5$, denotes the individual telescopes.

As expected, it may be observed that higher values of the simulation parameters μ_f and $\mu_{\Delta V}$ (respectively, first and third plot from the top of Figures E.4 until E.6) promote a more leveled use of resources among spacecraft, independently of the metric considered. Additionally, the peaks in fuel consumption and ΔV expenditure of section 9.4.2 (Figures 9.3 and E.1) are also visible in the bottom plot of Figures E.4 until E.6, whereby a three-fold increase in fuel or ΔV use is distinguishable for the ninth and tenth maneuvers, respectively '$S_{10} - M_{500}$' and '$M_{500} - S_{10}$'. Interestingly, the impact on the distance traveled is not linearly related to resource consumption, as the spacecraft are commanded to travel more than 10 times further compared to the other maneuvers.

E.2. Effective Envelopes

E.2.1. Case A

The ΔV-associated results of Section 9.4.3 for Case A are shown in Figures E.7(a) and E.7(b). Figure E.7(c) shows the maneuver duration for the $J_{\Delta V}$ cost function.

Variability

In addition, the present subsection provides a short analysis of the spread of the results of the repetitions concerning the four metrics described in Table 9.2: fuel used, sum of fuel differences, ΔV expended and sum of ΔV differences. Figure E.8 shows the relative standard deviation of the four metrics featured in Table 9.2, as

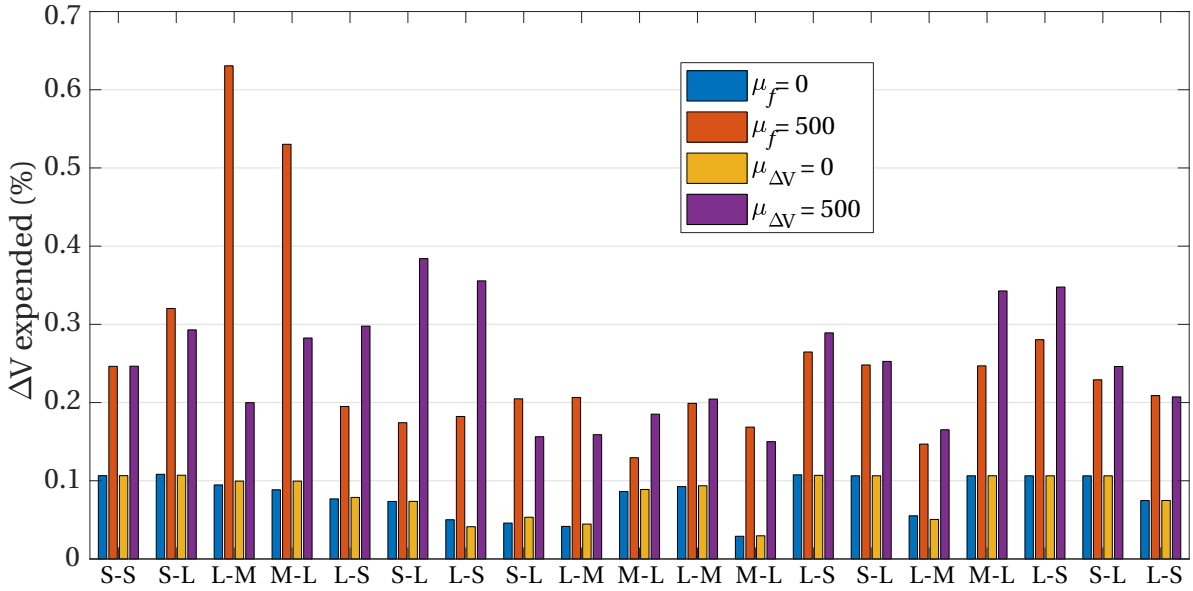

Figure E.1: Expended ΔV per maneuver for Example IRASSI Tour.

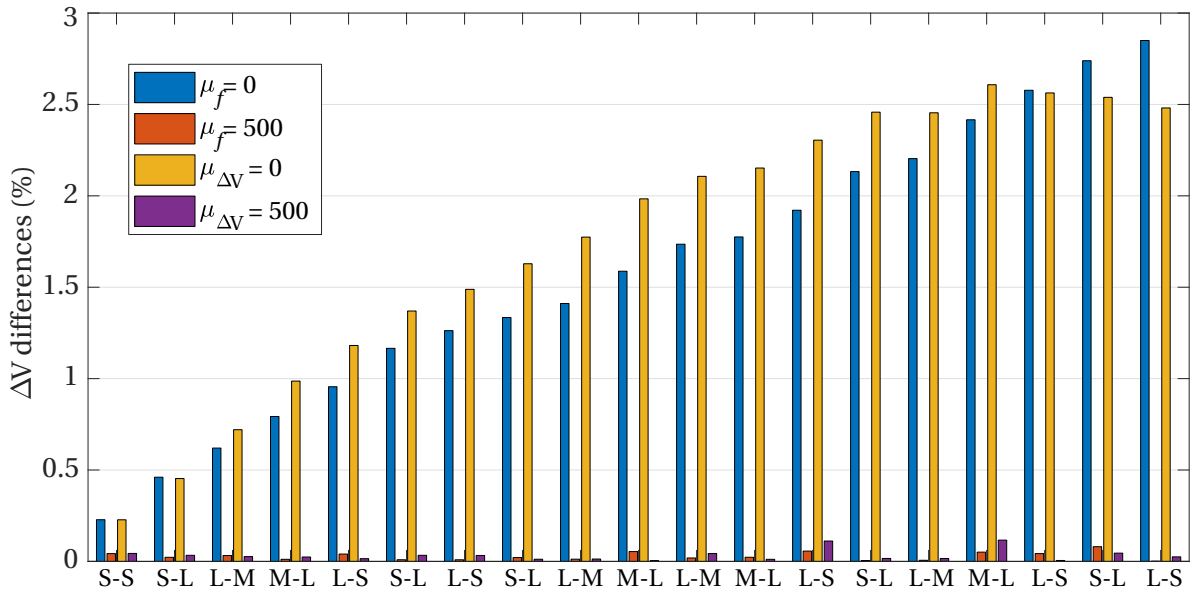

Figure E.2: ΔV differences per maneuver for Example IRASSI Tour.

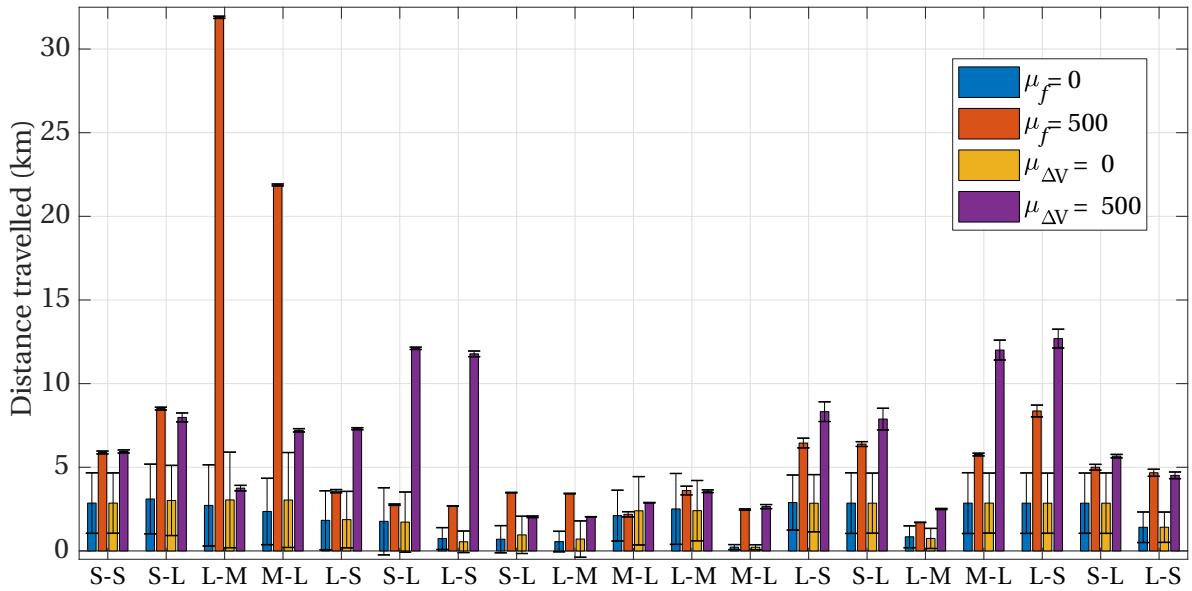

Figure E.3: Mean and standard deviation of distance traveled across fleet for Example IRASSI Tour.

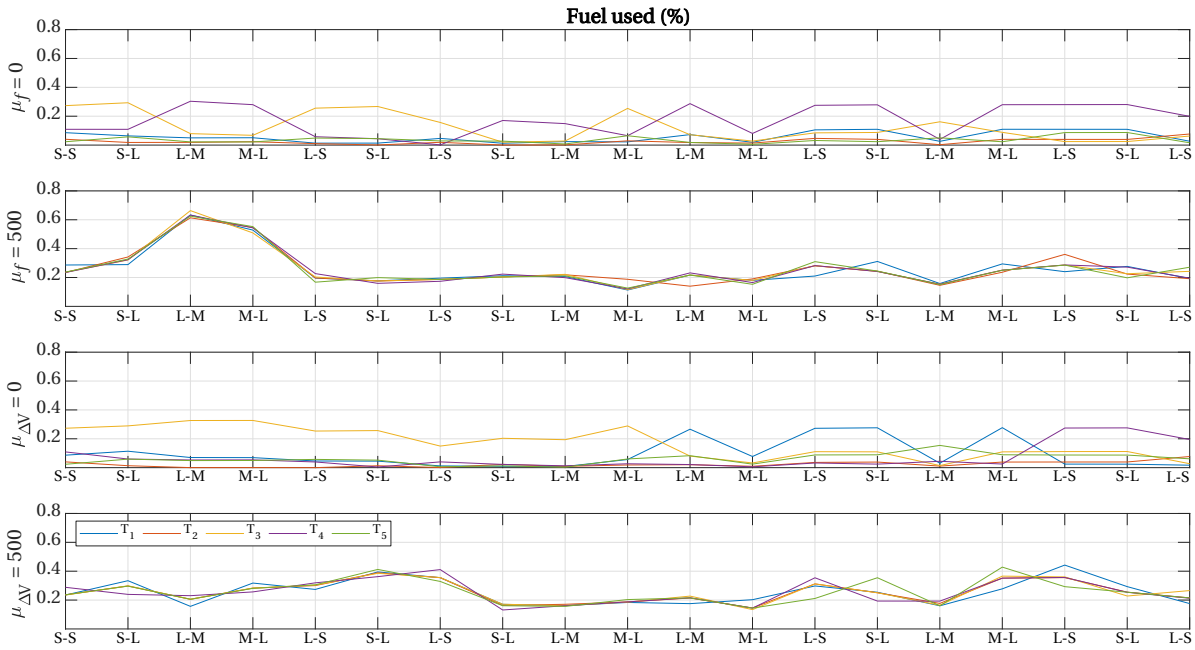

Figure E.4: Fuel used per telescope for Example IRASSI Tour, using two cost functions, the fuel-based and the ΔV-based, each with two different parameter values. The simulation parameters are $\mu_f = 0$, $\mu_f = 500$, $\mu_{\Delta V} = 0$ and $\mu_{\Delta V} = 500$.

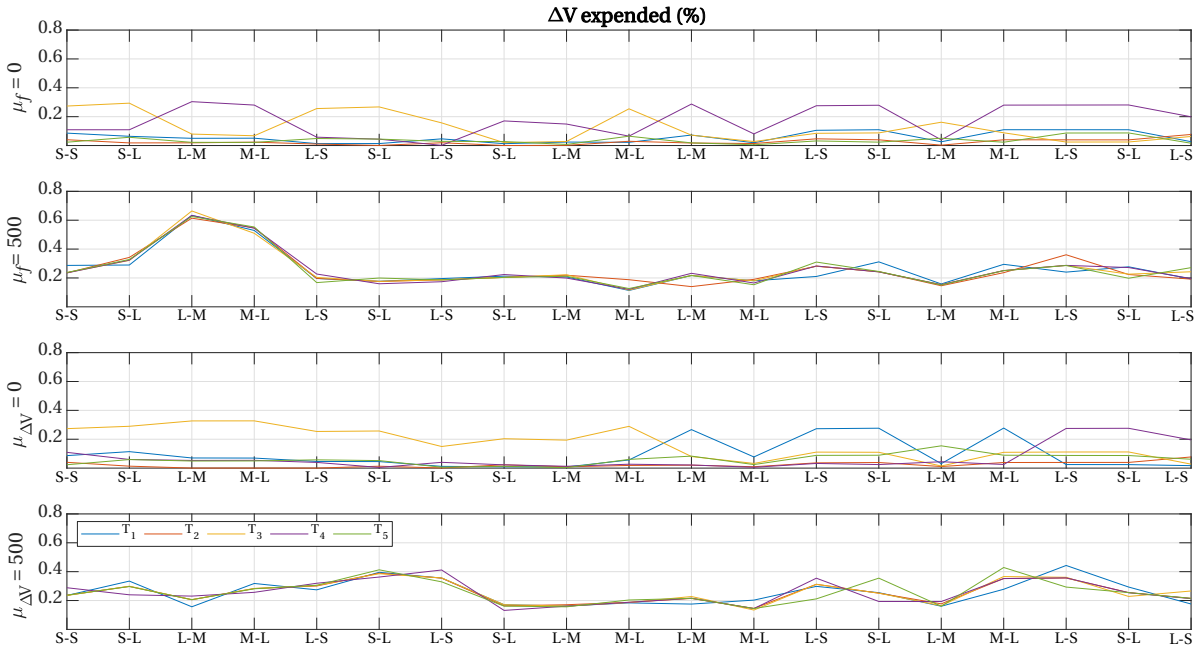

Figure E.5: ΔV per telescope for Example IRASSI Tour, using two cost functions, the fuel-based and the ΔV-based, each with two different parameter values. The simulation parameters are $\mu_f = 0$, $\mu_f = 500$, $\mu_{\Delta V} = 0$ and $\mu_{\Delta V} = 500$.

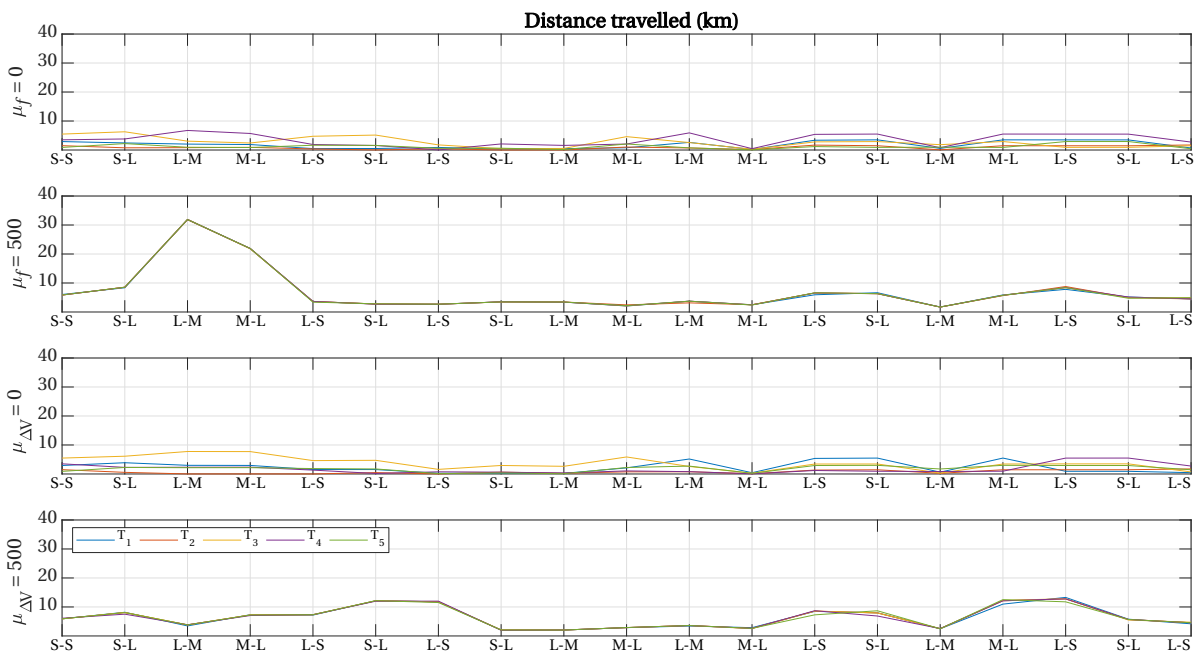

Figure E.6: Distance traveled per telescope for Example IRASSI Tour, using two cost functions, the fuel-based and the ΔV-based, each with two different parameter values. The simulation parameters are $\mu_f = 0$, $\mu_f = 500$, $\mu_{\Delta V} = 0$ and $\mu_{\Delta V} = 500$.

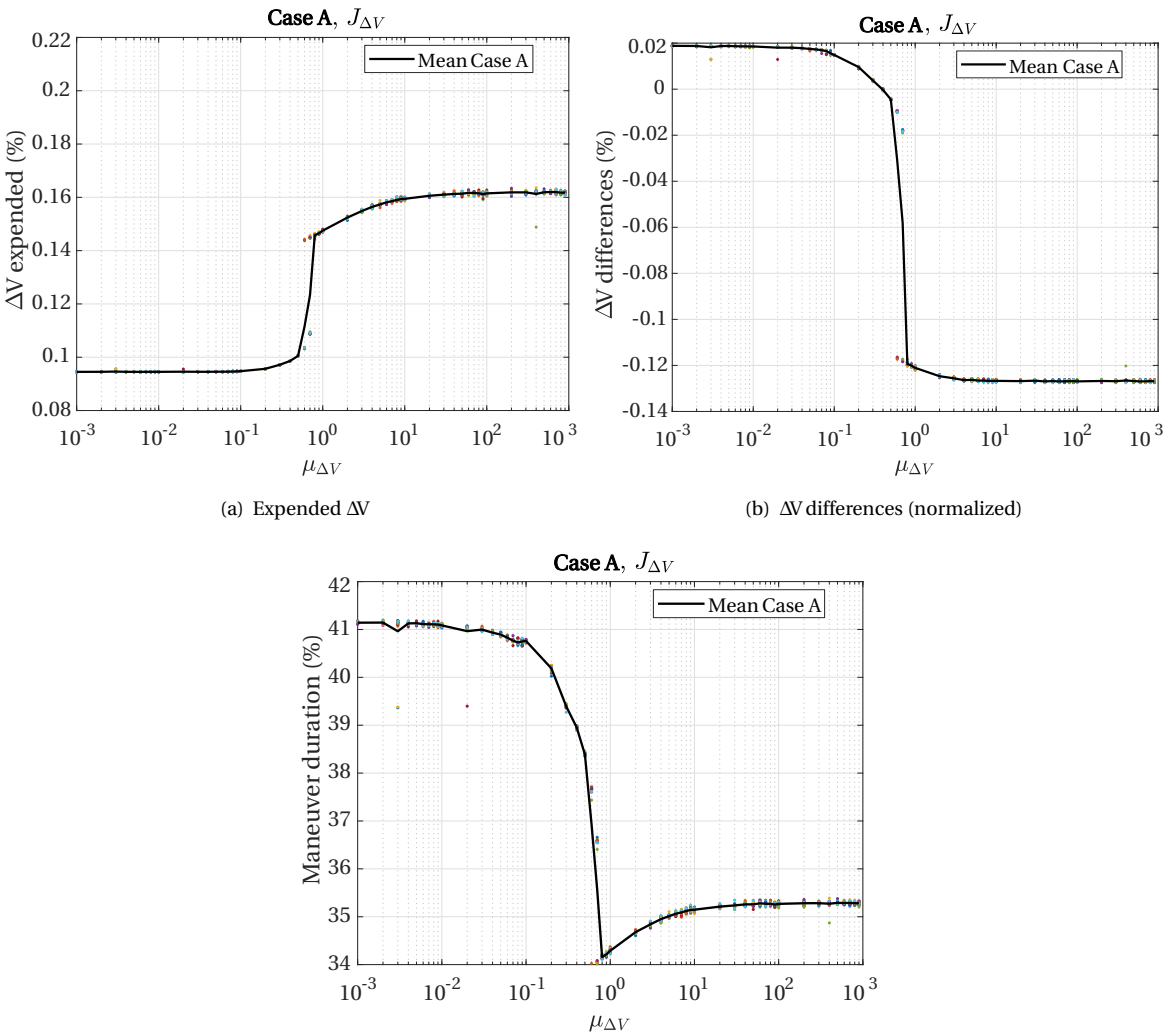

(a) Expended ΔV

(b) ΔV differences (normalized)

(c) Maneuver duration

Figure E.7: ΔV metrics and maneuver duration for Case A and $J_{\Delta V}$.

calculated by:

$$\sigma_r = \frac{\sqrt{\frac{1}{r-1}\sum_{i=1}^{r}(x_i - \bar{x})^2}}{\bar{x}} \tag{E.1}$$

where $\bar{x}$ is the mean of a metric considering the 20 repetitions of the single maneuver described in Chapter 9, x_i is the point value of the metric and r is the repetition number. The spread, or variability is analyzed in SI units (kg for fuel-related metrics and $\mathrm{m\,s^{-1}}$for ΔV-based ones).

A number of straightforward observations can be made from Figure E.8: the first one is that there is a relationship between the spread of the metrics and the value of the μ_f and $\mu_{\Delta V}$ parameters, whereby the spread starts to increase as the effective envelope values of each parameter are reached (at approximately $\mu_f = \mu_{\Delta V} > 0.1$), thereafter decreasing again and remaining approximately constant for $\mu_{\Delta V} > 0.8$ the ΔV-based function and $\mu_f > 10$ the fuel-based function. The second one is that the variability of the J_f function is generally higher than the $J_{\Delta V}$ one for all $\mu_f = \mu_{\Delta V} > 0.2$, (with the exception of the 0.6 to 0.7 range of the $\mu_{\Delta V}$ weighting parameter for the first two plots, fuel used and ΔV expended), whereas the spread is marginally higher for $J_{\Delta V}$ for $\mu_f = \mu_{\Delta V} \leq 0.2$. The third one is that two pronounced peaks for each cost function, respectively for $\mu_f = 0.8$ and $\mu_{\Delta V} \approx 0.4$ to 0.7 are observed for the bottom plot, the ΔV differences. This is because the average value $\bar{x}$ is very close to zero for these μ_f and $\mu_{\Delta V}$ values.

Overall, and for the effective envelopes of each cost function ($0.1 \leq \mu_f \leq 10$ and $0.1 \leq \mu_f \leq 5$), the variabil-

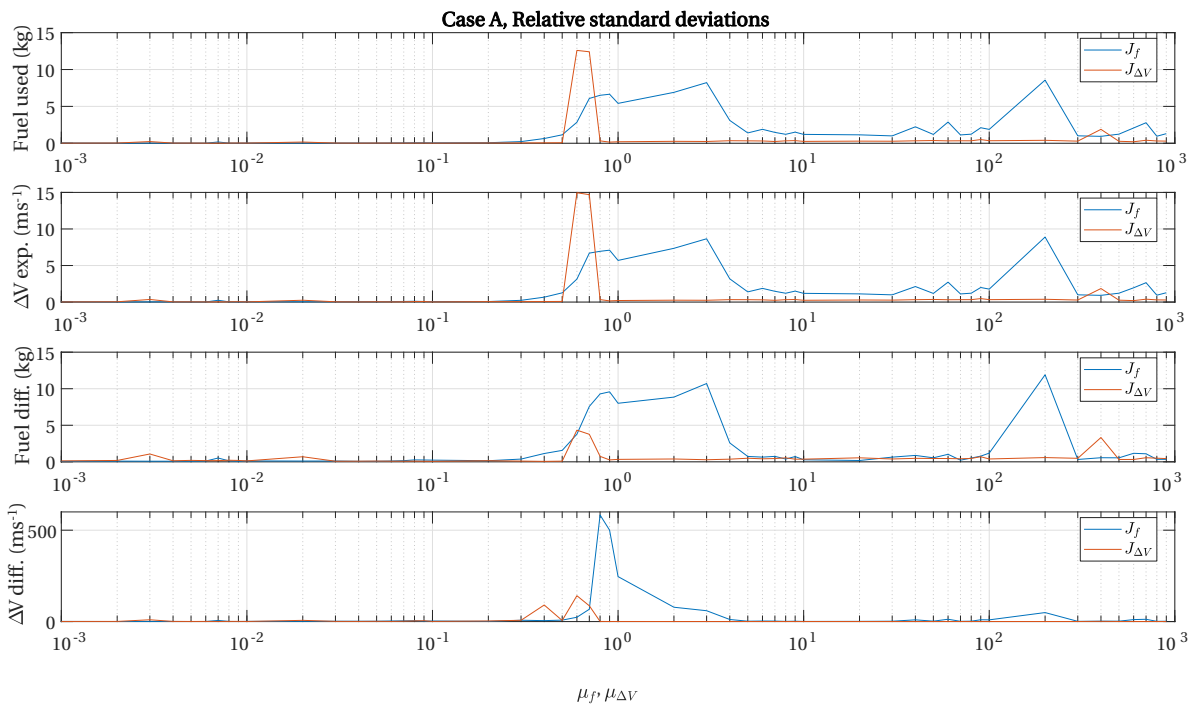

Figure E.8: Relative standard deviation of metrics for the two cost functions, J_f and $J_{\Delta V}$.

ity of the J_f function can exceed that of the $J_{\Delta V}$ one by one order of magnitude. The variability is also less constant for J_f. This is attributed to the fact that due to the nature of the fuel-based cost function, the solution space is larger (for instance, the algorithm may command systematically heavier spacecraft to spend more fuel than lighter spacecraft to achieve fuel-balancing) and this effect becomes evident with the stochasticity of the mesh-adaptive pattern search algorithm. The $J_{\Delta V}$ cost function, on the other hand, has a smaller solution space for equaling resources regardless of wet mass and is more consistent across different simulation conditions. The consequence of this is primarily that it makes the ΔV-based optimization more predictable in uncertain scenarios for heterogeneous formations.

ΔVMETRICS AS A FUNCTION OF F_i AND I_{sp}

The trends observed with the nominal engine parameters (F_i = 20 mN and I_{sp} = 2500 s) are applicable to other values of thrust magnitude and specific impulse, as demonstrated in Figures E.9 and E.9. At higher $\mu_{\Delta V}$ values, the variation of the expended ΔV seems nonetheless to be higher.

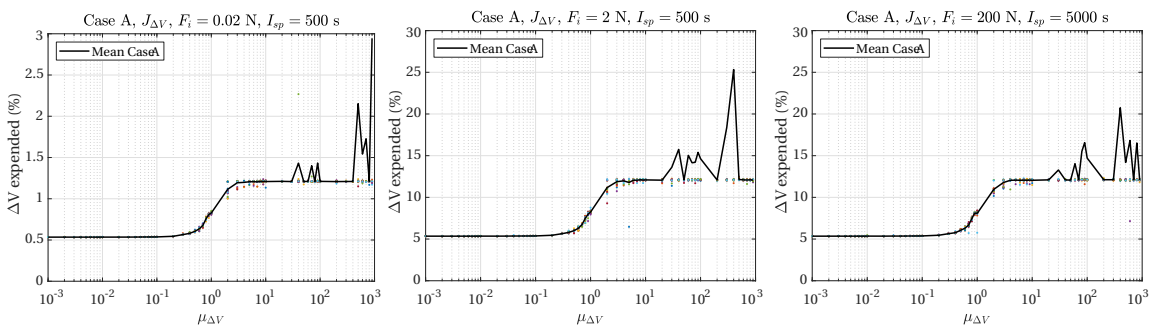

(a) F_i = 20 mN, I_{sp} = 500 s (b) F_i = 2 N, I_{sp} = 500 s (c) F_i = 200 N, I_{sp} = 5000 s

Figure E.9: Expended ΔVfor varying values of thrust magnitude F_i and specific impulse I_{sp}.

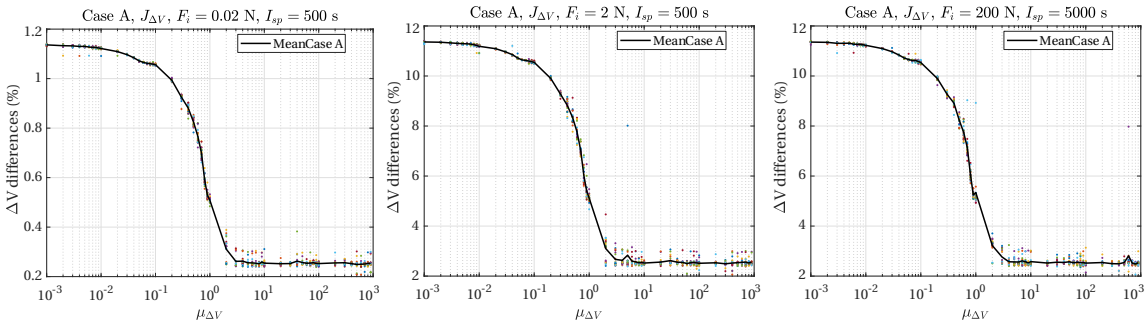

(a) $F_i = 20$ mN, $I_{sp} = 500$ s (b) $F_i = 2$ N, $I_{sp} = 500$ s (c) $F_i = 200$ N, $I_{sp} = 5000$ s

Figure E.10: ΔV differences (normalized) for varying values of thrust magnitude F_i and specific impulse I_{sp}.

E.2.2. CASE B

The ΔV-associated results of Section 9.4.3 for Case B are shown in Figures E.11(a) and E.11(b). Figure E.11(c) shows the maneuver duration for the $J_{\Delta V}$ cost function.

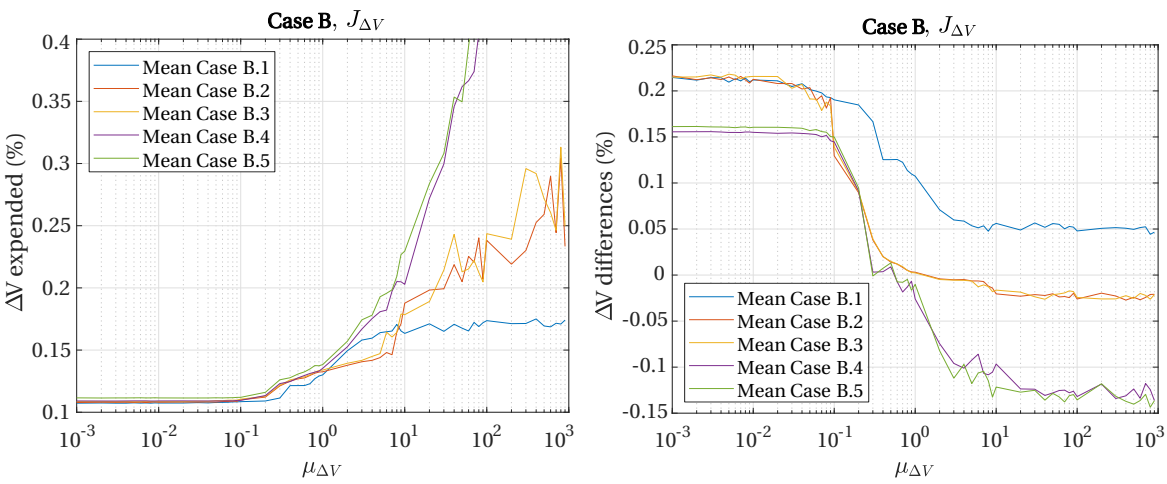

(a) Expended ΔV (b) ΔV differences (normalized)

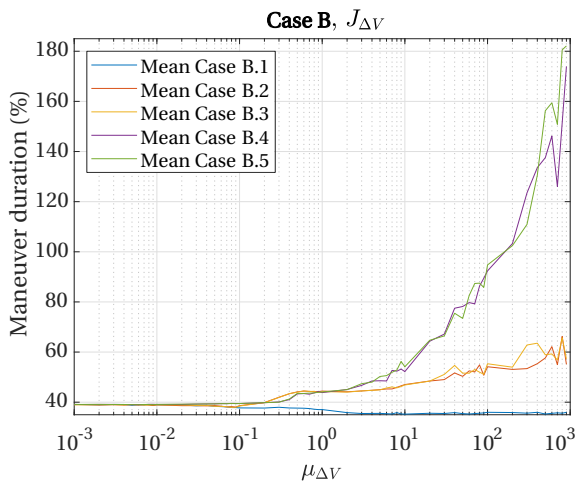

(c) Maneuver duration

Figure E.11: ΔV metrics and maneuver duration for Case B and $J_{\Delta V}$

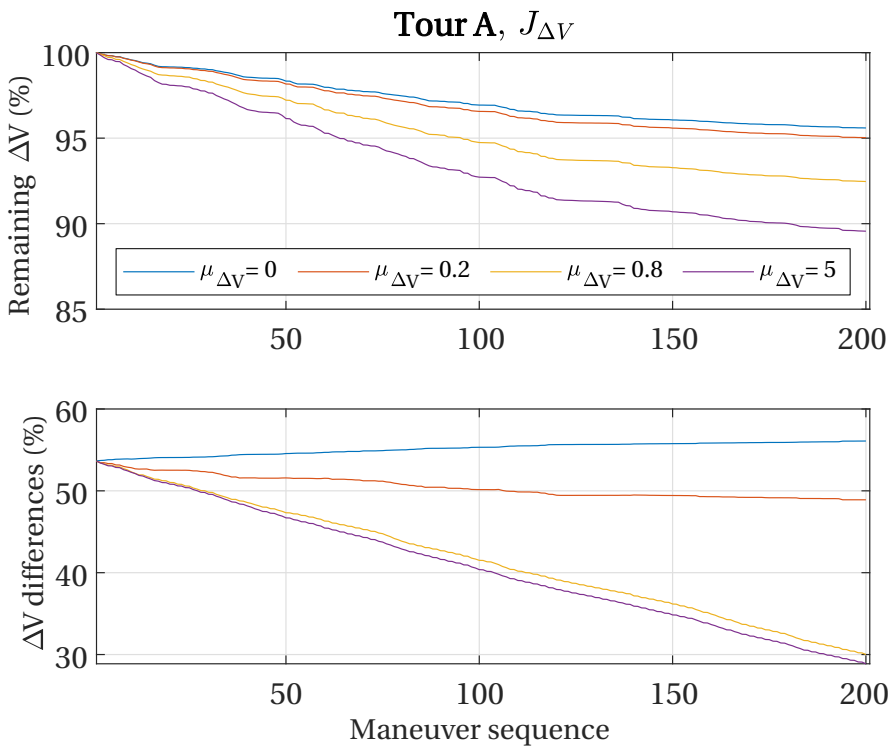

Figure E.12: IRASSI Tour A with varying $\mu_{\Delta V}$ parameter: total ΔV remaining (top) and ΔV differences (bottom).

E.3. IRASSI TOUR ANALYSIS

The ΔV-associated results of Section 9.4.4 for Tour A are shown in Figures E.12.

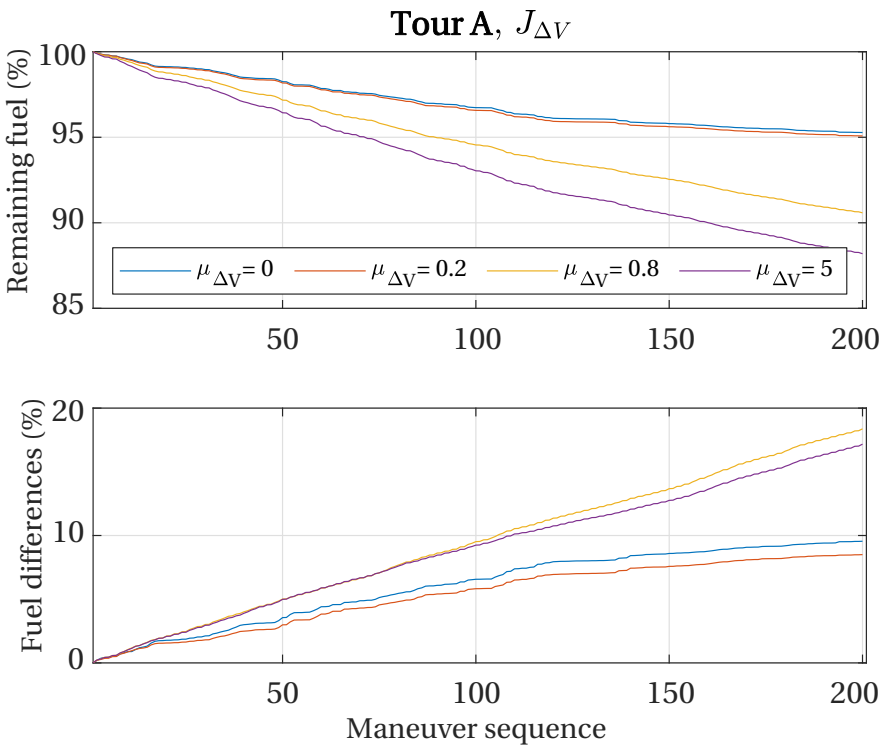

Figure E.13: IRASSI Tour A with varying $\mu_{\Delta V}$ parameter: total fuel remaining (top) and fuel differences (bottom).

F

Complementary Analysis of CAM

This appendix presents the number of collisions and instances of invisibility detected in the ReM maneuvers.

F.1. Collision and Invisibility Events for ReM Effective Envelopes

Safety violations within the single-maneuvers of the ReM, presented in section 9.4.3, are firstly presented. The simulation parameters are recalled below, each applying to Cases A and B:

- Two cost functions (J_f and $J_{\Delta V}$)
- 54 different μ_f and $\mu_{\Delta V}$ parameter values ($10^{-3} \leq \mu_f, \mu_{\Delta V} < 10^{-3}$)
- 1 maneuver
- 20 repetitions

These give a total of 1080 different simulations for each cost function and for each case. Table F.1 summarizes the total number of occurrences for each constraint. For each tour and cost function, the values reflect overall means, that is, across all repetitions and across all μ_f and $\mu_{\Delta V}$ parameter values. The 'Total' columns show the ratio between the number of maneuvers with detected collision or invisibility violation and the number of tour maneuvers. The 'Pairs' columns show the mean number of spacecraft pairs involved in collision or invisibility events over the tours. The last column, 'Duration', shows the ratio between the duration of invisibility and the duration of the reconfiguration maneuver.

There were no instances where both collision and invisibility were detected in a single maneuver. For Case A, one single collision-prone occurrence was detected across all conditions ($2 \times 54 \times 1 \times 20$=2160), whereas for Case B only invisibility periods materialized. On average, each invisibility instance lasted for 32 %–33 % of the reconfiguration maneuver (or between 5.4 and 5.6 hours) for both cost functions. Mean invisibility detections are generally consistent between J_f and $J_{\Delta V}$, except for B.2, where 34% more violations are detected with J_f.

For both Case A and Case B, collisions or invisibility instances only occurred between a single spacecraft pair (not necessarily the same pair, naturally). Only Case B.1 was free of both collisions and invisibility situations.

Figure F.1 shows the number of repetitions for which invisibility has been detected for both cost functions. It is interesting to note that invisible pairs are detected solely within the range $0.4 \leq \mu_f, \mu_{\Delta V} \leq 3$. The mean duration of invisibility periods for these repetitions is shown in Figure F.2, again, for both cost functions. On average, invisibility instances last between approximately 4.7 and 5.8 hours.

Table F.1: Detected collisions and invisible pairs during reconfiguration maneuver.

	Collisions				Invisibilities					
Tours	**Total (%)**		**Pairs**		**Total (%)**		**Pairs**		**Dur.[i] (%)**	
	J_f	$J_{\Delta V}$	J_f	$J_{\Delta V}$	J_f	$J_{\Delta V}$	J_f	$J_{\Delta V}$	J_f	$J_{\Delta V}$
A	0.1	0.0	1.0	0.0	0.0	0.0	0.0	0.0	0.0	0.0
B.1	0.0	0.0	0.0	0.0	0.0	0.0	0.0	0.0	0.0	0.0
B.2	0.0	0.0	0.0	0.0	4.1	5.5	1.0	1.0	32.7	32.8
B.3	0.0	0.0	0.0	0.0	6.3	5.8	1.0	1.0	32.8	32.4
B.4	0.0	0.0	0.0	0.0	5.4	5.5	1.0	1.0	33.0	33.1
B.5	0.0	0.0	0.0	0.0	5.6	5.8	1.0	1.0	32.2	32.2

[i] Duration

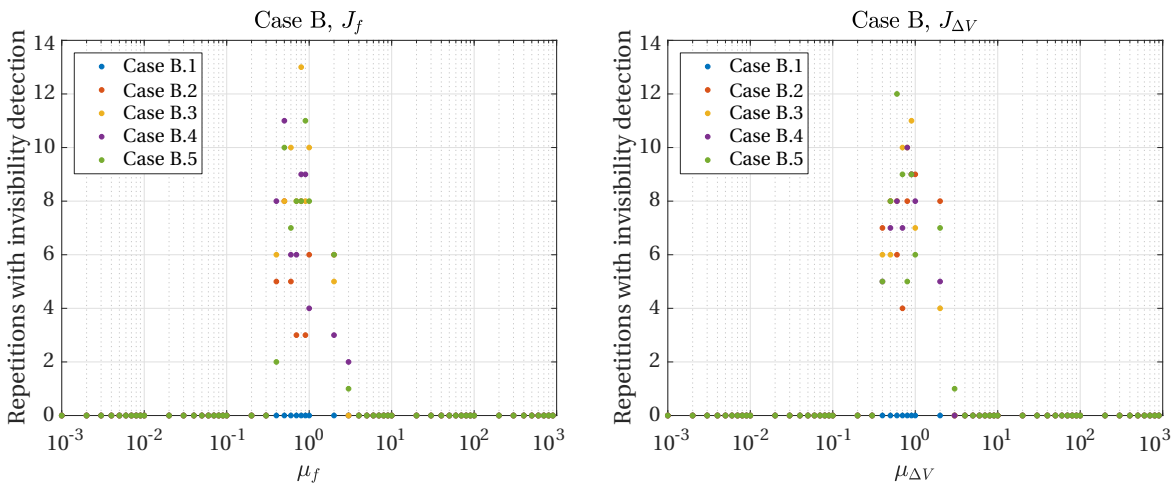

(a) J_f (b) $J_{\Delta V}$

Figure F.1: Number of repetitions with detected invisible pairs during reconfiguration maneuver.

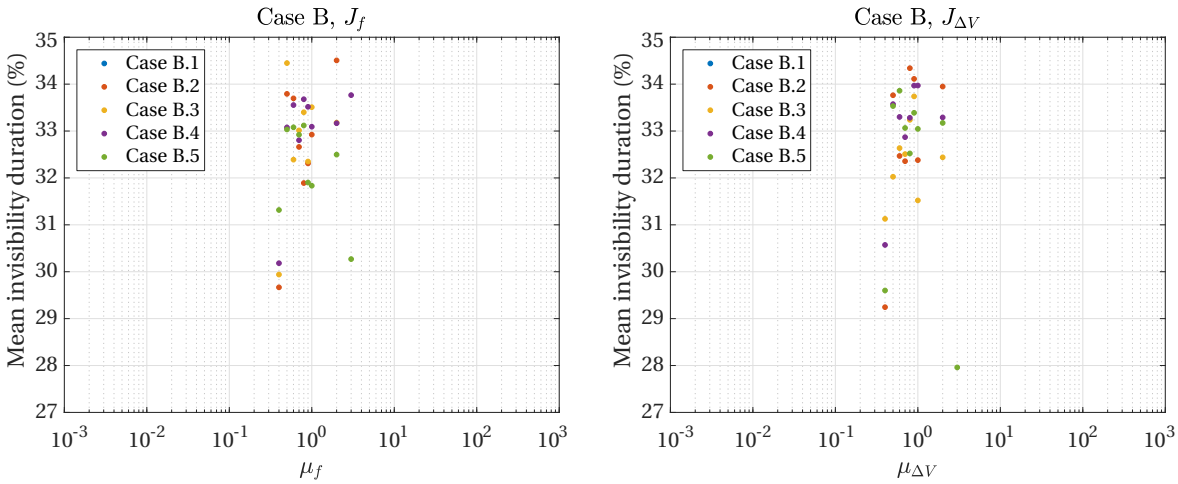

(a) J_f (b) $J_{\Delta V}$

Figure F.2: Mean duration of invisibility events over detected repetitions during reconfiguration maneuver.

F

Curriculum Vitæ

Luisa dos Santos Buinhas

01-08-1987 Born in Lisbon, Portugal.

Education

2020 PhD., Aerospace Engineering
Faculty of Aerospace Engineering, Institute of Space Technology and Space Applications
University of the German Federal Armed Forces, Neubiberg, Bayern, Germany
Thesis: Spacecraft Formation Flying Dynamics at L_2 and Operational Maneuvers Design: the Case of the IRASSI Space Interferometer
Promotor: Prof. Dr.-Ing. R. Förstner

2010–2011 Research Internship
Department of Aeronautics and Astronautics, Humans and Automation Laboratory
Massachusetts Institute of Technology, Cambridge, MA, United States of America

2009–2012 MSc., Aerospace Engineering
Faculty of Aerospace Engineering, Control & Simulation Department
Delft University of Technology, Delft, The Netherlands
Thesis: Prediction of Coherence Zones in Flight Simulation During Yaw Maneuvers - A modeling approach based on psychophysical laws
Supervisors: Prof. Dr. Ir. M. Mulder, Prof. Dr. Ir. M. van Passen, Dr. A. R. Valente Pais, Dr. B. J. Grácio

2009–2012 BSc., Aerospace Engineering
Instituto Superior Técnico, Lisbon, Portugal

Professional Experience

2020–present Space Systems Engineer & Co-founder
Vyoma GmbH, Munich/Darmstadt, Germany

2014–2020 Research Associate
Faculty of Aerospace Engineering, Institute of Space Technology and Space Applications
University of the German Federal Armed Forces, Neubiberg, Bayern, Germany

2013–2014 Junior Engineer
AEVO Technologies GmbH, Munich, Germany

2011–2012 Communications Assistant
Faculty of Aerospace Engineering, Control & Simulation Department
Delft University of Technology, Delft, The Netherlands

2010–2012 Academic Coach
Delft University of Technology, Delft, The Netherlands

VOLUNTEERING

2021–present	Member of the Space Traffic Management technical committee of the International Astronautical Federation
2020–2021	Mentor for TU Delft AE Mentor Alumni Program
2019–present	Space Generation Advisory Council Volunteer
2018–present	Pint of Science Germany Co-organizer
2013	Educational Teacher in Southeast Asia

ACHIEVEMENTS

2016	Amelia Earhart Fellowship
2012	Best Student Paper at the 56th Annual Meeting of the Human Factors and Ergonomics Society, October 2012
2010	Prof. Dr. Ir. H. J. Van der Maas scholarship for research internship at MIT
2010	TU Delft Executive Board Fund scholarship for research internship at MIT

LIST OF PUBLICATIONS

17. **L. Buinhas** and R. Förstner, *Formation Reconfiguration Optimization for the IRASSI Space Interferometer*, Advances in Space Research, **67(11)**, 3819-3839 (2021).

16. **L. Buinhas**, H. Linz, M. Philips-Blum and R. Förstner, *iSCOUT: Formation Reconfiguration and Science Planning Architecture for the IRASSI Space Interferometer*, Advances in Space Research, **67(11)**, 3840-3867 (2021).

15. J. Teuber, R. Weller, **L. Buinhas**, D. Kühn, P. Dittmann, A. Srinivas, F. Kirchner, R. Förstner, O. Funke and G. Zachmann, *Virtual Validation and Verification of the VaMEx Initative*, Proceedings of the 70th International Astronautical Congress (2019).

14. H. Linz, D. Bhatia, **L. Buinhas**, L. Lezius, E. Ferrer, R. Förstner, K. Frankl, M. Philips-Blum, M. Steen, U. Bestmann, W. Hänsel, R. Holzwarth, O. Krause and T. Pany, *InfraRed Astronomy Satellite Swarm Interferometry (IRASSI): Overview and study results*, Advances in Space Research, **65(2)**, 831-849 (2020).

13. **L. Buinhas**, G. Peytaví and R. Förstner, *Navigation and Communication Network for the Valles Marineris Explorer (VaMEx)*, Acta Astronautica, **160**, 280-296 (2019).

12. H. Linz, **L. Buinhas**, R. Förstner, L. Lezius, D. Bhatia, S. Batzdorfer, K. Beha, U. Bestmann, B. Eissfeller, M. Eren, E. Ferrer, K. Frankl, O. Krause, Y. Moon, M. Philips-Blum, S. Scheithauer, M. Steen, *The far-infrared space interferometer study IRASSI: motivation, principle design and technical aspects*, In Space Telescopes and Instrumentation 2018: Optical, Infrared, and Millimeter Wave, **10698**, p. 52. International Society for Optics and Photonics, (2018).

11. **L. Buinhas**, D. Grosse, S. Santra, A. Probst, G. Johnson, J. Murdza, R. Imam, S. Wittig and N. Shearer, *Key Challenges in Establishing Laser Space Communication Standards and Recommendations of the SGC Space Technologies Working Group*, Proceedings of the 69th International Astronautical Congress (2018).

10. **L. Buinhas**, A. Probst and R. Förstner, *Coverage Analysis for Positioning in the Asteroid Main Belt Using a Space Navigation Infrastructure*, Proceedings of the 2018 AAS/AIAA Astrodynamics Specialist Conference (2018).

9. M. Philips-Blum, T. Pany, H. Gomez, K. Frankl, **L. Buinhas**, and B. Eissfeller, *Advancements of the Relative Positioning in Space Within IRASSI Mission Concept*, Proceedings of the 2018 AAS/AIAA Astrodynamics Specialist Conference (2018).

8. **L. Buinhas**, M. Philips-Blum, K. Frankl, T. Pany, B. Eissfeller and R. Förstner, *Formation Operations and Navigation Concept Overview for the IRASSI Space Interferometer*, Proceedings of the 2018 IEEE Aerospace Conference (2018).

7. **L. Buinhas**, K. Frankl, H. Linz and R. Förstner, *IRASSI InfraRed Space Interferometer: Formation Geometry and Relative Dynamics Analysis*, Acta Astronautica **153**, 394-409 (2018).

6. N. Lemke, O. Funke, R. Ernst, B. Eissfeller, R. Föstner, F. te Hennepe and **L. Buinhas**, *Verification Mission of a Satellite Telescope Swarm (ESTS): One Candidate for the Next Large German Mission*, Proceedings of the 68th International Astronautical Congress (2017).

5. **L. Buinhas**, E. Ferrer-Gil and R. Förstner, *IRASSI InfraRed Space Interferometer: Mission Analysis, Spacecraft Design and Formation Flying Overview*, Proceedings of the 68th International Astronautical Congress (2017).

4. E. Ferrer-Gil, **L. Buinhas** and R. Förstner, *System Design and Thermal Stability Analysis for the IRASSI Infrared Space Interferometer*, Proceedings of the 2016 AIAA Space Conference (2016).

3. **L. Buinhas**, E. Ferrer-Gil and R. Förstner, *IRASSI InfraRed Astronomy Satellite Swarm Interferometry: Mission Concept and Description*, Proceedings of the 2016 IEEE Aerospace Conference (2016).

2. **L. Buinhas**, B. J. Grácio, A. R. Pais, M. van Paassen, M. Mulder, *Modeling Coherence Zones in Flight Simulation During Yaw Motion*, Proceedings of the AIAA Modeling and Simulation Technologies (MST) Conference, p. 5223 (2013).

1. A. Stimpson, **L. Buinhas**, B. Scott, Y. Boussemart and M. Cummings, *A Model-Based Measure to Assess Operator Adherence to Procedure*, Proceedings of the Human Factors and Ergonomics Society Annual Meeting, **56**, no. 1, 2452-2456 (2012).